



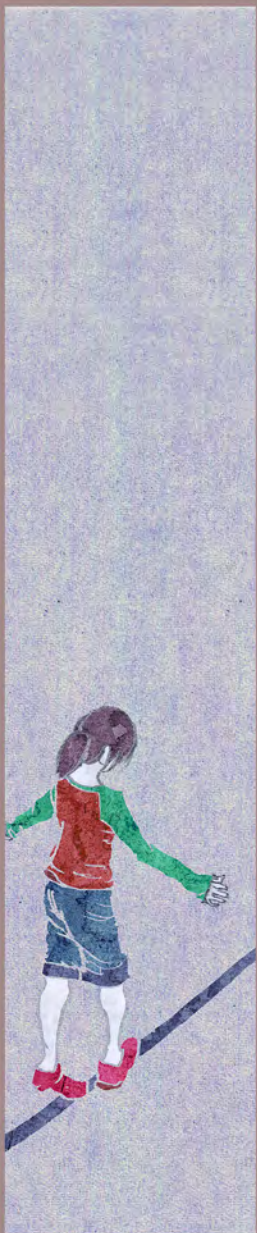
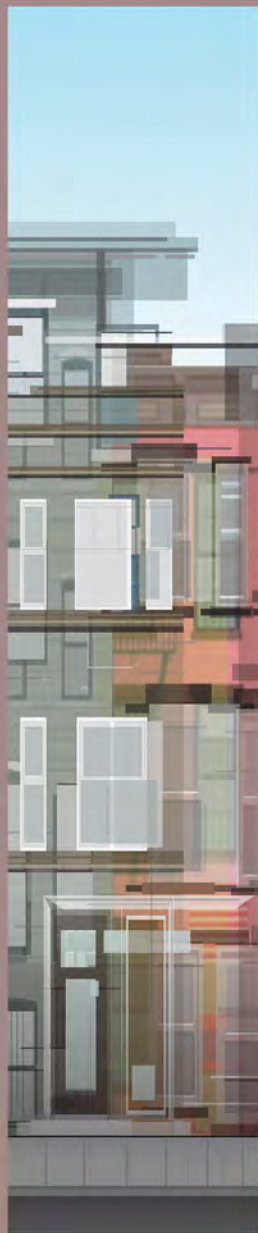
# THE BENCHMARK IN ANTIBODIES

Since the day it was founded, Proteintech has been making all of its products to the highest standards possible while taking complete responsibility for the quality of each product.

- **Proteintech makes every single antibody in its 12,000-strong catalog.**
- **Each Proteintech product is unique and cannot be bought under a different label.**
- **Antibodies tested in siRNA knockdown experiment to demonstrate specificity.**
- **It works in any species and any application or get a full money-back refund.**

# Neuron

Best of 2015–2016



Seahorse Bioscience is  
now Agilent Technologies

# A MAJOR LEAP FORWARD IN PHENOTYPING

Determine the functional impact of genes, proteins  
or compounds on metabolism in an hour



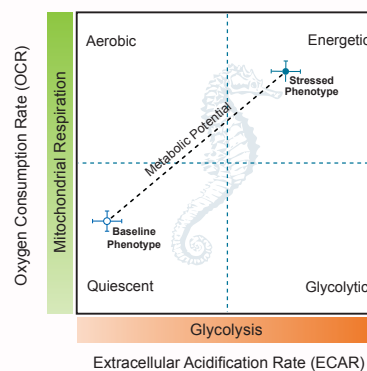
## Agilent Seahorse XFp Cell Energy Phenotype Test Kit

Using as few as 15,000 live cells and an Agilent Seahorse XFp Analyzer, the Seahorse XFp Cell Energy Phenotype Test Kit identifies your cells' metabolic phenotype as well as their metabolic potential — the utilization of mitochondrial respiration and glycolysis.

**LEARN MORE** at [www.agilent.com](http://www.agilent.com)



For Research Use Only. Not for use in diagnostic procedures.





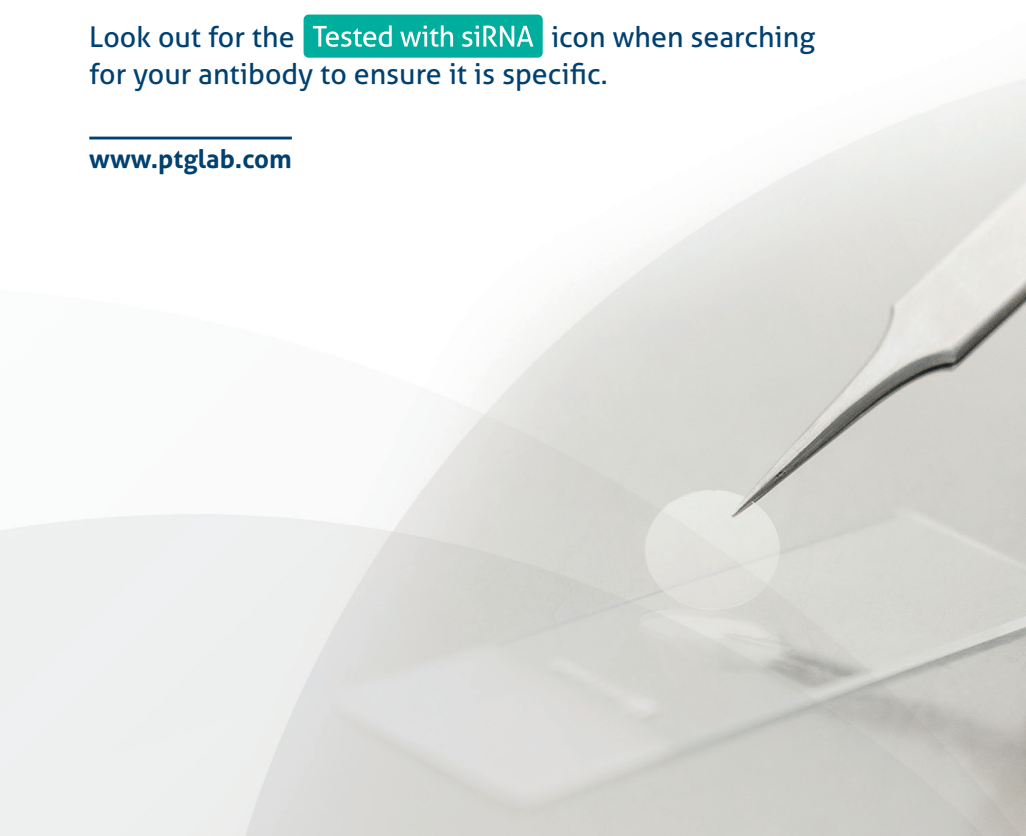
# THE BENCHMARK IN ANTIBODIES

Antibodies validated with siRNA  
knockdown to demonstrate specificity.

Look out for the **Tested with siRNA** icon when searching  
for your antibody to ensure it is specific.

---

[www.ptglab.com](http://www.ptglab.com)





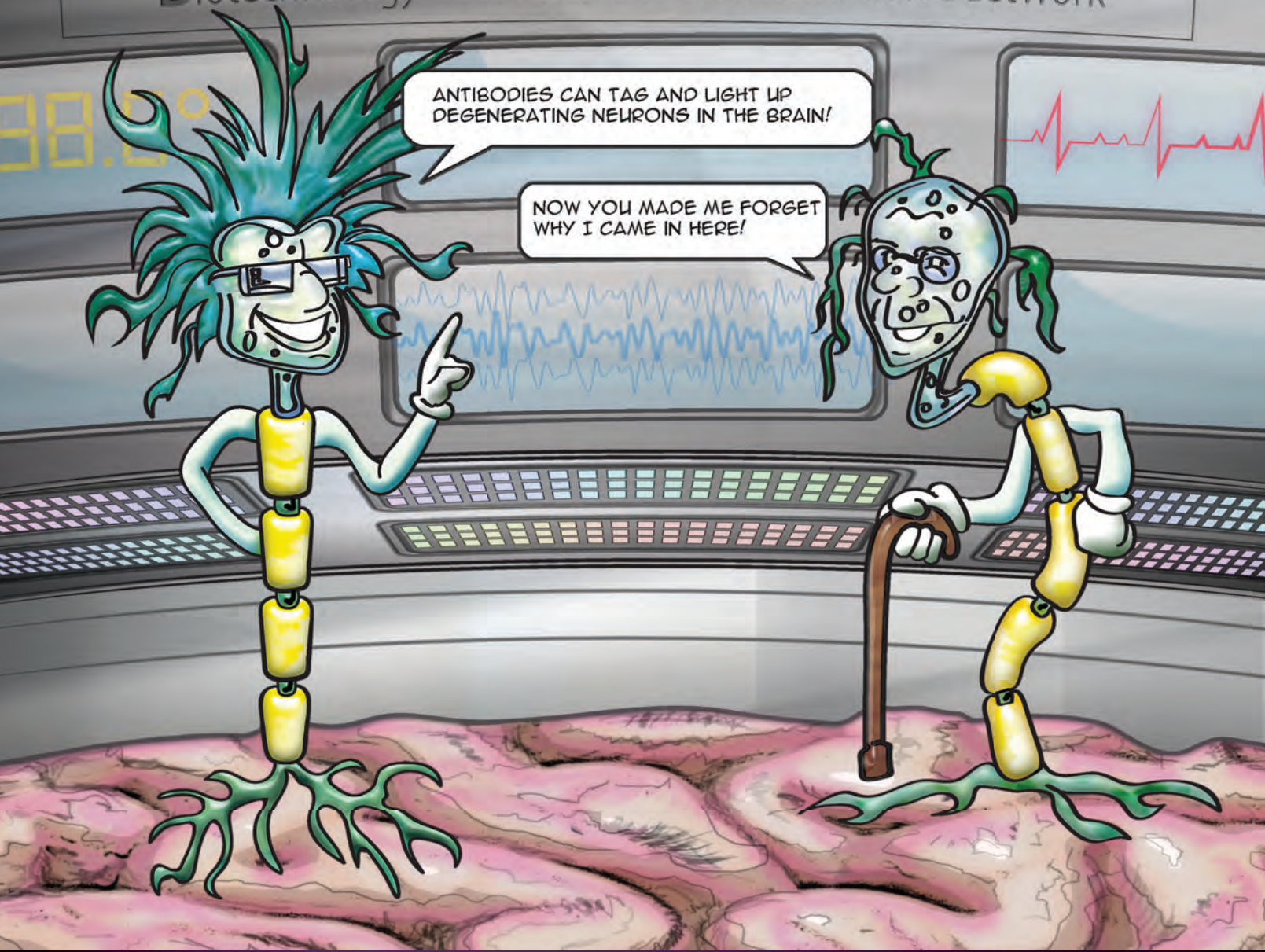
# THE BENCHMARK IN ANTIBODIES

Antibodies against 12,000 targets  
available to buy online.

---

[www.ptglab.com](http://www.ptglab.com)



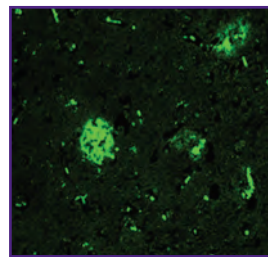


## Remember BioLegend as your Neuroscience Antibodies source

With the recent acquisition of the Covance legacy antibodies, BioLegend has expanded its portfolio to offer high quality and specificity antibodies for neuroscience research. We offer a great selection of human- and rodent-specific antibodies provided in multiple formats for use in research applications such as IHC, IF, WB, and more. BioLegend supports research within multiple neuroscience areas with a great focus on the field of neurodegeneration.

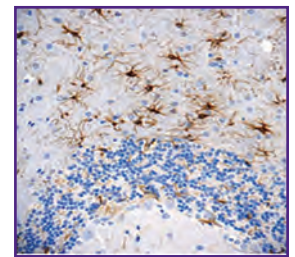
Learn more at: [biolegend.com/neuro/neuron](http://biolegend.com/neuro/neuron)

$\beta$ -Amyloid , 1-16



IHC staining of amyloid beta plaques with anti- $\beta$ -Amyloid antibody (clone 6E10) conjugated to Alexa Fluor® 488 on FFPE human AD brain.

GFAP



IHC staining of anti-GFAP antibody (clone MCA-5C10) on FFPE rat brain tissue. Nuclei were counterstained with Hoechst and are shown in blue.

BioLegend is ISO 9001:2008 and ISO 13485:2003 Certified

Toll-Free Tel: (US & Canada): 1.877.BIOLEGEND (246.5343)

Tel: 858.768.5800

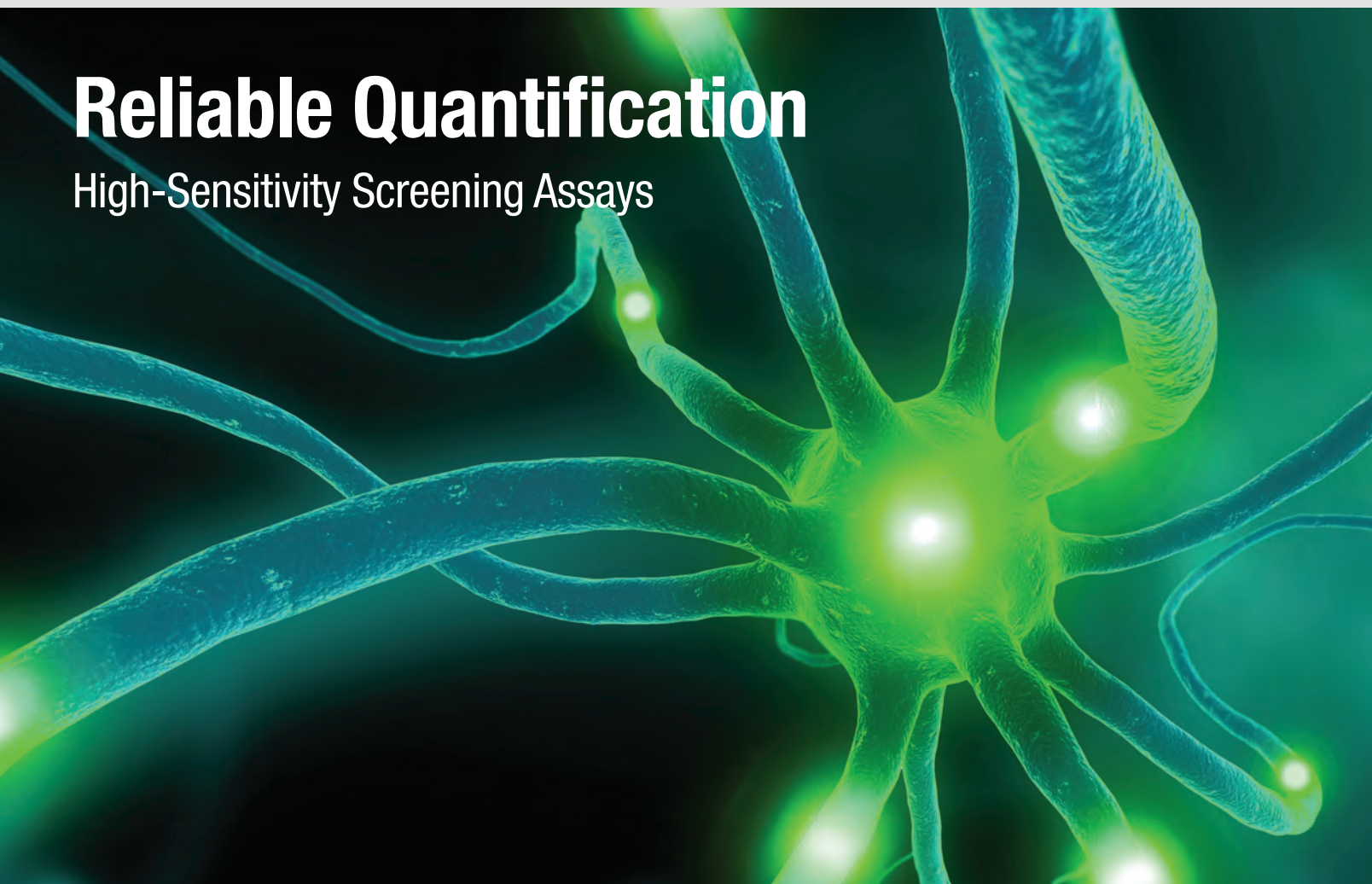
[biolegend.com](http://biolegend.com)

08-0060-10



# Reliable Quantification

## High-Sensitivity Screening Assays

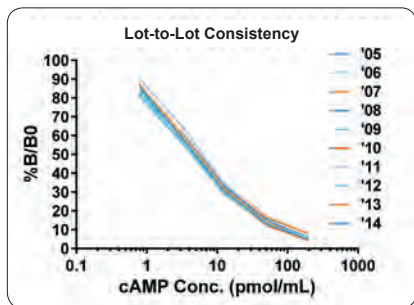


### Rapidly and Reliably Quantify Second Messengers with High-Sensitivity Assays

As our understanding of neurodegenerative disease origins increases, so does the need for innovative, high-quality screening assays for identifying potential therapeutics. Enzo's expertise in assay development and labeling and detection provide a unique collection of innovative research tools to monitor neural signaling networks.

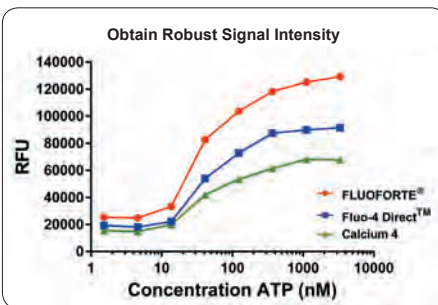
#### cAMP/cGMP ELISA Kits

Most sensitive and reliable ELISA kits for detection of cAMP/cGMP



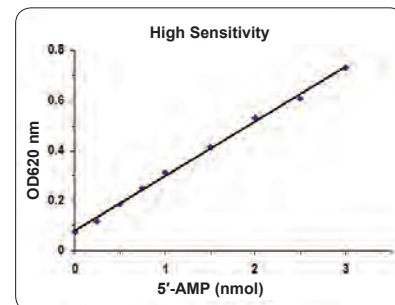
#### FLUOFORTE® Calcium Assays

Brighter, more robust fluorescent calcium mobilization assays



#### Cyclic Nucleotide Phosphodiesterase Assay

Unique colorimetric assay used to screen inhibitors and modulators of cyclic nucleotide PDE activity



# Consistency

# Is



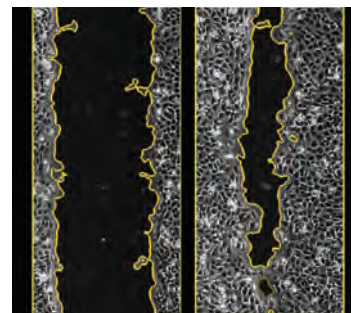
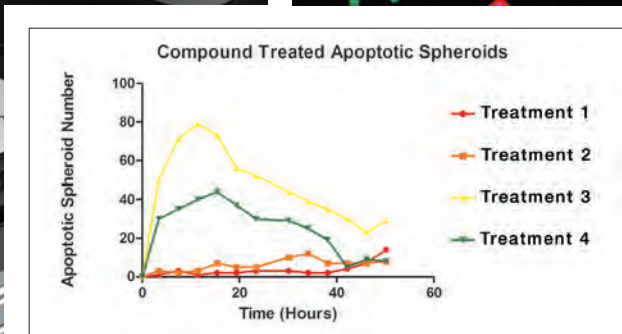
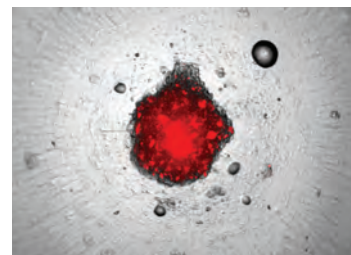
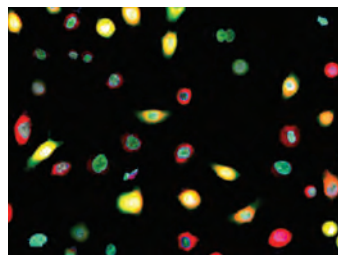
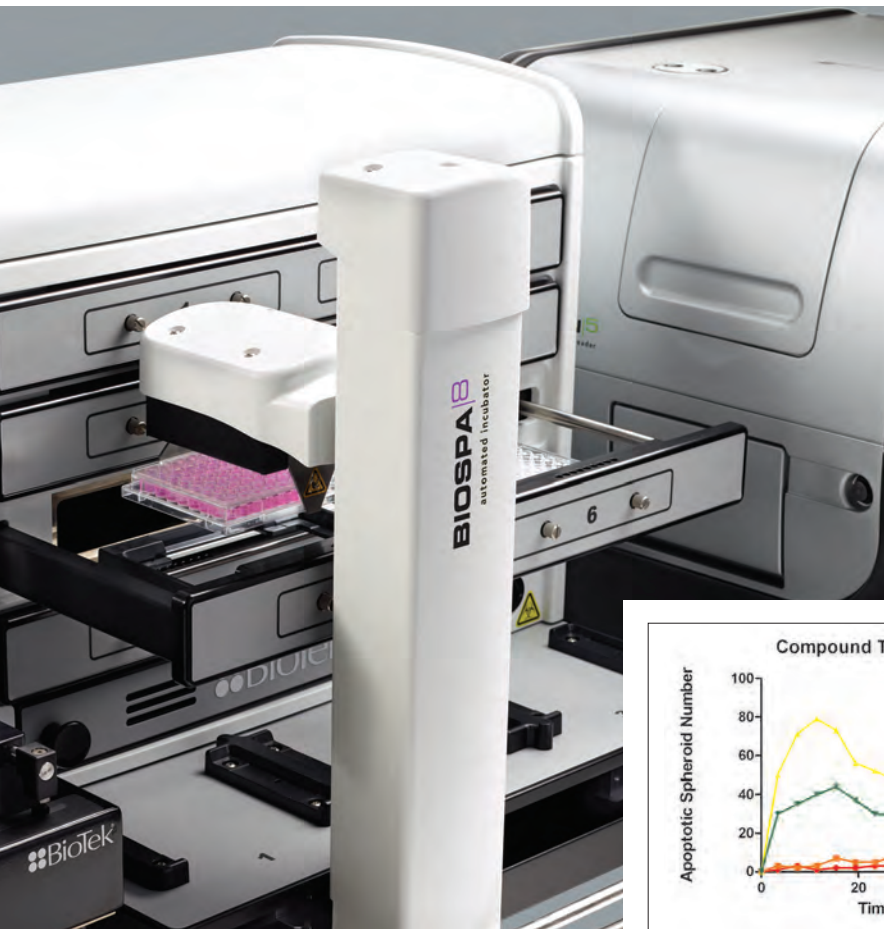
## N21-MAX and N-2 Neural Media Supplements from R&D Systems

Each lot of serum-free media is checked for performance consistency by our in-house quality team.



**LEARN MORE**  
[rndsystems.com/  
neuralmedia](https://rndsystems.com/neuralmedia)

# BIOSPA SYSTEM FOR LIVE CELL IMAGING



## More Than an IncuCyte®

	BioSpa™ System	IncuCyte® Zoom
Live cell imaging	✓	✓
Temperature, humidity, gas control	Integrated, monitored	Incubator required
Labware capacity	8	6
Objective capacity	6	1
Magnification range	1.25x to 60x	4x to 20x
Fluorescence colors available	>15	2
Z-stacking for 3D biology	✓	
Laser autofocus	✓	
Advanced cell-level analysis	✓	
Washing, media replacement	✓	
Reagent dispensing	✓	

\*BioSpa system includes BioSpa 8 and Cytation 5

Think Possible



Learn more. Visit [www.biotek.com/biospasystem](http://www.biotek.com/biospasystem)

IncuCyte® ZOOM is a registered trademark of Essen BioScience

[www.biotek.com](http://www.biotek.com)

THE FUTURE

AT YOUR

FINGERTIPS

Innovative Design Feature  
ICONIC gas mixing technology

Innovative Design Feature  
Removable Pop-Off™ front cover for easy set-up and cleaning

Quick and easy access with Ezee Sleeve™ Gloveless Access ports

Fast interlock purge cycle time



Dual chambers available for multiple atmospheres

Intuitive user controls and clean display

The InvivoO<sub>2</sub> workstation was designed and built to mimic the physiology of your subject matter, giving you the reassurance of precise results under controlled conditions. It allows you to study the most complex of cell interactions under precise physiological conditions, regulating and maintaining oxygen, carbon dioxide, temperature and humidity. Whether you're hoping to replicate the environment of blood vessels or lung tissue, the InvivoO<sub>2</sub> is the best tool for the job.

Get in touch today to hear how we can work with you. | U.S.: (800) 992-2537 | [www.bakerruskinn.com](http://www.bakerruskinn.com)

# Knock Out Any Gene!



## CRISPR/CAS 9 Genome Editing Kits

OriGene's system for genome disruption and gene replacement delivers pre-designed plasmids and all the vectors needed to knock out any human or mouse gene. Knockout is as simple as 1-2-3:

- 1 Search the gene symbol on [origene.com](http://origene.com) and order
- 2 Follow the simple protocol for transfection and Puro selection
- 3 Validate the knockout

### Kit Components Include:

- 2 guide RNA vectors to ensure efficient cleavage
- Donor vector with predesigned homologous arms
- Knockin GFP-Puro for selection
- Scramble gRNA as negative control included



Scan to view  
CRISPR/Cas-9 Video

Come to OriGene,  
the trusted molecular biology  
expert, for your CRISPR needs.

 **ORIGENE**

[www.origene.com/CRISPR-CAS9](http://www.origene.com/CRISPR-CAS9)

## Foreword

---



We are happy to present the latest edition in our annual *Best of Neuron* series. In this edition, we've looked back on the work we had the privilege to publish at the tail end of 2015 and throughout 2016 and have compiled this collection of articles, reviews, and essays. We're extremely proud of all of the work found within the pages of *Neuron*, and choosing a "best of" list is always a challenge. We considered several factors when selecting articles for this edition. To ensure that our readers' voices were heard, we looked through our most highly downloaded articles to find those that captured the greatest interest from the community. We also wanted to represent the broad scope of *Neuron*, so inside you'll find articles touching on a wide range of topics, encapsulating the breadth of the journal's coverage.

This collection presents two NeuroResources, two perspective pieces, one primer, one review, and nine full-length articles spanning the most exciting research of the last year. The wealth of subjects and article formats contained in this collection is an exciting representation of the journal's commitment to provide the neuroscience community with the most insightful and important research in the world.

We hope that you will enjoy reading this special collection. We'd like to thank all of our authors and reviewers: your contributions are what make *Neuron* great. Please be sure to check out the latest findings published in *Neuron* by visiting our homepage ([www.cell.com/neuron](http://www.cell.com/neuron)) and signing up for our email alerts. And if you can't wait until next year's Best of *Neuron* edition to see what your colleagues find most exciting, stay on top of what they've been reading over the past 30 days at [www.cell.com/neuron/mostread](http://www.cell.com/neuron/mostread). Also be sure to visit [www.cell.com](http://www.cell.com) to find other high-quality papers from all of our sister journals at Cell Press.

Finally, we are grateful for the generosity of our sponsors, who helped make this reprint collection possible, and we look forward to many more years of excellent neuroscience.

# Neuron



**For information for the Best of Series, please contact:**

Jonathan Christison  
Program Director, Best of Cell Press  
e: [jchristison@cell.com](mailto:jchristison@cell.com)  
p: 617-397-2893  
t: @CellPressBiz

QUALIFIED ANTIBODIES | MADE IN THE USA | VALIDATED IN THE USA

HOLY  
@Y#!

  
**BETHYL**  
LABORATORIES, INC  
Really Good Antibodies

**Holy Cow!—Great Reactions Start with Really Good Antibodies**

That's because every antibody is manufactured and validated on-site using a unique process that verifies target specificity with paired antibodies raised against distinct protein epitopes. We've heard our customers' great reactions for over 40 years and now we'd like to hear what you'll say.

Request a free trial size antibody by visiting [bethyl.com/9909](http://bethyl.com/9909)

Terms & Conditions Apply. Please see webpage for complete details.

©2016 Bethyl Laboratories, Inc. All rights reserved.

Your neurons are  
talking.  
Are you listening?



Maestro MEA platform with AxIS™ software showing real-time neural activity across a 96-well plate.

## Maestro™ microelectrode array (MEA) *in vitro* neural activity analysis

Record network-level neural activity directly on the benchtop with Maestro. Over minutes or months, gain unprecedented access to electrical network function from cultured neural populations.

Straightforward and easy to use, any researcher can measure activity from neurons in 12-, 48-, or 96-well plates.

**Connect to your network.**

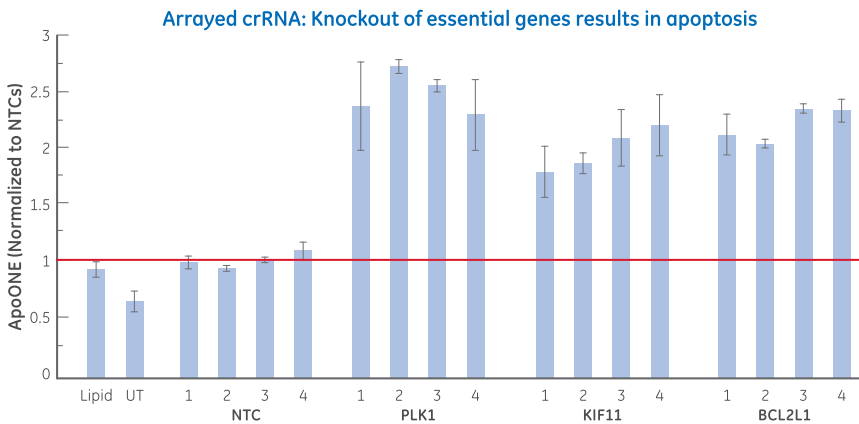


# CRISPR

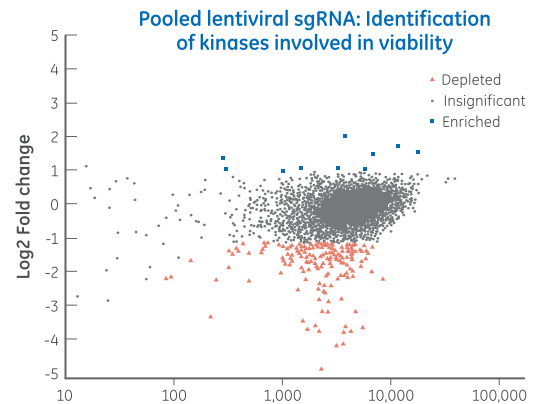
## Fast, efficient, loss-of-function screening with Dharmacon CRISPR Libraries

Rapidly assess multiple target sites per gene across hundreds or thousands of genes with Dharmacon™ Edit-R™ CRISPR-Cas9 screening libraries. Our arrayed synthetic crRNA and pooled lentiviral sgRNA collections leverage our powerful CRISPR RNA design algorithm to deliver high functionality and superior specificity – for high-confidence, loss-of-function screens.

**Edit-R crRNA Libraries | Edit-R Pooled Lentiviral sgRNA Libraries**



U2OS-UbiiEGFP-Cas9 stable cell seeded at 10,000 cells/well in 96-well format were transfected the following day with four different crRNA:tracrRNA complexes at 25 nM concentration targeting PLK1, KIF11 or BCL2L1 or four non-targeting crRNA controls (NTC). Wells transfected with lipid alone (Lipid) or left untreated (UT) were also included as controls. The effects on apoptosis were assayed using Casp3/9 homogeneous assay (ApoONE, Promega) at 48 hours post-transfection. Data normalized to average of NTC (non-targeting) crRNA controls.



Hits are identified by how strongly and significantly the experimental constructs are depleted at T1 compared to the constructs in the reference sample (T0).  $\geq 1.5$ -fold depletion |  $\leq 0.05$  padj value

# Over 16,000 citations. 2,600 test agents administered.



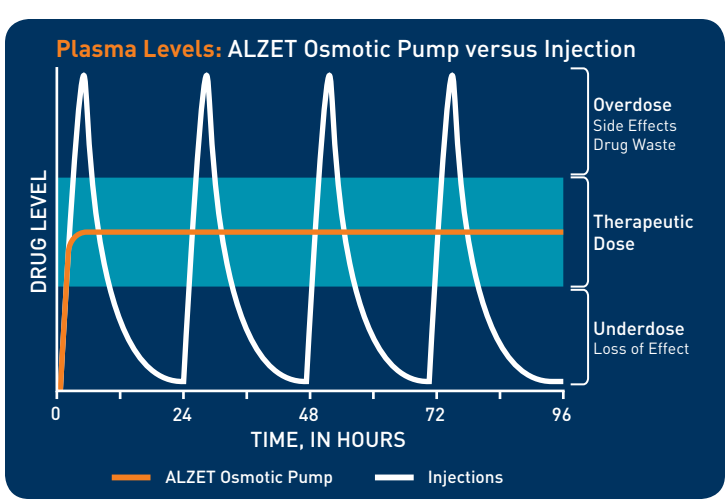
Visit us at  
Neuroscience  
2016,  
exhibit #2020

Want to see how ALZET Osmotic pumps are used in your field? Contact us to request references from our 16,000+ publication collection.

Learn more at [alzet.com](http://alzet.com)

## One Remarkably Simple Technology

Simplify your research with automatic and continuous dosing. **ALZET® Osmotic Pumps** are a superior alternative to repetitive injections and other dosing methods that require frequent animal handling. These fully implantable pumps provide continuous and precise administration of test agents, in animals as small as mice, for up to six weeks.



Watch product demo videos



# Discover #Brainbow

[www.rockland-inc.com/neuro](http://www.rockland-inc.com/neuro)



## Neuroscience Antibodies

Epigenetics | Stem Cells | Ion Channels | Epitopes |  
NOTCH | Beta Amyloid | PTM

Neurological research relies heavily on antibodies that can help identify and elucidate reactions on the cellular, molecular and biochemical level, which may lead to a better understanding of a variety of neuroscience processes and neuronal diseases. Antibody-based approaches for isolation, characterization and localization of target proteins are among the most critical and widely used techniques in molecular and cellular neuroscience. Rockland's neuroscience antibodies yield reproducible results and lead to significant advances in the field.

# Neuron

Best of 2015–2016

## Perspectives

The Psychology and Neuroscience of Curiosity

*Celeste Kidd and Benjamin Y. Hayden*

Neuroscience Training for the 21st Century

*Huda Akil, Rita Balice-Gordon, David Lopes Cardozo, Walter Koroshetz, Sheena M. Posey Norris, Todd Sherer, S. Murray Sherman, and Edda Thiels*

## Primer

DREADDs for Neuroscientists

*Bryan L. Roth*

## Review

The Cellular and Molecular Landscapes of the Developing Human Central Nervous System

*John C. Silbereis, Sirisha Pochareddy, Ying Zhu, Mingfeng Li, and Nenad Sestan*

## NeuroResources

Simultaneous Multi-plane Imaging of Neural Circuits

*Weijian Yang, Jae-eun Kang Miller, Luis Carrillo-Reid, Eftychios Pnevmatikakis, Liam Paninski, Rafael Yuste, and Darcy S. Peterka*

Mapping Sub-Second Structure in Mouse Behavior

*Alexander B. Wiltschko, Matthew J. Johnson, Giuliano Iurilli, Ralph E. Peterson, Jesse M. Katon, Stan L. Pashkovski, Victoria E. Abraira, Ryan P. Adams, and Sandeep Robert Datta*

## Articles

A Systems-Level Analysis of the Peripheral Nerve Intrinsic Axonal Growth Program

*Vijayendran Chandran, Giovanni Coppola, Homaira Nawabi, Takao Omura, Revital Versano, Eric A. Huebner, Alice Zhang, Michael Costigan, Ajay Yekkirala, Lee Barrett, Armin Blesch, Izhak Michaelievski, Jeremy Davis-Turak, Fuying Gao, Peter Langfelder, Steve Horvath, Zhigang He, Larry Benowitz, Mike Fainzilber, Mark Tuszyński, Clifford J. Woolf, and Daniel H. Geschwind*

RAN Translation in Huntington Disease

*Monica Bañez-Coronel, Fatma Ayhan, Alex D. Tarabochia, Tao Zu, Barbara A. Perez, Solaleh Khoramian Tusi, Olga Pletnikova, David R. Borchelt, Christopher A. Ross, Russell L. Margolis, Anthony T. Yachnis, Juan C. Troncoso, and Laura P.W. Ranum*

TREM2 Haplodeficiency in Mice and Humans Impairs the Microglia Barrier Function Leading to Decreased Amyloid Compaction and Severe Axonal Dystrophy

*Peng Yuan, Carlo Condello, C. Dirk Keene, Yaming Wang, Thomas D. Bird, Steven M. Paul, Wenjie Luo, Marco Colonna, David Baddeley, and Jaime Grutzendler*

Discovery of Novel Blood-Brain Barrier Targets to Enhance Brain Uptake of Therapeutic Antibodies

*Y. Joy Yu Zuchero, Xiaocheng Chen, Nga Bien-Ly, Daniela Bumbaca, Raymond K. Tong, Xiaoying Gao, Shuo Zhang, Kwame Hoyte, Wilman Luk, Melanie A. Huntley, Lilian Phu, Christine Tan, Dara Kallop, Robby M. Weimer, Yanmei Lu, Donald S. Kirkpatrick, James A. Ernst, Ben Chih, Mark S. Dennis, and Ryan J. Watts*

(continued)

**Positive Allosteric Modulators of  
GluN2A-Containing NMDARs with Distinct Modes  
of Action and Impacts on Circuit Function**

*David H. Hackos, Patrick J. Lupardus, Teddy Grand,  
Yelin Chen, Tzu-Ming Wang, Paul Reynen, Amy Gustafson,  
Heidi J.A. Wallweber, Matthew Volgraf, Benjamin D. Sellers,  
Jacob B. Schwarz, Pierre Paoletti, Morgan Sheng,  
Qiang Zhou, and Jesse E. Hanson*

**Transsynaptic Modulation of Kainate  
Receptor Functions by C1q-like Proteins**

*Keiko Matsuda, Timotheus Budisantoso, Nikolaos Mitakidis,  
Yuki Sugaya, Eriko Miura, Wataru Kakegawa, Miwako  
Yamasaki, Kohtarou Konno, Motokazu Uchigashima, Manabu  
Abe, Izumi Watanabe, Masanobu Kano, Masahiko Watanabe,  
Kenji Sakimura, A. Radu Aricescu, and Michisuke Yuzaki*

**Divergent Routing of Positive and Negative Information  
from the Amygdala during Memory Retrieval**

*Anna Beyeler, Praneeth Namburi, Gordon F. Glover,  
Clémence Simonnet, Gwendolyn G. Calhoun, Garrett F.  
Conyers, Robert Luck, Craig P. Wildes, and Kay M. Tye*

**Distinct Contribution of Adult-Born Hippocampal  
Granule Cells to Context Encoding**

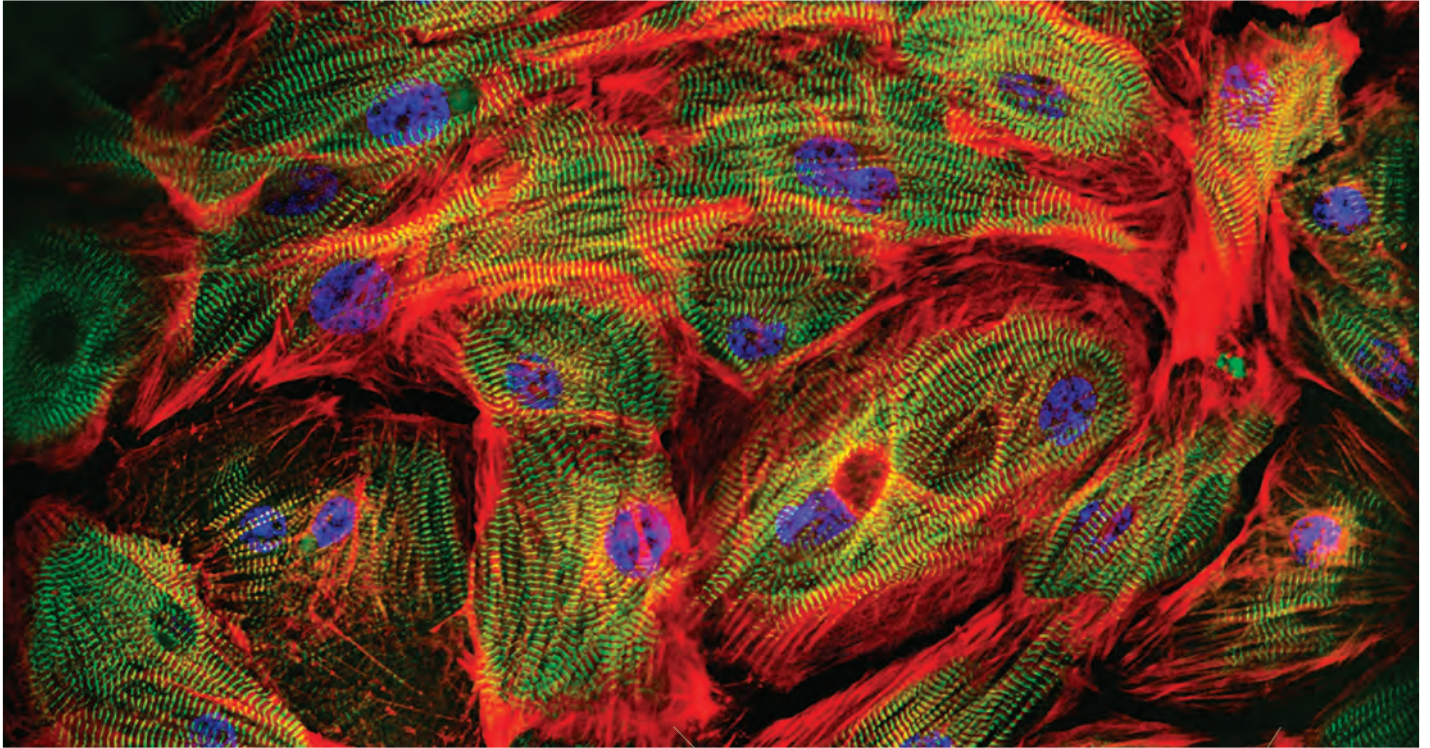
*Nathan B. Danielson, Patrick Kaifosh, Jeffrey D. Zaremba,  
Matthew Lovett-Barron, Joseph Tsai, Christine A. Denny,  
Elizabeth M. Balough, Alexander R. Goldberg, Liam J. Drew,  
René Hen, Attila Losonczy, and Mazen A. Kheirbek*

**Congenital Nystagmus Gene FRMD7 Is Necessary  
for Establishing a Neuronal Circuit Asymmetry  
for Direction Selectivity**

*Keisuke Yonehara, Michele Fiscella, Antonia Drinnenberg,  
Federico Esposti, Stuart Trenholm, Jacek Krol, Felix Franke,  
Brigitte Gross Scherf, Akos Kusnyerik, Jan Müller, Arnold  
Szabo, Josephine Jüttner, Francisco Cordoba, Ashrithpal  
Police Reddy, János Németh, Zoltán Zsolt Nagy, Francis  
Munier, Andreas Hierlemann, and Botond Roska*



**CELLular**  
**Dynamics**  
international  
a FUJIFILM company



## Human Cells.

### Endless Possibilities from Discovery to Regenerative Medicine.

Cellular Dynamics International (CDI) has designed an induced pluripotent stem cell (iPSC)-based technology platform that enables the large scale production of high-quality, fully functioning human cells. Stem cells are early stage, undifferentiated cells that are found in all multicellular organisms. They are unique because they can survive and replicate indefinitely. CDI's technology offers the potential to create iPSCs from anyone, starting with a standard blood draw, and followed by the powerful capability to develop into virtually any cell type in the human body.

Our iCell® and donor-specific MyCell® products are highly pure, highly reproducible, and available in industrial quantity to enable drug discovery, toxicity testing, stem cell banking, and cell therapy development.

[cellulardynamics.com](http://cellulardynamics.com)



# Discover what's beneath.

Explore the depths of amplicon sequencing with the NEXTflex™ Amplicon Panels. The NEXTflex Amplicon Panels are complete solutions for your targeted resequencing needs. These panels are designed to detect and screen relevant germline and somatic mutations using either Illumina or Ion Torrent-based sequencing platforms. Visit [BioScientific.com/panels](http://BioScientific.com/panels) to learn how the ready-to-use predesigned amplicon panels or validated NEXTflex™ custom solutions simplify targeted sequencing protocols.



AMPLICON PANELS
Custom
Mediterranean Fever
BRCA 1/2
Obesity
Colon
TP53
CEBPA
Phenylketonuria

*Your Discovery Awaits.*  
Visit [bioscientific.com/panels](http://bioscientific.com/panels) to learn more.

For research use only. Not for use in diagnostic procedures.  
Manufactured to the international quality standard ISO 13485.

THE NGS EXPERTS™

 **BIOO SCIENTIFIC®**  
a PerkinElmer company

# Illuminate your pathway to discovery

MBLI has over 5000 antibodies and immunoassay kits, including S100 ELISA kits and a variety of antibodies for neuroscience research.

Learn why our antibodies and kits are used worldwide among academic institutions, pharmaceutical and biotech companies.

[www.mblintl.com](http://www.mblintl.com)

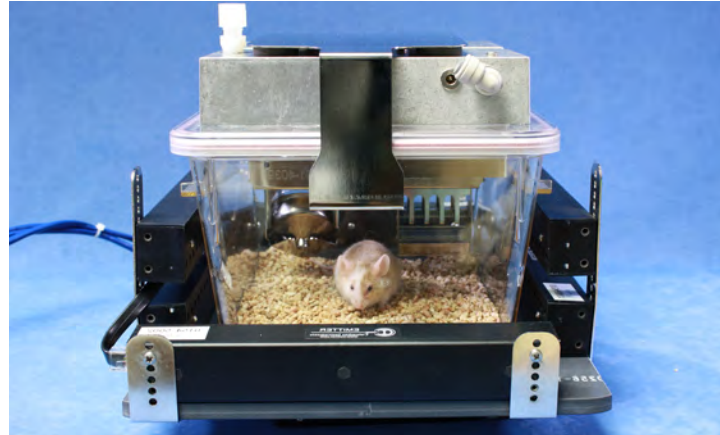


**MBL**<sup>®</sup>  
International Corporation

## **NEW** Metabolic Phenotyping Monitor: Oxymax CLAMS-HC

The Columbus Instruments Oxymax - CLAMS-HC (Comprehensive Lab Animal Monitoring System for Home Cages) is a versatile device for monitoring metabolic performance of mice and rats in their natural home cage environment.

- VO<sub>2</sub>/VCO<sub>2</sub> & RER
- Food Intake
- Drinking Volume
- Body Mass
- Core Body Temp. & Heart Rate
- Breaths / Minute
- Animal Activity
- Sleeping Bouts
- Running Wheel Activity
- **Optional Environmental enclosure with temperature and LED light color control**

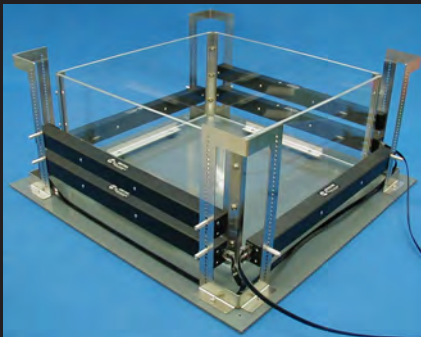


For more information: [clams@colinst.com](mailto:clams@colinst.com)

## Animal Activity Monitor

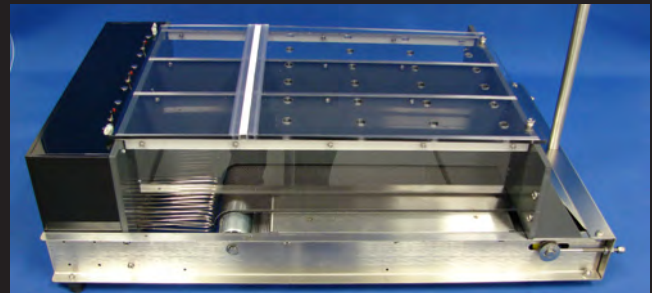
The Columbus Instruments Auto-Track Activity Meter presents the **ultimate flexibility** for measuring in home or special cages. Measures these parameters:

- Distance Traveled
- Path of Movement
- Zone Entries
- Rearing (Vertical)
- Rotations
- Open Field
- Hole Poke
- Light / Dark
- Contextual Place Preference

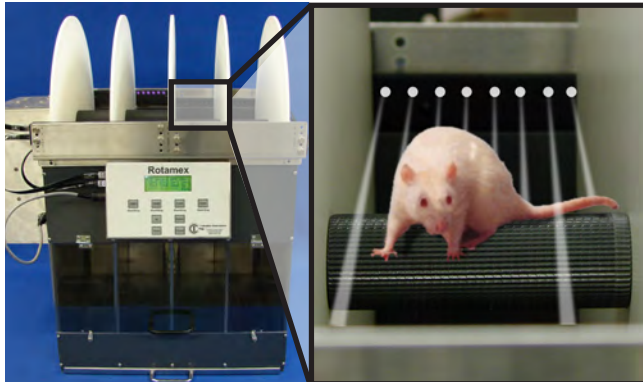


## Animal Treadmill

The Exer 3/6 Treadmill provides 6 mouse lanes or 3 rat lanes for general purpose exercise. Adjustable speed, acceleration, and incline on all models. Available with or without electric stimulus or our **NEW Air Puff Stimulus!**



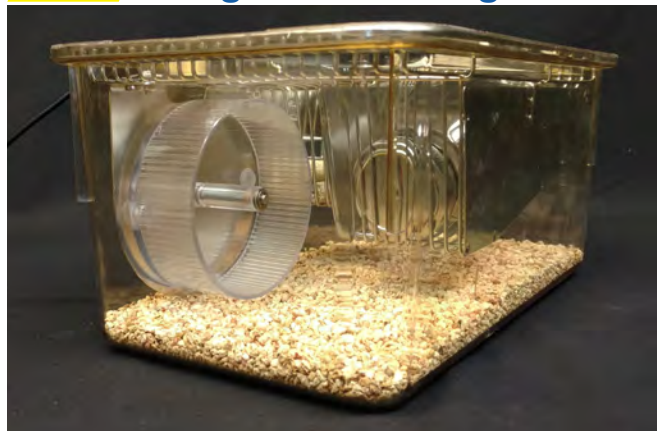
## Rota-Rod: Rotamex-5



The Rotamex-5 measures coordination in up to four mice or rats by recording the latency to fall from a spinning rod. Key features include:

- Reports latency time to fall for each subject
- Reports rod speed in RPMin. or in cm/sec.
- Adjustable speed from 0-99.9 RPMin.
- Fully adjustable acceleration 0.1-20 RPMin/sec.
- Fall detection by photocells above the rod
- Detection of passive rotation (looping) in mice

## **NEW** Weighted Running Wheel



The loaded running wheel applies a precise resistance during voluntary running for the purpose of increasing the load and measuring Work.

- Connects to PC via USB
- Software automatically calculates Work
- Adjustable load between 0 - 0.025 Newton-Meters in 0.00000038 Nm increments.

**ADVANCED FLUORESCENCE  
IMAGING SYSTEMS**



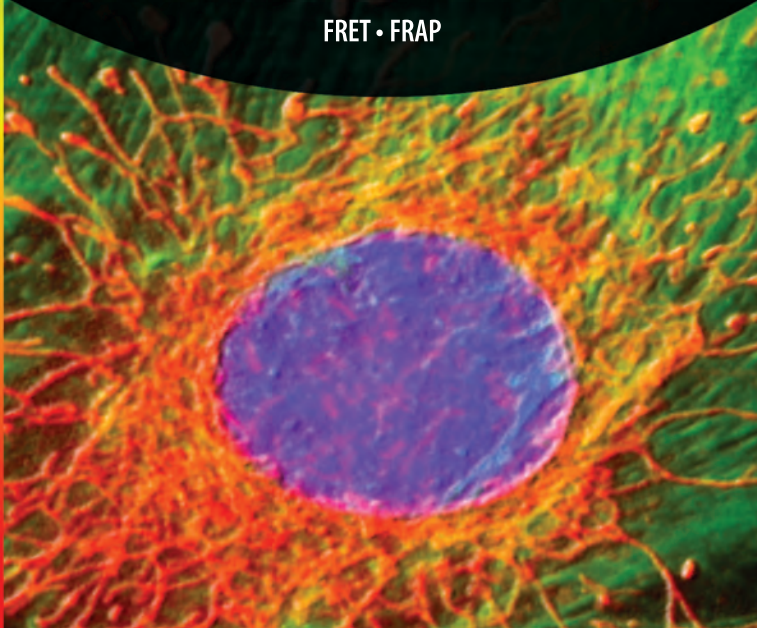
Imaging products from 89 North, Cairn Research  
and CrestOptics create light re-engineered.

Confocal Imaging • Super-Resolution Imaging

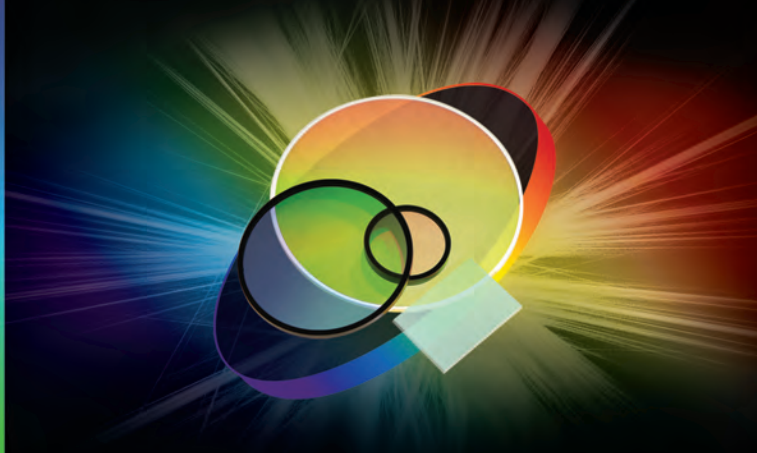
High-Speed Ratiometric Imaging • Optogenetics • Photoactivation

Photoconversion • Simultaneous Multichannel Imaging

FRET • FRAP



**DURABLE HIGH TRANSMISSION  
SPUTTERED FILTERS FROM UV TO NIR**



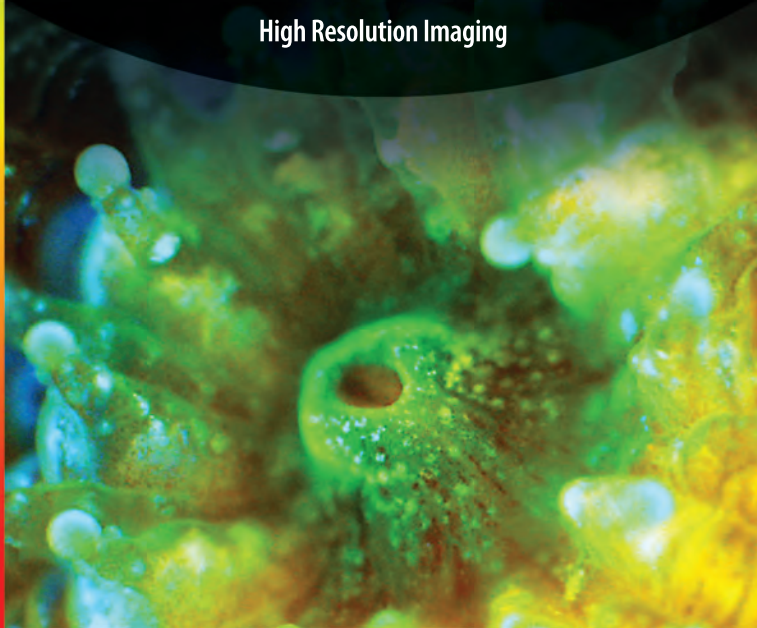
From super-resolution to Raman spectroscopy,  
Chroma filters give you more options.

Flow Cytometry • Machine Vision

Point-of-Care • Laser Applications

Raman • Fluorescence • Astronomy

High Resolution Imaging





# Quantify with Confidence

*Ever wonder about the quantitative nature of image data?  
We do. Introducing the new **ORCA-Flash4.0 V3** and the  
**W-VIEW GEMINI-2C** dual channel, dual camera optics.*

**ENGINEERED FOR SUPER RESOLUTION—READY FOR ANYTHING.**

Society for Neuroscience [Booth 1613](#)  
American Society for Cell Biology [Booth 309](#)

**HAMAMATSU**  
PHOTON IS OUR BUSINESS

908-231-0960 [hamamatsucameras.com](http://hamamatsucameras.com)

# The Psychology and Neuroscience of Curiosity

Celeste Kidd<sup>1</sup> and Benjamin Y. Hayden<sup>1,\*</sup>

<sup>1</sup>Department of Brain and Cognitive Sciences and Center for Visual Science, University of Rochester, Rochester, NY 14620, USA

\*Correspondence: benhayden@gmail.com

<http://dx.doi.org/10.1016/j.neuron.2015.09.010>

Curiosity is a basic element of our cognition, but its biological function, mechanisms, and neural underpinning remain poorly understood. It is nonetheless a motivator for learning, influential in decision-making, and crucial for healthy development. One factor limiting our understanding of it is the lack of a widely agreed upon delineation of what is and is not curiosity. Another factor is the dearth of standardized laboratory tasks that manipulate curiosity in the lab. Despite these barriers, recent years have seen a major growth of interest in both the neuroscience and psychology of curiosity. In this Perspective, we advocate for the importance of the field, provide a selective overview of its current state, and describe tasks that are used to study curiosity and information-seeking. We propose that, rather than worry about defining curiosity, it is more helpful to consider the motivations for information-seeking behavior and to study it in its ethological context.

## Background

Curiosity is such a basic component of our nature that we are nearly oblivious to its pervasiveness in our lives. Consider, though, how much of our time we spend seeking and consuming information, whether listening to the news or music; browsing the internet; reading books or magazines; watching television, movies, and sports; or otherwise engaging in activities not directly related to eating, reproduction, and basic survival. Our insatiable demand for information drives a much of the global economy and, on a micro-scale, motivates learning and drives patterns of foraging in animals. Its diminution is a symptom of depression, and its overexpression contributes to distractibility, a symptom of disorders such as attention deficit hyperactivity disorder (ADHD). Curiosity is thought of as the noblest of human drives but is commonly denigrated as dangerous (as in the expression “curiosity killed the cat”). Despite its link with the most abstract human thoughts, some rudimentary forms of it can be observed even in the humble worm *C. elegans*.

Despite its pervasiveness, we lack even the most basic integrative theory of the basis, mechanisms, and purpose of curiosity. Nonetheless, as a psychological phenomenon, curiosity—and the desire for information more broadly—has attracted the interest of the biggest names in the history of psychology (e.g., James, 1913; Pavlov, 1927; Skinner, 1938). Despite this interest, only recently have psychologists and neuroscientists begun widespread and coordinated efforts to unlock its mysteries (e.g., Gottlieb et al., 2013; Gruber et al., 2014; Kang et al., 2009). This Perspective aims to summarize this recent research, motivate new interest in the problem, and tentatively propose a framework for future studies of the neuroscience and psychology of curiosity.

## Definition and Taxonomy of Curiosity

One factor that has hindered the development of a formal study of curiosity is the lack of a single widely accepted definition of the term. In particular, many observers think that curiosity is a special type of the broader category of information-seeking. But carving out a formal distinction between curiosity and infor-

mation-seeking has proven difficult. As a consequence, much research that is directly relevant to the problem of curiosity does not use the term curiosity and, instead, focuses on what are considered to be distinct phenomena. These phenomena include, for example, play, exploration, reinforcement learning, latent learning, neophilia, and self-reported desire for information (e.g., Deci, 1975; Gruber et al., 2014; Jirout and Klahr, 2012; Kang et al., 2009; Sutton and Barto, 1998; Tolman and Gleitman, 1949). Conversely, studies that do use the term curiosity range quite broadly in topic area. In laboratory studies, the term curiosity itself is broad enough to encompass both the desire for answers to trivia questions and the strategic deployment of gaze in free viewing (Gottlieb et al., 2013).

We consider this diversity of definitions to be both characteristic of a nascent field and healthy. Here we consider some classic views with an aim toward helping us think about how to study curiosity in the future.

## Classic Descriptions of Curiosity

Philosopher and psychologist William James called curiosity “the impulse towards better cognition,” meaning that it is the desire to understand that which you do not (James, 1899). He noted that, in children, it drives them toward objects of novel, sensational qualities—that which is “bright, vivid, startling.” This early definition of curiosity, he said, later gives way to a “higher, more intellectual form”—an impulse toward more complete scientific and philosophic knowledge. Psychologist-educators G. Stanley Hall and Theodate L. Smith pioneered some of the earliest experimental work on the development of curiosity by collecting questionnaires and child biographies from mothers on the development of interest and curiosity (Hall and Smith, 1903). From these data, they describe children’s progression through four stages of development, starting with “passive staring” as early as the second week of life through “curiosity proper” at around the fifth month.

The history of studies of animal curiosity is nearly as long as the history of the study of human curiosity. Ivan Pavlov, for example, wrote about the spontaneous orienting behavior in dogs to novel stimuli (which he called the “what-is-it?” reflex)

as a form of curiosity (Pavlov, 1927). In the mid-20<sup>th</sup> century, exploratory behavior in animals began to fascinate psychologists, in part because of the challenge of integrating it into strict behaviorist approaches (e.g., Tolman, 1948). Some behaviorists counted curiosity as a basic drive, effectively giving up on providing a direct cause (e.g., Pavlov, 1927). This stratagem proved useful even as behaviorism declined in popularity. For example, this view was held by Harry Harlow—the psychologist best known for demonstrating that infant rhesus monkeys prefer the company of a soft, surrogate mother over a bare wire mother. Harlow referred to curiosity as a basic drive in and of itself—a “manipulatory motive”—that drives organisms to engage in puzzle-solving behavior that involved no tangible reward (e.g., Harlow et al., 1950, 1956; Harlow and McCleary, 1954).

Psychologist Daniel Berlyne is among the most important figures in the 20<sup>th</sup> century study of curiosity. He distinguished between the types of curiosity most commonly exhibited by human and non-humans along two dimensions: perceptual versus epistemic and specific versus diversive (Berlyne, 1954). Perceptual curiosity refers to the driving force that motivates organisms to seek out novel stimuli, which diminishes with continued exposure. It is the primary driver of exploratory behavior in non-human animals and, potentially, also in human infants as well as a possible driving force of human adults' exploration. Opposite perceptual curiosity was epistemic curiosity, which Berlyne described as a drive aimed “not only at obtaining access to information-bearing stimulation, capable of dispelling uncertainties of the moment, but also at acquiring knowledge.” He described epistemic curiosity as applying predominantly to humans, therefore distinguishing the curiosity of humans from that of other species (Berlyne, 1966).

The second dimension of curiosity that Berlyne described is informational specificity. Specific curiosity referred to desire for a particular piece of information, whereas diversive curiosity referred to a general desire for perceptual or cognitive stimulation (e.g., in the case of boredom). For example, monkeys robustly exhibit specific curiosity when solving mechanical puzzles, even without food or any other extrinsic incentive (e.g., Davis et al., 1950; Harlow et al., 1950; Harlow, 1950). However, rats exhibit diversive curiosity when, devoid of any explicit task, they robustly prefer to explore unfamiliar sections of a maze (e.g., Dember, 1956; Hughes, 1968; Kivy et al., 1956). Both specific and diversive curiosity were described as species-general information-seeking behaviors.

### **Contemporary Views of Curiosity**

A common contemporary view of curiosity is that it is a special form of information-seeking distinguished by the fact that it is internally motivated (Loewenstein, 1994; Oudeyer and Kaplan, 2007). By this view, curiosity is strictly an intrinsic drive, whereas information-seeking refers more generally to a drive that can be either intrinsic or extrinsic. An example of an extrinsic type of information-seeking is paying a nominal price to know the outcome of a gamble before choosing it to make a more profitable choice. In other words, contexts in which agents seek information for immediate strategic reasons are not considered curiosity in the strict sense. Although this definition is intuitively appealing (and most consistent with the use of the term curiosity in everyday speech), it is accompanied by some problems.

For example, it is often difficult for an external observer to know whether a decision-maker is motivated intrinsically or extrinsically. Animals and preverbal children, for example, cannot tell us why they do what they do, and may labor under biased theories about the structure of their environment or other unknown cognitive constraints. Consider a child choosing between a safe door and a risky one (Butler, 1953). If the child chooses the risky option, should we call her curious or just risk-seeking? Or consider a rhesus monkey who performs a color discrimination task to obtain the opportunity to visually explore its environment. Perhaps the monkey is laboring under the assumption that the view of the environment offers some actionable information, and we should put him in the same place on the curiosity spectrum as the child (whatever that place is). To make things more complicated, perhaps the monkey has decided—or even experienced selective pressure—to favor a policy of information-seeking in most contexts. It would be a challenging philosophical problem to classify this behavior as true or ersatz curiosity by the intrinsic definition.

Therefore, for the moment, we favor the rough-and-ready formulation of curiosity as a drive state for information. Decision-makers can be thought of as wanting information for several overlapping reasons just as they want food, water, and other basic goods. This drive may be internal or external, conscious or unconscious, slowly evolved, or some mixture of the above. We hope that future work will provide a solid taxonomy of different factors that constitute our umbrella term.

Instead of figuring out the taxonomy, we advocate a different approach. We suggest that it is helpful to think about curiosity in the context of Tinbergen's four questions. Named after Dutch biologist Nikolaas Tinbergen, these questions are designed to provide four complementary scientific perspectives on any particular type of behavior (Tinbergen, 1963). These questions, in turn, offer four vantage points from which we can describe a behavior or a broad class of behaviors even if its boundaries are not yet fully delineated. In this spirit, our Perspective will discuss current work on curiosity as seen through the lens of Tinbergen's four questions, here simplified to one word each: (1) function, (2) evolution, (3) mechanism, and (4) development.

### **The Function of Curiosity**

Although information is intangible, it has real value to any organism with the capacity to make use of it. The benefits may accrue immediately or in the future; the delayed benefits require a learning system. Not surprisingly, then, the most popular theory about the function of curiosity is to motivate learning. George Loewenstein described curiosity as “a cognitive induced deprivation that arises from the perception of a gap in knowledge and understanding” (Loewenstein, 1994). Loewenstein's information gap theory holds that curiosity functions like other drive states, such as hunger, which motivates eating. Building on this theory, Loewenstein suggests that a small amount of information serves as a priming dose that greatly increases curiosity. Consumption of information is rewarding, but, eventually, when enough information is consumed, satiation occurs, and information serves to reduce further curiosity.

Loewenstein's idea is supported by a recent study by Kang et al. (2009) (Figure 1B). They found that curiosity about the

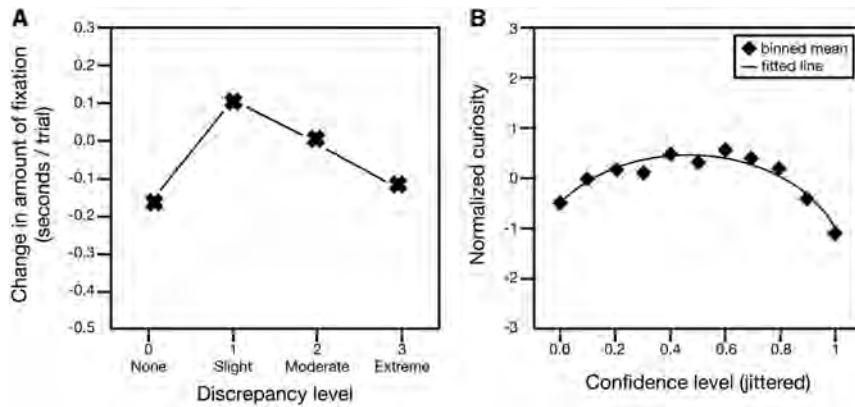


**Figure 1. Curiosity and Information-Seeking** (A) Data from Kinney and Kagan (1976). Attention to auditory stimuli shows an inverted U-shaped pattern, with infants making the most fixations to auditory stimuli estimated to be moderately discrepant from the auditory stimuli for which infants already possessed mental representations. (B) Data from Kang et al. (2009). Subjects were most curious about the answers to trivia questions for which they were moderately confident about their answers. This pattern suggests that subjects exhibited the greatest curiosity for information that was partially—but not fully—encoded.

answer to a trivia question is a U-shaped function of confidence about knowing that answer. Decision-makers were least curious when they had no clue about the answer and when they were extremely confident. They were most curious when they had some idea about the answer but lacked confidence. Under these circumstances, the compulsion to know the answer was so great that they were even willing to pay for the information even though curiosity could have been sated for free after the session. (The neural findings of this study are discussed below.)

Kang et al. (2009) also found that curiosity enhances learning, consistent with the theory that the primary function of curiosity is to facilitate learning. This idea also motivated O’Keefe and Nadel’s thinking about the factors that promote spatial learning in rodents (O’Keefe and Nadel, 1978). This idea is also popular in the education literature (e.g., Day, 1971; Engel, 2011, 2015; Gray, 2013) and has been for quite some time, as evidenced by attempts by education researchers to develop scales to quantify children’s degree of curiosity both generally and in specific learning materials (e.g., Harty and Beall, 1984; Jirout and Klahr, 2012; Pelz et al., 2015; Penney and McCann, 1964). One potential benefit of such research would be to improve education. More recently, the role of curiosity in enhancing learning is gaining adherents in cognitive science (see Gureckis and Markant, 2012, for a review). The idea is that allowing a learner to indulge his curiosity allows him to focus his effort on useful information that he does not yet possess. Furthermore, there is a growing body of evidence suggesting that curiosity enables even infant learners to play an active role in optimizing their learning experiences (P. Oudeyer, personal communication). This work suggests that allowing a learner to expose the information he requires himself—which would be inaccessible via passive observation—may further benefit the learner by enhancing the encoding and retention of the new information.

### The Evolution of Curiosity

Information allows for better choices, more efficient searches, more sophisticated comparisons, and better identification of conspecifics. Acquiring information, of course, is the primary evolutionary purpose of the sense organs and has been a major driver of evolution for hundreds of millions of years. Complex organisms actively control their sense organs to maximize the intake of information. For example, we choose our visual fixa-

tions strategically to learn about the things that are important to us in the context (Yarbus 1956; Gottlieb, 2012; Gottlieb et al., 2013, 2014). Given its important role, it is not surprising that our visual search is highly efficient. It is nearly optimal compared with an “ideal searcher” that uses precise statistics of the visual scene to maximize search efficiency (Najemnik and Geisler 2005). Moreover, the strong base of information we have about the visual system makes it an appealing target for studies of curiosity (Gottlieb et al., 2013, 2014). Just as eye movements can be highly informative, our overt behaviors, including choice, can provide evidence for and against specific theories about how we seek information, which can, in turn, help us understand the root causes of evolution. In this section, we discuss the spectrum of basic information-seeking behaviors.

### Elementary Information-Seeking

Even very simple organisms trade off information for reward. Although their information-seeking behavior is not typically categorized as curiosity, the simplicity of their neural systems makes them ideally suited for studies that may provide its foundation. For example, *C. elegans* is a roundworm whose nervous system contains 302 neurons and that actively forages for food, mostly bacteria. When placed on a new patch (such as a Petri dish in a lab), it first explores locally (for about 15 min), then abruptly adjusts strategies and makes large, directed movements in a new direction (Calhoun et al., 2014). This search strategy is more sophisticated and beneficial than simply moving toward food scents (or guesses about where food may be). Instead, it provides better long-term payoff because it provides information as well. It maximizes a conjoint variable that includes both expected reward and information about the reward. This behavior, although computationally difficult, is not too difficult for worms. A small network of three neurons can plausibly implement it. Other organisms that have simple information-seeking behavior include crabs (Zeil, 1998), bees (Gould, 1986; Dyer, 1991) ants (Wehner et al., 2002), and moths (Vergassola et al., 2007). Information gained from such organisms can help us understand how simple networks can perform information-seeking.

### Information Tradeoff Tasks

In primates (including humans), one convenient way to study information-seeking is the k-arm bandit task (Gittins and Jones, 1974; Figure 2). In this task, decision-makers are faced with a series of choices between stochastic reward (Whittle, 1988).

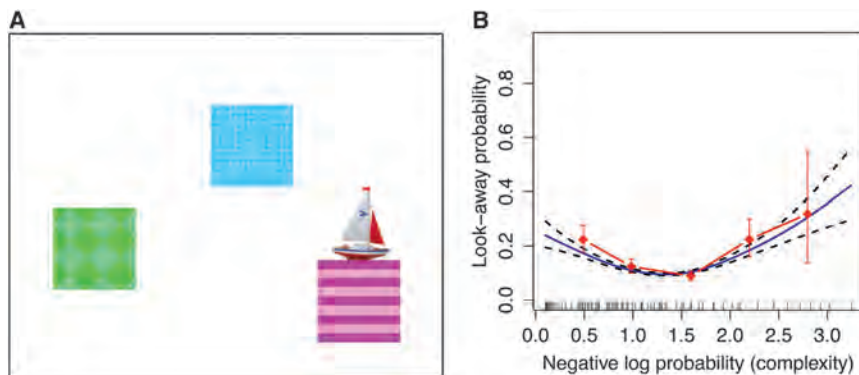


**Figure 2. Curiosity and Attention**

(A) Example display from Kidd et al. (2012). Each display featured three unique boxes hiding three unique objects that revealed themselves one at a time according to one of 32 sequences of varying complexity. The sequence continued until the infant looked away for 1 s.

(B) Infant look-away data plotted by complexity (information content) as estimated by an ideal observer model over the transitional probabilities. The U-shaped pattern indicates that infants were least likely to look away at events with intermediate information content. The infants' probability of looking away was greatest to events of either very low information content (highly predictable) or very high information content (highly surprising), consistent with an attentional strategy that aims to maintain intermediate rates of information absorption.

The optimal strategy requires adjudication between exploration (sampling to improve knowledge and, therefore, future choices) and exploitation (choosing known best options). Sampling typically gives a lower immediate payoff but can provide information that improves choices in the future, leading to greater overall performance. Humans and monkeys can do quite well at this task (Daw et al., 2006; Pearson et al., 2009). One particular advantage of such tasks is that they allow for sophisticated formal models of information tradeoffs. This level of rigor is often absent in conventional curiosity studies (Averbeck, 2015).

Daw et al. (2006) have shown that humans performing a four-arm bandit task choose options probabilistically based on expected values of the options (a "softmax" policy). This probabilistic element causes them to occasionally explore other possibilities, leading them to better overall choices. The frontopolar cortex and intraparietal sulcus are significantly more active during exploration, whereas the striatum and ventromedial prefrontal cortex (vmPFC) are more active during exploitative choices (Daw et al., 2006). These are canonical reward areas; therefore, these results link curiosity to the reward system (a theme to which we will return). They proposed that the activation of higher-level prefrontal regions during exploration indicates a control mechanism overriding the exploitative tendency.

In a similar task, neurons in the posterior cingulate cortex (PCC) have greater tonic firing rates in exploratory trials than in exploitative trials (even after controlling for reward expectation; Pearson et al., 2009; Figure 2). Firing rates also predict adjustments from an exploitative to exploratory strategy and vice versa. These results highlight the contribution of the PCC, a critical but mostly mysterious hub of the reward system, in both the transition to exploration and in its maintenance (Pearson et al., 2011). The PCC is linked to both reward and regulation of learning, therefore underscoring the possible link between these processes and curiosity (Heilbronner and Platt, 2013; Hayden et al., 2008). PCC responses are also driven by the salience of an option, a factor that relates directly to its ability to motivate interest rather than reward value per se (Heilbronner et al., 2011). The precuneus, a region adjacent to and closely interconnected with the PCC, was also associated with curiosity in one study; it is enlarged in capuchins that are particularly curious (Phillips et al., 2012).

Above and beyond the strategic benefit of exploration, we have a tendency to seek out new and unfamiliar options, which

may offer more information than familiar ones. The bandit task can be modified to measure this tendency (Wittmann et al., 2008). In one case, subjects chose between four different images in each trial. The identity of the images was arbitrary and served to distinguish the options. The value of each image was stable but stochastic, so sampling was required to learn its value. Some images were familiar, others were novel; however, image novelty had no special meaning in the context of the task. Nonetheless, subjects were more likely to choose novel images (that is, they motivated exploratory choices). This bias toward choosing novel images was mathematically expressible as a novelty bonus (Gittins and Jones, 1974). Interestingly, this novelty bonus increased the expected reward for the novel images (as measured by an increase in reward prediction error [RPE] signal in the ventral striatum). These results support the idea that novelty-seeking reflects an injection into choice of motivation provided by the brain's reward systems.

Bandit tasks can also be used to measure the effect of strategic context on information-seeking. For example, if the information relates to future events that may not happen, then it ought to be discounted. Therefore, the horizon (the number of trials available to search the environment before it changes dramatically) matters (Wilson et al., 2014; see also Averbeck, 2015). Humans can adjust appropriately to changes in horizon. With longer horizons, subjects were more likely to choose an exploratory strategy than an exploitative one. Together, these results highlight the power and flexibility of bandit tasks as a way of studying information-seeking in a rigorous and highly quantifiable way.

#### **Temporal Resolution of Uncertainty Tasks**

What about when the drive for information has no clear benefit? One convenient way to study this is to take advantage of the preference for immediate information about the outcome of a risky choice (Kreps and Porteus, 1978; Lieberman et al., 1997; Luhmann et al., 2008; Prokasy, 1956; Wyckoff, 1952). In a temporal resolution of uncertainty task, monkeys choose between two gambles with identical probabilities (50/50) and identical payoffs (a large or a small squirt of juice delayed by 2.25 s) (Bromberg-Martin and Hikosaka, 2009). The only difference between the two gambles is that one offers immediate information about win versus loss (that is, immediate temporal resolution of uncertainty), whereas, in the other, the information is delayed. The reward is delayed in both cases, so preference for sooner

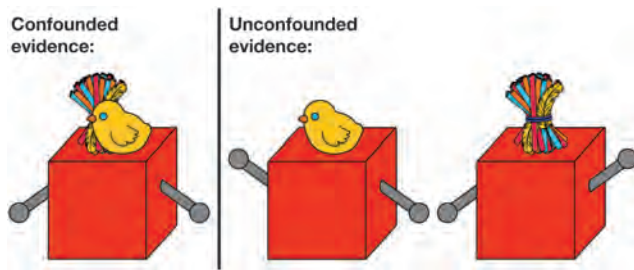


**Figure 3. Curiosity and Learning**

Experimental stimuli from Schulz and Bonawitz (2007). When both levers were pressed simultaneously, two puppets (a straw pom-pom and a chick) emerged from the center of the box. In this confounded case, the evidence was not informative about which of the two levers caused each puppet to rise. Under the unconfounded conditions, one lever was pressed at a time, making it clear which lever caused each puppet to rise. During a free play period following the toy's demonstration, children played more with the toy when the demonstrated evidence was confounded.

reward would not affect choice. Despite the brevity of the delay, monkeys reliably choose the option with the immediate resolution of uncertainty (the informative option; Bromberg-Martin and Hikosaka, 2009, 2011; Blanchard et al., 2015). This preference for earlier temporal resolution of uncertainty is not strategic because the information cannot improve choices. Therefore, these tasks satisfy a stricter notion of curiosity.

We modified this task to quantify the value of information by titrating the values of the reward (Blanchard et al., 2015; Figure 3). In the curiosity tradeoff task, by determining the indifference point between informative and uninformative options, we found that the value of information about a reward is about 25% of the value of the reward itself—surprisingly high. This finding indicates that monkeys choose information even when it has a measurable cost. In addition, the value of information increases with the stakes. In other words, monkeys will pay more for information about a high-stakes gamble than for information about a low-stakes gamble. These results are similar to some recent findings observed in pigeons (Stagner and Zentall, 2010). Pigeons will choose a risky option that provides an average of two pellets over one that provides an average of three pellets as long as the one that provides two pellets also provides what they call a discriminative cue—meaning a cue that reliably predicted whether a reward would come (see also Gipson et al., 2009).

Zentall and Stagner (2011) did make the link between their risk-seeking pigeons and human gamblers. This link is potentially important. Curiosity is often mooted as an explanation for risk-seeking behavior (Bromberg-Martin and Hikosaka, 2009). Rhesus monkeys, for example, are often risk-seeking in laboratory tasks (Blanchard and Hayden, 2014; Heilbronner and Hayden 2013; Monosov and Hikosaka, 2012; O'Neill and Schultz, 2010; So and Stuphorn, 2012; Strait et al., 2014, 2015). Risky choices provide information about the status of uncertain stimuli in the world, so animals may naturally seek such information. We trained monkeys to perform a gambling task in which both the location and value of a preferred high-variance option are uncertain. Knowing the location of that option allowed the monkeys to perform better in the future, but knowing its value was irrelevant

(Hayden et al., 2009). We found that, following choices of the low variance (and, therefore, non-preferred) option, when it was too late to change anything, monkeys will spontaneously shift gaze to its position, suggesting that they want to know information about it.

These findings demonstrate the power of the desire for temporal resolution of uncertainty as a motivator for choice and, therefore, as a potential tool for the study of information-seeking. This phenomenon is particularly useful because the information sought is demonstrably useless, making it a good potential model for more basic and fundamental (i.e., non-strategic) forms of information-seeking than the bandit task. It is also, like the bandit task, one that works well in animals (meaning behavior is reliable and stable across large numbers of trials), so it has potential utility in circuit-level studies.

### The Neural Mechanisms of Curiosity

Tinbergen's third question is about the proximate mechanism of a behavior. The mechanism of any behavior is in device that produces it—the brain.

As noted above, Kang et al. (2009) used a curiosity induction task to test Loewenstein's hypothesis that curiosity reflects an information gap (Loewenstein, 1994). Human subjects read trivia questions and rated their feelings of curiosity while undergoing fMRI (Kang et al., 2009). Brain activity in the caudate nucleus and inferior frontal gyrus (IFG) was associated with self-reported curiosity. These structures are activated by anticipation of many types of reward, so these results suggest that curiosity elicits an anticipation of a reward state—consistent with Loewenstein's theory (Delgado et al., 2000, 2003, 2008; de Quervain et al., 2004; Fehr and Camerer, 2007; King-Casas et al., 2005; Rilling et al., 2002). Puzzlingly, the nucleus accumbens, which is one of the most reliably activated structures for reward anticipation, was not activated (Knutson et al., 2001). When the answer was revealed, activations generally were found in structures associated with learning and memory, such as the parahippocampal gyrus and hippocampus. Again, this is a bit puzzling because classic structures that respond to receipt of reward were not particularly activated. In any case, the learning effect was particularly strong on trials on which subjects' guesses were incorrect—the trials on which learning was greatest.

Jepma et al. (2012) showed subjects blurry photos with ambiguous contents that piqued their curiosity. Curiosity activated the anterior cingulate cortex and anterior insula, regions sensitive to aversive conditions (but to many other things too). Resolution of curiosity activated striatal reward circuits. Like Kang et al. (2009), they found that resolution of curiosity activated learning structures and also drove learning. However, the differences between the two studies were larger than the similarities. In the Jepma study, curiosity is a fundamentally aversive state (Jepma et al., 2012), whereas, in the Kang study it is pleasurable (Kang et al., 2009). Specifically, curiosity is seen as a lack of something wanted (information) and, therefore, unpleasant, and this unpleasantness motivates information, which will alleviate it.

Gruber et al. (2014) measured brain activity while subjects answered trivia questions and rated their curiosity for each question. They were also shown interleaved photographs of neutral, unknown faces that acted as a probe for learning. When tested

later, subjects recalled the faces shown in high-curiosity trials better than faces shown on low-curiosity trials. Therefore, the curiosity state led to better learning, even for the things people were not curious about. Curiosity drove activity in both the midbrain (implying the dopaminergic regions) and nucleus accumbens. Memory was correlated with midbrain and hippocampal activity. These results suggest that, although curiosity reflects intrinsic motivation, it is mediated by the same mechanisms as extrinsically motivated reward.

Single-unit recordings from the temporal resolution of an uncertainty task further support this overlap. In this task, dopamine neuron activity (DA) is enhanced by the prospect of both a possible reward and early information. Dopamine neurons provide a key learning and motivation signal that is critical for many types of reward-related cognition (Redgrave and Gurney, 2006; Bromberg-Martin et al., 2010; Schultz and Dickinson, 2000). The phasic dopamine response is thought to serve as a general reward prediction error—indicating reward or reward prospects of any type that are greater than expected (Schultz et al., 1997). Information is not a primary reward (as juice or water would be in this context) but a more indirect kind of reward. The fact that dopamine neurons signal both the primary and informational reward suggests that the dopamine response reflects an integration of multiple reward components to generate an abstract reward response. This finding further suggests that dopamine responses not associated with a reward—such as surprising and aversive events—may reflect the value that information provides (Horvitz, 2000; Matsumoto and Hikosaka, 2009; Redgrave and Gurney, 2006).

These results suggest that, to subcortical reward structures, informational value is treated the same as any other valued good. To further test this idea, the authors asked whether midbrain neurons encode information prediction errors (Bromberg-Martin and Hikosaka, 2011). Although the positive RPE is carried by DA neurons, its inverse, the negative RPE, is carried by neurons in the lateral habenula (LHb). They made use of this fact in a task in which there was an option to choose a stochastically informative gamble, meaning it would provide (50/50 chance) valid or invalid information about the upcoming reward. They found that neurons in the LHb encode the unexpected occurrence of information and the unexpected denial of information—just as they do with a basic reward (water and juice).

Where does the domain-general curiosity signal come from? It has recently been proposed that the dopamine reward signal is constructed of input signals originating in the orbitofrontal cortex (OFC), which, in turn, receives input from basic sensory and association structures (Ongür and Price, 2000; Schoenbaum et al., 2011; Takahashi et al., 2011; Rushworth et al., 2011). If OFC is an input to the evaluation system, then it should carry information about the reward value of curiosity but may not carry a single general reward signal. In other words, OFC may serve as a kind of workshop that represents elements of reward that can guide choice but not a single domain general value signal. In the curiosity tradeoff task (see above and Figure 3), OFC neurons encode both the stakes of the gamble and also the information value of the options (Blanchard et al., 2015), but it does not integrate them into a single value signal. Therefore, at least within this one task, curiosity is computed separately from other factors

that influence value and combined at a specific point (or points) in the pathway between the OFC and the DA nuclei.

### The Development of Curiosity

The fourth of Tinbergen's questions concerns the development of a behavior. Curiosity has been central to the study of infant and child attention and learning and a major focus in research on early education for decades (e.g., Berlyne, 1978; Dember and Earl, 1957; Kinney and Kagan, 1976; Sokolov, 1963). The world of infants is full of potential sources for learning, but they possess limited information-processing resources. Therefore, infants must solve what is known as the sampling problem: their attentional mechanisms must select a subset of material from everything available in their environments to make learning tractable. Furthermore, they must sample in a way that ensures that learning is efficient, which is tricky considering the fact that what material is most useful changes as the infant gains more knowledge.

Infants enter the world with some simple, low-level heuristics for guiding their attention toward certain informative features of the world. Haith (1980) argued that these organizing principles for visual behavior are fundamentally stimulus-driven. For example, an infant's gaze is pulled toward areas of high contrast, which is useful for detecting objects and perceiving their shapes (e.g., Salapatek and Kessen, 1966), and motion onset, which is useful for detecting animacy (e.g., Aslin and Shea, 1990). Infants also have an innate bias to orient toward faces (e.g., Farroni et al., 2005; Johnson et al., 1991), which relay both social information and cues that guide language learning (e.g., Baldwin, 1993). Although this desire for information is surely intrinsic, whether or not these low-level mechanisms that guide infants' early attentional behavior could be explained with curiosity depends on the chosen definition. If curiosity requires an explicit mental representation of the need for new information, these low-level heuristics do not qualify. However, they do by a broader definition, which sees curiosity as any mechanism that guides an organism toward new information regardless of mental substrate. Regardless of how you classify them, these attentional biases get the infant started down the road of knowledge acquisition.

Externally driven motivation is not sufficient. Learners must also adapt to changing needs as they build up and modify their mental representations of the world. Many early researchers posited that novelty was the primary stimulus feature of relevance for infants (e.g., Sokolov, 1963). Infants prefer novel stimuli in many paradigms, such as those used by Fantz (1964), the high-amplitude sucking procedure (Siqueland and DeLucia, 1969), and the head turn preference procedure (Kemler Nelson et al., 1995). Novelty preference is also seen in habituation procedures in which infants' attention to a recurring stimulus decreases with lengthened exposure. Novelty theories, however, cannot account for infants' attested familiarity preferences, such as their affinity for their native languages and familiar faces (e.g., Bushnell et al., 1989; DeCasper and Spence, 1986).

Later theories sought to unify infants' novelty and familiarity preferences by explaining them in terms of infants' changing knowledge states. In other words, an infant's interest in a particular stimulus was theorized to be determined by that infant's

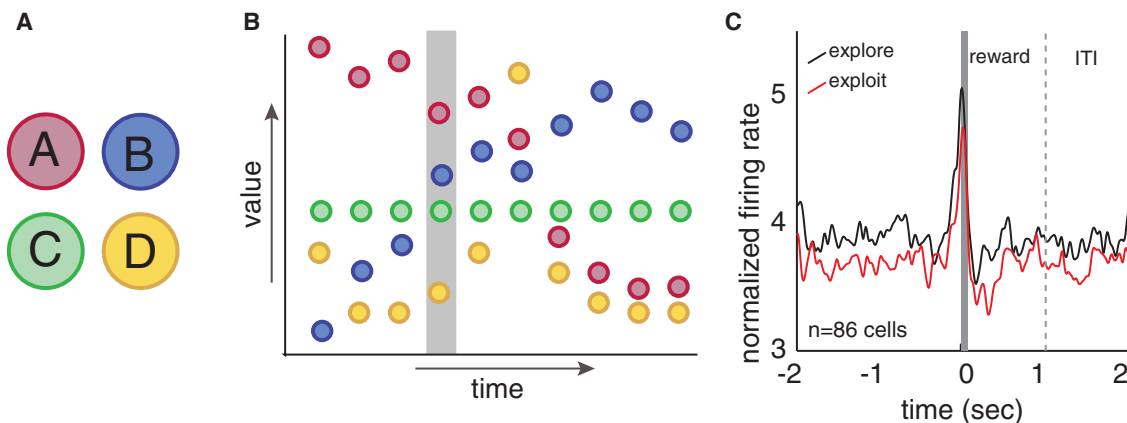


**Figure 4. Bandit Task**

(A) In a four-arm restless bandit task, subjects choose one of four targets in each trial.

(B) The value associated with each option changes stochastically in value (uncued) in each trial. Consequently, when the subject has identified the best target, there is a benefit to occasionally interspersing trials where an alternative is chosen (exploration) into the more common pattern of choosing the known best option (exploitation). For example, the subject may choose option A (red color) for several trials but would not know that blue (B) will soon overtake A in value without occasionally exploring other options.

(C) In this task, neurons in the posterior cingulate cortex show higher tonic firing in explore trials than in exploit trials. ITI, inter-trial interval.

particular mental status. For example, as infants attempt to encode various features of a visual stimulus, the efficiency or depth of this encoding process determines their subsequent preferences. Infants were theorized to exhibit a preference for stimuli that were partially—but not fully—encoded into memory (e.g., Dember and Earl, 1957; Hunter and Ames, 1988; Kinney and Kagan, 1976; Roder et al., 2000; Rose et al., 1982; Wagner and Sakovits, 1986). This idea recalls the fact that we are curious about things of which we are moderately certain (Kang et al., 2009).

Among these theories was Kinney and Kagan's moderate discrepancy hypothesis, which suggested that infants preferentially attend to stimuli that were "optimally discrepant," meaning those that were just the right amount of distinguishable from mental representations the infant already possessed (Kinney and Kagan, 1976). Under Dember and Earl's theory of choice/preference, learners seek stimuli that match their preferred level of complexity, which increases over time as they build up mental representations and acquire more knowledge (Dember and Earl, 1957). Similarly, Berlyne (1960) noted that complexity-driven preferences could represent an optimal strategy for learning. Such processing-based theories of curiosity predict that learners will exhibit a U-shaped pattern of preference for stimulus complexity, where complexity is defined in terms of the learner's current set of mental representations. The theories predict that learners will preferentially select stimuli of an intermediate level of complexity—material that is neither overly simple (already encoded into memory) nor overly complex (too disparate from existing representations already encoded into memory).

Recent infant research supports these accounts (e.g., Kidd et al., 2012, 2014; Figure 4). We showed 7- and 8-month-old infants visual event sequences of varying complexity, as measured by an idealized learning model, and measured points at which infants' attention drifted (as indicated by looks away from the display). We found that the infants' probability of looking away was greatest to events of either very low information con-

tent (highly predictable) or very high information content (highly surprising). This attentional strategy holds in multiple types of visual displays (Kidd et al., 2012), for auditory stimuli (Kidd et al., 2014), and even within individual infants (Piantadosi et al., 2014). These results suggest that infants implicitly decide to direct attention to maintain intermediate rates of information absorption. This attentional strategy likely prevents them from wasting cognitive resources on overly predictable or overly complex events, therefore helping to maximize their learning potential.

Related findings show that children structure their play in a way that reduces uncertainty and allows them to discover causal structures in the world (e.g., Schulz and Bonawitz, 2007). This work is in line with the earlier theories of Jean Piaget that asserted that the purpose of curiosity and play was to "construct knowledge" through interactions with the world (Piaget, 1945). If curiosity aims to reduce uncertainty in the world, then we would expect learners to exhibit increased curiosity to stimuli in the world that they do not understand. In fact, this is a behavior that is well attested in recent developmental psychology studies, such as work by Bonawitz et al., 2012), which demonstrates that children prefer to play with toys that violate their expectations. Children also exhibit increased curiosity outside of pedagogical contexts in the absence of explicitly given explanations (Bonawitz et al., 2011). In an experiment in which Bonawitz et al. (2011) gave children a novel toy to explore, either prefaced or not with partial instructions on how the toy works, children played for longer and discovered more of the toys' functions under the non-pedagogical conditions.

In line with the idea that the function of curiosity is to reduce uncertainty, children exhibit increased interest in situations with high degrees of uncertainty, such as preferentially playing with toys whose underlying mechanisms are not yet understood. Perhaps even more impressively, Schulz and Bonawitz (2007) found that children preferentially engaged with toys that allowed them to deconfound potential causal variables underlying the

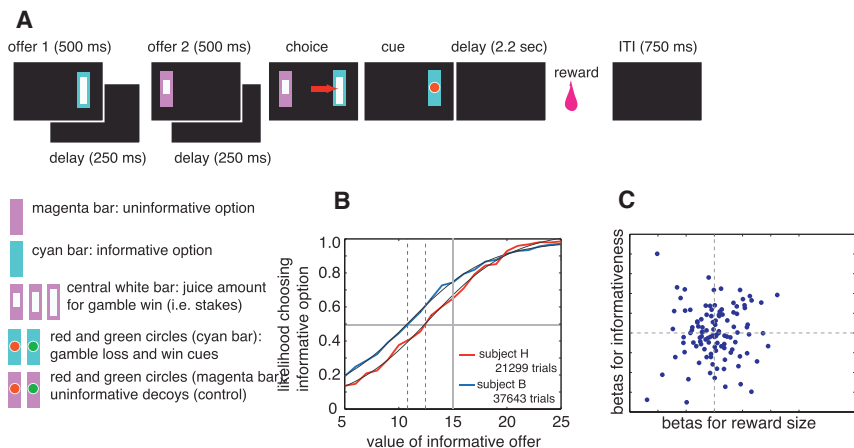


**Figure 5. Curiosity Tradeoff Task**

(A) In the curiosity tradeoff task, subjects choose between two gambles that vary in informativeness (cyan versus magenta) and gamble stakes (the size of the white inset bar). In each trial, two gambles appear in sequence on a computer screen (indicated by a black rectangle). When both options appear, subjects shift their gaze to one to select it. Then, after 2.25 s, they receive a juice reward. Following choice of the informative option, they receive a cue telling them whether they get the reward (50% chance). Following choice of the uninformative option, subjects get not valid information.

(B) Two subjects both showed a preference for informative options (indicated by a left shift of the psychometric curve) over uninformative ones despite the fact that this information provided no strategic benefit.

(C) In this task, OFC does not integrate value because of information (vertical axis) with value because of reward size (horizontal axis).

toys' inner workings. In these experiments, Schulz and Bonawitz (2007) had children play with toys consisting of boxes and levers. Under both the confounded and unconfounded conditions, the researcher would help a child play with a red box with two levers. Under the confounded condition, the researcher and the child each pressed down on a lever at the same time, and, in response, two small puppets (a chick and a pom-pom) popped out of the top of the red box (Figure 5). The puppets' location—dead center—was not informative about which of the two levers caused each one to rise. Under the unconfounded conditions, the researcher and child took turns pressing down on their respective levers one at a time or the researcher demonstrated each lever independently. Therefore, in both cases, it was clear which lever controlled each puppet. After this demonstration, the researcher uncovered a second, yellow box. After the demonstration and yellow box reveal, children were left alone and instructed to play in the researcher's absence for 60 s. During this period, children in the confounded condition preferentially explored the demonstrated red box over the novel yellow one.

The idea that children structure their play in a way that is sensitive to information gain is further bolstered by a recent study by Cook et al., (2011). They manipulated the ambiguity of various causal variables for a toy box that played music when certain—but not all—beads were placed on top of it. A researcher initially demonstrated how the box worked by placing a pair of connected beads on top, thereby making it ambiguous which of the two beads was causally responsible for the music playing. Children were effective at both selecting and designing informative interventions to figure out the underlying causal structure when it was unclear from the demonstration. When given ambiguous evidence, children tested individual beads when possible, and—even more impressively—when the bead pair was permanently stuck together, children held it so that only one side was touching the box to isolate the effect of that particular bead on the box.

This hypothesis-testing behavior is now widely attested in the developmental psychology literature. Children appear to structure their play to deconfound variables when causal mechanisms at play in the world are unclear (e.g., Denison et al., 2013; Gopnik et al., 1999; Gweon et al., 2014; Schulz et al.,

2007; van Schijndel et al., 2015) and also make efficient use of information that they encounter in the world to learn correct causal structures (e.g., Gopnik and Schulz, 2007; Gopnik et al., 2001). These findings are important because they highlight the fact that children's curiosity appears specifically well suited to teaching them about the causal structure of the world. Therefore, these strategic information-seeking behaviors in young children are far more sophisticated than the simple attentional heuristics that characterize early infant attention.

## Conclusions

Curiosity has long fascinated laymen and scholars alike but remains poorly understood as a psychological phenomenon. We argue that one factor impeding our understanding has been too much focus on delineating what is and is not curiosity. Another has been too much emphasis on taxonomy. These divide-then-conquer approaches are premature because they do not rely on empirical data. Perhaps the plethora of definitions and schemes attests more to differences in scholars' intuitions than to differences in their data. Therefore, we recommend that the definition stage should follow a relatively solid characterization of curiosity, defined as broadly as possible. For this reason, we are reluctant to commit to a strict definition now. This approach has risks, of course. It means that there will be a variety of studies using similar terms to describe different phenomena, and different terms to describe the same phenomena, which can be confusing. Nonetheless, we think the benefits of open-mindedness outweigh the costs.

Broadening the scope of inquiry has several advantages. First, it allows us to study information-seeking in non-humans, including monkeys, rats, and even roundworms. Animal techniques allow for a granular view of mechanism, a greater range of manipulations, and cross-species comparisons. Second, it allows us to temporarily put aside speculation about decision-makers' motivations and focus on other questions, by refusing to isolate curiosity from other cognitive processes, we can make bridges with other phenomena, especially reward and learning. Finally, it lets us take advantage of powerful new tasks invented in the past decade for studying the cognitive neuroscience of information-seeking.

Tinbergen's four questions are designed to provide a way to explain the causes of any behavior. This approach already provides a convenient framework for considering the knowledge we have so far. In the domain of function, it seems clear that curiosity serves to motivate the acquisition of knowledge and learning. In the domain of evolution, it seems that curiosity can tentatively be said to improve performance, yielding fitness benefits to organisms with it, and is likely to be an evolved trait. In the domain of mechanisms, it seems that the drive for information augments internal representations of value, therefore biasing decision-makers toward informative options and actions. It also seems that curiosity activates learning systems in the brain. In the domain of development, we can infer that curiosity is critical for learning and that it reflects both external features and internal representations of own knowledge.

In the future we hope to see answers to some of these questions:

- In what ways does curiosity resemble other basic drive states? How does it differ? To what extent is curiosity fundamentally different from drives like hunger and thirst?
- What is the most useful taxonomy of curiosity? How well does Berlyne's categorization hold up? Which factors unite distinct forms of curiosity?
- How is curiosity controlled? Which factors govern curiosity, and how does the brain integrate these factors into decision-making to produce decisions? To what extent is curiosity context-dependent?
- To what extent does curiosity in nematodes overlap (if at all) with curiosity in children? How useful is it to think of curiosity as being a single construct across a broad range of taxa?
- Does our continuing curiosity in adulthood serve a purpose or is it vestigial? Does continued curiosity serve to maintain cognitive abilities throughout adulthood?
- What is the link between curiosity and learning?
- Why and how is curiosity affected by diseases like depression and ADHD? Can sensitive measures of curiosity be used to predict and measure cognitive decline, senility, and Alzheimer's disease?

We can already sketch out rough guesses about how some of these questions will be answered. For example, we anticipate that, although useful in the past, Berlyne's categories will be replaced with other, differently formulated subtypes and that these newer ones will be motivated by new neural and developmental data. We suspect that curiosity serves a similar purpose in adulthood as it does in childhood, albeit, perhaps, in a more refined way. Even as adults we need to continue to adjust our understanding of the world. Finally, we are optimistic that scientists will eventually uncover a consistent set of principles that characterize curiosity across a wide range of taxa.

#### ACKNOWLEDGMENTS

This research was supported by a grant from the NIH, R01 (DA038615) (to B.Y.H.). We thank Sarah Heilbronner, Steve Piantadosi, Shradha Shah, Maya Wang, Habiba Azab, and Maddie Pelz for helpful comments.

#### REFERENCES

- Aslin, R.N., and Shea, S.L. (1990). Velocity thresholds in human infants: implications for the perception of motion. *Dev. Psychol.* *26*, 589–598.
- Averbeck, B.B. (2015). Theory of choice in bandit, information sampling and foraging tasks. *PLoS Comput. Biol.* *11*, e1004164.
- Baldwin, D.A. (1993). Infants' ability to consult the speaker for clues to word reference. *J. Child Lang.* *20*, 395–418.
- Berlyne, D.E. (1954). A theory of human curiosity. *Br. J. Psychol.* *45*, 180–191.
- Berlyne, D.E. (1960). *Conflict, Arousal, and Curiosity* (McGraw-Hill).
- Berlyne, D.E. (1966). Curiosity and exploration. *Science* *153*, 25–33.
- Berlyne, D.E. (1978). Curiosity and learning. *Motiv. Emot.* *2*, 97–175.
- Blanchard, T.C., and Hayden, B.Y. (2014). Neurons in dorsal anterior cingulate cortex signal postdecisional variables in a foraging task. *J. Neurosci.* *34*, 646–655.
- Blanchard, T.C., Hayden, B.Y., and Bromberg-Martin, E.S. (2015). Orbitofrontal cortex uses distinct codes for different choice attributes in decisions motivated by curiosity. *Neuron* *85*, 602–614.
- Bonawitz, E.B., Shafto, P., Gweon, H., Goodman, N., Spelke, E., and Schulz, L.E. (2011). The double-edged sword of pedagogy: Instruction limits spontaneous exploration and discovery. *Cognition* *120*, 322–330.
- Bonawitz, E.B., van Schijndel, T., Friel, D., and Schulz, L. (2012). Children balance theories and evidence in exploration, explanation, and learning. *Cognit. Psychol.* *64*, 215–234.
- Bromberg-Martin, E.S., and Hikosaka, O. (2009). Midbrain dopamine neurons signal preference for advance information about upcoming rewards. *Neuron* *63*, 119–126.
- Bromberg-Martin, E.S., and Hikosaka, O. (2011). Lateral habenula neurons signal errors in the prediction of reward information. *Nat. Neurosci.* *14*, 1209–1216.
- Bromberg-Martin, E.S., Matsumoto, M., and Hikosaka, O. (2010). Dopamine in motivational control: rewarding, aversive, and alerting. *Neuron* *68*, 815–834.
- Bushnell, E.W., Sai, F., and Mullin, J.T. (1989). Neonatal recognition of the mother's face. *Br. J. Dev. Psychol.* *7*, 3–15.
- Butler, R.A. (1953). Discrimination learning by rhesus monkeys to visual-exploration motivation. *J. Comp. Physiol. Psychol.* *46*, 95–98.
- Calhoun, A.J., Chalasani, S.H., and Sharpee, T.O. (2014). Maximally informative foraging by *Caenorhabditis elegans*. *eLife* *3*, e04220.
- Cook, C., Goodman, N.D., and Schulz, L.E. (2011). Where science starts: spontaneous experiments in preschoolers' exploratory play. *Cognition* *120*, 341–349.
- Davis, R.T., Settlage, P.H., and Harlow, H.F. (1950). Performance of normal and brain-operated monkeys on mechanical puzzles with and without food incentive. *J. Genet. Psychol.* *77*, 305–311.
- Daw, N.D., O'Doherty, J.P., Dayan, P., Seymour, B., and Dolan, R.J. (2006). Cortical substrates for exploratory decisions in humans. *Nature* *441*, 876–879.
- Day, H.I. (1971). The measurement of specific curiosity. In *Intrinsic Motivation: A New Direction in Education*, H.I. Day, D.E. Berlyne, and D.E. Hunt, eds. (Holt, Rinehart & Winston).
- de Quervain, D.J.F., Fischbacher, U., Treyer, V., Schellhammer, M., Schnyder, U., Buck, A., and Fehr, E. (2004). The neural basis of altruistic punishment. *Science* *305*, 1254–1258.
- DeCasper, A.J., and Spence, M.J. (1986). Prenatal maternal speech influences newborns' perception of speech sounds. *Infant Behav. Dev.* *9*, 133–150.
- Deci, E.L. (1975). *Intrinsic Motivation* (Plenum).
- Delgado, M.R., Nystrom, L.E., Fissell, C., Noll, D.C., and Fiez, J.A. (2000). Tracking the hemodynamic responses to reward and punishment in the striatum. *J. Neurophysiol.* *84*, 3072–3077.

- Delgado, M.R., Locke, H.M., Stenger, V.A., and Fiez, J.A. (2003). Dorsal striatum responses to reward and punishment: effects of valence and magnitude manipulations. *Cogn. Affect. Behav. Neurosci.* *3*, 27–38.
- Delgado, M.R., Schotter, A., Ozbay, E.Y., and Phelps, E.A. (2008). Understanding overbidding: using the neural circuitry of reward to design economic auctions. *Science* *321*, 1849–1852.
- Dember, W.N. (1956). Response by the rat to environmental change. *J. Comp. Physiol. Psychol.* *49*, 93.
- Dember, W.N., and Earl, R.W. (1957). Analysis of exploratory, manipulatory, and curiosity behaviors. *Psychol. Rev.* *64*, 91–96.
- Denison, S., Bonawitz, E., Gopnik, A., and Griffiths, T.L. (2013). Rational variability in children's causal inferences: the Sampling Hypothesis. *Cognition* *126*, 285–300.
- Dyer, F.C. (1991). Bees acquire route-based memories but not cognitive maps in a familiar landscape. *Animal Behav.* *41*, 239–246.
- Engel, S. (2011). Children's need to know: curiosity in schools. *Harv. Educ. Rev.* *81*, 625–645.
- Engel, S. (2015). *The Hungry Mind: The Origins of Curiosity in Childhood* (Harvard University Press).
- Fant, R.L. (1964). Visual experience in infants: decreased attention to familiar patterns relative to novel ones. *Science* *146*, 668–670.
- Farroni, T., Johnson, M.H., Menon, E., Zulian, L., Faraguna, D., and Csibra, G. (2005). Newborns' preference for face-relevant stimuli: effects of contrast polarity. *Proc. Natl. Acad. Sci. USA* *102*, 17245–17250.
- Fehr, E., and Camerer, C.F. (2007). Social neuroeconomics: the neural circuitry of social preferences. *Trends Cogn. Sci.* *11*, 419–427.
- Gipson, C.D., Alessandri, J.J., Miller, H.C., and Zentall, T.R. (2009). Preference for 50% reinforcement over 75% reinforcement by pigeons. *Learn. Behav.* *37*, 289–298.
- Gittins, J., and Jones, D. (1974). *Progress in Statistics* (North-Holland).
- Gopnik, A. and Schulz, L., eds. (2007). *Causal Learning: Psychology, Philosophy, and Computation* (Oxford University Press).
- Gopnik, A., Meltzoff, A.N., and Kuhl, P.K. (1999). *The Scientist in the Crib: Minds, Brains, & How Children Learn* (William Morrow & Co.).
- Gopnik, A., Sobel, D.M., Schulz, L.E., and Glymour, C. (2001). Causal learning mechanisms in very young children: two-, three-, and four-year-olds infer causal relations from patterns of variation and covariation. *Dev. Psychol.* *37*, 620–629.
- Gottlieb, J. (2012). Attention, learning, and the value of information. *Neuron* *76*, 281–295.
- Gottlieb, J., Oudeyer, P.-Y., Lopes, M., and Baranes, A. (2013). Information-seeking, curiosity, and attention: computational and neural mechanisms. *Trends Cogn. Sci.* *17*, 585–593.
- Gottlieb, J., Hayhoe, M., Hikosaka, O., and Rangel, A. (2014). Attention, reward, and information seeking. *J. Neurosci.* *34*, 15497–15504.
- Gould, J.L. (1986). The locale map of honey bees: do insects have cognitive maps? *Science* *232*, 861–863.
- Gray, P. (2013). *Free to Learn: Why Unleashing the Instinct to Play Will Make Our Children Happier, More Self-Reliant, and Better Students for Life* (Basic Books).
- Gruber, M.J., Gelman, B.D., and Ranganath, C. (2014). States of curiosity modulate hippocampus-dependent learning via the dopaminergic circuit. *Neuron* *84*, 486–496.
- Gureckis, T.M., and Markant, D.B. (2012). Self-Directed Learning: A Cognitive and Computational Perspective. *Perspect. Psychol. Sci.* *7*, 464–481.
- Gweon, H., Pelton, H., Konopka, J.A., and Schulz, L.E. (2014). Sins of omission: children selectively explore when teachers are under-informative. *Cognition* *132*, 335–341.
- Haith, M.M. (1980). *Rules That Babies Look By* (L. Erlbaum Associates).
- Hall, G.S., and Smith, T.L. (1903). Curiosity and interest. *Pedagogical Seminary* *10*, 315–358.
- Harlow, H.F. (1950). Learning and satiation of response in intrinsically motivated complex puzzle performance by monkeys. *J. Comp. Physiol. Psychol.* *43*, 289–294.
- Harlow, H.F., and McClearn, G.E. (1954). Object discrimination learned by monkeys on the basis of manipulation motives. *J. Comp. Physiol. Psychol.* *47*, 73.
- Harlow, H.F., Blazek, N.C., and McClearn, G.E. (1956). Manipulatory motivation in the infant rhesus monkey. *J. Comp. Physiol. Psychol.* *49*, 444.
- Harlow, H.F., Harlow, M.K., and Meyer, D.R. (1950). Learning motivated by a manipulation drive. *J. Exp. Psychol.* *40*, 228–234.
- Harty, H., and Beall, D. (1984). Toward the development of a children's science curiosity measure. *J. Res. Sci. Teach.* *21*, 425–436.
- Hayden, B.Y., Nair, A.C., McCoy, A.N., and Platt, M.L. (2008). Posterior cingulate cortex mediates outcome-contingent allocation of behavior. *Neuron* *60*, 19–25.
- Hayden, B.Y., Pearson, J.M., and Platt, M.L. (2009). Fictive reward signals in the anterior cingulate cortex. *Science* *324*, 948–950.
- Heilbronner, S.R., and Hayden, B.Y. (2013). Contextual factors explain risk-seeking preferences in rhesus monkeys. *Front. Neurosci.* *7*, 7.
- Heilbronner, S.R., and Platt, M.L. (2013). Causal evidence of performance monitoring by neurons in posterior cingulate cortex during learning. *Neuron* *80*, 1384–1391.
- Heilbronner, S.R., Hayden, B.Y., and Platt, M.L. (2011). Decision salience signals in posterior cingulate cortex. *Front. Neurosci.* *5*, 55.
- Horvitz, J.C. (2000). Mesolimbocortical and nigrostriatal dopamine responses to salient non-reward events. *Neuroscience* *96*, 651–656.
- Hughes, R.N. (1968). Behaviour of male and female rats with free choice of two environments differing in novelty. *Anim. Behav.* *16*, 92–96.
- Hunter, M.A., and Ames, E.W. (1988). A multifactor model of infant preferences for novel and familiar stimuli. *Adv. Infancy Res.* *5*, 69–95.
- James, W. (1899). *Talks to Teachers on Psychology: And to Students on Some of Life's Ideals* (Henry Holt & Company).
- James, W. (1913). *The Principles of Psychology, Volume II* (Henry Holt & Company).
- Jepma, M., Verdonschot, R.G., van Steenbergen, H., Rombouts, S.A.R.B., and Nieuwenhuis, S. (2012). Neural mechanisms underlying the induction and relief of perceptual curiosity. *Front. Behav. Neurosci.* *6*, 5.
- Jirout, J., and Klahr, D. (2012). Children's scientific curiosity: in search of an operational definition of an elusive concept. *Dev. Rev.* *32*, 125–160.
- Johnson, M.H., Dziurawiec, S., Ellis, H., and Morton, J. (1991). Newborns' preferential tracking of face-like stimuli and its subsequent decline. *Cognition* *40*, 1–19.
- Kang, M.J., Hsu, M., Krajbich, I.M., Loewenstein, G., McClure, S.M., Wang, J.T.Y., and Camerer, C.F. (2009). The wick in the candle of learning: epistemic curiosity activates reward circuitry and enhances memory. *Psychol. Sci.* *20*, 963–973.
- Kemler Nelson, D.G., Jusczyk, P.W., Mandel, D.R., Myers, J., Turk, A., and Gerken, L. (1995). The head-turn preference procedure for testing auditory perception. *Infant Behav. Dev.* *18*, 111–116.
- Kidd, C., Piantadosi, S.T., and Aslin, R.N. (2012). The Goldilocks effect: human infants allocate attention to visual sequences that are neither too simple nor too complex. *PLoS ONE* *7*, e36399.
- Kidd, C., Piantadosi, S.T., and Aslin, R.N. (2014). The Goldilocks effect in infant auditory attention. *Child Dev.* *85*, 1795–1804.

- King-Casas, B., Tomlin, D., Anen, C., Camerer, C.F., Quartz, S.R., and Montague, P.R. (2005). Getting to know you: reputation and trust in a two-person economic exchange. *Science* 308, 78–83.
- Kinney, D.K., and Kagan, J. (1976). Infant attention to auditory discrepancy. *Child Dev.* 47, 155–164.
- Kivy, P.N., Earl, R.W., and Walker, E.L. (1956). Stimulus context and satiation. *J. Comp. Physiol. Psychol.* 49, 90.
- Knutson, B., Adams, C.M., Fong, G.W., and Hommer, D. (2001). Anticipation of increasing monetary reward selectively recruits nucleus accumbens. *J. Neurosci.* 21, RC159.
- Kreps, D.M., and Porteus, E.L. (1978). Temporal resolution of uncertainty and dynamic choice theory. *Econometrica* 46, 185–200.
- Lieberman, D.A., Cathro, J.S., Nichol, K., and Watson, E. (1997). The role of S- in human observing behavior: bad news is sometimes better than no news. *Learn. Motiv.* 28, 20–42.
- Loewenstein, G. (1994). The psychology of curiosity: a review and reinterpretation. *Psychol. Bull.* 116, 75–98.
- Luhmann, C.C., Chun, M.M., Yi, D.J., Lee, D., and Wang, X.J. (2008). Neural dissociation of delay and uncertainty in intertemporal choice. *J. Neurosci.* 28, 14459–14466.
- Matsumoto, M., and Hikosaka, O. (2009). Two types of dopamine neuron distinctly convey positive and negative motivational signals. *Nature* 459, 837–841.
- Monosov, I.E., and Hikosaka, O. (2012). Regionally distinct processing of rewards and punishments by the primate ventromedial prefrontal cortex. *J. Neurosci.* 32, 10318–10330.
- Najemnik, J., and Geisler, W.S. (2005). Optimal eye movement strategies in visual search. *Nature* 434, 387–391.
- O’Keefe, J., and Nadel, L. (1978). *The Hippocampus as a Cognitive Map* (Oxford, UK: Clarendon Press).
- O’Neill, M., and Schultz, W. (2010). Coding of reward risk by orbitofrontal neurons is mostly distinct from coding of reward value. *Neuron* 68, 789–800.
- Öngür, D., and Price, J.L. (2000). The organization of networks within the orbital and medial prefrontal cortex of rats, monkeys and humans. *Cereb. Cortex* 10, 206–219.
- Oudeyer, P.-Y., and Kaplan, F. (2007). What is intrinsic motivation? A typology of computational approaches. *Front. Neurobot.* 1, 6.
- Pavlov, I.P. (1927). *Conditioned Reflexes: An Investigation of the Physiological Activity of the Cerebral Cortex* (Oxford University Press).
- Pearson, J.M., Hayden, B.Y., Raghavachari, S., and Platt, M.L. (2009). Neurons in posterior cingulate cortex signal exploratory decisions in a dynamic multioption choice task. *Curr. Biol.* 19, 1532–1537.
- Pearson, J.M., Heilbronner, S.R., Barack, D.L., Hayden, B.Y., and Platt, M.L. (2011). Posterior cingulate cortex: adapting behavior to a changing world. *Trends Cogn. Sci.* 15, 143–151.
- Pelz, M., Yung, A., and Kidd, C. (2015). Quantifying curiosity and exploratory play on touchscreen tablets. G. Gordon, J. Jirout, S. Engel, and A. Chang, eds. *Proceedings of the IDC 2015 Workshop on Digital Assessment and Promotion of Children’s Curiosity*, <http://www.bcs.rochester.edu/people/mpelz/PelzYungKiddIDC2015.pdf>.
- Penney, R.K., and McCann, B. (1964). The children’s reactive curiosity scale. *Psychol. Rep.* 15, 323–334.
- Phillips, K.A., Subiaul, F., and Sherwood, C.C. (2012). Curious monkeys have increased gray matter density in the precuneus. *Neurosci. Lett.* 518, 172–175.
- Piaget, J. (1945). *Play, Dreams, and Imitation in Childhood* (Heinemann).
- Piantadosi, S.T., Kidd, C., and Aslin, R. (2014). Rich analysis and rational models: inferring individual behavior from infant looking data. *Dev. Sci.* 17, 321–337.
- Prokasy, W.F., Jr. (1956). The acquisition of observing responses in the absence of differential external reinforcement. *J. Comp. Physiol. Psychol.* 49, 131–134.
- Redgrave, P., and Gurney, K. (2006). The short-latency dopamine signal: a role in discovering novel actions? *Nat. Rev. Neurosci.* 7, 967–975.
- Rilling, J., Gutman, D., Zeh, T., Pagnoni, G., Berns, G., and Kilts, C. (2002). A neural basis for social cooperation. *Neuron* 35, 395–405.
- Roder, B.J., Bushnell, E.W., and Sasseville, A.M. (2000). Infants’ preferences for familiarity and novelty during the course of visual processing. *Infancy* 1, 491–507.
- Rose, S.A., Gottfried, A.W., Melloy-Carminar, P., and Bridger, W.H. (1982). Familiarity and novelty preferences in recognition memory: implications for information processing. *Dev. Psychol.* 18, 704–713.
- Rushworth, M.F.S., Noonan, M.P., Boorman, E.D., Walton, M.E., and Behrens, T.E. (2011). Frontal cortex and reward-guided learning and decision-making. *Neuron* 70, 1054–1069.
- Salapatek, P., and Kessen, W. (1966). Visual scanning of triangles by the human newborn. *J. Exp. Child Psychol.* 3, 155–167.
- Schoenbaum, G., Takahashi, Y., Liu, T.L., and McDannald, M.A. (2011). Does the orbitofrontal cortex signal value? *Ann. N Y Acad. Sci.* 1239, 87–99.
- Schultz, W., and Dickinson, A. (2000). Neuronal coding of prediction errors. *Annu. Rev. Neurosci.* 23, 473–500.
- Schultz, W., Dayan, P., and Montague, P.R. (1997). A neural substrate of prediction and reward. *Science* 275, 1593–1599.
- Schulz, L., and Bonawitz, E.B. (2007). Serious fun: preschoolers engage in more exploratory play when evidence is confounded. *Dev. Psychol.* 43, 1045–1050.
- Schulz, L.E., Gopnik, A., and Glymour, C. (2007). Preschool children learn about causal structure from conditional interventions. *Dev. Sci.* 10, 322–332.
- Siqueland, E.R., and DeLucia, C.A. (1969). Visual reinforcement of nonnutritive sucking in human infants. *Science* 165, 1144–1146.
- Skinner, B.F. (1938). *The Behavior of Organisms: An Experimental Analysis* (Appleton-Century).
- So, N., and Stuphorn, V. (2012). Supplementary eye field encodes reward prediction error. *J. Neurosci.* 32, 2950–2963.
- Sokolov, E. (1963). *Perception and the Conditioned Reflex* (Pergamon).
- Stagner, J.P., and Zentall, T.R. (2010). Suboptimal choice behavior by pigeons. *Psychon. Bull. Rev.* 17, 412–416.
- Strait, C.E., Blanchard, T.C., and Hayden, B.Y. (2014). Reward value comparison via mutual inhibition in ventromedial prefrontal cortex. *Neuron* 82, 1357–1366.
- Strait, C.E., Slezzer, B.J., and Hayden, B.Y. (2015). Signatures of value comparison in ventral striatum neurons. *PLoS Biol.* 13, e1002173.
- Sutton, R.S., and Barto, A.G. (1998). *Introduction to Reinforcement Learning* (MIT Press).
- Takahashi, Y.K., Roesch, M.R., Wilson, R.C., Toreson, K., O’Donnell, P., Niv, Y., and Schoenbaum, G. (2011). Expectancy-related changes in firing of dopamine neurons depend on orbitofrontal cortex. *Nat. Neurosci.* 14, 1590–1597.
- Tinbergen, N. (1963). On aims and methods of ethology. *Z. Tierpsychol.* 20, 410–433.
- Tolman, E.C. (1948). Cognitive maps in rats and men. *Psychol. Rev.* 55, 189–208.
- Tolman, E.C., and Gleitman, H. (1949). Studies in learning and motivation; equal reinforcements in both end-boxes; followed by shock in one end-box. *J. Exp. Psychol.* 39, 810–819.
- van Schijndel, T.J.P., Visser, I., van Bers, B.M.C.W., and Raijmakers, M.E.J. (2015). Preschoolers perform more informative experiments after observing theory-violating evidence. *J. Exp. Child Psychol.* 131, 104–119.

- Vergassola, M., Villermaux, E., and Shraiman, B.I. (2007). 'Infotaxis' as a strategy for searching without gradients. *Nature* 445, 406–409.
- Wagner, S.H., and Sakovits, L.J. (1986). A process analysis of infant visual and crossmodal recognition memory: implications for an amodal code. *Advances in Infancy Research* 4, 195–217.
- Wehner, R., Gallizzi, K., Frei, C., and Vesely, M. (2002). Calibration processes in desert ant navigation: vector courses and systematic search. *J. Comp. Physiol. A Neuroethol. Sens. Neural Behav. Physiol.* 188, 683–693.
- Whittle, P. (1988). Restless bandits: Activity allocation in a changing world. *J. Appl. Probab.* 25, 287–298.
- Wilson, R.C., Geana, A., White, J.M., Ludvig, E.A., and Cohen, J.D. (2014). Humans use directed and random exploration to solve the explore-exploit dilemma. *J. Exp. Psychol. Gen.* 143, 2074–2081.
- Wittmann, B.C., Daw, N.D., Seymour, B., and Dolan, R.J. (2008). Striatal activity underlies novelty-based choice in humans. *Neuron* 58, 967–973.
- Wyckoff, L.B., Jr. (1952). The role of observing responses in discrimination learning. *Psychol. Rev.* 59, 431–442.
- Yarbus, A.L. (1956). The motion of the eye in the process of changing points of fixation. *Biofizika* 1, 76–78.
- Zeil, J. (1998). Homing in fiddler crabs (*Uca lactea annulipes* and *Uca vomeris*: Ocypodidae). *J. Comp. Physiol. A Neuroethol. Sens. Neural Behav. Physiol.* 183, 367–377.
- Zentall, T.R., and Stagner, J. (2011). Maladaptive choice behaviour by pigeons: an animal analogue and possible mechanism for gambling (sub-optimal human decision-making behaviour). *Proc. Biol. Sci.* 278, 1203–1208.

# Neuroscience Training for the 21st Century

Huda Akil,<sup>1,\*</sup> Rita Balice-Gordon,<sup>2</sup> David Lopes Cardozo,<sup>3</sup> Walter Koroshetz,<sup>4</sup> Sheena M. Posey Norris,<sup>5</sup> Todd Sherer,<sup>6</sup> S. Murray Sherman,<sup>7</sup> and Edda Thiels<sup>8</sup>

<sup>1</sup>University of Michigan, Ann Arbor, MI 48109, USA

<sup>2</sup>Neuroscience and Pain Research Unit, Pfizer, Inc., Cambridge, MA 02139, USA

<sup>3</sup>Harvard Medical School, Boston, MA 02115, USA

<sup>4</sup>National Institute of Neurological Disorders and Stroke, Bethesda, MD 20892, USA

<sup>5</sup>Forum on Neuroscience and Nervous System Disorders, National Academies of Sciences, Engineering, and Medicine, Washington, DC 20001, USA

<sup>6</sup>The Michael J. Fox Foundation for Parkinson's Research, New York, NY 10163, USA

<sup>7</sup>The University of Chicago, Chicago, IL 60637, USA

<sup>8</sup>National Science Foundation, Arlington, VA 22230, USA

\*Correspondence: akil@med.umich.edu

<http://dx.doi.org/10.1016/j.neuron.2016.05.030>

The field of neuroscience is enjoying a rapid expansion in scope, coupled with a remarkable broadening of conceptual approaches, scientific tools, and clinical applications. This growth poses new challenges for academic training programs as they prepare young neuroscientists for a more complex, competitive, and diverse career landscape. Multiple stakeholders, including academia, federal funding agencies, industry, scientific societies, private foundations, and other public and private sector contributors, need to be actively engaged in supporting this broad training effort. A renewed commitment to a more forward-looking, flexible yet integrative training vision offers opportunities for a bright future for young neuroscientists as they assume the role of vanguard of the enterprise that enriches our understanding of the brain.

## Introduction

The brain is a remarkable piece of biological machinery that fascinates both scientists and the general public, while testing the limits of our ability to understand our own minds. Every facet of neural function requires intricate orchestration and ongoing fine-tuning and remodeling. Neural circuits exhibit an additional layer of integration that transcends the complexity of any given cell, with dynamic characteristics whose analysis requires sophisticated computation. It is not surprising that this machinery can malfunction in innumerable ways, leading to debilitating, sometimes devastating disorders across the lifespan. Thus, understanding the brain is both intrinsically fascinating and highly relevant to the well-being of humans and animals. It is often seen as the greatest challenge in the biosciences, possibly in all of modern science. Consequently, over the last two decades, the field of neuroscience has undergone a quiet revolution, redefining its boundaries beyond the biomedical sciences to incorporate knowledge and tools from physics, mathematics, and engineering, as well as the social sciences and the humanities.

The increasing integration between neuroscience and other scientific fields is having a major impact on the footprint of neuroscience both within and beyond the walls of academia. The influence of basic neuroscience research on biology and medicine continues to increase as advances in many areas are being translated into therapeutic approaches, including better tools for studying brain structure and function in health and disease; molecular analysis of receptors, ion channels, and broad molecular pathways; powerful approaches to examine and manipulate neural circuits; and more sophisticated electrophysiological strategies to monitor and modify neural function. Recently, there has been a trend to focus more resources in the pursuit of neuroscience research, as seen in a number of developments such as the

Brain Research through Advancing Innovative Neurotechnologies (BRAIN) initiative (<https://www.whitehouse.gov/share/brain-initiative>) and research priorities seen in other countries (e.g., China Brain; Japan Brain/MINDS Project, <http://brainminds.jp/en/>; and the Human Brain Project in Europe, <https://www.humanbrainproject.eu/>). Moreover, there is an increasing need to communicate neuroscience information at all levels, from editing scholarly journals to educating the general public. On a national level, there is an ever-increasing need for informed regulators and policy makers.

The growth of the field, together with its commercialization of new products and services, will result in the expansion of career opportunities in the public and private sector, including bench scientists, entrepreneurs, analysts, consultants, and intellectual property experts. Given that the number of PhDs in neuroscience has risen much more rapidly than in any other field of biomedical research in the United States (see Figure 1), one challenge we must address is whether training programs are meeting the current and future workforce needs of the field. Clearly, we need to attract the best and the brightest from diverse backgrounds to take on the task of understanding the brain. The challenge before us is how to train and retain a talented work force to ensure a bright future both for neuroscience in general and for the individual young scientists entering the field. The discussion below focuses primarily on the landscape in the United States, although we would venture to guess that many of the same trends, challenges, and opportunities exist globally.

## Developing the Expertise Needed to Advance Neuroscience in the 21st Century

In October 2014, the Forum on Neuroscience and Nervous System Disorders of the National Academies of Sciences,

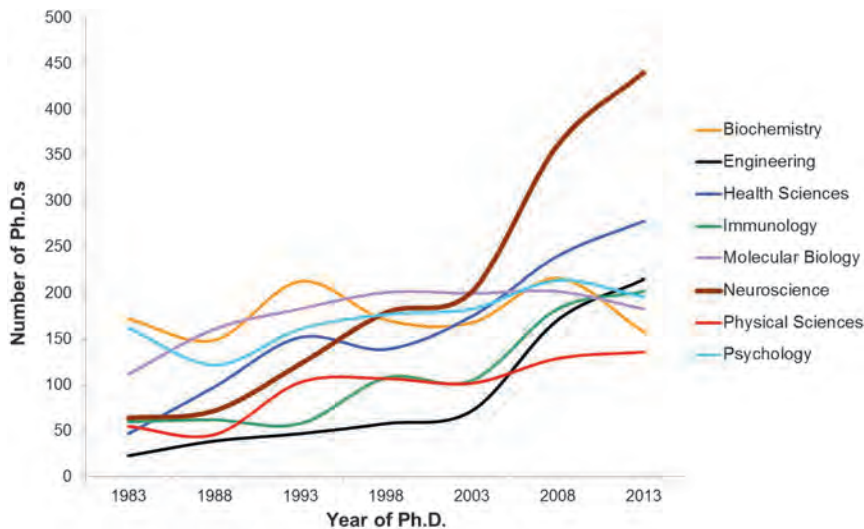


**Figure 1. Trends in Fields of Study of Trainees and Fellows Receiving Ph.D.s**

Data taken from the NIH Office of Extramural Research (OER) Training and Advisory Committee June 2015 meeting on education and selected career outcomes of graduate trainees and fellows.

Engineering, and Medicine held a workshop on how best to develop the next generation of scientists to advance neuroscience (IOM, 2014). Neuroscience was characterized as fundamentally interdisciplinary and currently in a stage that requires greater incorporation of computational science, applied mathematics, and engineering. This raises two major challenges that are not new but are increasingly important: (1) how to best impart rigorous quantitative, analytic, and statistical skills required by emerging technologies among trainees in neuroscience, and (2) how to best integrate scientists from different disciplines into neuroscience.

#### **Strengthening Experimental, Analytical, and Communication Skills**

A challenge currently being addressed across the biomedical sciences is the need to improve the quality of published work. Improved training is probably the most important means to achieve this goal. A deep understanding of the statistical basis for interpreting experimental data needs to drive not only the analysis but also the design of experiments. Robust science requires rigorous experimental design, including blinded allocation to groups, blinded assessment of outcomes, prospective sample size calculations, and prospective accounting for exclusion of outliers. This is in particular true for animal experiments, but also applies to in vitro and cell-based experiments. Although a generic statistics course is commonly included in neuroscience graduate programs, very few programs include statisticians on their faculty. A more intensive and disciplined effort to improve the level of statistical reasoning and facility with statistical methods should be a high training priority for the future.

Data analytics have become increasingly complex, and to exploit these tools appropriately, training in areas such as programming, data management platforms, multi-dimensional cloud computing, data visualization and feature extraction, algorithm development, machine learning, and computer modeling may be valuable for neuroscience trainees. Current experimental approaches, such as gene expression arrays, deep sequencing, multi-electrode recordings, and image analysis, all produce large datasets that pose challenging analytical problems. The interpre-

tion of these datasets demands more sophisticated quantitative skills to visualize complex, high-dimensional data and to perform appropriate statistical analyses. Moreover, many types of neuroscience data are not readily amenable to analysis by off-the-shelf software and thus require computational skills, including programming in high-level languages such as Python, “R,” or MATLAB. The majority of our graduate students lack these skills, and it is essential that we

revise our curricula to ensure that neuroscience students achieve competence in the area of computation and programming.

There are several potential points of intervention. Doctoral programs could require increased prerequisites in quantitative training on the part of applicants, especially in the area of statistics and programming. Additionally, individual programs should develop curricula to provide these necessary skills. Computational training can be jump-started by intensive instruction in a high-level programming language during pre-matriculation “boot camps,” thus allowing subsequent core courses to incorporate quantitative exercises that build on and reinforce these skills. Students can also take advantage of a plethora of web-based resources, such as massive open online courses (MOOCs). It would be helpful to the neuroscience community if there were some level of coordination of such resources, for instance, through the Society for Neuroscience (SfN).

Students are coming to neuroscience graduate programs with ever more sophisticated science backgrounds. Though a major benefit, one casualty may be the communication and writing skills of the neuroscience trainees, in spite of the fact that these skills are critical for a successful career in science. As neuroscience coursework has become increasingly common in undergraduate curricula and more students are arriving in graduate school with experience in the field, the graduate course requirements are decreasing and students move on to laboratory work earlier in their graduate training. While a positive development, this may lead to students focusing on a specialized domain earlier and potentially lead to gaps in training. It will be important to track whether abbreviation of a broad-based neuroscience experience in graduate school adversely affects the ability of neuroscientists to interact across fields. Certainly, attention to key items such as grant-writing skills, laboratory and office management, ethics in science, fundamental neuroscience knowledge and its history, teaching, and mentoring are important for all neuroscience trainees. As important, however, is the ability to understand other scientific languages—for example, biologically trained neuroscientists should receive sufficient mathematical training to communicate with informaticians and

**Box 1. NSF's Integrative Graduate Education and Research Traineeship Program**

NSF's IGERT program was initiated in 1998 to address the need for a workforce of PhD scientists and engineers with interdisciplinary backgrounds. The IGERT program supported research-based graduate training programs that integrate research and education around an interdisciplinary theme and empower their trainees not only with deep knowledge and research skills in a major field but also with the ability, breadth, and depth of knowledge and skills to participate in cross-disciplinary collaborations that require teamwork. Since its inception, the IGERT program has made 278 awards and provided funding for approximately 6,500 graduate students. Studies of the impact of IGERT programs indicate that the dissertation research of IGERT trainees is more interdisciplinary than that of non-IGERT trainees in similar academic departments, and that over 75% of IGERT graduates report using two or more disciplines in their post-PhD positions (Carney and Neishi, 2010). Moreover, more IGERT graduates than non-IGERT PhD graduates were found to consider their graduate training programs as having prepared them well for research faculty positions at universities, and, in agreement with that perception, more IGERT graduates (75%) than non-IGERT graduates (63%) identified their primary job responsibility after graduation to be research (Carney et al., 2011). An added positive effect of IGERT programs is that they also foster interdisciplinary collaborative research and interdisciplinary teaching by participant faculty (Carney et al., 2006). Based on their analyses of past IGERT projects, Gamse et al. (2013) offer valuable insights about interdisciplinary graduate training programs in STEM (science, technology, engineering, and mathematics) fields, including core competencies for conducting interdisciplinary research, and the challenges faced by as well as the most successful aspects of interdisciplinary, team-science-promoting graduate training programs such as IGERT programs. The success of IGERT projects focused on neuroscience demonstrates that application of the IGERT concept to the field of neuroscience is not only feasible but also fruitful and may present a useful path for meeting emergent neuroscience workforce needs while both preserving academic rigor and offering trainees greater professional flexibility.

The IGERT program, whose last competition was held in 2013, helped lay the foundation for the NSF Research Traineeship (NRT) program, launched in 2014. Similar to the IGERT program, and as described in more detail below, the NRT program emphasizes interdisciplinary graduate research training.

computational scientists. In turn, computational neuroscientists must translate ideas conceptually as a means of communicating with colleagues with less mathematical training.

**Fostering Transdisciplinary Training**

The growth in neuroscience has necessarily led to the development of an ever-increasing number of subfields, e.g., molecular, cellular, systems, behavioral, and translational neuroscience. The deepening silos within neuroscience carry the risk of slowing scientific advancement. More deliberate attention to promote cross-fertilization and communication across neuroscience fields is necessary in the 21st century with teams of scientists with different types of expertise working together to attack problems that would never be solved with a single approach. Likewise, the tools available for neuroscience research have become increasingly sophisticated. There is a growing need to “demystify” these tools by imparting to trainees a working knowledge of the underlying principles of their operation. Students need to be required to think deeply about the limits and utility of new tools and analytical techniques, exploring outside their departments to learn from experts and developers of new technologies. Some graduate programs may choose to focus on promoting skills required for team science that promote cross-disciplinary approaches to addressing research questions (Stokols et al., 2008), with tracks that integrate trainees with backgrounds in the physical, engineering, and/or computational sciences with biologists, or that provide more intensive experiences in clinical neuroscience, technology development, data analytics, and other facets of neurobiology. These new directions pose challenges for neuroscience training programs, including (1) what additional disciplines to incorporate, (2) what level of competence in additional disciplines to train, and (3) how to teach these additional disciplinary competences as well as an understanding

of and skill in team science. One potential solution would be for funding agencies that support graduate training programs, such as the NIH and the National Science Foundation (NSF), to encourage training programs in the neurosciences to incorporate in their curricula training in multiple disciplines. NSF's Integrative Graduate Education and Research Traineeship (IGERT) program may present a useful model (see Box 1).

Basic research is the foundation of the entire neuroscience enterprise. At the 2014 workshop hosted by the Forum on Neuroscience and Nervous System Disorders, several participants highlighted the importance of trainees who pursue careers in this area and for training programs to incorporate such training into their core courses. Equally important is enabling the process by which basic science discoveries add fundamental knowledge to the field and inform solutions for disabling neurological and psychiatric conditions. The process requires a cadre of investigators with a deep understanding of the complexity of the clinical disorders to engage in the very substantial research efforts on the neurobiology of disease. Building venues for mixing of basic neuroscience and clinical neuroscience training could promote translational potential of trainees from both the clinical and medical fields. The actual development of therapies or diagnostics that improve care of patients is as complex as any other field in neuroscience. For those interested in translation, special training is critical to avoid dedicating time and effort into “pseudo translation.” Training in teams that include biotechnology or industry partners, clinicians, patient advocates, experts in regulatory affairs, and bioethicists, among others, would foster more successful translation from the bench than in the past. The increasingly transdisciplinary future of neuroscience makes it difficult for any given program to excel in all these facets of training, and programs need to build their curricula to take

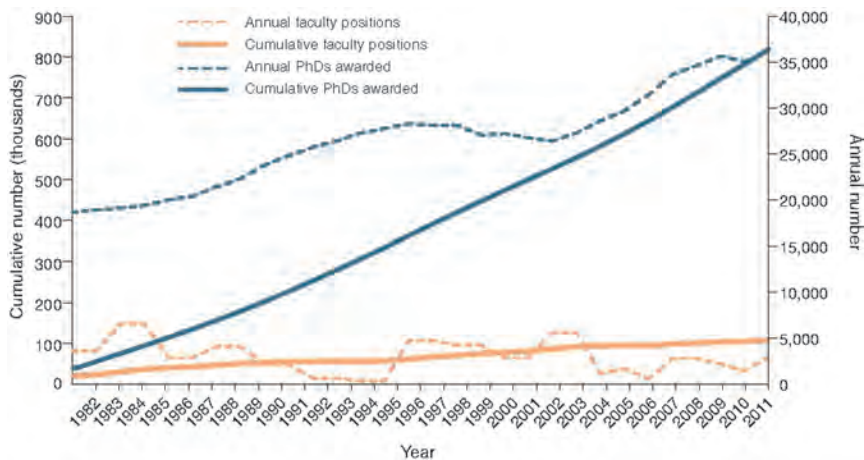


**Figure 2. New Faculty Positions versus New PhDs**

Since 1982, almost 800,000 PhDs were awarded in science and engineering (S&E) fields, whereas only about 100,000 academic faculty positions were created in those fields within the same time frame. The number of S&E PhDs awarded annually has also increased over this time frame, from ~19,000 in 1982 to ~36,000 in 2011. The number of faculty positions created each year, however, has not changed, with roughly 3,000 new positions created annually. Reprinted by permission from Macmillan Publishers Ltd (Schillebeeckx et al., 2013).

optimal advantage of the strengths within their institutions and in the surrounding environment. There may be value in considering the existence of two major types of training programs: those that are geared toward the more traditional training “of neuroscientists,” and new programs that train people from a variety of backgrounds “in neuroscience,” an approach seen in other disciplines (see Gould, 2015).

### Training for Different Career Opportunities

Students entering neuroscience have become increasingly aware of the challenging academic job market and the wide range of opportunities outside of academia. Whereas in the past, a non-academic career was viewed as “plan B,” many students now entering graduate school are very receptive to the wide variety of available opportunities both within and outside of academia. It is the responsibility of neuroscience training programs to provide trainees with the tools, skills, and knowledge that enable the trainees to make effective contributions to the workforce. This includes informing students about the range of careers available to them, establishing supplementary curricular offerings tailored to different career paths, and providing internship opportunities. Equally important is the need to ensure that the academic enterprise continues to flourish and that young neuroscientists will have an opportunity to make critical future discoveries about the brain. A critical part of this effort should include appropriate mentoring; however, there is a concern that appropriate mentoring has suffered as competition for funding has become more acute and the demands of laboratory management have burgeoned (Barres, 2013).

### Trends in Training Neuroscientists versus Available Future Academic Positions

Research at United States academic institutions is a primary engine that drives most innovation in the neuroscience space. Data and concepts derived from academia provide the backbone for private sector advances. However, the rapid increase in numbers of neuroscientists in training is not balanced by any such expected increase in future positions (see Figure 2 from Schillebeeckx et al., 2013, for science and engineering fields). In addition, academia has been slow to adjust its model for career advancement and employee satisfaction. Graduate stu-

dents often express concern around pursuing an academic career path, a concern reinforced by many mentors frustrated by the funding situation and the challenging criteria for promotions and tenure. As a result of this sense of uncertainty, we are likely losing promising scientists from the academic career path.

Since 1983, a decreasing percentage of neuroscience PhD students planned to pursue postdoctoral training—training that is seen as a necessary step in securing an academic research position (see Figure 3). According to data in 2013 from NSF’s National Center for Science and Engineering Statistics, 55% of neuroscience PhDs were in careers in academia 6–10 years post-doctorate, compared to 42% of those 11–15 years post-doctorate (see Figure 4). These numbers suggest that an increasing percentage of PhD students are working toward careers outside traditional academia. Two factors seem to underlie this trend: one is that these students recognize that future prospects for academic careers are declining, and the other is that non-academic careers (e.g., in publishing, public policy, and industry) are becoming more attractive and available. However, funders, academic institutions, and prospective PhD students need much better numbers regarding trends for both the demand (for example, the future availability of academic research positions or positions in the pharmaceutical industry) and supply (i.e., the “pipeline”).

As a whole, academia needs to take a step back and understand what forces may be pushing people away from the academic career path and work proactively to address these issues in order to maintain the best and brightest scientists in the workforce. The vitality and research opportunities in neuroscience are enormous, and it is critical to ensure that other sources of funding are identified to compensate for some of the loss in federal funding. As in other industries, issues like employee engagement and empowerment should be seriously addressed, and changes implemented. Greater departmental and institutional support of promising scientists is needed to bolster early career advancement. There are many advantages to an academic career, including intellectual freedom, collaborations, access to world-class facilities, interactions with ambitious and talented colleagues, flexible schedules, and the ongoing thrill of creating new knowledge while continuing to learn and contribute to the greater good. These values should be preserved and supported, and trainees should be exposed to their existence and encouraged to contemplate them even in the face of some risk.

Trend in Post-Ph.D. Plans of NIH Supported Trainees and Fellows  
Years 1983 - 2013

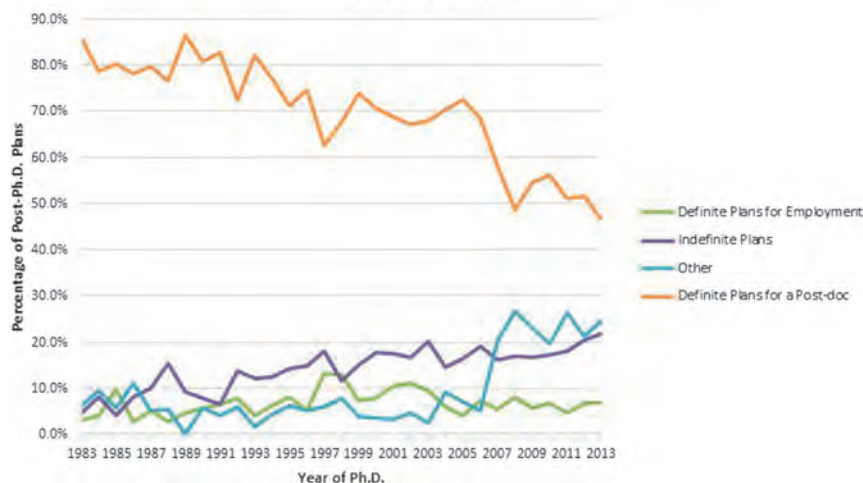


**Figure 3. Trend in Post-PhD Plans of NIH-Supported Trainees and Fellows Receiving PhDs in Neuroscience from 1983 to 2013**

Data taken from the NIH Office of Extramural Research (OER) Training and Advisory Committee June 2015 meeting on education and selected career outcomes of graduate trainees and fellows.

### Opportunities for Careers outside Academia

The increasing number of neuroscience PhD students opting for careers not involving postdoctoral training (Figure 3) indicates that these students, now representing the majority, are preparing for careers outside of academic research. The depicted numbers do not include the subset of students who pursue postdoctoral training and still opt for non-academic careers. This shift in students' post-PhD plans raises the question as to whether current training programs are equipped and organized to provide adequate training for non-academic careers.

One problem is that current PhD training programs are operated by faculty scientists who typically have no experience in the non-academic careers to which many of their students aspire. An informal survey of chairs of medical neuroscience departments (this was run through the Association of Medical School Neuroscience Department Chairs, <http://www.amsndc.org/>) shows that the vast majority of neuroscience PhD programs have either already begun to expand their training scope to incorporate non-academic curricula or are discussing ways to do so. There are many examples of such efforts, including at institutions that have been recipients of NIH's Broadening Experiences in Scientific Training (BEST) award program (see Box 2), designed to expose students to research-related career options. Although graduate programs are taking a diversity of approaches to this challenge, there are common themes. Some of the salient elements of a non-academic career training program are as follows: (1) institutional legitimization of the students' pursuit of non-academic careers, (2) educating students about the range of career options, (3) preparing and mentoring students for their chosen career paths, and (4) tracking career outcomes.

These points can be illustrated using one example (among many) from Harvard's Division of Medical Sciences Paths program, which was established in 2011 to expose and mentor students seeking non-traditional academic careers (see Box 3).

The nation benefits from the PhD training of neuroscientists, both those in academic and non-academic roles. The experience students receive by successfully navigating a rigorous PhD program provides them with a deep understanding and critical perspective of research that cannot be obtained in any other way. Future PhD candidates who pursue careers outside of academia without such training will be without the basic foundation for evaluating and understanding

research and the accompanying literature. And it can be argued that as neuroscience knowledge becomes more complex, we need to find the right balance between those who generate it and those who help translate it and apply it to many facets of life. We thus suggest that as training programs evolve mechanisms to incorporate non-academic career paths (e.g., training in neuroscience), they not abandon the core research training that currently characterizes PhD programs.

Career-focused curriculum offerings are going to continue to increase in importance in neuroscience training programs. These are still early times, and it is likely that many approaches will be tested before the most successful are identified. It will be important for programs to have a mechanism to facilitate the sharing of resources and reporting on best practices. It will be even more important for the neuroscience community to achieve a reasonable perspective concerning the future career landscape, including the types of available careers and the projected numbers of jobs. This information will be critical for career training and for considerations concerning the number of trainees who should be entering the field.

### Addressing Diversity Challenges in Neuroscience

Importantly, we must also consider ways to improve the representation of women and diverse groups in neuroscience careers. In neuroscience and in other biomedical sciences, women outnumber men in graduate school programs but remain underrepresented in faculty positions. Clearly, the system is losing talented women neuroscientists who could be leading us into the next innovations. There is work underway to address this gender imbalance at NIH, NSF, and SfN, including the NIH's Working Group on Women in Biomedical Careers (<https://womenin-science.nih.gov/>), NSF's ADVANCE: Increasing the Participation and Advancement of Women in Academic Science and Engineering Careers program ([http://www.nsf.gov/funding/pgm\\_summ.jsp?pims\\_id=5383](http://www.nsf.gov/funding/pgm_summ.jsp?pims_id=5383)), and SfN's Increasing Women in Neuroscience (iWiN) program. The NIH Working Group on Women in Biomedical Careers was formed in 2007 and serves

## Career Choices of *Neuroscience* PhDs

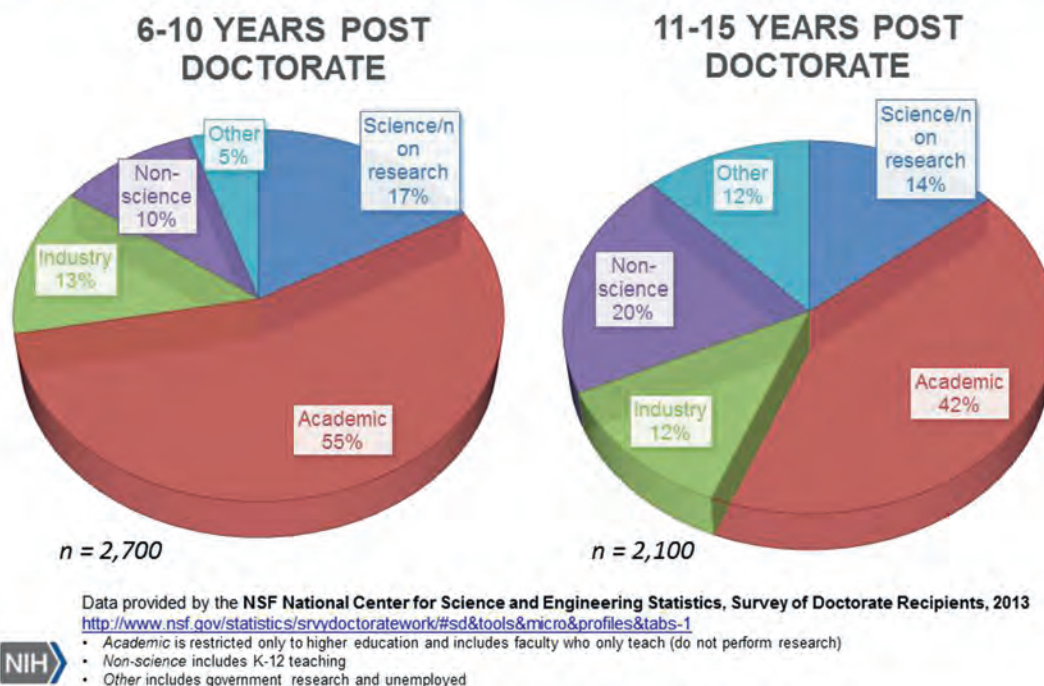


**Figure 4. Career Choices of Neuroscience PhDs**

“Academic” is restricted only to higher education and includes faculty who only teach (do not perform research), “non-science” includes K–12 teaching, and “other” includes government research and unemployed. Data provided by the National Science Foundation Center for Science and Engineering Statistics 2013 Survey of Doctorate Recipients (<http://www.nsf.gov/statistics/srvydoctoratework/#sd&tools&micro&profiles&tabs-1>).

as a trans-NIH effort that considers barriers for women in science and develops innovative strategies to promote entry, recruitment, retention, and sustained advancement of women in biomedical and research careers. Derived from recognition of the intellectual strength and value of a diverse workforce, the goal of NSF’s ADVANCE program is to increase representation and advancement of women in academic science and engineering by supporting efforts aimed at transforming academic culture and institutional practices, policies, and structure. SfN’s iWiN program is an example of one type of project supported by the ADVANCE program to provide opportunities for women neuroscientists and address challenges they may confront in the field. NIH and NSF also have underway various efforts to diversify the workforce by increasing the representation and advancement of underrepresented minorities in biomedical science. The National Institute of Neurological Disorders and Stroke (NINDS) “supports diverse individuals through general training programs as well as with targeted efforts to increase the number of scientists from diverse population groups who are prepared to pursue careers in neuroscience research” ([http://www.ninds.nih.gov/diversity\\_programs/index.htm](http://www.ninds.nih.gov/diversity_programs/index.htm)). Some examples include the Individual NRSA for Diversity PhD Students ([http://www.ninds.nih.gov/funding/areas/training\\_and\\_career\\_development/pre-doctoral-fellowship.htm#f31c](http://www.ninds.nih.gov/funding/areas/training_and_career_development/pre-doctoral-fellowship.htm#f31c)), the NINDS Faculty Development Award

to Promote Diversity in Neuroscience Research ([http://www.ninds.nih.gov/funding/areas/training\\_and\\_career\\_development/mentored-research-scientist.htm#k01](http://www.ninds.nih.gov/funding/areas/training_and_career_development/mentored-research-scientist.htm#k01)), the NINDS Advanced Postdoctoral Career Transition Award to Promote Diversity in Neuroscience Research ([http://www.ninds.nih.gov/funding/areas/training\\_and\\_career\\_development/mentored-research-scientist.htm#k22](http://www.ninds.nih.gov/funding/areas/training_and_career_development/mentored-research-scientist.htm#k22)), and the NINDS Neuroscience Development for Advancing the Careers of a Diverse Research Workforce (R25) ([http://www.ninds.nih.gov/funding/areas/training\\_and\\_career\\_development/institutional-programs.htm#r25](http://www.ninds.nih.gov/funding/areas/training_and_career_development/institutional-programs.htm#r25)). NSF encourages efforts that broaden participation in all of its training and core funding mechanisms through the agency’s merit review criteria, and it promotes efforts at the institutional level through programs such as the Louis Stokes Alliances for Minority Participation ([https://www.nsf.gov/funding/pgm\\_summ.jsp?pims\\_id=13646](https://www.nsf.gov/funding/pgm_summ.jsp?pims_id=13646)), the Alliances of Graduate Education and the Professoriate ([https://www.nsf.gov/funding/pgm\\_summ.jsp?pims\\_id=5474](https://www.nsf.gov/funding/pgm_summ.jsp?pims_id=5474)), and the recently launched Inclusion across the Nation of Communities of Learners and Underrepresented Discoverers in Engineering and Science ([http://www.nsf.gov/publications/pub\\_summ.jsp?ods\\_key=nsf16544](http://www.nsf.gov/publications/pub_summ.jsp?ods_key=nsf16544)). However, continued comprehensive and coordinated efforts with long-term impact are needed to address the systemic issue of insufficient diversity in academic science.

**Box 2. NIH's Broadening Experiences in Scientific Training Awards Program**

In March 2013, the NIH Common Fund program issued a funding opportunity entitled “NIH Director’s Biomedical Research Workforce Innovation Award: Broadening Experiences in Scientific Training (BEST)” (<http://grants.nih.gov/grants/guide/rfa-files/RFA-RM-12-022.html>). The purpose of this funding opportunity is to “seek, identify, and support bold and innovative approaches to broaden graduate and postdoctoral training, such that training programs reflect the range of career options that trainees (regardless of funding source) ultimately may pursue and that are required for a robust biomedical, behavioral, social, and clinical research enterprise.” Currently, 17 institutions across the country have been awarded a 5-year, one-time NIH BEST grant, aimed at identifying and implementing bold and innovative approaches to broaden career and professional development for graduate and postdoctoral training. Each institution employs a unique programmatic approach—some include voluntary workshops for trainees, some are integrated into the core curricula as courses, while others are customized as “BESTernships” that offer full- or part-time experiences for trainees at industry labs, as well as in federal STEM policy and advocacy, regulatory, legal, government, and public affairs; innovation; and academia (<http://www.nihbest.org/about-best/>). Some examples include:

- (1) Track-based training: Entrepreneurship and Business, Science Communication and Public Policy, Education and Outreach, Tech Transfer and Intellectual Property, Government and Nonprofit Research and Research Administration, and Biotech/Pharma Industry Research and Management.
- (2) Education/course work: Science Policy Bootcamp, business as a second language, pre-seed workshop (identifies potential paths to commercialization of high-tech ideas), team building and leadership development, scientific and technical writing, drug discovery, networking, grant writing, time management, responsible conduct of research, regulatory science, clinical innovations, and communication to broad audiences such as policymakers, K–12 educators, and the general public.
- (3) Internships/externships: experience available to graduate students and postdocs includes 160 hr internships that can take place as a 1 month full-time effort or part time over 2–3 months (at this point mostly paid by the institution), mostly at industry labs (Merck, Bristol Myers Squibb, Allergen, etc.) but also in Federal Stem Policy and Advocacy, Regulatory, Legal, Government and Public Affairs, Innovation, and Academia.

There are roughly 100 career development experts among the 17 sites, and the NIH BEST Coordinating Center works to develop, evaluate, and share challenges and best practices (Meyers et al., 2016).

**Identifying the Roles of Each Sector for Supporting the Future Neuroscience Workforce  
Academic Institutions**

The vitality and future of neuroscience depends on the ability of the field to continue to attract, train, and nurture the brightest and most capable graduate students and postdoctoral fellows. In addition to representing the future of the field, this group forms the bulk of the laboratory workforce, which is the backbone of the research enterprise. It is therefore incumbent on academic institutions to develop alternative or complementary strategies for funding graduate training in the biosciences, as well as supporting the early careers of young scientists to include securing private funds and providing other opportunities for work relevant to career development. Besides these additional contributions from academia and the need for more robust and stable federal funding to support academic faculty positions in neuroscience, there are other changes that can be made to improve the allure of academic research careers.

One issue is the narrowness of options for students interested in academic research options. Currently, the only real model in the United States is to obtain a tenure-track faculty position depending largely upon being head of a laboratory. However, many students are vitally interested in research careers but find some of the negative features of running a laboratory, including dealing with constant funding pressures and an increased bureaucratic load, to be severely off-putting. A more attractive career option for these individuals would be one that encouraged them to do research in a role that supports an ongoing program run by others (e.g., a staff scientist; see Box 4). Such a career track, which is available in other scientific cultures (e.g., many Euro-

pean countries), would need to be developed, respected, and stably supported by United States academic research institutions. Overall, it is important for academia to correct the pessimistic view that many young scientists have developed toward a career path in academic scientific research. What is offered here are just a few ideas of what might be done to improve the attractiveness of research careers for forthcoming neuroscientists. The lack of clear options within an academic research career is already being discussed and confronted by many, if not most, neuroscience training programs, so it seems likely that many other potential solutions to this issue will be found. It is thus imperative that we find a means to track and evaluate various potential solutions and make such data available to the neuroscience community.

Another issue that poses a barrier for young investigators is the “two-body problem.” It is much more common now than in past decades for beginning investigators to be in a relationship with another career-minded individual, often another hopeful academic, which means that many such aspiring neuroscientists must find two positions, often leading to significant compromise or failure in career development. The two-body problem may be a particular challenge for women and may contribute to the leaky pipeline for female trainees. The challenge of dual-career couples may make it more difficult for women to secure their first faculty position and seems likely to be a major contributor to the large exodus of women from the pipeline between their postdoctoral and faculty levels. However, even for men, the two-body problem poses a barrier to career development. Academic institutions have been slow to recognize, much less address, this problem.

**Box 3. Program Highlight: Harvard's Division of Medical Sciences Paths Program**

Harvard's Division of Medical Sciences Paths program includes individual paths centered on career interests such as biotechnology, writing and editing, intellectual property, science policy, and consulting. Each path includes a student interest group, an associated set of courses, internship opportunities, and alumni mentors. Legitimization was achieved by making Paths an integral part of graduate education. This included giving the program official status, listing it on all program webpages, and awarding academic credit for career courses and internships. Faculty rapidly became supportive of these efforts, especially as they observed their students and postdocs struggle with an increasingly challenging academic job market. Students are exposed to career options through courses that survey the career landscape and through informational sessions sponsored by individual paths. Once a student has identified a career path, he/she engages in a variety of activities designed to position the student for a successful transition following graduation. This includes career-specific enrichment courses, focused extracurricular activities, alumni mentoring, and internship opportunities. Finally, career outcomes are tracked by maintaining close contact with alumni who have pursued these paths.

Career programs do not necessarily require a large influx of new institutional resources as there are economies that can be achieved by harnessing or repurposing current resources. Existing student organizations such as biotechnology and consulting clubs can be incorporated into the program. Enrichment course offerings are typically available from allied institutions including business, education, government, and public health institutions. The Paths program has experienced an exceptional level of involvement from alumni and local private enterprises. There is a genuine enthusiasm on the part of alumni to re-engage with the institution and to mentor students who wish to follow in their paths. They have been willing partners in offering career courses and networking events, and providing internship opportunities at minimal or no cost to the institution. Not surprisingly, the graduate students are the single greatest driving force behind these programs, and it is essential that they have a strong voice in directing these endeavors. The students are highly motivated to explore different career options and bring nearly limitless creativity and energy to the enterprise. For example, students in the biotechnology path established a course in healthcare innovation that is taught by biotechnology leaders, and students in the writing path created an open access journal, the *Journal of Emerging Investigators*, that encourages middle and high school students to pursue science through publication of their science fair projects.

**The Private Sector**

After a several-year period of decline, there has been renewed investment in neuroscience from pharmaceutical companies, startup biotechnology companies, and the technology sector (Google, Apple, etc.). Even though neuroscience research and development remains a risky proposition compared to other therapeutic areas, including oncology, cardiovascular disease, and metabolism, more than three billion dollars was invested in 2014 in companies developing drugs for neurodegenerative and psychiatric disease, more than in any of the last 10 years (Tracy, 2015). Although the unmet medical need for these and other CNS disorders remains high and is a strong commercial driver, ongoing investment is built on a foundation of advances in understanding of brain circuit function, disease genetics and pathophysiology, and the rapid development of technologies to monitor the brain and behavior in real time. Across the private sector, there is real promise of developing new, impactful treatments for patients who desperately need them.

Realizing the commercial potential of these investments requires a well-trained neuroscience workforce able to interact collaboratively in multi-disciplinary teams focused on advancing projects through the drug discovery pipeline, including in the many attendant areas of specialization that are a hallmark of end-to-end drug development (clinical, regulatory, commercial, partnerships, external opportunities, policy, etc.). Investment in training for neuroscientists by the private sector has increased in recent years. Many small, mid-sized, and big pharma have summer internship programs for undergraduates and offer lab rotation opportunities to graduate master's and PhD degree students, sometimes as part of a broader collaborative platform with individual academic institutions. Some companies offer

postdoctoral training programs that recruit individuals that have met similar metrics of success as do academic principal investigators (PIs). During their training, industry postdocs typically pursue discovery work that is readily publishable, joining large collaborative teams that are a sine qua non of drug discovery. Whereas historically, molecular, cellular, and behavioral expertise were highly valued in neuroscientists applying for industry positions, the imperative to successfully translate findings to the clinic has seen increased recruitment of neuroscientists with circuits and systems, electrophysiology, and human biology and clinical expertise. Across the private sector, concerns with rigor, reproducibility, and robustness of research findings have raised awareness of the importance of training in experimental design, statistics and data analytics, responsible conduct, and research ethics. Postdocs that complete an industry training program are highly recruited for opportunities across the private sector, and there is a small but growing trend for neuroscientists who have completed industry postdocs to pursue positions in academia, where their drug discovery and translational experience makes them valuable future collaborators and external advisors for the industry, and valuable to academic institutions with burgeoning target validation, assay development/screening, and other drug discovery-relevant efforts. Because the private sector continually looks to partner with academia through pre-competitive consortia and other models, understanding how neuroscience is advanced in both arenas becomes a particularly valuable professional credential.

**Societies and Patient-Advocacy Organizations**

Well-funded and active philanthropic organizations, such as the Cure Huntington's Disease Initiative and the Michael J.

**Box 4. A New Class of Academic Biomedical Scientists: The “Staff Scientist”**

A new type of academic researcher, one that often is referred to as a “staff scientist,” would be a well-trained researcher who serves as a vital team member in a laboratory. Currently, the personnel of most laboratories are dominated by trainees: PhD students and postdoctoral fellows. Such trainees represent the bulk of the biomedical research enterprise in the United States. The faculty head of the laboratory thus oversees numerous trainees, and this is emblematic of the imbalance between the large training pipeline and the small endpoint of positions for those trainees. Another problem with this arrangement is lack of stability: trainees are involved with a given laboratory for only 4 years or so, meaning that long-range research programs must constantly deal with the upheaval of personnel changes. Alberts et al. (2014) deal with this issue as follows:

“We believe that staff scientists can and should play increasingly important roles in the biomedical workforce. Within individual laboratories, they can oversee the day-to-day work of the laboratory, taking on some of the administrative burdens that now tend to fall on the shoulders of the laboratory head; orient and train new members of the laboratory; manage large equipment and common facilities; and perform scientific projects independently or in collaboration with other members of the group. Within institutions, they can serve as leaders and technical experts in core laboratories serving multiple investigators and even multiple institutions.”

The creation of such positions would provide many more career opportunities for PhD students for academic research careers and thereby partially ameliorate the concern that too many PhDs are being trained given the predicted availability of future tenure-track faculty positions in institutions. To be attractive, such positions would need to be seen as reasonably stable and not, for instance, dependent on a given laboratory maintaining continuous NIH funding. This would require institutions to support such positions. As noted by Alberts et al. (2014), “To succeed, universities will need employment policies that provide these individuals with attractive career paths, short of guaranteed employment.” Funding and support for such positions already exist within the NIH intramural research program and are currently being explored by several institutions.

Fox Foundation for Parkinson’s Research, and nonprofit organizations such as the Simons Foundation, have entered the arena and require individuals with high levels of neuroscience expertise and skill to advance their work. Such individuals hold senior leadership positions within those organizations and are critical players in helping to identify and manage potential research priorities. In addition, the Society for Neuroscience’s Neuroscience Training Committee (<https://www.sfn.org/About/Volunteer-Leadership/Committees/Neuroscience-Training-Committee>) brings together individuals from many sectors to discuss topics and plan activities around neuroscience education, life-long learning, and workforce policy.

**Funding Agencies: NIH and NSF**

NIH institutes vary in the percentage of their budget devoted to training. The National Institute of Mental Health assigns approximately 7%–8% (<http://www.nimh.nih.gov/about/budget/fy-2016-budget-congressional-justification.shtml>), and NINDS 4%–5% ([http://www.ninds.nih.gov/funding/ninds\\_funding\\_strategy.htm](http://www.ninds.nih.gov/funding/ninds_funding_strategy.htm)) to training, which includes Research Career Development Awards. NIH funds graduate and post-graduate neuroscience training with its traditional National Research Service Awards (NRSA). However, the vast majority of neuroscience trainees are funded on RO1s or other funding sources, and NIH has exercised very little influence on this training. The NRSA programs include fellowship awards to individual trainees at the predoctoral graduate school level or the postdoctoral level. NIH also funds two major types of institutional training awards: (1) multi-institute sponsored programs for broad-based neuroscience training in the early years of graduate school, and (2) institute-specific training programs usually for thematic neuroscience training of graduate students or fellows in specific areas of neuroscience. The latter would provide the flexibility to include creative solutions for the future of neuroscience training. For instance, the NIH Blueprint for Neuroscience ([\[neuroscienceblueprint.nih.gov/\]\(http://neuroscienceblueprint.nih.gov/\)\) funds a number of training programs in computational neuroscience, and short courses in computational neuroscience are funded as part of the BRAIN Initiative.](http://</a></p></div><div data-bbox=)

NIH is also concerned with the growing and long training times before becoming independent scientists, and a number of programs, e.g., Pathway to Independence Award and Director’s Early Independence Award, were created to shorten that time. In addition, NIH funds specific programs to promote diversity in the neuroscience workforce at the college, graduate, postdoctoral, and early-career stage. The neuroscience institutes and centers are currently planning to promote greater quantitative and experimental skill training in their jointly sponsored, broad-based institutional training award. The neuroscience institutes are also examining timing the award of fellowship grants to better empower trainees with their own funding to choose labs based on their interests as opposed to the funding situation of the PIs.

One of NSF’s approaches to advancing the frontiers of science and technology is to invest in training of the next generation of scientists and engineers. Among the agency’s current priority goals is STEM graduate student preparedness for entering the STEM workforce and pursuing productive careers in- and outside academia. NSF funds training at the graduate student level through its Graduate Research Fellowship Program (GRFP) (<https://www.nsfgrfp.org/>) and the NSF Research Traineeship (NRT) program ([https://www.nsf.gov/funding/pgm\\_summ.jsp?pims\\_id=505015](https://www.nsf.gov/funding/pgm_summ.jsp?pims_id=505015)). The GRFP provides fellowship support for individual master’s and PhD students in science and engineering in the early stages of their graduate training and offers fellowship recipients the freedom to conduct research at any accredited United States institution of graduate education of their choosing. Additionally, the program provides mechanisms for fellows to enhance their professional development through international research collaborations and/or research internships at federal

facilities and national laboratories. Different from the GRFP, the NRT program provides support for cohorts of graduate students by funding STEM education programs that emphasize innovative, evidence-based traineeship approaches in interdisciplinary research areas (Traineeship Track) and projects that test and validate innovative and potentially transformative graduate STEM education strategies (Innovations in Graduate Education Track). Similar to the IGERT program (see Box 1), the Traineeship Track promotes training and collaborative research that transcend traditional disciplinary boundaries, to enable trainees to bridge research areas and engage in cross-disciplinary team science. Furthermore, it encourages the development and implementation of training curricula that prepare students for multiple career pathways. As part of NSF's engagement in the BRAIN Initiative and in recognition of the need for investigators skilled in developing and applying new technologies, complex data analytics, and theoretical frameworks to reveal the fundamental principles of nervous system function and complex behavior, a current priority area of the NRT Traineeship Track is "Understanding the Brain." NSF also funds Research Experiences for Undergraduates (REU) ([http://www.nsf.gov/funding/pgm\\_summ.jsp?pims\\_id=5517&from=fund](http://www.nsf.gov/funding/pgm_summ.jsp?pims_id=5517&from=fund)) by supporting REU Sites, programs that offer mentored participation in research for groups of undergraduate students through a single department and discipline or multiple departments that coalesce around a coherent intellectual theme, and by making REU supplements to an individual-investigator research award. In addition to these targeted programs, NSF invests in workforce preparation by supporting trainees at all levels, including the postdoctoral level, through a core research award made to individual investigators. Although the educational and research experiences embedded in core research grants are not organized around specific, strategic training goals, their quality and potential impact on trainee professional development are evaluated as part of NSF's merit review criteria.

### Conclusions

The future of neuroscience rests in the hands of a new generation of scientists who are willing to confront and overcome the great challenges of the field. This new generation has grown in the midst of an unprecedented explosion in knowledge, technologies, data, and tools. These young scientists begin their training with great talent, know-how, curiosity, and enthusiasm. Moreover, our field is vibrant, exciting, and in the midst of a revolution that aims to integrate human knowledge across many levels of analysis. This should be the best of times for both the scientists and the field. The shared task of all the stakeholders—academia, government, industry, scientific societies, foundations, and other components of the private and public sectors—is to ensure that we do not kill this hope. Rather, we should work collaboratively to offer the thoughtfulness, flexibility, nimbleness, and necessary support that will ensure the success of this next generation of neuroscientists.

The rewards for a better understanding of the brain are difficult to overstate. Such knowledge will not only inform how we treat devastating brain disorders, but it will also alter our self-concept as humans and inform how we see and treat each other. The key step is to train and support the talented neuroscientists of the 21st century who will continue this exciting journey of discovery.

### ACKNOWLEDGMENTS

The authors would like to thank Meghan Mott (NINDS), Stephen Korn (NINDS), Story Landis (Director Emeritus, NINDS), Alan Leshner (CEO Emeritus, American Association for the Advancement of Science), and Claire Hemingway (NSF) for helpful discussions. The authors also acknowledge useful background discussions convened by Forum on Neuroscience and Nervous System Disorders of the National Academies of Sciences, Engineering, and Medicine. The authors' views are personal views and do not necessarily represent those of the NIH and NSF, the Federal Government, or the National Academies of Sciences, Engineering, and Medicine. R.B.-G. is an employee of Pfizer, Inc. in the Neuroscience and Pain Research Unit.

### REFERENCES

- Alberts, B., Kirschner, M.W., Tilghman, S., and Varmus, H. (2014). Rescuing US biomedical research from its systemic flaws. *Proc. Natl. Acad. Sci. USA* *111*, 5773–5777.
- Barres, B.A. (2013). How to pick a graduate advisor. *Neuron* *80*, 275–279.
- Carney, J.G., and Neishi, K. (2010). Bridging disciplinary divides: developing an interdisciplinary STEM workforce. Prepared for the National Science Foundation. Abt Associates, Inc., [http://www.abtassociates.com/reports/ES\\_IGERT\\_SUMMARY\\_REPORT\\_October\\_2010.pdf](http://www.abtassociates.com/reports/ES_IGERT_SUMMARY_REPORT_October_2010.pdf).
- Carney, J.G., Chawla, D., Wiley, A., and Young, D. (2006). Evaluation of the initial impacts of the National Science Foundation's Integrative Graduate Education and Research Traineeship (IGERT) program. Prepared for the National Science Foundation, National Science Foundation, <http://www.nsf.gov/pubs/2006/nsf0617/index.jsp>.
- Carney, J.G., Martinez, A., Dreier, J., Neishi, K., and Parsad, A. (2011). Evaluation of the National Science Foundation's Integrative Graduate Education and Research Traineeship Program (IGERT): follow-up study of IGERT graduates. IGERT, [http://www.igert.org/system/content\\_item\\_assets/files/1535/ES\\_IGERT\\_FOLLOWUP\\_STUDY\\_FULLREPORT\\_May\\_2011.pdf?1340382040](http://www.igert.org/system/content_item_assets/files/1535/ES_IGERT_FOLLOWUP_STUDY_FULLREPORT_May_2011.pdf?1340382040).
- Gamse, B.C., Espinosa, L.L., and Roy, R. (2013). Essential competencies for interdisciplinary graduate training in IGERT. Prepared for the National Science Foundation. Abt Associates, Inc., <http://www.abtassociates.com/AbtAssociates/files/dc/dc390ed2-8e10-4c01-bcaa-24e5a837e7ff.pdf>.
- Gould, J. (2015). How to build a better PhD. *Nature* *528*, 22–25.
- IOM (Institute of Medicine) (2014). *Developing a 21st Century Neuroscience Workforce: Workshop Summary* (The National Academies Press).
- Meyers, F.J., Mathur, A., Fuhrmann, C.N., O'Brien, T.C., Wefes, I., Labosky, P.A., Duncan, D.S., August, A., Feig, A., Gould, K.L., et al. (2016). The origin and implementation of the Broadening Experiences in Scientific Training programs: an NIH common fund initiative. *FASEB J.* *30*, 507–514.
- Schillebeeckx, M., Maricque, B., and Lewis, C. (2013). The missing piece to changing the university culture. *Nat. Biotechnol.* *31*, 938–941.
- Stokols, D., Hall, K.L., Taylor, B.K., and Moser, R.P. (2008). The science of team science: overview of the field and introduction to the supplement. *Am. J. Prev. Med.* *35* (2, Suppl), S77–S89.
- Tracy, H. (2015). CNS funds raised 2014. *NeuroPerspective* *230/231*, 4.

# DREADDs for Neuroscientists

Bryan L. Roth<sup>1,\*</sup>

<sup>1</sup>Department of Pharmacology, University of North Carolina Chapel Hill Medical School, Chapel Hill, NC 27514, USA

\*Correspondence: bryan\_roth@med.unc.edu

<http://dx.doi.org/10.1016/j.neuron.2016.01.040>

To understand brain function, it is essential that we discover how cellular signaling specifies normal and pathological brain function. In this regard, chemogenetic technologies represent valuable platforms for manipulating neuronal and non-neuronal signal transduction in a cell-type-specific fashion in freely moving animals. Designer Receptors Exclusively Activated by Designer Drugs (DREADD)-based chemogenetic tools are now commonly used by neuroscientists to identify the circuitry and cellular signals that specify behavior, perceptions, emotions, innate drives, and motor functions in species ranging from flies to nonhuman primates. Here I provide a primer on DREADDs highlighting key technical and conceptual considerations and identify challenges for chemogenetics going forward.

Chemogenetics has been defined as a method by which proteins are engineered to interact with previously unrecognized small molecule chemical actuators (Forkmann and Dangelmayr, 1980; Sternson and Roth, 2014; Strobel, 1998). Over the past two decades, a large number of chemogenetic (also known as “chemical genetic”; (Bishop et al., 1998; Strader et al., 1991; Chen et al., 2005; Sternson and Roth, 2014) platforms have been invented that have been useful for biologists in general and most especially for neuroscientists.

A number of protein classes (Table 1) have been chemogenetically engineered including kinases (Bishop et al., 1998; Bishop et al., 2000; Chen et al., 2005; Cohen et al., 2005; Dar et al., 2012; Liu et al., 1998), non-kinase enzymes (Collot et al., 2003; Häring and Distefano, 2001; Klein et al., 2005; Strobel, 1998), G protein-coupled receptors (GPCRs) (Alexander et al., 2009; Armbruster and Roth, 2005; Armbruster et al., 2007; Redfern et al., 1999; Redfern et al., 2000; Vardy et al., 2015), and ligand-gated ion channels (Arenkiel et al., 2008; Lerchner et al., 2007; Magnus et al., 2011; Zemelman et al., 2003) (for recent review, see Sternson and Roth, 2014). Of these various classes of chemogenetically engineered proteins, the most widely used to date have been Designer Receptors Exclusively Activated by Designer Drugs (DREADDs) (Armbruster and Roth, 2005; Armbruster et al., 2007), and this *Neuron* Primer is devoted to them.

## How an Understanding of GPCR Molecular Pharmacology Facilitates the Appropriate Use of DREADD Technology

Before discussing DREADDs in detail, I will first summarize essential foundational concepts of GPCR molecular pharmacology and signaling. This background information is essential for all readers so that they may understand how DREADDs may be most effectively used. According to classical models of GPCR action GPCRs exist in multiple ligand-dependent and -independent states. These multiple GPCR states range from “fully inactive” to “partially active” to “fully active” to “signaling complexes” (Roth and Marshall, 2012; Samama et al., 1993). As depicted in Figure 1, GPCRs (R) are modulated by ligands (L) and can interact with both heterotrimeric G proteins (G) and  $\beta$ -ar-

restins ( $\beta$ Arr). According to the most recent findings, multiple inactive (e.g., “ground”) states exist that can be stabilized by ligands ( $R_1L$ ,  $R_2L$ , and so on) or can even occur in the absence of ligands (R). Sodium ions stabilize the ground state by exerting a negative allosteric modulation via a highly conserved allosteric site (Fenalti et al., 2014; Katritch et al., 2014). Drugs that stabilize the  $R_1L$ ,  $R_2L$  ground states function as inverse agonists (Samama et al., 1993, 1994). Inverse agonists are also known as “antagonists with negative intrinsic activity” (Costa and Herz, 1989). The evidence for multiple GPCR states is supported by classical molecular pharmacological (Samama et al., 1993, 1994), biophysical (Gether et al., 1995), and structural studies (Manglik et al., 2015).

Both full and partial agonists stabilize the active state ( $R^*L$ ) and promote the formation of a signaling complex (e.g., the “ternary complex”) consisting of (1) the active receptor, (2) an agonist, and (3) the heterotrimeric G protein ( $R^*LG$ ) (De Lean et al., 1980; Samama et al., 1993). In addition to the ligand-induced activation and inactivation of GPCRs, GPCRs can also spontaneously isomerize to an active state ( $R^*$ ) in the absence of ligand. Further, this active state can spontaneously interact with G proteins to yield a binary signaling complex in the absence of ligand ( $R^*G$ ) (Samama et al., 1993). This active state in the absence of ligand is termed “constitutive activity.”

GPCRs (R) also interact with arrestins ( $\beta$ Arr) to form alternative signaling complexes ( $R^{**}L$  and  $R^{**}L \beta$ Arr) (Luttrell et al., 1999; Wacker et al., 2013; Kroeze et al., 2015). GPCRs with high levels of basal (e.g., constitutive) activity can spontaneously interact with  $\beta$ Arr to form an  $R^{**}\beta$ Arr complex in the absence of agonist (Marion et al., 2004; Kroeze et al., 2015). Based on high-resolution crystal structures of GPCR-arrestin complexes, the  $R^*L \beta$ Arr state appears to sterically occlude G-protein interactions with the receptor thereby abolishing G-protein signaling (Shukla et al., 2014; Kang et al., 2015). Accordingly, the interaction of GPCRs with  $\beta$ Arr also represents a “desensitized” or inactive G-protein state of the complex. At the single molecule level, when GPCRs are activated by agonists, they can couple to either G-proteins or arrestins, but not both. At the cellular level conformational ensembles of all of the states identified above exist. Biasing for one particular state is dependent upon both the

**Table 1. Representative Chemogenetic Technologies**

Name	Protein(s)	Ligand	Reference
<b>Representative kinases</b>			
Allele-specific kinase inhibitors	v-I388G	Compound 3g	Liu et al., 1998
Analogue-sensitive kinases	v-Src (I338G, v-Src-as1), c-Fyn (T339G, c-Fyn-as1), c-Abl (T315A, c-Abl-as2), CAMK II $\alpha$ (F89G, CAMK II $\alpha$ -as1) and CDK2 (F80G, CDK2-as1)	K252a and PPI analogues	Bishop et al., 1998
Rapamycin-insensitive TOR complex 2	TORC2 V2227L	BEZ235	Bishop et al., 2000
ATP-binding pocket mutations in EphB1, EphB2 and EphB3	<i>Ephb1</i> <sup>T697G</sup> , <i>Ephb2</i> <sup>T699A</sup> , and <i>Ephb3</i> <sup>T706A</sup>	PP1 analogues	Soskis et al., 2012
ATP-binding pocket mutations of TrkA, TrkB and TrkC	<i>TrkA</i> <sup>F592A</sup> , <i>TrkB</i> <sup>F616A</sup> , and <i>TrkC</i> <sup>F617A</sup>	1NMPP1 and 1NaPP1	Chen et al., 2005
<b>Representative Enzymes</b>			
Metalloenzymes	Achiral biotinylated rhodium-diphosphine complexes		Collot et al., 2003
Engineered transaminases	Chemically conjugating a pyridoxamine moiety within the large cavity of intestinal fatty acid binding protein	Enhanced activity	Håring and Distefano, 2001
<b>Representative GPCRs</b>			
Allele-specific GPCRs	$\beta$ 2-adrenergic receptor, D113S	1-(3',4'-dihydroxyphenyl)-3-methyl-L-butanone (L-185,870)	Strader et al., 1991
RASSL-Gi (receptors activated solely by synthetic ligands)	$\kappa$ -opioid chimeric receptor	Spiradoline	Coward et al., 1998
Engineered GPCRs	5-HT2A serotonin receptor F340 $\rightarrow$ L340	Ketanserin analogues	Westkaemper et al., 1999
Gi-DREADD	M2- and M4 mutant muscarinic receptors	Clozapine-N-Oxide	Armbruster and Roth, 2005; Armbruster et al., 2007
Gq-DREADD	M1, M3, and M5- mutant muscarinic receptors	Clozapine-N-oxide	Armbruster and Roth, 2005; Armbruster et al., 2007
Gs-DREADD	Chimeric M3-turkey erythrocyte Adrenergic receptor	Clozapine-N-oxide	Guettier et al., 2009
Arrestin-DREADD	M3Dq R165L	Clozapine-N-oxide	Nakajima and Wess, 2012
Axonally-targeted silencing	hM4D-neurexin variant	Clozapine-N-oxide	Stachniak et al., 2014
KORD	$\kappa$ -opioid receptor D138N mutant	Salvinorin B	Vardy et al., 2015
<b>Representative Channels</b>			
GluCl	Insect Glutamate chloride channel; Y182F mutation	Ivermectin	Lerchner et al., 2007
TrpV1	TrpV1 in TrpV1 KO mice	Capsaicin	Arenkiel et al., 2008
PSAM	Chimeric channels PSAM <sup>G79G,L141S</sup>	PSEM <sup>9S</sup>	Magnus et al., 2011
PSEM	PSAM-GlyR fusions	PSEM <sup>89S</sup> , PSSEM <sup>22S</sup>	Magnus et al., 2011

cellular context and the available ligand (Vardy and Roth, 2013; Wacker et al., 2013).

A clear understanding of the implications of this extended and modified ternary complex model—for which there is now compelling biochemical (Strachan et al., 2014), biophysical (Sounier et al., 2015; Nygaard et al., 2013), pharmacological (Weiss et al., 2013; Fenalti et al., 2014), and structural evidence (Fenalti et al., 2014; Manglik et al., 2015; Rasmussen et al., 2011; Wacker et al., 2013)—is crucial for understanding how GPCR-based

chemogenetic technologies can be harnessed in neuroscience. Thus, for instance, a major concern for chemogenetic technologies is the possibility that high levels of expression of an engineered protein might have effects in the absence of chemical activation (Conklin et al., 2008). Indeed, many of the second-generation chemogenetic GPCRs (e.g., receptors activated solely by synthetic ligands [RASSLs]) had high basal levels of activity leading to phenotypes in the absence of chemical actuators (Hsiao et al., 2008; Sweger et al., 2007).

R=Receptor; L=Ligand; G=G protein;  $\beta$ Arr= $\beta$ Arrestin

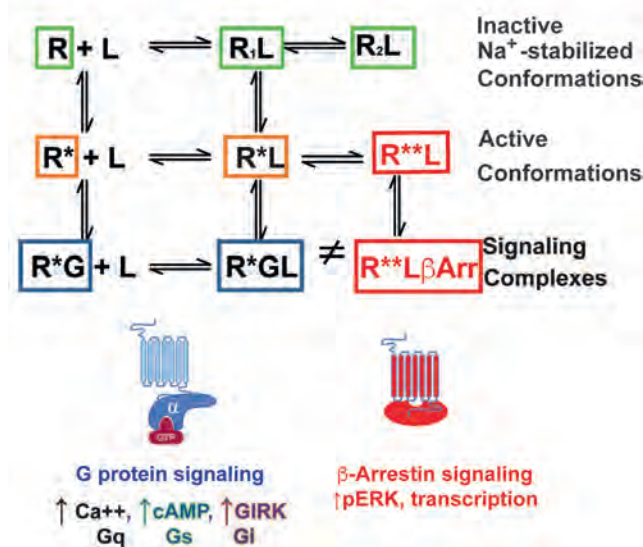


**Figure 1. A Modified and Extended Ternary Complex Model of GPCR Action**

As shown in the top panel GPCRs (R) may interact with ligands (L), heterotrimeric G proteins (G), and arrestins ( $\beta$ Arr) and thereby form a variety of inactive (green boxes), active (orange and red boxes), and signaling complexes (blue and red boxes). The bottom panel shows a cartoon of the various signaling complexes for canonical G protein signaling (L) and  $\beta$ -Arrestin signaling (R).

As depicted in Figure 1, a GPCR with constitutive activity would be more likely to exist in the R\* state and thus to spontaneously interact with G proteins to yield a signaling complex in the absence of ligand (R\*G). As shown in Figure 2A, high levels of expression of a GPCR with constitutive activity leads to signaling in the absence of ligand. Although no studies to date have demonstrated a basal phenotype for any of the known DREADDs, it is important to express DREADDs at the lowest level consistent with experimental design. For hM3Dq (Alexander et al., 2009) and hM4Di (Zhu et al., 2014), life-long and extremely high levels of expression were attained using a genetically encoded tetracycline-sensitive induction system without basal electrophysiological, behavioral, or anatomical abnormalities being observed. More modest life-long expression of the Gs-DREADD (GsD) also was attained without any detectable electrophysiological, behavioral, or anatomical phenotype (Farrell et al., 2013). High levels of virally mediated expression of various DREADDs have not yet been reported to yield any significant basal phenotypes (Urban et al., 2015; Vardy et al., 2015; Denis et al., 2015; Isosaka et al., 2015; Hayashi et al., 2015). Of course, the absence of reports of basal activity does not imply the absence of basal activity. Going forward, if basal activity is observed, it would be prudent to simply lower the level of DREADD expression using (1) a lower titer of virus, (2) a weaker promoter, or (3) modifying post-transcriptional expression (e.g., deleting a woodchuck hepatitis virus [WPRE] element from the 3' end of the construct). Thus, based on the law of mass action, decreasing [R] decreases the prob-

ability of  $[R] \rightarrow [R^*] \rightarrow [R^*G]$  (e.g., inactive, active, and signaling state) transitions.

An additional concern with DREADD technologies relates to issues of desensitization and subsequent receptor downregulation. Thus, following repeated dosing with a DREADD chemical actuator, one might observe diminished responses due to receptor desensitization and downregulation. This diminished response might be predicted because it is well known that GPCRs can be desensitized and subsequently internalized and downregulated following agonist-induced activation (DeWire et al., 2007).

As depicted in Figure 2A, the degree of desensitization depends greatly on the extent to which receptors are over-expressed and the subsequent amount of "receptor reserve." "Receptor reserve" is a pharmacological term that describes the phenomenon whereby a maximum agonist response can be achieved with less than full occupancy of all of the receptors by agonists (Ruffolo, 1982). From a practical perspective, the concept of receptor reserve predicts that when DREADD expression is quite high, lower concentrations of the chemical actuator are needed to achieve a maximal response (Figure 2A). Additionally, when receptors are desensitized or downregulated, there may be no change in the maximum response elicited by the agonist, but there may be a shift in the dose-response curve to the right because of receptor reserve (2A). Thus, when DREADDs are expressed at high levels relative to native GPCRs via viral or transgenic approaches, the cellular and behavioral responses will be less sensitive to repeated dosing than when they are expressed at lower levels. This phenomenon might explain why no significant desensitization was seen when DREADDs were virally or transgenically expressed (Alexander et al., 2009; Krashes et al., 2011)

Another conceptual issue specific to DREADD technology relates to whether the effects observed regarding neuronal output and behavior occur due to canonical or non-canonical GPCR signaling. As shown in Figure 1, agonists may activate multiple downstream effector pathways, and it is likely that actions other than simply enhancing or silencing neural activity can result when DREADDs are activated. Specifically, one might be concerned about conditions in which  $\beta$ Arr signaling is activated. To date, there have been no reports suggesting that the actions of the silencing (e.g., Gi-based DREADDs) or activating (e.g., Gq-based DREADDs) DREADDs on neuronal activity and subsequent physiological readouts could be explained by any mechanism other than altered neuronal firing. Pertinent to this issue, many studies have used DREADD and optogenetic technologies on the same neuronal populations. These studies have invariably identified essentially equivalent effects in terms of both the valence and magnitude of the effect on the physiological readout, although the duration is typically longer with DREADDs (Table 2 for representative examples). Indeed, many investigators now use both DREADD and optogenetic technologies to provide independent and converging lines of evidence in terms of both sufficiency and necessity when deconstructing neural circuits.

### Current DREADDs

As shown in Table 1 (for recent reviews, see Sternson and Roth, 2014; Urban and Roth, 2015; English and Roth, 2015), there now

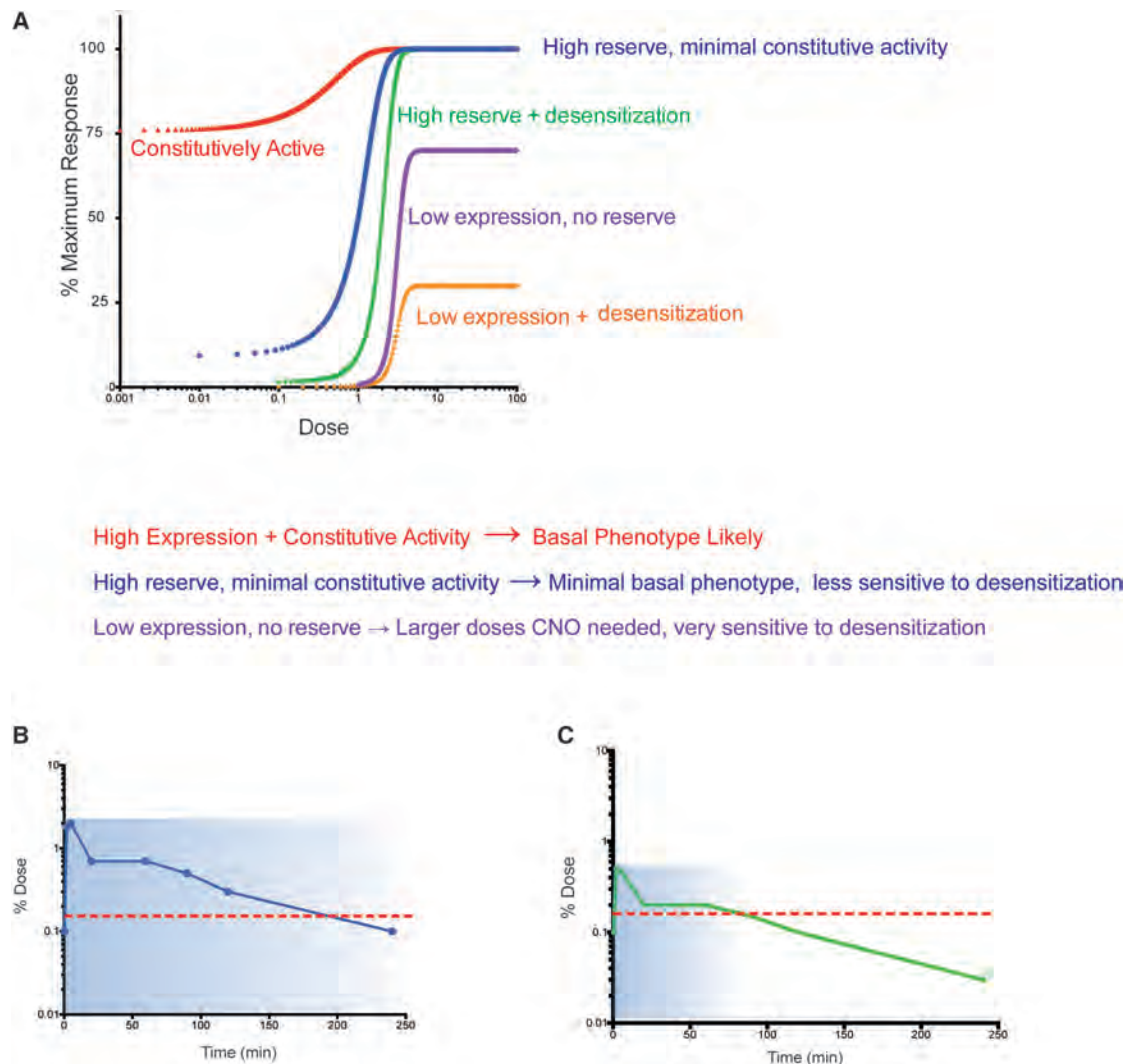


**Figure 2. How Receptor Reserve and Constitutive Activity may Modify DREADD Actions In Vitro and In Vivo**

(A) Simulations of receptor activity using a standard four-parameter logistic equation for GPCR activation, and variable receptor expression (DeLean et al., 1978) was used to simulate the effects of over-expression of a DREADD with constitutive activity (red circles); high receptor reserve, minimal constitutive activity (blue circles); high receptor reserve + desensitization (green circles); low expression and no receptor reserve (purple circles); and low expression, no receptor reserve, and desensitization (orange circles).

(B and C) Potential pharmacokinetic parameters of CNO following high (B) and lower (C) doses. The dotted red line indicates the threshold concentration required for activation of the DREADD in situ.

exist many GPCR-based chemogenetic tools. These include first- (“Allele-specific GPCRs”; Strader et al., 1991), second- (RASSLs and “Engineered GPCRs”; Coward et al., 1998; Westkaemper et al., 1999), and third-generation (DREADDs; Armbruster and Roth, 2005; Armbruster et al., 2007) platforms. Currently, DREADDs are the most widely used chemogenetic tool; the available DREADDs are shown in Figure 3A.

#### **Gq-DREADDs, CNO Analogues, and Basal Activity**

For enhancing neuronal firing and activating Gq signaling in neuronal and non-neuronal cells, the hM3Dq DREADD is typically used (Alexander et al., 2009; Armbruster et al., 2007). hM3Dq can be activated by clozapine-N-oxide (CNO)—a pharmacologically inert metabolite of the atypical antipsychotic drug clozapine (Armbruster et al., 2007; Roth et al., 1994).

When the original DREADDs were invented, three Gq-coupled DREADDs were created, each of which was based on a different human muscarinic receptor: hM1Dq, hM3Dq, and hM5Dq (Armbruster et al., 2007). All three Gq-DREADDs are activated by low nM concentrations of CNO and mobilize intracellular calcium (Armbruster et al., 2007). All three Gq-DREADDs could be used as excitatory DREADDs, although hM3Dq appears to be most frequently used.

CNO (Figure 3B) represents the prototypical chemical actuator for Gq-DREADDs. Based on many reports, CNO appears to be pharmacologically and behaviorally inert in mice (Alexander et al., 2009; Krashes et al., 2011; Farrell et al., 2013; Guettier et al., 2009; Urban et al., 2015; Zhu et al., 2014) and rats (Ferguson et al., 2011, 2013) when administered at the

**Table 2. Examples for Apparent Equivalency of Chemo- and Optogenetic Modulation**

Cell Type	DREADD	Opsin	Electrophysiology	Behavior
AgRP Neurons	hM3Dq (Krashes et al., 2011)	ChR2 (Aponte et al., 2011)	Increased firing	Enhanced feeding
ETV-1 subfornical area neurons	hM3Dq (Betley et al., 2015)	ChR2 (Betley et al., 2015)	Increased firing	Enhanced drinking
Medial entorhinal cortex cells	hM4Di (Miao et al., 2015)	Arch (Miao et al., 2015)	Decreased firing	Remapping place cells
PBN CGRP Projection neurons	hM3Dq (Cai et al., 2014)	ChR2 (Cai et al., 2014)	Increased firing	Diminished feeding
Orexin neurons	hM4Di (Sasaki et al., 2011)	Halorhodopsin (Tsunematsu et al., 2011)	Decreased firing	Decreased wakefulness
Hippocampus	hM4Di (Zhu et al., 2014)	Arch (Sakaguchi et al., 2015)	Decreased firing	Suppression of contextual fear conditioning
Raphe serotonergic neurons	hM3Dq (Urban et al., 2015)	ChR2 (Ohmura et al., 2014)	Increased firing	Anxiogenic

recommended doses (generally 0.1–3 mg/kg). CNO may be metabolized via back-transformation to clozapine—especially in guinea pigs, humans (Jann et al., 1994), and nonhuman primates (unpublished observations). Although the amount of back-metabolism to clozapine is low even in humans (10% or less by mass; Jann et al., 1994), care should be taken to ensure that clozapine-like side-effects (e.g., hypotension, sedation, and anticholinergic syndrome) do not occur by keeping the dose as small as possible and by always performing appropriate controls (e.g., administering CNO to animals expressing GFP or similarly irrelevant protein).

CNO has excellent drug-like properties with rapid CNS penetration and distribution in mice (Bender et al., 1994). CNO appears to have at least a 60 min residence in vivo in mice following intraperitoneal administration (Bender et al., 1994). Given the long residence time of CNO, it is not surprising that the in vivo effects of CNO-mediated activation of hM3Dq can be both robust and prolonged (Alexander et al., 2009; Krashes et al., 2013). Clearly, unless long-term activation of Gq signaling and neuronal firing is needed, it is recommended that the lowest effective dose of CNO be administered so that only peak CNO concentrations activate the DREADD (Figures 2B and 2C). As can be seen in Figure 2B, when a large dose of CNO is administered, the effects of CNO may be greatly prolonged because brain levels of CNO remain higher than the threshold for activation of the DREADD receptor. By contrast, lower systemic doses of CNO (Figure 2C) would result in transient peak activation and then a relatively rapid decay of activity.

Because of the potential for back-metabolism of CNO to clozapine and other clozapine metabolites in non-rodent species—including the pharmacologically diverse compound N-desmethyl-clozapine (NDMC) (Davies et al., 2005)—we have developed new non-CNO chemical actuators (Chen et al., 2015). The first of these—Compound 21 (Figure 3B)—has minimal off-target activity and exquisite selectivity for activating hM3Dq versus muscarinic and other GPCRs (Chen et al., 2015). Preliminary studies indicate that Compound 21 has equivalent potency in studies in vivo when compared with CNO (unpublished data). Compound 21 likely cannot be metabolized via normal routes to clozapine or any related compound and

thus represents an alternative to CNO for studies in which back metabolism of CNO to clozapine is problematic.

An additional compound especially suited for translational studies is perlapine (Figure 3B), a drug that is approved for use in Japan for insomnia. Perlapine has >10,000-fold selectivity for activating hM3Dq versus muscarinic receptors with an EC<sub>50</sub> at hM3Dq of 2.8 nM (Chen et al., 2015). Given perlapine's modest affinity for some biogenic amine receptors (e.g., 5-HT<sub>2A</sub>, 5-HT<sub>6</sub>, 5-HT<sub>7</sub>, and D<sub>4</sub>) (Davies et al., 2005; Roth et al., 1992, 1994, 1995), it is essential to test perlapine at the lowest possible dose in animals not expressing DREADDs before embarking on studies involving DREADDs. These preliminary studies would ensure that off-target actions of perlapine do not interfere with the phenomena studied. Perlapine will likely find its greatest utility in translational studies of DREADDs in primates and, perhaps, in humans given that it is approved for use in humans. It is likely that further investigation of the scaffolds for compound 21 and perlapine will yield even more effective, potent, and selective chemical actuators for muscarinic-based DREADDs.

The first report that CNO-induced activation of hM3Dq depolarized and excited genetically defined neurons appeared in 2009 (Alexander et al 2009). Since then, hM3Dq has been widely used to enhance neuronal firing, and I here cite only representative examples in which feeding (Krashes et al., 2011; Atasoy et al., 2012), energy expenditure (Kong et al., 2012), locomotion and striatal synaptogenesis (Kozorovitskiy et al., 2012), memory (Garner et al., 2012), and social behaviors (Peñagarikano et al., 2015) have been modulated by hM3Dq in vivo. Because hM3Dq activation induces intracellular calcium release, it has also been used to “activate” astrocytes (Agulhon et al., 2013; Bull et al., 2014; Scofield et al., 2015), hepatocytes (Li et al., 2013), pancreatic  $\beta$  cells (Guettier et al., 2009; Jain et al., 2013), vascular smooth muscle cells (Armbruster et al., 2007), and iPS-derived neuroblasts (Del’Anno et al., 2014).

Multiple options are currently available for expressing hM3Dq in genetically specified cells. Thus, genetically engineered mice are now available for expressing hM3Dq under control of tetracycline (*tet-off*) promoter (Alexander et al., 2009; Garner et al.,

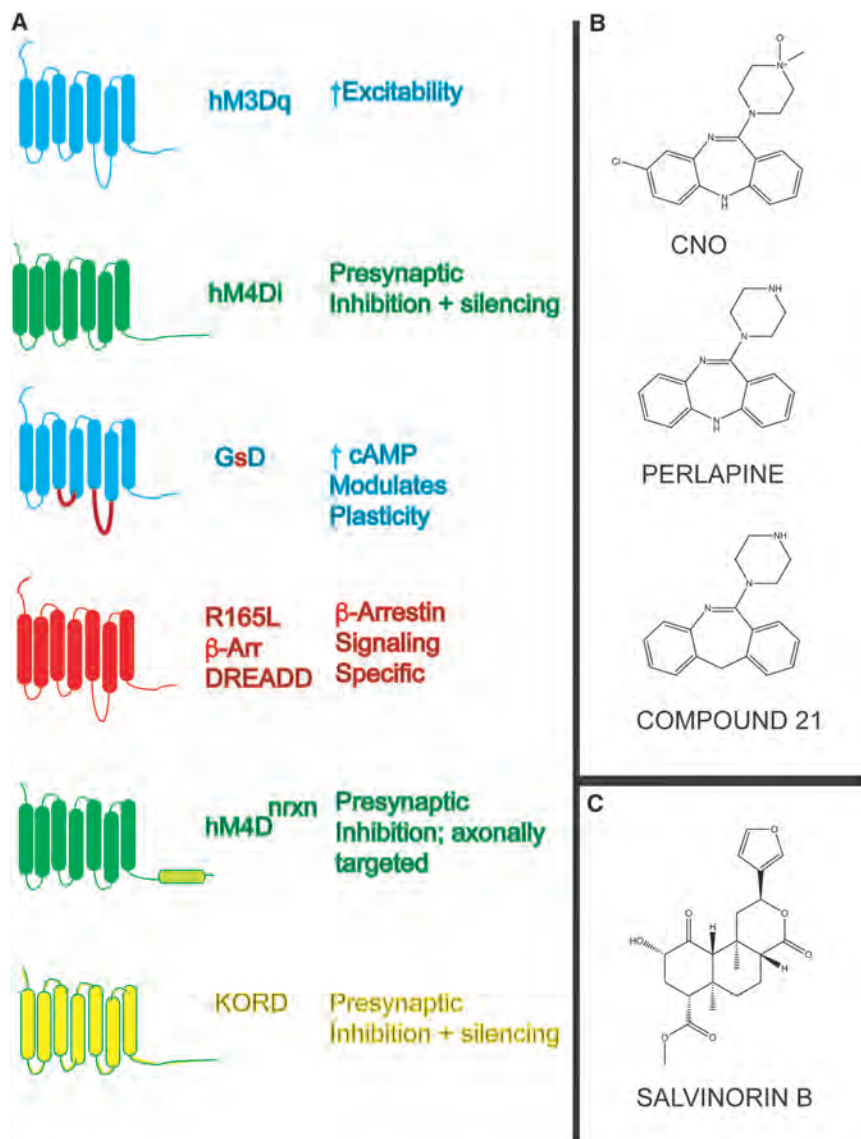


**Figure 3. Available DREADDs and Chemical Actuators**

(A) The available DREADDs, their current accepted nomenclature, and the potential downstream neuronal effects of activation.

(B and C) (B) Shows the structures of currently available chemical actuators for CNO-based DREADDs, while (C) shows the structure of the KOR ligand salvinorin B.

Aston-Jones, 2014). Finally, the use of canine adenovirus (CAV) expressing Cre-recombinase (CAV-Cre) allows for the projection-specific expression of DREADDs. Projection-specific expression of DREADD is possible because CAV-Cre is preferentially retrogradely transported to neuronal somas. In the neuronal cell bodies, recombination of AAV-FLEX-DREADD constructs can occur to allow expression of DREADDs in a projection-specific fashion (Boender et al., 2014) (Figure 4B). The use of CAV-Cre and FLEX-DREADD constructs has been dubbed the “Retro-DREADD” technique (Marchant et al., 2016) and in theory could be used for intersectional and multiplexed applications.

#### **Gi-DREADDs**

To date there are three Gi-DREADDs: hM2Di, hM4Di, and KORD. Of these, hM2Di and hM4Di can be activated by CNO (Armbruster et al., 2007), compound 21, and perlapine (B.L. Roth, unpublished data). Currently, hM4Di is the most commonly used inhibitory DREADD (for review, see Urban and Roth, 2015). Many labs have reported successful neuronal silencing with hM4Di, and only representative reports are cited wherein DREADDs silenced neurons (Armbruster

et al., 2007), modulated amphetamine sensitization (Ferguson et al., 2011) and synaptic plasticity (Kozorovitskiy et al., 2012), regulated breathing (Ray et al., 2011), feeding (Carter et al., 2013), itching (Bourane et al., 2015), and emotional (Teissier et al., 2015) behaviors.

The  $\kappa$ -opioid-derived DREADD (KORD) is a new chemogenetic GPCR that is activated by the pharmacologically inert compound. Thus, salvinorin B has no activity at any other tested molecular target (>350 GPCRs, ion channels, transporters, and enzymes evaluated) and thus has no apparent off-target activity (Figure 3C) (Chavkin et al., 2004; Vardy et al., 2015). Salvinorin B does retain modest affinity for KOR (>100 nM) so that investigators using the KORD should use the lowest dose possible and verify no effects of salvinorin B in the absence of KORD. Several labs have reported successful inhibition of neural activity with KORD (Marchant et al., 2016; Vardy et al., 2015; Denis et al., 2015).

et al., 2007), modulated amphetamine sensitization (Ferguson et al., 2011) and synaptic plasticity (Kozorovitskiy et al., 2012), regulated breathing (Ray et al., 2011), feeding (Carter et al., 2013), itching (Bourane et al., 2015), and emotional (Teissier et al., 2015) behaviors.

The  $\kappa$ -opioid-derived DREADD (KORD) is a new chemogenetic GPCR that is activated by the pharmacologically inert compound. Thus, salvinorin B has no activity at any other tested molecular target (>350 GPCRs, ion channels, transporters, and enzymes evaluated) and thus has no apparent off-target activity (Figure 3C) (Chavkin et al., 2004; Vardy et al., 2015). Salvinorin B does retain modest affinity for KOR (>100 nM) so that investigators using the KORD should use the lowest dose possible and verify no effects of salvinorin B in the absence of KORD. Several labs have reported successful inhibition of neural activity with KORD (Marchant et al., 2016; Vardy et al., 2015; Denis et al., 2015).

**Table 3. Mice Engineered to Express DREADDs**

Mouse Name Genotype	Expression Type	First Publication	Availability
TRE-hM3Dq Tg(tetO-CHRM3*)1Blr/J	Conditional Tet-off/Tet-on driven expression of hM3Dq	Alexander et al., 2009	JAX Mice; <a href="https://www.jax.org/strain/014093">https://www.jax.org/strain/014093</a>
TRE-hM4Di B6.Cg-Tg(tetO-CHRM4*)2Blr/J	Conditional Tet-off/Tet-on driven expression of hM4Di	Zhu et al., 2014	JAX Mice; <a href="https://www.jax.org/strain/024114">https://www.jax.org/strain/024114</a>
Adora2A-rM3Ds B6.Cg-Tg(Adora2a-Chrm3*, -mCherry)AD6Blr/j	Selective expression in Adora2a-expressing D2 neurons in striatum	Farrell et al., 2013	JAX Mice; <a href="https://www.jax.org/strain/017863">https://www.jax.org/strain/017863</a>
FLOXED-Gi-DREADD mice B6N.129-Gt(ROSA)26Sor <sup>tm1(CAG-CHRM4*, -mCitrine)Ute</sup> /J	Conditional Cre-mediated expression of hM4Di	Unpublished resource	JAX Mice; <a href="https://www.jax.org/strain/026219">https://www.jax.org/strain/026219</a>
FLOXED-Gq-DREADD mice Gt(ROSA)26Sor <sup>tm2(CAG-CHRM3*, -mCitrine)Ute</sup> /J	Conditional Cre-mediated expression of hM3Dq	Unpublished resource	JAX Mice; <a href="https://www.jax.org/strain/026220">https://www.jax.org/strain/026220</a>
FLOXED/FLP conditional Gi-DREADD mice; RC::FPDi; RC::PDi; RC::FDi	Conditional and intersectional Cre- and FLX-mediated expression of Gi-DREADD	Ray et al., 2011; Brust et al., 2014	Dymecki Lab; <a href="http://genepath.med.harvard.edu/~dymecki/requests.html">http://genepath.med.harvard.edu/~dymecki/requests.html</a>
$\beta$ -cell-specific GqDRADD; $\beta$ -R-q	Pancreatic $\beta$ -cell-specific M3Gq DREADD	Guettier et al., 2009	Jurgen Wess lab; <a href="mailto:jurgenw@helx.nih.gov">jurgenw@helx.nih.gov</a>
$\beta$ -cell-specific GsDREADD; $\beta$ -R-S	Pancreatic $\beta$ -cell-specific Gs DREADD	Guettier et al., 2009	Jurgen Wess lab; <a href="mailto:jurgenw@helx.nih.gov">jurgenw@helx.nih.gov</a>

Both hM4Di and KORD appear to inhibit neuronal activity via two mechanisms: (a) induction of hyperpolarization by G $\beta$ / $\gamma$ -mediated activation of G-protein inwardly rectifying potassium channels (GIRKs) (Armbruster et al., 2007; Vardy et al., 2015) and (b) via inhibition of the presynaptic release of neurotransmitters (e.g., synaptic silencing) (Stachniak et al., 2014; Vardy et al., 2015). Thus, unlike bacterial opsins, which silence neurons via a strong hyperpolarization and with millisecond precision, DREADDs induce a modest hyperpolarization and an apparently strong inhibition of axonal release of neurotransmitter (Stachniak et al., 2014; Vardy et al., 2015) in the seconds-minutes-hours time frame. Because of the dependence upon G $\beta$ / $\gamma$ -mediated activation of GIRKs for inducing hyperpolarization, it is possible that hM4Di and KORD might not hyperpolarize all neurons. To date, there have been no reports that hM4Di or KORD fail to silence or inhibit neuronal activity.

Given that the Gi-coupled DREADDs have effects on terminal release the possibility that CNO (or an analogue) or SalB (or analogue) could micro-infused to locally suppress neural activity has been tested (Figure 4C). Thus, at least two groups (Stachniak et al., 2014; Mahler et al., 2014) have successfully silenced terminal projections via local infusion of CNO. Terminal axons have also been activated by local CNO infusion into rats expression hM3Dq (Vazey and Aston-Jones, 2014). For selective axonal silencing, an hM4Di variant has been created (Figure 3A; hM4D<sup>IRXN</sup>) that is targeted preferentially to axons and axon terminals (Stachniak et al., 2014).

The availability of a new inhibitory DREADD—KORD—activated by a ligand orthogonal to CNO now allows for the multiplexed and bidirectional chemogenetic modulation of neural activity and behavior (Vardy et al., 2015). Thus, we recently demonstrated that KORD may be expressed simultaneously with hM3Dq to allow for the sequential chemogenetic activation (with hM3Dq and CNO) and inhibition (with SalB and KORD) (Vardy et al., 2015) of neuronal activity (Figure 4D). It is likely

that KORD and hM3Dq could be combined in a combinatorial fashion with various opsins and other chemogenetic tools (e.g., PSEM and PSAMs) to afford highly multiplexed control of neuronal activity with millisecond precision (e.g., with opsins) and for long periods of time for behavioral studies (e.g., with DREADDs or PSAMs).

#### Gs- and $\beta$ -Arrestin-DREADDs

The only DREADD coupled to Gs was created by swapping the intracellular regions of the turkey erythrocyte  $\beta$  adrenergic receptor for equivalent regions of a rat M3 DREADD to create a rat Gs-DREADD (Guettier et al., 2009) (Figure 3A). Unlike the current Gq and Gi-DREADDs, the Gs-DREADD (GsD) has a small degree of constitutive activity in transfected cells (Guettier et al., 2009) leading to a modest basal phenotype in pancreatic  $\beta$  cells (Guettier et al., 2009; Jain et al., 2013). Given that G $\alpha_{\text{off}}$  is the major Gs-like G $\alpha$  protein in some brain regions (Zhuang et al., 2000), it was critical to determine if GsD can also activate G $\alpha_{\text{off}}$ . Importantly, we demonstrated that GsD efficiently couples to G $\alpha_{\text{off}}$  in vitro and in vivo (Farrell et al., 2013) and that GsD had minimal constitutive activity for G $\alpha_{\text{off}}$ -mediated signaling in vitro and in vivo (Farrell et al., 2013). GsD has been used by several groups to probe the role(s) of Gs-like signaling for a number of behaviors including ethanol consumption (Pleil et al., 2015), reward (Ferguson et al., 2013), locomotor sensitization (Farrell et al., 2013), and circadian rhythms (Brancaccio et al., 2013).

Finally, a DREADD that apparently signals exclusively via  $\beta$ -arrestin has been developed (Nakajima and Wess, 2012) (Figure 3A). This  $\beta$ -arrestin-specific DREADD (Rq(R165L)) has not yet been used in vivo but has the potential to illuminate specific behaviors downstream of  $\beta$ -arrestin signaling (for discussion, see Allen and Roth, 2011; Allen et al., 2011).

#### Areas for Enhancement of DREADD Technologies

Chemogenetic technologies are now widely used by many neuroscientists with publications appearing at the rate of one to

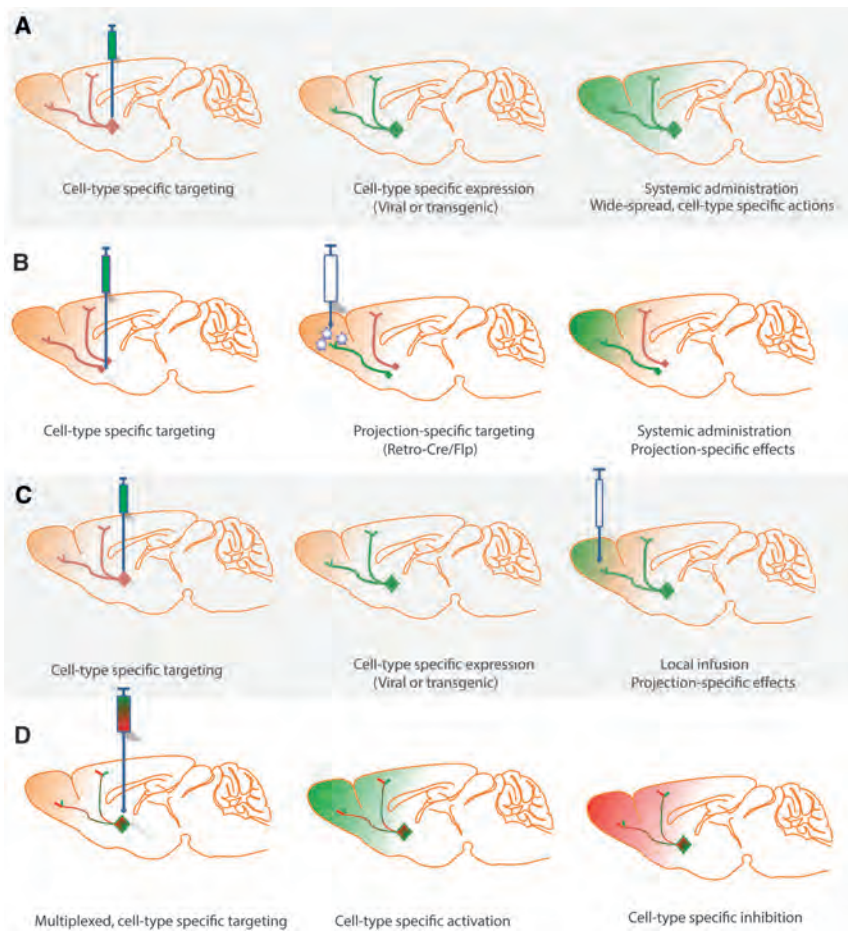


**Figure 4. Potential Approaches for Cell- and Projection-Specific Modulation of Neuronal Activity Using DREADDs**

(A) The standard approach whereby DREADDs are expressed in a cell-type-specific manner (either virally or transgenically) and then activated by systemic administration of chemical actuator.

(B) How a combination of cell-type-specific expression (e.g., localized injection of AAV-FLEX-hSyn-DREADD) and projection-specific infusion of CAV-Cre allows for the projection-specific expression and activation of DREADDs.

(C) How local infusion of a chemical actuator provides for projection-specific effects with a limited area of activation.

(D) How distinct DREADDs may be expressed in a cell-type-specific fashion to afford multiplexed chemogenetic modulation of neural activity and physiology.

tures of GPCRs including a 1.8 Å structure of the human  $\delta$ -opioid receptor (Katritch et al., 2014), two serotonin receptors in partially active states (Wang et al., 2013), active and coupled states of the  $\mu$ -opioid (Huang et al., 2015a), M1-muscarinic (Kruse et al., 2013),  $\beta$ 2-adrenergic receptors (Rasmussen et al., 2011), and many other inactive state structures (Katritch et al., 2014). Additionally, my lab and collaborators have used these structures for the successful structure-guided discovery of novel small molecule modulators (Weiss et al., 2013; Carlsson et al., 2011; Shoichet and Kobilka, 2012; Huang et al.,

two per day. To date, hM4Di (for silencing) and hM3Dq (for activating) neurons have been the most frequent used DREADDs. DREADDs have been used to modulate neural activity and behavior in flies (Becnel et al., 2013), mice (Alexander et al., 2009), rats (Ferguson et al., 2011), and nonhuman primates (El-dridge et al., 2016). Although DREADD technology has clearly been useful, there are several ways in which the technological platform could be enhanced.

#### **Outlook for New DREADDs and Chemical Actuators**

In terms of creating new DREADDs, we have described a generic platform wherein human GPCRs can be expressed in yeast with engineered selectable markers and chimeric G proteins (Armbruster et al., 2007; Dong et al., 2010) and have used this platform to express dozens of human GPCRs (Huang et al., 2015b). In theory it should be possible to create new DREADDs by directed molecular evolution of human GPCRs using the prior yeast-based platforms (Armbruster et al., 2007; Dong et al., 2010; Huang et al., 2015b).

An alternative approach is to use structure-guided docking of drug-like and pharmacologically inert small molecules against GPCRs for which there are available structures. This structure-guided approach was used by us to create KORD (Vardy et al., 2015). Currently there are many high-resolution struc-

tures of GPCRs including a 1.8 Å structure of the human  $\delta$ -opioid receptor (Katritch et al., 2014), two serotonin receptors in partially active states (Wang et al., 2013), active and coupled states of the  $\mu$ -opioid (Huang et al., 2015a), M1-muscarinic (Kruse et al., 2013),  $\beta$ 2-adrenergic receptors (Rasmussen et al., 2011), and many other inactive state structures (Katritch et al., 2014). Additionally, my lab and collaborators have used these structures for the successful structure-guided discovery of novel small molecule modulators (Weiss et al., 2013; Carlsson et al., 2011; Shoichet and Kobilka, 2012; Huang et al.,

2015b). It is thus possible that new DREADDs could be created using these sorts of approaches.

With regard to new small molecule actuators, it would be useful to identify other CNO- and salvinorin B analogues with (a) good drug-like properties, (b) excellent CNS penetrability, (c) clean off-target pharmacology, and (d) favorable pharmacokinetic and toxicological features (Arrowsmith et al., 2015). Additionally the availability of salvinorin B analogues which are water soluble—as salvinorin B is typically dissolved in dimethylsulfoxide—would also be useful. The development of these sorts of tool compounds could be achieved via conventional medicinal chemistry approaches (Chen et al., 2015) and by new technologies developed by my lab and my collaborators. These new chemical biology technologies allow for the design and validation of novel drug-like molecules using a combination of *in silico* and *in vitro* approaches (Keiser et al., 2009; Besnard et al., 2012; Huang et al., 2015b; Kroeze et al., 2015). Additionally, new chemical biology platforms that allow for the unbiased assessment of on- and off-target pharmacologies of chemical actuators across the GPCR-ome (Kroeze et al., 2015), kinome (Elkins et al., 2015), and other targets (Arrowsmith et al., 2015) are key to validating the specificity of DREADD ligands.

Other areas of enhancement for DREADD technology would include the design of DREADDs with differential neuronal

subdomain-specific targeting. Thus, in addition to the axonal targeting DREADDs previously reported (Stachniak et al., 2014), cell body, dendritically targeted, and spine-specifically targeted DREADDs would all be broadly useful. Enhancing the diversity of signaling cascades to include  $G_{12/13}$ ,  $G_o$ ,  $G_{olf}$ , and so on would also be highly valuable to the community. Here, structure-based approaches might be especially valuable. Finally, improving the temporal resolution via photo-caging DREADDs or via creation of DREADD antagonists would also be potentially highly useful—particularly given the large number of laboratories currently using DREADD technology.

#### Potential Therapeutic Applications for Chemogenetics

Many therapeutic applications of DREADD-based therapeutics have been suggested, including diabetes (Jain et al., 2013), metabolic disorders (Li et al., 2013), Parkinson's Disease (Dell'Anno et al., 2014), psychostimulant (Ferguson et al., 2011) and ethanol (Pleil et al., 2015) abuse, depression (Urban et al., 2015), post-traumatic stress disorder (Zhu et al., 2014), intractable seizures (Kätzel et al., 2014), inflammatory disorders (Park et al., 2014), autism (Peñagarikano et al., 2015), and many other disorders (English and Roth, 2015). DREADDs have been successfully expressed in nonhuman primates without apparent toxicity, and an exciting new report demonstrates that CNO-DREADDs can modulate circuitry, electrophysiology, and behavior in nonhuman primates (Eldridge et al., 2016). As AAV is a commonly used gene delivery platform in humans, the most likely viral vector for human studies would be AAV. In terms of the chemical actuator, given the fact that perlapine is an approved medication with a long history of safety in humans, it would be the most likely DREADD ligand for activating CNO-based DREADDs in humans. Although CNO has been given to humans without ill-effects, given its propensity for back-metabolism to clozapine and NDMC in humans, it might not be the first choice for translational studies. Salvinorin B has not been administered to humans, although salvinorin A—its precursor—has been used in many human studies without any apparent toxicity. Going forward it would be valuable to identify additional drugs that are approved for use in humans to accelerate translation of DREADD technology to humans.

In summary, DREADDs have transformed basic and translational neuroscience research. The availability of multiple DREADDs activated by chemically and pharmacologically distinct actuators will continue to facilitate the multiplexed, chemogenetic interrogation of circuits and cell types involved in behavior, cognition, emotion, memory, and perception.

#### ACKNOWLEDGEMENTS

Work involving chemogenetics in my lab is supported by an NIH BRAIN Initiative Award (U01MH105892), the National Institute of Mental Health Psychoactive Drug Screening Program (271201300017C-1-0-1), and the Michael Hooker Distinguished Professorship in Protein Therapeutics and Translational Proteomics.

#### REFERENCES

Agulhon, C., Boyt, K.M., Xie, A.X., Friocourt, F., Roth, B.L., and McCarthy, K.D. (2013). Modulation of the autonomic nervous system and behaviour by acute glial cell Gq protein-coupled receptor activation in vivo. *J. Physiol.* 591, 5599–5609.

Alexander, G.M., Rogan, S.C., Abbas, A.I., Armbruster, B.N., Pei, Y., Allen, J.A., Nonneman, R.J., Hartmann, J., Moy, S.S., Nicoletti, M.A., et al. (2009). Remote control of neuronal activity in transgenic mice expressing evolved G protein-coupled receptors. *Neuron* 63, 27–39.

Allen, J.A., and Roth, B.L. (2011). Strategies to discover unexpected targets for drugs active at G protein-coupled receptors. *Annu. Rev. Pharmacol. Toxicol.* 51, 117–144.

Allen, J.A., Yost, J.M., Setola, V., Chen, X., Sassano, M.F., Chen, M., Peterson, S., Yadav, P.N., Huang, X.P., Feng, B., et al. (2011). Discovery of  $\beta$ -arrestin-biased dopamine D2 ligands for probing signal transduction pathways essential for antipsychotic efficacy. *Proc. Natl. Acad. Sci. USA* 108, 18488–18493.

Aponte, Y., Atasoy, D., and Sternson, S.M. (2011). AGRP neurons are sufficient to orchestrate feeding behavior rapidly and without training. *Nat. Neurosci.* 14, 351–355.

Arenkiel, B.R., Klein, M.E., Davison, I.G., Katz, L.C., and Ehlers, M.D. (2008). Genetic control of neuronal activity in mice conditionally expressing TRPV1. *Nat. Methods* 5, 299–302.

Armbruster, B., and Roth, B. (2005). Creation of Designer Biogenic Amine Receptors via Directed Molecular Evolution. *Neuropsychopharmacology* 30, S265.

Armbruster, B.N., Li, X., Pausch, M.H., Herlitze, S., and Roth, B.L. (2007). Evolving the lock to fit the key to create a family of G protein-coupled receptors potently activated by an inert ligand. *Proc. Natl. Acad. Sci. USA* 104, 5163–5168.

Arrowsmith, C.H., Audia, J.E., Austin, C., Baell, J., Bennett, J., Blagg, J., Bountra, C., Brennan, P.E., Brown, P.J., Bunnage, M.E., et al. (2015). The promise and peril of chemical probes. *Nat. Chem. Biol.* 11, 536–541.

Atasoy, D., Aponte, Y., Su, H.H., and Sternson, S.M. (2008). A FLEX switch targets Channelrhodopsin-2 to multiple cell types for imaging and long-range circuit mapping. *J. Neurosci.* 28, 7025–7030.

Atasoy, D., Betley, J.N., Su, H.H., and Sternson, S.M. (2012). Deconstruction of a neural circuit for hunger. *Nature* 488, 172–177.

Becnel, J., Johnson, O., Majeed, Z.R., Tran, V., Yu, B., Roth, B.L., Cooper, R.L., Kerut, E.K., and Nichols, C.D. (2013). DREADDs in *Drosophila*: a pharmacogenetic approach for controlling behavior, neuronal signaling, and physiology in the fly. *Cell Rep.* 4, 1049–1059.

Bender, D., Holschbach, M., and Stöcklin, G. (1994). Synthesis of n.c.a. carbon-11 labelled clozapine and its major metabolite clozapine-N-oxide and comparison of their biodistribution in mice. *Nucl. Med. Biol.* 21, 921–925.

Besnard, J., Ruda, G.F., Setola, V., Abecassis, K., Rodriguiz, R.M., Huang, X.P., Norval, S., Sassano, M.F., Shin, A.I., Webster, L.A., et al. (2012). Automated design of ligands to polypharmacological profiles. *Nature* 492, 215–220.

Betley, J.N., Xu, S., Cao, Z.F., Gong, R., Magnus, C.J., Yu, Y., and Sternson, S.M. (2015). Neurons for hunger and thirst transmit a negative-valence teaching signal. *Nature* 521, 180–185.

Bishop, A.C., Shah, K., Liu, Y., Witucki, L., Kung, C., and Shokat, K.M. (1998). Design of allele-specific inhibitors to probe protein kinase signaling. *Curr. Biol.* 8, 257–266.

Bishop, A.C., Ubersax, J.A., Petsch, D.T., Matheos, D.P., Gray, N.S., Blethrow, J., Shimizu, E., Tsien, J.Z., Schultz, P.G., Rose, M.D., et al. (2000). A chemical switch for inhibitor-sensitive alleles of any protein kinase. *Nature* 407, 395–401.

Boender, A.J., de Jong, J.W., Boekhoudt, L., Luijendijk, M.C., van der Plasse, G., and Adan, R.A. (2014). Combined use of the canine adenovirus-2 and DREADD-technology to activate specific neural pathways in vivo. *PLoS ONE* 9, e95392.

Bourane, S., Duan, B., Koch, S.C., Dalet, A., Britz, O., Garcia-Campmany, L., Kim, E., Cheng, L., Ghosh, A., Ma, Q., and Goulding, M. (2015). Gate control of mechanical itch by a subpopulation of spinal cord interneurons. *Science* 350, 550–554.

- Brancaccio, M., Maywood, E.S., Chesham, J.E., Loudon, A.S., and Hastings, M.H. (2013). A Gq-Ca<sup>2+</sup> axis controls circuit-level encoding of circadian time in the suprachiasmatic nucleus. *Neuron* 78, 714–728.
- Brust, R.D., Corcoran, A.E., Richerson, G.B., Nattie, E., and Dymecki, S.M. (2014). Functional and developmental identification of a molecular subtype of brain serotonergic neurons specialized to regulate breathing dynamics. *Cell Rep.* 9, 2152–2165.
- Bull, C., Freitas, K.C., Zou, S., Poland, R.S., Syed, W.A., Urban, D.J., Minter, S.C., Shelton, K.L., Hauser, K.F., Negus, S.S., et al. (2014). Rat nucleus accumbens core astrocytes modulate reward and the motivation to self-administer ethanol after abstinence. *Neuropsychopharmacology* 39, 2835–2845.
- Cai, H., Haubensak, W., Anthony, T.E., and Anderson, D.J. (2014). Central amygdala PKC- $\delta$ (+) neurons mediate the influence of multiple anorexigenic signals. *Nat. Neurosci.* 17, 1240–1248.
- Carlsson, J., Coleman, R.G., Setola, V., Irwin, J.J., Fan, H., Schlessinger, A., Sali, A., Roth, B.L., and Shoichet, B.K. (2011). Ligand discovery from a dopamine D<sub>3</sub> receptor homology model and crystal structure. *Nat. Chem. Biol.* 7, 769–778.
- Carter, M.E., Soden, M.E., Zweifel, L.S., and Palmiter, R.D. (2013). Genetic identification of a neural circuit that suppresses appetite. *Nature* 503, 111–114.
- Chavkin, C., Sud, S., Jin, W., Stewart, J., Zjawiony, J.K., Siebert, D.J., Toth, B.A., Hufeisen, S.J., and Roth, B.L. (2004). Salvinorin A, an active component of the hallucinogenic sage *salvia divinorum* is a highly efficacious kappa-opioid receptor agonist: structural and functional considerations. *J. Pharmacol. Exp. Ther.* 308, 1197–1203.
- Chen, X., Ye, H., Kuruville, R., Ramanan, N., Scangos, K.W., Zhang, C., Johnson, N.M., England, P.M., Shokat, K.M., and Ginty, D.D. (2005). A chemical-genetic approach to studying neurotrophin signaling. *Neuron* 46, 13–21.
- Chen, X., Choo, H., Huang, X.P., Yang, X., Stone, O., Roth, B.L., and Jin, J. (2015). The first structure-activity relationship studies for designer receptors exclusively activated by designer drugs. *ACS Chem. Neurosci.* 6, 476–484.
- Cohen, M.S., Zhang, C., Shokat, K.M., and Taunton, J. (2005). Structural bioinformatics-based design of selective, irreversible kinase inhibitors. *Science* 308, 1318–1321.
- Collot, J., Gradinaru, J., Humbert, N., Skander, M., Zocchi, A., and Ward, T.R. (2003). Artificial metalloenzymes for enantioselective catalysis based on biotin-avidin. *J. Am. Chem. Soc.* 125, 9030–9031.
- Conklin, B.R., Hsiao, E.C., Claeysen, S., Dumuis, A., Srinivasan, S., Forsayeth, J.R., Guettier, J.M., Chang, W.C., Pei, Y., McCarthy, K.D., et al. (2008). Engineering GPCR signaling pathways with RASSLs. *Nat. Methods* 5, 673–678.
- Costa, T., and Herz, A. (1989). Antagonists with negative intrinsic activity at delta opioid receptors coupled to GTP-binding proteins. *Proc. Natl. Acad. Sci. USA* 86, 7321–7325.
- Coward, P., Wada, H.G., Falk, M.S., Chan, S.D., Meng, F., Akil, H., and Conklin, B.R. (1998). Controlling signaling with a specifically designed Gi-coupled receptor. *Proc. Natl. Acad. Sci. USA* 95, 352–357.
- Dar, A.C., Das, T.K., Shokat, K.M., and Cagan, R.L. (2012). Chemical genetic discovery of targets and anti-targets for cancer polypharmacology. *Nature* 486, 80–84.
- Davies, M.A., Compton-Toth, B.A., Hufeisen, S.J., Meltzer, H.Y., and Roth, B.L. (2005). The highly efficacious actions of N-desmethylclozapine at muscarinic receptors are unique and not a common property of either typical or atypical antipsychotic drugs: is M1 agonism a pre-requisite for mimicking clozapine's actions? *Psychopharmacology (Berl.)* 178, 451–460.
- De Lean, A., Stadel, J.M., and Lefkowitz, R.J. (1980). A ternary complex model explains the agonist-specific binding properties of the adenylate cyclase-coupled beta-adrenergic receptor. *J. Biol. Chem.* 255, 7108–7117.
- DeLean, A., Munson, P.J., and Rodbard, D. (1978). Simultaneous analysis of families of sigmoidal curves: application to bioassay, radioligand assay, and physiological dose-response curves. *Am. J. Physiol.* 235, E97–E102.
- Dell'Anno, M.T., Caiazzo, M., Leo, D., Dvoretzskova, E., Medrihan, L., Colasante, G., Giannelli, S., Theka, I., Russo, G., Mus, L., et al. (2014). Remote control of induced dopaminergic neurons in parkinsonian rats. *J. Clin. Invest.* 124, 3215–3229.
- Denis, R.G., Joly-Amado, A., Webber, E., Langlet, F., Schaeffer, M., Padilla, S.L., Cansell, C., Dehouck, B., Castel, J., Delbès, A.S., et al. (2015). Palatability Can Drive Feeding Independent of AgRP Neurons. *Cell Metab.* 22, 646–657.
- DeWire, S.M., Ahn, S., Lefkowitz, R.J., and Shenoy, S.K. (2007). Beta-arrestins and cell signaling. *Annu. Rev. Physiol.* 69, 483–510.
- Dong, S., Rogan, S.C., and Roth, B.L. (2010). Directed molecular evolution of DREADDs: a generic approach to creating next-generation RASSLs. *Nat. Protoc.* 5, 561–573.
- Eldridge, M.A.G., Lerchner, W., Saunders, R.C., Kaneko, H., Krausz, K.W., Gonzalez, F.J., Ji, B., Higuchi, M., Minamimoto, T., and Richmond, B.J. (2016). Chemogenetic disconnection of monkey orbitofrontal and rhinal cortex reversibly disrupts reward value. *Nat. Neurosci.* 19, 37–39.
- Elkins, J.M., Fedele, V., Szklarz, M., Abdul Azeez, K.R., Salah, E., Mikolajczyk, J., Romanov, S., Sepetov, N., Huang, X.P., Roth, B.L., et al. (2015). Comprehensive characterization of the Published Kinase Inhibitor Set. *Nat. Biotechnol.* 34, 95–103.
- English, J.G., and Roth, B.L. (2015). Chemogenetics—A Transformational and Translational Platform. *JAMA Neurol.* 72, 1361–1366.
- Farrell, M.S., Pei, Y., Wan, Y., Yadav, P.N., Daigle, T.L., Urban, D.J., Lee, H.M., Sciaky, N., Simmons, A., Nonneman, R.J., et al. (2013). A G $\alpha$ s DREADD mouse for selective modulation of cAMP production in striatopallidal neurons. *Neuropsychopharmacology* 38, 854–862.
- Fenalti, G., Giguere, P.M., Katritch, V., Huang, X.P., Thompson, A.A., Cherezov, V., Roth, B.L., and Stevens, R.C. (2014). Molecular control of  $\delta$ -opioid receptor signalling. *Nature* 506, 191–196.
- Ferguson, S.M., Eskenazi, D., Ishikawa, M., Wanat, M.J., Phillips, P.E., Dong, Y., Roth, B.L., and Neumaier, J.F. (2011). Transient neuronal inhibition reveals opposing roles of indirect and direct pathways in sensitization. *Nat. Neurosci.* 14, 22–24.
- Ferguson, S.M., Phillips, P.E., Roth, B.L., Wess, J., and Neumaier, J.F. (2013). Direct-pathway striatal neurons regulate the retention of decision-making strategies. *J. Neurosci.* 33, 11668–11676.
- Forkmann, G., and Dangelmayr, B. (1980). Genetic control of chalcone isomerase activity in flowers of *Dianthus caryophyllus*. *Biochem. Genet.* 18, 519–527.
- Garner, A.R., Rowland, D.C., Hwang, S.Y., Baumgaertel, K., Roth, B.L., Kentros, C., and Mayford, M. (2012). Generation of a synthetic memory trace. *Science* 335, 1513–1516.
- Gether, U., Lin, S., and Kobilka, B.K. (1995). Fluorescent labeling of purified beta 2 adrenergic receptor. Evidence for ligand-specific conformational changes. *J. Biol. Chem.* 270, 28268–28275.
- Gradinaru, V., Zhang, F., Ramakrishnan, C., Mattis, J., Prakash, R., Diester, I., Goshen, I., Thompson, K.R., and Deisseroth, K. (2010). Molecular and cellular approaches for diversifying and extending optogenetics. *Cell* 141, 154–165.
- Guettier, J.M., Gautam, D., Scarselli, M., Ruiz de Azua, I., Li, J.H., Rosemond, E., Ma, X., Gonzalez, F.J., Armbruster, B.N., Lu, H., et al. (2009). A chemical-genetic approach to study G protein regulation of beta cell function in vivo. *Proc. Natl. Acad. Sci. USA* 106, 19197–19202.
- Häring, D., and Distefano, M.D. (2001). Enzymes by design: chemogenetic assembly of transamination active sites containing lysine residues for covalent catalysis. *Bioconjug. Chem.* 12, 385–390.
- Hayashi, Y., Kashiwagi, M., Yasuda, K., Ando, R., Kanuka, M., Sakai, K., and Itohara, S. (2015). Cells of a common developmental origin regulate REM/non-REM sleep and wakefulness in mice. *Science* 350, 957–961.
- Hsiao, E.C., Boudignon, B.M., Chang, W.C., Bencsik, M., Peng, J., Nguyen, T.D., Manalac, C., Halloran, B.P., Conklin, B.R., and Nissenson, R.A. (2008). Osteoblast expression of an engineered Gs-coupled receptor dramatically increases bone mass. *Proc. Natl. Acad. Sci. USA* 105, 1209–1214.
- Huang, W., Manglik, A., Venkatakrishnan, A.J., Laeremans, T., Feinberg, E.N., Sanborn, A.L., Kato, H.E., Livingston, K.E., Thorsen, T.S., Kling, R.C., et al.

- (2015a). Structural insights into  $\mu$ -opioid receptor activation. *Nature* 524, 315–321.
- Huang, X.P., Karpiak, J., Kroeze, W.K., Zhu, H., Chen, X., Moy, S.S., Sadorris, K.A., Nikolova, V.D., Farrell, M.S., Wang, S., et al. (2015b). Allosteric ligands for the pharmacologically dark receptors GPR68 and GPR65. *Nature* 527, 477–483.
- Isosaka, T., Matsuo, T., Yamaguchi, T., Funabiki, K., Nakanishi, S., Kobayakawa, R., and Kobayakawa, K. (2015). Htr2a-Expressing Cells in the Central Amygdala Control the Hierarchy between Innate and Learned Fear. *Cell* 163, 1153–1164.
- Jain, S., Ruiz de Azua, I., Lu, H., White, M.F., Guettier, J.M., and Wess, J. (2013). Chronic activation of a designer G(q)-coupled receptor improves  $\beta$  cell function. *J. Clin. Invest.* 123, 1750–1762.
- Jann, M.W., Lam, Y.W., and Chang, W.H. (1994). Rapid formation of clozapine in guinea-pigs and man following clozapine-N-oxide administration. *Arch. Int. Pharmacodyn. Ther.* 328, 243–250.
- Kang, Y., Zhou, X.E., Gao, X., He, Y., Liu, W., Ishchenko, A., Barty, A., White, T.A., Yefanov, O., Han, G.W., et al. (2015). Crystal structure of rhodopsin bound to arrestin by femtosecond X-ray laser. *Nature* 523, 561–567.
- Katritch, V., Fenalti, G., Abola, E.E., Roth, B.L., Cherezov, V., and Stevens, R.C. (2014). Allosteric sodium in class A GPCR signaling. *Trends Biochem. Sci.* 39, 233–244.
- Kätzel, D., Nicholson, E., Schorge, S., Walker, M.C., and Kullmann, D.M. (2014). Chemical-genetic attenuation of focal neocortical seizures. *Nat. Commun.* 5, 3847.
- Keiser, M.J., Setola, V., Irwin, J.J., Laggner, C., Abbas, A.I., Hufeisen, S.J., Jensen, N.H., Kuijter, M.B., Matos, R.C., Tran, T.B., et al. (2009). Predicting new molecular targets for known drugs. *Nature* 462, 175–181.
- Klein, G., Humbert, N., Gradinaru, J., Ivanova, A., Gilardoni, F., Rusbandi, U.E., and Ward, T.R. (2005). Tailoring the active site of chzymes by using a chemogenetic-optimization procedure: towards substrate-specific artificial hydrogenases based on the biotin-avidin technology. *Angew. Chem. Int. Ed. Engl.* 44, 7764–7767.
- Kong, D., Tong, Q., Ye, C., Koda, S., Fuller, P.M., Krashes, M.J., Vong, L., Ray, R.S., Olson, D.P., and Lowell, B.B. (2012). GABAergic RIP-Cre neurons in the arcuate nucleus selectively regulate energy expenditure. *Cell* 151, 645–657.
- Kozorovitskiy, Y., Saunders, A., Johnson, C.A., Lowell, B.B., and Sabatini, B.L. (2012). Recurrent network activity drives striatal synaptogenesis. *Nature* 485, 646–650.
- Krashes, M.J., Koda, S., Ye, C., Rogan, S.C., Adams, A.C., Cusher, D.S., Maratos-Flier, E., Roth, B.L., and Lowell, B.B. (2011). Rapid, reversible activation of AgRP neurons drives feeding behavior in mice. *J. Clin. Invest.* 121, 1424–1428.
- Krashes, M.J., Shah, B.P., Koda, S., and Lowell, B.B. (2013). Rapid versus delayed stimulation of feeding by the endogenously released AgRP neuron mediators GABA, NPY, and AgRP. *Cell Metab.* 18, 588–595.
- Kroeze, W.K., Sassano, M.F., Huang, X.P., Lansu, K., McCorvy, J.D., Giguère, P.M., Sciak, N., and Roth, B.L. (2015). PRESTO-Tango as an open-source resource for interrogation of the druggable human GPCRome. *Nat. Struct. Mol. Biol.* 22, 362–369.
- Kruse, A.C., Ring, A.M., Manglik, A., Hu, J., Hu, K., Eitel, K., Hübner, H., Pardon, E., Valant, C., Sexton, P.M., et al. (2013). Activation and allosteric modulation of a muscarinic acetylcholine receptor. *Nature* 504, 101–106.
- Lee, G., and Saito, I. (1998). Role of nucleotide sequences of loxP spacer region in Cre-mediated recombination. *Gene* 216, 55–65.
- Lerchner, W., Xiao, C., Nashmi, R., Slimko, E.M., van Trigt, L., Lester, H.A., and Anderson, D.J. (2007). Reversible silencing of neuronal excitability in behaving mice by a genetically targeted, ivermectin-gated Cl<sup>-</sup> channel. *Neuron* 54, 35–49.
- Li, J.H., Jain, S., McMillin, S.M., Cui, Y., Gautam, D., Sakamoto, W., Lu, H., Jou, W., McGuinness, O.P., Gavrilova, O., and Wess, J. (2013). A novel experimental strategy to assess the metabolic effects of selective activation of a G(q)-coupled receptor in hepatocytes in vivo. *Endocrinology* 154, 3539–3551.
- Liu, Y., Shah, K., Yang, F., Witucki, L., and Shokat, K.M. (1998). Engineering Src family protein kinases with unnatural nucleotide specificity. *Chem. Biol.* 5, 91–101.
- Luttrell, L.M., Ferguson, S.S., Daaka, Y., Miller, W.E., Maudsley, S., Della Rocca, G.J., Lin, F., Kawakatsu, H., Owada, K., Luttrell, D.K., et al. (1999). Beta-arrestin-dependent formation of beta2 adrenergic receptor-Src protein kinase complexes. *Science* 283, 655–661.
- Magnus, C.J., Lee, P.H., Atasoy, D., Su, H.H., Looger, L.L., and Sternson, S.M. (2011). Chemical and genetic engineering of selective ion channel-ligand interactions. *Science* 333, 1292–1296.
- Mahler, S.V., Vazey, E.M., Beckley, J.T., Keistler, C.R., McGlinchey, E.M., Kaufling, J., Wilson, S.P., Deisseroth, K., Woodward, J.J., and Aston-Jones, G. (2014). Designer receptors show role for ventral pallidum input to ventral tegmental area in cocaine seeking. *Nat. Neurosci.* 17, 577–585.
- Manglik, A., Kim, T.H., Masurell, M., Altenbach, C., Yang, Z., Hilger, D., Lerch, M.T., Kobilka, T.S., Thian, F.S., Hubbell, W.L., et al. (2015). Structural Insights into the Dynamic Process of  $\beta$ 2-Adrenergic Receptor Signaling. *Cell* 161, 1101–1111.
- Marchant, N.J., Whitaker, L.R., Bossert, J.M., Harvey, B.K., Hope, B.T., Kaganovsky, K., Adhikary, S., Prinszano, T.E., Vardy, E., Roth, B.L., and Shaham, Y. (2016). Behavioral and Physiological Effects of a Novel Kappa-Opioid Receptor-Based DREADD in Rats. *Neuropsychopharmacology* 41, 402–409.
- Marion, S., Weiner, D.M., and Caron, M.G. (2004). RNA editing induces variation in desensitization and trafficking of 5-hydroxytryptamine 2c receptor isoforms. *J. Biol. Chem.* 279, 2945–2954.
- Miao, C., Cao, Q., Ito, H.T., Yamahachi, H., Witter, M.P., Moser, M.B., and Moser, E.I. (2015). Hippocampal Remapping after Partial Inactivation of the Medial Entorhinal Cortex. *Neuron* 88, 590–603.
- Nakajima, K.I., and Wess, J. (2012). Design and Functional Characterization of a Novel, Arrestin-Biased Designer G Protein-Coupled Receptor. *Mol. Pharmacol.* 82, 575–582.
- Nygaard, R., Zou, Y., Dror, R.O., Mildorf, T.J., Arlow, D.H., Manglik, A., Pan, A.C., Liu, C.W., Fung, J.J., Bokoch, M.P., et al. (2013). The dynamic process of  $\beta$ (2)-adrenergic receptor activation. *Cell* 152, 532–542.
- Ohmura, Y., Tanaka, K.F., Tsunematsu, T., Yamanaka, A., and Yoshioka, M. (2014). Optogenetic activation of serotonergic neurons enhances anxiety-like behaviour in mice. *Int. J. Neuropsychopharmacol.* 17, 1777–1783.
- Park, J.S., Rhau, B., Hermann, A., McNally, K.A., Zhou, C., Gong, D., Weiner, O.D., Conklin, B.R., Onuffer, J., and Lim, W.A. (2014). Synthetic control of mammalian-cell motility by engineering chemotaxis to an orthogonal bioinert chemical signal. *Proc. Natl. Acad. Sci. USA* 111, 5896–5901.
- Peñagarikano, O., Lázaro, M.T., Lu, X.H., Gordon, A., Dong, H., Lam, H.A., Peles, E., Maidment, N.T., Murphy, N.P., Yang, X.W., et al. (2015). Exogenous and evoked oxytocin restores social behavior in the Cntnap2 mouse model of autism. *Sci. Transl. Med.* 7, 271ra8.
- Pleil, K.E., Rinker, J.A., Lowery-Gionta, E.G., Mazzone, C.M., McCall, N.M., Kendra, A.M., Olson, D.P., Lowell, B.B., Grant, K.A., Thiele, T.E., and Kash, T.L. (2015). NPY signaling inhibits extended amygdala CRF neurons to suppress binge alcohol drinking. *Nat. Neurosci.* 18, 545–552.
- Rasmussen, S.G., DeVree, B.T., Zou, Y., Kruse, A.C., Chung, K.Y., Kobilka, T.S., Thian, F.S., Chae, P.S., Pardon, E., Calinski, D., et al. (2011). Crystal structure of the  $\beta$ 2 adrenergic receptor-Gs protein complex. *Nature* 477, 549–555.
- Ray, R.S., Corcoran, A.E., Brust, R.D., Kim, J.C., Richerson, G.B., Nattie, E., and Dymecki, S.M. (2011). Impaired respiratory and body temperature control upon acute serotonergic neuron inhibition. *Science* 333, 637–642.
- Redfern, C.H., Coward, P., Degtyarev, M.Y., Lee, E.K., Kwa, A.T., Hennighausen, L., Bujard, H., Fishman, G.I., and Conklin, B.R. (1999). Conditional expression and signaling of a specifically designed Gi-coupled receptor in transgenic mice. *Nat. Biotechnol.* 17, 165–169.
- Redfern, C.H., Degtyarev, M.Y., Kwa, A.T., Salomonis, N., Cotte, N., Nanevicz, T., Fidelman, N., Desai, K., Vranizan, K., Lee, E.K., et al. (2000). Conditional expression of a Gi-coupled receptor causes ventricular conduction delay and a lethal cardiomyopathy. *Proc. Natl. Acad. Sci. USA* 97, 4826–4831.

- Roth, B.L., and Marshall, F.H. (2012). NOBEL 2012 Chemistry: Studies of a ubiquitous receptor family. *Nature* *492*, 57.
- Roth, B.L., Ciaranello, R.D., and Meltzer, H.Y. (1992). Binding of typical and atypical antipsychotic agents to transiently expressed 5-HT<sub>1C</sub> receptors. *J. Pharmacol. Exp. Ther.* *260*, 1361–1365.
- Roth, B.L., Craigo, S.C., Choudhary, M.S., Uluer, A., Monsma, F.J., Jr., Shen, Y., Meltzer, H.Y., and Sibley, D.R. (1994). Binding of typical and atypical antipsychotic agents to 5-hydroxytryptamine-6 and 5-hydroxytryptamine-7 receptors. *J. Pharmacol. Exp. Ther.* *268*, 1403–1410.
- Roth, B.L., Tandra, S., Burgess, L.H., Sibley, D.R., and Meltzer, H.Y. (1995). D<sub>4</sub> dopamine receptor binding affinity does not distinguish between typical and atypical antipsychotic drugs. *Psychopharmacology (Berl.)* *120*, 365–368.
- Ruffolo, R.R., Jr. (1982). Review important concepts of receptor theory. *J. Auton. Pharmacol.* *2*, 277–295.
- Sakaguchi, M., Kim, K., Yu, L.M., Hashikawa, Y., Sekine, Y., Okumura, Y., Kawano, M., Hayashi, M., Kumar, D., Boyden, E.S., et al. (2015). Inhibiting the Activity of CA1 Hippocampal Neurons Prevents the Recall of Contextual Fear Memory in Inducible ArchT Transgenic Mice. *PLoS ONE* *10*, e0130163.
- Samama, P., Cotecchia, S., Costa, T., and Lefkowitz, R.J. (1993). A mutation-induced activated state of the beta 2-adrenergic receptor. Extending the ternary complex model. *J. Biol. Chem.* *268*, 4625–4636.
- Samama, P., Pei, G., Costa, T., Cotecchia, S., and Lefkowitz, R.J. (1994). Negative antagonists promote an inactive conformation of the beta 2-adrenergic receptor. *Mol. Pharmacol.* *45*, 390–394.
- Sasaki, K., Suzuki, M., Mieda, M., Tsujino, N., Roth, B., and Sakurai, T. (2011). Pharmacogenetic modulation of orexin neurons alters sleep/wakefulness states in mice. *PLoS ONE* *6*, e20360.
- Schnütgen, F., Doerflinger, N., Calléja, C., Wendling, O., Chambon, P., and Ghyselinck, N.B. (2003). A directional strategy for monitoring Cre-mediated recombination at the cellular level in the mouse. *Nat. Biotechnol.* *21*, 562–565.
- Scofield, M.D., Boger, H.A., Smith, R.J., Li, H., Haydon, P.G., and Kalivas, P.W. (2015). Gq-DREADD Selectively Initiates Glial Glutamate Release and Inhibits Cue-induced Cocaine Seeking. *Biol. Psychiatry* *78*, 441–451.
- Shoichet, B.K., and Kobilka, B.K. (2012). Structure-based drug screening for G-protein-coupled receptors. *Trends Pharmacol. Sci.* *33*, 268–272.
- Shukla, A.K., Westfield, G.H., Xiao, K., Reis, R.I., Huang, L.Y., Tripathi-Shukla, P., Qian, J., Li, S., Blanc, A., Oleskie, A.N., et al. (2014). Visualization of arrestin recruitment by a G-protein-coupled receptor. *Nature* *512*, 218–222.
- Soskis, M.J., Ho, H.Y., Bloodgood, B.L., Robichaux, M.A., Malik, A.N., Ataman, B., Rubin, A.A., Zieg, J., Zhang, C., Shokat, K.M., et al. (2012). A chemical genetic approach reveals distinct EphB signaling mechanisms during brain development. *Nat. Neurosci.* *15*, 1645–1654.
- Sounier, R., Mas, C., Steyaert, J., Laeremans, T., Manglik, A., Huang, W., Kobilka, B.K., Démené, H., and Granier, S. (2015). Propagation of conformational changes during  $\mu$ -opioid receptor activation. *Nature* *524*, 375–378.
- Stachniak, T.J., Ghosh, A., and Sternson, S.M. (2014). Chemogenetic synaptic silencing of neural circuits localizes a hypothalamus  $\rightarrow$  midbrain pathway for feeding behavior. *Neuron* *82*, 797–808.
- Sternson, S.M., and Roth, B.L. (2014). Chemogenetic tools to interrogate brain functions. *Annu. Rev. Neurosci.* *37*, 387–407.
- Strachan, R.T., Sun, J.P., Rominger, D.H., Violin, J.D., Ahn, S., Rojas Bie Thomsen, A., Zhu, X., Kleist, A., Costa, T., and Lefkowitz, R.J. (2014). Divergent transducer-specific molecular efficacies generate biased agonism at a G protein-coupled receptor (GPCR). *J. Biol. Chem.* *289*, 14211–14224.
- Strader, C.D., Gaffney, T., Sugg, E.E., Candelore, M.R., Keys, R., Patchett, A.A., and Dixon, R.A. (1991). Allele-specific activation of genetically engineered receptors. *J. Biol. Chem.* *266*, 5–8.
- Strobel, S.A. (1998). Ribozyme chemogenetics. *Biopolymers* *48*, 65–81.
- Sweger, E.J., Casper, K.B., Scearce-Levie, K., Conklin, B.R., and McCarthy, K.D. (2007). Development of hydrocephalus in mice expressing the G(i)-coupled GPCR Ro1 RASSL receptor in astrocytes. *J. Neurosci.* *27*, 2309–2317.
- Teissier, A., Chemiakine, A., Inbar, B., Bagchi, S., Ray, R.S., Palmiter, R.D., Dymekci, S.M., Moore, H., and Ansorge, M.S. (2015). Activity of raphe serotonergic neurons controls emotional behaviors. *Cell Rep.* *13*, 1965–1976.
- Tsunematsu, T., Kilduff, T.S., Boyden, E.S., Takahashi, S., Tominaga, M., and Yamanaka, A. (2011). Acute optogenetic silencing of orexin/hypocretin neurons induces slow-wave sleep in mice. *J. Neurosci.* *31*, 10529–10539.
- Urban, D.J., and Roth, B.L. (2015). DREADDs (designer receptors exclusively activated by designer drugs): chemogenetic tools with therapeutic utility. *Annu. Rev. Pharmacol. Toxicol.* *55*, 399–417.
- Urban, D.J., Zhu, H., Marcinkiewicz, C.A., Michaelides, M., Oshibuchi, H., Rhea, D., Aryal, D.K., Farrell, M.S., Lowery-Gionta, E., Olsen, R.H., et al. (2015). Elucidation of The Behavioral Program and Neuronal Network Encoded by Dorsal Raphe Serotonergic Neurons. *Neuropsychopharmacology*. <http://dx.doi.org/10.1038/npp.2015.293>.
- Vardy, E., and Roth, B.L. (2013). Conformational ensembles in GPCR activation. *Cell* *152*, 385–386.
- Vardy, E., Robinson, J.E., Li, C., Olsen, R.H., DiBerto, J.F., Giguere, P.M., Sassano, F.M., Huang, X.P., Zhu, H., Urban, D.J., et al. (2015). A New DREADD Facilitates the Multiplexed Chemogenetic Interrogation of Behavior. *Neuron* *86*, 936–946.
- Vazey, E.M., and Aston-Jones, G. (2014). Designer receptor manipulations reveal a role of the locus coeruleus noradrenergic system in isoflurane general anesthesia. *Proc. Natl. Acad. Sci. USA* *111*, 3859–3864.
- Wacker, D., Wang, C., Katritch, V., Han, G.W., Huang, X.P., Vardy, E., McCorvy, J.D., Jiang, Y., Chu, M., Siu, F.Y., et al. (2013). Structural features for functional selectivity at serotonin receptors. *Science* *340*, 615–619.
- Wang, C., Jiang, Y., Ma, J., Wu, H., Wacker, D., Katritch, V., Han, G.W., Liu, W., Huang, X.P., Vardy, E., et al. (2013). Structural basis for molecular recognition at serotonin receptors. *Science* *340*, 610–614.
- Weiss, D.R., Ahn, S., Sassano, M.F., Kleist, A., Zhu, X., Strachan, R., Roth, B.L., Lefkowitz, R.J., and Shoichet, B.K. (2013). Conformation guides molecular efficacy in docking screens of activated  $\beta$ -2 adrenergic G protein coupled receptor. *ACS Chem. Biol.* *8*, 1018–1026.
- Westkaemper, R., Glennon, R., Hyde, E., Choudhary, M., Khan, N., and Roth, B. (1999). Engineering in a region of bulk tolerance into the 5-HT<sub>2A</sub> receptor. *Eur. J. Med. Chem.* *34*, 441–447.
- Zemelman, B.V., Nesnas, N., Lee, G.A., and Miesenbock, G. (2003). Photochemical gating of heterologous ion channels: remote control over genetically designated populations of neurons. *Proc. Natl. Acad. Sci. USA* *100*, 1352–1357.
- Zhu, H., Pleil, K.E., Urban, D.J., Moy, S.S., Kash, T.L., and Roth, B.L. (2014). Chemogenetic inactivation of ventral hippocampal glutamatergic neurons disrupts consolidation of contextual fear memory. *Neuropsychopharmacology* *39*, 1880–1892.
- Zhuang, X., Belluscio, L., and Hen, R. (2000). G(olf)alpha mediates dopamine D1 receptor signaling. *J. Neurosci.* *20*, RC91.

Introducing  
**STAR★METHODS**

**Empowering methods,  
to empower you.**

STAR Methods promote rigor and robustness with an intuitive, consistent framework that integrates seamlessly into the scientific information flow—making reporting easier for the author and replication easier for the reader.

STAR Methods—a new methods section designed with authors and readers in mind—are now available in *Cell* and *Cell Systems*. Learn more about how we're empowering methods.

Visit [www.cell.com/star-methods](http://www.cell.com/star-methods) today!

**CellPress**

# The Cellular and Molecular Landscapes of the Developing Human Central Nervous System

John C. Silbereis,<sup>1,7</sup> Sirisha Pochareddy,<sup>1,7</sup> Ying Zhu,<sup>1</sup> Mingfeng Li,<sup>1</sup> and Nenad Sestan<sup>1,2,3,4,5,6,\*</sup>

<sup>1</sup>Department of Neuroscience

<sup>2</sup>Department of Genetics and Department of Psychiatry

<sup>3</sup>Program in Cellular Neuroscience, Neurodegeneration and Repair

<sup>4</sup>Section of Comparative Medicine

<sup>5</sup>Yale Child Study Center

<sup>6</sup>Kavli Institute for Neuroscience

Yale School of Medicine, New Haven, CT 06510, USA

<sup>7</sup>Co-first author

\*Correspondence: nenad.sestan@yale.edu

<http://dx.doi.org/10.1016/j.neuron.2015.12.008>

The human CNS follows a pattern of development typical of all mammals, but certain neurodevelopmental features are highly derived. Building the human CNS requires the precise orchestration and coordination of myriad molecular and cellular processes across a staggering array of cell types and over a long period of time. Dysregulation of these processes affects the structure and function of the CNS and can lead to neurological or psychiatric disorders. Recent technological advances and increased focus on human neurodevelopment have enabled a more comprehensive characterization of the human CNS and its development in both health and disease. The aim of this review is to highlight recent advancements in our understanding of the molecular and cellular landscapes of the developing human CNS, with focus on the cerebral neocortex, and the insights these findings provide into human neural evolution, function, and dysfunction.

The human CNS exhibits the organizing principles and developmental pattern typical of all mammals; it begins as a simple neural tube that breaks off from the embryonic ectoderm and gradually acquires mature organizational features through immensely complex and strictly regulated molecular and cellular processes. Studies of model organisms have provided fundamental insights into many human neurodevelopmental processes (Bae et al., 2015; Leone et al., 2008; Lui et al., 2011; Molyneaux et al., 2007; Nord et al., 2015; O'Leary et al., 2007; Rakic et al., 2009; Rash and Grove, 2006; Shibata et al., 2015; Taverna et al., 2014). However, despite commonalities in neurodevelopmental processes in mammals, there are compelling interspecies differences that yield clade and species-specific (or defining) features and, ultimately, differences in cognition and behavior. For example, the human brain as a whole, but most especially the association areas of the cerebral neocortex, develops more slowly than the brains of other primates, and humans have a particularly long gestational time as well as childhood and adolescence (Figure 1) (Bogin, 1994; Gogtay et al., 2004; Petanjek et al., 2011; Stiles and Jerinigan, 2010; Tau and Peterson, 2010; Yakovlev and Lecours, 1967). This prolonged developmental course and period of dependency allows, more so than in other primates, environmental factors to shape the development of cognitive, emotional, and social capacities. In addition, the developing human CNS possesses certain divergent and highly derived features, such as expanded proliferative zones and diverse subtypes of neural stem and progenitor cells with enhanced proliferative capacities that facilitate brain expansion, especially of the neocortex (Bae et al., 2015; Bystron et al., 2006;

Dehay et al., 2015; Gulden and Sestan, 2014; Howard et al., 2008; Lui et al., 2011; Taverna et al., 2014).

Indicative of the biological challenge of precisely regulating diverse molecular and cellular processes over a protracted period of time and across myriad cell types and regions, the CNS exhibits regionally and temporally distinct patterns of vulnerability to various diseases and insults (Figure 2) (Kessler et al., 2007; Lee et al., 2014; Semple et al., 2013; Tebbenkamp et al., 2014). Thus, the emergence of the many neurodevelopmental processes that have enabled human brain complexity may have required a trade-off that rendered it particularly susceptible to certain disorders. Not surprisingly, it has become increasingly evident that studies involving commonly used experimental animals can neither fully model human neurodevelopment or disorders nor reliably predict if potential therapeutic compounds will work against human disease or have adverse effects. Moreover, the use of model organisms is limited by our evolutionary distance from these species. As such, null mutations of orthologous genes can result in vastly different phenotypes across species (Liao and Zhang, 2008). Therefore, a true understanding of how the human CNS is built and functions also requires direct analyses of human neural tissues and cells.

Unfortunately, the human CNS, in particular its development, is challenging to study for many reasons. However, the procurement of high-quality post-mortem tissues from different periods of development, as well as recent advances in directed differentiation of induced human pluripotent stem cells (iPSCs) towards neural fates and other neural cell preparations (Brennand et al., 2011; Lancaster et al., 2013; Mariani et al., 2015; Paşca et al., 2015; Stein et al., 2014; van de Leemput et al., 2014; van den

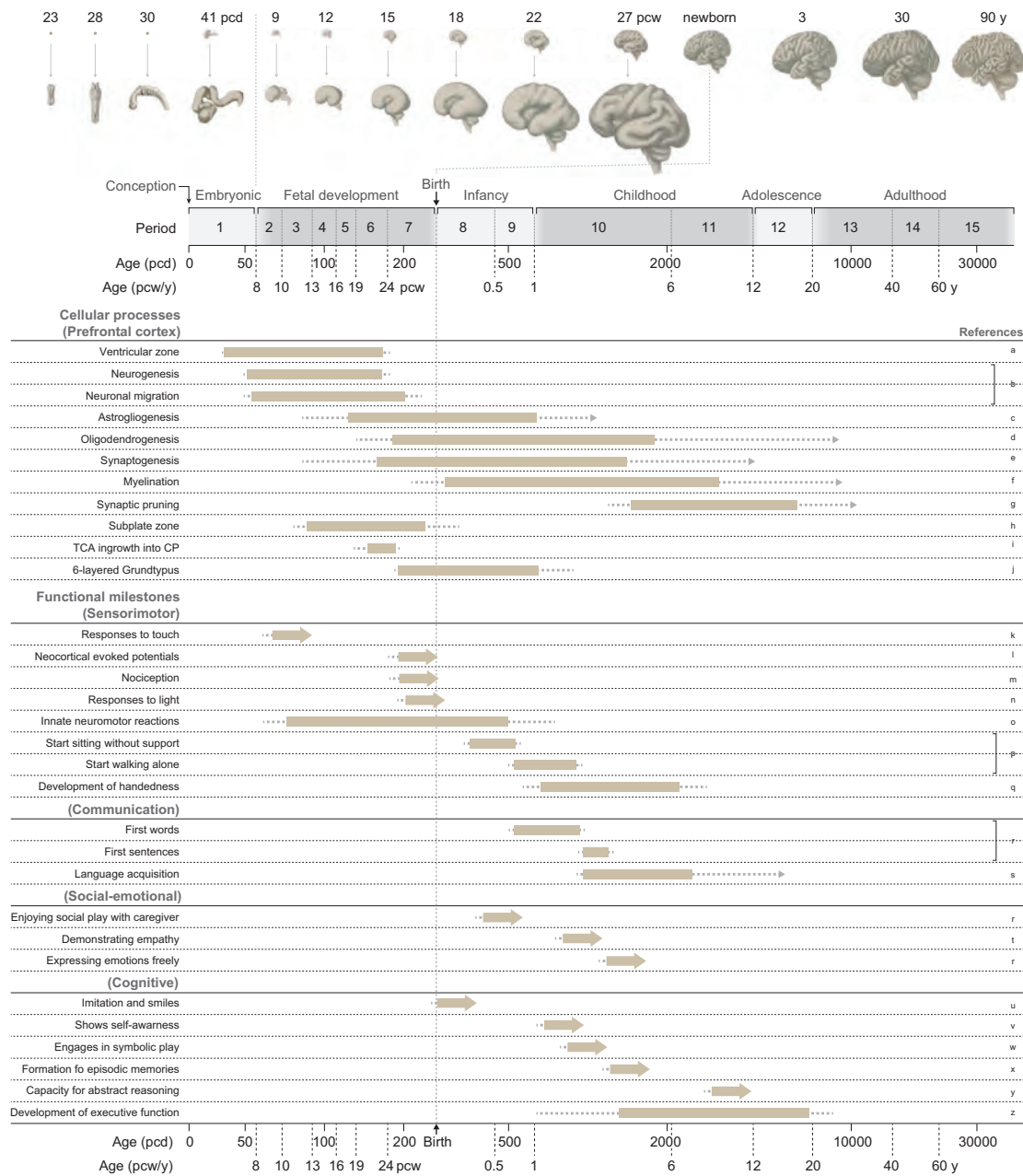


**Figure 1. Timeline of Key Human Neurodevelopmental Processes and Functional Milestones**

The figure provides a summary of some key cellular processes in the developing prefrontal cortex and functional milestones. Illustrations in the top panel show the gross anatomical features of the developing and adult CNS, with prenatal brain features magnified. The second panel, which is duplicated at the bottom of the figure, provides a timeline of human development and the associated periods (designed by Kang et al., 2011), and age in postconceptional weeks (pcw), and postnatal years (y). The schematic below details the approximate timing and sequence of key cellular processes and developmental milestones. Bars indicate the peak developmental period in which each feature is acquired; dotted lines indicate that feature acquisition occurs at these ages, though to a relatively minor degree; and arrows indicate that the feature is present thereafter. Relevant references pertaining to each process or milestone are provided in the rightmost column: a, Gould et al. (1990) and Malik et al. (2013); b, Bystron et al. (2006), Meyer (2007), and Workman et al. (2013); c, Choi and Lapham (1978), deAzevedo et al. (2003), and Kang et al. (2011); d, Kang et al. (2011) and Yeung et al. (2014); e, Huttenlocher (1979), Kwan et al. (2012), Molliver et al. (1973), and Petanjek et al. (2011); f, Miller et al. (2012) and Yakovlev and Lecours (1967); g, Huttenlocher (1979) and Petanjek et al. (2011); h, Kostovic and Rakic (1990); i, Kostovic and Judas (2006) and Kwan et al. (2012); j, Aldama (1930) and Brodmann (1909); k, Humphrey and Hooker (1959); l, Eswaran et al. (2007); m, Bellieni and Buonocore (2012); n, Polishuk et al. (1975); o, Clowry (2007), de Vries et al. (1985), Ianniruberto and Tajani (1981), Johnson and Blasco (1997), and Van Dongen and Goudie (1980); p, WHO Multicentre Growth Reference Study Group (2006); q, McManus et al. (1988) and Ramsay (1980); r, Dosman et al. (2012), Gerber et al. (2010), and Johnson and Newport (1989); s, Johnson and Newport (1989); t, Zahn-Waxler et al. (1992); u, Meltzoff and Moore (1977); v, Amsterdam (1972) and Butterworth (1990); w, Harris (2000); x, Dumontheil (2014); y, Rajan et al. (2014); z, Catts et al. (2013) and Heaton et al. (1993).

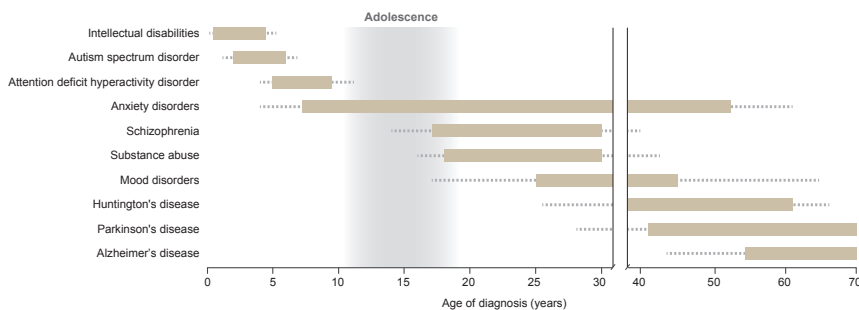


**Figure 2. Psychiatric and Neurological Disorders Have Discrete Ages of Onset**

The bars indicate the age range that each disorder commonly affects, with less frequent ages of diagnosis denoted as dotted lines. The light gray shading corresponds to adolescence. Note that the age of diagnosis is highly variable between brain disorders. Many psychiatric disorders emerge in adolescence and early adulthood. This variability is indicative of dysregulation of tightly controlled developmental processes and highlights the necessity of defining the spatiotemporal molecular and cellular processes in healthy and diseased human CNS. Based in part on data from Kessler et al. (2007) and Lee et al. (2014).

Ameele et al., 2014), coupled with the application of advanced histological, imaging, molecular, cellular, and genomic techniques, has provided new insights into dynamic cellular and molecular processes in human neurodevelopment and dysfunction in a wide array of neurological and psychiatric disorders (Brennan et al., 2011; Hu et al., 2014; Jeste and Geschwind, 2015; Lancaster et al., 2013; Mariani et al., 2015; Marin-Valencia et al., 2014; Stiles and Jernigan, 2010; Tau and Peterson, 2010; Tebbenkamp et al., 2014; Wen et al., 2014). Despite these advances, a more thorough understanding of the intricate processes underlying normal human CNS development is needed to answer many fundamental questions in biology and medicine and better recapitulate normal and abnormal human neurodevelopmental processes in model systems.

In this review, we will first briefly overview the basic principles of the organization and development of the human CNS and highlight certain developmental features that differ from commonly studied mammals. Particular emphasis will be given to studies of the cerebral neocortex, also called the isocortex and neopallium, both because it has been the focus of many developmental and comparative studies and because of its importance in higher-order cognition, emotional regulation, and complex behaviors. We will next detail the current understanding of the transcriptional, epigenomic, and regulatory landscapes of the developing human neocortex and other regions of the CNS, noting the essential conserved features, as well as clade and species-specific differences, revealed by these studies. For a more comprehensive description of the state of knowledge on the evolution of the human CNS, we recommend a number of recent reviews (Clowry et al., 2010; Dehay et al., 2015; Geschwind and Rakic, 2013; Lui et al., 2011; Marín-Padilla, 2014; Molnár and Pollen, 2014; Sherwood et al., 2012).

### A Brief Overview of Human CNS Cellular Organization and Complexity

The human CNS is possibly the most complex biological tissue, comprising on average 86.1 billion neurons in the brain and spinal cord (as estimated in adult males), along with a roughly equal number of glial cells (Azevedo, 2009; Herculano-Houzel et al., 2015). The combined white and gray matter of the cerebral cortex alone contains approximately 16.34 billion neurons (Azevedo, 2009). The neocortex has 164 trillion synapses, points of communication between neurons (Tang et al., 2001). In the entire adult CNS, there may be between several hundred trillion to well over a quadrillion synapses (see Box 1). Equally remarkable, the

cerebral white matter of young adults contains approximately 149,000 to 176,000 km of myelinated axons connecting these neurons (Marnier et al., 2003). This immensely complex cellular organization comes at substantial metabolic cost, as the human brain uses 18% of the body's oxygen at rest, but accounts for only 2.5% of a human's total body weight (Kety and Schmidt, 1948).

Owing to its remarkable complexity, the human CNS takes over two decades to build via precisely regulated molecular and cellular processes governed both by a genetic blueprint and environmental factors. These processes are particularly dynamic during neurogenesis, when neurons are generated at staggering rates—approximately 3.86 million each hour during prenatal cortical neurogenesis and 4.6 million each hour in the whole CNS over the course of developmental neurogenesis (Box 2). Moreover, synapses are formed at a rate of approximately 42.3 million synapses per minute in the late fetal and early postnatal neocortex (Box 2). Thus, it is not surprising that the relative energy and oxygen demands of the developing brain are markedly greater than that of the adult brain (Kennedy and Sokoloff, 1957). How the proper number of neuronal and glial cells is generated and how the myriads of distinct cell types are specified and assembled into complex neural circuitry during human development are among the greatest of scientific mysteries.

### A Brief Overview of Human CNS Development

The CNS is among the earliest organ systems of the human body to begin its development prenatally and among the last to complete it postnatally; development continues into the mid-20s or perhaps even the 30s in certain regions and neural circuits (Gogtay et al., 2004; Petanjek et al., 2011; Yakovlev and Lecours, 1967). The human CNS undergoes remarkably rapid growth that exceeds the rate of any other organ systems from 4 post-conceptual weeks (pcw) to the third postnatal year (Gogtay et al., 2004; Petanjek et al., 2011; Yakovlev and Lecours, 1967). After this period, the rate of growth slows and processes such as synaptic maturation and/or pruning and myelination predominate. CNS development is also characterized by the emergence and disappearance of transient cellular compartments, cell types, and synaptic circuits (Bystron et al., 2008; Hoerder-Suabedissen and Molnár, 2015; Kostovic and Judas, 2006; Lui et al., 2011; Taverna et al., 2014). In humans, these cellular changes are arguably best understood in the cerebral neocortex, and we will use it as an example to highlight general features of neurodevelopment, some of which are illustrated in Figure 1.

**Box 1. The Human CNS in Numbers. How Many Neurons and Synapses Are there?**

The human CNS contains approximately 86.1 billion neurons on average in 50- to 70-year-old males (Herculano-Houzel, 2015). There are approximately 16.34 billion neurons in the cerebral cortex, which includes as many as 2.58 billion neurons in the cortical white matter (Herculano-Houzel, 2009; Sigaard et al., 2014). However, it should be noted that published estimates of the number of cerebral neocortical neurons varies by as much as a factor of 2 (between 14.7 to 32.0 billion neurons) (Pakkenberg and Gundersen, 1997; Pakkenberg et al., 2003). It was estimated that there are 164 trillion synapses in the adult human cerebral neocortex (Tang et al., 2001). The published estimates for the number of synapses an individual neocortical neuron receives also vary between approximately 7,200 (Pakkenberg et al., 2003; Tang et al., 2001), 29,642 (DeFelipe et al., 2002), and 80,000 (Huttenlocher, 1979) synapses. The present authors did not find calculations for other human CNS regions. However, the average number of synapses per neuron certainly varies tremendously in other mammals and brain regions. In the rat brain, the number of synapses associated with a neuron ranges from an average of 2,186 for a calretinin-positive hippocampal interneuron (Gulyás et al., 1999), 31,700 for a hippocampal CA1 pyramidal neuron, to 175,000 for a cerebellar Purkinje neuron (Napper and Harvey, 1988). Thus, if we take the lower estimate for human neocortical neurons (i.e., 7,200) and assume that this establishes a lower boundary for a typical CNS neuron, there may be around 620 trillion synapses in the entire adult CNS. Remarkably, if we take the higher of these estimates for neocortical neurons (i.e., 29,642 or 80,000), then there may be as many as several quadrillion synapses in the entire adult CNS.

**General Features of Prenatal and Postnatal Neurodevelopment**

During pregnancy, the developing CNS undergoes rapid and dramatic changes in its architecture. The average length of prenatal development (i.e., the time from the date of conception to birth) is 38 weeks and is typically divided into two primary periods—embryonic and fetal—or three equal trimesters. The embryonic period comprises the first 56 days or 8 weeks of pregnancy and can be divided into 23 Carnegie stages (CSs), based solely on changes in morphologic features (O’Rahilly and Muller, 2006; Yamada et al., 2010). During this time span, the organ anlagen, including the primordium of the CNS, arise. The embryonic phase is also when the vast majority of congenital abnormalities occur (O’Rahilly and Muller, 2006). Moreover, due to its prolonged and dynamic development, the CNS is also sensitive to damaging effects of genetic (i.e., somatic mutations), epigenetic, and environmental insults for a longer period of time than other organs.

The anatomy of the prenatal human CNS has recently been systematically illustrated by several groups (Bayer and Altman, 2007; O’Rahilly and Muller, 2006; Yamada et al., 2010). Thus, we will only briefly summarize the sequence and timing of some key human prenatal neurodevelopmental events here. Human neurulation happens quite early, as is the case in all mammals, with the induction of the neural plate within the ectoderm immediately after the formation of the notochord. This is followed by the emergence of the neural groove, which is formed by neural folds that arise along each side of the midline of the neural plate on approximately the 23<sup>rd</sup> postconceptional day (pcd) and corresponding to CS 8 (O’Rahilly and Muller, 2006). Shortly thereafter, the neural folds fuse to form the neural tube, beginning in the center of neural plate and then proceeding both rostrally and caudally. The neuropores at the rostral and caudal ends of the neural tube close to separate the ventricular system from the amniotic fluid by 29 (CS 11) and 30 pcd (CS 12), respectively.

Because of its unequal growth, the neural tube is patterned along the rostro-caudal dimension of the CNS (i.e., neuraxis) into the following three major vesicles of the future brain: forebrain (prosencephalon), midbrain (mesencephalon), and hind-

brain (rhombencephalon). The spinal cord forms in the caudal region (O’Rahilly and Muller, 2006; Yamada et al., 2010). The three primary brain vesicles are subdivided and grow rapidly as prenatal development proceeds. In addition, the neural tube is patterned along the dorsal-ventral axis to establish defined compartments of neural progenitor cells that generate specific types of neural cells.

The fetal period is mainly characterized by the growth, differentiation, and subregionalization of organs (organogenesis). With respect to the CNS, there is a nearly 40-fold increase in the weight of the brain during fetal development (O’Rahilly and Muller, 2006). Among the most prominent morphological changes is the massive growth of the cerebral hemispheres, which first appear around 33 pcd or CS 14 (O’Rahilly and Muller, 2006), and the appearance of sulci and gyri on the cerebral surface, around the middle of prenatal development.

By birth, the gross anatomy of the CNS is reminiscent of its adult appearance and the repertoire of neurons found in the adult neocortex has been largely established (see Box 1). However, neurogenesis continues in several other regions (most prominently in the cerebellum, see Box 2), and glial cells are rapidly generated throughout infancy and early childhood. Early postnatal development is also characterized by massive outgrowth of dendrites and axons, followed by synaptogenesis, glial proliferation, and myelination, predominately in the forebrain and cerebellum. Thus, a newborn’s brain weighs just 26.2% (males) to 26.8% (females) of what it will in late adolescence, when the brain is at its heaviest (Dekaban, 1978). During the first 3 postnatal years, the brain continues to grow at a remarkable rate, attaining approximately 81.3% (females) to 87.6% (males) of its greatest weight (Dekaban, 1978). Though less dramatic than they are prenatally and in early postnatal development, substantial structural changes and molecular reorganization of neural circuits continue through late childhood and adolescence, paralleling the emergence of higher-order cognition and complex behavior.

**Neuronal Generation and Migration**

Neurogenesis in the human CNS begins shortly after the fusion of neural folds and proceeds at different rates across the neuraxis.

**Box 2. The Human CNS in Numbers. What Is the Rate of Neurogenesis and Synaptogenesis?**

About 80% of the 16.34 billion neurons (13.07 billion) estimated to be present in the middle-aged adult male cerebral cortex (Azevedo et al., 2009) are thought to be excitatory glutamatergic projection neurons (i.e., pyramidal and modified pyramidal neurons) (DeFelipe et al., 2002), which are produced from neural stem or progenitor cells within the VZ and SVZ of the developing cerebral cortical wall. The rest are GABAergic inhibitory interneurons, which recent studies have shown mostly originate from the ganglionic eminences of the ventral telencephalon (i.e., the subpallium) (Fertuzinhos et al., 2009; Hansen et al., 2010, 2013; Ma et al., 2013; Radonjić et al., 2014). Thus, approximately 13 billion excitatory glutamatergic neurons must be generated in the VZ and SVZ of the cortical wall within the approximately 141 days or 3,384 hours of neurogenesis in prenatal development (from 50–51 pcd [CS 21 or the beginning of the seventh pcw] when immature neurons are first observed in the CP to 191 pcd [27 pcw], when neocortical excitatory neuron generation stops according to the <http://translatingtime.org> algorithm [Workman et al., 2013]). This suggests that approximately 3.86 million excitatory neurons are generated per hour during prenatal cortical neurogenesis.

If we extend this analysis to the entire CNS, we would need to know when neurogenesis begins and ceases. CNS neurogenesis begins at 32 pcd (4 pcw) in the spinal cord and brain stem (Bayer and Altman, 2007; O’Rahilly and Muller, 2006). The vast majority of neurons in the human telencephalon are generated before birth, and neocortical excitatory neuron generation ends around 27 pcw (Ernst et al., 2014; Larsen et al., 2006; Spalding et al., 2005). Additional neocortical interneurons (Sanai et al., 2011), dentate gyrus neurons (Eriksson et al., 1998), and striatal interneurons (Ernst et al., 2014) are generated after this age, extending postnatally in some instances. On the other hand, 85% of the cerebellar granule cells are generated by the 11<sup>th</sup> postnatal month (Kießling et al., 2014), and the external granule layer disappears by the end of the 18<sup>th</sup> postnatal month (Raaf and Kernohan, 1944). Thus, the bulk of CNS neurogenesis (i.e., approximately 86.1 billion neurons) occurs over approximately 781 days from 32 pcd to 813 pcd (i.e., approximately 234 prenatal pcd plus 547 postnatal days [birth to the 18<sup>th</sup> postnatal month]), which would mean that approximately 4.6 million neurons are generated per hour during the CNS developmental neurogenic period.

Neocortical plate synaptogenesis starts as early as 18 pcw (Kwan et al., 2012) and reaches its maximum synaptic density (the peak of formation) in the middle frontal gyrus (prefrontal cortex) after 15 months postpartum, which is considerably later than in the primary auditory and visual cortices (Huttenlocher and Dabholkar, 1997). The maximum dendritic spine density (a proxy for synapse) on pyramidal neurons of the dorsolateral prefrontal cortex occurs around the seventh postnatal year (Petanjek et al., 2011), after which there is a general decline in the density of spines, indicative of synapse elimination. Thus, the bulk of synapses found in the adult neocortex (i.e., approximately 164 trillion synapses in total according to Tang et al., 2001) are generated across approximately 2,695 days (140 prenatal [18 to 38 pcw] and 2,555 postnatal days) at the rate of approximately 42.3 million synapses per minute or 700,000 synapses per second. However, the rate is likely higher as the density and the total number of synapses in the neocortex of a toddler is much higher than in the adult (Huttenlocher, 1979; Petanjek et al., 2011).

The first neurons to appear are motor neurons in the ventral horn of the cervical spinal cord and neurons of certain cranial nerve nuclei in the brainstem at CS 13 (28–32 pcd or 4 pcw) (Bayer and Altman, 2007; O’Rahilly and Muller, 2006). Neurogenesis continues throughout embryonic and fetal development (most prominently in the neocortex and cerebellum) and extends postnatally in certain regions (see Box 2). The wall of the neural tube initially comprises a pseudostratified layer of neuroepithelial cells called the ventricular zone (VZ), which lines the central cavity. These cells serve as the stem or progenitor cells for all neurons and macroglia (i.e., astrocytes and oligodendrocytes) of the CNS. Initially, each neuroepithelial cell division gives rise to two progenitor daughter cells. This process of symmetric division exponentially expands the number of progenitor cells.

Beginning at approximately 50–51 pcd (CS 21 or the beginning of the seventh pcw), neocortical VZ cells begin to generate the earliest neurons of the emerging cortical plate (CP; anlage of the cerebral cortical layers 2–6) (Bayer and Altman, 2007; Bystron et al., 2006; Meyer, 2007; O’Rahilly and Muller, 2006). At this time, another neurogenic proliferative compartment called the subventricular zone (SVZ) appears above the VZ and enlarges dramatically over the course of early and mid-fetal development (Bystron et al., 2008; Dehay et al., 2015; Fietz et al., 2010, 2012; Florio et al., 2015; Hansen et al., 2010; Johnson

et al., 2015; Meyer, 2007; Smart et al., 2002). Together these two zones give rise to all excitatory projection neurons (also known as pyramidal neurons) within the telencephalon and subsequently glial cells. Early on in embryonic neurogenesis, neuroepithelial progenitor cells of the VZ transition into another form of neural stem or progenitor cell, called radial glia (RG), which extend a very long process to the pial surface of the expanding neocortical wall (Bystron et al., 2006; Howard et al., 2008; Lui et al., 2011; Taverna et al., 2014). RG cell bodies largely reside in the VZ (apical or inner RG [iRG] cells) and SVZ (basal or outer RG [oRG] cells), where they divide symmetrically or asymmetrically, giving rise to a daughter RG cell and either an intermediate progenitor cell (IPC, also known as a transit amplifying cell) or nascent neuron (Bae et al., 2015; Bystron et al., 2008; Dehay et al., 2015; Lui et al., 2011; Taverna et al., 2014). Comparative studies of oRG cells in mouse, ferret, macaque, and human brain indicate that the expansion of this population correlates with brain size (Dehay et al., 2015; Fietz et al., 2010; Lui et al., 2011; Reillo and Borrell, 2012). In mammals with a large brain, the oRG cell population further subdivides the SVZ into inner and outer zones, with the former populated mostly by iRG cells and IPCs and the latter composed mostly of oRG cells. While the oSVZ is negligible in rodents, its volume in macaque and human far exceeds that of the iSVZ (Smart et al., 2002). Therefore, the expansion of the neuronal cell population in the human brain

appears in part due to a vast increase in the number of oRG cells that gives rise to highly proliferative IPCs.

Much of the expansion of human brain size and complexity is also a result of a relatively protracted time course of neurogenesis. For example, neocortical plate neurogenesis is predicted (see <http://translatingtime.org> [Workman et al., 2013]) to last 11 days (11 to 22 pcd) in mouse, 67 days (45 to 112 pcd) in rhesus macaque, and 143 days (48 to 191 pcd) in human. These predictions appear quite accurate, as the first neurons forming the CP are detected within the wall of cerebral hemispheres in the incipient insula at approximately 50–51 pcd (Bayer and Altman, 2007; Bystron et al., 2006; Marín-Padilla, 2014; Meyer, 2007; O’Rahilly and Muller, 2006).

The subsequent migration of newly generated neurons from the SVZ and VZ and their postmitotic differentiation leads to the formation of new, often transient structures and rapid expansion of the CNS. As is the case throughout the CNS, different subgroups of neocortical neurons have origins and migration modes that vary by subtype. Similar to rodents and other commonly studied mammals, human neocortical excitatory glutamatergic projection neurons are generated from progenitor cells of the dorsal pallium and migrate radially into the CP (Fietz et al., 2010; Hansen et al., 2010). In contrast, human GABAergic interneurons are largely generated ventrally from the ganglionic eminences in the basal ganglia primordia and migrate tangentially into the CP (Fertuzinhos et al., 2009; Hansen et al., 2010, 2013; Ma et al., 2013; Radonjić et al., 2014). Unlike in the rodent, most stem cells in the human ganglionic eminences do not appear to be located in the epithelium, but rather comprise a more distributed population suggestive of a mechanism for expansion of the interneuron progenitor pool (Hansen et al., 2013).

Before the start of neurogenesis, a diverse group of early born “pioneer” neurons arrive by tangential migration from outside the neocortical primordium and settle immediately above the VZ to form the early marginal zone (MZ), also called the primordial plexiform layer or preplate (Bystron et al., 2008; Marín-Padilla, 2014). These early-born “pioneer” neurons comprise a diverse group of cell types, including reelin-expressing Cajal-Retzius cells, which are important for establishing early synaptic circuits and laminar organization of the incipient CP “predecessor cells” and other cell types (Bystron et al., 2006; Marín-Padilla, 2014; Meyer, 2007; Zecevic, 1998).

Subsequently, newly born projection neurons migrate radially to form the CP below the pial surface by splitting the preplate into a superficial MZ (i.e., future layer 1) and a deep future subplate (SP; pre-SP) zone (Bystron et al., 2006; Marín-Padilla, 2014; Meyer, 2007; Molliver et al., 1973; Zecevic, 1998). The SP zone expands dramatically during pregnancy to become the largest compartment of the human fetal neocortical wall and does not have a direct counterpart in the adult brain. The transient SP zone plays a critical role in various neurodevelopmental processes involved in the formation of neural circuits (Hoerder-Suabedissen and Molnár, 2015; Honig et al., 1996; Kostovic and Rakic, 1990; Molliver et al., 1973). For instance, it serves as an intermediate target (waiting compartment) for various afferent projection systems of the cerebral cortex. It is enriched in extracellular matrix and filled with postmigratory glutamatergic

projection neurons and GABAergic interneurons, migrating neurons, glial cells, and many ingrowing axon terminals forming transient synapses (Al-Jaberi et al., 2015; Hevner, 2007; Hoerder-Suabedissen and Molnár, 2015; Honig et al., 1996; Kostovic and Judas, 2006; Kostovic and Rakic, 1990; Molliver et al., 1973; Wang et al., 2010). At its peak around 31 pcw, the human SP zone has around 3.6 billion cells (Samuelsen et al., 2003), which is an order of magnitude more than the total number of cells in the brain of mouse, rat, and many other mammals (Herculano-Houzel, 2009). The SP zone is sensitive to various perinatal injuries (Kostovic and Judas, 2006). While the SP zone undergoes gradual dissolution during late fetal and early postnatal development, many SP neurons survive and remain embedded in the adult white matter as so-called interstitial neurons (Hoerder-Suabedissen and Molnár, 2015; Honig et al., 1996; Kostovic and Rakic, 1990).

Newly born projection neurons migrate to their final laminar position in the emerging CP in a precise inside-first, outside-last gradient (Bystron et al., 2008; Leone et al., 2008; Marín-Padilla, 2014; Meyer, 2007; Molyneaux et al., 2007; Shibata et al., 2015). Upon arriving at the CP, neurons are instructed to stop migrating and continue to differentiate. Most differentiation processes, such as the extension and elaboration of dendrites and the formation of synaptic connections, take place only after neurons have assumed their final position in the CP, and many differentiation processes likely last into early adulthood in humans (Huttenlocher, 1979; Koenderink and Uylings, 1995; Koenderink et al., 1994; Petanjek et al., 2008, 2011).

### Glial Cell Genesis and Differentiation

The generation of glial cells generally follows neurogenesis, peaking around birth, and is also a protracted postnatal process in humans (Jakovcevski et al., 2009; Miller et al., 2012; O’Rourke et al., 1992; Roessmann and Gambetti, 1986; Yeung et al., 2014). Astrocytes and oligodendrocyte precursor cells are derived from RG cells beginning in midgestation (Howard et al., 2008; Jakovcevski et al., 2009). Oligodendrocytes are robustly generated and migrate extensively through the first 3 postnatal years, while myelination continues postnatally in most brain regions, stretching well into the third decade in some areas such as fronto-parieto-temporal association cortex (Jakovcevski et al., 2009; Miller et al., 2012; Sigaard et al., 2014; Yeung et al., 2014). Myelination is developmentally protracted in humans compared to chimpanzees in which myelination is largely completed in mid-adolescence (Miller et al., 2012). Given the inhibitory effects that myelin has on synaptogenesis and plasticity, this extended postnatal period of myelination expands the capacity for learning activities, memory, and complex sensory perception. Moreover, it indicates that gene regulatory processes and axon-glial interactions that govern myelination in humans may differ from those in mouse and other species, highlighting the importance for cross-species analyses.

Less is known about human astrocyte development. The earliest astrocytes are generated from the direct transformation of RG cells followed by subsequent rounds of proliferation (Bystron et al., 2008; Choi and Lapham, 1978; deAzevedo et al., 2003; Howard et al., 2008). Neocortical astrocytes with mature-like morphological characteristics are observed as early as 15 pcw (Choi and Lapham, 1978; Howard et al., 2008). The

astroglial population continues to proliferate and differentiate during the first 3 postnatal years (Kang et al., 2011; Sanai et al., 2011; Sigaard et al., 2014), which coincides with the peak in synaptic density (Huttenlocher, 1979) and is consistent with its previously reported role in synaptic formation and elimination (Clarke and Barres, 2013).

### Laminar Organization, Regional Patterning, and Lateralization of the Human Neocortex

In all mammals, including humans, at least two types of spatial information must be encoded in nascent excitatory projection (pyramidal) neurons in the CP: (1) their position in the radial direction, corresponding to their laminar position (Leone et al., 2008; Molyneaux et al., 2007; Shibata et al., 2015), and (2) their position in the tangential plane, corresponding to their particular cortical areal identity, which mouse studies show is governed by graded expression of transcription factors during early embryonic development, followed by extrinsic signaling from thalamic axonal inputs (Chou et al., 2013; O'Leary et al., 2007; Rakic et al., 2009; Rash and Grove, 2006). The physical separation of layers and areas is functionally determined and maintained through distinct compositions of neuronal cell types and unique sets of afferent and efferent synaptic connections. The laminar identity of pyramidal neurons reflects their birth order, with first-born neurons occupying the deepest layers and later-born neurons present in more superficial layers. The most superficial pyramidal neurons (layers 2 to 3), which exclusively make intratelencephalic connections, have been proposed to be overrepresented in humans and contribute to certain human-specific cognitive and motor abilities (Marín-Padilla, 2014).

The formation of the human neocortical areal map is topographically matched, though slightly asymmetric, structurally and functionally, between the left and right hemispheres (Amunts et al., 2003; Dehaene-Lambertz and Spelke, 2015; Sun and Walsh, 2006). This asymmetry plays a crucial role in functional lateralization of certain cognitive and motor functions (e.g., language and handedness). Neocortical structural asymmetry is first observed during the late mid-fetal period (Chi et al., 1977; Kasprjan et al., 2011) and becomes more prominent during early postnatal development as functional asymmetries become more apparent (Amunts et al., 2003; Dehaene-Lambertz and Spelke, 2015; Sun and Walsh, 2006). Furthermore, the right hemisphere appears to mature faster than the left during late fetal and early postnatal development (Taylor, 1969; Thatcher et al., 1987).

### Neural Circuit Assembly, Maturation, and Developmental Plasticity

Dendritic and axonal outgrowth followed by the formation of synapses and myelination of axons are key cellular features associated with the functional maturation of the CNS. At midgestation, immature neocortical neurons have extended axons and begun to elaborate dendrites, initiating a protracted period of axon outgrowth, dendritic arborization, and synaptogenesis that extends into early childhood. These processes vary substantially between layers, areas, and subtypes of human neocortical neurons (Huttenlocher, 1979; Huttenlocher and Dabholkar, 1997; Koenderink and Uylings, 1995; Koenderink et al., 1994; Petanjek et al., 2011).

Synaptogenesis begins at the transition between embryonic and fetal development and follows a specific spatiotemporal sequence. The very first synapses are found in the cervical spinal cord at CS 17 (14-mm crown-rump length; estimated around 44 pcd or the beginning of the sixth pcw) (Okado et al., 1979) and precede precocious movements and the first signs of reflex activity (Figure 1). Within the neocortical wall, the first synapses appear in the preplate between the fourth and fifth pcw (Zecevic, 1998), followed by their bilaminar distribution in the MZ above and in the SP below the emerging CP (Molliver et al., 1973; Zecevic, 1998). The SP zone represents a major site of early neocortical synaptogenesis, and starting around 10 pcw there is a dramatic increase in synaptogenesis within this zone, consistent with its role as a “waiting” compartment for ingrowing cortical afferent axons (Hoerder-Suabedissen and Molnár, 2015; Honig et al., 1996; Kostovic and Rakic, 1990; Molliver et al., 1973). The basic features of the apical and basal dendrites of pyramidal neurons start to appear around 15 pcw, before the thalamocortical axons invade the CP (Mrzljak et al., 1988). The earliest synapses within the CP are observed around 18 pcw, terminating on prospective layer 5 projection (pyramidal) neurons (Kwan et al., 2012). Dendritic spines typically start to appear on immature neocortical pyramidal neurons and interneurons much later, between the 24<sup>th</sup> and 27<sup>th</sup> pcw (Mrzljak et al., 1988), which is after the massive ingrowth of thalamocortical axons into the CP starting around 21 pcw (Kostovic and Rakic, 1990; Molliver et al., 1973). This massive ingrowth of afferent axons coincides with intensive dendritic differentiation and synaptogenesis on dendrites of the prospective layer 3 and 5 pyramidal neurons; both of these processes rapidly increase during the late perinatal phase (Mrzljak et al., 1988).

As noted above, many of these prenatal synapses and neural circuits are thought to be transient and the bulk of synaptogenesis in the neocortex does not occur until later in prenatal development and early postnatal development (Huttenlocher, 1979). The ingrowth of thalamocortical axons and the intracortical burst of dendritic arborization and synaptogenesis that occurs in the late mid-fetal and early late-fetal periods also coincide with both the beginning of the transformation of the CP into a six-layered ontogenetic lamination (Brodmann, 1909) and the appearance of evoked potentials (Figure 1). Rapid synaptogenesis (i.e., overproduction) continues during the first 2 postnatal years, peaking between 3 and 15 months (depending on neocortical area) (Huttenlocher and Dabholkar, 1997). Subsequently, refinement of synaptic connections and dendritic pruning, mediated by the convergence of influences from intrinsic and extrinsic factors, seems a major task of the early postnatal brain, extending largely from the peak of synaptogenesis during the first few years (depending on the brain region) through the third decade in regions such as the prefrontal cortex (Huttenlocher and Dabholkar, 1997; Petanjek et al., 2011). This reorganization of synaptic circuits is thought to be essential for the functional specialization of neocortical areas and brain regions. There are two opposing scenarios that may describe spatiotemporal patterns of the reorganization and maturation of neocortical neural circuits in primates: (1) synaptogenesis proceeds concurrently in all areas (Rakic et al., 1986), and (2) synaptogenesis proceed heterochronically across areas (Huttenlocher and Dabholkar, 1997),

**Box 3. Organization of the Human Nuclear Genome**

The diploid human nuclear genome of approximately 6.2 (in males) or 6.4 (in females) billion base pairs distributed across 46 chromosomes provides the blueprint for building the body and its functions. Current GENCODE estimates ([www.genecodegenes.org/stats/current.html](http://www.genecodegenes.org/stats/current.html); version 23) predict 60,498 genes. Of these, 19,881 are protein-coding genes, 25,813 are non-coding RNA (long and short) genes, and the remaining are pseudogenes. A significant part of the remaining genome is believed to be *cis*-regulatory elements (CREs), the DNA sequences that regulate transcription. According to some estimates, the human nuclear genome harbors approximately 400,000 putative enhancers and 70,000 promoters (ENCODE Project Consortium, 2012). This highlights both the complexity of the human genome and the challenges in elucidating the molecular mechanisms underlying complex processes like neurodevelopment.

with the association areas pruning synapses and myelinating axons (Yakovlev and Lecours, 1967) later than many other areas and thus retaining longer juvenile characteristics.

Remarkably, the size of pyramidal neurons and length of dendrites increase dramatically during the first postnatal year, and continue, at a reduced rate, until around the fifth postnatal year (Koenderink and Uylings, 1995; Koenderink et al., 1994; Petanjek et al., 2008). Robust synaptic elimination and dendritic pruning are observed from early childhood through adolescence. Differential maturation of brain regions and neocortical areas helps explain many of the cognitive and behavioral changes seen in children, teens, and young adults. Not surprisingly, alterations in synaptogenesis, progression of myelination, and tractography over the same ages have been noted in certain neurological and psychiatric disorders (Lee et al., 2014; Stiles and Jernigan, 2010; Tau and Peterson, 2010), highlighting the importance of the appropriate regulation of these prolonged human neurodevelopmental processes.

These characterizations of human neurodevelopment represent a great effort to describe the cellular, physiological, and anatomical trajectories of the developing human brain, which extends deep into the 19<sup>th</sup> century. Only recently, however, have advancements in functional genomic techniques enabled comprehensive and unbiased characterizations of the molecular processes in the human postmortem developmental CNS tissues and neural cell culture systems. The remainder of this review will focus on our understanding of the spatiotemporal landscape of the RNA species (i.e., transcriptome), epigenetic features (i.e., “the epigenome”; see also an alternative view by Ptashne [2013]) and DNA regulatory elements (i.e., regulome) active in the developing human neocortex, and other brain structures, as well as insights into human developmental neurobiology provided by these studies.

**The Transcriptional Landscape of the Developing Human CNS**

The molecular and cellular processes discussed above are encoded in the immensely complex genome (see Box 3). Transcrip-

tion is the first step in transferring genetic information into specific phenotypes and establishing unique molecular and, subsequently, cellular properties. The development of high-throughput microarray and sequencing technologies have greatly advanced our ability to explore the transcriptome in the developing human CNS. Some of the relevant resources on the developmental transcriptome of the human CNS include <http://www.humanbraintranscriptome.org>, <http://braincloud.jhmi.edu>, and <http://www.brainspan.org>.

**Global Spatiotemporal Dynamics of the Human Brain Transcriptome**

Recent genome-wide profiling studies of the developmental transcriptome of the human brain by several groups (Colantuoni et al., 2011; Ip et al., 2010; Jaffe et al., 2015; Johnson et al., 2009; Kang et al., 2011; Lambert et al., 2011; Mazin et al., 2013; Miller et al., 2014; Pletikos et al., 2014; Somel et al., 2009, 2011) have generated comprehensive datasets on coding and non-coding RNAs across multiple time points and brain regions. Moreover, these initial analyses have shed new light on the transcriptional architecture of brain regions and neocortical areas, neurodevelopmental processes, and the underlying biology of complex neurodevelopmental disorders. This work has revealed that the great majority of protein coding genes (at least 86% according to Kang et al., 2011) and an ever-expanding number of non-coding genes (see Box 3) are used at some point in the building of the human CNS. Of these, 9 out of 10 genes appear to be differentially expressed or spliced across brain regions and/or time (Kang et al., 2011; Mazin et al., 2013). Such differences in the transcriptional architecture of brain regions and neocortical areas reflect their ontologies, different cellular makeups, biological processes, and developmental timing (Figures 3A and 3B). Another common finding of these studies is that transcriptomes differ more prominently across time and space than they do between sexes, ethnicities, or individuals, despite the underlying genetic differences. In particular, they have revealed remarkable dynamicity of gene expression during prenatal and early postnatal development (periods 1–9), accounting for approximately 2/3 of the variance in global expression, while the expression changes over several decades of adulthood (periods 13–15) accounted for a very small fraction of the variance (Figure 3A). When compared with dorsal pallial structures (amygdala, hippocampus, and neocortex), the cerebellum is the most transcriptionally distinctive region in the developing brain, followed by thalamus and striatum (Figure 3B) (Kang et al., 2011; Numata et al., 2012). The transcriptional differences between putative areas of the developing neocortex were less robust than those between neocortex and other analyzed brain regions. A majority of these spatially enriched genes were also temporally regulated, and some were transiently enriched during a specific time window, including protracted epochs of postnatal development—the late childhood and adolescence. These findings reveal that regional transcriptomes are developmentally regulated and reflect cellular and functional differences.

Transcriptional studies have also demonstrated correlations between gene expression dynamics and the morphological and functional development of brain regions and, consequently,

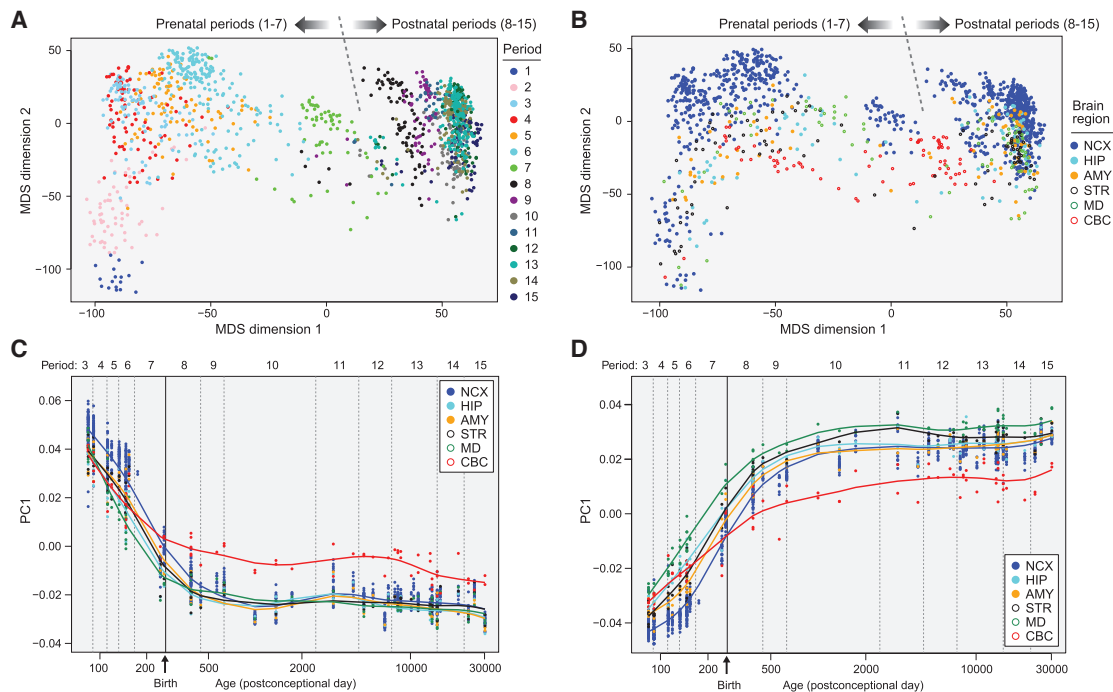


**Figure 3. Global Spatiotemporal Dynamics of the Human Brain Transcriptome**

(A) Multidimensional scaling (MDS) plot of global transcriptional differences across regions and time. The most pronounced differences (approximately two-thirds) occur during prenatal development (periods 1 to 7). By contrast, over four decades of adulthood (periods 13–15), less than 1% of genes are differentially expressed. Each dot represents a sample and is colored according to period as defined by Kang et al. (2011); the dotted line indicates birth.

(B) MDS plot in (A) colored by brain regions. The most prominent differences were between cerebellar cortex (CBC) and forebrain regions. Abbreviations are as follows: NCX, neocortex; HIP, hippocampus; AMY, amygdala; STR, striatum; and MD, mediodorsal nucleus of thalamus.

(C) Weighted gene co-expression analysis identifies modules of co-expressed genes associated with distinct spatiotemporal expression patterns and biological processes in human brain development. Module M20 from Kang et al. (2011) shown here comprises genes that are downregulated simultaneously in different regions, with the exception of postnatal CBC, as the brain matures. M20 is enriched for genes encoding transcription factors involved in neurogenesis and pan-neuronal differentiation.

(D) Module M2 shown here comprises genes that are upregulated simultaneously, peaking first in childhood, in all regions, with the exception of postnatal CBC, as the brain matures. This module was enriched for genes associated with neuronal maturation processes like synaptic transmission, ion transport, and calcium signaling.

(C) and (D) were adapted with permission from Kang et al. (2011).

shed light on the timing of developmental processes and the onset of specific biological functions. For example, gene co-expression network analyses have revealed that the developmental brain transcriptome can be segregated into distinct modules or clusters of genes with highly correlated expression. The expression trajectories of the modules, which can be summarized using the module eigengene or an intramodular hub gene, often exhibit dynamic expression patterns across development, consistent with their roles in distinct biological processes (Johnson et al., 2009; Kang et al., 2011; Miller et al., 2014; Parikshak et al., 2013; Willsey et al., 2013). In Kang et al. (2011), the expression trajectories of the two largest modules comprising genes that are co-regulated across brain regions and time indicate that many transcriptional processes are shared and coordinated across different regions as the brain develops (Figures 3C and 3D). In particular, the module enriched for genes associated with neuronal specification is most highly expressed embryonically and early fetally (Figure 3C), while the module enriched for genes associated with synaptic function and ion channels begins to rise late fetally and plateaus in early childhood (Figure 3D). In addition, many modules were very dynamic and

distinct across spatial and temporal dimensions and enriched for genes associated with distinct functions.

Recent studies of the developing postmortem human brains of individuals affected with autism spectrum disorder or fragile X syndrome have revealed distinct spatiotemporal patterns of transcriptional and post-transcriptional dysregulation (Kwan et al., 2012; Voineagu et al., 2011). Moreover, recent approaches have also successfully integrated the spatiotemporal dimensions of the human brain transcriptome with gene mutation discoveries to generate testable hypotheses about when and in which regions and/or cell types in the developing human CNS the expression of disease-associated genes converge. In particular, these approaches have implicated the projection neurons in the prefrontal and primary motor-somatosensory cortex during mid-fetal development in autism spectrum disorder and the frontal cortex during fetal development in schizophrenia (Gulsuner et al., 2013; Kang et al., 2011; Lin et al., 2015; Parikshak et al., 2013; State and Sestan, 2012; Willsey et al., 2013). It is intriguing to speculate that selective dysfunction of spatially and temporally regulated gene expression may in part explain differences in the age of onset and affected neural circuits in neurological

and psychiatric disorders (Figure 2). These observations further highlight the importance of deciphering the extent to which complex processes observed in the prolonged course of human development are recapitulated in model species.

Taken together, these recent transcriptomic analyses of human brain development across the spatial, temporal, and cellular dimensions have provided novel insights into normal neurodevelopmental processes and the interpretation of disease-associated mutations and underlying neuropathology.

### Transcriptomic Insights into Human Neural Stem Cell Biology and Evolution

In order to better understand the biology of and evolutionary changes in neural stem cell populations and the resultant expansion of certain progenitor compartments in brain evolution (e.g., oRG cell and the iSVZ) (see Figures 4A and 4B for schematic), recent studies have profiled differential gene expression in neocortical RG cells of humans and a few other species. In particular, by analyzing differential gene co-expression relationships between fetal human and mouse neocortical proliferative zones and cells, Lui et al. (2014) revealed a number of genes that were enriched in either mouse or human RG cells (Figure 4C). By assessing genes expressed in human, but not mouse, RG cells, the study went on to determine that *PDGFD* encodes a platelet derived growth factor acting through the PDGFRB receptor, which is likewise enriched in human fetal RG cells, to regulate cell-cycle progression and progenitor cell expansion in human, but not mouse, cortex.

In a complementary approach, Florio et al. (2015) used differential labeling of apical (iRG) and basal (oRG) RG cells to sort these two populations for RNA sequencing in mouse and human fetal neocortex. They found that global gene expression in mouse oRG cells was very similar to IPCs and immature neurons, while in human oRG cells it was highly similar to iRG cells. Of the genes that were preferentially expressed in human RG cells compared to IPCs and neurons, 56 lacked a mouse ortholog. Among these, the gene with the highest degree of iRG and oRG enrichment was the hominin-specific gene *ARHGAP11B*, which arose through a partial duplication of *ARGHGAP11A* after the human-chimpanzee split. Overexpression studies in mouse revealed that *ARHGAP11B*, but not *ARHGAP11A*, promoted basal progenitor cell proliferation and iRG delamination, ultimately leading to an increase in neuron numbers and ectopic cortical folding.

On the other hand, Johnson et al. (2015) employed a single-cell sequencing approach to further profile the similarities and differences of the RG population in human, ferret, and mouse. They found that most “classical” RG markers were commonly expressed, confirming that oRG cells do indeed retain a definitive RG identity. oRG cells were enriched in targets of the neurogenin family, which are proneural genes that are highly expressed in mouse IPCs, but not mouse RG cells. In ferret, neurogenin2 (*Neurog2*) was found to be expressed in oRG cells, suggesting that this is a shared property of large gyrencephalic brains. Consistent with that interpretation, overexpression of human *NEUROG2* in the developing ferret cortex promoted delamination of apical progenitors and an expansion of the oRG cell population with a concomitant increase in the rate of neurogenesis.

Together, these studies demonstrate that differential gene expression, including the emergence of hominin-specific genes, operated in evolution to promote increased diversity and complexity of neural stem or progenitor cells in species with large, and often gyrencephalic neocortices. One such example is the subdivision of SVZ in primates and in other mammals with a large brain (Fietz et al., 2010; Hansen et al., 2010; Lui et al., 2011; Smart et al., 2002) to establish the expanded proliferative zone in the oSVZ that generates a greater number of neurons and glial cells. Moreover, oRG cells in the oSVZ exhibit distinct gene expression patterns compared to iRG cells, indicating that these cells are not merely “displaced” RG cells, but rather a related but distinct cell type with divergent properties.

### Transcriptomic Insights into Laminar and Regional Patterning of Neocortical Neural Circuits

Recently, in depth transcriptome analyses of the human prenatal neocortical wall have been carried out and have identified transcriptional signatures of different transient zones and the cell types within them, revealing both conserved patterns and species differences (Figures 4D and 4E) (Fietz et al., 2012; Ip et al., 2010; Johnson et al., 2009; Miller et al., 2014; Pletikos et al., 2014; Pollen et al., 2014). For instance, many of the genes previously implicated in the generation and specification of distinct subtypes of cortical projection neurons (Leone et al., 2008; Molyneaux et al., 2007; Shibata et al., 2015) and interneurons (Southwell et al., 2014) have well conserved expression gradients and domains among neural stem or progenitor cells in the VZ and SVZ or neurons in the SP and CP (Bayatti et al., 2008; Hansen et al., 2013; Hevner, 2007; Kwan et al., 2008; Ma et al., 2013; Radonjić et al., 2014), indicating that human neocortical patterning employs many of the same principles observed across mammalian species. This suggests a degree of homology. However, some of the same studies have also identified differences between humans, non-human primates, and rodents in the expression of certain genes previously implicated in regional patterning, highlighting the role of species differences in the early patterning of the neocortex. For instance, species comparisons of the human and mouse SP zone transcriptomes have revealed many genes with enriched expression in the SP zone of both species, as well as genes that were enriched in human but not mouse (Hoerder-Suabedissen and Molnár, 2015; Miller et al., 2014). Given the essential role of the SP zone in establishing early neural circuits, it will be interesting to determine if human-enriched SP zone genes are important for establishing derived features of human early neocortical connectivity.

While the neocortex has a highly specialized laminar organization, its organization into functionally discrete regions and areas along the tangential dimension is arguably far more complex, especially in humans. Moreover, the molecular processes underlying the regional and areal parcellation of the neocortical CP are poorly understood, particularly in humans. Recent transcriptome studies have identified substantial regional and areal differences in the developing human neocortex (Johnson et al., 2009; Kang et al., 2011; Lambert et al., 2011; Miller et al., 2014; Pletikos et al., 2014). These works have revealed that each region and area has a unique temporally specified transcriptional profile, likely reflecting underlying biological processes involved in the

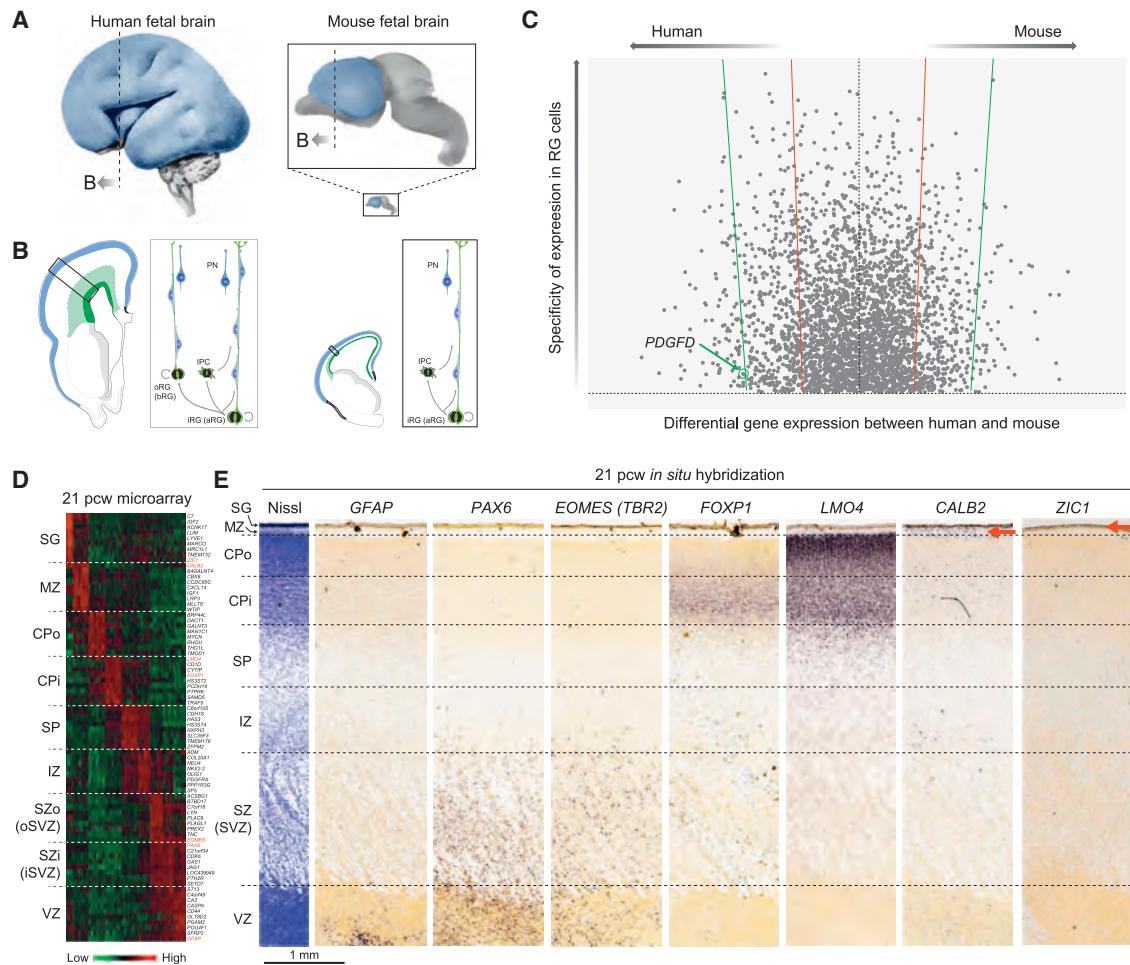


**Figure 4. Shared and Divergent Organization and Transcriptional Profiles of Human and Mouse Neocortical Stem or Progenitor Cells**

(A) Schematic representations of the mid-fetal human (left; 20 pcw) and mouse (right; 18.5 pcd) brain and neocortex (blue). The smaller image of the mouse brain indicates the approximate size difference between human and mouse brains and neocortex (blue) at approximately equivalent age. The zoomed image of the mouse brain highlights differences in brain size and the position along the rostral caudal axis (dotted line) of the illustrations in (B). Adapted with permission from Gulden and Sestan (2014).

(B) A schematic of the cellular composition of the human (left) and mouse (right) fetal forebrain wall detailing differences in neurogenic processes and stem/progenitor types between species. In mouse, VZ apical or inner RG (aRG or iRG) cells (dark green) divide asymmetrically to produce both a daughter intermediate progenitor cell (IPC) that subsequently divides symmetrically in the overlying SVZ (light green) and an excitatory projection neuron (PN) that migrates along RG fibers to the CP (blue). In human, the SVZ is greatly expanded and contains a large population of asymmetrically dividing basal or outer RG (bRG or oRG) cells, which enables the production of greater numbers of neurons.

(C) A plot of the top 5,000 genes found to be enriched in RG cells by Lui et al. (2014) are plotted. Ordinate values reflect the specificity of a gene within the neocortex to human RG cells, while values along the abscissa represent expression differences between human and mouse RG. Red lines and green lines denote 1 and 2 SDs from the mean differential expression score. The vast majority of RG-enriched genes are similarly expressed in mouse and human. However, a considerable number of genes with high differential expression between species are observed, including a number of genes with high expression in human, but not mouse, RG cells. Among these genes, *PDGFRD* was shown to increase the proliferative capacity of the neural progenitors. Adapted with permission from Figure 2d and Expanded Data Table 3 in Lui et al. (2014).

(D) A heatmap showing differential gene expression within discrete zones (layers) of the fetal neocortical wall at 21 pcw. These differences underlie the distinct cell types, cellular processes, and stages of maturation in each zone. Abbreviations are as follows: SG, subplate granular layer; MZ, marginal zone; CPo and CPi, outer and inner cortical plate; SP, subplate zone; IZ, intermediate zone; SZo and SZi, outer and inner subventricular zones; and VZ, ventricular zone.

(E) A Nissl stain on the left delineates each fetal neocortical zone. Notable genes enriched in each are shown by in situ hybridization in the panels to the right, confirming findings of zone enriched expression identified by microarrays. The red arrows mark bands of enriched expression of calretinin/calbindin2 (*CALB2*) and zic family member 1 (*ZIC1*) in the MZ and SG, respectively. Images in (D) and (E) were adapted with permission from Miller et al. (2014).

patterning and differentiation of neural circuits in that region or area (Figures 5B and 5C). Interestingly, these regional and areal transcriptional profiles were largely bilaterally symmetrical across the two hemispheres at the population level during fetal

development, early postnatal development, and in adulthood (Johnson et al., 2009; Kang et al., 2011; Lambert et al., 2011; Miller et al., 2014; Pletikos et al., 2014). These findings suggest that either transcriptional neocortical left-right asymmetry is

present at a level undetectable by using existing tissue-level transcriptomic methods and tissue samples or other non-transcriptional mechanisms, such as neural activity, may play a critical role.

Robust inter-areal transcriptional differences were particularly prominent during early and mid-fetal development and included specific transcriptional signatures associated with prospective prefrontal and perisylvian areas (Johnson et al., 2009; Kang et al., 2011; Miller et al., 2014; Pletikos et al., 2014), which are involved in some of the most distinctly human aspects of cognition and behavior. In addition, prefrontal or frontal-enriched graded expression along the anteroposterior axis of the CP and gradients with enrichment in temporal, occipital, occipito-temporal, perisylvian, and ventromedial areas were observed (Figures 5D–5K). These strong early and mid-fetal inter-areal transcriptional differences and gradients diminish during late fetal periods and postnatal development, especially during infancy and childhood, and increase again after adolescence (Figures 5B and 5C) (Pletikos et al., 2014). The authors hypothesize that the greater inter-areal differences observed during early and mid-fetal development may in part reflect the topographically dynamic transcriptional programs that are necessary to establish area specific cortical and subcortical connectivity patterns. By contrast, in late fetal periods and early postnatal development, perhaps more general molecular programs for glial development, synaptic formation and elimination, and dendritic remodeling predominate. Differences in adolescence may reflect the varied maturational trajectories between certain neocortical areas (e.g., associative versus primary areas), which may be important for late cognitive and sociobehavioral development.

Interestingly, the fetal gene co-expression modules that showed prominent differential patterns among areas and gradient-like expression patterns (Figures 5D–5G), particularly during fetal development, also displayed divergence between humans and rhesus macaques (Figures 5H–5K) (Pletikos et al., 2014), suggesting a possible role for differences in neocortical topographic patterns of gene expression in the evolution of neural circuitry. Other recent studies have also reported genes and protein products with species-biased expression pattern in the developing human neocortex (Charrier et al., 2012; Florio et al., 2015; Han et al., 2013; Johnson et al., 2009, 2015; Kang et al., 2011; Kwan et al., 2012; Lui et al., 2014; Miller et al., 2014; Pollard et al., 2006; Pollen et al., 2014). For instance, *CBLN2* exhibits shared mid-fetal rostral enrichment in human and mouse. However, in situ hybridization data revealed species differences in laminar localization; in the fetal human frontal neocortex, *CBLN2* is highly expressed throughout CP, while in mouse it is enriched selectively in the upper parts of CP (Figure 6A). Unlike *CBLN2*, *NPY* is expressed posteriorly in the occipital and parts of the temporal human CP compared to expression in anterior regions of mouse cortex (Figure 6B). Taken together, these findings indicate that, similar to other species, the generation and differentiation of neocortical cell types and their assembly into functional neural circuits in humans is achieved through precise regulation of spatiotemporal gene expression involving conserved and divergent developmental programs.

### The Regulatory and Epigenomic Landscapes of the Developing Human CNS

The spatiotemporal patterns of gene expression discussed above are achieved through complex regulatory processes involving several players that function in a combinatorial way (Nord et al., 2015; Shibata et al., 2015). But the tissue specificity, timing, and level of a gene's expression are greatly controlled by distal sequences like enhancers (sequences that increase expression), silencers (sequences that repress expression), and insulators (sequences that block interaction between enhancers and promoters), which along with core promoters are referred to as “cis-regulatory elements” (CREs). CREs contain binding sites for multiple *trans*-acting regulatory proteins, primarily transcription factors. According to some estimates, the human genome harbors approximately 400,000 putative enhancers (ENCODE Project Consortium, 2012). Enhancer bound transcription factors along with mediator complex proteins loop DNA and bring enhancers and promoters in close proximity, leading to activation of gene expression. In addition to CREs and regulatory proteins, chromatin state or structure plays a critical role in the regulation of gene expression. Chromatin state is affected by epigenomic modifications like DNA methylation and post-translational modification of histone proteins and chromatin remodeling complexes. Here, we will give an overview of the current understanding of transcriptional regulation in the developing human CNS.

### Regulatory Landscape of Human Neurodevelopment

Comparative genomic studies have shown that many of the genes encoding transcription factors and associated regulatory networks involved in the specification and differentiation of different subtypes of neurons and glia are highly conserved across mammals (Nord et al., 2015; Shibata et al., 2015). Moreover, studies indicate that nearly half of all pairwise regulatory interactions connecting mouse transcription factor genes have been maintained in orthologous human tissues, including brain (Ravasi et al., 2010; Stergachis et al., 2014). However, substantial turnover of CREs has been reported.

Evolutionary changes in CREs have been shown to directly underlie species differences, including in humans. For instance, in the case of *Fezf2*, a cortex specific enhancer, E4, is essential for corticospinal tract development mediated by SOX4 and SOX11 (Shim et al., 2012). The SOX binding sites in this enhancer emerged during tetrapod evolution and stabilized in mammals to establish a regulatory network that controls corticospinal tract specification and formation.

In addition to evolutionary changes in transcription factor binding sites, human-specific expansion, deletion, and de novo emergence of regulatory elements are also observed (Bae et al., 2014). For example, extensive variation in the *cis*-regulation of *GPR56*, a gene that promotes neural progenitor proliferation (Bae et al., 2014), is observed due to the expansion of the number of transcriptional start sites present in human *GPR56* (17 start sites) as compared to its mouse ortholog *Gpr56* (5 start sites; Figure 7A). The *cis*-element of one of these human alternative transcriptional start sites (E1m) can drive expression of a reporter gene in RG cells throughout the embryonic neocortex of a transgenic mouse (Figure 7B). Further experiments with sequences

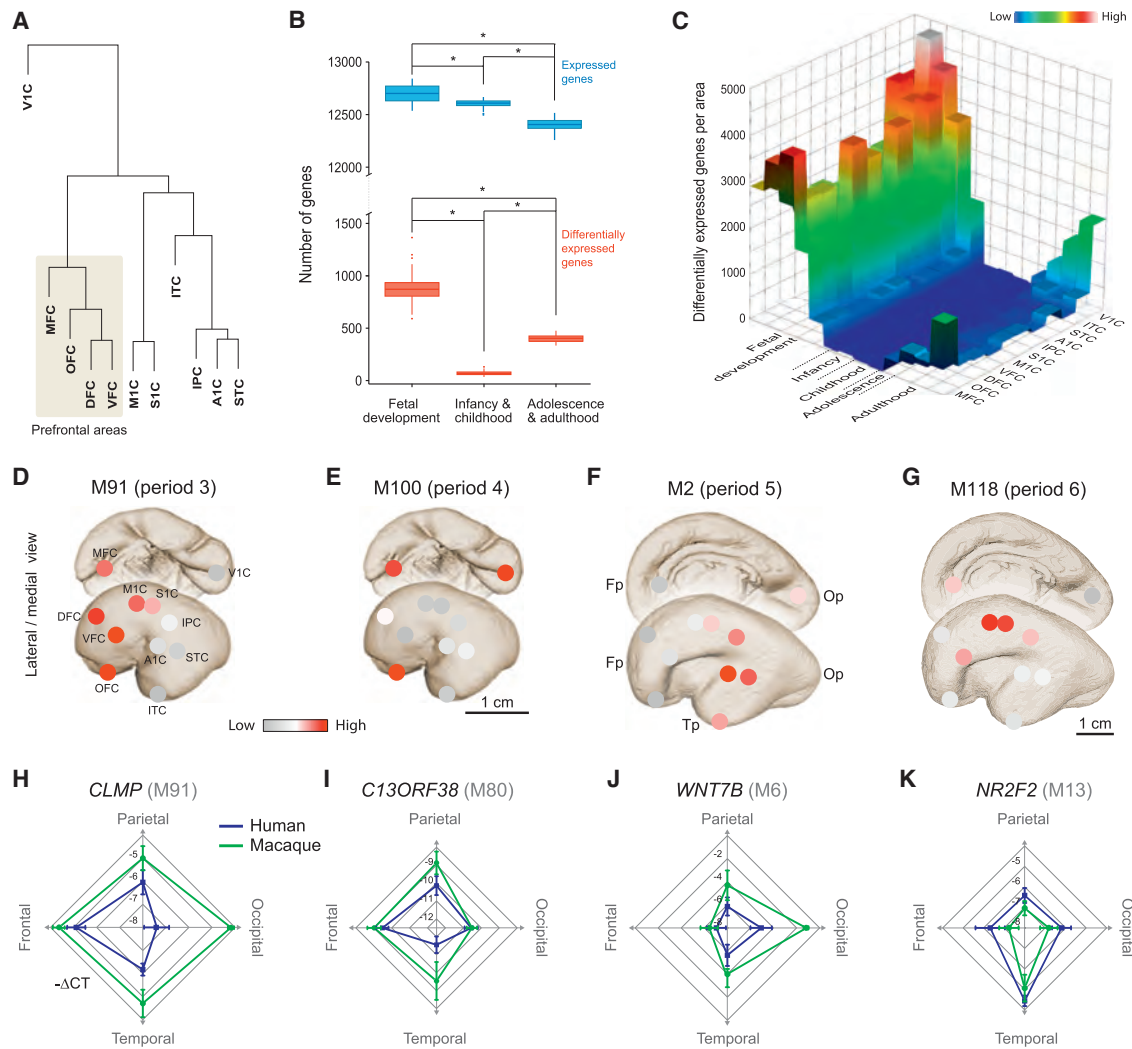


**Figure 5. Transcriptional Differences among Human Neocortical Areas Are Temporally Regulated**

(A) Unsupervised hierarchical clustering of the 11 neocortical areas profiled by Pletikos et al. (2014), based on the transcriptome of each area from the period of fetal development throughout adulthood, showing relative transcriptional differences. Abbreviations are as follows: OFC, orbital prefrontal cortex; DFC, dorsal prefrontal cortex; VFC, ventral prefrontal cortex; MFC, medial prefrontal cortex; M1C, primary motor cortex; S1C, primary somatosensory cortex; IPC, posterior inferior parietal cortex; A1C, primary auditory cortex; STC, superior temporal cortex; ITC, inferior temporal cortex; and V1C, primary visual cortex.

(B) Boxplots of subsampling permutations show the number of expressed (blue) and differentially expressed (red) genes among neocortical areas across fetal development (periods 3–7), infancy (periods 8 and 9), childhood (periods 10 and 11), adolescence (period 12), and adulthood (periods 13–15). Note that the total number of genes expressed decreases over development. However, the number of differentially expressed genes observed over development exhibits a temporal hourglass pattern with the highest number in fetal development, a marked decline in infancy and childhood, and an increase in adolescence through adulthood.

(C) A 3D heatmap showing the number (post hoc Tukey test) of genes with differential expression between any two neocortical areas, demonstrating that the hourglass pattern of inter-areal differential expression persists in all neocortical areas, but is most prominent in MFC and V1C.

(D–G) Examples of gene co-expression modules (M) with a temporally regulated gradient-like expression pattern in the fetal neocortex (see circles with colored scale overlaying each area). Modules M91, M100, M2, and M118 show frontal (D), medial fronto-occipital (E), posterior perisylvian (F), and middle perisylvian (G) enriched expression, respectively. Fp, frontal pole; Tp, temporal pole; Op, occipital pole.

(H–L) Radar charts showing shared and divergent expression gradients in human (blue) versus Rhesus macaque (green) fetal neocortex of specific intramodular hub genes (*CLMP* [M91], *C13ORF38* [M80], *WNT7B* [M6], and *NR2F2* [M13]).

(A)–(K) were adapted with permission from Pletikos et al. (2014).

found in other mammals with a prominent sylvian fissure and gyrencephalic brain recapitulated this pattern of expression, suggesting that *GPR56* was important for the evolutionary expansion of the perisylvian neocortex, a region involved in the processing of language and speech and other higher-order cognitive functions. Moreover, a 15-bp deletion of the E1m *cis*-element caused

perisylvian microgyria in humans and affected rostro-lateral *GPR56* expression in mouse (Figures 7C and 7D). Taken together, these findings indicate that species differences in *cis*-regulatory elements are important for driving region and species-specific patterns of gene expression and contribute to the expansion of the neocortex.

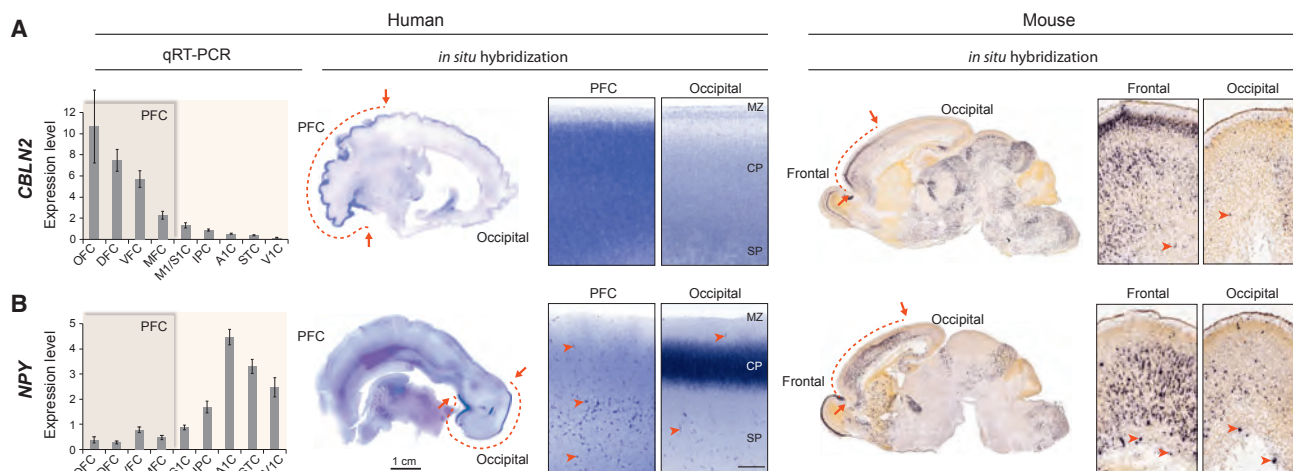


**Figure 6. Shared and Divergent Expression Patterns in the Fetal Human and Mouse Neocortex**

(A) *CBLN2* is enriched throughout the CP of the mid-fetal human prefrontal cortex (PFC), whereas in mouse, at a comparable period of development, expression is enriched in the upper layers of frontal cortex. (B) *NPY* has highly divergent expression along the rostral-caudal axis in human versus mouse mid-fetal neocortex. In human, but not mouse, *NPY* is enriched in the mid-fetal occipito-temporal CP. The expression of *NPY* in sparsely distributed interneurons of the CP and SP zone is conserved. Human data were adapted with permission from Johnson et al. (2009). Mouse in situ hybridization images were obtained from the Allen Developing Mouse Brain Atlas (<http://developingmouse.brain-map.org>; Thompson et al., 2014). Abbreviations are as given in the Figure 5 legend.

Moving beyond the incremental advances provided by studies of individual CREs to a comprehensive understanding of gene regulation in the human brain requires genome-wide knowledge of the CREs that are active in human neurodevelopment. Comparative genomic methods have been applied by several groups (Lindblad-Toh et al., 2011; Margulies et al., 2007; Pennacchio et al., 2006; Pollard et al., 2006; Prabhakar et al., 2006; Siepel et al., 2005) to identify putative conserved CREs or regulatory RNAs, a disproportionate number of which are proposed to regulate human brain-expressed genes (Johnson et al., 2009; Pennacchio et al., 2006; Pollard et al., 2006). In addition to conserved sequences, many genomic regions that display accelerated sequence divergence in humans are predicted to be enhancers active during development, with a disproportionate number predicted to regulate human brain-expressed genes (Capra et al., 2013; Franchini and Pollard, 2015; Johnson et al., 2009; Lambert et al., 2011; Miller et al., 2014; Prabhakar et al., 2006).

In addition to genomic sequences, hallmark features of active CREs like chromatin accessibility, nucleosome depletion, or enrichment for specific post-translational histone modifications can also be assayed globally through techniques including DNAase hypersensitivity and chromatin immunoprecipitation followed by deep sequencing. Visel et al. (2013) determined the genome-wide occupancy of the enhancer-associated proteins p300/CBP in human fetal neocortex to identify active enhancers. Enrichment of p300/CBP binding sites was observed near genes highly expressed in the fetal neocortex. By further characterizing a subset of highly conserved human enhancers that are active in the embryonic day 11.5 (e11.5) mouse telencephalon, Pattabiraman et al. (2014) determined which progenitor domains generated cells that populated different subdivisions of the cerebral cortex and provided insights into the transcription networks that generate these subdivisions. Other groups have identified

enhancers, on a genome-wide scale, in different brain regions and time points by mapping enrichment of histone 3 lysine 4 monomethylation (H3K4me1) and histone 3 lysine 27 acetylation (H3K27ac), characteristic marks of active enhancers (Reilly et al., 2015; Vermunt et al., 2014). Region specific enhancers along with co-regulated enhancers that form cell type and context specific networks have also been identified. Comparative epigenetic profiling of promoters and enhancers active during human, rhesus macaque, and mouse corticogenesis has identified many regions that were gained in humans (Reilly et al., 2015). These regions were shown to be significantly enriched in modules of co-expressed genes that function in neuronal proliferation, migration, and cortical-map organization. Thus, the regulatory networks that govern gene expression in the developing human CNS are beginning to be elucidated; however, this information has yet to be fully placed into a functional context.

#### DNA Methylation and Histone Modifications in Human Neurodevelopment

Epigenetic mechanisms, acting in concert with *trans* and *cis* components of the regulatory circuitry, play a critical role in regulating spatiotemporal expression patterns (Maze et al., 2014; Nord et al., 2015; Shibata et al., 2015). These mechanisms, including DNA methylation, histone modifications, and non-coding RNAs, can also be affected by various extrinsic factors, thus providing a molecular link between external cues and gene expression.

DNA methylation of cytosine, primarily at CpG nucleotides, plays a key role in neural development and function and can be profiled at millions of CpGs in the human genome at single base resolution in an unbiased manner by applying sequencing technologies. Several studies have mapped global methylation patterns in human brain development using microarray platforms

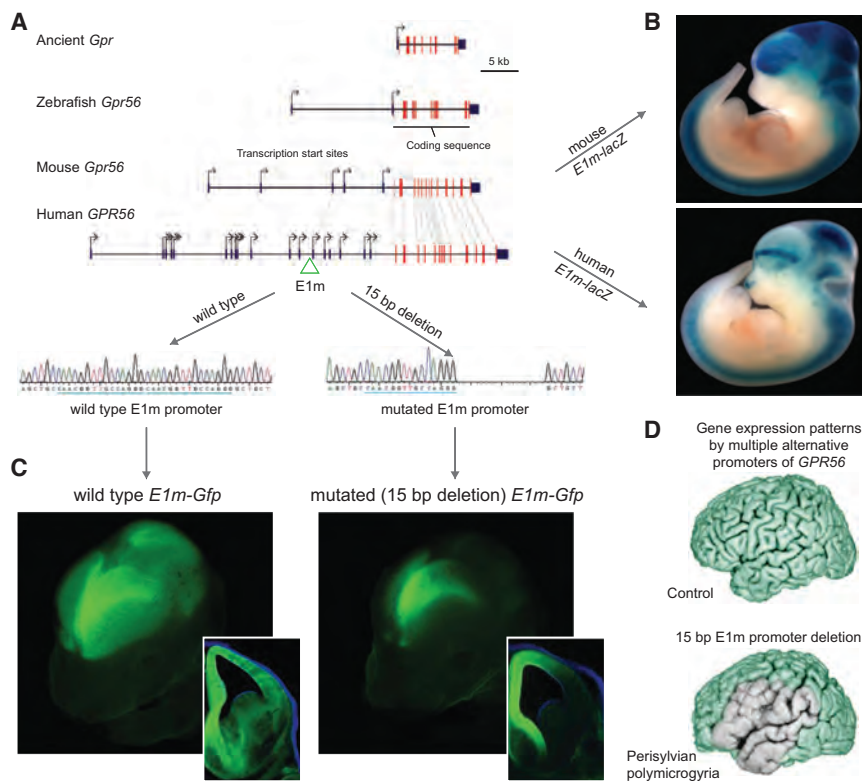


**Figure 7. Evolutionary Changes in a *cis*-Regulatory Element Active in Neocortical Stem or Progenitor Cells**

(A) Schematic demonstrating expansion of transcriptional start sites over evolution in noncoding exon 1 of the *Gpr56* gene (2 in zebra fish, 5 in mouse, and 17 in human), a gene that promotes proliferation of neural progenitor cells.

(B) A different expression pattern was observed after driving expression of *lacZ* (blue staining) with either the mouse or human variant of the promoter of one of the transcription start sites (E1m). The mouse element was able to recapitulate the full extent of mouse *Gpr56* expression, but expression driven from the human element was restricted to a rostra-lateral band.

(C) Consistent with a role in driving rostra-lateral expression specifically, a 15-bp deletion in the E1m element eliminated expression of GFP from the rostra-lateral forebrain in transgenic mice harboring an allele of *Gfp* driven by the E1m element.

(D) Deletion of this element was observed in patients with perisylvian polymicrogyria in accordance with a role in driving expression of *GPR56* in the lateral neocortex (light green). In these patients, this mutation likely led to malformations of the perisylvian neocortex important for language among other functions.

(A)–(D) were adapted with permission from Bae et al. (2014).

(Numata et al., 2012; Siegmund et al., 2007; Spiers et al., 2015). Global methylation in the human prefrontal cortex was observed to be age dependent, with fetal samples being the most distinct from early postnatal and adult samples (Numata et al., 2012), as DNA methylation levels changed rapidly during fetal development but slowed down after birth and with aging. Moreover, at loci that changed both in fetal and postnatal periods, demethylated states predominated during fetal periods with increasing methylation observed during the postnatal period.

DNA methylation patterns in the human prefrontal cortex during development were further studied by Lister et al. (2013) by genome sequencing. Similar to array-based studies, they too observed widespread methylome reconfiguration during fetal to young adult development. Another key finding of their study is the accumulation of methylation in the non-CpG context (mCH) during early postnatal development (first 2 years postpartum) through adolescence, with a small decrease thereafter. Lister et al. noted that mCH accumulation during the early post-natal development period coincided with the primary phase of synaptogenesis. Further examination of the DNA methylation patterns in a cell-type-specific manner found that mCH was more abundant than CpG methylation in adult neurons, but was at insignificant levels in glial cells. Accumulation of mCH and gene expression were negatively correlated; genes highly expressed in adult neurons lost both CpG and non-CpG methylation progressively during development.

Taken together these data indicate that dynamics in methylation of genomic DNA is an essential feature of gene regulation

in human neurodevelopment. Moreover, it is intriguing to speculate that increased DNA methylation in infancy and childhood may be a mechanism underlying the reduction in inter-areal differences in gene expression and the increase in the expression of genes associated with synapse formation and regulation observed during these periods (Figures 3 and 6).

In addition to DNA methylation, histone modification is an essential mechanism for establishing cellular diversity and regulating the timing of developmental processes. Methylation (mono-, di-, and tri-) and acetylation are the most extensively studied modifications, although many more have been observed (Tessarz and Kouzarides, 2014). Unfortunately, comprehensive chromatin immunoprecipitation sequencing (ChIP-seq) studies of histone modifications in human brain are limited due to the necessity for large amounts of tissue along with the variable quality of human post-mortem brain tissue. However, a few studies (Kundaje et al., 2015; Zhu et al., 2013) have generated chromatin state maps in a limited number of post-mortem human brains, which suggests that histone modification is indeed likely to be an important regulator of neuronal maturation in the human brain. Cheung et al. (2010) profiled histone 3 lysine 4 trimethylation (H3K4me3) across development in neuronal and non-neuronal cells of the human prefrontal cortex of 11 individuals ranging in age from 0.5 to 69 postnatal years. A key finding of their study was significant remodeling during postnatal development and aging of prefrontal neurons. Notably, H3K4me3 methylation of *NEUROD1* and several members of the cadherin and semaphorin families was increased in infants compared to the oldest samples (greater than 60 years of age).

### Non-coding RNAs in Human Neurodevelopment

Non-coding RNAs represent a large, but poorly characterized, component of the human transcriptome that plays a critical role in transcriptional and post-transcriptional regulation to influence the overall transcriptional landscape and proteomic diversity (Morris and Mattick, 2014; O'Carroll and Schaefer, 2013) (Box 3). They are broadly classified as short or long, based on their length. Short microRNAs (miRNAs) bind their substrate mRNA and target it for degradation or inhibit its translation (O'Carroll and Schaefer, 2013). On the other hand, long non-coding RNAs (lncRNAs) and pseudogenes can act as regulators of transcription (Morris and Mattick, 2014), compete with endogenous RNAs, or act as miRNA sponges to post-transcriptionally regulate the levels and dynamics of protein-coding transcripts (Tay et al., 2014).

Recent studies have shown that a large number of all identified miRNAs and lncRNAs are expressed in the human and non-human primate brains and are spatially and temporally regulated (O'Carroll and Schaefer, 2013; Somel et al., 2010, 2011). For example, 31% of the miRNAs in the human prefrontal cortex were found to be affected by age and miRNA expression was negatively correlated with the expression of predicted target RNAs (Somel et al., 2010). miRNA mediated regulation was also implicated in the evolution of gene expression across the postnatal development of the prefrontal cortex and cerebellum in humans, chimpanzees, and macaques (Somel et al., 2011). Taken together, these data indicate that non-coding RNAs are an important regulatory mechanism in establishing the regional and temporal landscape of gene expression and contributed to human brain development and evolution.

### Genome Mosaicism in Human Neurodevelopment

Recent advances in next generation sequencing and single-cell genomics have enabled the detection of somatic genomic variations in specific cells and healthy and diseased human brains (Cai et al., 2015; Hu et al., 2014; Marin-Valencia et al., 2014). This work has broad ranging implications from uncovering new disease mechanisms to providing new insights into neurotypical development. For example, these studies have demonstrated that certain neurodevelopmental diseases are caused by de novo somatic mutations in neural progenitors that then expand clonally to produce aberrations in specific neural cell types and brain regions (Cai et al., 2015; Hu et al., 2014; Marin-Valencia et al., 2014; D'Gama et al., 2015).

Recent studies have also shown that somatic mutations and mobile DNA elements play a role in the generation of diversity and complexity in the developing human brain (Coufal et al., 2009). For example, mutations driven by L1 mediated retrotransposition, in which mobile elements relocate throughout the genome to inactivate genes and alter their expression profile, appear to occur in normal brain development. However, reports also indicate such mutations are rare in the human brain and the extent to which retrotransposition functionally contributes to aspects of normal human development remains to be determined (Cai et al., 2015).

### Conclusions and Future Directions

The genomic revolution has left us in an unprecedented position, poised to decipher molecular and cellular processes underlying

neurodevelopment in humans and other not well studied mammals, such as non-human primates, more rapidly, precisely, and comprehensively than ever before. There is also an improved ability to detect genetic variations that confer risk for neurological and psychiatric disorders and an increased appreciation of the role of genomic mosaicism in development, evolution, and disease. However, a great deal of further work must be undertaken to know what makes us human—how our mind takes shape during development, why we suffer from certain diseases, how genetic and somatic variations cause diseases, and why certain therapeutic approaches developed using model systems do not work as effectively or lead to side effects in humans. Additional work is also needed to characterize the timing and sequence of cellular processes in human neurodevelopment, the sequence variants and gene expression differences observed in neurodevelopmental disorders, and the epigenetic and *cis*-regulatory elements that regulate the spatiotemporal dynamics of the transcriptome and proteomic diversity in both healthy and diseased individuals. Achieving these goals will require additional improvements in tissue procurement and processing to make tissue more accessible for advanced molecular and cellular techniques. Similar endeavors need to be applied for systematic comparisons with non-human primates, our closest relatives. Another major challenge before us is better understanding cellular heterogeneity and the properties of specific human cell types, which is now attainable through single-cell genomics and other techniques that allow for the isolation of discrete cell populations. Ultimately, advances in genomics and other disciplines must be leveraged to construct better experimental models of human neurodevelopment and diseases.

### AUTHOR CONTRIBUTIONS

Conceptualization, J.C.S., S.P., and N.S.; Writing – Original Draft, J.C.S., S.P., and N.S.; Writing – Review & Editing, J.C.S., S.P., Y.Z., M.L., and N.S.; Visualization, J.C.S., S.P., Y.Z., M.L., and N.S.

### ACKNOWLEDGMENTS

We thank members of our laboratory for thoughtful discussions and comments on the manuscript. We apologize to all colleagues whose relevant studies were not cited because of space limitations, the broad scope of this review, and the emphasis on recent studies. Work in our laboratory was supported by the NIH, the Foster-Davis Foundation (NARSAD), the Kavli Foundation, the James S. McDonnell Foundation, and the Simons Foundation.

### REFERENCES

- Al-Jaberi, N., Lindsay, S., Sarma, S., Bayatti, N., and Clowry, G.J. (2015). The early fetal development of human neocortical GABAergic interneurons. *Cereb. Cortex* 25, 631–645.
- Aldama, J. (1930). Cytoarchitektonik der Großhirnrinde eines 5 jährigen und eines 1 jährigen Kindes. *Z. Gesamte Neurol. Psychiatr.* 130, 532–626.
- Amsterdam, B. (1972). Mirror self-image reactions before age two. *Dev. Psychobiol.* 5, 297–305.
- Amunts, K., Schleicher, A., Ditterich, A., and Zilles, K. (2003). Broca's region: cytoarchitectonic asymmetry and developmental changes. *J. Comp. Neurol.* 465, 72–89.
- Azevedo, F.A., Carvalho, L.R., Grinberg, L.T., Farfel, J.M., Ferretti, R.E., Leite, R.E., Jacob Filho, W., Lent, R., and Herculano-Houzel, S. (2009). Equal

- numbers of neuronal and nonneuronal cells make the human brain an isometrically scaled-up primate brain. *J. Comp. Neurol.* **513**, 532–541.
- Bae, B.I., Tietjen, I., Atabay, K.D., Evrony, G.D., Johnson, M.B., Asare, E., Wang, P.P., Murayama, A.Y., Im, K., Lisgo, S.N., et al. (2014). Evolutionarily dynamic alternative splicing of GPR56 regulates regional cerebral cortical patterning. *Science* **343**, 764–768.
- Bae, B.I., Jayaraman, D., and Walsh, C.A. (2015). Genetic changes shaping the human brain. *Dev. Cell* **32**, 423–434.
- Bayatti, N., Sarma, S., Shaw, C., Eyre, J.A., Vouyiouklis, D.A., Lindsay, S., and Clowry, G.J. (2008). Progressive loss of PAX6, TBR2, NEUROD and TBR1 mRNA gradients correlates with translocation of EMX2 to the cortical plate during human cortical development. *Eur. J. Neurosci.* **28**, 1449–1456.
- Bayer, S.A., and Altman, J. (2007). Atlas of Human Central Nervous System Development, *Volumes 1–5* (CRC Press).
- Belliemi, C.V., and Buonocore, G. (2012). Is fetal pain a real evidence? *J. Matern. Fetal Neonatal Med.* **25**, 1203–1208.
- Bogin, B. (1994). Adolescence in evolutionary perspective. *Acta Paediatr. Suppl.* **406**, 29–35, discussion 36.
- Brennan, K.J., Simone, A., Jou, J., Gelboin-Burkhardt, C., Tran, N., Sangar, S., Li, Y., Mu, Y., Chen, G., Yu, D., et al. (2011). Modelling schizophrenia using human induced pluripotent stem cells. *Nature* **473**, 221–225.
- Brodmann, K. (1909). Vergleichende Lokalisationslehre der Grosshirnrinde in ihren Prinzipien dargestellt auf Grund des Zellenbaues (Johann Ambrosius Barth Verlag).
- Butterworth, G. (1990). Origins of Self-Perception in Infancy (University of Chicago Press).
- Bystron, I., Rakic, P., Molnár, Z., and Blakemore, C. (2006). The first neurons of the human cerebral cortex. *Nat. Neurosci.* **9**, 880–886.
- Bystron, I., Blakemore, C., and Rakic, P. (2008). Development of the human cerebral cortex: Boulder Committee revisited. *Nat. Rev. Neurosci.* **9**, 110–122.
- Cai, X., Evrony, G.D., Lehmann, H.S., Elhosary, P.C., Mehta, B.K., Poduri, A., and Walsh, C.A. (2015). Single-cell, genome-wide sequencing identifies clonal somatic copy-number variation in the human brain. *Cell Rep.* **10**, 645.
- Capra, J.A., Erwin, G.D., McKinsey, G., Rubenstein, J.L., and Pollard, K.S. (2013). Many human accelerated regions are developmental enhancers. *Philos. Trans. R. Soc. Lond. B Biol. Sci.* **368**, 20130025.
- Catts, V.S., Fung, S.J., Long, L.E., Joshi, D., Vercammen, A., Allen, K.M., Fillman, S.G., Rothmond, D.A., Sinclair, D., Tiwari, Y., et al. (2013). Rethinking schizophrenia in the context of normal neurodevelopment. *Front. Cell. Neurosci.* **7**, 60.
- Charrier, C., Joshi, K., Coutinho-Budd, J., Kim, J.E., Lambert, N., de Marchena, J., Jin, W.L., Vanderhaeghen, P., Ghosh, A., Sassa, T., and Polleux, F. (2012). Inhibition of SRGAP2 function by its human-specific paralogs induces neoteny during spine maturation. *Cell* **149**, 923–935.
- Cheung, I., Shulha, H.P., Jiang, Y., Matevosian, A., Wang, J., Weng, Z., and Akbarian, S. (2010). Developmental regulation and individual differences of neuronal H3K4me3 epigenomes in the prefrontal cortex. *Proc. Natl. Acad. Sci. USA* **107**, 8824–8829.
- Chi, J.G., Dooling, E.C., and Gilles, F.H. (1977). Left-right asymmetries of the temporal speech areas of the human fetus. *Arch. Neurol.* **34**, 346–348.
- Choi, B.H., and Lapham, L.W. (1978). Radial glia in the human fetal cerebrum: a combined Golgi, immunofluorescent and electron microscopic study. *Brain Res.* **148**, 295–311.
- Chou, S.J., Babot, Z., Leingärtner, A., Studer, M., Nakagawa, Y., and O’Leary, D.D. (2013). Geniculocortical input drives genetic distinctions between primary and higher-order visual areas. *Science* **340**, 1239–1242.
- Clarke, L.E., and Barres, B.A. (2013). Emerging roles of astrocytes in neural circuit development. *Nat. Rev. Neurosci.* **14**, 311–321.
- Clowry, G.J. (2007). The dependence of spinal cord development on corticospinal input and its significance in understanding and treating spastic cerebral palsy. *Neurosci. Biobehav. Rev.* **31**, 1114–1124.
- Clowry, G., Molnár, Z., and Rakic, P. (2010). Renewed focus on the developing human neocortex. *J. Anat.* **217**, 276–288.
- Colantuoni, C., Lipska, B.K., Ye, T., Hyde, T.M., Tao, R., Leek, J.T., Colantuoni, E.A., Elkhoulou, A.G., Herman, M.M., Weinberger, D.R., and Kleinman, J.E. (2011). Temporal dynamics and genetic control of transcription in the human prefrontal cortex. *Nature* **478**, 519–523.
- Coufal, N.G., Garcia-Perez, J.L., Peng, G.E., Yeo, G.W., Mu, Y., Lovci, M.T., Morell, M., O’Shea, K.S., Moran, J.V., and Gage, F.H. (2009). L1 retrotransposition in human neural progenitor cells. *Nature* **460**, 1127–1131.
- D’Gama, A.M., Pochareddy, S., Li, M., Jamuar, S.S., Reiff, R.E., Lam, A.T., Sestan, N., and Walsh, C.A. (2015). Targeted DNA sequencing from autism spectrum disorder brains implicates multiple genetic mechanisms. *Neuron* **88**, 910–917.
- deAzevedo, L.C., Fallet, C., Moura-Neto, V., Daumas-Duport, C., Hedin-Perreira, C., and Lent, R. (2003). Cortical radial glial cells in human fetuses: depth-correlated transformation into astrocytes. *J. Neurobiol.* **55**, 288–298.
- DeFelipe, J., Alonso-Nanclares, L., and Arellano, J.I. (2002). Microstructure of the neocortex: comparative aspects. *J. Neurocytol.* **31**, 299–316.
- Dehaene-Lambertz, G., and Spelke, E.S. (2015). The infancy of the human brain. *Neuron* **88**, 93–109.
- Dehay, C., Kennedy, H., and Kosik, K.S. (2015). The outer subventricular zone and primate-specific cortical complexification. *Neuron* **85**, 683–694.
- Dekaban, A.S. (1978). Changes in brain weights during the span of human life: relation of brain weights to body heights and body weights. *Ann. Neurol.* **4**, 345–356.
- de Vries, J.I., Visser, G.H., and Prechtl, H.F. (1985). The emergence of fetal behaviour. II. Quantitative aspects. *Early Hum. Dev.* **12**, 99–120.
- Dosman, C.F., Andrews, D., and Goulden, K.J. (2012). Evidence-based milestone ages as a framework for developmental surveillance. *Paediatr. Child Health* **17**, 561–568.
- Dumontheil, I. (2014). Development of abstract thinking during childhood and adolescence: the role of rostralateral prefrontal cortex. *Dev. Cogn. Neurosci.* **10**, 57–76.
- ENCODE Project Consortium (2012). An integrated encyclopedia of DNA elements in the human genome. *Nature* **489**, 57–74.
- Eriksson, P.S., Perfilieva, E., Björk-Eriksson, T., Alborn, A.M., Nordborg, C., Peterson, D.A., and Gage, F.H. (1998). Neurogenesis in the adult human hippocampus. *Nat. Med.* **4**, 1313–1317.
- Ernst, A., Alkass, K., Bernard, S., Salehpour, M., Perl, S., Tisdale, J., Possnert, G., Druid, H., and Frisén, J. (2014). Neurogenesis in the striatum of the adult human brain. *Cell* **156**, 1072–1083.
- Eswaran, H., Haddad, N.I., Shihabuddin, B.S., Preissl, H., Siegel, E.R., Murphy, P., and Lowery, C.L. (2007). Non-invasive detection and identification of brain activity patterns in the developing fetus. *Clin. Neurophysiol.* **118**, 1940–1946.
- Fertuzinhos, S., Krsnik, Z., Kawasawa, Y.I., Rasin, M.R., Kwan, K.Y., Chen, J.G., Judas, M., Hayashi, M., and Sestan, N. (2009). Selective depletion of molecularly defined cortical interneurons in human holoprosencephaly with severe striatal hypoplasia. *Cereb. Cortex* **19**, 2196–2207.
- Fietz, S.A., Kelava, I., Vogt, J., Wilsch-Bräuninger, M., Stenzel, D., Fish, J.L., Corbeil, D., Riehn, A., Distler, W., Nitsch, R., and Huttner, W.B. (2010). OSVZ progenitors of human and mouse fetal neocortex are epithelial-like and expand by integrin signaling. *Nat. Neurosci.* **13**, 690–699.
- Fietz, S.A., Lachmann, R., Brandl, H., Kircher, M., Samusik, N., Schröder, R., Lakshmanaperumal, N., Henry, I., Vogt, J., Riehn, A., et al. (2012). Transcriptional zones of human and mouse fetal neocortex suggest a role of extracellular matrix in progenitor self-renewal. *Proc. Natl. Acad. Sci. USA* **109**, 11836–11841.
- Florio, M., Albert, M., Taverna, E., Namba, T., Brandl, H., Lewitus, E., Haffner, C., Sykes, A., Wong, F.K., Peters, J., et al. (2015). Human-specific gene ARHGAP11B promotes basal progenitor amplification and neocortex expansion. *Science* **347**, 1465–1470.

- Franchini, L.F., and Pollard, K.S. (2015). Can a few non-coding mutations make a human brain? *BioEssays* 37, 1054–1061.
- Gerber, R.J., Wilks, T., and Erdie-Lalena, C. (2010). Developmental milestones: motor development. *Pediatr. Rev.* 31, 267–276, quiz 277.
- Geschwind, D.H., and Rakic, P. (2013). Cortical evolution: judge the brain by its cover. *Neuron* 80, 633–647.
- Gogtay, N., Giedd, J.N., Lusk, L., Hayashi, K.M., Greenstein, D., Vaituzis, A.C., Nugent, T.F., 3rd, Herman, D.H., Clasen, L.S., Toga, A.W., et al. (2004). Dynamic mapping of human cortical development during childhood through early adulthood. *Proc. Natl. Acad. Sci. USA* 101, 8174–8179.
- Gould, S.J., Howard, S., and Papadaki, L. (1990). The development of ependyma in the human fetal brain: an immunohistological and electron microscopic study. *Brain Res. Dev. Brain Res.* 55, 255–267.
- Gulden, F.O., and Sestan, N. (2014). Neurobiology: building a bigger brain. *Nature* 515, 206–207.
- Gulsuner, S., Walsh, T., Watts, A.C., Lee, M.K., Thornton, A.M., Casadei, S., Rippey, C., Shahin, H., Nimgaonkar, V.L., Go, R.C., et al.; Consortium on the Genetics of Schizophrenia (COGS); PAARTNERS Study Group (2013). Spatial and temporal mapping of de novo mutations in schizophrenia to a fetal prefrontal cortical network. *Cell* 154, 518–529.
- Gulyás, A.I., Megias, M., Emri, Z., and Freund, T.F. (1999). Total number and ratio of excitatory and inhibitory synapses converging onto single interneurons of different types in the CA1 area of the rat hippocampus. *J. Neurosci.* 19, 10082–10097.
- Han, K., Gennarino, V.A., Lee, Y., Pang, K., Hashimoto-Torii, K., Choufani, S., Raju, C.S., Oldham, M.C., Weksberg, R., Rakic, P., et al. (2013). Human-specific regulation of MeCP2 levels in fetal brains by microRNA miR-483-5p. *Genes Dev.* 27, 485–490.
- Hansen, D.V., Lui, J.H., Parker, P.R., and Kriegstein, A.R. (2010). Neurogenic radial glia in the outer subventricular zone of human neocortex. *Nature* 464, 554–561.
- Hansen, D.V., Lui, J.H., Flandin, P., Yoshikawa, K., Rubenstein, J.L., Alvarez-Buylla, A., and Kriegstein, A.R. (2013). Non-epithelial stem cells and cortical interneuron production in the human ganglionic eminences. *Nat. Neurosci.* 16, 1576–1587.
- Harris, P.L. (2000). *The Work of the Imagination* (Blackwell Publishers).
- Heaton, R.K., Chelune, G.J., Talley, J.L., Kay, G.G., and Curtiss, G. (1993). *Wisconsin Card Sorting Test Manual: Revised and Expanded* (Psychological Assessment Resources).
- Herculano-Houzel, S. (2009). The human brain in numbers: a linearly scaled-up primate brain. *Front. Hum. Neurosci.* 3, 31.
- Herculano-Houzel, S., Kaas, J.H., and de Oliveira-Souza, R. (2015). Corticalization of motor control in humans is a consequence of brain scaling in primate evolution. *J. Comp. Neurol.* Published online April 18, 2015. <http://dx.doi.org/10.1002/cne.23792>.
- Hevner, R.F. (2007). Layer-specific markers as probes for neuron type identity in human neocortex and malformations of cortical development. *J. Neuropathol. Exp. Neurol.* 66, 101–109.
- Hoerder-Suabedissen, A., and Molnár, Z. (2015). Development, evolution and pathology of neocortical subplate neurons. *Nat. Rev. Neurosci.* 16, 133–146.
- Honig, L.S., Herrmann, K., and Shatz, C.J. (1996). Developmental changes revealed by immunohistochemical markers in human cerebral cortex. *Cereb. Cortex* 6, 794–806.
- Howard, B.M., Zhicheng Mo, Filipovic, R., Moore, A.R., Antic, S.D., and Zecevic, N. (2008). Radial glia cells in the developing human brain. *Neuroscientist* 14, 459–473.
- Hu, W.F., Chahrour, M.H., and Walsh, C.A. (2014). The diverse genetic landscape of neurodevelopmental disorders. *Annu. Rev. Genomics Hum. Genet.* 15, 195–213.
- Humphrey, T., and Hooker, D. (1959). Double simultaneous stimulation of human fetuses and the anatomical patterns underlying the reflexes elicited. *J. Comp. Neurol.* 112, 75–102.
- Huttenlocher, P.R. (1979). Synaptic density in human frontal cortex - developmental changes and effects of aging. *Brain Res.* 163, 195–205.
- Huttenlocher, P.R., and Dabholkar, A.S. (1997). Regional differences in synaptogenesis in human cerebral cortex. *J. Comp. Neurol.* 387, 167–178.
- Ianniruberto, A., and Tajani, E. (1981). Ultrasonographic study of fetal movements. *Semin. Perinatol.* 5, 175–181.
- Ip, B.K., Wappler, I., Peters, H., Lindsay, S., Clowry, G.J., and Bayatti, N. (2010). Investigating gradients of gene expression involved in early human cortical development. *J. Anat.* 217, 300–311.
- Jaffe, A.E., Shin, J., Collado-Torres, L., Leek, J.T., Tao, R., Li, C., Gao, Y., Jia, Y., Maher, B.J., Hyde, T.M., et al. (2015). Developmental regulation of human cortex transcription and its clinical relevance at single base resolution. *Nat. Neurosci.* 18, 154–161.
- Jakovcevski, I., Filipovic, R., Mo, Z., Rakic, S., and Zecevic, N. (2009). Oligodendrocyte development and the onset of myelination in the human fetal brain. *Front. Neuroanat.* 3, 5.
- Jeste, S.S., and Geschwind, D.H. (2015). Developmental disorders. *Curr. Opin. Neurol.* 28, 89–90.
- Johnson, C.P., and Blasco, P.A. (1997). Infant growth and development. *Pediatr. Rev.* 18, 224–242.
- Johnson, J.S., and Newport, E.L. (1989). Critical period effects in second language learning: the influence of maturational state on the acquisition of English as a second language. *Cognit. Psychol.* 21, 60–99.
- Johnson, M.B., Kawasawa, Y.I., Mason, C.E., Krsnik, Z., Coppola, G., Bogdanović, D., Geschwind, D.H., Mane, S.M., State, M.W., and Sestan, N. (2009). Functional and evolutionary insights into human brain development through global transcriptome analysis. *Neuron* 62, 494–509.
- Johnson, M.B., Wang, P.P., Atabay, K.D., Murphy, E.A., Doan, R.N., Hecht, J.L., and Walsh, C.A. (2015). Single-cell analysis reveals transcriptional heterogeneity of neural progenitors in human cortex. *Nat. Neurosci.* 18, 637–646.
- Kang, H.J., Kawasawa, Y.I., Cheng, F., Zhu, Y., Xu, X., Li, M., Sousa, A.M., Plelikos, M., Meyer, K.A., Sedmak, G., et al. (2011). Spatio-temporal transcriptome of the human brain. *Nature* 478, 483–489.
- Kasprian, G., Langs, G., Brugger, P.C., Bittner, M., Weber, M., Arantes, M., and Prayer, D. (2011). The prenatal origin of hemispheric asymmetry: an in utero neuroimaging study. *Cereb. Cortex* 21, 1076–1083.
- Kennedy, C., and Sokoloff, L. (1957). An adaptation of the nitrous oxide method to the study of the cerebral circulation in children; normal values for cerebral blood flow and cerebral metabolic rate in childhood. *J. Clin. Invest.* 36, 1130–1137.
- Kessler, R.C., Amminger, G.P., Aguilar-Gaxiola, S., Alonso, J., Lee, S., and Ustün, T.B. (2007). Age of onset of mental disorders: a review of recent literature. *Curr. Opin. Psychiatry* 20, 359–364.
- Kety, S.S., and Schmidt, C.F. (1948). The nitrous oxide method for the quantitative determination of cerebral blood flow in man: Theory, procedure and normal values. *J. Clin. Invest.* 27, 476–483.
- Kiessling, M.C., Büttner, A., Butti, C., Müller-Starck, J., Milz, S., Hof, P.R., Frank, H.G., and Schmitz, C. (2014). Cerebellar granule cells are generated postnatally in humans. *Brain Struct. Funct.* 219, 1271–1286.
- Koenderink, M.J., and Uylings, H.B. (1995). Postnatal maturation of layer V pyramidal neurons in the human prefrontal cortex. A quantitative Golgi analysis. *Brain Res.* 678, 233–243.
- Koenderink, M.J., Uylings, H.B., and Mrzljak, L. (1994). Postnatal maturation of the layer III pyramidal neurons in the human prefrontal cortex: a quantitative Golgi analysis. *Brain Res.* 653, 173–182.
- Kostovic, I., and Judas, M. (2006). Prolonged coexistence of transient and permanent circuitry elements in the developing cerebral cortex of fetuses and preterm infants. *Dev. Med. Child Neurol.* 48, 388–393.
- Kostovic, I., and Rakic, P. (1990). Developmental history of the transient subplate zone in the visual and somatosensory cortex of the macaque monkey and human brain. *J. Comp. Neurol.* 297, 441–470.

- Kundaje, A., Meuleman, W., Ernst, J., Bilenky, M., Yen, A., Heravi-Moussavi, A., Kheradpour, P., Zhang, Z., Wang, J., Ziller, M.J., et al.; Roadmap Epigenomics Consortium (2015). Integrative analysis of 111 reference human epigenomes. *Nature* 518, 317–330.
- Kwan, K.Y., Lam, M.M., Krsnik, Z., Kawasawa, Y.I., Lefebvre, V., and Sestan, N. (2008). SOX5 postmitotically regulates migration, postmigratory differentiation, and projections of subplate and deep-layer neocortical neurons. *Proc. Natl. Acad. Sci. USA* 105, 16021–16026.
- Kwan, K.Y., Lam, M.M., Johnson, M.B., Dube, U., Shim, S., Rašin, M.R., Sousa, A.M., Fertuzinhos, S., Chen, J.G., Arellano, J.I., et al. (2012). Species-dependent posttranscriptional regulation of NOS1 by FMRP in the developing cerebral cortex. *Cell* 149, 899–911.
- Lambert, N., Lambot, M.A., Bilheu, A., Albert, V., Englert, Y., Libert, F., Noel, J.C., Sotiriou, C., Holloway, A.K., Pollard, K.S., et al. (2011). Genes expressed in specific areas of the human fetal cerebral cortex display distinct patterns of evolution. *PLoS ONE* 6, e17753.
- Lancaster, M.A., Renner, M., Martin, C.A., Wenzel, D., Bicknell, L.S., Hurles, M.E., Homfray, T., Penninger, J.M., Jackson, A.P., and Knoblich, J.A. (2013). Cerebral organoids model human brain development and microcephaly. *Nature* 501, 373–379.
- Larsen, C.C., Bonde Larsen, K., Bogdanovic, N., Laursen, H., Graem, N., Saemuelson, G.B., and Pakkenberg, B. (2006). Total number of cells in the human newborn telencephalic wall. *Neuroscience* 139, 999–1003.
- Lee, F.S., Heimer, H., Giedd, J.N., Lein, E.S., Sestan, N., Weinberger, D.R., and Casey, B.J. (2014). Mental health. Adolescent mental health—opportunity and obligation. *Science* 346, 547–549.
- Leone, D.P., Srinivasan, K., Chen, B., Alcamo, E., and McConnell, S.K. (2008). The determination of projection neuron identity in the developing cerebral cortex. *Curr. Opin. Neurobiol.* 18, 28–35.
- Liao, B.Y., and Zhang, J. (2008). Null mutations in human and mouse orthologs frequently result in different phenotypes. *Proc. Natl. Acad. Sci. USA* 105, 6987–6992.
- Lin, G.N., Corominas, R., Lemmens, I., Yang, X., Tavernier, J., Hill, D.E., Vidal, M., Sebat, J., and Iakoucheva, L.M. (2015). Spatiotemporal 16p11.2 protein network implicates cortical late mid-fetal brain development and KCTD13-Cul3-RhoA pathway in psychiatric diseases. *Neuron* 85, 742–754.
- Lindblad-Toh, K., Garber, M., Zuk, O., Lin, M.F., Parker, B.J., Washietl, S., Kheradpour, P., Ernst, J., Jordan, G., Mauceli, E., et al.; Broad Institute Sequencing Platform and Whole Genome Assembly Team; Baylor College of Medicine Human Genome Sequencing Center Sequencing Team; Genome Institute at Washington University (2011). A high-resolution map of human evolutionary constraint using 29 mammals. *Nature* 478, 476–482.
- Lister, R., Mukamel, E.A., Nery, J.R., Urich, M., Puddifoot, C.A., Johnson, N.D., Lucero, J., Huang, Y., Dwork, A.J., Schultz, M.D., et al. (2013). Global epigenomic reconfiguration during mammalian brain development. *Science* 341, 1237905.
- Lui, J.H., Hansen, D.V., and Kriegstein, A.R. (2011). Development and evolution of the human neocortex. *Cell* 146, 18–36.
- Lui, J.H., Nowakowski, T.J., Pollen, A.A., Javaherian, A., Kriegstein, A.R., and Oldham, M.C. (2014). Radial glia require PDGFR $\beta$  signalling in human but not mouse neocortex. *Nature* 515, 264–268.
- Ma, T., Wang, C., Wang, L., Zhou, X., Tian, M., Zhang, Q., Zhang, Y., Li, J., Liu, Z., Cai, Y., et al. (2013). Subcortical origins of human and monkey neocortical interneurons. *Nat. Neurosci.* 16, 1588–1597.
- Malik, S., Vinukonda, G., Vose, L.R., Diamond, D., Bhimavarapu, B.B., Hu, F., Zia, M.T., Hevner, R., Zecevic, N., and Ballabh, P. (2013). Neurogenesis continues in the third trimester of pregnancy and is suppressed by premature birth. *J. Neurosci.* 33, 411–423.
- Margulies, E.H., Cooper, G.M., Asimenos, G., Thomas, D.J., Dewey, C.N., Siepel, A., Birney, E., Keefe, D., Schwartz, A.S., Hou, M., et al. (2007). Analyses of deep mammalian sequence alignments and constraint predictions for 1% of the human genome. *Genome Res.* 17, 760–774.
- Mariani, J., Coppola, G., Zhang, P., Abyzov, A., Provini, L., Tomasini, L., Amenduni, M., Szekely, A., Palejev, D., Wilson, M., et al. (2015). FOXP1-dependent dysregulation of GABA/glutamate neuron differentiation in autism spectrum disorders. *Cell* 162, 375–390.
- Marín-Padilla, M. (2014). The mammalian neocortex new pyramidal neuron: a new conception. *Front. Neuroanat.* 7, 51.
- Marín-Valencia, I., Guerrini, R., and Gleeson, J.G. (2014). Pathogenetic mechanisms of focal cortical dysplasia. *Epilepsia* 55, 970–978.
- Marner, L., Nyengaard, J.R., Tang, Y., and Pakkenberg, B. (2003). Marked loss of myelinated nerve fibers in the human brain with age. *J. Comp. Neurol.* 462, 144–152.
- Maze, I., Shen, L., Zhang, B., Garcia, B.A., Shao, N., Mitchell, A., Sun, H., Akbarian, S., Allis, C.D., and Nestler, E.J. (2014). Analytical tools and current challenges in the modern era of neuroepigenomics. *Nat. Neurosci.* 17, 1476–1490.
- Mazin, P., Xiong, J., Liu, X., Yan, Z., Zhang, X., Li, M., He, L., Somel, M., Yuan, Y., Phoebe Chen, Y.P., et al. (2013). Widespread splicing changes in human brain development and aging. *Mol. Syst. Biol.* 9, 633.
- McManus, I.C., Sik, G., Cole, D.R., Mellon, A.F., Wong, J., and Kloss, J. (1988). The development of handedness in children. *Br. J. Dev. Psychol.* 6, 257–273.
- Meltzoff, A.N., and Moore, M.K. (1977). Imitation of facial and manual gestures by human neonates. *Science* 198, 74–78.
- Meyer, G. (2007). Genetic control of neuronal migrations in human cortical development. *Adv. Anat. Embryol. Cell Biol.* 189, 1–111.
- Miller, D.J., Duka, T., Stimpson, C.D., Schapiro, S.J., Baze, W.B., McArthur, M.J., Fobbs, A.J., Sousa, A.M., Sestan, N., Wildman, D.E., et al. (2012). Prolonged myelination in human neocortical evolution. *Proc. Natl. Acad. Sci. USA* 109, 16480–16485.
- Miller, J.A., Ding, S.L., Sunkin, S.M., Smith, K.A., Ng, L., Szafer, A., Ebbert, A., Riley, Z.L., Royall, J.J., Aiona, K., et al. (2014). Transcriptional landscape of the prenatal human brain. *Nature* 508, 199–206.
- Molliver, M.E., Kostović, I., and van der Loos, H. (1973). The development of synapses in cerebral cortex of the human fetus. *Brain Res.* 50, 403–407.
- Molnár, Z., and Pollen, A. (2014). How unique is the human neocortex? *Development* 141, 11–16.
- Molyneaux, B.J., Arlotta, P., Menezes, J.R., and Macklis, J.D. (2007). Neuronal subtype specification in the cerebral cortex. *Nat. Rev. Neurosci.* 8, 427–437.
- Morris, K.V., and Mattick, J.S. (2014). The rise of regulatory RNA. *Nat. Rev. Genet.* 15, 423–437.
- Mrzljak, L., Uylings, H.B., Kostovic, I., and Van Eden, C.G. (1988). Prenatal development of neurons in the human prefrontal cortex: I. A qualitative Golgi study. *J. Comp. Neurol.* 271, 355–386.
- Napper, R.M., and Harvey, R.J. (1988). Number of parallel fiber synapses on an individual Purkinje cell in the cerebellum of the rat. *J. Comp. Neurol.* 274, 168–177.
- Nord, A.S., Pattabiraman, K., Visel, A., and Rubenstein, J.L. (2015). Genomic perspectives of transcriptional regulation in forebrain development. *Neuron* 85, 27–47.
- Numata, S., Ye, T., Hyde, T.M., Guitart-Navarro, X., Tao, R., Winger, M., Colantuoni, C., Weinberger, D.R., Kleinman, J.E., and Lipska, B.K. (2012). DNA methylation signatures in development and aging of the human prefrontal cortex. *Am. J. Hum. Genet.* 90, 260–272.
- O’Carroll, D., and Schaefer, A. (2013). General principals of miRNA biogenesis and regulation in the brain. *Neuropsychopharmacology* 38, 39–54.
- Okado, N., Kakimi, S., and Kojima, T. (1979). Synaptogenesis in the cervical cord of the human embryo: sequence of synapse formation in a spinal reflex pathway. *J. Comp. Neurol.* 184, 491–518.
- O’Leary, D.D., Chou, S.J., and Sahara, S. (2007). Area patterning of the mammalian cortex. *Neuron* 56, 252–269.
- O’Rahilly, R., and Muller, F. (2006). *The Embryonic Human Brain: An Atlas of Developmental Stages*, Third Edition (Wiley-Liss).

- O'Rourke, N.A., Dailey, M.E., Smith, S.J., and McConnell, S.K. (1992). Diverse migratory pathways in the developing cerebral cortex. *Science* 258, 299–302.
- Pakkenberg, B., and Gundersen, H.J. (1997). Neocortical neuron number in humans: effect of sex and age. *J. Comp. Neurol.* 384, 312–320.
- Pakkenberg, B., Pelvig, D., Marnier, L., Bundgaard, M.J., Gundersen, H.J., Nyengaard, J.R., and Regeur, L. (2003). Aging and the human neocortex. *Exp. Gerontol.* 38, 95–99.
- Parikshak, N.N., Luo, R., Zhang, A., Won, H., Lowe, J.K., Chandran, V., Horvath, S., and Geschwind, D.H. (2013). Integrative functional genomic analyses implicate specific molecular pathways and circuits in autism. *Cell* 155, 1008–1021.
- Paşca, A.M., Sloan, S.A., Clarke, L.E., Tian, Y., Makinson, C.D., Huber, N., Kim, C.H., Park, J.Y., O'Rourke, N.A., Nguyen, K.D., et al. (2015). Functional cortical neurons and astrocytes from human pluripotent stem cells in 3D culture. *Nat. Methods* 12, 671–678.
- Pattabiraman, K., Golonzhka, O., Lindtner, S., Nord, A.S., Taher, L., Hoch, R., Silberberg, S.N., Zhang, D., Chen, B., Zeng, H., et al. (2014). Transcriptional regulation of enhancers active in protodomains of the developing cerebral cortex. *Neuron* 82, 989–1003.
- Pennacchio, L.A., Ahituv, N., Moses, A.M., Prabhakar, S., Nobrega, M.A., Shoukry, M., Minovitsky, S., Dubchak, I., Holt, A., Lewis, K.D., et al. (2006). In vivo enhancer analysis of human conserved non-coding sequences. *Nature* 444, 499–502.
- Petanjek, Z., Judas, M., Kostović, I., and Uylings, H.B. (2008). Lifespan alterations of basal dendritic trees of pyramidal neurons in the human prefrontal cortex: a layer-specific pattern. *Cereb. Cortex* 18, 915–929.
- Petanjek, Z., Judaš, M., Šimic, G., Rasin, M.R., Uylings, H.B., Rakic, P., and Kostovic, I. (2011). Extraordinary neoteny of synaptic spines in the human prefrontal cortex. *Proc. Natl. Acad. Sci. USA* 108, 13281–13286.
- Pletikos, M., Sousa, A.M., Sedmak, G., Meyer, K.A., Zhu, Y., Cheng, F., Li, M., Kawasawa, Y.I., and Sestan, N. (2014). Temporal specification and bilaterality of human neocortical topographic gene expression. *Neuron* 81, 321–332.
- Polishuk, W.Z., Laufer, N., and Sadovsky, E. (1975). [Fetal reaction to external light]. *Harefuah* 89, 395–396.
- Pollard, K.S., Salama, S.R., Lambert, N., Lambot, M.A., Coppens, S., Pederesen, J.S., Katzman, S., King, B., Onodera, C., Siepel, A., et al. (2006). An RNA gene expressed during cortical development evolved rapidly in humans. *Nature* 443, 167–172.
- Pollen, A.A., Nowakowski, T.J., Shuga, J., Wang, X., Leyrat, A.A., Lui, J.H., Li, N., Szpankowski, L., Fowler, B., Chen, P., et al. (2014). Low-coverage single-cell mRNA sequencing reveals cellular heterogeneity and activated signaling pathways in developing cerebral cortex. *Nat. Biotechnol.* 32, 1053–1058.
- Prabhakar, S., Noonan, J.P., Pääbo, S., and Rubin, E.M. (2006). Accelerated evolution of conserved noncoding sequences in humans. *Science* 314, 786.
- Ptashne, M. (2013). Epigenetics: core misconception. *Proc. Natl. Acad. Sci. USA* 110, 7101–7103.
- Raaf, J., and Kernohan, J.W. (1944). A study of the external granular layer in the cerebellum. The disappearance of the external granular layer and the growth of the molecular and internal granular layers in the cerebellum. *Am. J. Anat.* 75, 151–172.
- Radonjić, N.V., Ayoub, A.E., Memi, F., Yu, X., Maroof, A., Jakovcevski, I., Anderson, S.A., Rakic, P., and Zecevic, N. (2014). Diversity of cortical interneurons in primates: the role of the dorsal proliferative niche. *Cell Rep.* 9, 2139–2151.
- Rajan, V., Cuevas, K., and Bell, M.A. (2014). The contribution of executive function to source memory development in early childhood. *J. Cogn. Dev.* 15, 304–324.
- Rakic, P., Bourgeois, J.P., Eckenhoff, M.F., Zecevic, N., and Goldman-Rakic, P.S. (1986). Concurrent overproduction of synapses in diverse regions of the primate cerebral cortex. *Science* 232, 232–235.
- Rakic, P., Ayoub, A.E., Breunig, J.J., and Dominguez, M.H. (2009). Decision by division: making cortical maps. *Trends Neurosci.* 32, 291–301.
- Ramsay, D.S. (1980). Onset of unimanual handedness in infants. *Infant Behav. Dev.* 3, 377–385.
- Rash, B.G., and Grove, E.A. (2006). Area and layer patterning in the developing cerebral cortex. *Curr. Opin. Neurobiol.* 16, 25–34.
- Ravasi, T., Suzuki, H., Cannistraci, C.V., Katayama, S., Bajic, V.B., Tan, K., Akalin, A., Schmeier, S., Kanamori-Katayama, M., Bertin, N., et al. (2010). An atlas of combinatorial transcriptional regulation in mouse and man. *Cell* 140, 744–752.
- Reillo, I., and Borrell, V. (2012). Germinal zones in the developing cerebral cortex of ferret: ontogeny, cell cycle kinetics, and diversity of progenitors. *Cereb. Cortex* 22, 2039–2054.
- Reilly, S.K., Yin, J., Ayoub, A.E., Emera, D., Leng, J., Cotney, J., Sarro, R., Rakic, P., and Noonan, J.P. (2015). Evolutionary genomics. Evolutionary changes in promoter and enhancer activity during human corticogenesis. *Science* 347, 1155–1159.
- Roessmann, U., and Gambetti, P. (1986). Astrocytes in the developing human brain. An immunohistochemical study. *Acta Neuropathol.* 70, 308–313.
- Samuelsen, G.B., Larsen, K.B., Bogdanovic, N., Laursen, H., Graem, N., Larsen, J.F., and Pakkenberg, B. (2003). The changing number of cells in the human fetal forebrain and its subdivisions: a stereological analysis. *Cereb. Cortex* 13, 115–122.
- Sanai, N., Nguyen, T., Ihrie, R.A., Mirzadeh, Z., Tsai, H.H., Wong, M., Gupta, N., Berger, M.S., Huang, E., Garcia-Verdugo, J.M., et al. (2011). Corridors of migrating neurons in the human brain and their decline during infancy. *Nature* 478, 382–386.
- Semple, B.D., Blomgren, K., Gimlin, K., Ferriero, D.M., and Noble-Haeusslein, L.J. (2013). Brain development in rodents and humans: Identifying benchmarks of maturation and vulnerability to injury across species. *Prog. Neurobiol.* 106–107, 1–16.
- Sherwood, C.C., Bauernfeind, A.L., Bianchi, S., Raghanti, M.A., and Hof, P.R. (2012). Human brain evolution writ large and small. *Prog. Brain Res.* 195, 237–254.
- Shibata, M., Gulden, F.O., and Sestan, N. (2015). From trans to cis: transcriptional regulatory networks in neocortical development. *Trends Genet.* 31, 77–87.
- Shim, S., Kwan, K.Y., Li, M., Lefebvre, V., and Sestan, N. (2012). Cis-regulatory control of corticospinal system development and evolution. *Nature* 486, 74–79.
- Siegmund, K.D., Connor, C.M., Campan, M., Long, T.I., Weisenberger, D.J., Biniszkiwicz, D., Jaenisch, R., Laird, P.W., and Akbarian, S. (2007). DNA methylation in the human cerebral cortex is dynamically regulated throughout the life span and involves differentiated neurons. *PLoS ONE* 2, e895.
- Siepel, A., Bejerano, G., Pedersen, J.S., Hinrichs, A.S., Hou, M., Rosenbloom, K., Clawson, H., Spieth, J., Hillier, L.W., Richards, S., et al. (2005). Evolutionarily conserved elements in vertebrate, insect, worm, and yeast genomes. *Genome Res.* 15, 1034–1050.
- Sigaard, R.K., Kjær, M., and Pakkenberg, B. (2014). Development of the cell population in the brain white matter of young children. *Cereb. Cortex*, bhu178.
- Smart, I.H., Dehay, C., Giroud, P., Berland, M., and Kennedy, H. (2002). Unique morphological features of the proliferative zones and postmitotic compartments of the neural epithelium giving rise to striate and extrastriate cortex in the monkey. *Cereb. Cortex* 12, 37–53.
- Somel, M., Franz, H., Yan, Z., Lorenc, A., Guo, S., Giger, T., Kelso, J., Nickel, B., Dannemann, M., Bahn, S., et al. (2009). Transcriptional neoteny in the human brain. *Proc. Natl. Acad. Sci. USA* 106, 5743–5748.
- Somel, M., Guo, S., Fu, N., Yan, Z., Hu, H.Y., Xu, Y., Yuan, Y., Ning, Z., Hu, Y., Menzel, C., et al. (2010). MicroRNA, mRNA, and protein expression link development and aging in human and macaque brain. *Genome Res.* 20, 1207–1218.
- Somel, M., Liu, X., Tang, L., Yan, Z., Hu, H., Guo, S., Jiang, X., Zhang, X., Xu, G., Xie, G., et al. (2011). MicroRNA-driven developmental remodeling in the brain distinguishes humans from other primates. *PLoS Biol.* 9, e1001214.

- Southwell, D.G., Nicholas, C.R., Basbaum, A.I., Stryker, M.P., Kriegstein, A.R., Rubenstein, J.L., and Alvarez-Buylla, A. (2014). Interneurons from embryonic development to cell-based therapy. *Science* *344*, 1240622.
- Spalding, K.L., Bhardwaj, R.D., Buchholz, B.A., Druid, H., and Frisén, J. (2005). Retrospective birth dating of cells in humans. *Cell* *122*, 133–143.
- Spiers, H., Hannon, E., Schalkwyk, L.C., Smith, R., Wong, C.C., O'Donovan, M.C., Bray, N.J., and Mill, J. (2015). Methylomic trajectories across human fetal brain development. *Genome Res.* *25*, 338–352.
- State, M.W., and Sestan, N. (2012). Neuroscience. The emerging biology of autism spectrum disorders. *Science* *337*, 1301–1303.
- Stein, J.L., de la Torre-Ubieta, L., Tian, Y., Parikhshak, N.N., Hernández, I.A., Marchetto, M.C., Baker, D.K., Lu, D., Hinman, C.R., Lowe, J.K., et al. (2014). A quantitative framework to evaluate modeling of cortical development by neural stem cells. *Neuron* *83*, 69–86.
- Stergachis, A.B., Neph, S., Sandstrom, R., Haugen, E., Reynolds, A.P., Zhang, M., Byron, R., Canfield, T., Stelting-Sun, S., Lee, K., et al. (2014). Conservation of trans-acting circuitry during mammalian regulatory evolution. *Nature* *515*, 365–370.
- Stiles, J., and Jernigan, T.L. (2010). The basics of brain development. *Neuropsychol. Rev.* *20*, 327–348.
- Sun, T., and Walsh, C.A. (2006). Molecular approaches to brain asymmetry and handedness. *Nat. Rev. Neurosci.* *7*, 655–662.
- Tang, Y., Nyengaard, J.R., De Groot, D.M., and Gundersen, H.J. (2001). Total regional and global number of synapses in the human brain neocortex. *Synapse* *41*, 258–273.
- Tau, G.Z., and Peterson, B.S. (2010). Normal development of brain circuits. *Neuropsychopharmacology* *35*, 147–168.
- Taverna, E., Götz, M., and Huttner, W.B. (2014). The cell biology of neurogenesis: toward an understanding of the development and evolution of the neocortex. *Annu. Rev. Cell Dev. Biol.* *30*, 465–502.
- Tay, Y., Rinn, J., and Pandolfi, P.P. (2014). The multilayered complexity of ceRNA crosstalk and competition. *Nature* *505*, 344–352.
- Taylor, D.C. (1969). Differential rates of cerebral maturation between sexes and between hemispheres. Evidence from epilepsy. *Lancet* *2*, 140–142.
- Tebbenkamp, A.T., Willsey, A.J., State, M.W., and Sestan, N. (2014). The developmental transcriptome of the human brain: implications for neurodevelopmental disorders. *Curr. Opin. Neurol.* *27*, 149–156.
- Tessarz, P., and Kouzarides, T. (2014). Histone core modifications regulating nucleosome structure and dynamics. *Nat. Rev. Mol. Cell Biol.* *15*, 703–708.
- Thatcher, R.W., Walker, R.A., and Giudice, S. (1987). Human cerebral hemispheres develop at different rates and ages. *Science* *236*, 1110–1113.
- Thompson, C.L., Ng, L., Menon, V., Martinez, S., Lee, C.K., Glattfelder, K., Sunkin, S.M., Henry, A., Lau, C., Dang, C., et al. (2014). A high-resolution spatiotemporal atlas of gene expression of the developing mouse brain. *Neuron* *83*, 309–323.
- van de Leemput, J., Boles, N.C., Kiehl, T.R., Corneo, B., Lederman, P., Menon, V., Lee, C., Martinez, R.A., Levi, B.P., Thompson, C.L., et al. (2014). CORTECON: a temporal transcriptome analysis of in vitro human cerebral cortex development from human embryonic stem cells. *Neuron* *83*, 51–68.
- van den Aamele, J., Tiberi, L., Vanderhaeghen, P., and Espuny-Camacho, I. (2014). Thinking out of the dish: what to learn about cortical development using pluripotent stem cells. *Trends Neurosci.* *37*, 334–342.
- Van Dongen, L.G., and Goudie, E.G. (1980). Fetal movement patterns in the first trimester of pregnancy. *Br. J. Obstet. Gynaecol.* *87*, 191–193.
- Vermunt, M.W., Reinink, P., Korving, J., de Bruijn, E., Creghton, P.M., Basak, O., Geeven, G., Toonen, P.W., Lansu, N., Meunier, C., et al.; Netherlands Brain Bank (2014). Large-scale identification of coregulated enhancer networks in the adult human brain. *Cell Rep.* *9*, 767–779.
- Visel, A., Taher, L., Girgis, H., May, D., Golonzhka, O., Hoch, R.V., McKinsey, G.L., Pattabiraman, K., Silberberg, S.N., Blow, M.J., et al. (2013). A high-resolution enhancer atlas of the developing telencephalon. *Cell* *152*, 895–908.
- Voineagu, I., Wang, X., Johnston, P., Lowe, J.K., Tian, Y., Horvath, S., Mill, J., Cantor, R.M., Blencowe, B.J., and Geschwind, D.H. (2011). Transcriptomic analysis of autistic brain reveals convergent molecular pathology. *Nature* *474*, 380–384.
- Wang, W.Z., Hoerder-Suabedissen, A., Oeschger, F.M., Bayatti, N., Ip, B.K., Lindsay, S., Supramaniam, V., Srinivasan, L., Rutherford, M., Møllgård, K., et al. (2010). Subplate in the developing cortex of mouse and human. *J. Anat.* *217*, 368–380.
- Wen, Z., Nguyen, H.N., Guo, Z., Lalli, M.A., Wang, X., Su, Y., Kim, N.S., Yoon, K.J., Shin, J., Zhang, C., et al. (2014). Synaptic dysregulation in a human iPSC cell model of mental disorders. *Nature* *515*, 414–418.
- WHO Multicentre Growth Reference Study Group (2006). WHO Child Growth Standards based on length/height, weight and age. *Acta Paediatr. Suppl.* *450*, 76–85.
- Willsey, A.J., Sanders, S.J., Li, M., Dong, S., Tebbenkamp, A.T., Muhle, R.A., Reilly, S.K., Lin, L., Fertuzinhos, S., Miller, J.A., et al. (2013). Coexpression networks implicate human midfetal deep cortical projection neurons in the pathogenesis of autism. *Cell* *155*, 997–1007.
- Workman, A.D., Charvet, C.J., Clancy, B., Darlington, R.B., and Finlay, B.L. (2013). Modeling transformations of neurodevelopmental sequences across mammalian species. *J. Neurosci.* *33*, 7368–7383.
- Yakovlev, P.I., and Lecours, A.R. (1967). The myelogenetic cycles of regional maturation of the brain. In *Regional Development of the Brain in Early Life*, A. Minowski, ed. (F.A. Davis Co.), pp. 3–70.
- Yamada, S., Samtani, R.R., Lee, E.S., Lockett, E., Uwabe, C., Shiota, K., Anderson, S.A., and Lo, C.W. (2010). Developmental atlas of the early first trimester human embryo. *Dev. Dyn.* *239*, 1585–1595.
- Yeung, M.S., Zdunek, S., Bergmann, O., Bernard, S., Salehpour, M., Alkass, K., Perl, S., Tisdale, J., Possnert, G., Brundin, L., et al. (2014). Dynamics of oligodendrocyte generation and myelination in the human brain. *Cell* *159*, 766–774.
- Zahn-Waxler, C., Radke-Yarrow, M., Wagner, E., and Chapman, M. (1992). Development of concern for others. *Dev. Psychol.* *28*, 126–136.
- Zecevic, N. (1998). Synaptogenesis in layer I of the human cerebral cortex in the first half of gestation. *Cereb. Cortex* *8*, 245–252.
- Zhu, J., Adli, M., Zou, J.Y., Verstappen, G., Coyne, M., Zhang, X., Durham, T., Miri, M., Deshpande, V., De Jager, P.L., et al. (2013). Genome-wide chromatin state transitions associated with developmental and environmental cues. *Cell* *152*, 642–654.

# Simultaneous Multi-plane Imaging of Neural Circuits

Weijian Yang,<sup>1,\*</sup> Jae-eun Kang Miller,<sup>1</sup> Luis Carrillo-Reid,<sup>1</sup> Eftychios Pnevmatikakis,<sup>2,3</sup> Liam Paninski,<sup>1,3</sup> Rafael Yuste,<sup>1</sup> and Darcy S. Peterka<sup>1</sup>

<sup>1</sup>Neurotechnology Center, Department of Biological Sciences, Columbia University, New York, NY 10027, USA

<sup>2</sup>Center for Computational Biology, Simons Foundation, New York, NY 10010, USA

<sup>3</sup>Department of Statistics, Center for Theoretical Neuroscience, and Grossman Center for the Statistics of Mind, Columbia University, New York, NY 10027, USA

\*Correspondence: wy2221@columbia.edu

<http://dx.doi.org/10.1016/j.neuron.2015.12.012>

## SUMMARY

Recording the activity of large populations of neurons is an important step toward understanding the emergent function of neural circuits. Here we present a simple holographic method to simultaneously perform two-photon calcium imaging of neuronal populations across multiple areas and layers of mouse cortex *in vivo*. We use prior knowledge of neuronal locations, activity sparsity, and a constrained nonnegative matrix factorization algorithm to extract signals from neurons imaged simultaneously and located in different focal planes or fields of view. Our laser multiplexing approach is simple and fast, and could be used as a general method to image the activity of neural circuits in three dimensions across multiple areas in the brain.

## INTRODUCTION

The coherent activity of individual neurons, firing in precise spatiotemporal patterns, is likely to underlie the function of the nervous system, and so methods to record the activity of large neuronal populations appear necessary to identify these emergent patterns in animals and humans (Alivisatos et al., 2012). Calcium imaging can be used to capture the activity of neuronal populations (Yuste and Katz, 1991), and one can use it, for example, to image the firing of nearly the entire brain of the larval zebrafish with single-cell resolution (Ahrens et al., 2013). However, the larval zebrafish is transparent; in scattering tissue, where nonlinear microscopy is necessary (Denk et al., 1990; Williams et al., 2001; Zipfel et al., 2003; Helmchen and Denk, 2005), progress toward imaging large numbers of neurons in three dimensions has been slower. In fact, in nearly all existing two-photon microscopes, a single laser beam is serially scanned in a continuous trajectory across the sample in a raster pattern or with a specified trajectory that intersects targets of interest along the path. To image several focal planes, one needs to change the focus and then reimage. This serial scanning leads to low imaging speeds, which necessarily become slower with increases in the number of neurons or focal planes to be imaged. Since the inception of two-photon microscopy, there have been many efforts to increase the speed and depth of imaging. One approach is to use

inertia-free scanning using acousto-optic deflectors (AODs) (Duemani Reddy et al., 2008; Otsu et al., 2008; Grewe et al., 2010; Kirkby et al., 2010; Katona et al., 2012). Another approach is to parallelize the light and use many laser beams instead of a single one. Parallelized multifocal scanning has been developed (Bewersdorf et al., 1998; Carriles et al., 2008; Watson et al., 2009), as well as scanless approaches utilizing spatial light modulators (SLMs), which build holograms that target specific regions of interest (Nikolenko et al., 2008; Ducros et al., 2013; Quirin et al., 2014). As a further innovation of SLM-based imaging, we describe a novel “hybrid” multiplexed approach, combining traditional galvanometers and an SLM to provide a powerful, flexible, and cost-effective platform for 3D two-photon imaging. We demonstrate its performance by simultaneously imaging multiple areas and layers of the mouse cortex *in vivo*.

In particular, one key challenge in nonlinear microscopies is expanding the spatial extent of imaging while still maintaining high temporal resolution and high sensitivity. This is because of the inverse relationship between the total volume scanned per second and the signal collected per voxel in that time. Our SLM hybrid-multiplexed scanning approach helps overcome this limitation by creating multiple beamlets that scan the sample simultaneously, and leverages advanced computational methods (Pnevmatikakis et al., 2016 [companion paper in this issue of *Neuron*]) to extract the underlying signals reliably.

## RESULTS

The basic configuration of our SLM microscope consists of a two-photon microscope, with traditional galvanometers, along with an added SLM module. Figure 1A shows a schematic of the SLM-based multiplexed two-photon microscope. The layout is based on that described in detail in Nikolenko et al. (2008) and Quirin et al., (2014) and is similar to that in Dal Maschio et al. (2010). The SLM module was created by diverting the input path of the microscope, prior to the galvanometer mirrors, with retractable kinematic mirrors onto a compact optical breadboard with the SLM and associated components. The essential features of the SLM module are folding mirrors for redirection, a pre-SLM afocal telescope to resize the incoming beam to match the active area of the SLM, the SLM itself, and a post-SLM afocal telescope to resize the beam again to match the open aperture of the galvanometers and fill the back focal plane of the objective appropriately. The SLM is optically conjugated to the galvanometers and to the back aperture of the microscope objective (see Experimental

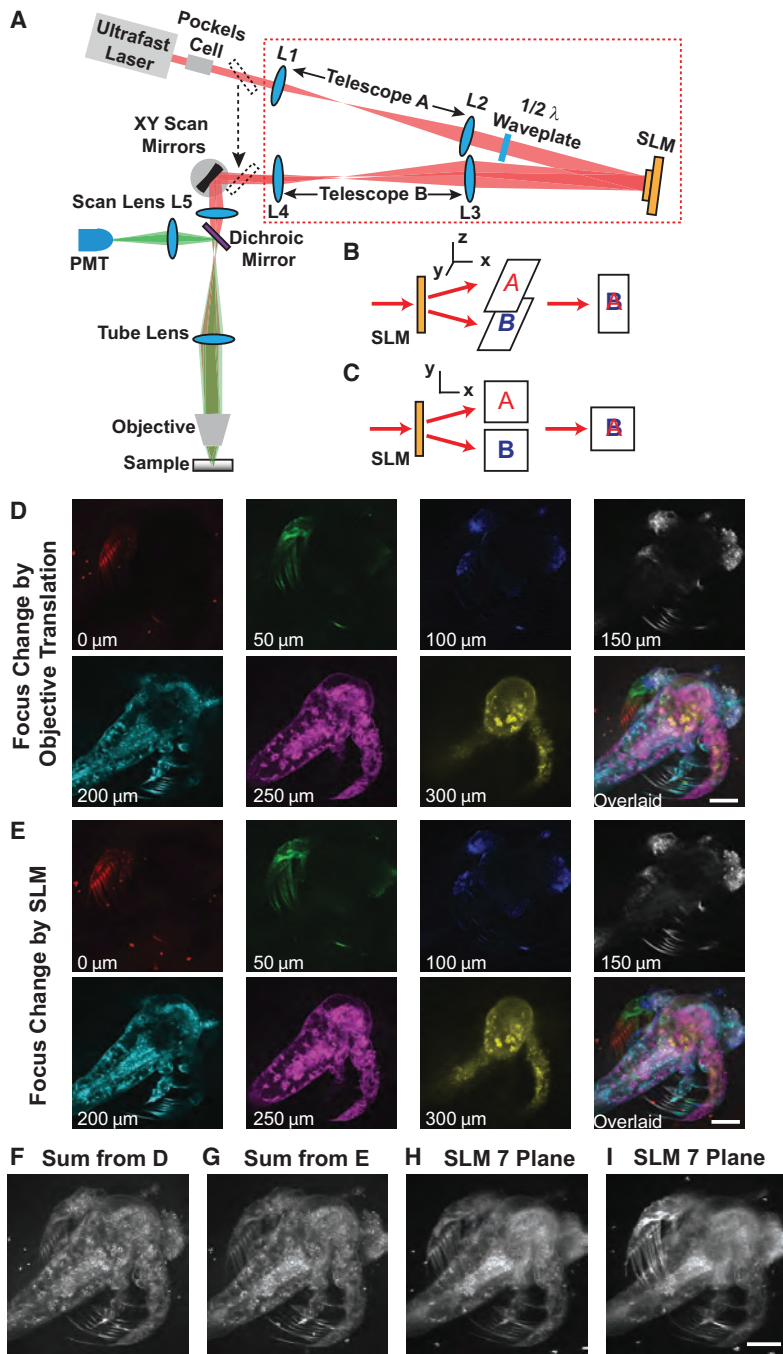


**Figure 1. SLM Two-Photon Microscope and Multi-plane Structural Imaging**

(A) SLM two-photon microscope. The laser beam from the Ti:sapphire laser is expanded to illuminate the SLM. The spatially modulated reflected beam from the SLM passes through a telescope, followed by an XY galvanometric mirror pair and is directed into a two-photon microscope. This setup is thus composed of a conventional two-photon microscope and an SLM beam-shaping module (red dashed box).

(B) Illustration of axial dual-plane imaging, where two planes at different depths can be simultaneously imaged.

(C) Illustration of lateral dual-plane imaging, where two fields of view at the same depth can be simultaneously imaged.

(D) Two-photon structural imaging of a shrimp at different depths through the sample, obtained by mechanically moving the objective with a micrometer. Each imaging depth is pseudocolored. The last image is constructed by overlaying all other images together. The scale bar represents 100  $\mu\text{m}$ .

(E) Software-based SLM focusing of the same shrimp as in (D). The SLM is used to modify the wavefront of the light to control the focal depth while the position of the objective is fixed. The nominal focus of the objective is fixed at the 100- $\mu\text{m}$  plane. This set of images looks similar to that in (D). The scale bar represents 100  $\mu\text{m}$ .

(F) Arithmetic sum of all the images at the seven planes shown in (D).

(G) Arithmetic sum of all the images at the seven planes shown in (E).

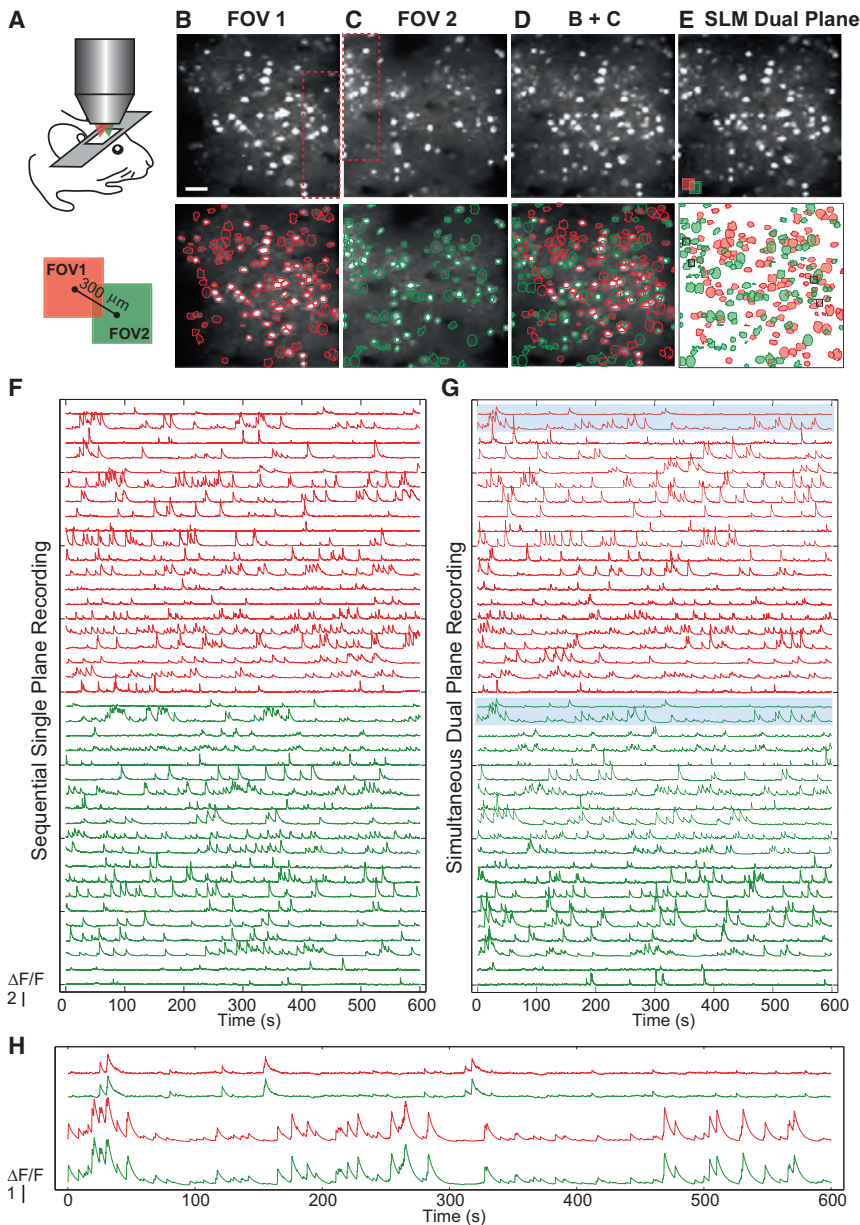
(H) Seven-axial-plane imaging of the same shrimp as in (D)–(G), using the SLM to create seven beamlets that simultaneously target all seven planes.

(I) Same as (H), but using the SLM to selectively increase the illumination intensity of the 50- $\mu\text{m}$  plane. Features on that plane are highlighted compared to (H). The scale bar represents 100  $\mu\text{m}$ .

Procedures for details). We coupled this module, with negligible mechanical changes, to a home-built two-photon microscope, as well as to a lightly modified Prairie/Bruker system. The SLM is used as a programmable optical multiplexer that allows for high-speed independent control of each generated beamlet. The SLM performs this beam splitting by imprinting a phase profile across the incoming wavefront, resulting in a far-field diffraction pattern that yields the desired illumination pattern. These multiple beamlets are directed to different regions or depths of the sample simultaneously. When the galvanometers are scanned, each indi-

vidual beamlet sweeps across its targeted area on the sample, and the total fluorescence is collected by a single photomultiplier tube. The resultant “image” is a superposition of all of the individual images that would have been produced by scanning each separate beamlet individually (see Figures 1B and 1C).

To demonstrate the multi-plane imaging system, we first performed structural imaging of a brine shrimp, *Artemia nauplii*, collecting its intrinsic autofluorescence. First, we acquired a traditional serial “z stack,” with seven planes, by moving the objective 50  $\mu\text{m}$  axially between each plane (Figure 1D). Next, we acquired a serial z stack with seven planes separated by 50  $\mu\text{m}$  each, but with the objective fixed and the axial displacements generated by imparting a lens phase function on the SLM (Figure 1E). In Figures 1F and 1G, we show the arithmetic sums of the individual sections in Figures 1D and 1E,



respectively. Finally, we used the SLM to generate all seven axially displaced beamlets *simultaneously*, and scanned them across the sample (Figure 1H). We note that we can control the power delivered to each beamlet independently, which differentiates this method from traditional extended depth-of-field approaches, where near-uniform intensity is imposed across the entire depth of field. Figure 1I shows an image where the power at the 50- $\mu\text{m}$  plane is selectively increased to enhance the signal at that depth. This flexibility is important for inhomogeneously stained samples, and is especially critical for multidepth in vivo imaging in scattering tissue. Additionally, we can effectively control the complexity of the final image—we deterministically control the number of sections we illuminate.

To demonstrate functional imaging in our system, we performed in vivo two-photon imaging at 10 Hz in Layer 2/3 (L2/3, 280  $\mu\text{m}$  depth) of the primary visual cortex (V1) of an awake head-fixed mouse that expresses the genetically encoded calcium indicator GCaMP6f (Chen et al., 2013) (see details in Experimental Procedures). We configured the SLM as illustrated in Figure 1C. We split the beam laterally, creating two beams with an on-sample separation of  $\sim 300$   $\mu\text{m}$ , centered on the original field of view (FOV) (Figure 2A). A small beam block is placed in the excitation path to eliminate the zero-order beam, leaving only the two SLM steered beams for imaging (see details in Experimental Procedures). Figures 2B–2D (top) show images of the intensity standard deviation (SD) of the time series image stack that results from scanning each of these displaced beams individually and their arithmetic sum, respectively, whereas Figure 2E (top) shows the SD image acquired when both beams are simultaneously scanned across the sample. The lower images in Figures 2B–2E show the spatial components of detected sources from the images, with the colors coded to reflect the original FOV. The areas contained in the red rectangles in Figures 2B and 2C highlight the area that is scanned by both beams, and

## Figure 2. Lateral Dual-Plane In Vivo Functional Imaging of Mouse V1

(A) Schematic of the in vivo experiment, imaging V1 in the mouse. In this experiment, two fields of view (FOVs), laterally displaced by 300  $\mu\text{m}$ , are simultaneously imaged.

(B and C) Top: temporal SD images of the sequential single-plane recording (10 fps) of FOV 1 (B) and FOV 2 (C) of mouse V1 at a depth of 280  $\mu\text{m}$  from the pial surface. Bottom: spatial component contours overlaid on the top panel. The boxes in dashed lines show the overlapped region, shared in both FOVs. The scale bar represents 50  $\mu\text{m}$ .

(D) Arithmetic sum of (B) and (C).

(E) Top: temporal SD image of the simultaneous dual-plane recording (10 fps) of the two FOVs. Bottom: overlaid spatial component contours from the two FOVs.

(F) Representative extracted  $\Delta F/F$  traces, using the CNMF algorithm, of the selected spatial components from the two fields of view (red, FOV 1; green, FOV 2) from the sequential single-plane recording. (G) Extracted  $\Delta F/F$  traces, using the CNMF algorithm, of the same spatial components shown in (F) from the simultaneous dual plane recording. The areas highlighted in blue in the dual-plane  $\Delta F/F$  traces are two spatial components taken from the overlapped area of the two FOVs. Their spatial contours are shown with the black box in the bottom panel in (E).

(H) Zoomed-in view of the  $\Delta F/F$  traces in the shaded areas in (G), showing the extremely high correlation between the independently extracted dynamics from the twinned spatial components.

hence their spatial components are present twice in the dual-plane image.

Figures 2F and 2G show some representative fluorescence time series extracted from the detected spatial components (40 out of 235 shown) from the sequential single-plane imaging and simultaneous dual-plane imaging, respectively. The same spatial components are displayed in both Figures 2F and 2G, with the same ordering, to facilitate direct comparison of the single- and dual-plane traces. For Figure 2F, the red and green traces from the two FOVs were collected sequentially, whereas in Figure 2G, they were collected simultaneously. Because of the spatial sparsity of active neurons (see Figure 2E, bottom), many of the spatial components are separable even in the overlaid dual-region image, and fluorescence time series data can be easily extracted using conventional techniques. However, some spatial components show clear overlap, and more sophisticated methods, such as independent component analysis (ICA) (Mukamel et al., 2009) or nonnegative matrix factorization (NMF) methods (Maruyama et al., 2014), perform better at extracting the activity. The traces shown were extracted using a novel constrained NMF (CNMF) method, which is discussed in greater detail later in this paper (Figure 4), and is described fully in the companion paper by Pnevmatikakis et al. (2016). The collected multiregion image is simply the arithmetic sum of the two single-region images, and thus we can use the detected spatial components from the single-region images as priors for source localization. We leverage this to get very good initial estimates of the number of independent sources and their spatial locations in the dual-region image. We examine the “uniqueness” of signal recovery by looking at the spatial components that appear twice in the dual-plane image and hence should display identical dynamics. Two examples are highlighted in blue in Figure 2G and expanded in Figure 2H; each respective color shows the source copy generated from each beamlet, and shows the extremely high correlation between the extracted traces ( $R > 0.985$ ).

Compared to the original FOV, the dual-region image includes signals from a significantly larger total area, with no loss in temporal resolution. The maximal useful lateral displacement of each beamlet from the center of the FOV depends on the whole optical system, and is discussed in detail in Supplemental Information. Besides increasing the effective imaged FOV, we can instead choose to also increase the effective frame rate, while keeping the same FOV (see Supplemental Information).

Although the lateral imaging method increases performance, the full power of multiplexed SLM imaging lies in its ability to address axially displaced planes, with independent control of beamlet power and position. We can introduce a defocus aberration to the wavefront, which shifts the beam focus away from the nominal focal plane. In practice, we also include higher-order axially dependent phase terms to correct higher-order aberrations (see Supplemental Information), and impose lateral displacements between the beamlets if desired. The SLM could also be used for further wavefront engineering, such as adaptive optics to correct any beam distortion from the system or the sample, but it was not necessary in these experiments. Our current system can address axial planes separated by  $\sim 500$   $\mu\text{m}$  while maintaining the total collected two-photon fluorescence at  $>50\%$  of that generated at the objective's natural focal

plane (see Figure S1B). This gives considerable range for scanning without moving the objective, which eliminates vibrations and acoustic noise and simplifies coupling with independently targetable photostimulation (Packer et al., 2015).

Using the SLM, we can address multiple axial planes simultaneously (see the schematic shown in Figure 3A). Figures 3B and 3C show two examples of conventional “single-plane” two-photon images (intensity SD of the time series image stack) in mouse V1, the first 170  $\mu\text{m}$  below the pial surface, in L2/3, and the second 500  $\mu\text{m}$  below the surface, in L5. These images were acquired with SLM focusing—the objective's focal plane was fixed at a depth of 380  $\mu\text{m}$ , and the axial displacements were generated by imposing the appropriate lens phase on the SLM (see Experimental Procedures for details). At each depth, we recorded functional signals at 10 Hz, with Figure 3F showing some representative extracted fluorescence traces from L2/3 and L5 in red and green, respectively (154 and 191 total spatial components were detected across the upper and lower planes, respectively). The SLM was then used to simultaneously split the incoming beam into two axially displaced beams, directed to these two cortical depths, and scanned over the sample at 10 Hz (Figure 3E). The power delivered to the two layers is adjusted such that the collected fluorescence from each plane was approximately equal (see Supplemental Information for details). Scanning these beamlets over the sample, we collect the dual-plane image. This is shown together with the spatial components in Figure 3E, which corresponds very well to the arithmetic sum of the individual plane images as shown in Figure 3D. In Figure 3G, we show 20 representative traces (out of 345 spatial source components) showing spontaneous activity across L2/3 and L5. The ordering of traces is identical to that of Figure 3F, which facilitates comparison. The lightly shaded regions in Figures 3F and 3G are enlarged and shown in Figures 3H and 3I. The signals show very clear events, with high apparent signal-to-noise ratio (SNR). Further zooms of small events are shown in Figure 3J, which reveals expanded views of the small peaks labeled i–iv in Figures 3H and 3I.

In the dual-plane image, it is clear that there is significant overlap between a number of sources. As mentioned earlier, CNMF (Pnevmatikakis et al., 2016) is used to demix the signal. We use a statistical model to relate the detected fluorescence from a source (neuron) to the underlying activity (spiking) (Vogelstein et al., 2009, 2010). We extend this to cases where the total detected signal (fluorescence plus noise) in each single pixel may come from multiple underlying sources, which produces a spatiotemporal mixing of signals in that pixel. The goal is, given a set of pixels of time-varying intensity, to infer the low-rank matrix of underlying signal sources that generated the measured signals. We take advantage of the nonnegativity of the underlying neuronal activity to allow computationally efficient constrained nonnegative matrix factorization methods to perform the source separation.

Operationally, to extract signals from the multi-plane image, we initialize the algorithm with the expected number of sources (the rank), along with the nominal expected spatial location of the sources as prior knowledge, as identified by running the algorithm on the previously acquired single-plane image sequences. For the single-plane images, the complexity and number of overlapping sources are significantly less than for the multi-plane images, and the algorithm works very well for

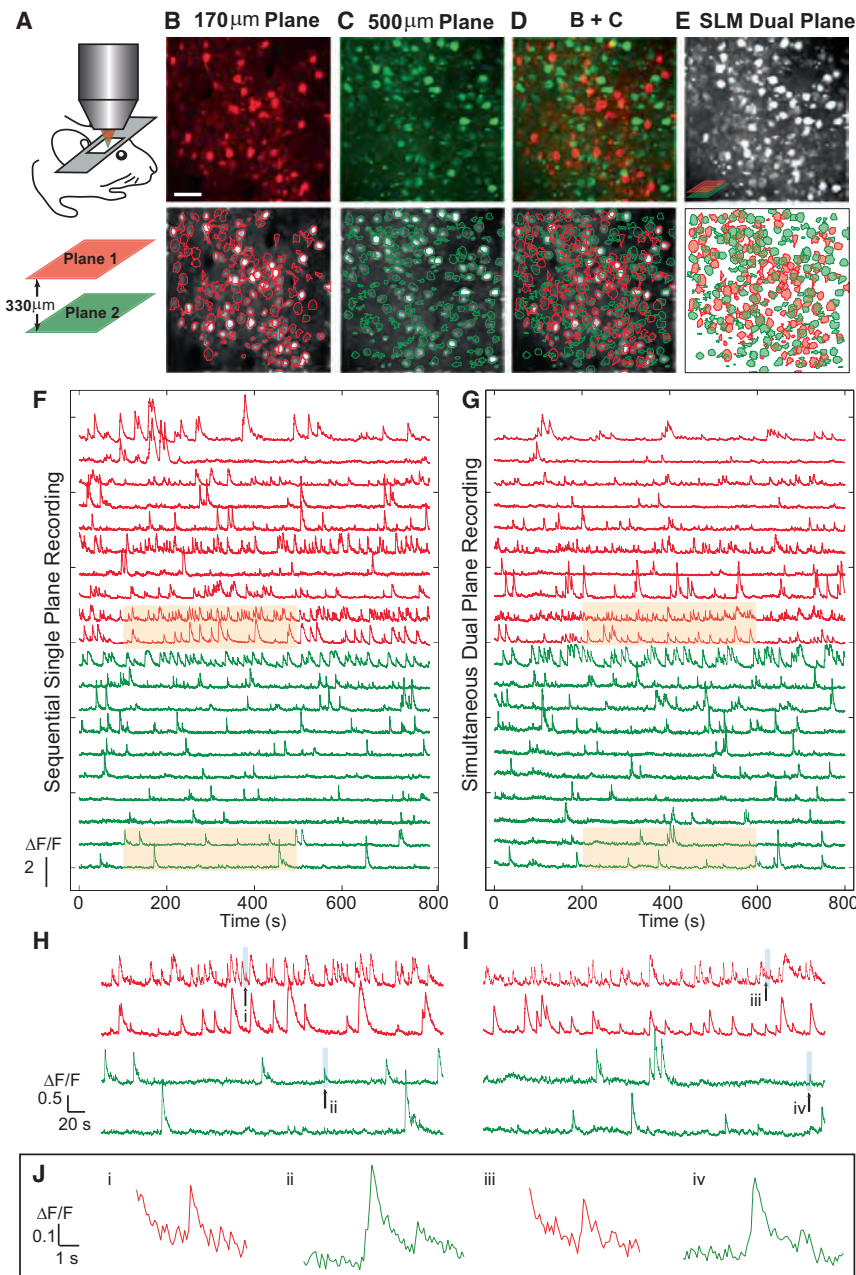


**Figure 3. Axial Dual-Plane In Vivo Functional Imaging of Mouse V1 at Layers 2/3 and 5**

(A) Schematic of the in vivo experiment, imaging V1 in the mouse. In this experiment, two different planes, axially separated by 330  $\mu\text{m}$ , are simultaneously imaged.

(B and C) Top: temporal SD images of the sequential single-plane recording (10 fps) of mouse V1 at a depth of 170  $\mu\text{m}$  (layer 2/3) (B) and 500  $\mu\text{m}$  (layer 5) (C) from the pial surface. The images are false colored. Bottom: spatial component contours overlaid on the top panel. The scale bar represents 50  $\mu\text{m}$ .

(D) Arithmetic sum of (B) and (C).

(E) Top: temporal SD image of the simultaneous dual-plane (10 fps) recording of the two planes shown in (B) and (C). Bottom: overlaid spatial component contours from the two planes.

(F) Representative extracted  $\Delta F/F$  traces, using the CNMF algorithm, of 20 spatial components out of 345 from the two planes (red, layer 2/3; green, layer 5) from the sequential single-plane recording.

(G) Extracted  $\Delta F/F$  traces, using the CNMF algorithm, of the same spatial components shown in (F) from the simultaneous dual-plane recording.

(H and I) Zoomed-in views of the extracted  $\Delta F/F$  traces in the shaded areas in (F) and (G), respectively.

(J) Further enlargement of the small events in the  $\Delta F/F$  traces shown in the blue-shaded areas in (H) and (I).

In Figures 4A and 4B, we show progressively more complex spatial patches of the dual-plane image series. The overall structure of Figures 4A and 4B is identical. In each panel, the uppermost row of images shows first the boundary of the spatial component contour and then the maximum-intensity projection of the time series, along with the subsequent images showing representative time points where the component sources are independently active. The spatial components in red and green come from L2/3 and L5, respectively. The leftmost column of images shows the weighted mask, labeled with the spatial component selection scheme

(binary mask from maximum-intensity projection, human-selected nonoverlapped region [NOL], ICA, or CNMF) that produces the activity traces presented immediately to the right of these boxes. On top of the full CNMF extracted traces in red, we also show, in cyan, the signal extracted considering only the CNMF spatial component but with uniform pixel weighting and no spatiotemporal demixing. This comparison shows the power and effectiveness of the source separation.

identifying sources without additional guidance (see Supplemental Information). Figure S2 shows a single-plane imaging example from which various spatial components, including doughnut-shape cell body and perisomatic dendritic processes, can be automatically extracted using CNMF, together with various calcium dynamics in the extracted temporal signals. The effectiveness of this method applied to multi-plane imaging is highlighted in Figure 4, where we compare it against our “best” human effort at selecting only the non- or minimally overlapping pixels from each source, and against ICA, which previously has proved successful in extracting individual sources from mixed signals in calcium imaging movies (Mukamel et al., 2009).

We first discuss the spatial component selection scheme using NOL. In simple cases, like in Figure 4A, we see only a subset of the events in the combined binary mask. In more complex cases (Figure 4B; Figures S4B–S4D), where multiple distinct

Neuron 89, 269–284, January 20, 2016 ©2016 Elsevier Inc. 273

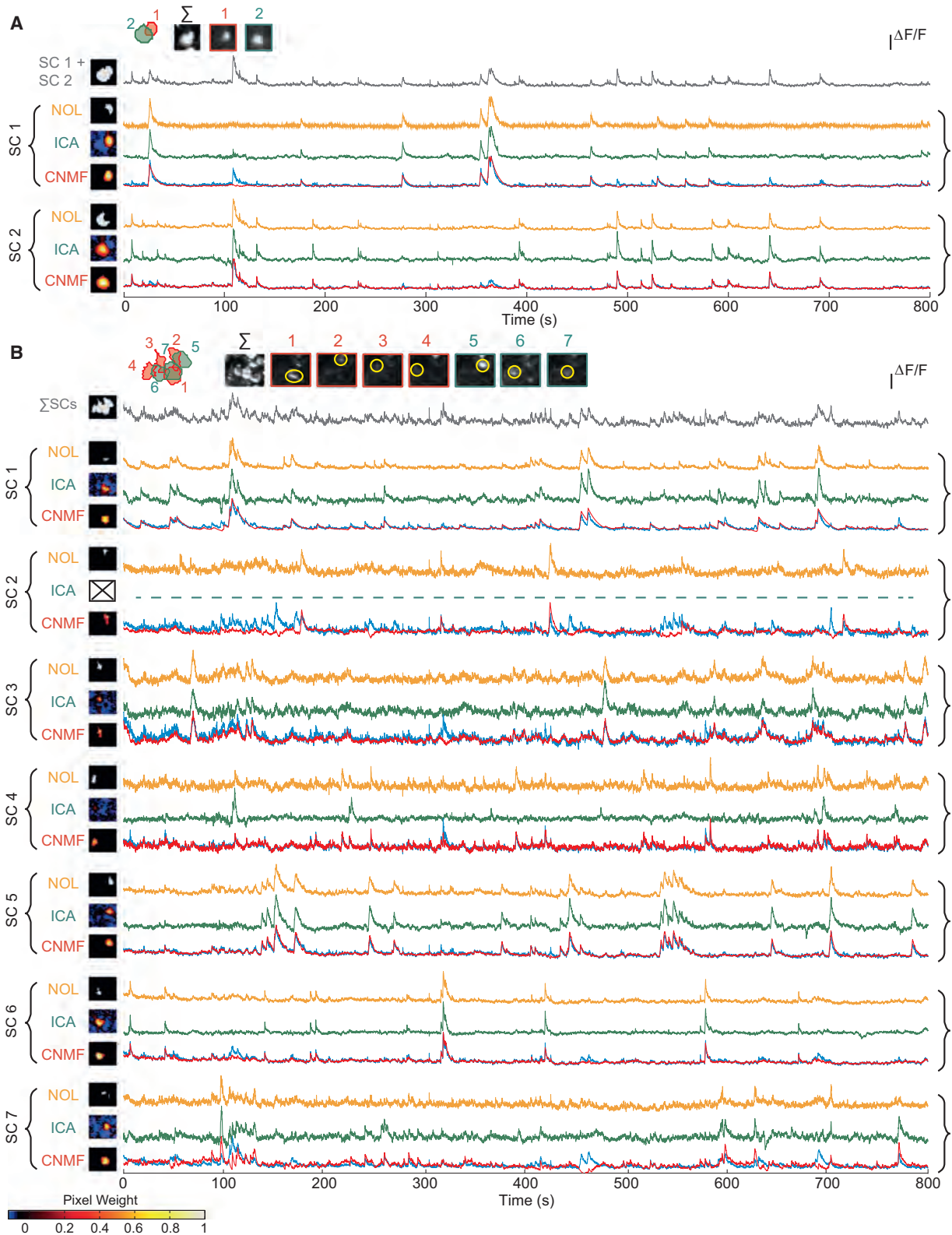


**Figure 4. Source Separation**

Source separation of the fluorescence signal from spatially overlapped spatial components (SCs) in the dual-plane images shown in Figure 3. (A) and (B) show two different examples with increasing complexity. In each example, the contours of the overlapped spatial components are plotted in red (from layer 2/3) and green (legend continued on next page)

sources can overlap with the chosen source, the nonoverlapped portion may only contain a few pixels, yielding poor SNR, or those pixels may not be fully free from contamination, yielding mixed signals. Nevertheless, in regions where the nonoverlapped portion is identifiable, we can use this as a reference to evaluate the other two algorithms.

We then examine the ICA extracted sources. ICA identifies the sources automatically without human intervention, and with high speed. For cases where the number of sources in space is low and there are “clean” nonoverlapping pixels with high SNR (Figure 4A), the extracted components are spatially consistent with the known source location (cf. top row of images). In many cases, they include a region of low-magnitude negative weights, which, on inspection, appear to spatially overlap with adjacent detected sources, presumably because this decreases the apparent mixing of signals between the components. More consequential is that for the complex overlapping signals in our experiment, ICA routinely fails to identify human- and CNMF-identified spatial source components, and appears to have less clean separation of mixed signals (cf. activity traces in Figure 4A and the complete failure of ICA to identify spatial component 2 in Figure 4B). See also Figure S3 for the comparison in a large population.

We further compare CNMF traces against the human-selected nonoverlapping traces for a larger population in Figure 5 (and additionally in Figures S4 and S5). Figure 5A shows the cross-correlation between 250 CNMF sources and the NOL source related to it. The correlation is high, as would be expected if the CNMF traces accurately detect the underlying source. The majority of the signals show a correlation coefficient of  $>0.94$ , and the mean correlation coefficient is 0.91. The distribution of coefficients is strongly asymmetric, and contains some notable outliers. Examining the underlying traces of these outliers (Figure 5C; Figures S4B–S4E), we can identify the origin of the poor correlation between the NOL traces and the CNMF traces. In these cases, the NOL spatial component consists of only a few pixels, and is extremely noisy; they also contain contamination from neighboring sources. The related spatial component from CNMF contains more pixels, has less noise, and shows clean demixed signal. They have generally higher SNR, especially for those NOL spatial components with low SNR (Figures 5B–5E; see Experimental Procedures for the calculation of SNR).

The fractions of cells with low correlation between the NOL and CNMF components are *exactly* the sources that simple signal extraction techniques *cannot* cleanly separate—they are the imaged sources that *require* CNMF. Without CNMF, extracted signals would falsely show high correlation between sources that are imaged into the same region in the dual-plane image. In the dual-plane image collected in Figure 3 and

analyzed here, we find that  $\sim 26\%$  of the cells have correlations below 0.9. The SNR comparison in Figure 5B is between the NOL signal and that from CNMF *with residue* (i.e., noise; see Experimental Procedures), to not simply boost the CNMF SNR from full deconvolution. Globally, the SNR of CNMF is 13% higher than that from NOL. The pooled data ( $\sim 1,800$  spatial components from ten dual-plane imaging sessions across five mice) presented in Figure S5 show similar results.

The power of our simultaneous multi-plane imaging and source separation approach can be seen in Figure 6, where we are able to record spontaneous and evoked activity across multiple layers, which is critical for understanding microcircuit dynamics in the brain. We examined visually evoked activity in L2/3 and L5 simultaneously, while we projected drifting gratings to probe the orientation and directional sensitivity of the neuronal responses (OS and DS; see Experimental Procedures). This paradigm was chosen because drifting gratings produce robust responses in V1 (Niell and Stryker, 2008). They are used frequently in the community (Huberman and Niell, 2011; Rochefort et al., 2011), and can be used to examine the performance of our imaging method in a functional context. Figure 6A shows some representative extracted traces from cells with different OS, along with an indicator showing the timings of presentation of stimuli (traces shown were acquired under the dual-plane paradigm). During the entire recording period, this mouse had particularly strong spontaneous activity in nearly all of the cells in the FOV. Nonetheless, many cells showed strong and consistent orientation tuning across the trials (76 out of 260 cells). For these cells, we compared the computed single-plane DS and OS to those computed from the same neurons, but from the dual-plane image series. If the dual-plane images had increased noise or, more seriously, if overlapping sources could not be cleanly separated, we would expect decreased, or even altered, OS. This is neither the case on the population level nor on the single-cell level, as seen in Figures 6B and 6C. In Figure 6D, we show the SD dual-plane image and the extracted spatial component contours. The two small boxes in the contour image indicate two pairs of cells with significant spatial overlap in the dual-plane image. We examine the DS of these cells in more detail in Figure 6E, and it is clear that we can fully separate the functional activity of even strongly overlapping cells, without cross-contamination.

The data shown in Figures 3, 4, 5, and 6 were taken with two planes, with interplane spacing of  $330\ \mu\text{m}$  (Figures 3, 4, and 5) and  $250\ \mu\text{m}$  (Figure 6), which is far from the limit of the method. In Figures 7A–7I, we show experimental results from simultaneous three-plane imaging of mouse V1. The intermediate plane is set to be the same as the nominal focal plane (the undiffracted beam's location). Figures 7A–7C show the images of the intensity SD of

---

(from layer 5) with their source ID. A pixel maximum projection of the recorded movie is shown to illustrate the spatial overlap of these SCs. Raw image frames from the recorded movie show the neuronal activity of these individual spatial components. For the temporal traces, the first trace (in gray) shows that extracted from all the pixels of the overlapped SCs. The following traces show the demixed signal of the individual SCs. Three different methods are used to extract the signal from individual SCs: nonoverlapped pixel (NOL), with the extracted signal shown in orange, independent component analysis (ICA) in green, and constrained nonnegative matrix factorization (CNMF) in red. The corresponding SC contours resulting from these methods are shown next to their  $\Delta F/F$  traces, and the color code of the pixel weighting is shown immediately below (B). Using the SC contour from CNMF, but with uniform pixel weighting and without temporal demixing, the extracted  $\Delta F/F$  trace is plotted in cyan, superimposed onto the traces extracted from CNMF. In (B), ICA fails to find SC 2. The traces are plotted independently scaled for display convenience. The scaling applied is as follows: the scale bars of  $\Delta F/F$  represent 1.27 for SC 1 and 1.46 for SC 2 in (A) and 1.24 for SC 1, 0.48 for SC 2, 0.36 for SC 3, 0.24 for SC 4, 0.78 for SC 5, 0.85 for SC 6, and 0.79 for SC 7 in (B).

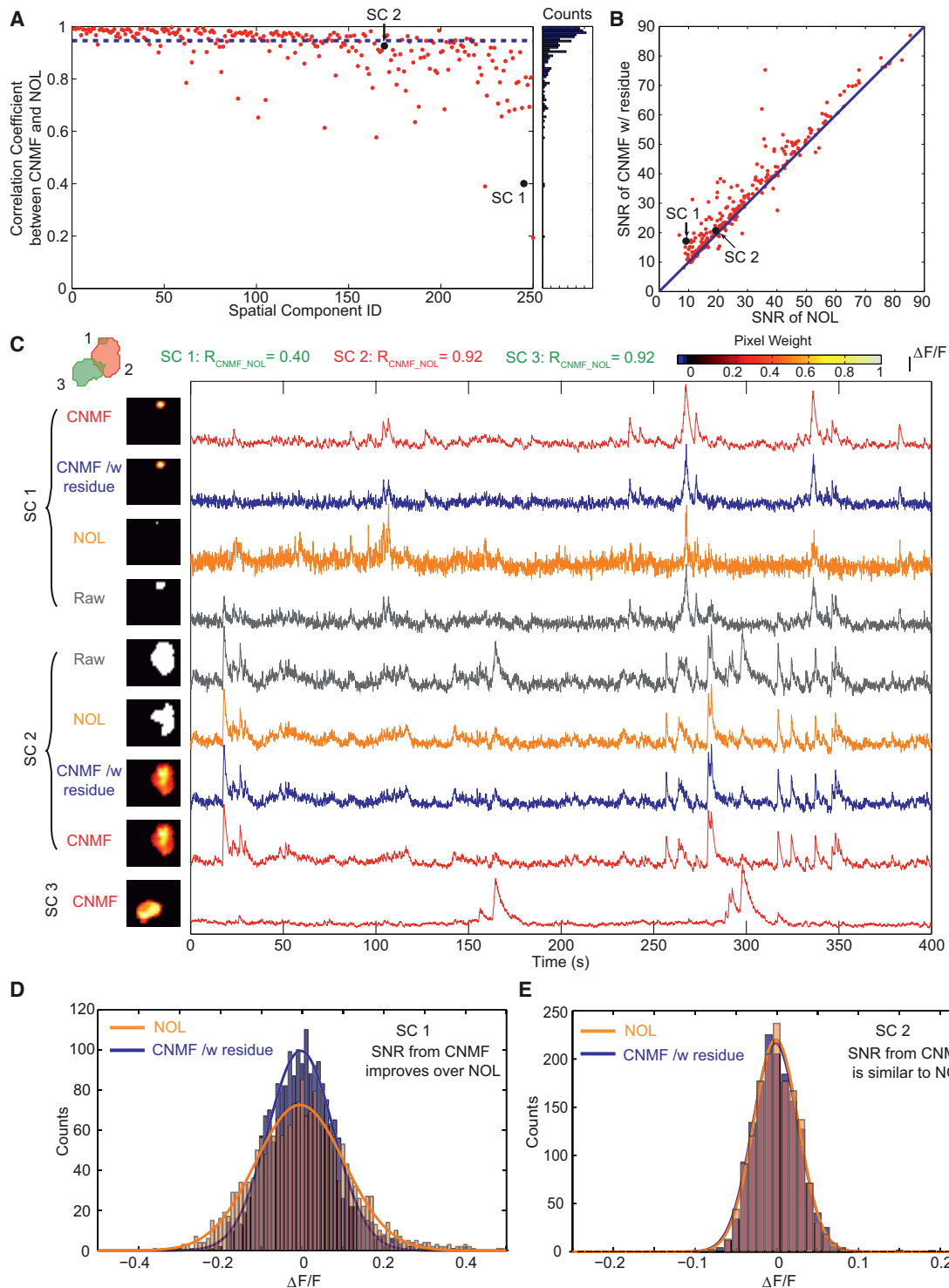


**Figure 5. Comparison between CNMF and NOL**

(A) Correlation coefficient between the  $\Delta F/F$  extracted from CNMF and NOL for a total of 250 spatial components in the dual-plane imaging shown in Figure 3. The blue dashed line indicates the median (0.947) of the correlation coefficients. The SC IDs are sorted by the signal-to-noise ratio (from high to low) of the signals extracted by NOL.

(B) Signal-to-noise ratio (SNR) comparison between the  $\Delta F/F$  extracted from CNMF (with residue) and the  $\Delta F/F$  extracted from NOL for the 250 SCs. The overall SNR of CNMF (with residue) is 13% higher than that from NOL.

(legend continued on next page)

the time series image stack from single-plane imaging at three different depths. The SLM simultaneous three-plane imaging is shown in Figure 7E, corresponding well to the arithmetic sum of Figures 7A–7C shown in Figure 7D. The spatial contours of the extracted source components are shown in Figure 7F, along with the representative fluorescence traces shown in Figures 7G and 7H for sequential single-plane and simultaneous three-plane imaging, respectively. In Figure 7I, we show an example where three overlapped sources from the three planes can be clearly separated using CNMF. We can further extend the extremal range between planes to over 500  $\mu\text{m}$ , as shown in Figures S6A–S6G.

The multi-plane imaging can be further extended with a time-multiplexed scheme. The SLM used in our experiments can switch between different holograms at high speed (>300 Hz). In Figure 7J, we show that we can fully transition between two sets of simultaneous dual-plane images in <3 ms, a switching time confirmed “offline,” using a simple structured Rhodamine 6G target, in Figure 7K. This spatial-multi-plane imaging and time-multiplexed scheme paves the path toward high-speed volumetric imaging (see the schematic shown in Figure S6H).

## DISCUSSION

In this work, we extend two-photon holographic microscopy (Nikolenko et al., 2008; Anselmi et al., 2011) to demonstrate successful simultaneous 3D multi-plane *in vivo* imaging with a hybrid SLM multiplexed-scanning approach that leverages spatiotemporal sparseness of activity and prior structural information to efficiently extract single-cell neuronal activity. We can extend the effective area that can be sampled, target multiple axial planes over an extended range (>500  $\mu\text{m}$ ), or do both, at depth within the cortex. This enables the detailed examination of intra- and interlaminar functional activity. The method can be easily implemented on any microscope with the addition of a relatively simple SLM module to the excitation path, and without any additional hardware modifications in the detection path. The regional targeting is performed remotely, through holography, without any motion of the objective, which makes the technique a strong complement to 3D two-photon activation (Packer et al., 2012, 2015; Rickgauer et al., 2014). This approach is an initial demonstration of an essential paradigm for future high-speed *in vivo* volumetric imaging in scattering tissue, combining structured multiplexed excitation along with computational reconstruction that is aided by additional prior knowledge—in this case, the simplified single-plane source locations.

### Comparisons to Alternative Methods

There are many imaging modalities today that are capable of collecting functional data within a 3D volume. The simplest systems

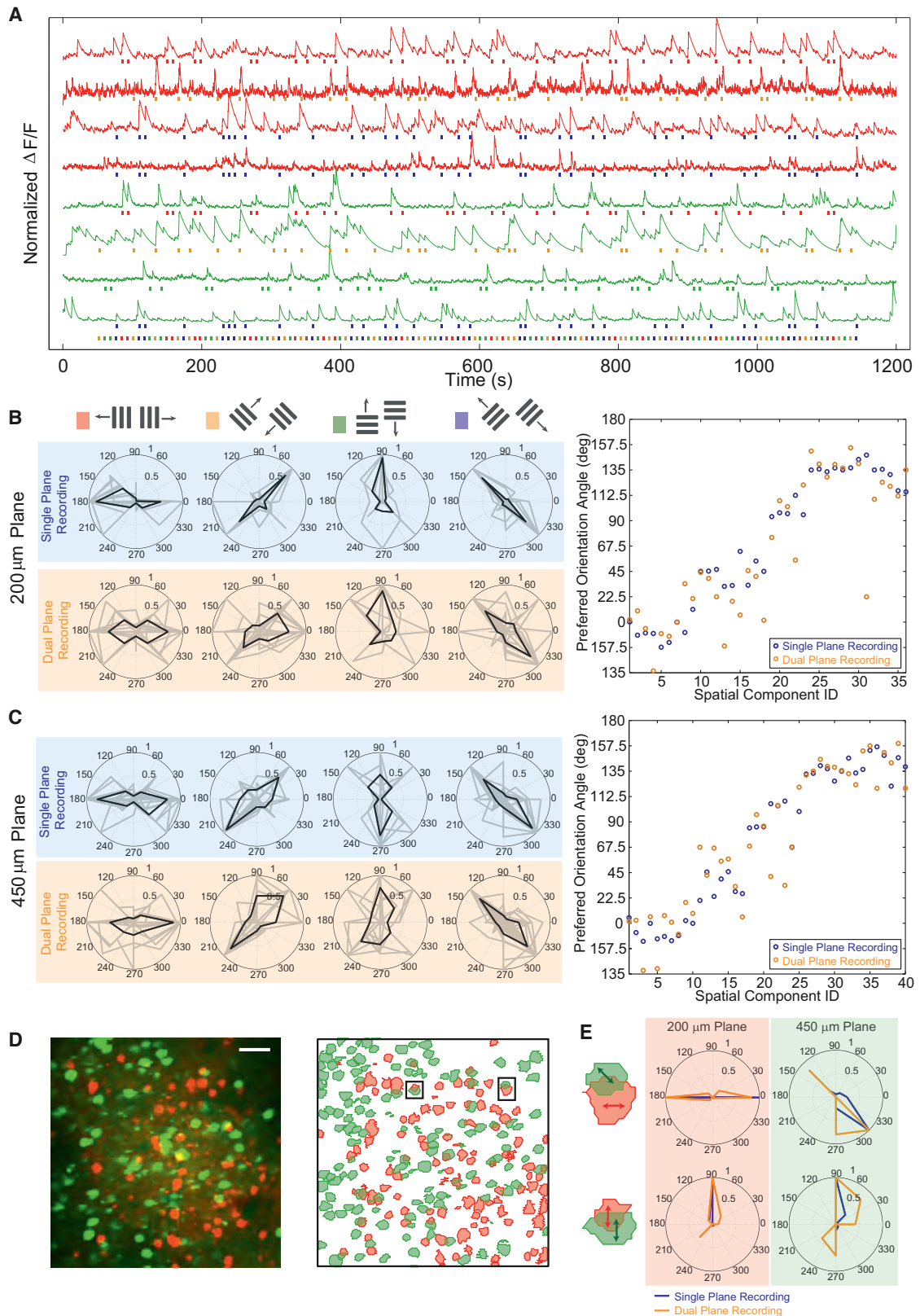
that provide volumetric imaging combine a piezo-mounted objective with resonant galvanometers, which have high optical performance throughout their focusing range. A critical component for determining the imaging rate is the speed of the piezo—how fast the objective can be translated axially. For deep imaging in scattering tissue, the fluorescence collection efficiency scales as  $NA^2/M^2$ , with  $M$  being the objective magnification (Beaurepaire and Mertz, 2002). The combination of high numerical aperture (N.A.) with low-magnification inevitably means that the objectives are large and heavy. This large effective mass lowers the resonant frequency of the combined piezo-objective system, and necessitates significant forces to move axially quickly, as well as lengthens the settle times ( $\sim 15$  ms); this lowers the duty cycles, because imaging cannot take place during objective settling. The distance that the piezo can travel is also limited, with current state-of-the-art systems offering 400  $\mu\text{m}$  of total travel. Compared to piezo-based systems, our SLM-based approach has significantly greater axial range and couples no vibrations into the sample. Additionally, we can change between different planes throughout the full range very rapidly, in <3 ms, which allows for axial switching *within* a frame (Figures 7J and 7K).

Remote focusing has also been used for faster volumetric imaging, either with the use of a secondary objective and movable mirror (Botcherby et al., 2012), electro-tunable lenses (ETLs) (Grewe et al., 2011), and, very recently, ultrasound lenses (Kong et al., 2015). Although these have higher performance than piezo-mounted objectives, none of these has yet been demonstrated to allow for *in vivo* functional imaging at the axial span that we show here. For applications where a perfect point spread function (PSF) is paramount, remote focusing with a mirror may offer better optical performance but requires careful alignment and engineering. Ultrasound lenses give very high speed axial scanning, but must be continuously scanned, a severe limitation of the technology. The stand-alone ETL, when properly inserted into the microscope, represents perhaps the most cost-effective solution for fast focusing. Although the ETL provides a lower-cost solution, it is not as fast as the SLM and cannot provide any adaptive optics capabilities, nor flexible beam reconfiguration, such as lateral shift or multiplexed excitation. Ultrasound lenses also lack convenient beam multiplexing or complex optical corrections. SLMs, on the other hand, allow for all of these.

Although fast sequential imaging strategies such as acousto-optic deflector systems offer good performance, with state-of-the-art 3D AOD systems currently providing high-performance imaging over relatively large volumes of tissue (Duemani Reddy et al., 2008; Kirkby et al., 2010; Katona et al., 2012), these systems are very complex and expensive, with a cost that is at least a few times that of conventional two-photon microscopes, severely limiting their practical use. They are also very sensitive

(C) An example where three sources that are spatially overlapped in the dual-plane imaging is studied. The contours of the overlapped SCs are plotted in red (from layer 2/3) and green (from layer 5) with their spatial component ID. The CNMF and NOL extracted  $\Delta F/F$  signals are plotted in red and orange, respectively. The signal that CNMF extracted with residual noise is plotted in blue. Using the SC contour in the CNMF but with uniform pixel weighting and without temporal demixing, the extracted  $\Delta F/F$  trace is plotted in gray and labeled as “raw.” The corresponding correlation and SNR values for SC 1 and SC 2 are labeled in (A) and (B). The traces are plotted independently scaled for display convenience. The scaling applied is as follows: the scale bars of  $\Delta F/F$  represent 0.29 for SC 1, 0.14 for SC 2, and 0.51 for SC 3.

(D and E) Histograms of the  $\Delta F/F$  noise for SC 1 (D) and SC 2 (E). Orange color shows that for the NOL extracted signal, whereas blue shows that for CNMF with residue. The histograms are fitted with a Gaussian function, shown as a solid-line curve.



(legend on next page)

to wavelength, requiring extensive realignment with changes in wavelength. An additional complication of any point targeting strategy, such as AOD systems, is that sample motions are significantly more difficult to treat (Cotton et al., 2013).

A larger limitation of all of these serially scanned systems is that all are near the fundamental limits on their speed, as finite dwell times are required on each pixel to maintain SNR. Because fluorophore saturation ultimately limits the maximum emission rate regardless of excitation intensity, increases in intensity simply cause photodamage, bleaching, and reduced spatial resolution. Wide-field fluorescence imaging can overcome the speed limit with the development of high-speed cameras. Despite their high performance, wide-field imaging schemes such as light-sheet microscopy (Ahrens et al., 2013), light-field microscopy (Prevedel et al., 2014), or swept confocally aligned planar excitation (SCAPE) (Bouchard et al., 2015) suffer from light scattering in deep tissues, and are thus better suited for relatively superficial imaging or imaging in weakly scattering samples.

Multiplexed two-photon-based approaches offer a clear way to increase overall system performance by taking advantage of the benefits of nonlinear imaging while maintaining sufficient dwell times for high sensitivity. Spatially multiplexed strategies have been used before (Bewersdorf et al., 1998; Fricke and Nielsen, 2005; Bahlmann et al., 2007; Kim et al., 2007; Matsumoto et al., 2014) but with very limited success for imaging neuronal activity in scattering samples. The fluorescence produced deep in the samples scatters extensively while traveling through the sample, which limits the ability to “assign” each fluorescence photon to its source (Andresen et al., 2001; Kim et al., 2007; Cha et al., 2014). A more successful approach has been to temporally multiplex each separate excitation beam (Egner and Hell, 2000; Fittinghoff et al., 2000; Andresen et al., 2001; Cheng et al., 2011) and use customized electronics for temporal demixing. For multilayer imaging, our current system exceeds the demonstrated FOV and axial range of published implementations using temporally multiplexed beams and provides a cleaner signal demixing, with significantly greater flexibility and speed in choosing targeted depths. However, we do not consider other spatially separated multibeam or temporally multiplexed strategies as competitors but rather as complementary methods that could be leveraged to further increase the overall system performance.

### Current Limitations and Technical Outlook Phase-Only SLMs for Beam Steering

The performance of our current system is strongly dependent on the SLM, a  $512 \times 512$ -pixel phase-only device that performs beam splitting by imparting phase modulation on the incoming laser pulse and uses diffraction to redirect the beams to their targeted sites. Multiple factors need to be considered when designing an SLM-based imaging system. First, the efficiency of the SLM diffraction is notably affected by the fill factor and the effective number of phase levels per “feature.” The effective power throughput from the SLM module ranges from  $\sim 82\%$  to  $40\%$  for the patterns used in this paper. This is significantly better than  $<20\%$  overall efficiency of a full 3D AOD system. The efficiency of this method can be improved by better SLMs, that is, devices that have higher fill factors, increased pixel number, and increased phase modulation, all of which are the subject of active development. Second, any diffractive device is inherently chromatic—the deflection depends on the wavelength of the light. This chromatic dispersion can be reduced with the incorporation of a custom dispersion compensation optical element. For axial displacements in our system, the effect of chromatic dispersion on performance is markedly less. More details are presented in Supplemental Information.

Regarding the maximal number of planes addressable, and limitations to the axial spacing, practically, we find acceptable results when the separation between planes is at least five times the axial PSF for shifts without lateral displacements. Shorter separations appear to give decreased sectioning. In our experiments, the maximal number of planes (three) demonstrated for functional imaging was limited by the total power deliverable to the sample, as we specifically aimed to target deeper layers, where scattering losses are significant. By targeting more superficial layers, more planes were addressable. Adaptive optics could also extend the gains to deeper layers. Fundamentally, the maximal usable number of planes is limited by the biology and functional indicators—relatively sparse signals with little background would promote the use of more planes, whereas dense, complex sources may require limiting the number of planes to low numbers to achieve effective demixing. In the dual-plane experiments shown in Figures 3, 4, and 5, the strongly overlapped sources represent  $\sim 30\%$  of all detected sources (as can be seen in the correlation between NOL and CNMF in

#### Figure 6. Orientation and Direction Selectivity Analysis with Simultaneous Dual-Plane Imaging

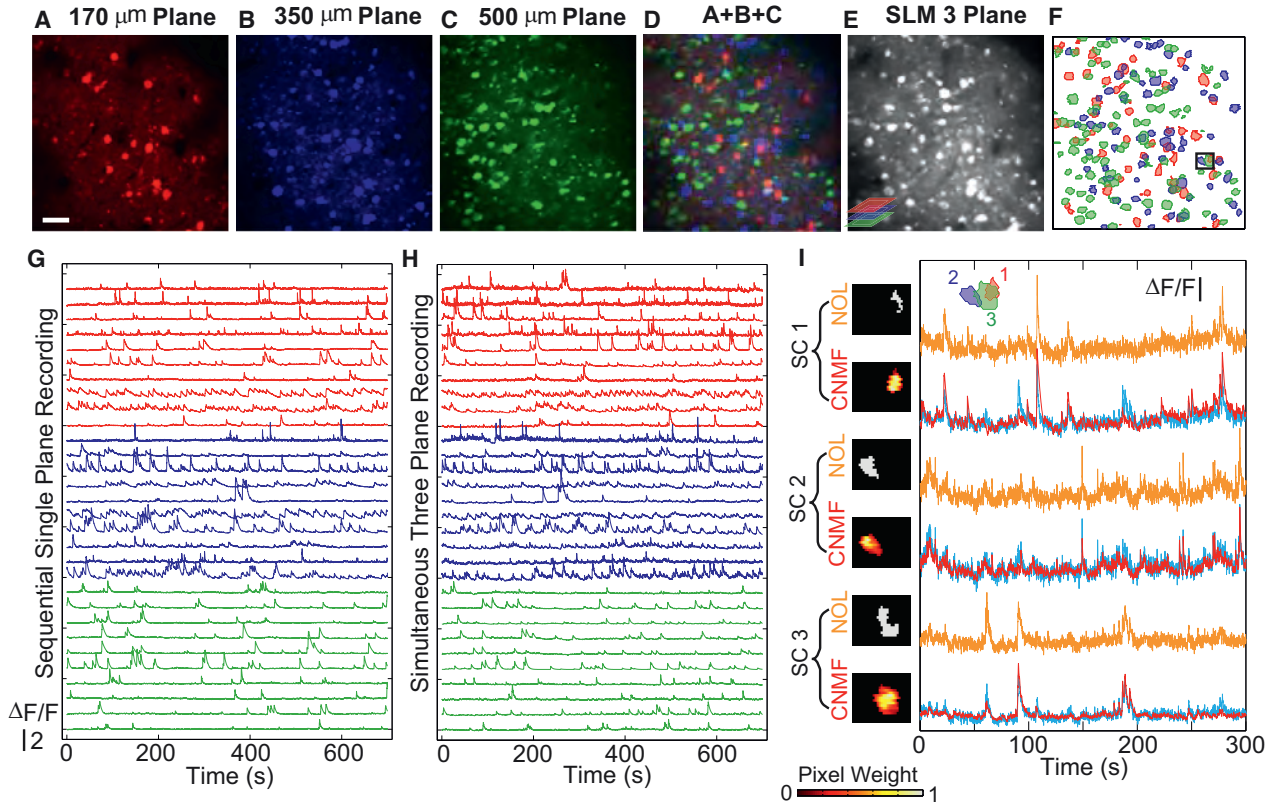
(A) Normalized  $\Delta F/F$  traces for selected spatial components with strong response to drifting grating visual stimulation, recorded with simultaneous dual-plane imaging. The red and green color traces are from SCs at depths of 200 and 450  $\mu\text{m}$  from the pial surface of mouse V1, respectively. The color bar at the bottom of each trace indicates the visual stimulation orientation of the drifting grating, with the legend shown at the top of (B): red,  $0^\circ/180^\circ$ ; yellow,  $45^\circ/225^\circ$ ; green,  $90^\circ/270^\circ$ ; purple,  $135^\circ/315^\circ$ .

(B) Left: response of the SCs to the drifting grating in visual stimulation. The SCs are on the 200- $\mu\text{m}$  plane. The SCs are separated into four groups, corresponding to a preferred orientation angle of  $0^\circ/180^\circ$ ,  $45^\circ/225^\circ$ ,  $90^\circ/270^\circ$ , and  $135^\circ/315^\circ$ . The black curves are the average response of the group. Right: comparison of the SCs' preferred orientation angle to the drifting gratings, between signals extracted from the single-plane recording (blue dots) and the dual-plane recording (orange dots).

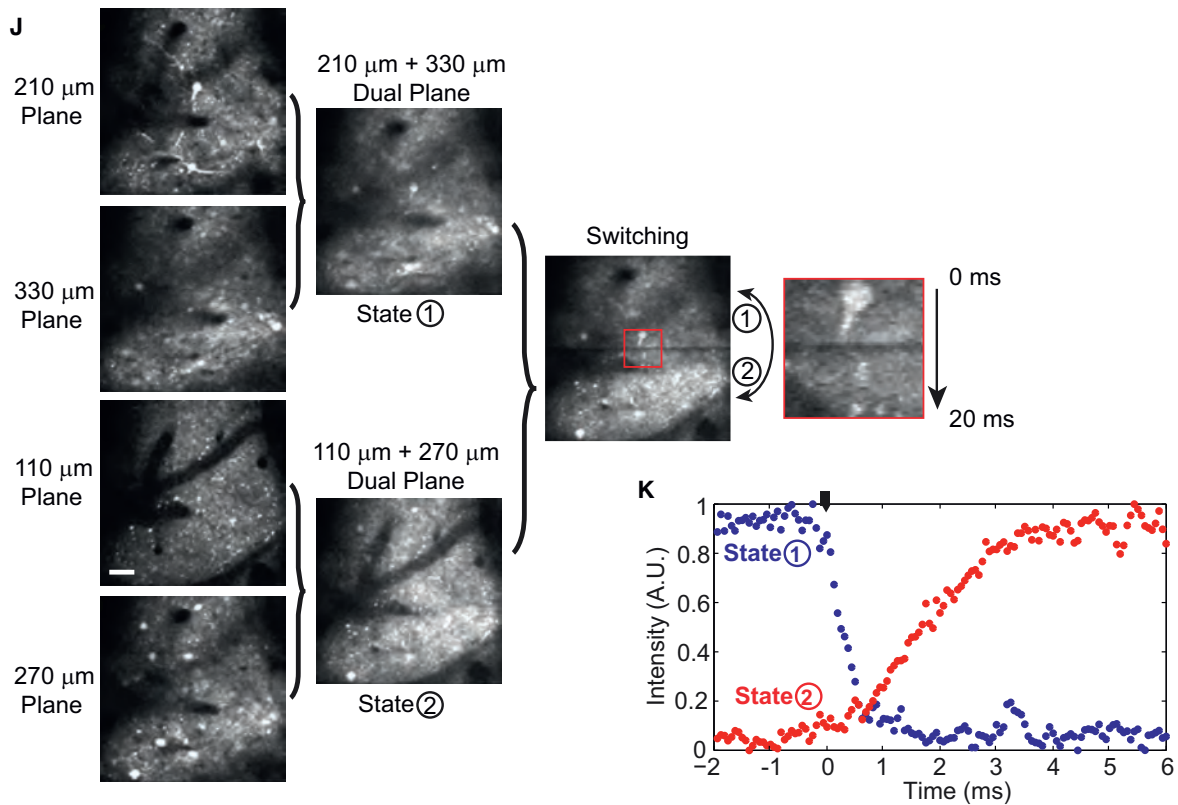
(C) Same as (B), for SCs located at 450- $\mu\text{m}$  depth from the pial surface.

(D) Left: overlaid temporal SD image (with false color) of the sequential single-plane recording from the 200- $\mu\text{m}$  plane (red) and the 450- $\mu\text{m}$  plane (green). Right: extracted SC contours from the two planes. The scale bar represents 50  $\mu\text{m}$ .

(E) Examples of the evoked responses of the SCs with spatial lateral overlaps from the two planes. Blue color shows that extracted from single-plane recording, and orange shows that extracted from dual-plane recording. The arrow inside each SC indicates its preferred direction. The locations of these SCs are indicated in the small black boxes in the SC contours in (D).



### Towards High Speed Volumetric Imaging: Fast SLM Switching



(legend on next page)

Figure 5A), so we believe there is significant room to push the total number of planes with the current setup.

### Volumetric Imaging

The overall speed of multi-plane imaging can be increased with additional simple methods. With the current system's high apparent sensitivity, we anticipate that we could reduce the nominal dwell time per pixel and still collect enough photons for effective detection. By transitioning our microscope from conventional galvanometers to resonant galvanometers, we could speed up the imaging by at least a factor of three. Combined with the fast switching time of our device (<3 ms; see Figures 7J and 7K and Thalhammer et al., 2013), we anticipate being able to image large volumes of neural tissue at high speed. Our strategy is to rapidly interleave multi-plane images in successive scans to generate a complete picture of neural activity (see the schematics shown in Figure S6H).

### Outlook

SLM-based multiregion imaging is one implementation of the general strategy of computationally enhanced projective imaging, which will make possible the ability to interrogate neurons over a very large area, with high temporal resolution and SNR. Projective imaging is extremely powerful, especially when combined with prior information about the system to be studied. Basic knowledge of the underlying physical structure of the neural circuit and the sparsity of its activity is used to define constraints for the recovery of the underlying signal and allow for higher-fidelity reconstruction and increased imaging speed in complex samples. With our multiplexed SLM approach, we determine the number of areas simultaneously illuminated and have direct control over the effective number of sources, in contrast to alternate extended two-photon approaches, such as Bessel beam scanning (Botcherby et al., 2006; Thériault et al., 2014), where the sample alone controls the complexity of the signal.

There are many questions that can be addressed by high-speed volumetric imaging. First, the simple increase in total neurons monitored in the local circuit greatly increases the chances for capturing the richness and variability of the dynamics in cortical processing (Alivisatos et al., 2013a, 2013b; Insel et al.,

2013). For instance, what is the organization of functionally or behaviorally relevant ensembles in cortical columns? How do upstream interneurons affect downstream activity and synchrony, and output (Helmstaedter et al., 2008, 2009; Meyer et al., 2011)? Without the ability to probe interlaminar activity simultaneously, answering these questions definitively will be very difficult, if not impossible. Although we have focused on somatic imaging in this paper, this technique works equally well for imaging dendrites or dendrites and soma together (data not shown; see the companion paper [Pnevmatikakis et al., 2016] for dendritic source separation with CNMF). The extended axial range of our method would allow exploring L5 soma and their apical tufts simultaneously, and may give direct insight into the role of dendritic spikes and computation in neuronal output (London and Häusser, 2005; Shai et al., 2015). Thus, SLM-based multi-plane imaging appears to be a powerful method for addressing these and other questions that require high-speed volumetric imaging with clear cellular resolution. The system is flexible, easily configurable, and compatible with most existing two-photon microscopes, and could thus provide a novel powerful platform with which to study neural circuit function and computation.

## EXPERIMENTAL PROCEDURES

### Animals and Surgery

All experimental procedures were carried out in accordance with animal protocols approved by the Columbia University Institutional Animal Care and Use Committee. All experiments were performed with C57BL/6 wild-type mice at postnatal day 60–120. Virus AAV1synGCaMP6f (Chen et al., 2013) was injected into both layer 2/3 and layer 5 of the left V1 of the mouse cortex 4–5 weeks prior to craniotomy. The virus ( $6.91 \times 10^3$  genome copies per ml) was front loaded into the injection pipette and injected at a rate of 80 nl/min. The injection sites were at 2.5 mm lateral and 0.3 mm anterior from the lambda, in the putative monocular region of the left hemisphere. Injections (500 nl per site) were made at two different depths from the cortical surface, at 200–250 and 400–500  $\mu\text{m}$ , respectively.

After 4–5 weeks of expression, mice were anesthetized with isoflurane (1%–2% [v/v] in air). Before surgery, dexamethasone sodium phosphate (2 mg per kg of body weight; to prevent cerebral edema) and bupivacaine (5 mg/ml) were administered subcutaneously, and enrofloxacin (4.47 mg/kg) and carprofen

### Figure 7. Axial Three-Plane In Vivo Functional Imaging of Mouse V1 and Fast SLM Switching between Different Holograms

(A–C) Temporal SD image of the sequential single-plane recording (10 fps) of mouse V1 at depths of 170  $\mu\text{m}$  (A), 350  $\mu\text{m}$  (B), and 500  $\mu\text{m}$  (C) from the pial surface. The images are false colored. The scale bar represents 50  $\mu\text{m}$ .

(D) Arithmetic sum of (A)–(C).

(E) Temporal SD image of the simultaneous three-plane recording (10 fps) of the same planes shown in (A)–(C).

(F) Overlaid SC contours from the three planes.

(G) Representative extracted  $\Delta F/F$  traces of the selected SCs from the three planes (red, 170- $\mu\text{m}$  plane, 10 SCs out of 58; blue, 350- $\mu\text{m}$  plane, 10 SCs out of 65; green, 500- $\mu\text{m}$  depth, 10 SCs out of 95), from the sequential single-plane recording.

(H) Extracted  $\Delta F/F$  traces of the same SCs shown in (G), from the simultaneous three-plane recording.

(I) An example of source separation of the fluorescence signal from spatially overlapped components in the three-plane imaging. The locations of these SCs are shown in the small black box in (F). The contours of the overlapped SCs are plotted in color with their SC ID. For each SC, the signal is extracted using NOL shown in orange and CNMF in red. The corresponding SC contours resulting from these methods are shown next to their  $\Delta F/F$  traces. A raw trace, generated from the CNMF SC, but with uniform pixel weighting and without temporal demixing, is plotted in cyan, superimposed onto the traces extracted with CNMF. Fluorescence traces are independently scaled for display convenience. The scale bars of  $\Delta F/F$  represent 0.268 for SC 1, 0.376 for SC 2, and 0.351 for SC 3.

(J) SLM switching between two sets of dual-plane imaging of mouse V1. State 1 is the dual plane for a depth of 210 and 330  $\mu\text{m}$  from the pial surface, and state 2 is the dual plane for a depth of 110 and 270  $\mu\text{m}$  from the pial surface. Imaging frame rate is 10 fps. The SLM switching happens at the middle and end of each frame. The zoom-in view of the switching region shows that the switching time between the two states is less than 3 ms. The scale bar represents 50  $\mu\text{m}$ .

(K) SLM switching time between two different states, measured from the change in fluorescence signal emitted from spatially localized planes of Rhodamine 6G. The switching time between different states is less than 3 ms. The black indicator marks when the switching starts. A.U., arbitrary units.

(5 mg/kg) were administered intraperitoneally. A 2-mm-diameter circular craniotomy was made over the injection cite with a dental drill and the dura mater was removed. Agarose (1.5%) was placed over the craniotomy, and a 3-mm circular glass coverslip (Warner Instruments) was placed and sealed using a cyanoacrylate adhesive. A titanium head plate was attached to the skull using dental cement. The imaging experiments were performed 1–14 days after the chronic window implantation. During imaging, the head-fixed mouse is awake and can walk on a circular treadmill.

The shrimp used in the structural imaging were *A. nauplii* (Brine Shrimp Direct).

### Two-Photon SLM Laser Scanning Microscope

The setup of the two-photon SLM laser scanning microscope is illustrated in Figure 1. The laser source is a pulsed Ti:sapphire laser (Coherent; Mira) tuned to 940 nm with a maximum output power of  $\sim 1.4$  W ( $\sim 140$ -fs pulse width, 80-MHz repetition rate). The laser power is controlled with a Pockels cell (Conoptics; EO350-160-BK). A  $\lambda/2$  waveplate (Thorlabs; AHWP05M-980) is used to rotate the laser polarization so that it is parallel to the active axis of the spatial light modulator (Meadowlark Optics; HSP512-1064;  $7.68 \times 7.68$ -mm<sup>2</sup> active area,  $512 \times 512$  pixels). The laser beam is expanded by a 1:1.5 telescope (focal length [f]1, 50 mm; f2, 75 mm; Thorlabs; plano-convex lenses, “B” coated) to fill the active area of the SLM. The light incident angle to the SLM is  $\sim 3.5^\circ$ . The reflected beam is scaled by a 4:1 telescope (f3, 400 mm; f4, 100 mm; Thorlabs; achromatic doublets lenses, “B” coated) and imaged onto a set of close-coupled galvanometer mirrors (Cambridge Technology; 6215HM40B). In dual-lateral plane imaging, a beam block made of a small metallic mask on a thin pellicle is placed at the intermediate plane of this 4:1 telescope to remove the zero-order beam. The galvanometer mirrors are located conjugate to the microscope objective pupil of a modified Olympus BX-51 microscope through an Olympus pupil transfer lens (f5, 50 mm) and tube lens (fTL, 180 mm). An Olympus 25 $\times$  N.A. 1.05 XLPan N objective is used for the imaging. The fluorescence signal from the sample is detected with a photomultiplier tube (PMT; Hamamatsu; H7422P-40) and a low-noise amplifier (Stanford Research Systems; SR570). ScanImage 3.8 (Pologruto et al., 2003) is used to control the galvanometer mirrors and digitize and store the signal from the PMT amplifier. The line scanning is bidirectional, with a single line scan rate of 2 kHz. For a 256  $\times$  200-pixel image, the frame rate is 10 frames per second (fps).

A detailed characterization of the performance of SLM beam steering and its dependence on other optics in the microscope, such as the objective, is presented in Supplemental Information.

### Hologram Generation

Custom software using MATLAB (The MathWorks) was developed to generate and project the phase hologram pattern on the SLM through a PCIe interface (Meadowlark Optics). At the operating wavelength of 940 nm, the SLM outputs  $\sim 80$  effective phase levels over a  $2\pi$  phase range, with relatively uniform phase-level spacing (see Figure S1A).

To create a 3D beamlet pattern on the sample (a total of  $N$  beamlets, each with coordinates  $[x_i, y_i, z_i]$ ,  $i = 1, 2, \dots, N$ ), the phase hologram on the SLM,  $\phi(u, v)$ , can be expressed as

$$\phi(u, v) = \text{phase} \left\{ \sum_{i=1}^N A_i e^{2\pi j \{ x_i u + y_i v + [Z_m^0(u, v) C_m^0(z_i) + Z_m^1(u, v) C_m^1(z_i) + Z_m^2(u, v) C_m^2(z_i)] \}} \right\} \quad (\text{Equation 1})$$

$A_i$  is the electrical field weighting factor for the individual beamlet.  $Z_m^0(u, v)$  and  $C_m^0(z_i)$  are the Zernike polynomials and Zernike coefficients, respectively, which fulfills the defocusing functionality and compensates some of the higher-order spherical aberrations due to defocusing. The expressions of  $Z_m^0(u, v)$  and  $C_m^0(z_i)$  are shown in Table S1 (Anselmi et al., 2011). A 2D coordinate calibration between the SLM phase hologram and the PMT image is carried out on a pollen grain slide, and an affine transformation can be extracted to map the coordinates. For axial defocusing, the defocusing length set in the SLM phase hologram is matched with the actual defocusing length by adjusting the apparent “effective N.A.” in the Zernike coefficients after calibration following the procedure described in Quirin et al. (2013). This is done mainly for convenience, and it changes very little over the full axial range of the

SLM (range 0.43–0.48). In multi-plane imaging, the field weighting factors  $A_i$  in Equation 1 alter the power ratio of different imaging planes. We adjust the parameter empirically to achieve similar fluorescence signals from different imaging planes but we can also calculate the expected power ratio from first principles, considering the depths of each plane, the nominal scattering length of light in the tissue, the SLM steering efficiency (see Supplemental Information), and then perform numerical beam propagation of the electric field (Schmidt, 2010).

### Visual Stimulation

Visual stimuli were generated using MATLAB and the Psychophysics Toolbox (Brainard, 1997) and displayed on a monitor (Dell; P1914Sf, 19-inch, 60-Hz refresh rate) positioned 28 cm from the right eye, at  $\sim 45^\circ$  to the long axis of the animal. Each visual stimulus session consisted of eight different trials, each trial with a 3-s drifting square grating (100% contrast, 0.035 cycles per degree, two cycles per second), followed by 5 s of mean luminescence gray screen. Eight drifting directions (separated by  $45^\circ$ ) were presented in random order in the eight trials in each session. Seventeen sessions were recorded continuously (1,088 s).

### Image Analysis and Source Separation Algorithm

The raw images are motion corrected using a pyramid approach (Thévenaz et al., 1998) and analyzed using a novel constrained nonnegative matrix factorization algorithm detailed in the companion paper (Pnevmatikakis et al., 2016), coded in MATLAB. The core of the CNMF algorithm is that the spatiotemporal fluorescence signals  $Y$  from the whole recording can be expressed as a product of two matrices: a spatial matrix  $A$  that encodes the location of each spatial component and a temporal matrix  $C$  that characterizes the fluorescence signal of each spatial component, as well as the background  $B$  and noise (residue)  $E$ , expressed as  $Y = AC + B + E$ .

This can be solved using a constrained minimization method. The method imposes sparsity penalties on the matrix  $A$  to promote localized spatial footprints, and enforces the dynamics of the calcium indicator in the temporal components of  $C$ , which results in increased SNR. The individual single-plane recordings are first analyzed per Pnevmatikakis et al. (2016), and the resulting spatial matrix  $A$  for the spatial components and the background as well as the temporal calcium transient characteristics of each spatial component are used as initial estimates for the sources in the analysis of the multi-plane recording. The matrix  $A$ , which characterizes the individual pixel weights for each spatial component, is no longer reoptimized. We then apply the identical procedure as in the single-plane analysis to solve the convex optimization problem for the multi-plane data. Once  $C$  and  $B$  are estimated, the fluorescence signal, as well as the background baseline of each spatial component, can be extracted from these matrices, and  $\Delta F/F$  can be calculated.

To detect the events from the extracted fluorescence signal, the  $\Delta F/F$  is first normalized and then temporally deconvolved with the parameterized fluorescence decay (from fitting the autoregressive model). Independently, a temporal first derivative is also applied to the  $\Delta F/F$  signal. The deconvolved signal and the derivative are then thresholded with 2% and at least 2 SDs from the mean derivative signal, respectively. At each time point, if both are larger than the threshold, an activity event is recorded in binary format.

### Evaluation of CNMF, NOL, and ICA

To evaluate the signals extracted from CNMF, we compared them against signals extracted from pixels of each spatial component that do not have contribution from other sources. Temporal signals from these pixels are averaged with a uniform weighting, followed by subtraction of the background baseline obtained from CNMF. We term this nonoverlapped signal. This is similar to conventional fluorescence extraction methods, except that the background baseline subtraction is automated.

The signals extracted from CNMF are compared with the NOL signals in two aspects: similarity (or correlation) and signal-to-noise ratio. In the calculation of SNR, the “signal” is estimated by the maximum of the  $\Delta F/F$  trace, and the “noise” is estimated as described below. A histogram of the difference between the  $\Delta F/F$  values of adjacent time points is first calculated. Considering temporal regions where there are few transients, this histogram should have a maximum around 0, and the local distribution around 0 should characterize the

noise. The shape of this histogram can then be fitted with a Gaussian function, and the SD coefficient of this Gaussian function is considered as the “noise” in the SNR calculation.

ICA was also used to analyze the data, with software written in MATLAB (Mukamel et al., 2009). The motion-corrected image stack is first normalized, followed by principal component analysis for dimensionality reduction and noise removal. ICA is then applied to extract the spatiotemporal information of each independent source. Figure S3 provides a comparison between the performance of ICA and CNMF on a large population.

### Analysis of the Cell Orientation Selectivity of the Drifting Grating Visual Stimulation

To analyze the orientation and direction selectivity of the spatial components in response to the drifting grating visual stimulation, the total number of neuronal events is counted during the visual stimulation period in each session for all eight different grating angles. These event numbers are then mapped into a vector space (Mazurek et al., 2014). The direction and magnitude of their vector sum represent the orientation selectivity and orientation index, respectively. With  $N_{\text{visualsession}}$  visual stimulation sessions,  $N_{\text{visualsession}}$  vectors are obtained. Hotelling’s  $T^2$  test is used to calculate whether these vectors are significantly different from 0 (i.e., whether the spatial component has a strong orientation selectivity). Only spatial components with their vectors significantly different from 0 (<0.25 probability that null 0 is true) are selected, and their orientation selectivity is calculated by averaging the  $N_{\text{visualsession}}$  vectors and extracting the angle ( $N_{\text{visualsession}} = 17$  for the experiments shown in Figure 6).

### SUPPLEMENTAL INFORMATION

Supplemental Information includes six figures and one table and can be found with this article online at <http://dx.doi.org/10.1016/j.neuron.2015.12.012>.

### AUTHOR CONTRIBUTIONS

Conceptualization, D.S.P.; Methodology, W.Y., R.Y., and D.S.P.; Investigation, W.Y.; Software, E.P., L.P., W.Y., and D.S.P.; Formal Analysis, W.Y. and D.S.P.; Resources, J.-e.K.M. and L.C.-R.; Funding Acquisition, R.Y.; Writing – Original Draft, W.Y. and D.S.P.; Writing – Review & Editing, W.Y., E.P., L.P., R.Y., and D.S.P.; Supervision, R.Y. and D.S.P.

### ACKNOWLEDGMENTS

This work is supported by the NEI (DP1EY024503, R01EY011787), NIMH (R01MH101218, R41MH100895, R01MH100561), and DARPA under contract numbers W91NF-14-1-0269 and SIMPLEX N66001-15-C-4032. This material is based upon work supported by, or in part by, the U.S. Army Research Laboratory and the U.S. Army Research Office under contract number W911NF-12-1-0594 (MURI). The authors thank Yeonsook Shin for virus injection of the mice.

Received: April 7, 2015

Revised: July 28, 2015

Accepted: December 7, 2015

Published: January 7, 2016

### REFERENCES

Ahrens, M.B., Orger, M.B., Robson, D.N., Li, J.M., and Keller, P.J. (2013). Whole-brain functional imaging at cellular resolution using light-sheet microscopy. *Nat. Methods* *10*, 413–420.

Alivisatos, A.P., Chun, M., Church, G.M., Greenspan, R.J., Roukes, M.L., and Yuste, R. (2012). The Brain Activity Map Project and the challenge of functional connectomics. *Neuron* *74*, 970–974.

Alivisatos, A.P., Andrews, A.M., Boyden, E.S., Chun, M., Church, G.M., Deisseroth, K., Donoghue, J.P., Fraser, S.E., Lippincott-Schwartz, J.,

Looger, L.L., et al. (2013a). Nanotools for neuroscience and brain activity mapping. *ACS Nano* *7*, 1850–1866.

Alivisatos, A.P., Chun, M., Church, G.M., Deisseroth, K., Donoghue, J.P., Greenspan, R.J., McEuen, P.L., Roukes, M.L., Sejnowski, T.J., Weiss, P.S., and Yuste, R. (2013b). The Brain Activity Map. *Science* *339*, 1284–1285.

Andresen, V., Egnér, A., and Hell, S.W. (2001). Time-multiplexed multifocal multiphoton microscope. *Opt. Lett.* *26*, 75–77.

Anselmi, F., Ventalon, C., Bègue, A., Ogden, D., and Emiliani, V. (2011). Three-dimensional imaging and photostimulation by remote-focusing and holographic light patterning. *Proc. Natl. Acad. Sci. USA* *108*, 19504–19509.

Bahlmann, K., So, P.T.C., Kirber, M., Reich, R., Kosicki, B., McGonagle, W., and Belve, K. (2007). Multifocal multiphoton microscopy (MMM) at a frame rate beyond 600 Hz. *Opt. Express* *15*, 10991–10998.

Beaurepaire, E., and Mertz, J. (2002). Epifluorescence collection in two-photon microscopy. *Appl. Opt.* *41*, 5376–5382.

Bewersdorf, J., Pick, R., and Hell, S.W. (1998). Multifocal multiphoton microscopy. *Opt. Lett.* *23*, 655–657.

Botcherby, E.J., Juskaitis, R., and Wilson, T. (2006). Scanning two photon fluorescence microscopy with extended depth of field. *Opt. Commun.* *268*, 253–260.

Botcherby, E.J., Smith, C.W., Kohl, M.M., Débarre, D., Booth, M.J., Juskaitis, R., Paulsen, O., and Wilson, T. (2012). Aberration-free three-dimensional multiphoton imaging of neuronal activity at kHz rates. *Proc. Natl. Acad. Sci. USA* *109*, 2919–2924.

Bouchard, M.B., Voleti, V., Mendes, C.S., Lacefield, C., Grueber, W.B., Mann, R.S., Bruno, R.M., and Hillman, E.M.C. (2015). Swept confocally-aligned planar excitation (SCAPE) microscopy for high speed volumetric imaging of behaving organisms. *Nat. Photonics* *9*, 113–119.

Brainard, D.H. (1997). The Psychophysics Toolbox. *Spat. Vis.* *10*, 433–436.

Carriles, R., Sheetz, K.E., Hoover, E.E., Squier, J.A., and Barzda, V. (2008). Simultaneous multifocal, multiphoton, photon counting microscopy. *Opt. Express* *16*, 10364–10371.

Cha, J.W., Singh, V.R., Kim, K.H., Subramanian, J., Peng, Q., Yu, H., Nedivi, E., and So, P.T.C. (2014). Reassignment of scattered emission photons in multifocal multiphoton microscopy. *Sci. Rep.* *4*, 5153.

Chen, T.W., Wardill, T.J., Sun, Y., Pulver, S.R., Renninger, S.L., Baohan, A., Schreiter, E.R., Kerr, R.A., Orger, M.B., Jayaraman, V., et al. (2013). Ultrasensitive fluorescent proteins for imaging neuronal activity. *Nature* *499*, 295–300.

Cheng, A., Gonçalves, J.T., Golshani, P., Arisaka, K., and Portera-Cailliau, C. (2011). Simultaneous two-photon calcium imaging at different depths with spatiotemporal multiplexing. *Nat. Methods* *8*, 139–142.

Cotton, R.J., Froudarakis, E., Storer, P., Saggau, P., and Tolia, A.S. (2013). Three-dimensional mapping of microcircuit correlation structure. *Front. Neural Circuits* *7*, 151.

Dal Maschio, M., Difato, F., Beltramo, R., Blau, A., Benfenati, F., and Fellin, T. (2010). Simultaneous two-photon imaging and photo-stimulation with structured light illumination. *Opt. Express* *18*, 18720–18731.

Denk, W., Strickler, J.H., and Webb, W.W. (1990). Two-photon laser scanning fluorescence microscopy. *Science* *248*, 73–76.

Ducros, M., Goulam Houssen, Y., Bradley, J., de Sars, V., and Charpak, S. (2013). Encoded multisite two-photon microscopy. *Proc. Natl. Acad. Sci. USA* *110*, 13138–13143.

Duemani Reddy, G., Kelleher, K., Fink, R., and Saggau, P. (2008). Three-dimensional random access multiphoton microscopy for functional imaging of neuronal activity. *Nat. Neurosci.* *11*, 713–720.

Egnér, A., and Hell, S.W. (2000). Time multiplexing and parallelization in multifocal multiphoton microscopy. *J. Opt. Soc. Am. A Opt. Image Sci. Vis.* *17*, 1192–1201.

Fittinghoff, D., Wiseman, P., and Squier, J. (2000). Widefield multiphoton and temporally decorrelated multifocal multiphoton microscopy. *Opt. Express* *7*, 273–279.

- Fricke, M., and Nielsen, T. (2005). Two-dimensional imaging without scanning by multifocal multiphoton microscopy. *Appl. Opt.* *44*, 2984–2988.
- Grewe, B.F., Langer, D., Kasper, H., Kampa, B.M., and Helmchen, F. (2010). High-speed in vivo calcium imaging reveals neuronal network activity with near-millisecond precision. *Nat. Methods* *7*, 399–405.
- Grewe, B.F., Voigt, F.F., van 't Hoff, M., and Helmchen, F. (2011). Fast two-layer two-photon imaging of neuronal cell populations using an electrically tunable lens. *Biomed. Opt. Express* *2*, 2035–2046.
- Helmchen, F., and Denk, W. (2005). Deep tissue two-photon microscopy. *Nat. Methods* *2*, 932–940.
- Helmstaedter, M., Staiger, J.F., Sakmann, B., and Feldmeyer, D. (2008). Efficient recruitment of layer 2/3 interneurons by layer 4 input in single columns of rat somatosensory cortex. *J. Neurosci.* *28*, 8273–8284.
- Helmstaedter, M., Sakmann, B., and Feldmeyer, D. (2009). Neuronal correlates of local, lateral, and translaminar inhibition with reference to cortical columns. *Cereb. Cortex* *19*, 926–937.
- Huberman, A.D., and Niell, C.M. (2011). What can mice tell us about how vision works? *Trends Neurosci.* *34*, 464–473.
- Insel, T.R., Landis, S.C., and Collins, F.S. (2013). The NIH BRAIN Initiative. *Science* *340*, 687–688.
- Katona, G., Szalay, G., Maák, P., Kaszás, A., Veress, M., Hillier, D., Chiovini, B., Vizi, E.S., Roska, B., and Rózsa, B. (2012). Fast two-photon in vivo imaging with three-dimensional random-access scanning in large tissue volumes. *Nat. Methods* *9*, 201–208.
- Kim, K.H., Buehler, C., Bahlmann, K., Ragan, T., Lee, W.-C.A., Nedivi, E., Heffer, E.L., Fantini, S., and So, P.T.C. (2007). Multifocal multiphoton microscopy based on multianode photomultiplier tubes. *Opt. Express* *15*, 11658–11678.
- Kirkby, P.A., Nadella, K.M.N.S., and Silver, R.A. (2010). A compact acousto-optic lens for 2D and 3D femtosecond based 2-photon microscopy. *Optics Express* *18*, 13720–13744.
- Kong, L., Tang, J., Little, J.P., Yu, Y., Lämmermann, T., Lin, C.P., Germain, R.N., and Cui, M. (2015). Continuous volumetric imaging via an optical phase-locked ultrasound lens. *Nat. Methods* *12*, 759–762.
- London, M., and Häusser, M. (2005). Dendritic computation. *Annu. Rev. Neurosci.* *28*, 503–532.
- Maruyama, R., Maeda, K., Moroda, H., Kato, I., Inoue, M., Miyakawa, H., and Aonishi, T. (2014). Detecting cells using non-negative matrix factorization on calcium imaging data. *Neural Netw.* *55*, 11–19.
- Matsumoto, N., Okazaki, S., Fukushi, Y., Takamoto, H., Inoue, T., and Terakawa, S. (2014). An adaptive approach for uniform scanning in multifocal multiphoton microscopy with a spatial light modulator. *Opt. Express* *22*, 633–645.
- Mazurek, M., Kager, M., and Van Hooser, S.D. (2014). Robust quantification of orientation selectivity and direction selectivity. *Front. Neural Circuits* *8*, 92.
- Meyer, H.S., Schwarz, D., Wimmer, V.C., Schmitt, A.C., Kerr, J.N.D., Sakmann, B., and Helmstaedter, M. (2011). Inhibitory interneurons in a cortical column form hot zones of inhibition in layers 2 and 5A. *Proc. Natl. Acad. Sci. USA* *108*, 16807–16812.
- Mukamel, E.A., Nimmerjahn, A., and Schnitzer, M.J. (2009). Automated analysis of cellular signals from large-scale calcium imaging data. *Neuron* *63*, 747–760.
- Niell, C.M., and Stryker, M.P. (2008). Highly selective receptive fields in mouse visual cortex. *J. Neurosci.* *28*, 7520–7536.
- Nikolenko, V., Watson, B.O., Araya, R., Woodruff, A., Peterka, D.S., and Yuste, R. (2008). SLM microscopy: scanless two-photon imaging and photostimulation with spatial light modulators. *Front. Neural Circuits* *2*, 5.
- Otsu, Y., Bormuth, V., Wong, J., Mathieu, B., Dugué, G.P., Feltz, A., and Diudonné, S. (2008). Optical monitoring of neuronal activity at high frame rate with a digital random-access multiphoton (RAMP) microscope. *J. Neurosci. Methods* *173*, 259–270.
- Packer, A.M., Peterka, D.S., Hirtz, J.J., Prakash, R., Deisseroth, K., and Yuste, R. (2012). Two-photon optogenetics of dendritic spines and neural circuits. *Nat. Methods* *9*, 1202–1205.
- Packer, A.M., Russell, L.E., Dagleish, H.W.P., and Häusser, M. (2015). Simultaneous all-optical manipulation and recording of neural circuit activity with cellular resolution in vivo. *Nat. Methods* *12*, 140–146.
- Pnevmatikakis, E.A., Soudry, D., Gao, Y., Machado, T.A., Merel, J., Pfau, D., Reardon, T., Mu, Y., Lacefield, C., Yang, W., et al. (2016). Simultaneous denoising, deconvolution, and demixing of calcium imaging data. *Neuron* *89*, this issue, 285–299.
- Pologruto, T.A., Sabatini, B.L., and Svoboda, K. (2003). ScanImage: flexible software for operating laser scanning microscopes. *Biomed. Eng. Online* *2*, 13.
- Prevedel, R., Yoon, Y.-G., Hoffmann, M., Pak, N., Wetzstein, G., Kato, S., Schrödel, T., Raskar, R., Zimmer, M., Boyden, E.S., and Vaziri, A. (2014). Simultaneous whole-animal 3D imaging of neuronal activity using light-field microscopy. *Nat. Methods* *11*, 727–730.
- Quirin, S., Peterka, D.S., and Yuste, R. (2013). Instantaneous three-dimensional sensing using spatial light modulator illumination with extended depth of field imaging. *Opt. Express* *21*, 16007–16021.
- Quirin, S., Jackson, J., Peterka, D.S., and Yuste, R. (2014). Simultaneous imaging of neural activity in three dimensions. *Front. Neural Circuits* *8*, 29.
- Rickgauer, J.P., Deisseroth, K., and Tank, D.W. (2014). Simultaneous cellular-resolution optical perturbation and imaging of place cell firing fields. *Nat. Neurosci.* *17*, 1816–1824.
- Rocheffort, N.L., Narushima, M., Grienberger, C., Marandi, N., Hill, D.N., and Konnerth, A. (2011). Development of direction selectivity in mouse cortical neurons. *Neuron* *71*, 425–432.
- Schmidt, J.D. (2010). *Numerical Simulation of Optical Wave Propagation with Examples in MATLAB* (SPIE Press).
- Shai, A.S., Anastassiou, C.A., Larkum, M.E., and Koch, C. (2015). Physiology of layer 5 pyramidal neurons in mouse primary visual cortex: coincidence detection through bursting. *PLoS Comput. Biol.* *11*, e1004090.
- Thalhammer, G., Bowman, R.W., Love, G.D., Padgett, M.J., and Ritsch-Marte, M. (2013). Speeding up liquid crystal SLMs using overdrive with phase change reduction. *Opt. Express* *21*, 1779–1797.
- Thériault, G., Cottet, M., Castonguay, A., McCarthy, N., and De Koninck, Y. (2014). Extended two-photon microscopy in live samples with Bessel beams: steadier focus, faster volume scans, and simpler stereoscopic imaging. *Front. Cell. Neurosci.* *8*, 139.
- Thévenaz, P., Ruttimann, U.E., and Unser, M. (1998). A pyramid approach to subpixel registration based on intensity. *IEEE Trans. Image Process.* *7*, 27–41.
- Vogelstein, J.T., Watson, B.O., Packer, A.M., Yuste, R., Jedynak, B., and Paninski, L. (2009). Spike inference from calcium imaging using sequential Monte Carlo methods. *Biophys. J.* *97*, 636–655.
- Vogelstein, J.T., Packer, A.M., Machado, T.A., Sippy, T., Babadi, B., Yuste, R., and Paninski, L. (2010). Fast nonnegative deconvolution for spike train inference from population calcium imaging. *J. Neurophysiol.* *104*, 3691–3704.
- Watson, B.O., Nikolenko, V., and Yuste, R. (2009). Two-photon imaging with diffractive optical elements. *Front. Neural Circuits* *3*, 6.
- Williams, R.M., Zipfel, W.R., and Webb, W.W. (2001). Multiphoton microscopy in biological research. *Curr. Opin. Chem. Biol.* *5*, 603–608.
- Yuste, R., and Katz, L.C. (1991). Control of postsynaptic Ca<sup>2+</sup> influx in developing neocortex by excitatory and inhibitory neurotransmitters. *Neuron* *6*, 333–344.
- Zipfel, W.R., Williams, R.M., and Webb, W.W. (2003). Nonlinear magic: multiphoton microscopy in the biosciences. *Nat. Biotechnol.* *21*, 1369–1377.

# Mapping Sub-Second Structure in Mouse Behavior

Alexander B. Wiltschko,<sup>1,2</sup> Matthew J. Johnson,<sup>1,2</sup> Giuliano Iurilli,<sup>1</sup> Ralph E. Peterson,<sup>1</sup> Jesse M. Katon,<sup>1</sup> Stan L. Pashkovski,<sup>1</sup> Victoria E. Abraira,<sup>1</sup> Ryan P. Adams,<sup>2</sup> and Sandeep Robert Datta<sup>1,\*</sup>

<sup>1</sup>Department of Neurobiology, Harvard Medical School, Boston, MA 02115, USA

<sup>2</sup>School of Engineering and Applied Sciences, Harvard University, Cambridge, MA 02138, USA

\*Correspondence: [srdatta@hms.harvard.edu](mailto:srdatta@hms.harvard.edu)

<http://dx.doi.org/10.1016/j.neuron.2015.11.031>

## SUMMARY

Complex animal behaviors are likely built from simpler modules, but their systematic identification in mammals remains a significant challenge. Here we use depth imaging to show that 3D mouse pose dynamics are structured at the sub-second time-scale. Computational modeling of these fast dynamics effectively describes mouse behavior as a series of reused and stereotyped modules with defined transition probabilities. We demonstrate this combined 3D imaging and machine learning method can be used to unmask potential strategies employed by the brain to adapt to the environment, to capture both predicted and previously hidden phenotypes caused by genetic or neural manipulations, and to systematically expose the global structure of behavior within an experiment. This work reveals that mouse body language is built from identifiable components and is organized in a predictable fashion; deciphering this language establishes an objective framework for characterizing the influence of environmental cues, genes and neural activity on behavior.

## INTRODUCTION

Innate behaviors are sculpted by evolution into stereotyped forms that enable animals to accomplish particular goals (such as exploring or avoiding a predator). Ultimately understanding how neural circuits create these patterned behaviors requires a clear framework for characterizing how behavior is organized and evolves over time. One conceptual approach to addressing this challenge arises from ethology, which proposes that the brain builds coherent behaviors by expressing stereotyped modules of simpler action in specific sequences (Tinbergen, 1951).

Although behavioral modules have traditionally been identified, one at a time, through careful human observation, recent technical advances have enabled more comprehensive characterization of the components of behavior. For example, in invertebrates, behavioral modules and their associated transition probabilities can now be discovered systematically through automated machine vision, clustering, and classification algorithms (Berman et al., 2014; Croll, 1975; Garrity et al., 2010; Ste-

phens et al., 2008, 2010; Vogelstein et al., 2014). Furthermore, identifying behavioral modules and transition probabilities has uncovered context-specific strategies used by invertebrate brains to adapt behavior to changes in the environment, which include both the emission of new behavioral modules (such as when the animal switches from “exploring” to “mating”) and the generation of new behaviors through re-sequencing existing modules. In *C. elegans*, for example, neural circuits that respond to appetitive cues alter transition probabilities between a core set of locomotor-related behavioral modules, thereby creating new behavioral sequences that enable taxis toward attractive odorants (Gray et al., 2005; Pierce-Shimomura et al., 1999). Similar observations have been made for sensory-driven behaviors in fly larvae (Garrity et al., 2010).

Comparable systematic approaches to discovering behavioral modules have not yet been implemented in mice. Instead, traditional behavioral classification approaches have been instantiated in silico, enabling machine vision algorithms to replace tedious and unreliable human scoring of videotaped behavior (de Chaumont et al., 2012; Jhuang et al., 2010; Kabra et al., 2013; Weissbrod et al., 2013). These approaches are powerful and have been successfully used to quantify components of innate exploratory, grooming, approach, aggressive, and reproductive behaviors. However, because they depend upon the prior specification, by human observers, of what constitutes a meaningful behavioral module, the insight from these methods is bounded by human perception and intuition. Currently available approaches therefore focus on identifying a small number of pre-specified modules within a given experiment, rather than on discovering new behavioral modules (which potentially encapsulate novel patterns of action), describing the global structure of behavior, or predicting future actions based upon those in the past.

Systematically describing the structure of behavior in mice—and understanding how the brain alters that structure to enable adaptation—requires overcoming three challenges. First, it is not clear which features are important to measure when identifying candidate behavioral modules. Mice interact with the world by expressing complex 3D pose dynamics, but because these are difficult to capture, most current methods track 2D parameters such as the position, velocity, or 2D contour of the mouse (de Chaumont et al., 2012; Gomez-Marin et al., 2012; Jhuang et al., 2010; Kabra et al., 2013; Spink et al., 2001; but see Ouyang et al., 2011). Second, given that behavior evolves on many timescales in parallel, it is not clear how to objectively identify the relevant spatiotemporal scales at which to modularize behavior. Finally, even stereotyped modules of behavior exhibit

moment-to-moment and animal-to-animal variability (Colgan, 1978). This variability raises significant challenges for identifying the number and content of behavioral modules, and with associating observed actions with specific behavioral modules.

Here we describe a novel method, based upon recent advances in machine vision and learning, that identifies behavioral modules and their associated transition probabilities without human supervision. This approach uses 3D imaging to capture the pose dynamics of mice as they freely behave in a variety of experimental contexts; these data reveal a surprising regularity that appears to divide mouse behavior into recognizable behavioral motifs that are organized at the sub-second timescale. A computational model then takes advantage of the observed fast temporal structure to describe mouse behavior as a series of reused modules, each a brief and stereotyped 3D trajectory through pose space that is connected in time to other modules through predictable transitions. We use this combined 3D imaging/modeling approach to explore how the underlying structure of behavior is altered after distinct environmental, genetic, or neural manipulations and show that this method can detect both predicted changes in action and new features of behavior that had not been previously described. This work reveals that defining behavioral modules based upon structure in the 3D behavioral data itself—rather than using a priori definitions for what should constitute a measurable unit of action—can yield key information about the elements of behavior, offer insight into adaptive behavioral strategies used by mice, and enable discovery of subtle alterations in patterned action.

## RESULTS

### 3D Imaging Captures Inherent Structure in Mouse Pose Dynamics

We wished to develop a method that would allow unsupervised phenotyping of mice based upon patterns of 3D movement. However, it is not clear whether spontaneous behaviors exhibited by mice have a definable underlying structure that can be used to characterize action as it evolves over time. To ask whether such a structure might exist, we measured how the shape of a mouse's body changes as it freely explores a circular open field (Experimental Procedures). We used a single depth camera placed above the arena to capture these 3D pose dynamics and then extracted the image of the mouse from the arena; corrected imaging artifacts due to parallax effects; centered, and aligned the mouse along the inferred axis of its spine; and then quantified how the mouse's pose changed over time (Figures 1A and S1; Movie S1).

Plotting these 3D data over time revealed that mouse behavior is characterized by periods during which pose dynamics evolve slowly, punctuated by fast transitions that separate these periods; this pattern appears to divide the behavioral imaging data into blocks typically lasting 200–900 ms (Figures 1B and S2A). This temporal structure is apparent in the raw imaging pixels (Figure 1B, top), in the inferred shape of the mouse's spine (Figure 1B, middle), and in dimensionally reduced data that randomly samples from the depth images on the sensor (Figure 1B, bottom; see Supplemental Experimental Procedures). This structure is absent in data acquired from anesthetized or

dead mice but is present for the entire duration of each experiment in the pose dynamics data of mice exploring behavioral arenas of different shapes and after exposure to a wide variety of sensory cues, suggesting that it is a fundamental and ubiquitous feature of mouse behavior (data not shown; Figure S2).

To characterize this fast temporal structure, we performed three separate quantitative analyses. First, approximate boundaries between blocks in the behavioral imaging data were identified by a changepoints algorithm, which revealed that the mean block duration was about 350 ms, roughly matching the timescale of the blocks apparent upon visual inspection (Figures 1B and 1C; Supplemental Experimental Procedures). Second, we performed temporal autocorrelation analysis on the pose dynamics data, which demonstrated that autocorrelation in the mouse's pose largely dissipated after 400 ms ( $\tau = 340 \pm 58$  ms, Figures 1C and S2B). This pattern of autocorrelation reflects specific behavioral dynamics organized at sub-second timescales, as it was destroyed by shuffling the behavioral data at timescales of 500 ms or less, and was not observed in synthetic mouse behavioral data designed to evolve with either random walk or Levy flight characteristics (Figures 1C and S2C). Third, we used a Wiener filter analysis to compare power spectral densities taken from live and dead mice; this approach identifies frequencies that must be changed in imaging data taken from a dead mouse to match the power spectrum of a live mouse. Nearly all of the frequency content differentiating behaving from dead mice was concentrated between 1 and 6 Hz (measured by spectrum ratio, mean  $3.75 \pm 0.56$  Hz, Figures 1C and S2B). Taken together, the qualitative appearance of block structure in the pose dynamics data, along with the convergent results obtained with these three quantitative analyses, demonstrate that mouse pose dynamics exhibit structure at the sub-second timescale.

The observed temporal structure within the pose dynamics data suggests a timescale at which continuous behavior may be naturally segmented into meaningful components, as visual inspection of 3D movies revealed that each of the sub-second blocks of behavior appears to encode a recognizable action (e.g., a dart, a pause, the first half of a rear; see Movie S2). To explore the possibility that these sub-second actions are stereotyped (and therefore reproducibly performed at different times during an experiment), the 3D mouse imaging data was subjected to wavelet decomposition followed by principal-component analysis (PCA), which transformed each block in the pose dynamics data into a continuous trajectory through principal component (PC) space (Figures 1D). By scanning the behavioral data using a template matching method (using Euclidean distance among the first 10 PCs, which explain 88% of the data variance) (Figure S2D), additional instances were identified in which each template action was reused (Figure 1D; Supplemental Experimental Procedures; see Figure S3 for additional examples). These anecdotal observations suggest that mice create complex behaviors through the serial expression of stereotyped and reused behavioral modules (Tinbergen, 1951).

### Mouse Behavior Can Be Described and Predicted with Modules and Transitions

Although our analysis suggests a timescale at which behavioral modules might exist, and qualitative inspection of 3D video

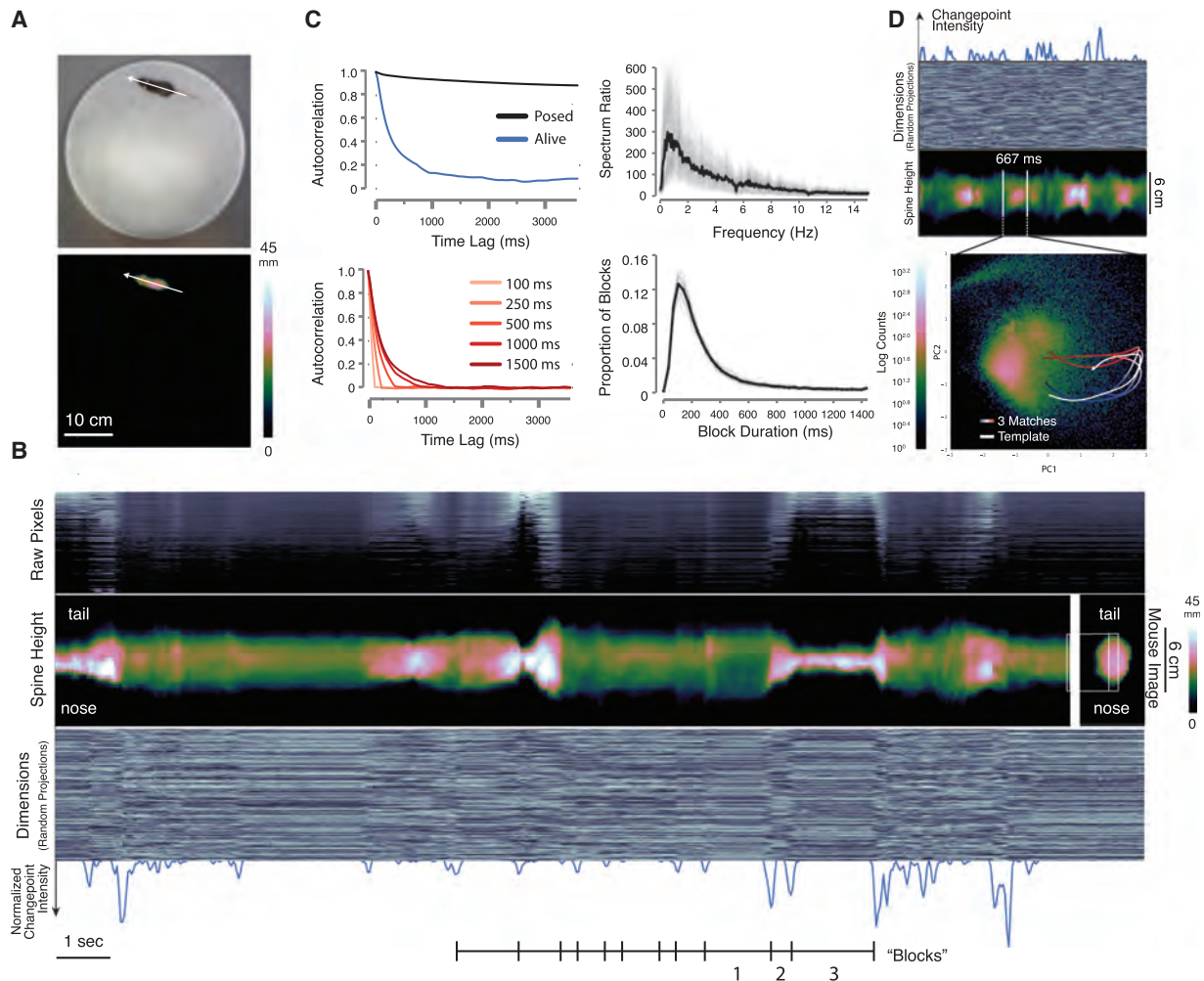


### Figure 1. Depth Imaging Reveals Block Structure in 3D Mouse Pose Dynamics Data

(A) Mouse imaged in the circular open field with a standard RGB (top) and 3D depth camera (bottom, mm = mm above floor). Arrow indicates the inferred axis of the animal's spine.

(B) Raw pixels of the extracted and aligned 3D mouse image (top panel, sorted by mean height), compressed data (bottom panel, 300 dimensions compressed via random projections arrayed on the y axis, pixel brightness proportional to its value), and height at each inferred position of the mouse's spine (middle panel, "spine" data extracted from the mouse as indicated on the right, mm = mm above floor) each reveal sporadic, sharp transitions in the pose data over time. Note that the cross-sectional profile of the spine with respect to the camera varies depending upon the morphology of the mouse; when reared, this profile becomes smaller, and when on all fours, it becomes larger. Changepoints analysis (bottom panel, blue trace = normalized changepoint probability) identifies approximate boundaries between blocks. Blocks encode a variety of behaviors including locomotion (1), a pointing rear with the mouse's body elongated with respect to the sensor (2), and a true rear (3).

(C) Upper left: Autocorrelation analysis performed on the top ten principal components (PCs) of the pose dynamics data reveals that temporal correlation in the mouse's pose stabilizes after about 400 ms ( $\tau = 340 \pm 58$  ms).

(C) Lower left: Shuffling behavioral data in blocks of 500 ms or shorter destroys autocorrelation structure (shuffle block size indicated).

(C) Upper right: Spectral power ratio between behaving and dead mice (mean plotted in black, individual mice plotted in gray) reveals most frequency content is represented between 1 and 6 Hz (mean =  $3.75 \pm 0.56$  Hz).

(C) Lower right: Changepoints-identified block duration distribution (mean = 358 ms, SD 495 ms, mean plotted in black, individual mice in gray,  $n = 25$  mice, 500 total min imaging).

(D) Projecting mouse pose data (top panels, random projections and spine data depicted as in [B] into PC space [bottom]) reveals that blocks of pose data encode reused trajectories (density of all recorded poses colormapped behind trajectories). Tracing out the path associated with a block highlighted by changepoint detection (top) identifies a trajectory through PC space (white). Similar trajectories identified through template matching (time indicated as progression from blue to red) are superimposed. Note that this procedure uses the first ten PCs to identify matched trajectories, although only the first two PCs are depicted here.

and PCA trajectories is consistent with the possibility that sub-second blocks of behavior correspond to reused modules, current methods do not allow for the systematic identification of

candidate behavioral modules in mice. Indeed, available approaches neither reveal whether dividing behavior into modules actually helps to explain the overall structure of behavior nor

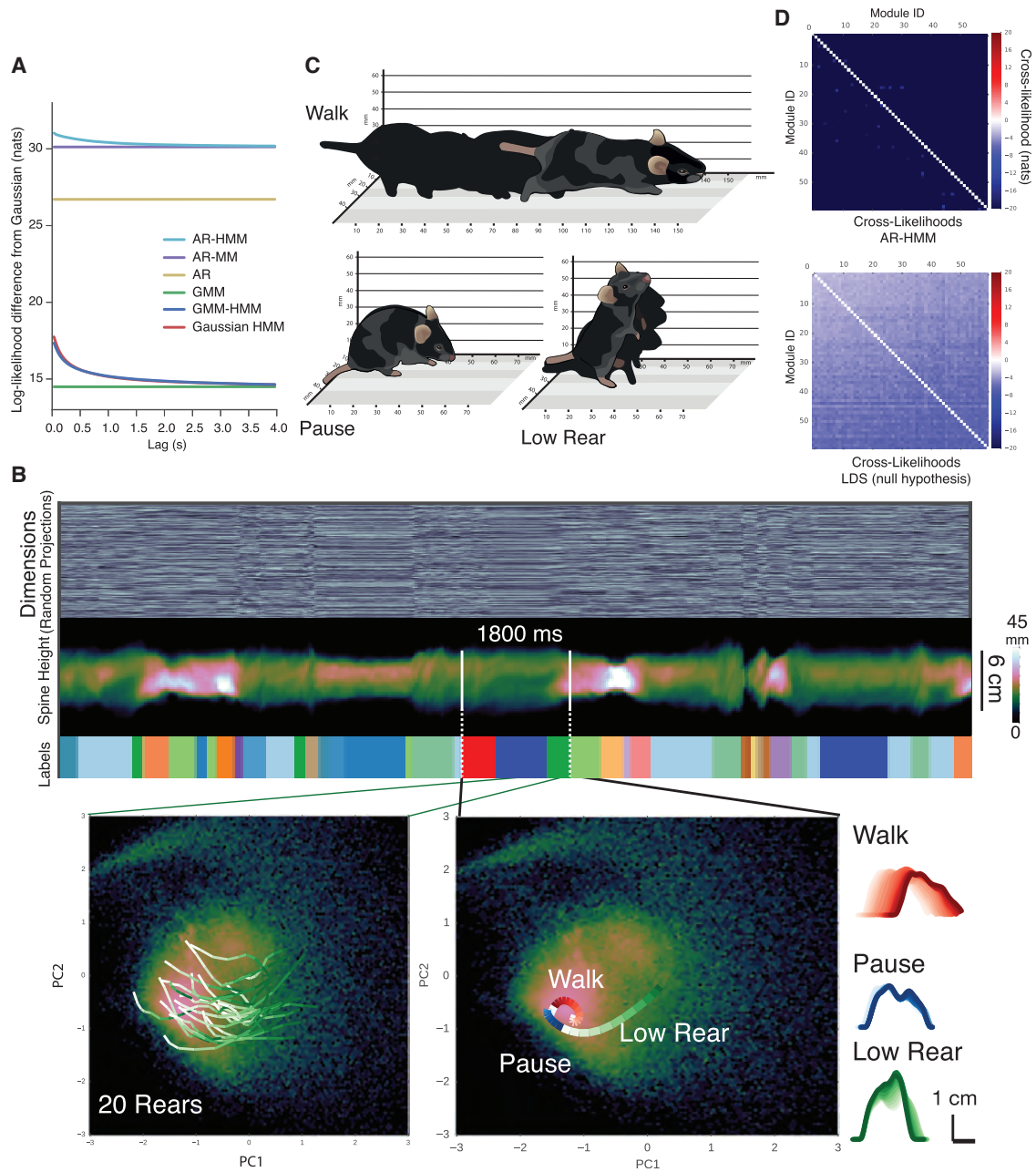


**Figure 2. Reused Behavioral Modules within Mouse Pose Dynamics Data**

(A) Predictive performance comparison of computational models describing possible structures for behavior (details of each model and the comparison metric provided in Supplemental Experimental Procedures). Models range from a Gaussian model (which proposes that mouse behavior is built from modules, each a single Gaussian in pose space) to an AR-HMM (which proposes that mouse behavior is built from modules, each of which encodes an autoregressive trajectory through pose space, and which transition from one to another with definable transition statistics; AR-MM, autoregressive mixture model; AR, autoregressive model; GMM, Gaussian mixture model; GMM-HMM, GMM hidden Markov model; Gaussian HMM, Gaussian hidden Markov model). Model performance plotted as the log likelihood (y axis) ascribed to held-out test data at some time lag (x axis) into the future (after subtracting Gaussian model performance).

(B) The AR-HMM parses behavioral data into identifiable modules (top panels—marked “labels,” each module is uniquely color coded). Multiple data instances associated with a single behavioral module (encoding a rear) each take a stereotyped trajectory through PC space (bottom left, trajectories progress from white to green over time, see Movie S4); multiple trajectories define behavioral sequences (bottom center, see Movie S6). Each trajectory within a sequence encodes a different elemental action (side-on view of the mouse calculated from depth data, bottom right, time indicated as increasingly darker lines, from module start to end).

*(legend continued on next page)*

identify the most likely number of modules expressed within any given dataset, or the content and durations of those modules.

To address these issues, we built a family of computational models, each of which proposes a unique underlying structure for behavior, and asked which of these models best predicts the pose dynamics of freely behaving mice (Figures 2A and S4); we reasoned that the model that most closely fit behavioral data (to which the model had not been exposed) would reveal key features of the underlying organization of behavior and could be used to characterize its components. After pre-processing the imaging data, the top ten PCs of the data (Figure S4E) were used to fit each model; this use of PCs (which directly reflect the pixel data) as a basis for modeling minimized potential biases from feature engineering. Models were fit using Bayesian nonparametric and Markov Chain Monte Carlo techniques that can automatically identify structure within large datasets, including the optimal state number for a given dataset and model (see Supplemental Experimental Procedures; Figure S4). Each model was trained on one set of pose dynamics data and then tested for its ability to explain a separate set of held-out data, a metric canonically used to compare unsupervised learning models (Hastie et al., 2009).

Our simplest model proposed that each behavioral module is a single fixed pose with no defined transition probabilities between the modules. We iteratively added structure to build increasingly complex models, which incorporated modules with more elaborate internal structures (ranging from mixtures of poses to smooth pose trajectories), allowed predictable transitions between specific modules (by embedding the modules within a Markov model), or both (Figure S4). Where relevant, the fitting procedures were explicitly focused to search for behavioral modules at the sub-second timescale matching the temporal structure identified using our model-free methods; this approach provided an important—and previously unavailable—constraint, given the multiple possible timescales upon which behavior evolves simultaneously.

The model that best fit previously unseen behavioral data describes mouse behavior as a sequence of modules (each capturing a brief motif of 3D body motion) that switch from one to another at the sub-second timescale identified by our model-free analysis of pose dynamics (Figures 2A and S4D; Supplemental Experimental Procedures). We refer to this model as an AR-HMM, as each behavioral module was modeled as a vector autoregressive (AR) process capturing a stereotyped trajectory through pose space, and the switching dynamics between different modules were modeled using a hidden Markov model (HMM). In other words, the model is a hierarchical description of behavior, with the “internals” of each module reflecting the mouse’s pose dynamics over short timescales, and the longer-timescale relationships between behavioral modules (i.e., the possible module sequences) governed by the transition probabilities specified by an HMM (Figures S4B and S4C). The observation that the AR-HMM outperforms alternative models

(Figure 2A) demonstrates that modularity and transition structure at fast timescales are critical for describing mouse behavior, a key prediction from ethology.

### Model-Identified Behavioral Modules Are Stereotyped and Distinct

The AR-HMM systematically identifies modules and their transition probabilities from behavioral data without human supervision; this suggests that the AR-HMM can be used to identify behavioral modules and their associated transition probabilities—and thereby expose the underlying structure of behavior—in a wide variety of experimental contexts. We therefore performed a series of control analyses to establish whether the AR-HMM can indeed reliably identify behavioral modules encoding repeatedly used and stereotyped motifs of distinguishable behavior that are organized at sub-second timescales.

Although the AR-HMM is tuned to identify modules at a particular timescale, it is possible that after training the model could fail to effectively capture temporal structure in behavior. However, the AR-HMM successfully identified modules at the fast behavioral timescale defined by the model-free methods, as the distribution of module durations was similar to the duration distribution for changepoints-identified blocks (Figure S5A). Importantly, the ability of the AR-HMM to identify behavioral modules depended upon the inherent sub-second organization of mouse pose data, as shuffling the behavioral data in small chunks (i.e., <500 ms) substantially degraded model performance, whereas shuffling the data in bigger chunks had little effect (Figure S5B).

We then asked whether model-identified modules encode repeatedly used and stereotyped motifs of behavior. The pose trajectories associated with a specific model-identified behavioral module took similar paths through PC space, and visual inspection of the 3D movies associated with multiple instances of this module revealed they all encoded a stereotyped rearing behavior (Figure 2B and 2C; Movie S3). In contrast, data instances drawn from different behavioral modules traced distinct (and stereotyped) paths through PC space (Figure 2B; see Figure S5C for additional examples). Furthermore, visual inspection of the 3D movies assigned to different modules reveals that each encoded a coherent pattern of 3D motion that post hoc can be distinguished and labeled with descriptors (see Movie S4 for “walk,” “pause,” and “low rear” modules depicted in Figure 2C, as well as additional examples).

The modules identified by the AR-HMM are distinct from each other, as a cross-likelihood analysis demonstrated that the imaging data associated with a given module are best assigned to that module, and not to any of the other behavioral modules (Figure 2D; Supplemental Experimental Procedures). In contrast, the AR-HMM failed to identify any well-separated modules in a synthetic mouse behavioral dataset that lacks modularity but otherwise matches all multidimensional and intertemporal correlations of the real data, demonstrating that the AR-HMM does not discover modularity where none exists (Figure 2D).

(C) Isometric-view illustrations of the 3D imaging data associated with walk, pause, and low rear modules (also see Movie S4).

(D) Cross-likelihood analysis depicting the likelihood that a data instance assigned to a particular module is well-modeled by another module. Cross-likelihoods were computed for the open field dataset (above, see Supplemental Experimental Procedures, units are nats, where  $e^{\text{nats}}$  is the likelihood ratio) and for module-free synthetic data whose autocorrelation structure matches actual mouse data (below).

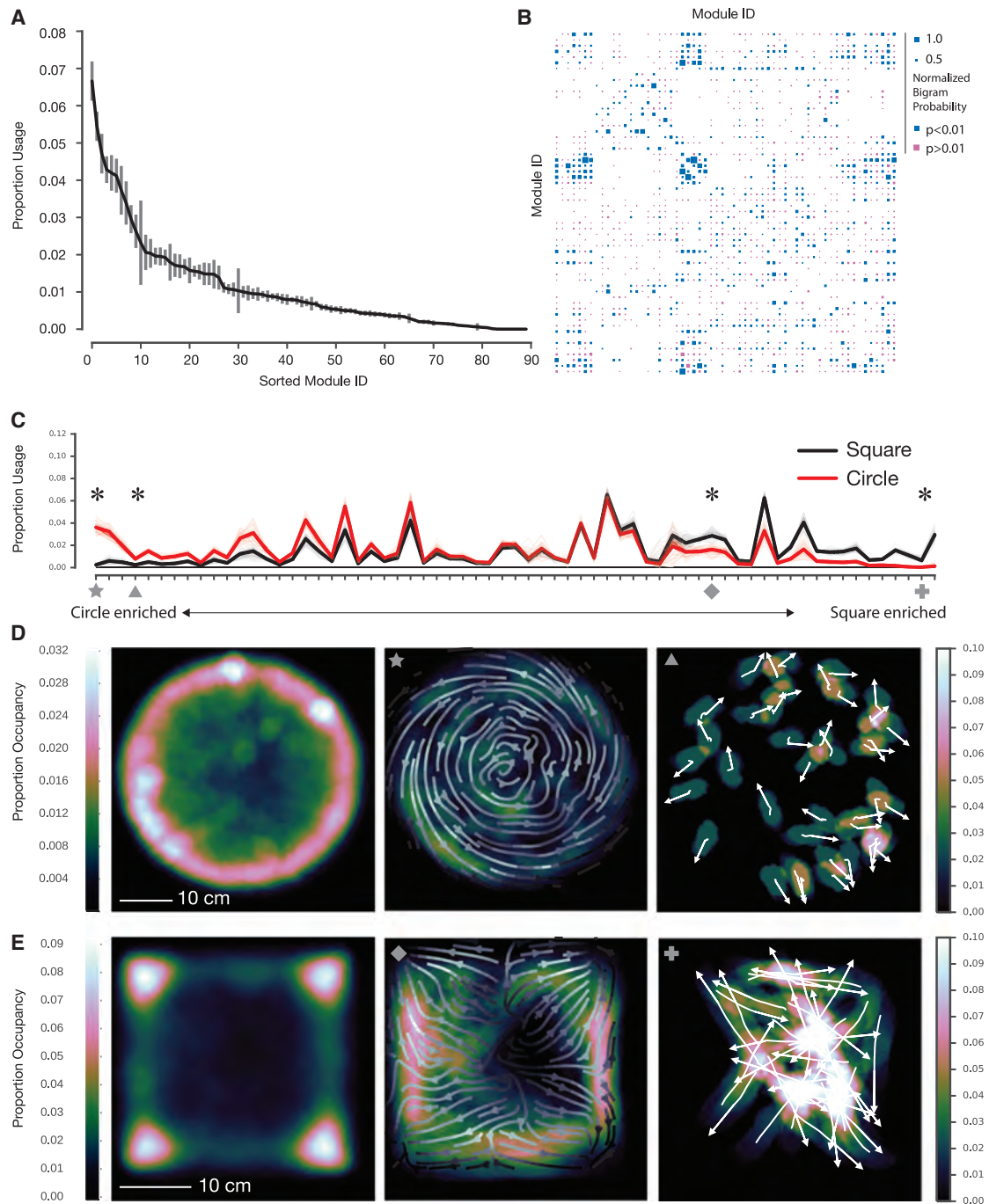


### Figure 3. The Physical Environment Influences Module Usage and Spatial Pattern of Expression

(A) Modules identified by the AR-HMM, sorted by usage ( $n = 25$  mice, 20 min per mouse, data from circular open field, error bars are SEs calculated using bootstrap estimation,  $n = 100$  bootstrap estimates, see Figure S5E for Bayesian credible intervals).

(B) Hinton diagram depicting the probability that any pair of modules is observed as an ordered pair ( $p$  values calculated via bootstrap estimation and color coded); modules were sorted by spectral clustering to emphasize neighborhood structure.

(C) Module usage, sorted by context (with “circleness” on left, overall usages differ significantly,  $p < 10^{-15}$ , Hotelling two-sample t-squared test, see Supplemental Experimental Procedures for sorting details). Mean usages across animals depicted with dark lines, with bootstrap estimates depicted in fainter lines ( $n = 100$ ). Marked modules discussed in main text and shown in (D): star, circular wall-hugging locomotion (“thigmotaxis”); triangle, outward-facing rears; diamond, square thigmotaxis; cross, square dart; see Movie S7. Usage for all marked modules significantly modulated by context (indicated by asterisk, Wald Test, Holm-Bonferroni adjusted  $p < 0.006$  for square dart, otherwise  $p < 10^{-5}$ ).

(legend continued on next page)

Furthermore, rerunning the AR-HMM training process from random starting points generated highly similar behavioral modules ( $R^2 = 0.94 \pm 0.03$ ,  $n = 15$  restarts, Supplemental Experimental Procedures); in comparison, models with lower held-out likelihood scores had lower consistency ( $R^2 < 0.4$ ), suggesting that these alternatives fail to reliably identify underlying structure in behavior. The AR-HMM output was also robust to the specific training data used, as models created from subsets of a larger dataset representing a single experiment were highly similar to each other ( $R^2 > 0.9$ ). These findings demonstrate that the AR-HMM converges on a consistent set of behavioral modules regardless of the specific training data (within a given experiment) or how the model is initialized.

Finally, the modules of behavior and the associated transition probabilities identified by the AR-HMM appear to fully capture the richness of mouse behavior, as a 3D movie of a behaving mouse generated by a trained AR-HMM was qualitatively difficult to distinguish from a 3D movie of behavior exhibited by a real animal (Movie S5; Figure S4E); in contrast, movies generated by more poorly performing models appeared discontinuous and were easily distinguished from actual mice (data not shown). Taken together with our model-free and model-based analyses and controls, the observation that after training our model can synthesize a convincing replica of 3D mouse behavior from learned modules and transition probabilities is consistent with the hypothesis that mouse behavior is organized into distinct sub-second modules that are combined to create coherent patterns of action.

### Using the AR-HMM to Characterize Baseline Patterns of Behavior

The AR-HMM identifies two key features of mouse behavior (from the perspective of 3D pose dynamics): which behavioral modules are expressed during behavior and how those modules transition into each other over time to create action. The AR-HMM identified  $\sim 60$  reliably used behavioral modules from a circular open field dataset, which is representative of normal mouse exploratory behavior in the laboratory (51 modules explained 95 percent of imaging frames, and 65 modules explained 99 percent of imaging frames) (Figures 3A, S5D, and S5E; subjective categorization of the 51 most-used modules is shown in Figure S6A). These modules were connected to each other over time in a highly non-uniform manner, with each module preferentially linked to some modules and not others (Figures 3B and S5F; average node degree after thresholding transitions that occur with  $<5\%$  probability,  $4.08 \pm 0.10$ ). This specific transition pattern among modules constrained the module sequences observed in the dataset ( $\sim 17,000 \sim 75,000$  possible sequences of three modules [“trigrams”] given the total data size), demonstrating that certain module sequences were favored over others and that mouse behavior is therefore predictable (per frame en-

tropy rate without self-transitions  $3.78 \pm 0.03$  bits, with self-transitions  $0.72 \pm 0.01$  bits, entropy rate in a uniform matrix  $6.02$  bits; average mutual information without self-transitions  $1.92 \pm 0.02$  bits, with self-transitions  $4.84$  bits  $\pm 0.03$  bits; see Movie S6 for multiple examples of the sequence of three modules depicted in Figure 2B). Note that while estimating coarse changes in specific trigram frequencies is possible, accurately estimating higher-order  $k$ -gram transition statistics is difficult, as the amount of data required grows exponentially with  $k$ . We therefore focus our analysis on lower-order statistics such as module usage frequencies and temporal interactions between pairs of modules.

### Using the AR-HMM to Characterize the Nature of Behavioral Change

We tested whether the AR-HMM could effectively capture changes in behavior (both predicted and unpredicted) elicited by a range of simple experimental interventions designed to probe the influence of the environment, genes, or neural circuit activity on behavior. We first asked how mice behavior adapts to changes in apparatus shape. We imaged mice within a small square box and then co-trained our model with both the circular open field and square box data, thereby enabling direct comparisons of modules and transitions under both conditions; the modules identified by this co-training procedure did not erroneously lump together data that would otherwise be distinguishable, as each behavioral module’s mean pose trajectory was stereotyped across the different experimental arenas (data not shown). Although mice tended to explore the corners of the square box and the walls of the circular open field, the overall usage of most modules was similar between these apparatuses, consistent with exploratory behavior sharing many common features across arenas (Figure 3C).

However, the AR-HMM also identified a small number of behavioral modules that were deployed selectively in just one context, suggesting that different physical environments drive expression of new behavioral modules (Figure 3C). For example, one circular arena-specific module encoded a behavior in which mice walk near the arena wall with a body posture that matches the curvature of the wall, while within the square box mice expressed a context-specific module that encodes a dart out of the center of the square (Figures 3D and 3E). Several behavioral modules were also differentially enriched (but not exclusively expressed) in one context or the other. In the circular arena, for example, mice preferentially executed a rear characterized by pointing outward while pausing near the center of the open field, whereas in the smaller square box mice preferentially expressed a high rear in the corners of the box (Figure 3D; data not shown).

These results demonstrate that the AR-HMM can effectively capture predictable changes in behavior resulting from altering the physical environment (like walking along a curved wall or

(D) Occupancy plot of mice in circular open field (left,  $n = 25$ , 500 min total) indicating cumulative spatial positions across all experiments. Occupancy plot depicting deployment of circular thigmotaxis module (middle, average orientation across the experiment indicated as arrow field) and circle-enriched outward-facing rear module (right, orientation of individual animals indicated with arrows).

(E) Occupancy plot of mice in square box (left,  $n = 15$ , 300 min total) indicating cumulative spatial positions across all experiments. Occupancy plot depicting a square-enriched thigmotaxis module (middle, average orientation across the experiment indicated as arrow field) and square-specific darting module (right, orientation of individual animals indicated with arrows).

rearing in a corner). Importantly, these results also demonstrate that the AR-HMM can unmask arena-specific patterns of behavior that are expressed in the center of both arenas, away from the physically constraining walls (like the darting across the center of the square box and the outward pointing behavior expressed in the circle); this surprisingly suggests that arena shape influences mouse behavior in a manner that extends significantly beyond the predictable changes in action at the walls themselves. Taken together, these experiments reveal that the AR-HMM can suggest strategies used by the mouse brain to adapt to new physical environments: in the case of a change in environmental geometry, this strategy includes the recruitment of a limited set of context-specific behavioral modules into baseline patterns of action, and a broad rewriting of where in space modules are expressed with respect to the arena boundaries.

The small number of behavioral modules distinguishing the circular and square arenas suggests only modest differences in the global pattern of behavior in these two experiments. To ask how the AR-HMM captures changes in the underlying structure of behavior after an overt change in behavioral state, we exposed mice to an ethologically relevant olfactory cue, the aversive fox odor trimethylthiazoline (TMT), which was delivered to one quadrant of the square box via an olfactometer. This odorant profoundly changes mouse behavior, inducing odor investigation, escape, and freezing behaviors that are accompanied by increases in corticosteroid and endogenous opioid levels (Fendt et al., 2005; Wallace and Rosen, 2000). Consistent with these known effects, mice sniffed the odor-containing quadrant and then avoided the quadrant containing the predator cue, displaying prolonged periods of immobility traditionally described as freezing behavior (Figure 4A and S6B).

Given that TMT-induced behaviors are dramatically different than those observed at baseline, one might predict that TMT should induce new behavioral modules that underlie the generation of these new actions. Surprisingly, the AR-HMM revealed that the TMT-induced suite of new behaviors was best explained by the same set of behavioral modules that were expressed during normal exploration; several modules were upregulated or downregulated after TMT exposure, but new modules were not introduced or eliminated relative to control (Figure 4B).

We therefore asked whether the changes in observed behavior were the consequence of altered connections between behavioral modules. Plotting the module transitions altered after exposure to TMT defined two neighborhoods within the behavioral statemap; the first included an expansive set of transitions that was modestly downregulated by TMT, and the second included a focused set of transitions that was upregulated by TMT (Figure 4C). Many of these newly interconnected modules encoded different forms of freezing behavior (average velocity  $0.14 \pm 0.54$  mm/s, for other modules  $34.7 \pm 53$  mm/s) (Movie S8; Figure S6B). In addition, the TMT-initiated modulation of transition probabilities altered the expression of specific behavioral sequences; for example, the most commonly observed sequence of three freezing modules was expressed 716 times after TMT exposure (in 300 min of imaging), as opposed to just 17 times under control conditions (in 480 min of imaging). The stimulus-evoked rewriting of transition probabilities was accom-

panied by an increase in the overall predictability of mouse behavior (per frame entropy rate fell from  $3.92 \pm 0.02$  bits to  $3.66 \pm 0.08$  bits without self-transitions, and from  $0.82 \pm 0.01$  bits to  $0.64 \pm 0.02$  bits with self-transitions) consistent with the mouse enacting an avoidance strategy that was more deterministic in nature than locomotor exploration.

Proximity to the odor source also governed the usage of specific behavioral modules (Figures 4D and 4E). For example, a set of freezing-related modules tended to be expressed in the quadrant most distant from the odor source, while the expression of an investigatory rearing module (whose overall usage was not altered by TMT) was specifically enriched within the odor quadrant (Figures 4D and 4E; Movie S9).

Although TMT is known to induce dramatic changes in behavior, it has not been possible to systematically identify those specific behavioral features altered in response to this odorant or to place those altered features in context with normal patterns of exploration. Analysis by the AR-HMM suggests that the strategy used by the mouse brain to adapt to the presence of TMT overlaps with—and yet is distinct from—that used to accommodate physical changes in the environment. As was true for a changed physical environment, exposure to TMT alters the spatial deployment of modules and sequences to support particular patterns of action; in contrast, the complete cohort of behaviors elicited by TMT, including seemingly “new” behaviors such as freezing, are the consequence of altered transition structure between individual modules. Behavioral modules are not, therefore, simply reused over time but instead act as flexibly interlinked components whose specific sequencing and deployment in space has profound consequences for the generation of adaptive behavior.

### Sub-Second Architecture of Behavior Reflects the Influence of Genes and Neural Activity

As described above, the AR-HMM shows the fine-timescale structure of behavior to be sensitive to persistent changes in the physical or sensory environment. However, manipulation of individual genes or neural circuits influences behavior across a range of spatiotemporal scales and with variable penetrance and reliability; these changes in behavior may or may not be effectively captured by a classification method designed to characterize the sub-second structure of action. We therefore directly asked whether the AR-HMM could systematically reveal the behavioral consequences of manipulating the mouse genome or activity within the nervous system.

To explore these possibilities, we first used the AR-HMM to characterize the phenotype of mice mutant for the retinoid-related orphan receptor  $1\beta$  (*Ror1\beta*) gene, which is expressed in neurons in the brain and spinal cord. This mouse was selected for analysis because adult homozygous mutant animals permanently exhibit abnormal gait, which would be expected to be observed during a brief open-field experiment (André et al., 1998; Eppig et al., 2015; Liu et al., 2013; Masana et al., 2007). Analysis with the AR-HMM revealed that littermate control mice are nearly indistinguishable from fully inbred C57/Bl6 mice, whereas homozygous mutant mice express a unique behavioral module encoding a waddling gait (Figure 5A and 5C; Movie S10; see Supplemental Experimental Procedures for

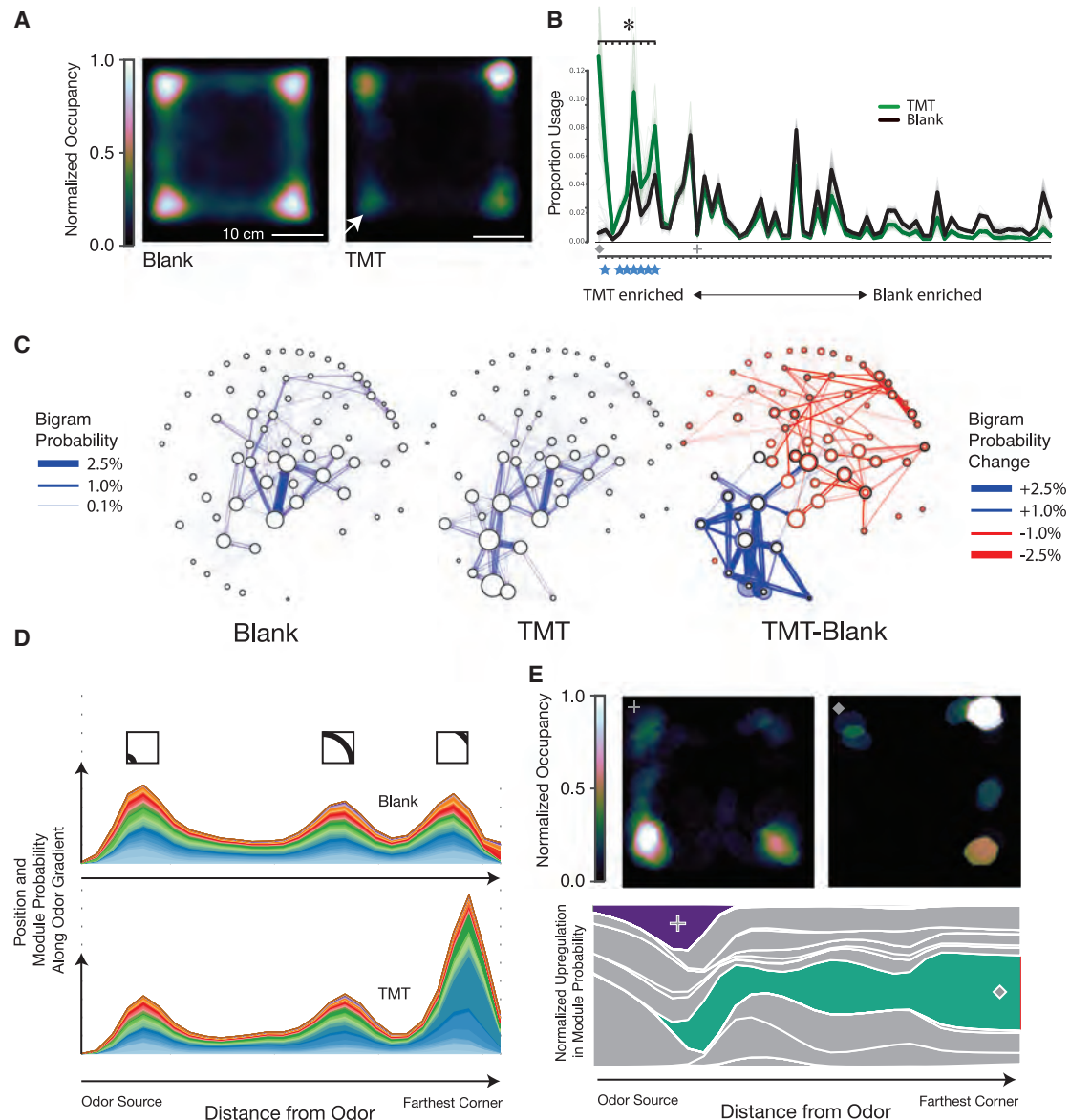


#### Figure 4. Odor-Driven Innate Avoidance Alters Transition Probabilities

(A) Occupancy plot of mice under control conditions ( $n = 24$ , 480 min total) and after exposure to the fox-derived odorant TMT (5% dilution,  $n = 15$ , 300 min total, model co-trained on both conditions) in the lower left quadrant (arrow). Plots normalized such that maximum occupancy = 1.

(B) Module usage plot sorted by “TMT-ness” (dark lines depict mean usages, bootstrap estimates depicted in fainter lines, sorting as in Figure 3). Marked modules discussed in main text and (E): cross, sniff in TMT quadrant; diamond, freeze away from TMT. See Movies S8 and S9. Blue stars indicate freezing events. Asterisk indicates statistically significant regulation (Wald test, Holm-Bonferroni corrected,  $p < 10^{-4}$ ).

(C) Left and middle: Behavioral state maps for mice exploring a square box before and after TMT exposure, with modules depicted as nodes (usage proportional to the diameter of each node), and bigram transition probabilities depicted as directional edges. Graph layout minimizes the length of edges and is seeded by spectral clustering to emphasize local structure.

(C) Right: Statemap depiction of the difference between blank and TMT. Usage differences are indicated by the newly sized colored circles (upregulation indicated in blue, downregulation indicated in red, previous usages in control conditions indicated in black). Altered bigram transition probabilities are indicated in the same color code; only those significant transition probabilities ( $p < 0.01$ ) are depicted.

(D) Mountain plot depicting the joint probability of module expression and spatial position, plotted with respect to the TMT corner (x axis); note that the “bump” two-thirds of the way across the graph occurs due to the two corners equidistant from the odor source (see inset for approximate position in square box, modules are color coded).

(E) Occupancy plot (upper) indicating spatial position at which mice after TMT exposure emit an investigatory sniffing module (left) or a pausing module (right, see Movie S8). Mountain plot (lower) indicating the differential deployment of these two modules (purple, green; other modules in gray) with respect to distance from the odor source.

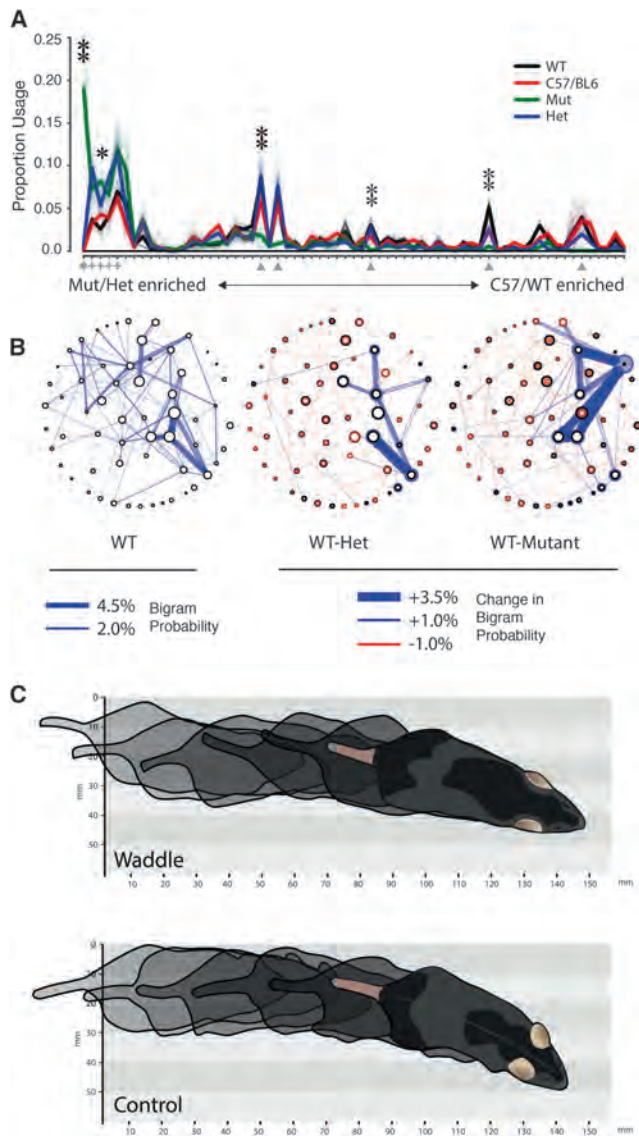


**Figure 5. The AR-HMM Disambiguates Wild-Type, Heterozygous, and Homozygous *Ror1β* Mice**

(A) Usage plot of modules exhibited by littermate *Ror1β* mice ( $n = 25$  C57/BL6,  $n = 3$  +/+,  $n = 6$  ±,  $n = 4$  −/−, open field assay, 20 min trials), sorted by “mutantness” (sorting and depiction as in Figure 3). Wild-type module usage is not statistically different from C57 but differs significantly from homozygote and heterozygote (Hotelling two-sample t-squared test,  $p < 10^{-15}$ ). Marked modules described in main text: diamond, waddle; triangle, normal locomotion; cross, pause. Single asterisk indicates significant usage difference between mutant and wild-type,  $p < 0.05$ ; double asterisk indicates  $p < 0.01$  under Wald test, Holm-Bonferroni corrected.

(B) State map depiction of baseline OFA behavior for +/+ animals as in Figure 4C (left); difference state maps as in Figure 4C between the +/+ and +/- genotype (middle) and +/+ and -/- genotype (right); all depicted transitions that distinguish genotypes are statistically significant,  $p < .01$ .

(C) Illustration of the “waddle” module in which the hind limbs of the animal are elevated during walking (see Movie S10).

statistical details, data were co-trained with both circular open field and TMT datasets to facilitate comparisons with C57 animals). Conversely, the expression of five behavioral modules encoding normal forward locomotion in wild-type and C57 mice was downregulated in *Ror1β* mutants (Figure 5A, average during-module velocity =  $114.6 \pm 76.3$  mm/s).

Previously unobserved phenotypes in the *Ror1β* mutant mice were also uncovered by the AR-HMM, as the expression of a set of four modules that encoded brief pauses and headbobs was upregulated in mutant mice (Figure 5A, average during-module velocity =  $8.8 \pm 25.3$  mm/s); this pausing phenotype had not been previously reported in the literature. Furthermore, heterozygous mice—which have no reported phenotype (André et al., 1998; Eppig et al., 2015; Liu et al., 2013; Masana et al., 2007), exhibit wild-type running wheel behavior (Masana et al., 2007), and appear normal by eye—were also found to express a fully penetrant mutant phenotype: they overexpressed the same set of pausing modules that were upregulated in the full *Ror1β* mutants while failing to express the more dramatic waddling phenotype (Figure 5A). Differences between wild-type animals and both heterozygotes and mutants were also observed in transition probabilities associated with these pausing modules (Figure 5B).

The AR-HMM therefore describes the pathological behavior of *Ror1β* mice as the combination of a single neomorphic waddling module, decreased expression of normal locomotion modules, and increased expression of a small group of physiological modules encoding pausing behaviors; heterozygous mice express a defined subset of these behavioral abnormalities, whose penetrance is not intermediate but equals that observed in the mutant. These results suggest that the sensitivity of the AR-HMM allows fractionation of severe and subtle behavioral abnormalities within the same litter of animals, facilitates comparisons among genotypes and enables discovery of new phenotypes.

In the case of the *Ror1β* animals, a permanent alteration in DNA sequence is translated into an ongoing change in the overall sub-second statistical structure of behavior, one that is expressed continuously over the lifetime of the animal. We also wished to characterize how transient changes in activity in specific neural circuits influence the moment-to-moment structure of behavior; furthermore, given that the relationship between neural circuit activity and behavior can vary on a trial-to-trial basis, we wanted to probe the ability of the AR-HMM to afford insight into the probabilistic relationships between neural circuit activity and behavior.

To address these questions, we unilaterally expressed the light-gated ion channel Channelrhodopsin-2 in a subset of layer 5 corticostriatal neurons in the right hemisphere and assessed behavioral responses before, during, and after 2 s of light-mediated activation of motor cortex (Glickfeld et al., 2013). At negligible power levels, no light-induced changes in behavior were observed, whereas at the highest power levels, the AR-HMM identified two behavioral modules whose expression was reliably induced by the light, as on nearly every trial either one or the other module was expressed (Figure 6A). As would be expected, both of these modules encode forms of spinning-to-the-left behavior, and neither of these modules was expressed during normal mouse locomotion (Figure 6B; Movie S11). In addition, we noted that approximately 40 percent of the time the overall

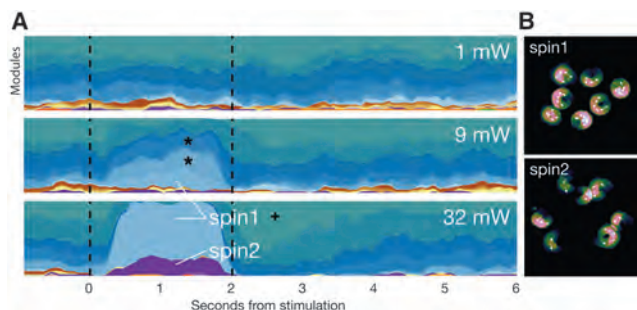


**Figure 6. Optogenetic Perturbation of Motor Cortex Yields Both Neomorphic and Physiological Modules**

(A) Mountain plot depicting the probability of expression of each behavioral module (assigned a unique color on the y axis) over time (x axis), with light stimulation indicated by dashed vertical lines (each plot is the average of 50 trials). Note that modest variations in the baseline pattern of behavior, due to trial structure, are captured before light onset. Stars indicate two modules expressed during baseline conditions that are also upregulated at intermediate powers (11 mW) but not high powers (32 mW, Wald test, Holm-Bonferroni adjusted  $p < 10^{-5}$ ); cross indicates pausing module upregulated at light offset (Wald test, Holm-Bonferroni adjusted,  $p < 10^{-5}$ ).

(B) Average position of example mice (with arrows indicating orientation over time) of the two modules induced under the highest stimulation conditions (see Movie S11). Note that (A) and (B) are generated from one animal and that the observed modulations are representative of the complete dataset ( $n = 4$  mice, model was trained separately from previous experiments).

pattern of behavior did not return to baseline for several seconds after the end of optogenetic stimulation. This deviation from baseline was not due to continued expression of the same spinning modules that were triggered at light onset; instead, mice often paradoxically expressed a pausing module at light offset (average during-module velocity =  $0.8 \pm 7$  mm/s, Figure 6A, see cross).

The behavioral changes induced by high-intensity optogenetic stimulation were reliable, as on nearly every trial the animal emitted one of the two spinning modules. To ask whether the AR-HMM could characterize the pattern of behavior observed when behavioral modules are generated more probabilistically, the levels of light stimulation were reduced; we identified conditions under which one of the two spinning modules was no longer detected, and the other was expressed in only 25 percent of trials. Under these conditions, the AR-HMM detected the upregulation of a distinct set of behavioral modules, each of which was expressed in a fraction of trials (Figure 6A, see stars). Unlike the spinning modules triggered by high-intensity stimulation, these modules were not neomorphic; rather, these modules were normally expressed during physiological exploration and encoded distinct forms of forward locomotion behavior (data not shown). Interestingly, although each of these individual light-regulated modules was emitted probabilistically on any given trial, low-intensity neural activation reliably influenced behavior across all trials when the behavioral modules were considered in aggregate (Figure 6A).

Thus, both low- and high-intensity optogenetic stimulation dramatically alters behavior, but the identity of the induced behaviors and their relative probabilities of expression vary across light levels. This effect would not have been apparent without the

ability of the AR-HMM to distinguish new from previously expressed behavioral modules and to identify the specific behavioral module induced at light onset on each trial; indeed, under low-light stimulation, the behavioral phenotype apparent by eye on any given trial often appears to be an extension of normal mouse exploratory behavior. Taken together, these data demonstrate that the AR-HMM can identify and characterize both obvious and subtle optogenetically induced phenotypes, distinguish “new” optogenetically induced behaviors from upregulated expression of “old” behaviors, and reveal the trial-by-trial relationships between neural activity and action.

## DISCUSSION

It has been long hypothesized that innate behaviors are composed of stereotyped modules and that specific sequences of these modules encode coherent and adaptive patterns of action (Bizzi et al., 2000; Brown, 1911; Draai et al., 2000; Lashley, 1967; Sherrington, 1907; Tinbergen, 1951). However, most efforts to explore the underlying structure of mouse behavior have relied on ad hoc definitions of what constitutes a behavioral module and have focused on specific behaviors rather than systematically considering behavior as a whole. As a consequence, we lack insight into the global organization of mouse behavior, the relationships between currently expressed actions and past or future behaviors, and the strategies used by the brain to generate behavioral change. Furthermore, we lack a comprehensive framework for characterizing the influence of individual genes or neural circuits on behavior.

Here we use 3D imaging to identify a sub-second spatiotemporal scale at which mouse behavior may be organized. Using this finding as a constraint, we then built a family of computational models, each of which represents a different hypothesis for the potential structure of behavior, and compared the ability of these models to predict and explain mouse behavior. The best performing model (the AR-HMM) specifically searches for modularity at sub-second timescales similar to those observed in the pose dynamics data and quantitatively describes behavior as a series of sub-second modules with defined transition probabilities. This combined 3D imaging/modeling approach can be used to automatically identify the behavioral modules expressed during a variety of experiments and to systematically discover how the architecture of behavior is altered as the mouse adapts to a changing world.

### The AR-HMM Automatically and Systematically Captures Known and New Phenotypes

Our experiments reveal that the AR-HMM identifies both predicted changes in action and new features of behavior that had not been previously described. The high sensitivity of the AR-HMM—illustrated by the identification of a previously undescribed phenotype in heterozygous *Ror1 $\beta$*  mice—raises the possibility that the AR-HMM could be useful for extracting subtle phenotypes from mouse models, including those in which single gene alleles are mutated; such patterns of mutation are common in human disease but are rarely explored in mouse models. Furthermore, the ability of the AR-HMM to place changes in behavior into context—illustrated by the ability of the AR-HMM

to identify the modules expressed after modest optogenetic stimulation on a trial-by-trial basis—suggests that the AR-HMM may be useful for relating unreliable or noisy patterns of neural activity to the probabilistic expression of specific actions. The AR-HMM (or similar approaches based upon unsupervised machine learning) may therefore be useful for discovering the behavioral consequences of a wide variety of experimental manipulations, particularly those enabled by the ever-growing toolbox of gene editing and optogenetic techniques.

### The AR-HMM Identifies Possible Mechanisms for Behavioral Change

The AR-HMM suggests three regulatory strategies that may be used by the brain to implement behavioral adaptation. First, behavioral modules and their transitions appear to be selectively—and to some extent independently—vulnerable to alteration. None of the physiological and pathological deviations from baseline described here, from freezing to a waddling gait, caused global changes in the underlying structure of action; instead, new behaviors were well-described as changes in a small number of specific modules or transitions. This suggests that the brain can focally manipulate individual modules or transitions to generate new behaviors, and furthermore that mice can accommodate pathological actions (such as waddling) without catastrophic alterations in behavioral patterning.

Second, dramatically new behaviors can be created by altering the transitions statistics between modules alone—without invoking new behavioral modules—as was observed in animals exposed to TMT. This strategy has been shown to underlie sensory-driven negative and positive taxis behaviors in bacteria, worms, and flies (Berg and Brown, 1972; Garrity et al., 2010; Gray et al., 2005; Pierce-Shimomura et al., 1999); here we show that this strategy is conserved in mice and used by vertebrate nervous systems to create complex patterns of action in response to an external cue. In the specific case of the TMT response, the induced behaviors extend beyond taxis to adaptations like freezing, suggesting that the restructuring of transition probabilities may be a general mechanism for creating new patterns of action.

Third, we find that modulation of where in space behavioral modules are expressed supports the generation of specific adaptive behaviors. For example, the rearing module used by mice to investigate TMT is not significantly upregulated or resequenced relative to control, and yet its spatial pattern of expression in the quadrant containing TMT facilitates detection (and therefore avoidance) of the aversive odorant. Characterizing where in space behavioral modules are expressed also reveals that changes in physical context—such as the difference between a square and circular arena—elicit “state”-like changes in mouse behavior that extend beyond predictable changes in action at apparatus boundaries. Because the training data for the AR-HMM do not include any explicit allocentric parameters (such as the mouse’s spatial position within the apparatus), the ability of the model to uncover meaningful relationships between allocentric space and egocentric pose dynamics is an important validation that its segmentation of behavior is informative.

### Potential Neural Underpinnings for Modules and Transitions

The observations generated by the AR-HMM lead to several predictions about the neural control of behavior. One such prediction is that specific behavioral modules and their associated transition probabilities will have explicit neural correlates, whose pattern of activity should reflect the ~2–5 Hz timescale at which modules are expressed; it is tempting to speculate that neural correlates representing transition probabilities between behavioral modules will be encoded in higher-order neural circuits tasked with behavioral sequencing, while neural correlates for the behavioral modules themselves might be encoded in central pattern generators or related circuit motifs in the brainstem or spinal cord. The relevant neural circuits may include both evolutionarily ancient regions of the brain involved in releasing innate behaviors, such as the amygdala, hypothalamus, and brainstem, as well as other areas, such as the striatum, that regulate fine-timescale behavioral sequencing (Aldridge et al., 2004; Swanson, 2000). Testing these predictions will require simultaneous characterization of neural activity and assessment of behavior; future embellishments of the modeling approach described here may allow for inference of joint structure between dense neural and behavioral data, and therefore be useful for revealing mechanistic relationships between the dynamics of neural activity and action.

### Unsupervised Behavioral Characterization via Modeling of 3D Data: Strengths, Caveats, and Future Directions

Although there are multiple possible approaches to acquiring 3D pose dynamics data, we chose to implement our imaging system using a single standard depth camera, because such cameras are widely available, adaptable to a variety of different experimental circumstances, and can characterize behavior under most lighting conditions and in animals with any coat color (due to the use of infrared light as an illumination source). The “unsupervised” modeling approach taken here is also transparent, insofar as the assumptions of the model are explicitly stated (with no constraints supplied by the researcher other than the structure of the model and the specification of a single parameter that acts as a tunable “lens” to focus the model on behavior at a particular timescale). This makes clear the precise bounds of human influence on the output of the AR-HMM and insulates key aspects of that output from the vagaries of human perception and intuition. Given that inter-observer reliability in scoring even single mouse behaviors can be low (from 50 to 70 percent, with reliability falling as the number of scored behaviors increases), developing methods free from observer bias is essential for informatively characterizing mouse behavior (Garcia et al., 2010).

In addition, the generative modeling and inferential fitting methods described herein offer several practical advantages over the approaches typically used to analyze mouse behavior (Crawley, 2003), including the explicit time-series modeling of behavioral data (as opposed to simple clustering of dimensionally reduced data); the ability to directly inspect and explore each behavioral module; the flexible discovery of previously unobserved behavioral modules (rather than characterization of behavior from the perspective of “known” phenotypes); and

the ability to generate synthetic behavioral data, thereby allowing quantitation of how well a given model predicts the structure of behavior. This quantitative framework for comparing the performance of different methods for dividing up and measuring behavior is critical for advancing behavioral neuroscience, as it enables objective evaluation of alternative models for behavior, and assessment of future extensions that incorporate inevitable improvements in camera resolution, model structure, and fitting procedures.

On the other hand, the conclusions drawn here regarding the underlying structure of behavior (including its timescale) are limited by the simplicity of our experimental manipulations, which were designed to expose differences in motor outputs. Furthermore “mouse behavior” as described by the model is restricted to the imaged pose dynamics of the mouse at a particular spatiotemporal resolution and within a controlled laboratory experiment. Because the AR-HMM directly models the pixel data (after pre-processing), comparisons can only be made between mice of roughly similar size and shape. In addition, there are clearly important physical features of mouse behavior (operating at a variety of spatiotemporal scales) not captured in the pose data and therefore not modeled—these range from individual joint dynamics and paw position to sniffing, whisking, and breathing. In the future, complementary datastreams that capture different facets of behavior could be integrated with 3D pose data to generate more comprehensive behavioral models.

The modeling approach itself also has several important limitations. The AR-HMM uses Bayesian nonparametric approaches to identify the most likely number of modules that describe behavior at a particular temporal scale. However, this insight also comes at a cost: as the amount of data fed to the algorithm increases, the number of discovered modules necessarily rises. This challenge parallels the well-described phenomenon in ethology in which the number of discovered behaviors increases in subjects that have been observed either more frequently or for longer (Colgan, 1978). This monotonic (although sublinear) relationship between data size and the number of discovered modules limits comparisons of behavior across experiments without co-training models, as was done here. One potential approach to address this challenge could be the incorporation of a “canonical” behavioral dataset against which additional data could be compared; such a framework (in which the “canonical” modules are either frozen or flexible) may enable analysis of new behavioral experiments within a fixed frame of reference.

Finally, the AR-HMM cannot explicitly disambiguate those features of behavior that are the consequence of the biomechanics of the mouse—for example, transitions between specific modules that are impossible due to physical constraints—from those that are the consequence of the action of the nervous system. Given that the nervous system and the body in which it is embedded co-evolved to facilitate action, ultimately disentangling the relative contributions of each to the organization of behavior may be difficult (for discussion of this issue, see, for example, Tresch and Jarc, 2009). However, changes in the structure of behavior that are induced by experimental intervention arise principally from the action of the nervous system; the

observed context-dependent flexibility of the transition statistics between modules, taken with the ability of the mouse to emit new behavioral modules in response to internal or external cues, together suggest that—at the spatiotemporal scale captured by our methods—the nervous system plays a key role in regulating the overall structure of behavior.

### Mouse Body Language: Syllables and Grammar

Candidate behavioral modules have been recognized in a variety of different contexts and on a wide range of spatiotemporal scales, and accordingly, researchers have given them a diverse set of names, including motor primitives, behavioral motifs, motor synergies, prototypes, and movemes (Anderson and Perona, 2014; Flash and Hochner, 2005; Tresch et al., 1999). The behavioral modules identified by the AR-HMM here find their origin in switching dynamics that are expressed on timescales of hundreds to milliseconds. Mouse behavior is clearly also organized at the varied and interdigitated timescales at which internal state (e.g., neural activity, endocrine function and development) and external state (e.g., daily, monthly, seasonal, and annual variation in behavior) unfold. The behavioral modules we have characterized therefore likely exist at an intermediate hierarchical level within the overall structure of behavior, albeit one that captures many of the behavioral changes induced by experimental manipulations carried out at both short and long timescales.

The modules identified by the AR-HMM do not exist in isolation; instead, they are given behavioral meaning through a transition structure that governs their sequencing. The observation of both modularity and transition structure within the pose dynamics of mice suggests strong analogies to birdsong, which is also hierarchically organized and composed of identifiable modules whose sequence is governed by definable transition statistics; importantly, birdsong has also been well described using generative modeling and low-order Markov processes (Berwick et al., 2011; Markowitz et al., 2013; Wohlgemuth et al., 2010). By analogy to birdsong, we therefore propose to refer to the modules we have identified as behavioral “syllables” and the statistical interconnections between these syllables as behavioral “grammar.” Such a grammatical structure has been previously proposed for restricted subsets of mouse behavior (such as grooming) in which behavioral modules were defined on an ad hoc basis (Berridge et al., 1987; Fentress and Stilwell, 1973); through unsupervised identification of behavioral syllables, here we show that the notion of a regulatory grammar is general and can be used to explain a wide variety of behavioral phenotypes. As is true for birdsong, the grammar we describe is highly restricted in nature (as only low-order interactions are modeled) and lacks the richness and flexibility of context-dependent grammars that have been explored in human language (Berwick et al., 2011). Despite this limitation, the experiments described herein expose an underlying structure for mouse body language organized at the sub-second timescale; this structure encapsulates mouse behavior (as detected by a depth sensor) within a given experiment and reveals a balance between stochasticity and determinism that is dynamically modulated as the mouse varies its pattern of action to adapt to challenges in the environment.

## EXPERIMENTAL PROCEDURES

All error bars indicated in the paper are SEM as determined by bootstrap analysis unless noted otherwise. For complete details on methods used, please consult Supplemental Experimental Procedures.

## SUPPLEMENTAL INFORMATION

Supplemental Information includes seven figures, eleven movies, and Supplemental Experimental Procedures and can be found with this article online at <http://dx.doi.org/10.1016/j.neuron.2015.11.031>.

A video abstract is available at <http://dx.doi.org/10.1016/j.neuron.2015.11.031#mmc14>.

## ACKNOWLEDGMENTS

We thank Michael Greenberg, Vanessa Ruta, David Ginty, Jesse Gray, Mike Springer, Aravi Samuel, Chris Harvey, Bernardo Sabatini, Rachel Wilson, Andreas Schaefer, and members of the Datta Lab for helpful comments on the manuscript; Joseph Bell for useful conversations; and Alexandra Nowlan and Christine Ashton for laboratory assistance. We thank David Roberson and Clifford Woolf for assistance with behavioral experiments and Ofer Mazor and Pavel Gorelik from the Research Instrumentation Core Facility for engineering support. We thank Sigrid Knemeyer for illustration assistance. Core facility support is provided by NIH grant P30 HD18655. A.B.W. is supported by an NSF Graduate Research Fellowship and is a Stuart H.Q. & Victoria Quan Fellow. G.I. is supported by the Human Frontiers Science Program. M.J.J. is supported by a fellowship from the Harvard/MIT Joint Grants program. S.L.P. is supported by an NSF Graduate Research Fellowship and is a Stuart H.Q. & Victoria Quan Fellow. R.P.A. is supported by NSF IIS-1421780. S.R.D. is supported by fellowships from the Burroughs Wellcome Fund, Searle Scholars Program, the Vallee Foundation, the McKnight Foundation, and the Khodadad Program; by the Fidelity Biosciences Research Initiative; by grants DP2OD007109 and RO11DC011558 from the NIH; and by the SFARI program and the Global Brain Initiative from the Simons Foundation. Code is available upon request ([datta.hms.harvard.edu/research.html](http://datta.hms.harvard.edu/research.html)).

Received: June 12, 2015

Revised: September 13, 2015

Accepted: November 18, 2015

Published: December 16, 2015

## REFERENCES

- Aldridge, J.W., Berridge, K.C., and Rosen, A.R. (2004). Basal ganglia neural mechanisms of natural movement sequences. *Can. J. Physiol. Pharmacol.* *82*, 732–739.
- Anderson, D.J., and Perona, P. (2014). Toward a science of computational ethology. *Neuron* *84*, 18–31.
- André, E., Conquet, F., Steinmayr, M., Stratton, S.C., Porciatti, V., and Becker-André, M. (1998). Disruption of retinoid-related orphan receptor beta changes circadian behavior, causes retinal degeneration and leads to vacillans phenotype in mice. *EMBO J.* *17*, 3867–3877.
- Berg, H.C., and Brown, D.A. (1972). Chemotaxis in *Escherichia coli* analysed by three-dimensional tracking. *Nature* *239*, 500–504.
- Berman, G.J., Choi, D.M., Bialek, W., and Shaevitz, J.W. (2014). Mapping the stereotyped behaviour of freely moving fruit flies. *J. R. Soc. Interface.* *11*, <http://dx.doi.org/10.1098/rsif.2014.0672>.
- Berridge, K.C., Fentress, J.C., and Parr, H. (1987). Natural syntax rules control action sequence of rats. *Behav. Brain Res.* *23*, 59–68.
- Berwick, R.C., Okanoya, K., Beckers, G.J.L., and Bolhuis, J.J. (2011). Songs to syntax: the linguistics of birdsong. *Trends Cogn. Sci.* *15*, 113–121.
- Bizzi, E., Tresch, M.C., Saltiel, P., and d'Avella, A. (2000). New perspectives on spinal motor systems. *Nat. Rev. Neurosci.* *1*, 101–108.
- Brown, T.G. (1911). The intrinsic factors in the act of progression in the mammal. *Proc. R. Soc. Lond. B* *84*, 308–319, <http://dx.doi.org/10.1098/rspb.1911.0077>.
- Colgan, P.W. (1978). *Quantitative ethology* (John Wiley & Sons).
- Crawley, J.N. (2003). Behavioral phenotyping of rodents. *Comp. Med.* *53*, 140–146.
- Croll, N.A. (1975). Components and patterns in the behaviour of the nematode *Caenorhabditis elegans*. *J. Zool.* *176*, 159–176.
- de Chaumont, F., Coura, R.D.-S., Serreau, P., Cressant, A., Chabout, J., Granon, S., and Olivo-Marin, J.-C. (2012). Computerized video analysis of social interactions in mice. *Nat. Methods* *9*, 410–417.
- Drai, D., Benjamini, Y., and Golani, I. (2000). Statistical discrimination of natural modes of motion in rat exploratory behavior. *J. Neurosci. Methods* *96*, 119–131.
- Eppig, J.T., Blake, J.A., Bult, C.J., Kadin, J.A., Richardson, J.E., and Group, M.G.D.; Mouse Genome Database Group (2015). The Mouse Genome Database (MGD): facilitating mouse as a model for human biology and disease. *Nucleic Acids Res.* *43*, D726–D736.
- Fendt, M., Endres, T., Lowry, C.A., Apfelbach, R., and McGregor, I.S. (2005). TMT-induced autonomic and behavioral changes and the neural basis of its processing. *Neurosci. Biobehav. Rev.* *29*, 1145–1156.
- Fentress, J.C., and Stilwell, F.P. (1973). Letter: Grammar of a movement sequence in inbred mice. *Nature* *244*, 52–53.
- Flash, T., and Hochner, B. (2005). Motor primitives in vertebrates and invertebrates. *Curr. Opin. Neurobiol.* *15*, 660–666.
- Garcia, V.A., Crispim Junior, C.F., and Marino-Neto, J. (2010). Assessment of observers' stability and reliability - a tool for evaluation of intra- and inter-concordance in animal behavioral recordings. *Conf. Proc. IEEE Eng. Med. Biol. Soc.* *2010*, 6603–6606.
- Garrity, P.A., Goodman, M.B., Samuel, A.D., and Sengupta, P. (2010). Running hot and cold: behavioral strategies, neural circuits, and the molecular machinery for thermotaxis in *C. elegans* and *Drosophila*. *Genes Dev.* *24*, 2365–2382.
- Glickfeld, L.L., Andermann, M.L., Bonin, V., and Reid, R.C. (2013). Corticocortical projections in mouse visual cortex are functionally target specific. *Nat. Neurosci.* *16*, 219–226.
- Gomez-Marin, A., Partoune, N., Stephens, G.J., Louis, M., and Brembs, B. (2012). Automated tracking of animal posture and movement during exploration and sensory orientation behaviors. *PLoS ONE* *7*, e41642.
- Gray, J.M., Hill, J.J., and Bargmann, C.I. (2005). A circuit for navigation in *Caenorhabditis elegans*. *Proc. Natl. Acad. Sci. USA* *102*, 3184–3191.
- Hastie, T., Tibshirani, R., and Friedman, J. (2009). *The Elements of Statistical Learning: Data Mining, Inference, and Prediction*, Second Edition (Springer).
- Jhuang, H., Garrote, E., Mutch, J., Yu, X., Khilnani, V., Poggio, T., Steele, A.D., and Serre, T. (2010). Automated home-cage behavioural phenotyping of mice. *Nat. Commun.* *1*, 68.
- Kabra, M., Robie, A.A., Rivera-Alba, M., Branson, S., and Branson, K. (2013). JAABA: interactive machine learning for automatic annotation of animal behavior. *Nat. Methods* *10*, 64–67.
- Lashley, K.S. (1967). The problem of serial order in behavior. In *Psycholinguistics: A book of readings*, L.A. Jeffress, ed.
- Liu, H., Kim, S.-Y., Fu, Y., Wu, X., Ng, L., Swaroop, A., and Forrest, D. (2013). An isoform of retinoid-related orphan receptor  $\beta$  directs differentiation of retinal amacrine and horizontal interneurons. *Nat. Commun.* *4*, 1813.
- Markowitz, J.E., Ivie, E., Kligler, L., and Gardner, T.J. (2013). Long-range order in canary song. *PLoS Comput. Biol.* *9*, e1003052.
- Masana, M.I., Sumaya, I.C., Becker-Andre, M., and Dubocovich, M.L. (2007). Behavioral characterization and modulation of circadian rhythms by light and melatonin in C3H/HeN mice homozygous for the RORbeta knockout. *Am. J. Physiol. Regul. Integr. Comp. Physiol.* *292*, R2357–R2367.
- Ou-Yang, T.-H., Tsai, M.-L., Yen, C.-T., and Lin, T.-T. (2011). An infrared range camera-based approach for three-dimensional locomotion tracking and pose reconstruction in a rodent. *J. Neurosci. Methods* *201*, 116–123.

- Pierce-Shimomura, J.T., Morse, T.M., and Lockery, S.R. (1999). The fundamental role of pirouettes in *Caenorhabditis elegans* chemotaxis. *J. Neurosci.* *19*, 9557–9569.
- Sherrington, C. (1907). *The Integrative Action of the Nervous System*. J. Nerv. Ment. Dis.
- Spink, A.J., Tegelenbosch, R.A., Buma, M.O., and Noldus, L.P. (2001). The EthoVision video tracking system—a tool for behavioral phenotyping of transgenic mice. *Physiol. Behav.* *73*, 731–744.
- Stephens, G.J., Johnson-Kerner, B., Bialek, W., and Ryu, W.S. (2008). Dimensionality and dynamics in the behavior of *C. elegans*. *PLoS Comput. Biol.* *4*, e1000028.
- Stephens, G.J., Johnson-Kerner, B., Bialek, W., and Ryu, W.S. (2010). From modes to movement in the behavior of *Caenorhabditis elegans*. *PLoS ONE* *5*, e13914.
- Swanson, L.W. (2000). Cerebral hemisphere regulation of motivated behavior. *Brain Res.* *886*, 113–164.
- Tinbergen, N. (1951). *The study of instinct* (Clarendon Press).
- Tresch, M.C., and Jarc, A. (2009). The case for and against muscle synergies. *Curr. Opin. Neurobiol.* *19*, 601–607.
- Tresch, M.C., Saltiel, P., and Bizzi, E. (1999). The construction of movement by the spinal cord. *Nat. Neurosci.* *2*, 162–167.
- Vogelstein, J.T., Park, Y., Ohyama, T., Kerr, R.A., Truman, J.W., Priebe, C.E., and Zlatic, M. (2014). Discovery of brainwide neural-behavioral maps via multi-scale unsupervised structure learning. *Science* *344*, 386–392.
- Wallace, K.J., and Rosen, J.B. (2000). Predator odor as an unconditioned fear stimulus in rats: elicitation of freezing by trimethylthiazoline, a component of fox feces. *Behav. Neurosci.* *114*, 912–922.
- Weissbrod, A., Shapiro, A., Vasserman, G., Edry, L., Dayan, M., Yitzhaky, A., Hertzberg, L., Feinerman, O., and Kimchi, T. (2013). Automated long-term tracking and social behavioural phenotyping of animal colonies within a semi-natural environment. *Nat. Commun.* *4*, 2018.
- Wohlgemuth, M.J., Sober, S.J., and Brainard, M.S. (2010). Linked control of syllable sequence and phonology in birdsong. *J. Neurosci.* *30*, 12936–12949.

# A Systems-Level Analysis of the Peripheral Nerve Intrinsic Axonal Growth Program

Vijayendran Chandran,<sup>1</sup> Giovanni Coppola,<sup>1,8</sup> Homaira Nawabi,<sup>2</sup> Takao Omura,<sup>2</sup> Revital Versano,<sup>1</sup> Eric A. Huebner,<sup>2</sup> Alice Zhang,<sup>3</sup> Michael Costigan,<sup>2</sup> Ajay Yekkirala,<sup>2</sup> Lee Barrett,<sup>2</sup> Armin Blesch,<sup>4,9</sup> Izhak Michaelievski,<sup>5,10</sup> Jeremy Davis-Turak,<sup>1,11</sup> Fuying Gao,<sup>8</sup> Peter Langfelder,<sup>6,7</sup> Steve Horvath,<sup>6,7</sup> Zhigang He,<sup>2</sup> Larry Benowitz,<sup>2</sup> Mike Fainzilber,<sup>5</sup> Mark Tuszynski,<sup>4</sup> Clifford J. Woolf,<sup>2</sup> and Daniel H. Geschwind<sup>1,6,\*</sup>

<sup>1</sup>Program in Neurogenetics, Department of Neurology, David Geffen School of Medicine, University of California, Los Angeles, Los Angeles, CA 90095, USA

<sup>2</sup>F.M. Kirby Neurobiology Center, Boston Children's Hospital and Harvard Medical School, Boston, MA 02115, USA

<sup>3</sup>Interdepartmental Program in Neuroscience, University of California, Los Angeles, Los Angeles, CA 90095, USA

<sup>4</sup>Department of Neurosciences, University of California, San Diego, La Jolla, CA 92093, USA

<sup>5</sup>Department of Biological Chemistry, Weizmann Institute of Science, 76100 Rehovot, Israel

<sup>6</sup>Department of Human Genetics, University of California, Los Angeles, Los Angeles, CA 90095, USA

<sup>7</sup>Department of Biostatistics, University of California, Los Angeles, Los Angeles, CA 90095, USA

<sup>8</sup>Department of Psychiatry, Semel Institute for Neuroscience and Human Behavior, David Geffen School of Medicine, University of California Los Angeles, Los Angeles, CA 90095, USA

<sup>9</sup>Present address: Stark Neurosciences Research Institute, Indiana University School of Medicine, Indianapolis, IN 46202, USA

<sup>10</sup>Present address: Department of Biochemistry and Molecular Biology, Sagol School of Neuroscience, Tel Aviv University, Tel Aviv 69978, Israel

<sup>11</sup>Present address: OnRamp Bioinformatics, San Diego, CA 92103, USA

\*Correspondence: dhg@mednet.ucla.edu

<http://dx.doi.org/10.1016/j.neuron.2016.01.034>

## SUMMARY

The regenerative capacity of the injured CNS in adult mammals is severely limited, yet axons in the peripheral nervous system (PNS) regrow, albeit to a limited extent, after injury. We reasoned that coordinate regulation of gene expression in injured neurons involving multiple pathways was central to PNS regenerative capacity. To provide a framework for revealing pathways involved in PNS axon regrowth after injury, we applied a comprehensive systems biology approach, starting with gene expression profiling of dorsal root ganglia (DRGs) combined with multi-level bioinformatic analyses and experimental validation of network predictions. We used this rubric to identify a drug that accelerates DRG neurite outgrowth in vitro and optic nerve outgrowth in vivo by inducing elements of the identified network. The work provides a functional genomics foundation for understanding neural repair and proof of the power of such approaches in tackling complex problems in nervous system biology.

## INTRODUCTION

The regenerative capacity of the injured adult mammalian CNS is extremely limited, which leads to permanent neurological deficits following CNS injury. In contrast, injured axons in the adult mammalian peripheral nervous system (PNS) maintain the capacity to regenerate, providing potential for functional recovery

after peripheral nerve injury (Abe and Cavalli, 2008; Ramón y Cajal et al., 1991). The failure of CNS axons to regenerate is due to many factors, primarily a lack of induction of a cell-intrinsic growth capacity after injury (Afshari et al., 2009; Giger et al., 2010) and the presence of extrinsic inhibitory effects (Filbin, 2003; Yiu and He, 2006), both mechanisms supported by many lines of experimental evidence (Hoffman, 2010; Neumann and Woolf, 1999; Sun et al., 2011; Yiu and He, 2006). The concept that specific intrinsic molecular differences contribute to the divergent neuronal growth states after PNS and CNS injuries is supported by the manipulation of individual candidate genes induced in neurons by PNS, but not CNS, injury, which can promote limited CNS regrowth after injury (Hoffman, 2010; Neumann and Woolf, 1999; Sun et al., 2011). The relative importance of intrinsic neuronal signals during injury in CNS regeneration failure (Sun and He, 2010) is highlighted by the very limited axon regeneration observed even after eliminating combinations of known extrinsic inhibitory signals (Yiu and He, 2006). Furthermore, a conditioning lesion of the peripheral axon of dorsal root ganglion (DRG) neurons in the PNS increases the intrinsic growth state of the neurons sufficiently to enable the regeneration of their central axons in the CNS (Neumann and Woolf, 1999).

One of the intrinsic molecular mechanisms contributing to the regenerative process is the retrograde transport of injury signals to the cell body of the neuron, leading to expression of regeneration-associated genes (RAGs; Abe and Cavalli, 2008). For example, injured PNS axons activate RAGs such as *Atf3*, *Jun*, *Hsp27*, *Sprr1a*, *Gap43*, and genes involved in the JAK-STAT3 pathway, whereas injury to CNS axons does not result in the activation of these RAGs (Afshari et al., 2009). Axonal injury also induces local activation and retrograde transport of several MAPKs, including ERK (Hanz et al., 2003; Perlson et al., 2005) and JNK (Cavalli et al., 2005; Lindwall and Kanje, 2005), while

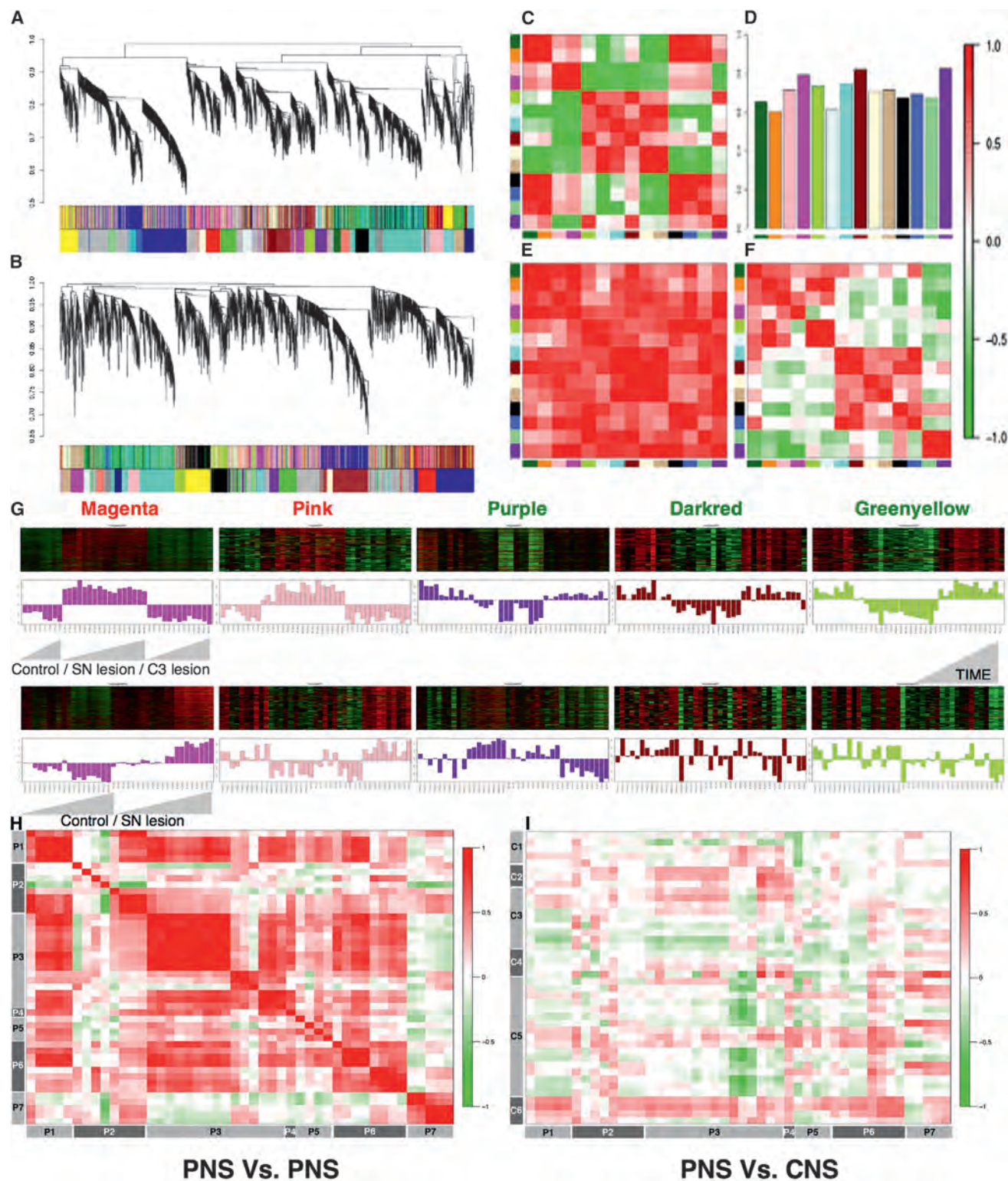


**Figure 1. Network Analysis of Sensory Neuron Profile Changes after SN Lesions**

(A and B) Gene dendrograms for two SN lesion datasets are shown.

(C–F) Consensus module preservation across datasets. (C and E) Eigengene (first principal component of gene expression) adjacencies of two datasets are shown; rows and columns correspond to one eigengene consensus module (red, positive correlation; green, negative correlation). (D) Preservation measure for

(legend continued on next page)

elevation of cAMP levels in the soma after axonal injury to the PNS neurons enhances axonal re-growth (Qiu et al., 2002). Elevated cAMP levels also increase regenerative responses of retinal ganglion cells (Chierzi et al., 2005) and the damaged spinal cord (Qiu et al., 2002). PNS nerve injury also triggers the expression of several cytokines, such as interleukin-6, leukemia inhibitory factor, and ciliary neurotrophic factor, at the lesion sites (Cao et al., 2006; Sendtner et al., 1992; Subang and Richardson, 2001). Subsequently, these cytokines activate the JAK-STAT pathway through gp130-containing receptor complexes (Taga and Kishimoto, 1997), resulting in the accumulation of phospho-STAT3 in the nucleus (Schweizer et al., 2002), which further activates the axon regeneration program (Bareyre et al., 2011).

Overexpression of a single RAG alone, including the transcription factors (TFs) ATF3 and STAT3 or the cytoskeletal protein GAP43, is usually not sufficient for effective successful regeneration (Bareyre et al., 2011; Bomze et al., 2001; Seiffers et al., 2007). For example, constitutive expression of a single TF (ATF3) increases axonal growth in the PNS after injury, but it does not overcome myelin inhibition in culture or enhance neuronal regeneration in the CNS (Seiffers et al., 2007). These findings demonstrate the necessity for the combined and cooperative intrinsic regulation of many RAGs involved in various pathways for the regeneration program to occur. This is consistent with the growing appreciation that genes do not act in isolation, but rather in coordinated networks in conjunction with other genes (Parikshak et al., 2015).

Recently, combinatorial knockout of two genes, *Pten* and *Socs3*, responsible for negative regulation of the mammalian target of rapamycin (mTOR) and JAK-STAT pathways, was shown to enhance regeneration in the CNS, providing important evidence that it is possible to reactivate central axonal growth in the injured adult (Sun et al., 2011). In many cases, modulation of expression of individual genes in these pathways has led to some increase in axonal outgrowth after injury, consistent with their functional role in neural repair. However, these findings also suggest that multiple pathways act in parallel to stimulate neuronal regeneration after injury.

We reasoned that differences in the regenerative potential between injured PNS neurons and injured CNS neurons likely reflect major differences in intrinsic transcriptional networks, rather than changes in expression of a few individual genes. We applied a multi-staged approach to characterize the transcriptional network associated with axon outgrowth in the PNS, and we experimentally validated several network predictions using bioinformatic and experimental approaches. By integration of protein-protein interactions (PPIs) with the RNA co-expression network, we identified a core RAG co-expression module highly enriched in a core set of hub genes, including TFs known to promote neurite outgrowth as well as novel TFs

not previously associated with axonal outgrowth. Our analysis indicates that, rather than acting in isolation, these enriched TFs provide crucial cross-talk between the signaling pathways involved in neuronal regeneration after PNS injury. We show, moreover, that the expression of these TFs is coordinately up-regulated following PNS injury, but not after CNS injury, consistent with the notion that coordinate regulation of this core network, rather than individual components, is necessary for axonal outgrowth. As a proof of principle, we show that top two hub TFs present in the core regeneration-associated gene network, ATF3 and JUN, when simultaneously over-expressed increased axonal outgrowth in mouse DRG neurons, when compared to the individual TF over-expression. Finally, we show that a compound that increases the expression of several components of the PNS coordinate transcriptional network, can promote CNS regeneration, validating this approach to screen for CNS growth-promoting treatments.

## RESULTS

### Construction of RAG Co-expression Networks

We first analyzed the genome-wide transcriptional changes that occur in DRG neurons during axon outgrowth following peripheral nerve injury at multiple time points, ranging from hours to days, after injury (see Table S1) in several experimental models of rodent peripheral nerve injury (Beggs and Salter, 2006) generated independently in collaborating laboratories as follows: sciatic nerve (SN) lesion (SN transection), spinal nerve ligation, spared nerve injury, and chronic nerve constriction, as well as a model where regeneration does not occur after a C3 lesion (cervical cord hemi-section at the C3 level cutting the central axons of DRG neurons in the dorsal columns). In total, 147 microarrays for 31 time points were analyzed in this initial study. We performed weighted gene co-expression network analysis (WGCNA) (Geschwind and Konopka, 2009; Langfelder and Horvath, 2008; Zhang and Horvath, 2005), a powerful method for understanding the modular network structure of the transcriptome, to identify the peripheral nerve regrowth-related network following SN lesions. WGCNA permits identification of modules of highly co-expressed genes whose grouping reflects shared biological functions and key functional pathways, as well as key hub genes within the modules (Langfelder and Horvath, 2008; Parikshak et al., 2015).

We first conducted WGCNA on two different microarray-based time series experiments on DRGs during the period of regrowth after nerve injury, performed independently in two different laboratories (Experimental Procedures). We applied consensus network analysis (Langfelder and Horvath, 2008) to define 14 robust and reproducible co-expression modules (Experimental Procedures; Figure 1) between the two SN lesion

each consensus eigengene is shown. (E) Overall module preservation among SN lesion datasets is shown; rows and columns correspond to a consensus module; red saturation denotes module preservation.

(G) Heatmaps depicting expression of genes (rows) across samples (columns) for five modules (red corresponds to gene upregulation and green to down-regulation). First principal component of gene expression is shown as a bar-plot. (Top) SN and C3 lesion datasets 1, 3, 7, 14, and 49 days after injury (left to right, ascending order) are shown. (Bottom) Same genes in another SN lesion dataset 1, 3, 8, 12, 16, 18, 24, and 28 hr post-injury are shown.

(H and I) Plots comparing direction of correlation of top 50 hub genes in magenta module in 16 (eight PNS and eight CNS) neuronal injury datasets (H) PNS versus PNS and (I) CNS versus PNS; correlation scores encoded  $-1$  (green, anti-correlated) to  $+1$  (red, correlated).

datasets generated 1, 3, 7, 14, and 49 days after injury and 1, 3, 8, 12, 16, 18, 24, and 28 hr post-injury (Figures 1A–1F). This analysis indicated that the gene co-expression relationships in the DRG following SN injury are highly preserved; these 14 modules represent common pathways associated with regeneration after nerve injury (Figures 1C–1F).

On the basis of the module eigengene correlation with time-dependent changes after injury, we first classified modules as upregulated, downregulated, and early regulated following injury (Experimental Procedures; Figure S1A). Next, based on the significant module-trait relationships (Experimental Procedures; Figure S1B; Bonferroni corrected  $p$  value  $< 0.01$ ), we identified five modules strongly associated with regeneration as follows: two modules (magenta and pink) whose genes are unregulated, and three (purple, dark red, and green-yellow) whose genes are downregulated after nerve injury (Figures 1A, 1B, and 1G; Table S2), all of which were conserved in a third, independent peripheral nerve injury dataset (Costigan et al., 2002; Table S1).

As a first step toward functional annotation, we examined each module's association with neuronal regeneration from published literature by testing association with the key words neuronal regeneration, axonal regeneration, and nerve injury in the PubMed database for every gene (Experimental Procedures). This analysis identified the magenta module as significantly enriched for genes associated with neuronal regeneration. Nearly 24% of the genes (108 of 435 genes in the module; hypergeometric  $p$  value  $3.3 \times 10^{-11}$ ; Experimental Procedures) were associated with neural regeneration and/or axon outgrowth (Table S2). To further annotate module function at a general level, we applied gene ontology (GO) enrichment analyses, which showed enrichment (Benjamini-corrected  $p$  values  $< 0.05$ ) for several GO categories in the upregulated RAG co-expression modules (magenta and pink) that are functionally associated with neuronal regeneration. Significant clusters included regulation of transcription, neuron differentiation, inflammation, stimulus related, signaling related, and cell proliferation/growth/migration (Table S3). GO functional analysis for downregulated RAG co-expression modules (purple and dark red) revealed enrichment for various categories related to plasma membrane, ion/gated channel, ion binding, and synapse/cell junction (Table S3). Several previous studies have observed the differential regulation of many TFs (Abe and Cavalli, 2008; Michaelevski et al., 2010) and membrane ion channel regulation after nerve injury (Abe and Cavalli, 2008; Yang et al., 2004), consistent with these observations.

### Validation of RAG Co-expression Modules

To validate these co-expression modules, we first compared the direction of differential expression of the top 50 hub genes, which represent the most central genes in the co-expression network in all five modules, in 16 independent datasets (eight PNS and eight CNS) containing 382 microarrays related to either PNS or CNS neuronal injury (Figures 1H and 1I; Figures S1C and S1D; Table S4). The co-expression relationships observed in our PNS data were also observed in these independent PNS datasets ( $r^2$  range, 0.5 to 1.0; Figures 1H and 1I; Figures S1C and S1D). In contrast, these relationships

were not as well preserved in datasets after CNS injury, where we observed a higher degree ( $>1.5$ -fold versus PNS) of anti-correlation ( $\leq -0.5$ ; Figures S1C and S1D), especially significant for magenta and purple modules. This analysis demonstrates that the core PNS injury-related co-expression network in the DRG is highly reproducible and is not observed in injured CNS neurons following a CNS lesion (Figures 1H and 1I).

The association of nearly 24% of magenta module genes with terms related to neuronal regeneration in the literature predicts that the other genes in this module and the other upregulated module also would modulate regeneration. To validate these network-based predictions, we selected the following upregulated genes from the magenta and pink modules based on their high intramodular connectivity (hub status; Experimental Procedures), requiring that they had not been previously associated with neuronal regeneration in the literature (i.e., were putative novel RAGs): *Smagp* (small trans-membrane and glycosylated protein), *Gfpt1* (glutamine fructose-6-phosphate transaminase 1), *Tsfp* (thymic stromal lymphopoietin), *Nudt6* (nucleoside diphosphate linked moiety X-type motif 6), *Cdc42se2* (CDC42 small effector 2), *Rfxap* (regulatory factor X-associated protein), *Grem2* (gremlin 2), and LOC688459. We augmented this validation set utilizing a knowledge-based semi-supervised approach (Experimental Procedures) to include the following additional genes with strong co-expression relationships in our datasets to neuronal regeneration: *Fxyd5* (FXID domain containing ion transport regulator 5), *Tacstd2* (tumor-associated calcium signal transducer 2), *Kif22* (kinesin family member 22), RGD1304563, *Cldn4* (claudin 4), *Fam46a* (family with sequence similarity 46, member A), *Pdcl3* (phosducin-like 3), and *Rrad* (Ras-related associated with diabetes).

To determine if these nominated genes were indeed RAGs, we first performed an in vitro assay by monitoring acute neurite outgrowth following overexpression of each candidate gene in adult mouse DRG neurons (Figures 2A and 2B; Figure S1E). Of the 16 putative RAGs tested, ten caused significant increases in both neurite length and the number of neurites after overexpression (ANOVA with Bonferroni-Holm post hoc test,  $p < 0.05$ ; Figures 2A, 2B, and 2D; Figure S1E) (genes *Fxyd5*, *Gfpt1*, *Smagp*, *Tacstd2*, *Kif22*, RGD1304563, *Cldn4*, *Fam46a*, *Rfxap*, and *Pdcl3*). We selected the top four (*Fxyd5*, *Gfpt1*, *Smagp*, and *Tacstd2*) for further loss-of-function validation, and we performed an in vitro assay monitoring neurite outgrowth in replated adult mouse DRG neurons following knockdown of the candidate RAGs *Fxyd5*, *Gfpt1*, *Smagp*, *Tacstd2*, and *Cdc42* by RNAi, compared with a small hairpin RNA (shRNA) control vector (containing a non-specific shRNA). In all cases, target knockdown significantly (ANOVA with Bonferroni-Holm post hoc test,  $p < 0.05$ ) reduced neurite outgrowth (Figures 2C and 2D).

### TF-Binding Site Enrichment in RAG Co-expression Modules

To uncover the potential regulatory network contributing to the consistent co-expression of multiple genes after nerve injury, we performed TF-binding site (TFBS) enrichment analysis for each of the RAG co-expression modules. To avoid confounders and identify the most statistically robust sites, we

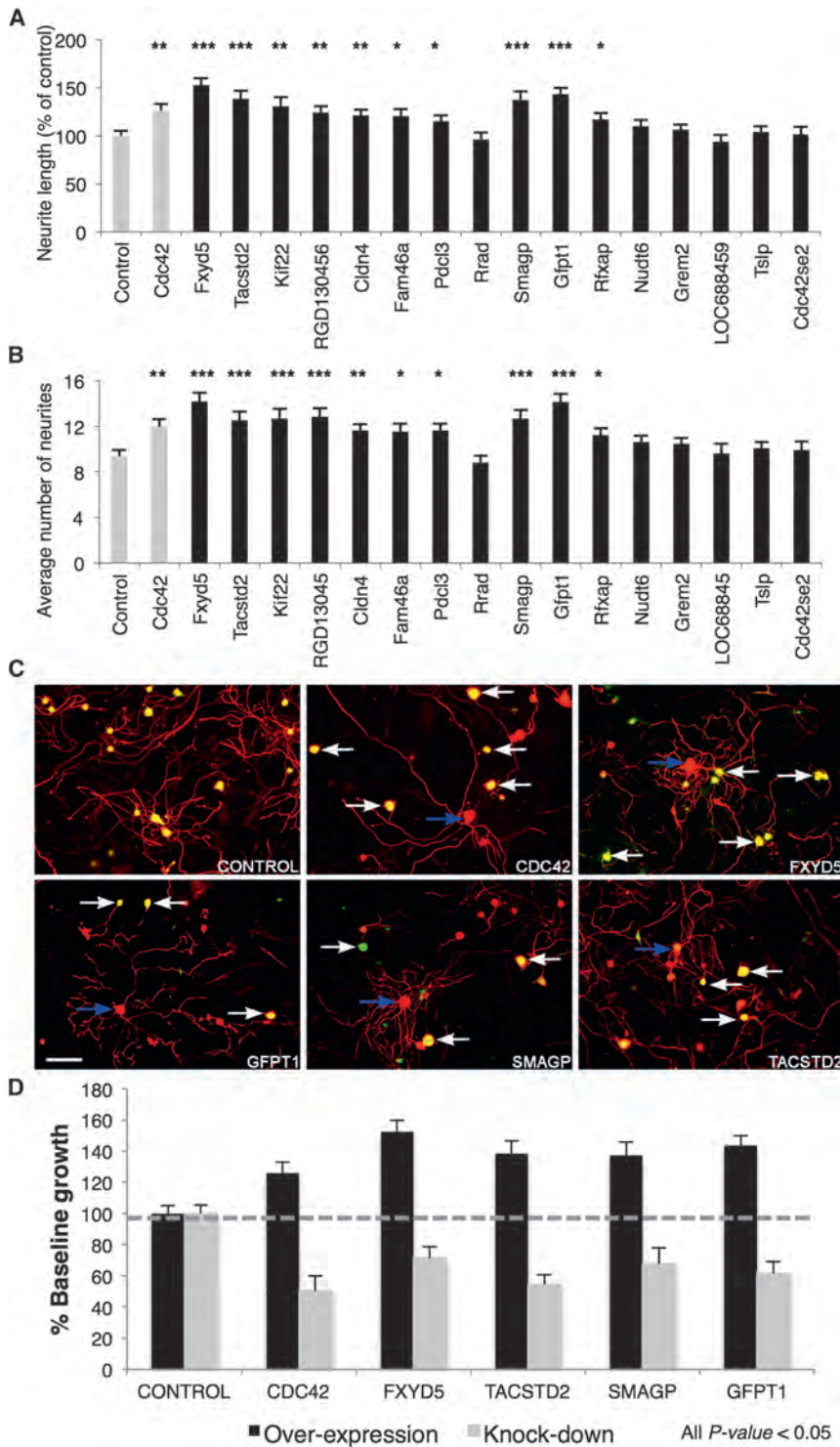


**Figure 2. Experimental Validation of Novel Candidate RAGs**

(A and B) Differences in neurite outgrowth produced by overexpression of 16 cDNA clones in lentiviral expression vectors with an IRES eGFP expression tag in cultured adult C57BL/6 DRG neurons with *Cdc42* as positive control. (A) Total neurite length and (B) number of neurites per neuron were quantified using ImageJ software (NeuronJ plugin), from 50 to 150 cells per view. Significant differences were determined by ANOVA with Bonferroni-Holm post hoc test; 10/16 candidates induce greater neurite growth.

(C) Knockdown of the top four selected genes using lentiviral delivery of shRNA with eGFP reporter in C57BL/6 DRGs. Transfected (white arrow) and non-transfected (blue arrow) individual DRG neurons are highlighted. Scale bar, 100 μm.

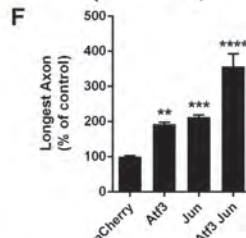
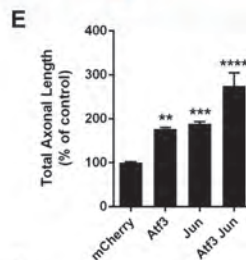
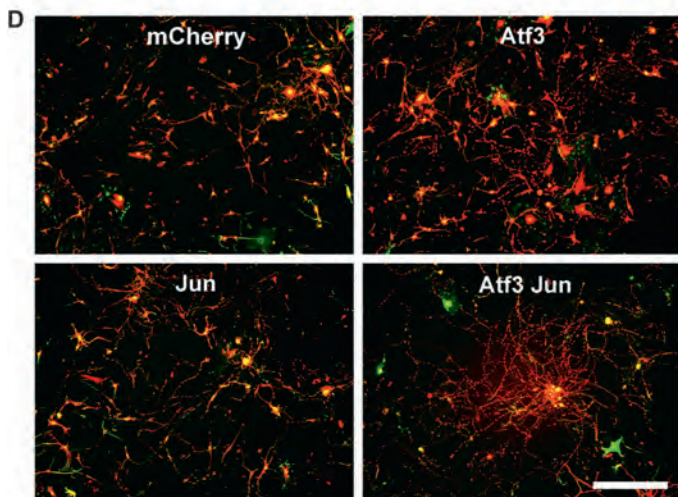
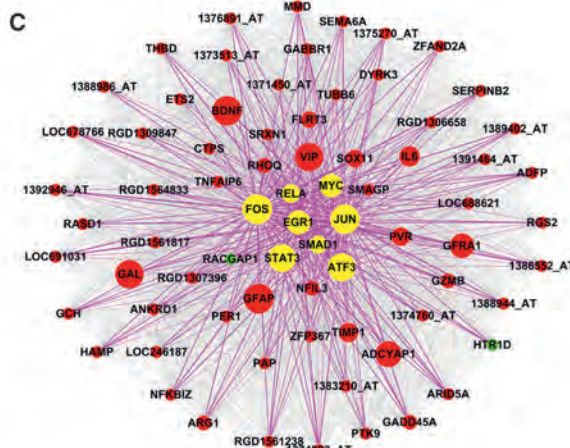
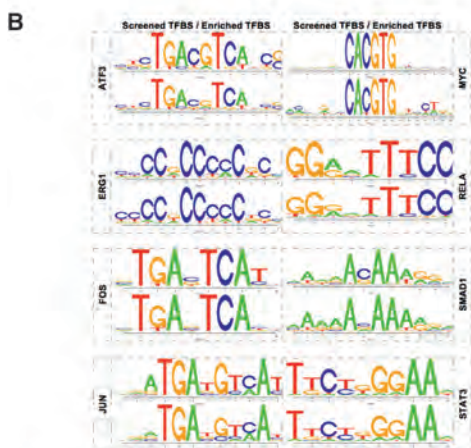
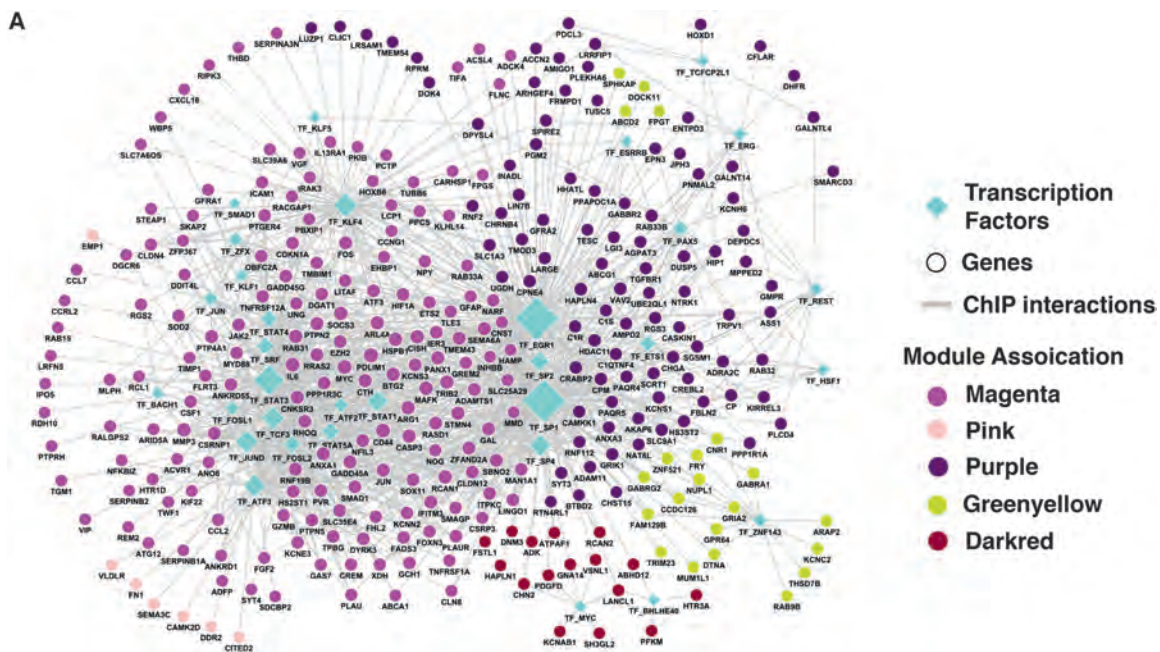
(D) Average total neurite length relative to control. All data shown is significant relative to control ( $p < 0.05$ , mean  $\pm$  SEM).

confirmation of predicted binding sites via chromatin immunoprecipitation (ChIP) experiments (hypergeometric  $p$  value  $3.4 \times 10^{-25}$ ; Figure 3A; Table S6; Experimental Procedures). Interestingly, up-regulated modules (purple, green-yellow and pink) and downregulated modules (dark red) occupied relatively distinct network territories that share different core TF regulators, as defined by network co-expression and ChIP data, suggesting quite distinct control of the regulation of these gene sets after peripheral nerve injury (Figure 3A). The two upregulated modules showed enrichment for 15 TFs previously associated with the axonal growth and neuronal injury response (Figure 3A; Table S5), including ATF3, EGR1, EGR2, FOS, JUN, KLF4, REL, RELA, SMAD1, SP1, SP2, STAT1, and STAT3 (Abe and Cavalli, 2008; Figure 3A). Remarkably, eight of these over-represented TFs (ATF3, EGR1, FOS, JUN, MYC, RELA, SMAD1, and STAT3) are present in the magenta module, the major upregulated module after PNS injury (Figures 3B and 3C).

Next, we cross-validated the TFBS enrichment analysis of the sequences upstream of the orthologous genes in mouse and human. We found that 51% of TFs

used three different background datasets (1,000-bp sequences upstream of all rat genes, rat CpG islands, and the rat chromosome 20 sequence). We identified 62 TFs (Experimental Procedures) significantly enriched in RAG co-expression modules ( $p$  value < 0.05 relative to all three background datasets; Table S5). Of these TFs, 39 had experimental data available, providing

that were over-represented in rats also were over-represented in the sequences of mouse or human homologs, demonstrating phylogenetic conservation of TFBS in the promoter regions of these co-expressed genes after nerve injury (Table S6). It is notable that the enriched TFs related to upregulated modules (ATF3, EGR2, FOS, JUN, KLF4, REL, RELA, SMAD1, SP1,



(legend on next page)

SP2, and STAT3 [Abe and Cavalli, 2008]) are well studied for involvement in the nerve injury process compared to TFs enriched in the downregulated modules (candidate transcriptional repressors).

During regeneration, many genes are dynamically down-regulated (Shim and Ming, 2010). To specifically identify TFs that could regulate this process, we screened for experimentally validated TFBS over-represented in modules down-regulated after injury—purple, dark red, and green-yellow (candidate transcriptional repressors; Experimental Procedures), which are enriched in genes related to the GO terms plasma membrane, ion/gated channel, ion binding, and synapse/cell junction related (Table S3). By screening for highly phylogenetically conserved regulatory regions (rat, mouse, and human) in these down-regulated modules, we found that TFBS for SP1, 2, EGR1, 2, KLF4, 5, and MZF1 were enriched in the promoter regions of these orthologous genes (Table S6b). A recent study has shown that MZF1 expression increases after nerve injury in DRG neurons and regulates a long noncoding RNA that contributes to neuropathic pain (Zhao et al., 2013), but little is known about its regulatory targets. We validated the network-predicted co-expression relationships via over-expression of MZF1 in adult DRG neurons and examination of its putative target's mRNA levels, validating two-thirds of the predicted targets (6 out of 9) including Ntrk1 (neurotrophic tyrosine kinase receptor type 1), Htr3a (5-hydroxytryptamine serotonin receptor 3A), and Gabbr2 (gamma-aminobutyric acid B receptor 2) (Figure S1F). Both Htr3a and Gabbr2 are present in the down-regulated modules whose members are enriched with MZF1 TFBS in their promoter regions, and both had been previously shown to be down regulated by nerve injury (Li et al., 2015).

### Co-expression of Two Hub TFs Induces a Combinatorial Increase in Axonal Growth

Next, to provide an experimental test of our TFBS enrichment predictions, we assessed the action of two of the transcription factors by over-expression in DRG neurons *in vitro*. We selected two critical TFs (ATF3 and JUN) based on their presence in the core regeneration associated magenta module (Figure 3C) and their increased expression levels after nerve injury *in vivo* (Figure S2). We assessed neurite outgrowth in the context of over-expression of each TF individually, as well with their combined over-expression. We observed that ATF3 and JUN increase neurite outgrowth significantly when over-expressed individually

(Figures 3E and 3F), consistent with previous findings (Dragunow et al., 2000; Seiffers et al., 2006). Their combinatorial over-expression synergistically increased neurite outgrowth; the total neurite outgrowth per neuron and the longest neurite per neuron were enhanced by  $2.7 \pm 0.3$ -fold, and  $3.6 \pm 0.4$ -fold, respectively (Figures 3D–3F) relative to the control. The magnitude of the increased growth on laminin induced by these two factors (2.7-fold increase in total neurite outgrowth per neuron) is significantly higher when compared to the over-expression of each TF individually, supporting the predictions of the network analysis.

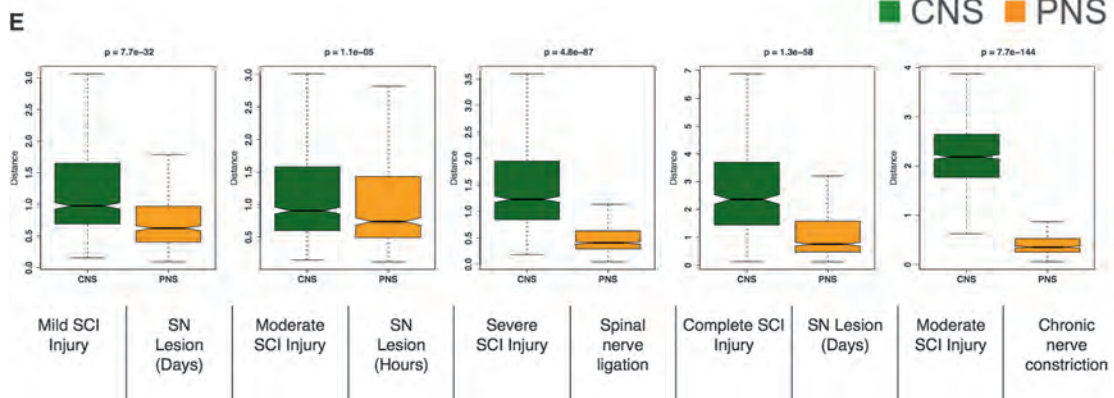
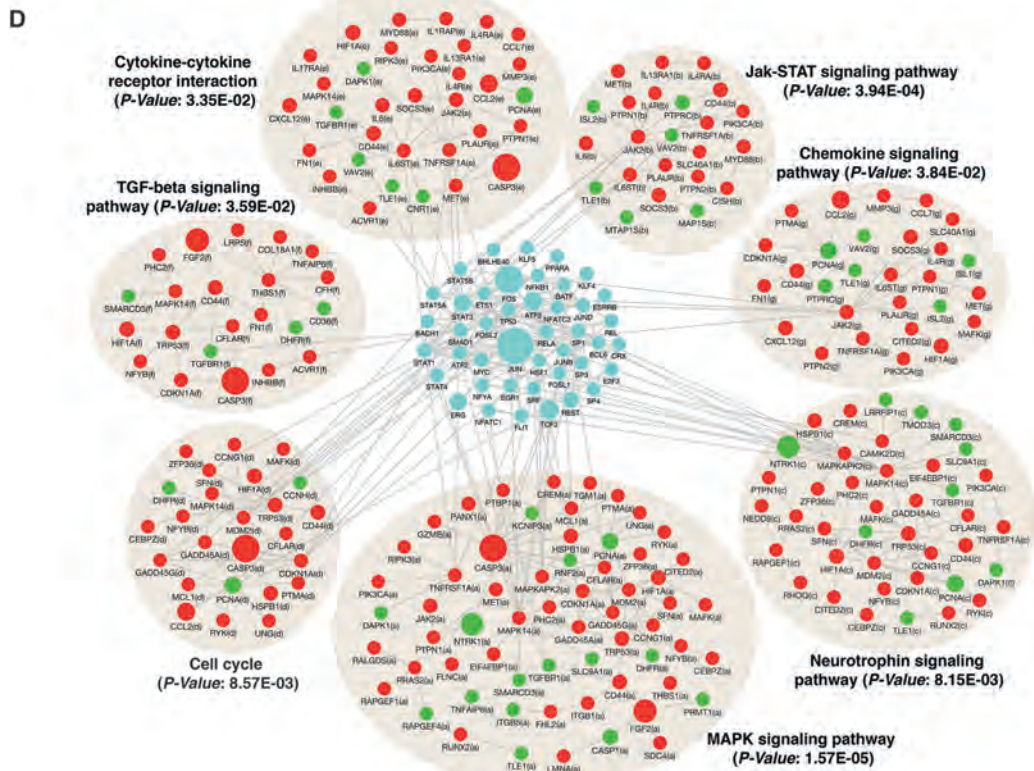
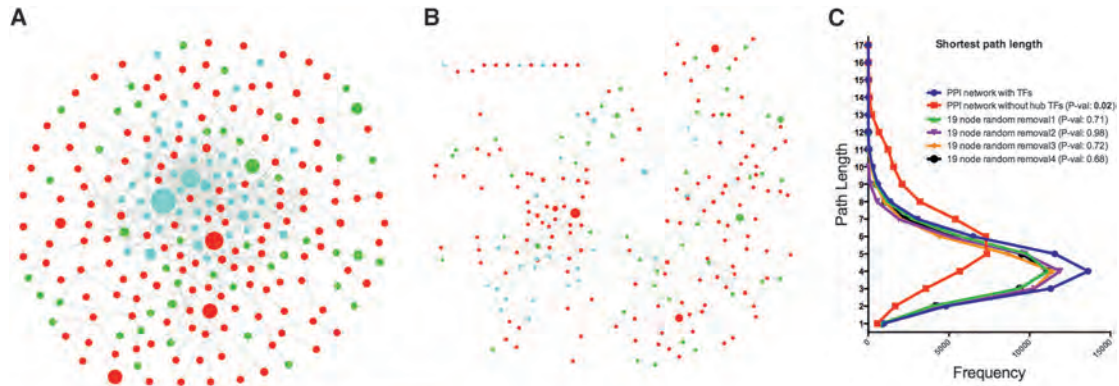
### Co-regulated Genes Represent Convergent Pathways

To extend this work to the level of specific proteins and identify potential mammalian conserved protein-signaling pathways represented by the RAG co-expression modules, we determined the PPI network represented by the genes in all the five modules. We reasoned that this would not only provide independent validation of the relationships inferred by RNA co-expression, but that the PPIs would provide important pathways for possible therapeutic intervention.

We screened experimentally validated PPIs among all possible combinations of gene pairs present in the co-expressed modules and over-represented TFs, obtaining a PPI network consisting of 280 nodes and 496 edges (Figure 4A; Experimental Procedures). Strikingly, despite the relatively small number of proteins in this network, we observed higher connectivity when compared to a random PPI network consisting of a similar number of nodes (clustering coefficient = 0.114, for random network = 0.016; average number of neighbors = 4.12, for random network = 1.83). We also observed enrichment of several important signaling pathways that contribute to the regulation of neuronal regeneration (Abe and Cavalli, 2008), including the Neurotrophin-, MAPK-, TGF-beta-, chemokine-, and JAK-STAT-signaling pathways (Abe and Cavalli, 2008; Figure 4D). Many of the TFs whose binding sites were over-represented in the RAG mRNA co-expression modules were also hubs in this protein network (Figures 4A and 4D; 19/62; hypergeometric  $p$  value  $5.8 \times 10^{-20}$ ); based on network centrality, 68% (19 TFs of the top 10%,  $n = 28$ ) of the most highly connected nodes represented TFs. Most genes belonging to the enriched signaling pathways also were enriched for the TFBSs of hub TFs in the PPI network (for 12 TFs with experimental ChIP data, 42 of 280 genes had three or more TFBSs for hub TFs; hypergeometric  $p$  value  $1.1 \times 10^{-12}$ ).

### Figure 3. TF-Binding Site Enrichment in Injured Regenerating Neurons

(A) Regulatory network of differentially expressed genes after nerve injury. Nodes correspond to genes or TFs and edges to ChIP interaction. Node color represents their corresponding module associations as denoted in the legends and over-represented TFs (diamond) are shown in cyan. Node size is based on its centrality.  
 (B) Sequence logo plots of reference (JASPAR/TRANSFAC) and identified position weight matrix for each TF significantly over-represented in magenta module are shown.  
 (C) Magenta module, showing eight over-represented TFs as hub genes. Nodes correspond to genes and edges to significant correlation. Larger nodes correspond to number of PubMed hits with co-occurrence of gene and neuronal regeneration, axonal regeneration, and nerve injury tags; upregulated (red), downregulated (green), and over-represented TFs (yellow) are shown. Only edges connected by over-represented TFs are highlighted.  
 (D–F) Combined TF overexpression. (D) Photomicrographs of dissociated DRG neurons transduced with the indicated viruses at 1 DIV, replated at 7 DIV, and cultured for an additional 20 hr on laminin. Red,  $\beta$ -tubulin; green, EGFP. (E and F) Quantification of total axonal length (E) and longest axon (F) reveal significant enhancement of axonal growth for ATF3 and JUN expression individually, compared to control (mCherry). Combined ATF3 and JUN overexpression enhances axonal growth significantly more than ATF3 or JUN individually. Data are mean  $\pm$  SE.  $n = 30$  wells. \*\* $p < 0.01$ , \*\*\* $p < 0.001$ , \*\*\*\* $p < 0.0001$ , one-way ANOVA with Bonferroni's post hoc test. Scale bar, 200 microns.



(legend on next page)

The presence of TFBS enrichment within genes representing these seven signaling pathways (Figure 4D) suggested that the coordinate regulation of core regeneration-associated hub TFs could provide the key regulatory cross-talk connecting these distinct pathways. To test this prediction, we removed these 19 TFs from the PPI network (Figure 4B), and we examined the resulting network mean path length, which is a measure of the connectivity of the remaining protein interactions in the absence of these TFs. We observed a drastic and significant reduction in protein connectivity, essentially causing nearly complete module disintegration (from 0.10 to 0.04 average clustering coefficient,  $p = 1.2 \times 10^{-4}$ ; Figures 4B and 4C). However, random removal of a similar number of nodes from the PPI network did not cause module disintegration (Figure 4C). This illustrates that these TFs provide critical cross-talk that coordinately links the core signaling pathways responsible for neuronal regeneration (Figures 4A and 4D).

Based on these observations, we reasoned that, rather than each of these pathways acting independently to facilitate regeneration, coordinate regulation of these regeneration-associated pathways is necessary for effective regeneration to occur after injury and that the identified hub TFs contribute to connecting these signaling pathways. To test this, we examined the gene expression levels of these over-represented TFs in independent published PNS and CNS spinal cord injury profiling data (Di Giovanni et al., 2003; Ryge et al., 2010; Table S4). Regardless of the model, these TFs were significantly co-expressed and upregulated after PNS injury (Figure 4E; Figure S2). In contrast, in five independent CNS injury datasets (spinal cord injury: mild, moderate, severe, and complete transection), the levels of these TFs were significantly variable or downregulated (Figure 4E) (non-parametric Kruskal-Wallis  $p < 1.1 \times 10^{-5}$ ; Figure S2). These data provide strong independent evidence that the coordinate regulation of all these TFs is associated with or related to nerve outgrowth after injury, as their coordinate upregulation is observed only in the PNS, and not in the CNS. This is also supported by the data shown in Figure 3, that two hub TFs present in the core regeneration-associated gene network, ATF3 and JUN, show cooperative (partially additive) effects when simultaneously over-expressed (increasing axonal outgrowth in mouse DRG neurons), when compared to either over-expressed individually (Figures 3D–3F).

In many cases, TF regulation of gene expression is often activated in a cooperative way by direct physical contact between two or more TFs forming transcriptional complexes (Ravasi et al., 2010). We next asked whether the over-represented TFs are known to physically interact, identifying experimentally vali-

dated interactions between several TFs, including ATF3, JUN, STAT3, and SP1 (Kiryu-Seo et al., 2008; Experimental Procedures; Figure S3). The TF SP1, when bound to the promoter region, recruits ATF3, JUN, and STAT3 and physically interacts with them to regulate gene expression in a synergistic fashion (Kiryu-Seo et al., 2008). Minimal regenerative effect after individual overexpression of these TFs in isolation has been observed previously (ATF3, Seiffers et al., 2007; STAT3, Bareyre et al., 2011). Hence, targeting the neuronal growth state network, rather than a single gene, may be more effective to mobilize a more complete range of signaling pathways necessary for recovery after injury, consistent with the cooperative effects that we observe with concurrent ATF3 and JUN over-expression.

### Regulation of Neurite Outgrowth in DRG Neurons Using Small Molecules

We reasoned that, if we could identify a small molecule whose effect on gene expression in injured neurons closely approximated the core signaling network associated with regeneration in the PNS, we could formally test the network biology prediction that such a compound should promote neurite outgrowth. In doing so, we extend this work to the level of initial screen for the discovery of therapeutics and provide further support for our strategy. We utilized the gene expression levels from the identified candidate up- and downregulated genes in the core 280-gene PPI network (M280; Figure 5A; Experimental Procedures) as a signature with which to query a publicly available database of drug-related expression profiles derived from non-neuronal cell lines known as the Connectivity Map (Lamb et al., 2006). We chose the top three matching expression patterns based on the connectivity and specificity score (Lamb et al., 2006), identifying the drugs ambroxol, lasalocid, and disulfiram (Experimental Procedures) for further analysis. Only ambroxol showed significant enhancement of axonal outgrowth in DRG neurons (Figure 5B).

Next, since the original pattern was derived from non-neuronal cell lines (Lamb et al., 2006), we tested if ambroxol regulates target marker genes in DRG neurons, observing that ambroxol-treated DRG neurons showed significant differential expression of eight genes ( $p$  value  $< 0.05$ ) among 14 tested genes from the M280 network (Figure S4). Interestingly, this included five of the core hub TFs (ATF3, FOS, JUN, SMAD1, and SP1) in the M280 network (Figure 5A; Figure S4). Ambroxol is a potent blocker of neuronal  $\text{Na}^+$  and  $\text{Ca}^{2+}$  channels and is used clinically as a mucolytic (Weiser, 2008). In animal models, ambroxol effectively suppresses symptoms of peripheral and central neuropathic pain (Gaida et al., 2005); but, the relationship of ambroxol to peripheral or central regeneration has not been described or predicted previously.

#### Figure 4. Over-Represented TFs Are Involved in Transcriptional Cross-Talk between Regeneration-Associated Pathways

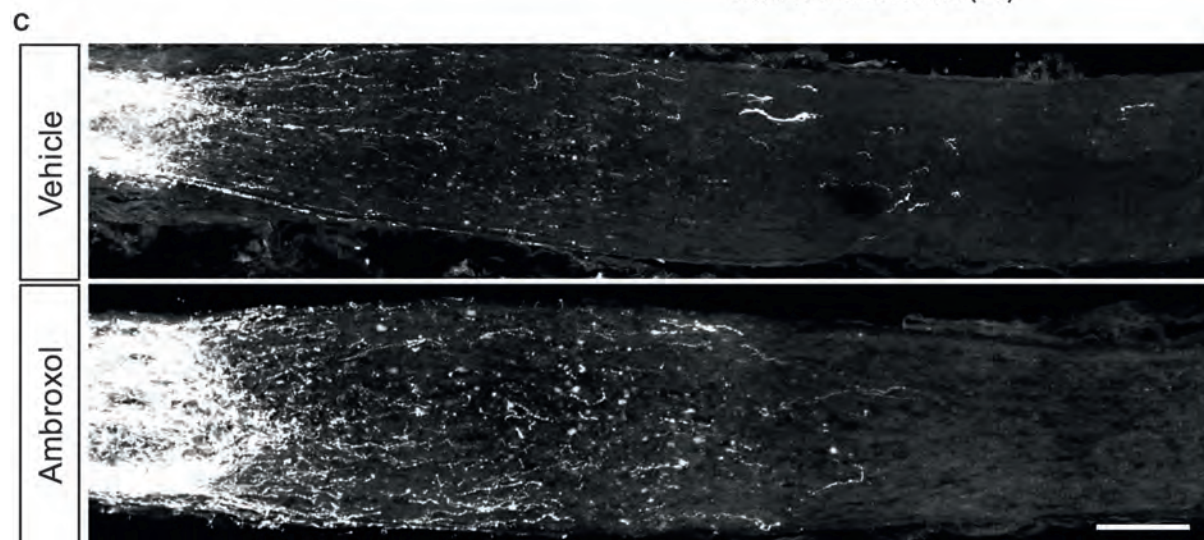
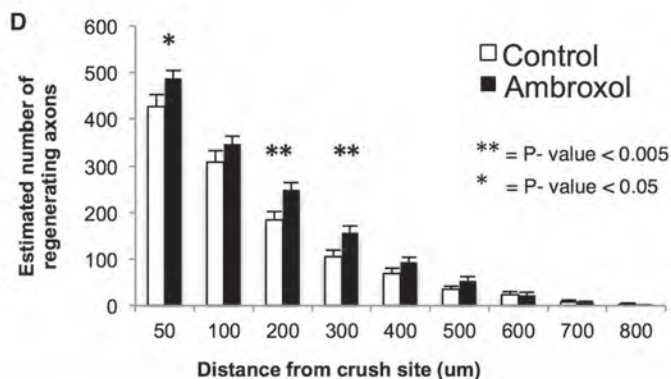
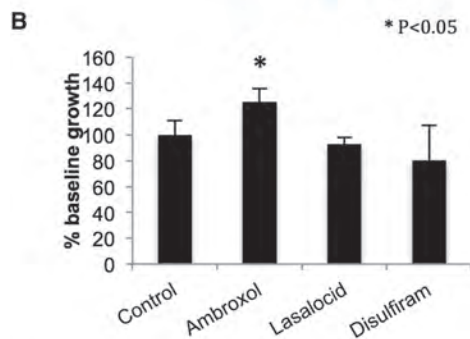
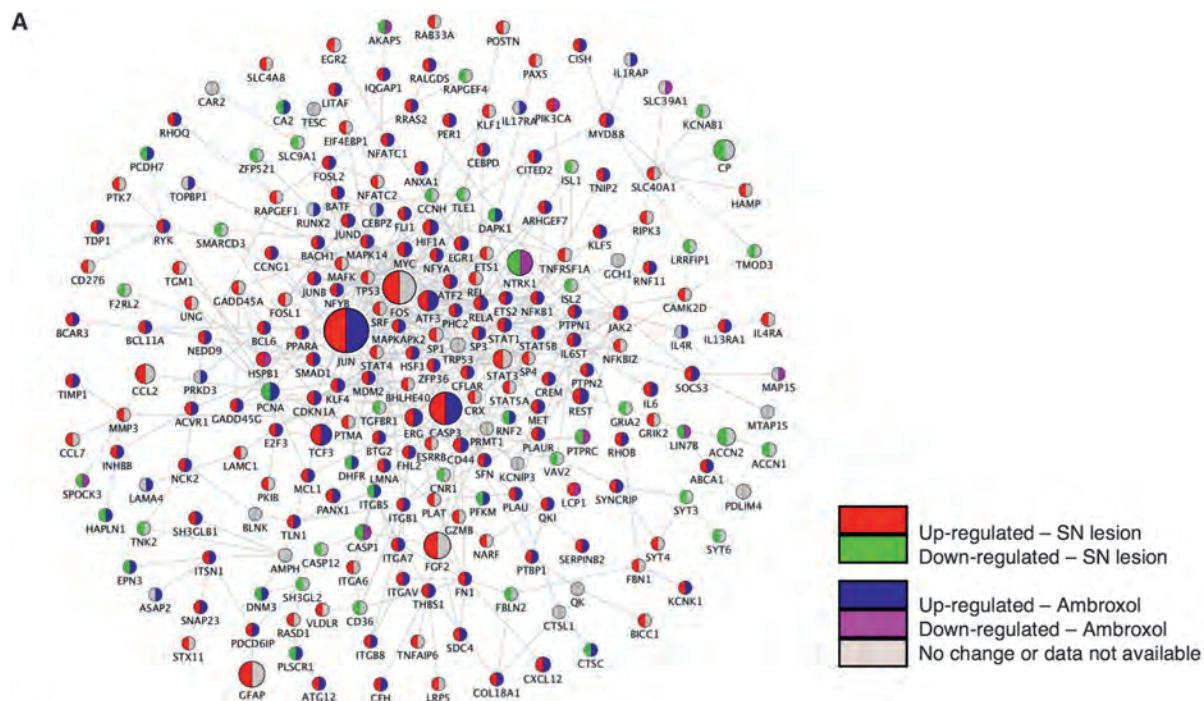
(A) Protein-protein interaction (PPI) network of differentially expressed genes after nerve injury. Nodes correspond to genes and edges to PPI. Larger nodes correspond to number of PubMed hits with co-occurrence of gene and neuronal regeneration, axonal regeneration, and nerve injury tags. Node color represents upregulated (red), downregulated (green), and over-represented (cyan) TFs.

(B) PPI network dissociation after *in silico* removal of 19 hub TFs is shown.

(C) Distribution of the shortest path between pairs of nodes in the PPI network with or without *in silico* removal of 19 hub TFs. Random removal of a similar number of nodes is shown for comparison.

(D) Significantly enriched KEGG pathways (Benjamini-corrected  $p$  values  $< 0.05$ ) in the PPI network.

(E) Boxplot representation of the variability in the expression levels of the over-represented TFs between CNS and PNS injuries (see Figures S1C and S1D). Time series data after CNS or PNS injury (see Figure S2) were used to create distance matrix using Euclidean distance measure to create the boxplot. Non-parametric Kruskal-Wallis test was used to compare differences between CNS and PNS injury datasets.



(legend on next page)

### Ambroxol Enhances CNS Regeneration In Vivo

Another prediction from our network analyses is that an appropriate co-regulation of the core regeneration-associated module, M280, which does not normally occur in CNS injury, might enable CNS regeneration. Since ambroxol recapitulates many of the core expression changes in the M280, we reasoned that it could potentially promote CNS regeneration. Optic nerve (ON) regeneration is a standard model for CNS regeneration (Sun et al., 2011), so we examined ON regeneration in C57BL/6 mice after a crush injury following treatment with ambroxol (Experimental Procedures). We observed a limited, but significant increase in axon regeneration beyond the site of the lesion (>1.5-fold increase between 200 and 500  $\mu\text{m}$ ;  $p < 0.04$ ) after 2 weeks in animals treated with ambroxol compared with control animals (Figures 5C and 5D; Figure S5A), confirming the predictive properties of the approach.

Next we compared ambroxol to one of the few proven genetic approaches to determine whether it would have a similar additive effect of enabling axonal regeneration after injury, on top of a genetic manipulation already shown to do so (Sun et al., 2011). For this, we examined the combinatorial activity of ambroxol treatment in PTEN homozygous knockout mice, which have significantly improved axonal regeneration after ON crush relative to wild-type (WT) animals (Park et al., 2008), which is further enhanced by double PTEN/SOCS knockout (Sun et al., 2011). We observed enhanced regeneration beyond the site of the lesion (>2.9-fold increase at 2,500  $\mu\text{m}$ ;  $p$  value 0.02) after 2 weeks in PTEN<sup>-/-</sup> (PTEN<sup>fl/fl</sup>) animals treated with ambroxol compared with PTEN<sup>-/-</sup> animals treated with vehicle (Figure 6; Figure S5B), confirming that ambroxol administration *in vivo* enhances ON regeneration combined with a known regeneration-promoting genetic manipulation.

### DISCUSSION

The limited regenerative potential of CNS neurons is due to both cell-extrinsic and cell-intrinsic factors (Afshari et al., 2009; Filbin, 2003; Giger et al., 2010; Yiu and He, 2006). Several decades of work devoted to identifying cell-intrinsic factors has resulted in dozens of individual RAGs, including cytoskeletal proteins, cell adhesion and axon guidance molecules, TFs, trophic factors, and their receptors (Costigan et al., 2002; Giger et al., 2010; Sun and He, 2010). Individual manipulation of these RAGs causes, though, only limited regeneration (Ferreira et al., 2012), while combinatorial reductions in cell-extrinsic factors Nogo, MAG, and OMgp have yielded inconclusive results (Cafferty et al., 2010; Lee et al., 2010).

We hypothesized that changing the growth state of differentiated adult CNS neurons by using drugs that activate relevant signaling pathways, TFs, and thereby regeneration effector genes would allow the neurons to re-grow without changing their molecular identity, making it possible to activate and enhance CNS regeneration. To achieve this, we applied a comprehensive systems genomics approach, starting with gene expression profiling combined with multi-level bioinformatic analyses and then experimental validation of network predictions, to provide a framework for understanding the precise molecular pathways involved in nerve regrowth after injury. We provide multiple lines of experimental support for the predictions of the regeneration network that we make, and we further apply this rubric for pathway discovery to identify a drug that accelerates nerve outgrowth after CNS injury, albeit modestly. This work provides a key proof of principle for the power of such systems genomic approaches in tackling complex problems in nervous system biology.

Our data describe that the injury-induced regulation of neuronal transcription in sensory neurons in the PNS includes a specific network of genes that are associated by coordinate action with the capacity for autonomous regeneration. The network includes many previously identified RAGs and related pathways, as well as many novel RAGs and the structure of the regulatory network in which they operate, building upon decades of research in this field. We speculate that failure of induction of this network after CNS injury at least partially explains why regeneration in CNS injury does not occur.

In support of this view, we show that ambroxol, a compound that increases expression of elements of the PNS coordinate transcriptional network, can promote CNS regeneration. We acknowledge that the effects of ambroxol are modest compared with combinatorial genetic manipulations (Sun et al., 2011), which is perhaps not unexpected given the paucity of drugs that enhance regeneration to any extent. We view this drug-screening component as a proof of principle that should be further refined in future experiments but that demonstrates the potential of coordinate regulation of the identified core network. Understanding the mechanism of ambroxol activity in this regard will also aid in the further development of mechanistic-based treatments. We also emphasize that the identified core network can be used as tool for screening additional drugs that may enhance neuronal regeneration. Moreover, the additive activity of ambroxol in combination with PTEN reduction provides support for the notion that combinatorial activation of RAGs and their pathways enhances CNS regeneration.

Combining approaches that activate the intrinsic regeneration network with suppression of inhibitory extrinsic cues will almost

#### Figure 5. Targeting Candidate RAG Regulatory Network Using Small Molecules

Gene expression signatures after PNS injury were used to query drug-related expression profiles in the Connectivity Map. Using a pattern-matching algorithm, we selected three drugs (ambroxol, disulfiram, and lasalocid) based on enrichment and specificity scores.

(A) PPI (edges) network of co-expressed and differentially expressed genes (nodes) after PNS injury is shown. Upregulation (red) and downregulation (green) after SN lesion; upregulation (blue) and downregulation (purple) after ambroxol treatment (from Connectivity Map).

(B) Differences in DRG neurite outgrowth after treatment with drugs. Ambroxol elicited more neuronal growth than control ( $p < 0.05$ ,  $t$  test).

(C and D) Ambroxol promotes retinal ganglion cell axonal regeneration. Ambroxol (Amb 25 mg/ml) or vehicle (Veh) was injected into the eye just before ON crush. Animals received daily 120 ml ambroxol (25 mg/ml) or vehicle by intraperitoneal (i.p.) injection from day 1 to day 14. At day 7 ambroxol (25 mg/ml) or vehicle was injected into the eye. Tracer CTB was injected into the eye on day 11 and animals were sacrificed on day 14. (C) Representative confocal images show ON sections from WT animals treated with vehicle ( $n = 10$ ) and WT animals treated with ambroxol (25 mg/ml,  $n = 13$ ). Axons are labeled with CTB. Scale bar, 100  $\mu\text{m}$ . Measurements were made blinded to treatment. (D) Quantification of number of axons in (C) is shown ( $t$  test, \*\* $p < 0.001$  and \* $p < 0.05$ ).

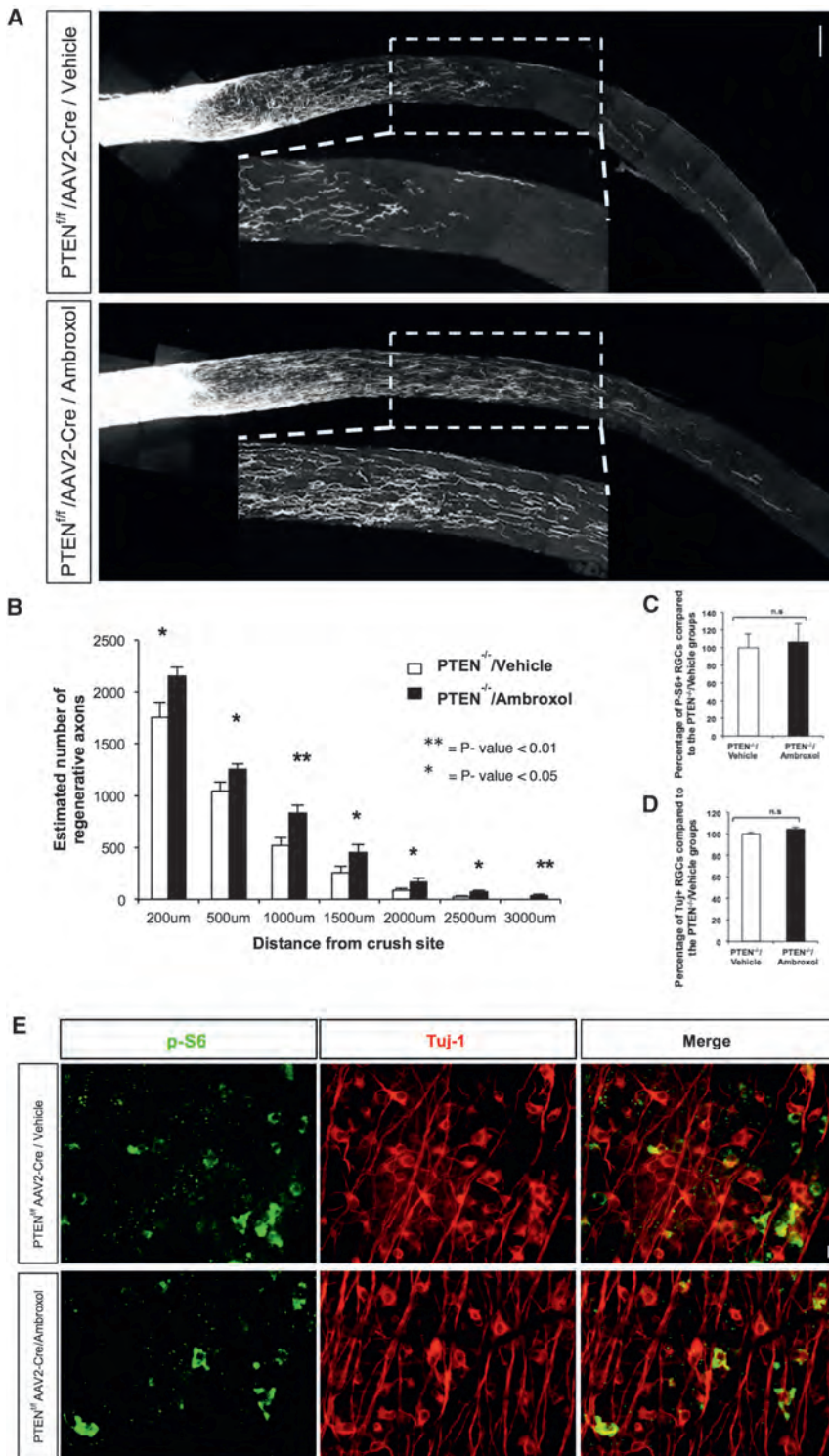


### Figure 6. Ambroxol Promotes Retinal Ganglion Cell Axonal Regeneration in PTEN Knockout Mice

Ambroxol (Amb 25 mg/ml) or vehicle was injected into the eye just before ON crush. Animals received daily 300 mg/kg ambroxol or vehicle by i.p. injection for the first 5 days after the crush and then they received 150 mg/kg until day 14. At day 7 ambroxol (25 mg/ml) or vehicle was injected into the eye. Tracer CTB was injected into the eye on day 11 and animals were sacrificed on day 14.

(A) Representative confocal images of ON sections from PTEN<sup>-/-</sup> animals treated with vehicle (n = 4) and PTEN<sup>-/-</sup> animals treated with ambroxol (n = 4). Axons are labeled with CTB. Scale bar, 100  $\mu$ m. Measurements were made blinded to treatment.

(B) Quantification of number of axons in (A) is shown (t test, \*\*p < 0.01 and \*p < 0.05).

(C and D) Quantifications of retinal ganglion cell (RGC) survival measured by Tuj1 and P-S6 antibody staining are shown.

(E) Representative retina whole-mount images with Tuj1 and P-S6 antibody staining 2 weeks post injury are shown. Scale bar, 25  $\mu$ m.

multiple TFs in vivo in the CNS exist. But, our network and bioinformatic analyses lead to the expectation that coordinate overexpression of the core set of TFs identified here will enhance both peripheral and central regeneration. We predict that changing the transcriptional state of differentiated adult CNS neurons, either by coordinate expression of sets of TFs or by using drugs that activate the relevant downstream functional signaling pathways, represents a worthwhile strategy, enhancing the possibility of creating CNS regenerative capacity after injury.

### EXPERIMENTAL PROCEDURES

#### Nerve Injury Expression Data

In total, 382 gene expression data from microarray experiments related to nerve injury were utilized in this study; preprocessing and normalization procedures were calculated according to the R functions as described in the Supplemental Experimental Procedures (see Table S4 for dataset details).

#### Weighted Gene Co-expression Network Analysis

We used the R package WGCNA (Langfelder and Horvath, 2008) to construct co-expression networks, as previously done (Oldham et al., 2006;

certainly further optimize recovery. An obvious conceptual parallel that was deemed improbable prior to its demonstration was the overexpression of four TFs to change the state of a cell from fully differentiated to pluripotent (Takahashi and Yamanaka, 2006). Technical challenges to coordinate overexpression of

Zhang and Horvath, 2005) and as described in detail in the Supplemental Experimental Procedures. To identify hub genes and modules shared across independent nerve injury datasets, we applied consensus network analysis (Langfelder and Horvath, 2007). GO and pathway enrichment analysis was performed using the Database for Annotation, Visualization and Integrated Discovery (DAVID) platform (<https://david.ncicrf.gov/>; Huang da et al.,

2009). All network plots were constructed using the Cytoscape software (Saito et al., 2012).

### Overexpression of Novel Candidate RAGs

The 16 lentiviral open reading frame (ORF) expression clones (candidate RAGs) and control vector (pReceiver-Lv122) were purchased from GeneCopoeia. Viral stocks were used to transduce DRGs for 24 hr. Then 1 week after infection, the cells were fixed with 4% paraformaldehyde 24 hr after replating. Fixed cells were immunostained for anti-beta-tubulin (1:800, Sigma, RRID: AB\_1844090). Neurite initiation and the longest neurite length of the cells expressing GFP and immunostained for beta-tubulin were quantified using NeuroMath and ImageJ. Data were obtained from at least three separate experiments.

### Knockdown of Novel Candidate RAGs

Mission control plasmid containing either shRNA sequences to *Fxyd5*, *Gfpt1*, *Smagp*, *Tacstd2*, and *Cdc42* were purchased from Sigma-Aldrich and shRNA control vector, containing a non-specific shRNA, was purchased from OpenBiosystems. Viral particles were produced as previously described (Sena-Esteves et al., 2004). Then 1 hr after plating the DRG neurons, 100 MOI shRNA was added to the DRG cultures and incubated for 24 hr. Then 1 week after infection, the cells were fixed with 4% paraformaldehyde 17 hr after replating. Fixed cells were immunostained for anti-beta-tubulin (1:800, Sigma, RRID: AB\_1844090). Neurite initiation and the longest neurite length of the cells expressing GFP and immunostained for beta-tubulin were quantified using NeuroMath. Data were obtained from at least three separate experiments repeated in quadruplicate. Measurements were made blinded to treatment (see the Supplemental Experimental Procedures for further details).

### TFBS Enrichment

TFBS enrichment analysis was performed by scanning the canonical promoter region (1,000 bp upstream of the transcription start site) for the genes (kME > 0.5) present in the regeneration-associated co-expression modules. We utilized TFBS position weight matrices from JASPAR and TRANSFAC databases (Matys et al., 2003; Portales-Casamar et al., 2010) to examine the enrichment using Clover algorithm (Frith et al., 2004; see the Supplemental Experimental Procedures for further details). We also integrated the existing ChIP data for TFs from either the Encyclopedia of DNA Elements (ENCODE, Landt et al., 2012) or other compiled genome-wide ChIP data (Lachmann et al., 2010) to generate the transcriptional network (Figure 3A).

### PPI Network Analyses

We constructed an experimentally validated PPI network using all the regeneration-associated co-expression gene network modules (two upregulated modules after nerve injury and three downregulated modules after injury). We created all possible combinations of gene pairs present in these co-expression networks and identified all experimentally verified interaction data (in human, mouse, or rat dataset) for their corresponding proteins in the STRING database (Franceschini et al., 2013), constructing the protein network by force-directed layout (Figure 4A).

### In Silico Small Molecule Screening

The Connectivity Map (cmap) database was used for screening and the database details have been described previously (Lamb et al., 2006). In this method, the similarity between the query signature (RAG signature) and more than 7,000 expression profiles for 1,309 compounds (reference signatures) in the cmap database was evaluated (Lamb et al., 2006). Enrichments of both the up- and downregulated nerve injury-induced genes in the profiles of each treatment instance were estimated as described previously (Lamb et al., 2006) and as described in detail in the Supplemental Experimental Procedures. Permutated results were used to evaluate the significance of the scores and to rank the molecules in order to select the top molecules for experimental validation (see the Supplemental Experimental Procedures). This methodology was applied for two query signatures related to nerve injury as follows: (1) PPI network consisting of 280 genes (Figure 4A), and (2) regeneration-associated co-expression modules (Figure 1; Table S2). The top three enriched small molecules intersecting in both the signature lists were utilized for experimental validation.

### Neurite Outgrowth Assay in Primary Adult DRG Neuron Culture

Adult C57BL/6J dissociated DRG neurons were plated in a tissue culture eight-well chamber slide dish (Nalge Nunc) coated with poly-D-lysine and laminin (Sigma) cultured in Neurobasal medium (Invitrogen) supplemented with B27 supplement, penicillin, streptomycin, 1 mM L-glutamine, 50 ng/ml NGF, 2 ng/ml GDNF, and 10 mM AraC at 37°C. For drug treatment, DRG neurons were cultured for 24 hr in the presence of 40 and 60  $\mu$ M concentrations of drugs. The cells were fixed with 4% paraformaldehyde. Fixed cells were immunostained for b-III-tubulin (RRID: AB\_2313773). Neurite initiation and the longest neurite length of the cells were quantified using NeuroMath. Data were obtained from at least three separate experiments repeated in quadruplicate.

### Mice Surgery, Drug Administration, and ON Injury

All experimental procedures were performed in compliance with animal protocols approved by Institutional Animal Care and Use Committee (IACUC) at Boston Children's Hospital. ONs from 6-week-old C57BL/6 mice were crushed as described previously (Park et al., 2008) just after intravitreal injection of 1  $\mu$ l ambroxol (Sigma, 25 mg/ml in 5% Tween80%–5% Polyethylene glycol 400 in water) or vehicle (5% Tween80%–5% PEG 400 in water). A second intravitreal injection of ambroxol or vehicle was performed 7 days post-ON crush. Daily mice received 120  $\mu$ l (25 mg/ml) ambroxol or vehicle intraperitoneally, i.e., from the day after the ON crush to the day prior to termination. For PTEN<sup>-/-</sup> animal experiments, P21 PTEN floxed mice received AAV2-Cre intravitreal injection within the eye. We injected (intraperitoneally) ambroxol at 300 mg/kg for the first 5 days after the crush and then we injected 150 mg/kg. Mice were injected twice a day every day. Regenerating axons were traced by intravitreal injection of 1  $\mu$ l CTB-Alexa-488 (1  $\mu$ g/ $\mu$ l in PBS, Invitrogen) 2 days before termination.

### ACCESSION NUMBERS

The accession numbers for the data reported in this paper are GEO: GSE30691, GSE26350, GSE2884, GSE33175, GSE21007, GDS63, and GSE19701. The network datasets generated and analyzed in this study also are available at [https://coppolab.ucla.edu/gclabapps/nb/browser?id=Consensus\\_Tuszynski;ver=vijay](https://coppolab.ucla.edu/gclabapps/nb/browser?id=Consensus_Tuszynski;ver=vijay) and [https://coppolab.ucla.edu/gclabapps/nb/browser?id=Consensus\\_Fainzilber;ver=vijay](https://coppolab.ucla.edu/gclabapps/nb/browser?id=Consensus_Fainzilber;ver=vijay).

### SUPPLEMENTAL INFORMATION

Supplemental Information includes Supplemental Experimental Procedures, five figures, and seven tables and can be found with this article online at <http://dx.doi.org/10.1016/j.neuron.2016.01.034>.

### AUTHOR CONTRIBUTIONS

V.C., G.C., and D.H.G. designed the experiments and V.C., C.J.W., and D.H.G. wrote the manuscript. G.C. and V.C. performed network analyses on the two initial PNS datasets, and V.C. performed all subsequent bioinformatic analyses with input from D.H.G. V.C. conducted or coordinated the in vitro validation experiments via gene overexpression. T.O. performed the in vitro knockdown experiments. E.A.H. performed the transcription factor co-expression experiments. H.N. performed the ON crush experiments with supervision by Z.H. R.V., A.Y., and L. Barrett provided technical assistance with experiments. G.C., F.G., J.D.-T., P.L., S.H., and A.Z. also contributed to aspects of the data analyses. M.T., M.F., C.J.W., M.C., A.B., I.M., and L. Benowitz provided microarray data utilized in this study. All authors discussed the results and provided comments and revisions on the manuscript.

### ACKNOWLEDGMENTS

We gratefully acknowledge support from the Dr. Miriam and Sheldon G. Adelson Medical Research Foundation, the NINDS Informatics Center for Neurogenetics and Neurogenomics (P30 NS062691) (G.C.), NIH R01 NS038253 (C.J.W.) and NS074430 (M.C.), and the Bertarelli Foundation (C.J.W.).

Received: September 25, 2015

Revised: January 12, 2016

Accepted: January 20, 2016

Published: February 18, 2016

## REFERENCES

- Abe, N., and Cavalli, V. (2008). Nerve injury signaling. *Curr. Opin. Neurobiol.* *18*, 276–283.
- Afshari, F.T., Kappagantula, S., and Fawcett, J.W. (2009). Extrinsic and intrinsic factors controlling axonal regeneration after spinal cord injury. *Expert Rev. Mol. Med.* *11*, e37.
- Bareyre, F.M., Garzorz, N., Lang, C., Misgeld, T., Büning, H., and Kerschensteiner, M. (2011). In vivo imaging reveals a phase-specific role of STAT3 during central and peripheral nervous system axon regeneration. *Proc. Natl. Acad. Sci. USA* *108*, 6282–6287.
- Beggs, S., and Salter, M.W. (2006). Neuropathic pain: symptoms, models, and mechanisms. *Drug Dev. Res.* *67*, 289–301.
- Bomze, H.M., Bulsara, K.R., Iskandar, B.J., Caroni, P., and Skene, J.H. (2001). Spinal axon regeneration evoked by replacing two growth cone proteins in adult neurons. *Nat. Neurosci.* *4*, 38–43.
- Cafferty, W.B., Duffy, P., Huebner, E., and Strittmatter, S.M. (2010). MAG and OMgp synergize with Nogo-A to restrict axonal growth and neurological recovery after spinal cord trauma. *J. Neurosci.* *30*, 6825–6837.
- Cao, Z., Gao, Y., Bryson, J.B., Hou, J., Chaudhry, N., Siddiq, M., Martinez, J., Spencer, T., Carmel, J., Hart, R.B., and Filbin, M.T. (2006). The cytokine interleukin-6 is sufficient but not necessary to mimic the peripheral conditioning lesion effect on axonal growth. *J. Neurosci.* *26*, 5565–5573.
- Cavalli, V., Kujala, P., Klumperman, J., and Goldstein, L.S. (2005). Sunday Driver links axonal transport to damage signaling. *J. Cell Biol.* *168*, 775–787.
- Chierzi, S., Ratto, G.M., Verma, P., and Fawcett, J.W. (2005). The ability of axons to regenerate their growth cones depends on axonal type and age, and is regulated by calcium, cAMP and ERK. *Eur. J. Neurosci.* *21*, 2051–2062.
- Costigan, M., Befort, K., Karchewski, L., Griffin, R.S., D'Urso, D., Allchorne, A., Sitariski, J., Mannion, J.W., Pratt, R.E., and Woolf, C.J. (2002). Replicate high-density rat genome oligonucleotide microarrays reveal hundreds of regulated genes in the dorsal root ganglion after peripheral nerve injury. *BMC Neurosci.* *3*, 16.
- Di Giovanni, S., Knobloch, S.M., Brandoli, C., Aden, S.A., Hoffman, E.P., and Faden, A.I. (2003). Gene profiling in spinal cord injury shows role of cell cycle in neuronal death. *Ann. Neurol.* *53*, 454–468.
- Dragunow, M., Xu, R., Walton, M., Woodgate, A., Lawlor, P., MacGibbon, G.A., Young, D., Gibbons, H., Lipski, J., Muraviev, A., et al. (2000). c-Jun promotes neurite outgrowth and survival in PC12 cells. *Brain Res. Mol. Brain Res.* *83*, 20–33.
- Ferreira, L.M., Floriddia, E.M., Quadrato, G., and Di Giovanni, S. (2012). Neural regeneration: lessons from regenerating and non-regenerating systems. *Mol. Neurobiol.* *46*, 227–241.
- Filbin, M.T. (2003). Myelin-associated inhibitors of axonal regeneration in the adult mammalian CNS. *Nat. Rev. Neurosci.* *4*, 703–713.
- Franceschini, A., Szklarczyk, D., Frankild, S., Kuhn, M., Simonovic, M., Roth, A., Lin, J., Minguez, P., Bork, P., von Mering, C., and Jensen, L.J. (2013). STRING v9.1: protein-protein interaction networks, with increased coverage and integration. *Nucleic Acids Res.* *41*, D808–D815.
- Frith, M.C., Fu, Y., Yu, L., Chen, J.F., Hansen, U., and Weng, Z. (2004). Detection of functional DNA motifs via statistical over-representation. *Nucleic Acids Res.* *32*, 1372–1381.
- Gaida, W., Klinder, K., Arndt, K., and Weiser, T. (2005). Ambroxol, a Nav1.8-preferring Na<sup>+</sup> channel blocker, effectively suppresses pain symptoms in animal models of chronic, neuropathic and inflammatory pain. *Neuropharmacology* *49*, 1220–1227.
- Geschwind, D.H., and Konopka, G. (2009). Neuroscience in the era of functional genomics and systems biology. *Nature* *461*, 908–915.
- Giger, R.J., Hollis, E.R., 2nd, and Tuszynski, M.H. (2010). Guidance molecules in axon regeneration. *Cold Spring Harb. Perspect. Biol.* *2*, a001867.
- Hanz, S., Perlson, E., Willis, D., Zheng, J.Q., Massarwa, R., Huerta, J.J., Koltzenburg, M., Kohler, M., van-Minnen, J., Twiss, J.L., and Fainzilber, M. (2003). Axoplasmic importins enable retrograde injury signaling in lesioned nerve. *Neuron* *40*, 1095–1104.
- Hoffman, P.N. (2010). A conditioning lesion induces changes in gene expression and axonal transport that enhance regeneration by increasing the intrinsic growth state of axons. *Exp. Neurol.* *223*, 11–18.
- Huang da, W., Sherman, B.T., and Lempicki, R.A. (2009). Systematic and integrative analysis of large gene lists using DAVID bioinformatics resources. *Nat. Protoc.* *4*, 44–57.
- Kiryu-Seo, S., Kato, R., Ogawa, T., Nakagomi, S., Nagata, K., and Kiyama, H. (2008). Neuronal injury-inducible gene is synergistically regulated by ATF3, c-Jun, and STAT3 through the interaction with Sp1 in damaged neurons. *J. Biol. Chem.* *283*, 6988–6996.
- Lachmann, A., Xu, H., Krishnan, J., Berger, S.I., Mazloom, A.R., and Ma'ayan, A. (2010). ChEA: transcription factor regulation inferred from integrating genome-wide ChIP-X experiments. *Bioinformatics* *26*, 2438–2444.
- Lamb, J., Crawford, E.D., Peck, D., Modell, J.W., Bhat, I.C., Wrobel, M.J., Lerner, J., Brunet, J.P., Subramanian, A., Ross, K.N., et al. (2006). The Connectivity Map: using gene-expression signatures to connect small molecules, genes, and disease. *Science* *313*, 1929–1935.
- Landt, S.G., Marinov, G.K., Kundaje, A., Kheradpour, P., Pauli, F., Batzoglou, S., Bernstein, B.E., Bickel, P., Brown, J.B., Cayting, P., et al. (2012). ChIP-seq guidelines and practices of the ENCODE and modENCODE consortia. *Genome Res.* *22*, 1813–1831.
- Langfelder, P., and Horvath, S. (2007). Eigengene networks for studying the relationships between co-expression modules. *BMC Syst. Biol.* *1*, 54.
- Langfelder, P., and Horvath, S. (2008). WGCNA: an R package for weighted correlation network analysis. *BMC Bioinformatics* *9*, 559.
- Lee, J.K., Geoffroy, C.G., Chan, A.F., Tolentino, K.E., Crawford, M.J., Leal, M.A., Kang, B., and Zheng, B. (2010). Assessing spinal axon regeneration and sprouting in Nogo-, MAG-, and OMgp-deficient mice. *Neuron* *66*, 663–670.
- Li, S., Xue, C., Yuan, Y., Zhang, R., Wang, Y., Wang, Y., Yu, B., Liu, J., Ding, F., Yang, Y., and Gu, X. (2015). The transcriptional landscape of dorsal root ganglia after sciatic nerve transection. *Sci. Rep.* *5*, 16888.
- Lindwall, C., and Kanje, M. (2005). Retrograde axonal transport of JNK signaling molecules influence injury induced nuclear changes in p-c-Jun and ATF3 in adult rat sensory neurons. *Mol. Cell. Neurosci.* *29*, 269–282.
- Matys, V., Fricke, E., Geffers, R., Gössling, E., Haubrock, M., Hehl, R., Hornischer, K., Karas, D., Kel, A.E., Kel-Margoulis, O.V., et al. (2003). TRANSFAC: transcriptional regulation, from patterns to profiles. *Nucleic Acids Res.* *31*, 374–378.
- Michaevlevski, I., Segal-Ruder, Y., Rozenbaum, M., Medzihradzky, K.F., Shalem, O., Coppola, G., Horn-Saban, S., Ben-Yaakov, K., Dagan, S.Y., Rishal, I., et al. (2010). Signaling to transcription networks in the neuronal retrograde injury response. *Sci. Signal.* *3*, ra53.
- Neumann, S., and Woolf, C.J. (1999). Regeneration of dorsal column fibers into and beyond the lesion site following adult spinal cord injury. *Neuron* *23*, 83–91.
- Oldham, M.C., Horvath, S., and Geschwind, D.H. (2006). Conservation and evolution of gene coexpression networks in human and chimpanzee brains. *Proc. Natl. Acad. Sci. USA* *103*, 17973–17978.
- Parikshak, N.N., Gandal, M.J., and Geschwind, D.H. (2015). Systems biology and gene networks in neurodevelopmental and neurodegenerative disorders. *Nat. Rev. Genet.* *16*, 441–458.
- Park, K.K., Liu, K., Hu, Y., Smith, P.D., Wang, C., Cai, B., Xu, B., Connolly, L., Kramvis, I., Sahin, M., and He, Z. (2008). Promoting axon regeneration in the adult CNS by modulation of the PTEN/mTOR pathway. *Science* *322*, 963–966.
- Perlson, E., Hanz, S., Ben-Yaakov, K., Segal-Ruder, Y., Seger, R., and Fainzilber, M. (2005). Vimentin-dependent spatial translocation of an activated MAP kinase in injured nerve. *Neuron* *45*, 715–726.

- Portales-Casamar, E., Thongjuea, S., Kwon, A.T., Arenillas, D., Zhao, X., Valen, E., Yusuf, D., Lenhard, B., Wasserman, W.W., and Sandelin, A. (2010). JASPAR 2010: the greatly expanded open-access database of transcription factor binding profiles. *Nucleic Acids Res.* *38*, D105–D110.
- Qiu, J., Cai, D., Dai, H., McAtee, M., Hoffman, P.N., Bregman, B.S., and Filbin, M.T. (2002). Spinal axon regeneration induced by elevation of cyclic AMP. *Neuron* *34*, 895–903.
- Ramón y Cajal, S., DeFelipe, J., and Jones, E.G. (1991). *Cajal's Degeneration and Regeneration of the Nervous System* (Oxford University Press).
- Ravasi, T., Suzuki, H., Cannistraci, C.V., Katayama, S., Bajic, V.B., Tan, K., Akalin, A., Schmeier, S., Kanamori-Katayama, M., Bertin, N., et al. (2010). An atlas of combinatorial transcriptional regulation in mouse and man. *Cell* *140*, 744–752.
- Ryge, J., Winther, O., Wienecke, J., Sandelin, A., Westerdahl, A.C., Hultborn, H., and Kiehn, O. (2010). Transcriptional regulation of gene expression clusters in motor neurons following spinal cord injury. *BMC Genomics* *11*, 365.
- Saito, R., Smoot, M.E., Ono, K., Ruschinski, J., Wang, P.L., Lotia, S., Pico, A.R., Bader, G.D., and Ideker, T. (2012). A travel guide to Cytoscape plugins. *Nat. Methods* *9*, 1069–1076.
- Schweizer, U., Gunnarsen, J., Karch, C., Wiese, S., Holtmann, B., Takeda, K., Akira, S., and Sendtner, M. (2002). Conditional gene ablation of Stat3 reveals differential signaling requirements for survival of motoneurons during development and after nerve injury in the adult. *J. Cell Biol.* *156*, 287–297.
- Seiffers, R., Allchorne, A.J., and Woolf, C.J. (2006). The transcription factor ATF-3 promotes neurite outgrowth. *Mol. Cell Neurosci.* *32*, 143–154.
- Seiffers, R., Mills, C.D., and Woolf, C.J. (2007). ATF3 increases the intrinsic growth state of DRG neurons to enhance peripheral nerve regeneration. *J. Neurosci.* *27*, 7911–7920.
- Sena-Esteves, M., Tebbets, J.C., Steffens, S., Crombleholme, T., and Flake, A.W. (2004). Optimized large-scale production of high titer lentivirus vector pseudotypes. *J. Virol. Methods* *122*, 131–139.
- Sendtner, M., Stöckli, K.A., and Thoenen, H. (1992). Synthesis and localization of ciliary neurotrophic factor in the sciatic nerve of the adult rat after lesion and during regeneration. *J. Cell Biol.* *118*, 139–148.
- Shim, S., and Ming, G.L. (2010). Roles of channels and receptors in the growth cone during PNS axonal regeneration. *Exp. Neurol.* *223*, 38–44.
- Subang, M.C., and Richardson, P.M. (2001). Synthesis of leukemia inhibitory factor in injured peripheral nerves and their cells. *Brain Res.* *900*, 329–331.
- Sun, F., and He, Z. (2010). Neuronal intrinsic barriers for axon regeneration in the adult CNS. *Curr. Opin. Neurobiol.* *20*, 510–518.
- Sun, F., Park, K.K., Belin, S., Wang, D., Lu, T., Chen, G., Zhang, K., Yeung, C., Feng, G., Yankner, B.A., and He, Z. (2011). Sustained axon regeneration induced by co-deletion of PTEN and SOCS3. *Nature* *480*, 372–375.
- Taga, T., and Kishimoto, T. (1997). Gp130 and the interleukin-6 family of cytokines. *Annu. Rev. Immunol.* *15*, 797–819.
- Takahashi, K., and Yamanaka, S. (2006). Induction of pluripotent stem cells from mouse embryonic and adult fibroblast cultures by defined factors. *Cell* *126*, 663–676.
- Weiser, T. (2008). Ambroxol: a CNS drug? *CNS Neurosci. Ther.* *14*, 17–24.
- Yang, E.K., Takimoto, K., Hayashi, Y., de Groat, W.C., and Yoshimura, N. (2004). Altered expression of potassium channel subunit mRNA and alpha-dendrotoxin sensitivity of potassium currents in rat dorsal root ganglion neurons after axotomy. *Neuroscience* *123*, 867–874.
- Yiu, G., and He, Z. (2006). Glial inhibition of CNS axon regeneration. *Nat. Rev. Neurosci.* *7*, 617–627.
- Zhang, B., and Horvath, S. (2005). A general framework for weighted gene co-expression network analysis. *Stat. Appl. Genet. Mol. Biol.* *4*, Article 17.
- Zhao, X., Tang, Z., Zhang, H., Atianjoh, F.E., Zhao, J.Y., Liang, L., Wang, W., Guan, X., Kao, S.C., Tiwari, V., et al. (2013). A long noncoding RNA contributes to neuropathic pain by silencing *Kcna2* in primary afferent neurons. *Nat. Neurosci.* *16*, 1024–1031.

# RAN Translation in Huntington Disease

Monica Bañez-Coronel,<sup>1,2</sup> Fatma Ayhan,<sup>1,2</sup> Alex D. Tarabochia,<sup>1,2</sup> Tao Zu,<sup>1,2</sup> Barbara A. Perez,<sup>1,2</sup> Solaleh Khoramian Tusi,<sup>1,2,6</sup> Olga Pletnikova,<sup>7</sup> David R. Borchelt,<sup>1,4</sup> Christopher A. Ross,<sup>8,9,10,11,12,13,14</sup> Russell L. Margolis,<sup>8,9,10,12,14</sup> Anthony T. Yachnis,<sup>5</sup> Juan C. Troncoso,<sup>7,10</sup> and Laura P.W. Ranum<sup>1,2,3,6,\*</sup>

<sup>1</sup>Center for NeuroGenetics

<sup>2</sup>Department of Molecular Genetics and Microbiology

<sup>3</sup>Department of Neurology

<sup>4</sup>Department of Neuroscience

<sup>5</sup>Department of Pathology, Immunology and Laboratory Medicine, College of Medicine

<sup>6</sup>Genetics Institute

University of Florida, Gainesville, FL 32610, USA

<sup>7</sup>Department of Pathology

<sup>8</sup>Division of Neurobiology

<sup>9</sup>Department of Psychiatry

<sup>10</sup>Department of Neurology

<sup>11</sup>Department of Pharmacology

<sup>12</sup>Department of Neuroscience

<sup>13</sup>Program in Cellular and Molecular Medicine

<sup>14</sup>Baltimore Huntington's Disease Center

The John Hopkins University School of Medicine, Baltimore, MD 21205, USA

\*Correspondence: ranum@ufl.edu

<http://dx.doi.org/10.1016/j.neuron.2015.10.038>

## SUMMARY

Huntington disease (HD) is caused by a CAG•CTG expansion in the *huntingtin* (*HTT*) gene. While most research has focused on the HTT polyGln-expansion protein, we demonstrate that four additional, novel, homopolymeric expansion proteins (polyAla, polySer, polyLeu, and polyCys) accumulate in HD human brains. These sense and antisense repeat-associated non-ATG (RAN) translation proteins accumulate most abundantly in brain regions with neuronal loss, microglial activation and apoptosis, including caudate/putamen, white matter, and, in juvenile-onset cases, also the cerebellum. RAN protein accumulation and aggregation are length dependent, and individual RAN proteins are toxic to neural cells independent of RNA effects. These data suggest RAN proteins contribute to HD and that therapeutic strategies targeting both sense and antisense genes may be required for efficacy in HD patients. This is the first demonstration that RAN proteins are expressed across an expansion located in an open reading frame and suggests RAN translation may also contribute to other polyglutamine diseases.

## INTRODUCTION

Huntington disease (HD) is a progressive neurodegenerative disorder characterized by severe movement, cognitive, and behav-

ioral changes caused by a CAG•CTG expansion in the *HTT* gene (Orr and Zoghbi, 2007). Upon translation, this expansion mutation results in the production of a mutant huntingtin protein (HTT) with an expanded polyGln repeat tract. HD is one of nine neurologic diseases caused by CAG expansion mutations that encode broadly expressed proteins containing expanded polyGln tracts. While there is substantial evidence that mutant HTT and other polyGln expansion proteins are toxic and contribute to disease, the differential vulnerability of specific brain regions is not yet understood. In HD, expansions >40 repeats are fully penetrant, and longer alleles are associated with earlier, sometimes juvenile, onset and increased disease severity. While nearly all research into the molecular mechanisms of HD has focused on the downstream effects of the mutant HTT protein, CUG HD-antisense transcripts (Chung et al., 2011) and CAG microRNAs have also been reported and may play a role in disease (Bañez-Coronel et al., 2012). The discovery of repeat associated non-ATG (RAN) translation (Zu et al., 2011) in spinocerebellar ataxia type 8 (SCA8) raises the possibility that sense and antisense mutant proteins may be expressed from the HD CAG•CTG expansion mutation.

RAN translation has now been reported in several diseases with non-coding expansion mutations (Ash et al., 2013; Mori et al., 2013; Todd et al., 2013; Zu et al., 2011, 2013). It is not yet clear if RAN translation can occur across expansion mutations located in an open reading frame (ORF), such as the polyglutamine diseases. In these cases, RAN could be limited because these repeats are generally shorter than non-coding expansions and because the position of these repeats in conventional ORFs may inhibit RAN translation. To test if RAN translation can occur in a polyglutamine disease, we examined one of the most prevalent polyglutamine disorders, HD.

## RESULTS

### RAN Proteins Accumulate in Cells Expressing Mutant HTT and in Human HD Brains

To test if RAN translation can occur across the HTT ORF in transfected cells, we generated a series of minigenes containing *HTT* exon 1 with expansion mutations (Figure 1A). Immunoblots and immunofluorescence (IF) performed on transiently transfected HEK293T cells demonstrate that RAN translation occurs across a CAG<sub>EXP</sub> located in the ATG-initiated ORF of an HTT-exon 1 minigene and produces polyAla and polySer RAN proteins. Additionally, constructs lacking the ATG demonstrate that an ATG initiation codon is not required for expression of the polyGln, polyAla, or polySer expansion proteins (Figures 1B and S1Aa). Furthermore, polyAla and polySer are expressed at similar levels with and without an ATG initiation codon in the polyGln frame, indicating that frameshifting from an AUG-initiated polyGln reading frame is not required for polyAla or polySer expression in these minigenes. In contrast, (CAG)<sub>23</sub> and non-hairpin-forming (CAA)<sub>80</sub> constructs produce ATG-initiated polyGln but not RAN polyAla or polySer proteins (Figures 1B and S1Ab). In summary, these data show that HTT exon-1 (CAG)<sub>80</sub> transcripts can express RAN proteins in all three reading frames in transfected cells.

Because frameshifting has been previously reported in HD (Davies and Rubinsztein, 2006) and SCA3 (Gaspar et al., 2000; Toulouse et al., 2005), we performed a second series of experiments to test if frame-shifted products, which initiate at the AUG in the glutamine frame, can also produce hybrid polyGln/polyAla and polyGln/polySer proteins. We transfected cells using a modified HD exon 1 minigene with a 5' V5 tag in the polyGln frame and three C-terminal epitope tags to label proteins translated in each of the three reading frames (Figure S1Ac). Immunoprecipitations using antibodies against the C-terminal tags in the polyAla ( $\alpha$ -HA) and polySer ( $\alpha$ -Flag) frames followed by immunoblotting using the N-terminal and C-terminal tags shows that the polyAla and polySer proteins do not contain the N-terminal V5 tag in the ATG-initiated polyGln frame (Figure S1Ac).

To test if RAN proteins are expressed in vivo, a panel of polyclonal antibodies against the predicted C-terminal regions available for four of the five possible novel RAN proteins was generated (Figure 1C). The specificities of these antibodies, which recognize the putative polyAla (GCA), polySer (AGC), polyLeu (CUG), and polyCys (UGC) proteins, were demonstrated in transfected cells (Figure S1B). Next, we tested if HD-RAN proteins could be detected by immunohistochemistry (IHC) in the striatum, a prominently affected brain region in HD. We found striking positive staining using all four HD-RAN antibodies:  $\alpha$ -Ala-Ct,  $\alpha$ -Ser-Ct,  $\alpha$ -Leu-Ct, and  $\alpha$ -Cys-Ct (Figure 1D; Table 1) in HD but not HDL2 or control samples. No similar staining was seen with the corresponding pre-immune control sera for the various antibodies (Figure 1D). Protein blot analyses of insoluble lysates from human HD frontal cortex provide additional evidence that RAN proteins accumulate in HD but not control brains (Figure 1E). These results show that, in addition to the HTT polyGln expansion protein, the HD CAG·CTG expansion mutation also expresses four novel HD-RAN proteins and that these proteins are expressed from both sense and antisense transcripts.

### RAN Proteins Accumulate in Specific Striatal Regions

To explore areas of the striatum that are predominantly affected in HD (Figure 2A), we performed a series of IHC experiments using the HD-RAN protein antibodies in HD cases with Vonsattel grade II-IV. These experiments show strong HD-RAN protein staining in the caudate and putamen of the striatum, two regions severely affected in HD (Figure 2B, 2D–2G, and S2A–S2D; Table 1). Both nuclear and cytoplasmic RAN protein staining was found in neurons and can appear as diffuse staining or as punctate aggregates. Additional staining was seen in astrocytes and microglia in the caudate and putamen. HD-RAN antibodies also show consistently strong nuclear staining in the white matter bundle regions of the caudate and putamen, a region containing astrocytes and oligodendrocytes (Figure 2B, 2D–2G, and S2A–S2D; Table 1). In contrast, HD-RAN staining is only rarely observed in the internal capsule, a white matter structure containing both ascending and descending axons that separate the caudate nucleus from the putamen, and which is relatively preserved in HD. While the pattern of sense and antisense RAN protein staining across the caudate-putamen is strikingly similar, the pattern of staining using the 1C2 or EM48 antibodies to detect the expanded HTT polyGln protein was distinct. First, although 1C2/EM48 staining of neurons in the caudate and putamen is present and detects previously reported nuclear aggregates, positive cells are much less frequent (Figures 2B, 2C, and S2E). A second notable difference is that polyGln aggregates detected by 1C2 or EM48 are not detected in regions with the most intense RAN-protein staining, the white matter bundles of the caudate and putamen (Figures 2B, 2C, and S2E).

### RAN Proteins Accumulate in Regions with Neuroinflammatory Changes

Neuroinflammatory changes including an increase in microglial cells have been reported in HD and correlate with neuronal loss. To test if neuroinflammatory changes are found in areas that are RAN positive, we stained serial sections of the human autopsy material with the IBA1 antibody that recognizes microglia. RAN-positive regions of the caudate and putamen were also strongly positive for IBA1, and similar to the HD-RAN staining, the most intense IBA1 staining was seen in the RAN-positive white matter bundles (Figures 2B, 2H, and S2F). Next, we performed a double labeling experiment in which RAN-positive cells were labeled with a brown chromogen using a mixture of the  $\alpha$ -polyAla-Ct,  $\alpha$ -polySer-Ct,  $\alpha$ -polyLeu-Ct, and  $\alpha$ -polyCys-Ct antibodies, and microglia/macrophages were labeled using the  $\alpha$ -IBA1 antibody with a blue chromogen. The IBA1/RAN double labeling experiments show that microglia and RAN-positive cells are distributed in three patterns in the various regions of striatum: (1) RAN-negative microglia, (2) RAN-negative microglia in close proximity to a RAN-positive cell, and (3) RAN-positive microglia (Figure 2J).

### RAN Proteins Accumulate in Regions Undergoing Cell Death

Because caspase-3 is a prominent marker of cell death in HD, we also stained serial sections to determine if RAN-positive areas are caspase-3 positive. Caspase-3-positive cells were found in both the caudate and putamen and also within the caudate and putamen white matter bundles, which are positive

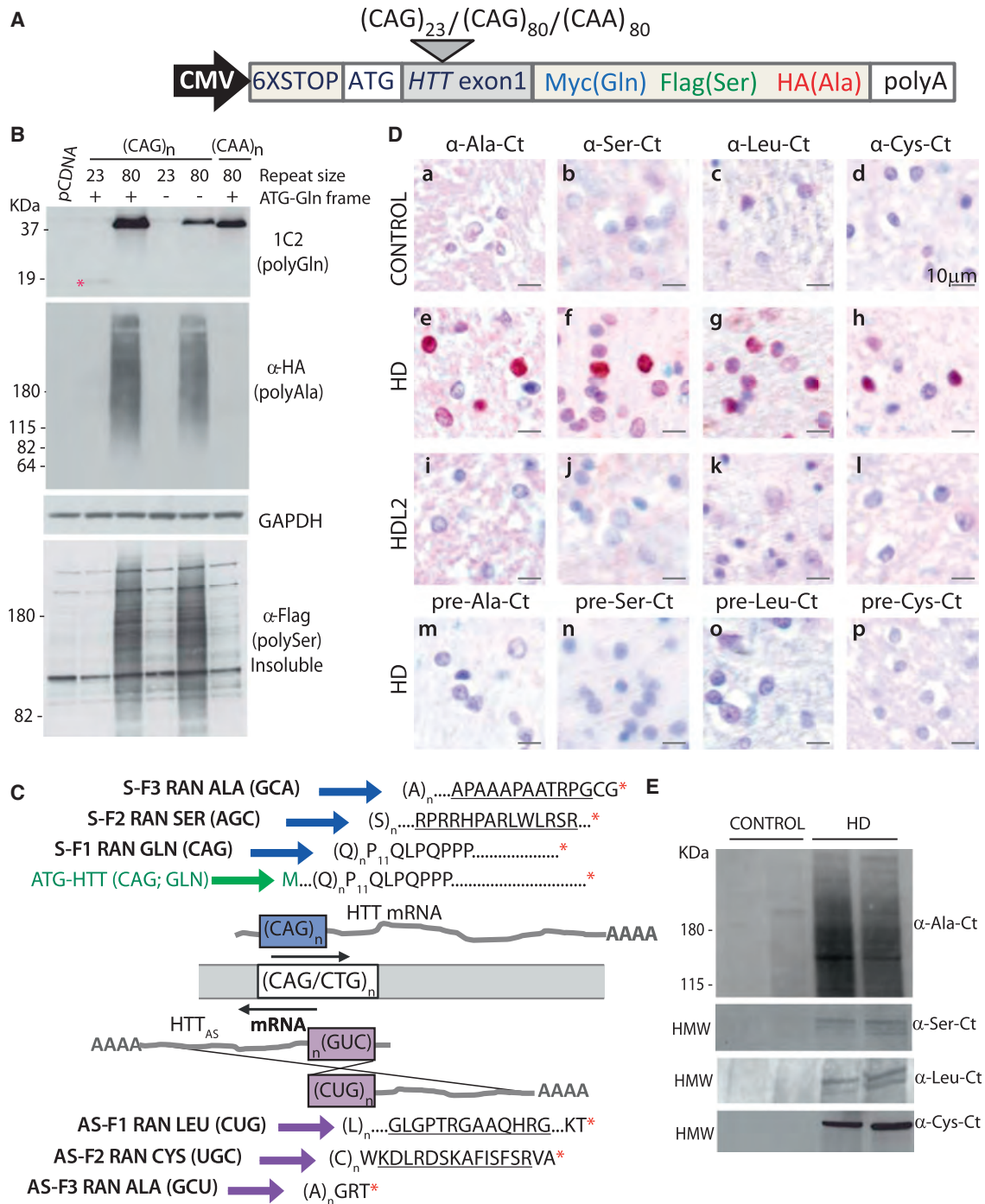


### Figure 1. RAN Translation in HD

(A) CAG and CAA HTT-exon1 minigenes with a 6× STOP codon cassette (two stops in each frame) upstream of *HTT* exon 1 and C-terminal epitope tags in each of the three reading frames.

(B) Immunoblots of HEK293T cells show polyGln expression from all +ATG-constructs and RAN polyGln, polyAla and polySer proteins from (CAG)<sub>80</sub> but not (CAG)<sub>23</sub> or non-hairpin-forming (CAA)<sub>80</sub> expansions.

(C) Schematic diagram of putative HD-RAN proteins. C-terminal regions used to generate peptide for HD-RAN polyclonal antibodies are underlined.

(D) IHC staining of human autopsy tissue shows positive staining (red) for sense (polyAla and polySer) and antisense (polyCys and polyLeu) RAN proteins in HD ([De]-[Dh]) but not HDL2 ([Di]-[Dl]), control ([Da]-[Dd]) or preimmune ([Dm]-[Dp]) controls. Red, positive staining; blue, nuclear counterstain.

(E) Protein blots showing RAN proteins detected from the insoluble fraction of HD but not control frontal cortex lysates. See also Figures S1A and S1B. HMW, high molecular weight.

**Table 1. Summary of RAN Protein Staining in HD Cases and Controls**

Case	Age	Sex/Race	Repeat	PMD	Vonsattel Grade	Striatum	Frontal Cortex	Cerebellum	
CTRL	1	40	M/W		6	–	–	–	
	2	56	F/W		13	–	–	–	
	3	45	F/W		20	–	–	–	
	4	57	M/W			–	–	–	
HD	1	47	M/W	N/A	30	2	++	++	++
	2	57	M/W	N/A	26	2	++	+	++
	3	60	F/W	N/A	24	3	+++	+	+
	4	57	F/W	N/A	9.5	3	+++	+	+
	5	52	M/B	49	24	3/4	+++	++	+
	6	41	M/W	52	8	4	+++	+	+
	7	46	F/W	N/A	7	4	+++	+	+
JHD	1	8	F/	>100*	–		+++	++	++++
	2	8	M/B	~100*	–	3	++++	+++	++
	3	27	M/W	69	22	4	+++	++	++
	4	23	F/B	76	14	4	++++	++	+
	5	23	F/W	64	13	4	+++	++	++
HDL2	1	58	M/B		11.5	4	–	–	–
	2	41	F/B		3	3	–	–	–
SCA8	80	F				NA	NA	–	

RAN staining: –, negative; +, low-intensity staining; ++, moderate intensity; +++, frequent and intense; +++++, highly frequent positive cells with high intensity staining. CTRL, control; HD, Huntington disease; JHD, juvenile Huntington disease; HDL2, Huntington disease like-2; SCA-8, Spinocerebellar ataxia type 8; N/A, not available; \*, repeat length estimated from autopsy brains; M, male; F, female.

for HD-RAN proteins but negative for the polyGln HTT protein (Figure S2G). Additional double labeling experiments show 40%–60% of cells positive for active caspase-3 are also positive for one or more RAN proteins in the caudate, caudate white-matter bundles, putamen white matter bundles, and putamen (Figure 2K). These studies show RAN-positive cells are found in regions with markers of cell death.

#### HD-RAN Proteins in Frontal Cortex and Cerebellum

Since neurodegenerative changes in HD also occur in additional regions of the brain including the frontal cortex and the cerebellum, we tested these regions for RAN protein staining. Neuropathology in the frontal cortex is well established in HD, with cortical degeneration, neuronal loss in all layers, and increased density of large glial cells (Bates et al., 2014). Additionally, variable involvement of the cerebellum has recently been reported in HD (Bates et al., 2014; Rüb et al., 2013).

In the frontal cortex, positive staining for the four HD-RAN proteins was found in clustered patches, with the most prominent staining found in cortical layers II and III in HD but not controls. Nuclear staining for HD-Ala, HD-Ser, HD-Leu, and HD-Cys was also found in HD cortical white matter (Figures 3A and S3A–S3D; Table 1). In the cerebellum, HD patients but not controls show RAN-protein staining (Figures 3B and S3A–S3D; Table 1). Staining is found in the molecular and granule cell layers and in areas of Bergmann-glia proliferation surrounding the Purkinje cells. Staining of neurons in both the cortex and cerebellum was nuclear, cytoplasmic, or perinuclear and was diffuse or localized to dense aggregates. In contrast, staining in cere-

bral and cerebellar white matter showed intense nuclear localization.

In summary, while RAN protein staining in the cortex and cerebellum is easily detected, staining in the striatum was consistently more intense. IHC using the 1C2 antibody to detect expanded polyGln protein also showed nuclear staining in the neuronal layers of the frontal cortex (Figures 3A and S3E), but no staining was evident in the white matter regions of the frontal cortex or the cerebellum (Figures 3B and S3E).

#### HD-RAN Proteins in N171-82Q HD Mice

Next, we tested if HD-RAN proteins can be expressed in a mouse model of HD. We chose the N171-82Q HD mice (Schilling et al., 1999) for analysis because the transgene contains both a RAN-competent CAG expansion mutation and human flanking sequences that allow detection with the C-terminal polySer and polyAla antibodies that we developed. Figure 3C shows that, similar to human HD autopsy tissue, HD-polyAla and HD-polySer are also detected in this mouse model by IHC (Figure 3C). It is not known at this time if antisense transcripts or antisense RAN proteins are expressed in these mice. Our findings of sense RAN proteins in these mice provide proof-of-principle evidence that RAN proteins can be expressed in mouse models of HD and that mice may be a useful tool for understanding the impact of HD-RAN proteins on disease.

In summary, RAN proteins accumulate in two additional affected brain regions, the frontal cortex and cerebellum. Additionally, prominent RAN-positive staining was observed in the absence of detectable polyGln staining in white matter regions.

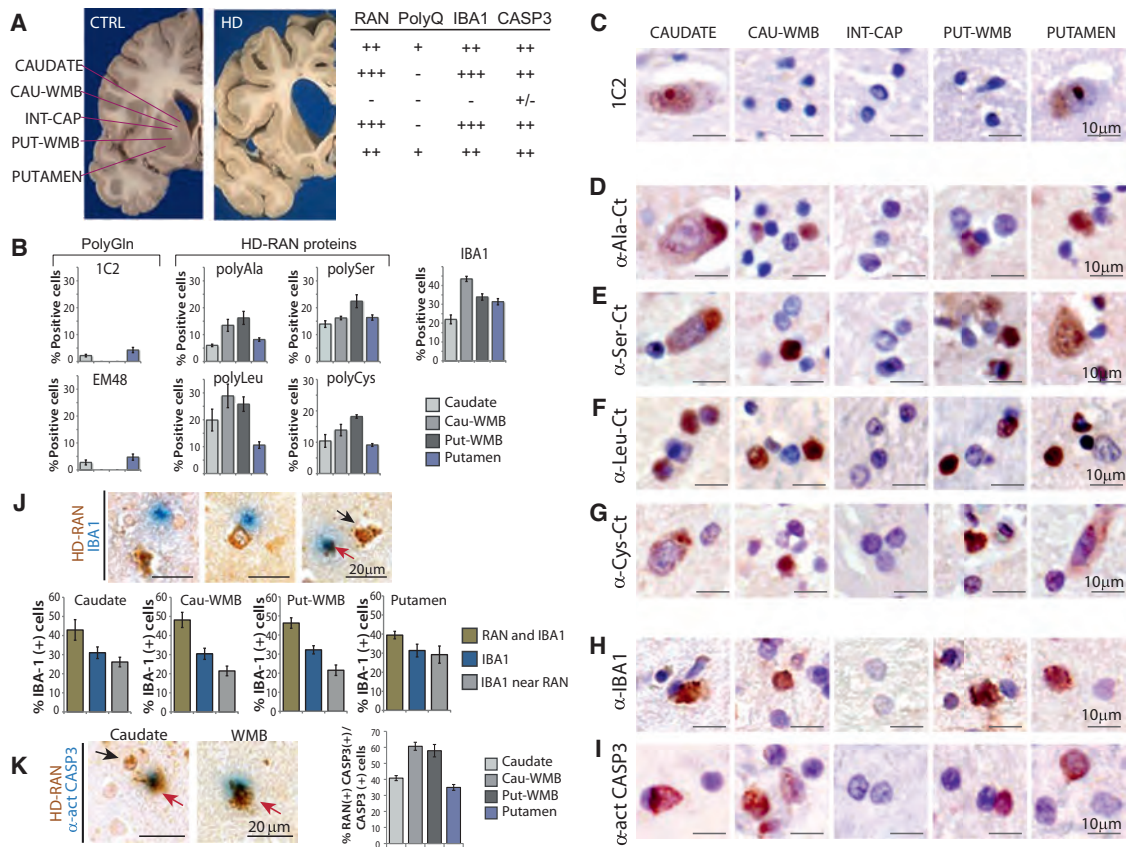


**Figure 2. HD-RAN Proteins in Striatum**

(A) Control and HD brain showing striatal sub-regions with summary of staining.

(B) Quantification of IHC-positive cells for  $\alpha$ -Gln,  $\alpha$ -RAN, and IBA1 staining  $\pm$  SEM in caudate nucleus.

(C–I) IHC of striatal sub-sections from HD brains using (C)  $\alpha$ -Gln antibody (1C2), (D)–[G])  $\alpha$ -RAN antibodies, (H)  $\alpha$ -IBA1 for microglia, and (I)  $\alpha$ -active caspase-3 for cell death. (A)–(I): red, positive staining; blue, nuclear counterstain.

(J) Double staining for RAN protein cocktail using mixture of all four anti-RAN antibodies (brown) plus anti-IBA1 antibody to label microglia with quantitation ( $\pm$  SEM) of single-, double-labeled, and IBA1 cells that are in close proximity to RAN-positive cells.

(K) Double staining for RAN protein cocktail using mixture of all anti-RAN antibodies (brown) plus anti-caspase-3 antibody to label apoptotic cells with quantitation of the percent active Caspase-3-positive cells that are also positive for RAN proteins. See also Figure S2. Cau-WMB, caudate white matter bundles; Int-Cap, internal capsule; Put-WMB, putamen white matter bundles.

This latter observation suggests that RAN proteins play a role in white matter abnormalities previously described in HD, such as gliosis and white matter changes detected by DTI/MRI imaging (Bohanna et al., 2011; Fennema-Notestine et al., 2004; Paulsen et al., 2010; Reading et al., 2005).

### RAN-Protein Accumulation and Aggregation Are Length Dependent

Longer CAG expansions are associated with earlier onset and increased severity in HD and other polyGln expansion disorders (Ross et al., 1999). To investigate the effects of repeat length on HD-RAN proteins, we developed a series of HTT-exon-1 minigenes with repeats ranging in length from 23 to 80 CAGs (Figure 4A). Transient transfections were performed and cell lysates examined for the accumulation of ATG-initiated polyGln and HD-RAN polyAla and polySer proteins. As expected, ATG-initiated polyGln proteins are expressed and accumulate at all repeat lengths (23–80 repeats) (Figures 4B, 4C, and S4A). In contrast,

RAN-protein accumulation and aggregation is length dependent. For example, protein blotting and IF show HD-polyAla RAN proteins accumulate in cells expressing CAG repeats  $\geq 52$  but not at repeats  $\leq 45$ . In the polySer frame, RAN protein accumulation is evident at  $\geq 35$  repeats, and as the repeats get longer, RAN-polySer shifts from being in the soluble (35–40 repeats) to the insoluble fraction (45–80 repeats) by protein blot (Figure 4B). Similarly, in transfected cells, polySer staining changes from a diffuse pattern (35–40 repeats) to a progressively more punctate, almost pin-like staining pattern forming granular cytoplasmic inclusions (45–80 repeats) (Figures 4C and S4A). In summary, the selective accumulation of RAN polyAla and punctate polySer proteins in this in vitro system occurs at repeat lengths typically associated with early-onset and juvenile cases of HD.

### HD-RAN Proteins Decrease Cell Survival In Vitro

The discovery of HD-RAN proteins in caspase-3-positive brain regions strongly suggests that RAN proteins are toxic. To

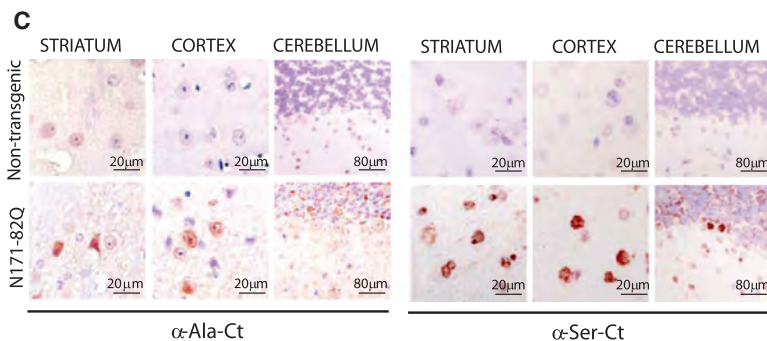
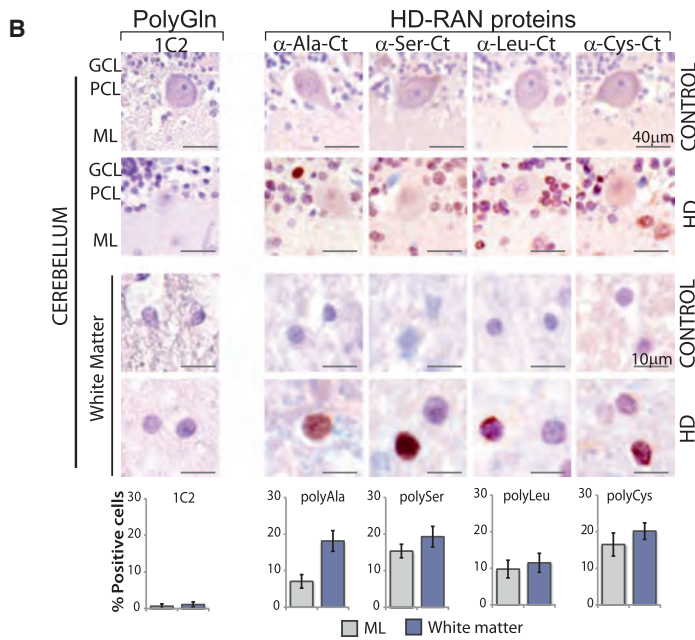
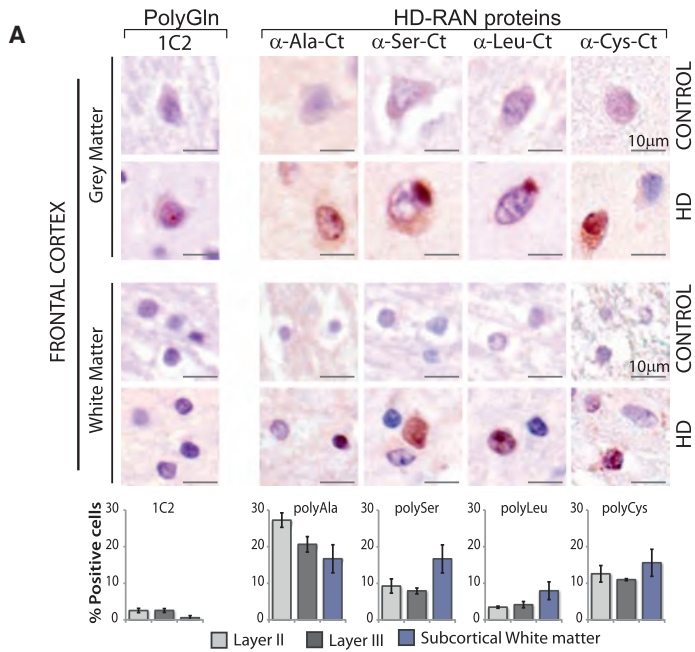


**Figure 3. HD-RAN Proteins in Human Frontal Cortex and Cerebellum and HD Mice**

(A and B) IHC staining of control and HD gray and white matter of (A) frontal cortex and (B) cerebellum using  $\alpha$ -RAN and  $\alpha$ -Gln (1C2) antibodies show punctate nuclear and cytoplasmic staining with  $\alpha$ -polyAla,  $\alpha$ -polySer,  $\alpha$ -polyLeu, and  $\alpha$ -polyCys. GCL, granule cell layer; PCL, Purkinje-cell layer; ML, molecular layer. Staining of the cortex and cerebellum in adult-onset HD cases is variable. IHC images and quantification of percent positive cells represent typical positive regions.

(C) IHC staining of indicated brain regions in N171-82Q and control mice using the  $\alpha$ -polyAla,  $\alpha$ -polySer. Red, positive staining; blue, nuclear counterstain. See also Figures S3A-S3E.

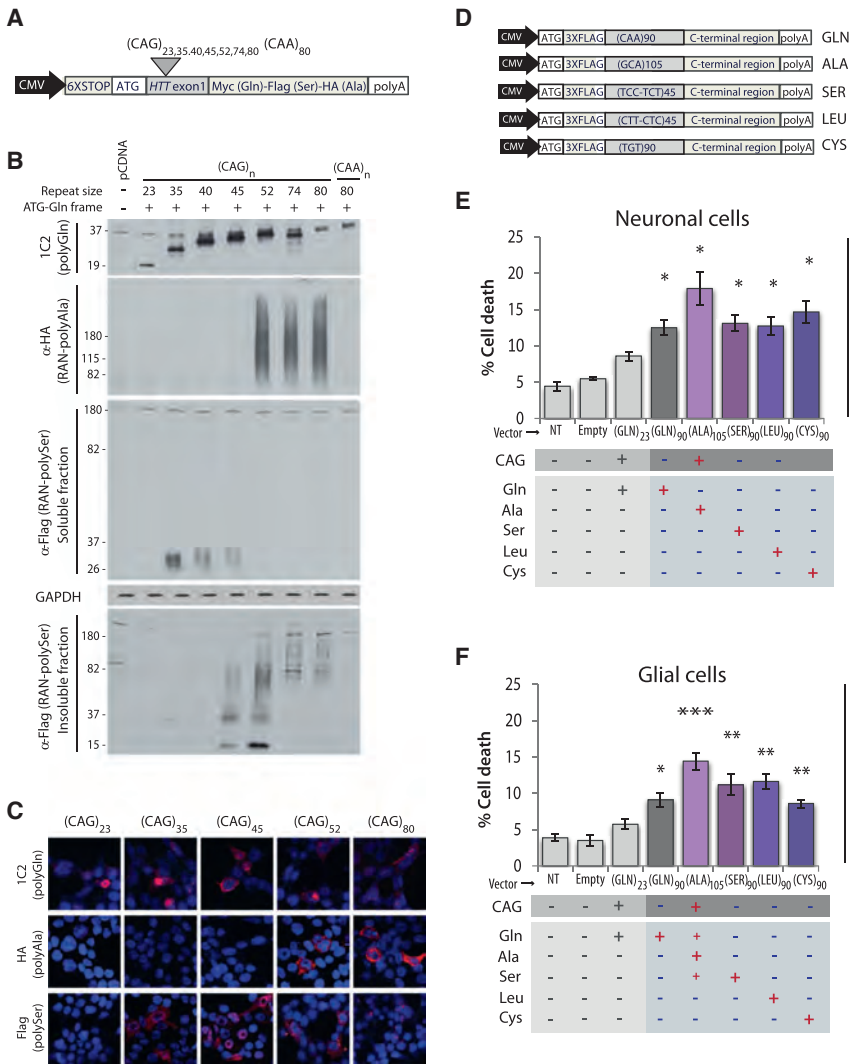


**Figure 4. Length-Dependent RAN Protein Expression, Aggregation, and Toxicity**

(A) CAG and CAA HTT-exon1 minigenes. (B and C) (B) Immunoblots and (C) IF of HEK293T cells after transfection with indicated constructs. (D) Transfected minigenes (top) containing non-hairpin-forming alternative codons in the repeat region for polyGln<sub>90</sub> (CAA), polySer<sub>90</sub> (TCC-TCT), polyLeu<sub>90</sub> (CTT-CTC), and polyCys<sub>90</sub> (TGT) constructs. Because non-hairpin forming codon substitutions encoding polyAla were not available, polyAla was expressed by a +ATG-GCA construct using a slightly longer repeat tract of 105 repeats. (E and F) LDH assays of SH-SY5Y and T98 cells expressing polyGln and individual HD-RAN proteins 42 hr post-transfection. Values equal percent of cell death ± SEM (n = 5; \*p < 0.05, \*\*p < 0.01, and \*\*\*p < 0.001). See also Figures S4A–S4F.

transfection (Figures S4B, S4C, and S4F), suggesting that the vulnerability to HD-RAN proteins is cell type specific. Taken together, these data demonstrate that the expression of individual polySer, polyLeu, and polyCys HD-RAN proteins using non-hairpin-forming alternative codons increases cell death in neuronal and glial cells.

**HD-RAN Proteins Accumulate in Severely Affected Cerebellar Regions in Juvenile HD**

In adult-onset HD, there is a predictable disease progression that first, and most severely, affects the caudate/putamen followed by the frontal cortex and other brain regions. In contrast, disease progression in juvenile-onset cases shows a

examine the effect of each individual RAN protein independently of RNA-mediated effects, we generated polyGln, polySer, polyLeu, and polyCys minigenes using alternative codons to prevent RNA hairpin formation and RAN translation (Zu et al., 2011). Because non-hairpin forming codons are not available for polyAla, we increased polyAla expression relative to polyGln and polySer by including an ATG-initiation codon in the polyAla reading frame. ATG-initiated polyAla was generated with a GCA expansion (Figure 4D). All the minigenes expressed proteins with the repeat expansion and the complete C-terminal region for each protein.

SH-SY5Y neuronal and T98 glial cells transfected with these constructs showed a significant increase in cell death compared to cells expressing a short repeat. HD-RAN polySer, polyLeu, and polyCys proteins are equally or more toxic than polyGln alone. The transfection with the polyAla construct, which expresses high polyAla levels, but also low levels of polyGln and polySer, dramatically increased cell death (Figures 4E, 4F, and S4C). In contrast, toxic effects of these proteins were less robust or not found in transfected HEK293T cells at 18, 24, or 42 hr post-

more widespread pathology, with some patients showing severe involvement of the caudate and putamen while others show relative sparing of this region but severe atrophy of the cortex or cerebellum (Figure 5A) (Bates et al., 2014). Given that RAN protein expression increases with repeat length, we tested if RAN protein staining is more prominent in juvenile HD cases and if severely affected regions show increased RAN protein accumulation. To explore this question, we analyzed autopsy tissue from five juvenile-onset cases. All five cases showed increased frequency and more intense staining for all four RAN proteins in striatum, frontal cortex, and cerebellum (Table 1). Two of these cases, which came to autopsy at 8 years of age with repeats greater than 100, showed marked cerebellar atrophy with abundant RAN protein staining in all layers of the cerebellum (Figures 5B, 5C, and S5A; Tables 1 and 2).

In the most severely affected juvenile HD case (JHD-1), the cerebellum showed more intense RAN polySer and polyCys staining compared to adult HD (Table 1; Figure S5A) with JHD showing ubiquitous, densely reactive, often punctate nuclear or perinuclear staining in regions throughout the cerebellum. Positive

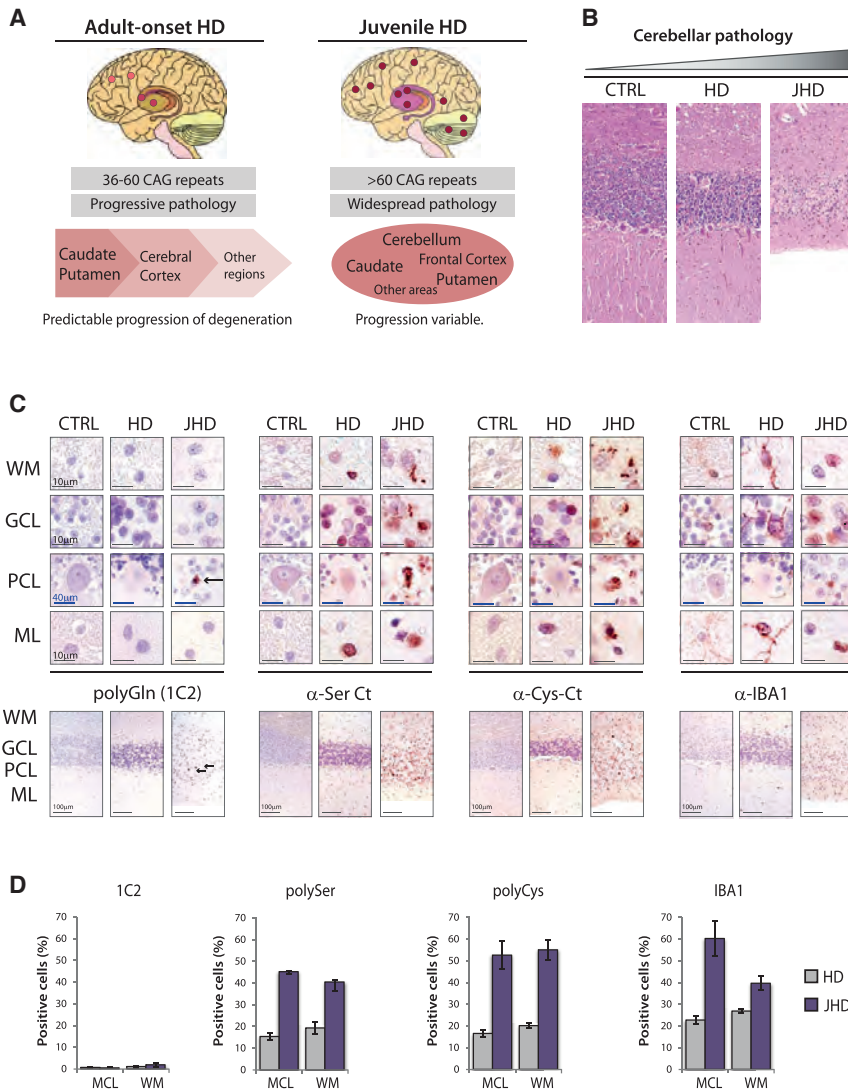


**Figure 5. Increased RAN Protein Staining in Juvenile HD**

(A) Schematic diagram summarizing features of adult-onset and juvenile HD pathology. (B) H&E staining in control, adult-onset, and juvenile-onset HD cases with cerebellar atrophy. (C)  $\alpha$ -polyGln,  $\alpha$ -polySer,  $\alpha$ -polyCys and  $\alpha$ -IBA1 staining in cerebellar layers. (D) Quantitation of IHC-positive cells with 1C2 (polyGln) and  $\alpha$ -polySer-Ct,  $\alpha$ -polyCys-Ct, and  $\alpha$ -IBA1 antibodies. WM, white matter; GCL, granule cell layer; PCL, Purkinje-cell layer; ML, molecular layer. Red, positive staining; blue, nuclear counterstain. Staining of cerebellum in adult-onset HD cases is variable. IHC images and quantification of percent positive cells represent typical positive regions. See also Figures S5A and S5B.

played a ramified morphology in the adult and less affected juvenile cerebellum. In contrast, IBA1-positive cells were more abundant in the severely affected juvenile cerebellum and displayed active, round amoeboid morphology, with a similar distribution pattern to that observed for  $\alpha$ -polySer and  $\alpha$ -polyCys staining (Figures 5C and S5A). These results show high levels of RAN protein accumulation in severely affected regions with minimal polyGln staining.

**DISCUSSION**

Our understanding of HD has been built on studying the effects of the AUG-initiated polyGln expansion protein. In this report, we provide evidence that additional expansion proteins, polyAla, polySer, polyLeu, and polyCys, are ex-

pressed; accumulate in HD patient brains; and contribute to disease pathology. First, HD-RAN proteins show abundant positive staining in regions of the brain most affected by HD, including the caudate/putamen and, in juvenile-onset cases, also the cerebellum. Second, regions with intense RAN-positive staining show pathologic features of HD, including activated caspase-3 staining, activated microglia, and gliosis. Third, prominent RAN-positive staining was observed in the absence of detectable polyGln (Herndon et al., 2009) staining in several white matter regions, suggesting RAN proteins play a role in HD white matter abnormalities (Bohanna et al., 2011; Fennema-Notestine et al., 2004; Paulsen et al., 2010; Reading et al., 2005). Fourth, in vitro studies indicate that HD-RAN proteins are toxic to neural cells. Fifth, increased polyAla accumulation and aggregation of polySer RAN proteins occurs in cells expressing longer repeats >52, which are typically associated with earlier disease onset and more severe juvenile HD. Additionally, the accumulation of RAN polySer at 35, but not 23 repeats, is worth considering as a possible trigger of disease, since 35

regions included molecular layer interneurons, Bergmann glia and basket cells surrounding the Purkinje cells, the granular layer and subcortical and deep white matter regions including regions surrounding the dentate nuclei (Figure 5C, S5A, and S5B). Additionally, RAN protein staining in the white matter surrounding the dentate nucleus was found in regions of gliosis, with prominent  $\alpha$ -polyCys staining of astrocytes and microglia-like cells (Figures S5A and S5B). A second juvenile case (JHD-2), also with cerebellar atrophy, showed polySer- and polyCys-positive staining in similar regions as well as in the remaining Purkinje cells (Figure S5A). In contrast, polyglutamine staining in the cerebellum was rare in all cases, with no positive staining detected in the adult-onset cases or JHD-2 using the 1C2 or EM48 antibodies (Figures 5C and S5A), and few positive cells per 20 $\times$  field in JHD-1 detected with 1C2 but not EM48 (Figure S5A).

Similar to the results obtained in the adult-onset HD striatum (Figure 2), IBA1 staining of juvenile HD cerebella showed abundant microglial-like cells in regions strongly positive for HD-RAN polySer and polyCys. Microglia/monocyte staining mostly dis-

**Table 2. HD-RAN Protein Staining and Cerebellar Atrophy in Juvenile HD**

Cases JHD	Age	Repeat	PMD	CBL Atrophy	RAN
1	8	>100*	–	++++	++++
2	8	~100*	–	++	++
3	27	69	22	+	++
4	23	76	14	+	+
5	23	64	13	+	++

RAN staining: +, low-intensity staining; ++, moderate intensity; +++, frequent and intense; +++++, highly frequent positive cells with high intensity staining. JHD, juvenile HD. \* repeat length estimated from autopsy brains.

repeats is near the threshold at which HD can manifest. Finally, increased HD-RAN protein staining is found in highly affected juvenile-onset cerebellar tissue.

It was previously suggested that the CAG expansions can undergo frameshifting that results in the production of fusion proteins that start with an AUG-initiation codon in the glutamine frame and shift to alternative reading frames to produce hybrid polyGln/polyAla or polyGln/polySer proteins (Davies and Rubinsztein, 2006; Gaspar et al., 2000; Stochmanski et al., 2012; Toulouse et al., 2005). Here we demonstrate that neither frameshifting nor an AUG initiation codon is required for the expression of polyAla or polySer and that both sense and antisense HD-RAN proteins are abundantly expressed in affected regions of HD autopsy brains. (Figure 1 and S1Ac). While the detection of HD-RAN proteins with C-terminal antibodies demonstrates that these proteins include C-terminal flanking sequences, future studies will be important to characterize their specific initiation and termination sites. Additionally, it will be important to determine the stability and aggregation properties of these proteins as well as the mechanisms of protein clearance.

The discovery that RAN proteins are expressed and accumulate at sites of HD pathology provides new insights that may explain the selective vulnerability of the caudate/putamen in adult-onset cases and the variability of affected regions of the brain in juvenile-onset HD. First, RAN proteins are frequently found in cells expressing active-caspase-3, including in white-matter-bundle regions that show RAN but not HTT-polyGln accumulation. Additionally, the observation that 40%–50% of IBA1 cells are also RAN-positive suggests microglia/macrophages are recruited to RAN-positive regions and engulf RAN proteins or RAN-positive cells. Alternatively, it is possible that a subset of microglia/macrophages express RAN proteins. Taken together, these results raise the possibility that HD-RAN proteins trigger neuroinflammatory changes (Björkqvist et al., 2008, 2009; Myers et al., 1991; Pavese et al., 2006; Tai et al., 2007) and cell death in HD.

As recently described, cerebellar atrophy has been reported in both adult and juvenile HD cases (Nance et al., 1999; Rüb et al., 2013; Seneca et al., 2004) and may contribute to balance, speech, and gait problems found in HD patients (Koller and Trimble, 1985; Margolis and Ross, 2003; Rüb et al., 2013). The preferential accumulation of HD-RAN versus HD-polyGln proteins in the cerebellum (Figures 3, 5, and S5; Table 1) in both adult and juvenile cases suggests the possibility that RAN proteins trigger

the neurodegeneration seen in juvenile cases (Table 2) and may also cause functional problems in adults.

It is striking that RAN but not polyGln proteins accumulate in white matter regions of the striatum, frontal cortex, and cerebellum. These data suggest several possibilities that may explain the region-specific accumulation of HD-RAN proteins: (1) the shorter RAN proteins may be more aggregate prone and easier to detect than HTT-polyGln, (2) degradation pathways may less efficiently target RAN proteins leading to their preferential accumulation, and (3) RAN translation may be more efficient in specific cell types. Additional research will be required to determine if the accumulation of RAN proteins in specific white matter regions underlies the early white matter abnormalities seen by diffusion tensor imaging in HD patients (Rosas et al., 2006; Rüb et al., 2013) and cause early signs of the disease.

While additional work will be required to sort out the contributions of HD-RAN proteins in disease, two mouse models that show HD-like phenotypes were developed using a mixed CAG/CAA repeat encoding a polyGln tract (Gray et al., 2008; O'Brien et al., 2015). While these animals express a polyGln expansion across the CAG/CAA repeat, the CAG/CAA mixed repeat is also predicted to form a complex hairpin-containing structure that may also produce two novel di-peptide (Thr/Ala and Asn/Ser) RAN proteins, which may contribute to the phenotypes found in these models. Additional animal models that allow direct comparisons of the effects of polyGln, individual RAN proteins and sense and antisense RNAs will be required to fully understand how each of these CAG•CTG expansion mutation products contributes to disease.

Although additional work will be needed to understand the individual and combined effects of HD-RAN proteins, it is possible that one or more of these proteins is highly toxic and that strategies to target or increase turnover of selected proteins may mitigate disease (Cleary and Ranum, 2014). It may also be possible to downregulate RAN translation without inhibiting canonical AUG-initiated translation and that decreasing overall RAN protein load will have beneficial effects (Cleary and Ranum, 2014). Alternatively, targeting the HTT sense transcript using antisense oligonucleotides has been described as a promising therapeutic approach for HD (Hu et al., 2012; Kordasiewicz et al., 2012). While preclinical strategies to target the HD sense RNAs, as well as other therapeutic approaches (Lee et al., 2013; Menalled and Brunner, 2014; Switonski et al., 2012), are promising, it will be important to determine which of these mouse models accurately reproduce the sense and antisense expression seen in humans and to correlate these findings with the recovery seen in each of the models studied.

In summary, the accumulation of both sense and antisense RAN proteins in human autopsy brains and their toxicity suggests strategies targeting both transcripts may be required to effectively treat disease in humans. Additionally, HD-RAN proteins may prove to be useful biomarkers to predict disease onset and progression and responses to future therapeutic treatments. Finally, the discovery that RAN translation can occur when an expansion mutation is located in an ORF raises the possibility that RAN proteins also contribute to eight other CAG polyglutamine expansion disorders.

## SUPPLEMENTAL INFORMATION

Supplemental Information includes five figures and Supplemental Experimental Procedures and can be found with this article online at <http://dx.doi.org/10.1016/j.neuron.2015.10.038>.

## AUTHOR CONTRIBUTIONS

Author contributions: M.B.-C., T.Z., and L.P.W.R. designed research; M.B.-C., F.A., A.D.T., T.Z., B.A.P., S.K.T., and O.P. performed research; O.P., D.R.B., C.A.R., R.L.M., A.T.Y., and J.C.T. contributed new reagents/analytic tools/samples; M.B.-C., F.A., T.Z., A.T.Y., J.C.T., and L.P.W.R. analyzed data; and M.B.-C. and L.P.W.R. wrote the paper with input from all authors.

## ACKNOWLEDGMENTS

We thank Dr. M. Swanson for helpful suggestions and discussions, Drs. E. Marti and X. Estivill for the generous gift of HTT exon1 plasmids, and Dr. J. Streit for helpful technical suggestions in detecting microglia. This work was funded by CHDI Foundation, Inc., a grant from the W.F. Keck Foundation and start-up funding from the University of Florida (L.P.W.R.); a Sara Borrell contract from the Spanish Ministry of Health, ISCIII (M.B.-C.); a University of Florida Alumni Fellowship (F.A.); and an NIH Training Grant (NS082168) (B.A.P.) and the John Hopkins University Alzheimer's Disease Research Center (NIH P50AG05146) (C.A.R., R.L.M., and J.C.T.). M.B.-C., T.Z., and L.P.W.R. have patents pending on RAN translation. No other authors have conflicts.

Received: May 6, 2015

Revised: September 5, 2015

Accepted: October 15, 2015

Published: November 18, 2015

## REFERENCES

- Ash, P.E., Bieniek, K.F., Gendron, T.F., Caulfield, T., Lin, W.L., DeJesus-Hernandez, M., van Blitterswijk, M.M., Jansen-West, K., Paul, J.W., 3rd, Rademakers, R., et al. (2013). Unconventional translation of C9ORF72 GGGGCC expansion generates insoluble polypeptides specific to c9FTD/ALS. *Neuron* 77, 639–646.
- Bañez-Coronel, M., Porta, S., Kagerbauer, B., Mateu-Huertas, E., Pantano, L., Ferrer, I., Guzmán, M., Estivill, X., and Martí, E. (2012). A pathogenic mechanism in Huntington's disease involves small CAG-repeated RNAs with neurotoxic activity. *PLoS Genet.* 8, e1002481.
- Bates, G., Tabrizi, S.J., and Jones, L., eds. (2014). *Huntington's Disease*, Fourth Edition (Oxford University Press).
- Björkqvist, M., Wild, E.J., Thiele, J., Silvestroni, A., Andre, R., Lahiri, N., Raibon, E., Lee, R.V., Benn, C.L., Soulet, D., et al. (2008). A novel pathogenic pathway of immune activation detectable before clinical onset in Huntington's disease. *J. Exp. Med.* 205, 1869–1877.
- Björkqvist, M., Wild, E.J., and Tabrizi, S.J. (2009). Harnessing immune alterations in neurodegenerative diseases. *Neuron* 64, 21–24.
- Bohanna, I., Georgiou-Karistianis, N., Sriharan, A., Asadi, H., Johnston, L., Churchyard, A., and Egan, G. (2011). Diffusion tensor imaging in Huntington's disease reveals distinct patterns of white matter degeneration associated with motor and cognitive deficits. *Brain Imaging Behav.* 5, 171–180.
- Chung, D.W., Rudnicki, D.D., Yu, L., and Margolis, R.L. (2011). A natural antisense transcript at the Huntington's disease repeat locus regulates HTT expression. *Hum. Mol. Genet.* 20, 3467–3477.
- Cleary, J.D., and Ranum, L.P. (2014). Repeat associated non-ATG (RAN) translation: new starts in microsatellite expansion disorders. *Curr. Opin. Genet. Dev.* 26, 6–15.
- Davies, J.E., and Rubinsztein, D.C. (2006). Polyalanine and polyserine frame-shift products in Huntington's disease. *J. Med. Genet.* 43, 893–896.
- Fennema-Notestine, C., Archibald, S.L., Jacobson, M.W., Corey-Bloom, J., Paulsen, J.S., Peavy, G.M., Gamst, A.C., Hamilton, J.M., Salmon, D.P., and Jernigan, T.L. (2004). In vivo evidence of cerebellar atrophy and cerebral white matter loss in Huntington disease. *Neurology* 63, 989–995.
- Gaspar, C., Jannatipour, M., Dion, P., Laganière, J., Sequeiros, J., Brais, B., and Rouleau, G.A. (2000). CAG tract of MJD-1 may be prone to frameshifts causing polyalanine accumulation. *Hum. Mol. Genet.* 9, 1957–1966.
- Gray, M., Shirasaki, D.I., Cepeda, C., André, V.M., Wilburn, B., Lu, X.H., Tao, J., Yamazaki, I., Li, S.H., Sun, Y.E., et al. (2008). Full-length human mutant huntingtin with a stable polyglutamine repeat can elicit progressive and selective neuropathogenesis in BACHD mice. *J. Neurosci.* 28, 6182–6195.
- Herndon, E.S., Hladik, C.L., Shang, P., Burns, D.K., Raisanen, J., and White, C.L., 3rd (2009). Neuroanatomic profile of polyglutamine immunoreactivity in Huntington disease brains. *J. Neuropathol. Exp. Neurol.* 68, 250–261.
- Hu, J., Liu, J., Yu, D., Chu, Y., and Corey, D.R. (2012). Mechanism of allele-selective inhibition of huntingtin expression by duplex RNAs that target CAG repeats: function through the RNAi pathway. *Nucleic Acids Res.* 40, 11270–11280.
- Koller, W.C., and Trimble, J. (1985). The gait abnormality of Huntington's disease. *Neurology* 35, 1450–1454.
- Kordasiewicz, H.B., Stanek, L.M., Wancewicz, E.V., Mazur, C., McAlonis, M.M., Pytel, K.A., Artates, J.W., Weiss, A., Cheng, S.H., Shihabuddin, L.S., et al. (2012). Sustained therapeutic reversal of Huntington's disease by transient repression of huntingtin synthesis. *Neuron* 74, 1031–1044.
- Lee, C.Y., Cantle, J.P., and Yang, X.W. (2013). Genetic manipulations of mutant huntingtin in mice: new insights into Huntington's disease pathogenesis. *FEBS J.* 280, 4382–4394.
- Margolis, R.L., and Ross, C.A. (2003). Diagnosis of Huntington disease. *Clin. Chem.* 49, 1726–1732.
- Menalled, L., and Brunner, D. (2014). Animal models of Huntington's disease for translation to the clinic: best practices. *Mov. Disord.* 29, 1375–1390.
- Mori, K., Weng, S.M., Arzberger, T., May, S., Rentzsch, K., Kremmer, E., Schmid, B., Kretschmar, H.A., Cruts, M., Van Broeckhoven, C., et al. (2013). The C9orf72 GGGGCC repeat is translated into aggregating dipeptide-repeat proteins in FTL/ALS. *Science* 339, 1335–1338.
- Myers, R.H., Vonsattel, J.P., Paskevich, P.A., Kiely, D.K., Stevens, T.J., Cupples, L.A., Richardson, E.P., Jr., and Bird, E.D. (1991). Decreased neuronal and increased oligodendroglial densities in Huntington's disease caudate nucleus. *J. Neuropathol. Exp. Neurol.* 50, 729–742.
- Nance, M.A., Mathias-Hagen, V., Brenningstall, G., Wick, M.J., and McGlennen, R.C. (1999). Analysis of a very large trinucleotide repeat in a patient with juvenile Huntington's disease. *Neurology* 52, 392–394.
- O'Brien, R., DeGiacomo, F., Holcomb, J., Bonner, A., Ring, K.L., Zhang, N., Zafar, K., Weiss, A., Lager, B., Schilling, B., et al. (2015). Integration-independent Transgenic Huntington Disease Fragment Mouse Models Reveal Distinct Phenotypes and Life Span in Vivo. *J. Biol. Chem.* 290, 19287–19306.
- Orr, H.T., and Zoghbi, H.Y. (2007). Trinucleotide repeat disorders. *Annu. Rev. Neurosci.* 30, 575–621.
- Paulsen, J.S., Nopoulos, P.C., Aylward, E., Ross, C.A., Johnson, H., Magnotta, V.A., Juhl, A., Pierson, R.K., Mills, J., Langbehn, D., and Nance, M.; PREDICT-HD Investigators and Coordinators of the Huntington's Study Group (HSG) (2010). Striatal and white matter predictors of estimated diagnosis for Huntington disease. *Brain Res. Bull.* 82, 201–207.
- Pavese, N., Gerhard, A., Tai, Y.F., Ho, A.K., Turkheimer, F., Barker, R.A., Brooks, D.J., and Piccini, P. (2006). Microglial activation correlates with severity in Huntington disease: a clinical and PET study. *Neurology* 66, 1638–1643.
- Reading, S.A., Yassa, M.A., Bakker, A., Dziorny, A.C., Gourley, L.M., Yallapragada, V., Rosenblatt, A., Margolis, R.L., Aylward, E.H., Brandt, J., et al. (2005). Regional white matter change in pre-symptomatic Huntington's disease: a diffusion tensor imaging study. *Psychiatry Res.* 140, 55–62.
- Rosas, H.D., Tuch, D.S., Hevelone, N.D., Zaleta, A.K., Vangel, M., Hersch, S.M., and Salat, D.H. (2006). Diffusion tensor imaging in presymptomatic and early Huntington's disease: Selective white matter pathology and its relationship to clinical measures. *Mov. Disord.* 21, 1317–1325.

- Ross, C.A., Wood, J.D., Schilling, G., Peters, M.F., Nucifora, F.C., Jr., Cooper, J.K., Sharp, A.H., Margolis, R.L., and Borchelt, D.R. (1999). Polyglutamine pathogenesis. *Philos. Trans. R. Soc. Lond. B Biol. Sci.* *354*, 1005–1011.
- Rüb, U., Hoche, F., Brunt, E.R., Heinsen, H., Seidel, K., Del Turco, D., Paulson, H.L., Bohl, J., von Gall, C., Vonsattel, J.P., et al. (2013). Degeneration of the cerebellum in Huntington's disease (HD): possible relevance for the clinical picture and potential gateway to pathological mechanisms of the disease process. *Brain Pathol.* *23*, 165–177.
- Schilling, G., Becher, M.W., Sharp, A.H., Jinnah, H.A., Duan, K., Kotzuc, J.A., Slunt, H.H., Ratovitski, T., Cooper, J.K., Jenkins, N.A., et al. (1999). Intranuclear inclusions and neuritic aggregates in transgenic mice expressing a mutant N-terminal fragment of huntingtin. *Hum. Mol. Genet.* *8*, 397–407.
- Seneca, S., Fagnart, D., Keymolen, K., Lissens, W., Hasaerts, D., Debulpaep, S., Desprechins, B., Liebaers, I., and De Meirleir, L. (2004). Early onset Huntington disease: a neuronal degeneration syndrome. *Eur. J. Pediatr.* *163*, 717–721.
- Stochmanski, S.J., Therrien, M., Laganière, J., Rochefort, D., Laurent, S., Karemera, L., Gaudet, R., Vyboh, K., Van Meyel, D.J., Di Cristo, G., et al. (2012). Expanded ATXN3 frameshifting events are toxic in *Drosophila* and mammalian neuron models. *Hum. Mol. Genet.* *21*, 2211–2218.
- Switonski, P.M., Szlachcic, W.J., Gabka, A., Krzyzosiak, W.J., and Figiel, M. (2012). Mouse models of polyglutamine diseases in therapeutic approaches: review and data table. Part II. *Mol. Neurobiol.* *46*, 430–466.
- Tai, Y.F., Pavese, N., Gerhard, A., Tabrizi, S.J., Barker, R.A., Brooks, D.J., and Piccini, P. (2007). Imaging microglial activation in Huntington's disease. *Brain Res. Bull.* *72*, 148–151.
- Todd, P.K., Oh, S.Y., Krans, A., He, F., Sellier, C., Frazer, M., Renoux, A.J., Chen, K.C., Scaglione, K.M., Basrur, V., et al. (2013). CGG repeat-associated translation mediates neurodegeneration in fragile X tremor ataxia syndrome. *Neuron* *78*, 440–455.
- Toulouse, A., Au-Yeung, F., Gaspar, C., Roussel, J., Dion, P., and Rouleau, G.A. (2005). Ribosomal frameshifting on MJD-1 transcripts with long CAG tracts. *Hum. Mol. Genet.* *14*, 2649–2660.
- Zu, T., Gibbens, B., Doty, N.S., Gomes-Pereira, M., Huguet, A., Stone, M.D., Margolis, J., Peterson, M., Markowski, T.W., Ingram, M.A., et al. (2011). Non-ATG-initiated translation directed by microsatellite expansions. *Proc. Natl. Acad. Sci. USA* *108*, 260–265.
- Zu, T., Liu, Y., Bañez-Coronel, M., Reid, T., Pletnikova, O., Lewis, J., Miller, T.M., Harms, M.B., Falchook, A.E., Subramony, S.H., et al. (2013). RAN proteins and RNA foci from antisense transcripts in C9ORF72 ALS and frontotemporal dementia. *Proc. Natl. Acad. Sci. USA* *110*, E4968–E4977.

# TREM2 Haplodeficiency in Mice and Humans Impairs the Microglia Barrier Function Leading to Decreased Amyloid Compaction and Severe Axonal Dystrophy

Peng Yuan,<sup>1,2,9</sup> Carlo Condello,<sup>1,9,10</sup> C. Dirk Keene,<sup>3</sup> Yaming Wang,<sup>4</sup> Thomas D. Bird,<sup>5</sup> Steven M. Paul,<sup>6</sup> Wenjie Luo,<sup>6</sup> Marco Colonna,<sup>4</sup> David Baddeley,<sup>7,8</sup> and Jaime Grutzendler<sup>1,2,\*</sup>

<sup>1</sup>Department of Neurology

<sup>2</sup>Department of Neuroscience

Yale University, New Haven, CT 06511, USA

<sup>3</sup>Department of Pathology, University of Washington, Seattle, WA 98195, USA

<sup>4</sup>Department of Pathology and Immunology, Washington University School of Medicine, St. Louis, MO 63110, USA

<sup>5</sup>Department of Neurology, University of Washington, Seattle, WA 98195, USA

<sup>6</sup>The Helen and Robert Appel Alzheimer's Disease Research Institute, Brain and Mind Research Institute, Weill Cornell Medical College, New York, NY 10065, USA

<sup>7</sup>Department of Cell Biology, Yale University, New Haven, CT 06511, USA

<sup>8</sup>Nanobiology Institute, Yale University, West Haven, CT 06515, USA

<sup>9</sup>Co-first author

<sup>10</sup>Present address: Department of Neurology, Institute for Neurodegenerative Diseases, University of California, San Francisco, San Francisco, CA 94158, USA

\*Correspondence: jaime.grutzendler@yale.edu

<http://dx.doi.org/10.1016/j.neuron.2016.05.003>

## SUMMARY

Haplodeficiency of the microglia gene *TREM2* increases risk for late-onset Alzheimer's disease (AD) but the mechanisms remain uncertain. To investigate this, we used high-resolution confocal and super-resolution (STORM) microscopy in AD-like mice and human AD tissue. We found that microglia processes, rich in TREM2, tightly surround early amyloid fibrils and plaques promoting their compaction and insulation. In *Trem2*- or *DAP12*-haplodeficient mice and in humans with R47H *TREM2* mutations, microglia had a markedly reduced ability to envelop amyloid deposits. This led to an increase in less compact plaques with longer and branched amyloid fibrils resulting in greater surface exposure to adjacent neurites. This was associated with more severe neuritic tau hyperphosphorylation and axonal dystrophy around amyloid deposits. Thus, TREM2 deficiency may disrupt the formation of a neuroprotective microglia barrier that regulates amyloid compaction and insulation. Pharmacological modulation of this barrier could be a novel therapeutic strategy for AD.

## INTRODUCTION

Microglia are the resident immune cells in the CNS, where they constantly survey their microenvironment and become activated in various neurological disorders (Davalos et al., 2005; Hanisch

and Kettenmann, 2007). In Alzheimer's disease (AD), a striking feature of microglia is their universal clustering around amyloid- $\beta$  (A $\beta$ ) deposits, one of the major pathological hallmarks of this condition. It has traditionally been thought that activated microglia remove A $\beta$  deposits via phagocytosis (Lee and Landreth, 2010). However, multiple recent lines of evidence indicate that microglia are ineffective at removing fibrillar A $\beta$  in vivo (Condello et al., 2011; Liu et al., 2010; Stalder et al., 2001). At the same time, given their ability to secrete cytokines and reactive oxygen species, microglia have the potential to be neurotoxic (Block et al., 2007). Thus, it remains unknown whether certain aspects of microglial function play beneficial or detrimental roles that could be important for disease pathogenesis.

*TREM2* (Triggering Receptor Expressed on Myeloid cells 2) gene is specifically expressed by microglia in the CNS (Schmid et al., 2002). A loss-of-function R47H (rs75932628, Arginine-47-Histidine) mutation in *TREM2* constitutes one of the strongest single allele genetic risk factors for AD (Guerreiro et al., 2013; Jin et al., 2014; Jonsson et al., 2013; Korvatska et al., 2015; Ruiz et al., 2014), providing the clearest link between microglia dysfunction and AD pathogenesis. While loss of *Trem2* in vitro disrupts A $\beta$  phagocytosis by microglia (Kleinberger et al., 2014), *Trem2*-haplodeficient AD-like mice have shown inconsistent results with respect to the amounts of cerebral A $\beta$  deposition (Jay et al., 2015; Ulrich et al., 2014; Wang et al., 2015). Thus, it remains unclear to what extent *Trem2* regulates microglia phagocytosis in vivo, suggesting that the increased risk of AD in *Trem2* haplodeficiency may not be due to differences in amyloid plaque load. Interestingly, most studies in *Trem2*-deficient AD-like mice have shown reduced number of microglia around amyloid plaques (Jay et al., 2015; Wang et al., 2015). However, it remains unknown how subtle changes in microglia around plaques could profoundly increase the risk of AD.

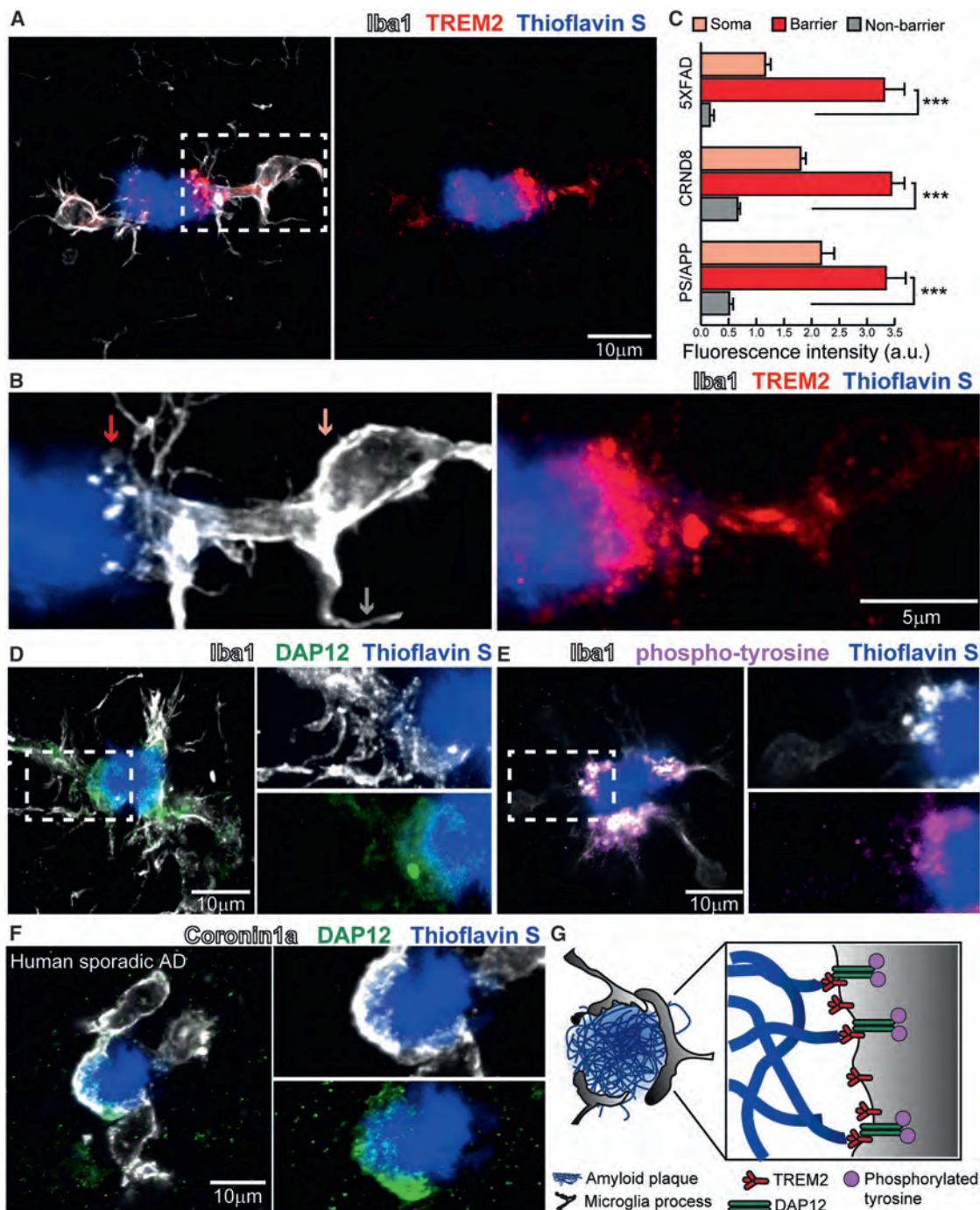


### Figure 1. Trem2-Mediated Signaling Is Activated within Microglia Processes Directly Contacting Amyloid Plaques

(A) Confocal images showing the subcellular localization of immunostained Trem2 (red) within Iba1-positive microglia (white) clustered around an amyloid plaque (blue) in a 5XFAD mouse.

(B) Zoomed images of Trem2 in plaque-associated microglia processes from the dashed box in (A). Microglia processes were divided into three subcellular compartments: (1) soma (pink arrow), (2) barrier (processes contacting plaque, red arrow), and (3) non-barrier (processes not engaged with plaque, gray arrow).

(C) Quantification of Trem2 fluorescence intensity in microglia associated with plaques in AD mouse models: 5XFAD, CRND8, and APPS1-21.  $n = 30$  microglia from each model. Student's *t* tests were used for statistical comparisons, \*\*\* $p < 0.001$ ; a.u., arbitrary unit. Data presented as mean  $\pm$  SEM.

(D and E) Confocal images showing elevated levels of immunostained-DAP12 (D, green) and phospho-tyrosine (E, magenta) at the microglia-plaque interface (white). Right: zoomed split channels from the dashed box.

(legend continued on next page)

Furthermore, it remains unclear how these mouse studies correlate with the human pathology.

Recently, we identified a protective function of microglia, whereby their processes tightly wrap around plaques and act as a physical barrier that prevents the outward extension of amyloid fibrils (Condello et al., 2015). This barrier function promotes formation of highly compact plaque microregions that have minimal affinity for soluble A $\beta$ 42 (Figure S1). Conversely, areas not covered by microglia processes display hotspots with very high soluble A $\beta$ 42 affinity, leading to markedly concentrated protofibrillar A $\beta$  plaque regions. These A $\beta$  hotspots are neurotoxic given that adjacent axons develop a greater extent of dystrophy compared to those next to non-hotspot regions covered by microglia (Condello et al., 2015). Despite these intriguing observations in mice, the importance of microglia in the pathogenesis of AD and more specifically the relevance of this newly discovered microglial barrier function in humans has not been demonstrated.

We thus hypothesized that disruption of the microglia barrier function is a cellular mechanism underlying association between loss-of-function *TREM2* mutations and increased risk of AD. To test this, we used quantitative high-resolution confocal microscopy and super-resolution Stochastic Optical Reconstruction Microscopy (STORM) in both human brains of patients with R47H *TREM2* mutations and in AD-like mice lacking either Trem2 or its adaptor protein DNAX-binding protein of 12 kDa (DAP12). This revealed unprecedented structural detail of the landscape of amyloid fibrils, axonal dystrophy, and microglia heterogeneity around plaques in *TREM2* haplodeficiency.

Our data in mice and humans indicate that microglia processes closely interact with individual amyloid fibrils in early non-compact filamentous plaques and later form specialized protrusions rich in *TREM2* and DAP12 that tightly wrap around the surface of compact plaques. We then demonstrate in both *TREM2* and *DAP12* haplodeficiency a striking microglia phenotype in which these cells fail to polarize and engage nascent amyloid fibrils and mature compact plaques. However, this was not associated with differences in amyloid phagocytosis or plaque numbers. Instead, we observed a marked reduction in amyloid plaque compaction and a subsequent increase in plaque surface area contacting neuropil, which was associated with a significant increase in the degree of axonal dystrophy. A strikingly similar phenotype was also observed in human *TREM2* R47H mutants, demonstrating that this neuroprotective microglia barrier is conserved in humans. Our data indicate that *TREM2* deficiency disrupts this specialized barrier function and may thus constitute a previously unknown cellular mechanism linking *TREM2* R47H variant with increased risk of dementia. Future studies may determine whether similar mechanisms play a role in the pathogenesis of late-onset AD associated with other microglia-related genetic risk alleles.

## RESULTS

### Microglia Processes Contacting Plaques Are Highly Enriched with Trem2

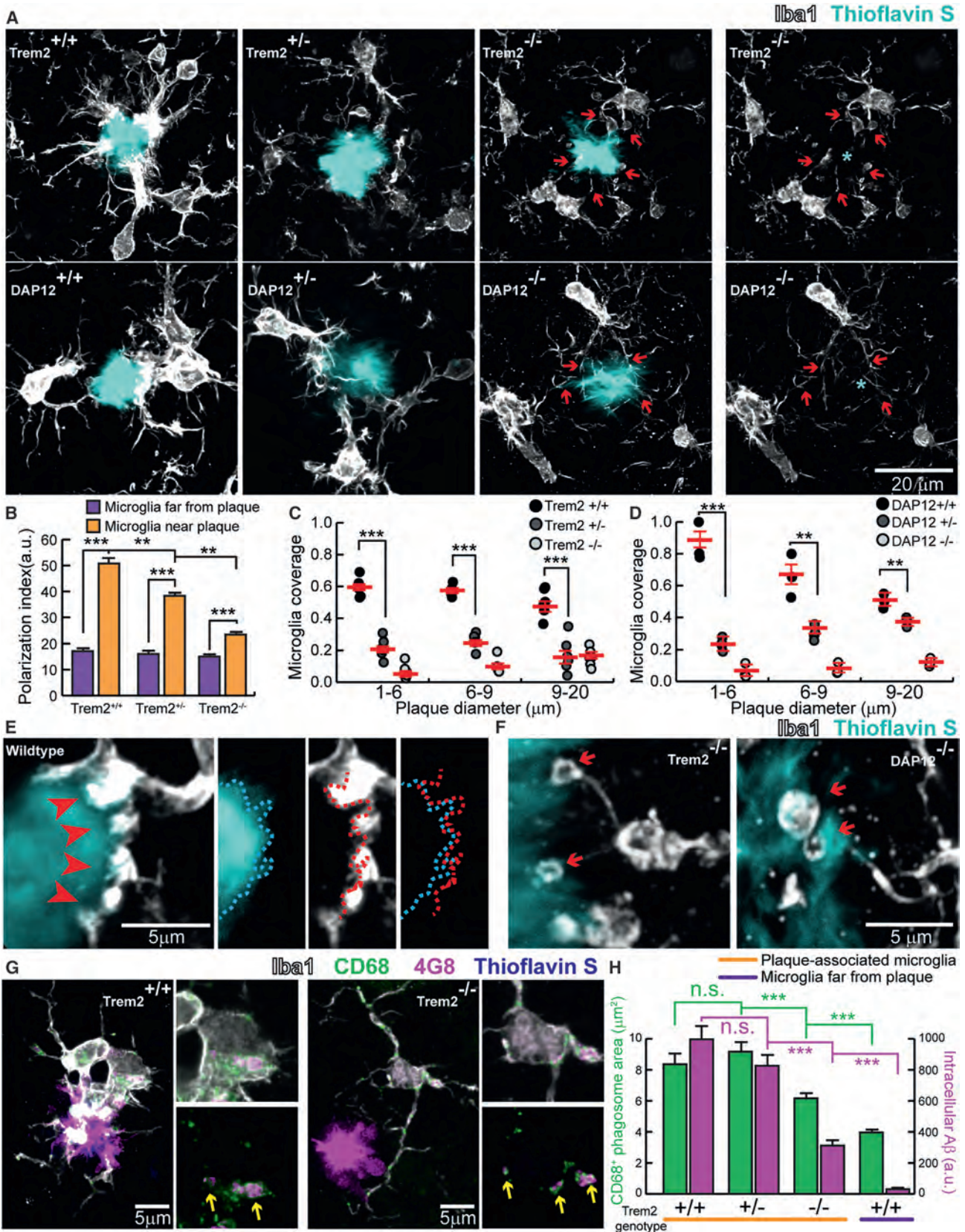
We first examined the expression pattern of Trem2 in the brains of three transgenic AD mouse models. Building upon previous reports (Frank et al., 2008; Lue et al., 2015; Matarin et al., 2015), high-resolution confocal microscopy revealed that Trem2 is enriched within plaque-associated microglia, but not in microglia away from plaques or other neural cells (Figure S2). Interestingly, we found that Trem2 expression was exceptionally high at the leading edges of microglia processes directly contacting amyloid plaques (Figures 1A–1C). We also detected polarized expression of its signaling adaptor protein DAP12 (Figure 1D), and a marker of phosphorylated tyrosine (Figure 1E) consistent with downstream kinase-mediated signal transduction (Colonna, 2003). Similar to mice, in postmortem human brain, we found enhanced DAP12 expression specifically polarized to microglia processes contacting amyloid plaques (Figure 1F and Table S1). The robust enrichment of Trem2, DAP12, and a marker of downstream tyrosine phosphorylation suggests that these signaling proteins could play a key role in the envelopment of the plaque surface by microglia processes and the establishment of the microglia barrier (Figure 1G).

### Trem2 Haplodeficiency Abolishes the Microglia Barrier but Does Not Impair A $\beta$ Phagocytosis

We next examined structural and functional features of microglia in AD-like transgenic mice carrying different copy numbers of the *Trem2* or *DAP12* genes (Figures 2, S2, and S4). High-resolution confocal microscopy revealed that *Trem2* or *DAP12* deletion markedly reduced the degree of plaque surface coverage by microglia processes (Figures 2A–2D). The dramatic change of plaque coverage in *Trem2* and *DAP12* deficiency cannot be explained alone by the modest ~20% reduction in the number of plaque-associated microglia (Figures S3 and S4). Instead, it appears that microglia in *Trem2* or *DAP12* deficiency have an impairment in the ability to polarize their processes toward the plaque surface and thus are unable to create an effective barrier around them (Figures 2A–2D). Interestingly, in *Trem2* deficiency, microglia processes contacting plaques did not show enrichment of phosphorylated tyrosine (Figure S3), a marker of downstream tyrosine kinase activation that is potentially necessary for triggering actin reorganization during process polarization (Peng et al., 2010). Indeed, contrary to the robust microglia processes seen in wild-type mice (Figure 2E), processes contacting plaques in either *Trem2*- or *DAP12*-deficient mice displayed characteristic dysmorphic features with fine processes and terminal loops that failed to closely track the boundaries of the plaque (Figure 2F). Thus, *Trem2* likely plays a critical role in signaling microglia process specialization underlying the formation of the microglia barrier around plaques.

(F) Confocal images of DAP12 (green) and microglia (white) in human sporadic AD postmortem brain showing strong polarization to processes contacting plaques.

(G) Diagram of specialized microglial processes wrapping around amyloid plaque microregions, with enriched *TREM2* and downstream signaling proteins. All analyses were performed in mouse somatosensory cortex human middle frontal gyrus.



(legend on next page)

To assess whether *Trem2* deficiency also affected A $\beta$  fibril engulfment by microglia, we performed immunohistochemistry and quantitative confocal image analysis to measure the A $\beta$  content within CD68-immunolabeled microglial phagosomes, a correlate of A $\beta$  phagocytosis efficiency. While in *Trem2*<sup>-/-</sup> mice, there was a significant reduction in A $\beta$  phagocytosis, we were surprised to see that in *Trem2*<sup>+/-</sup> mice, a more relevant model of human *TREM2* haplodeficiency leading to AD, there was no significant difference in either the number of phagosomes or amount of A $\beta$  within phagosomes (Figures 2G and 2H). This suggests that a defect in microglia phagocytosis of A $\beta$  is not the main cause of neuropathology in *Trem2* deficiency. Instead it suggests that inability of microglia processes to polarize and establish an effective barrier may be a neuropathological mechanism in *TREM2* R47H variant carriers.

### **Trem2 Haplodeficiency Decreases Amyloid Plaque Compaction and Increases Total Fibril Surface Area**

We next asked how deficiency in the microglia barrier may impact the structural organization of individual plaques. Quantitative confocal analyses of individual plaques labeled by the  $\beta$  sheet binding dye thioflavin S, in *Trem2*- and *DAP12*-deficient mice, showed a reduction in the fluorescence and a diffuse plaque morphology with amyloid fibrils projecting outward radially (Figures 3A–3C). To directly observe A $\beta$  fibrils, we next performed super-resolution nanoscopy using stochastic optical reconstruction microscopy (STORM) in brain slices fluorescently immunolabeled with an N terminus anti-A $\beta$  antibody. While plaques from *Trem2*<sup>+/+</sup> mice exhibited circumscribed borders, in *Trem2*<sup>+/-</sup> and *Trem2*<sup>-/-</sup> mice, plaques displayed spike-like fibrils extending radially (Figure 3D). We then defined three different plaque regions based on A $\beta$  fibril organization: (1) diffuse region; (2) mesh-like region (likely formed by interweaving of individual A $\beta$  fibrils); and (3) compact region (where densely packed fibrils limit antibody penetration (Figures 3E and S5)). *Trem2* deficiency markedly increased the proportion of diffuse fibrils and decreased the proportion of mesh-like and compact fibrils (Figure 3F). Furthermore, loss of *Trem2* increased the average length of diffuse fibrils radiating outward from the mesh-like compact core (Figures 3G and 3H) (average 231 nm in *Trem2*<sup>+/+</sup>, 396 nm in *Trem2*<sup>+/-</sup>, and 442 nm in *Trem2*<sup>-/-</sup>). This suggests that the microglia barrier prevents the radial extension of  $\beta$ -amyloid fibrils, promoting their intermingling and forma-

tion of mesh-like structures with various degrees of compaction. The longer amyloid fibers, coupled with their increased branching at the nano scale (Figure 4G), lead to a marked increase in fibril surface area in *Trem2* deficiency (see Supplemental Information).

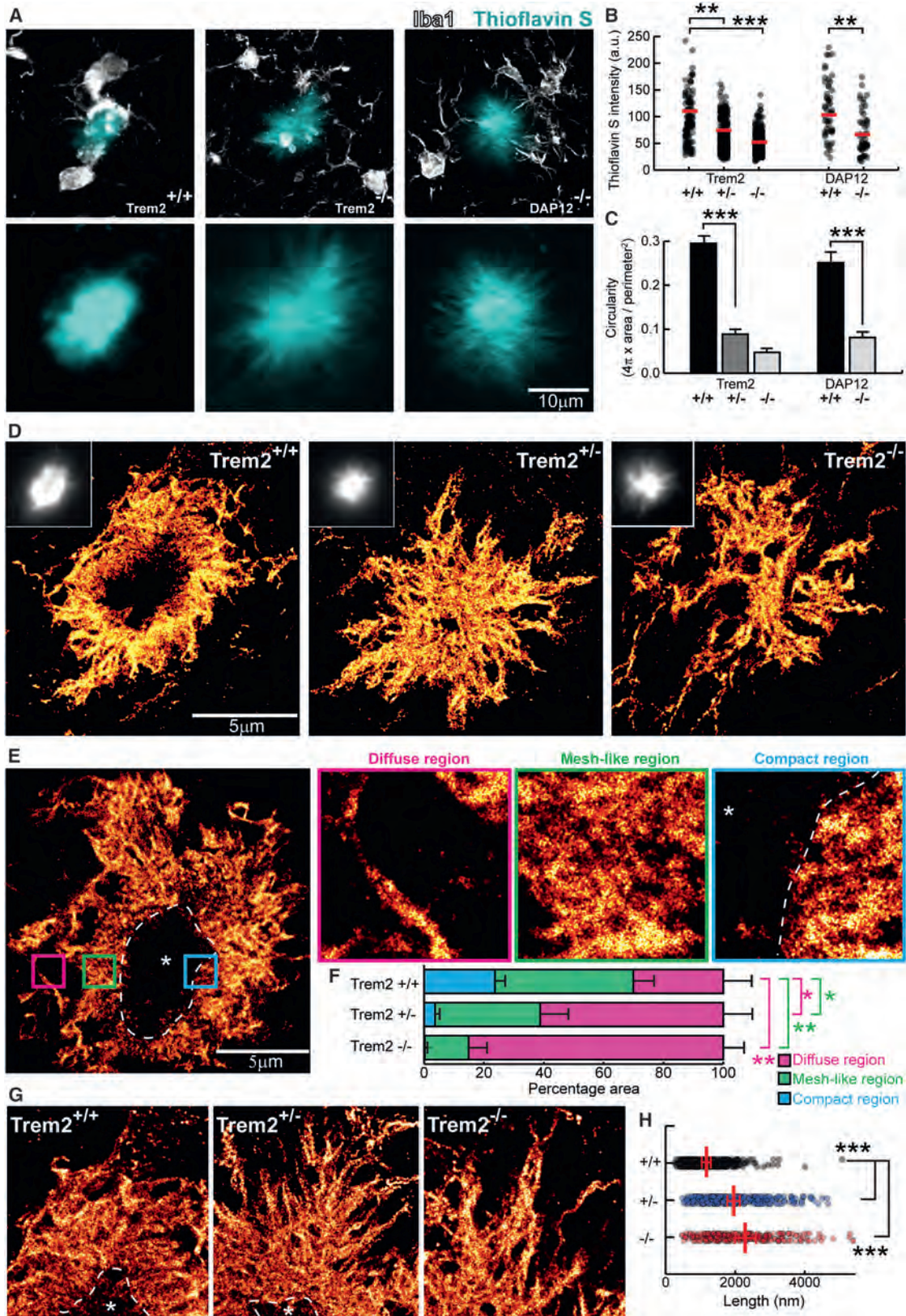
### **Microglia Processes Envelop Individual Fibrils in Early Filamentous Plaques and Promote Their Compaction**

To explore the role of microglia and *TREM2* deficiency in the earliest stages of amyloid deposition in mice, we obtained high-resolution confocal images of clusters of thioflavin S-positive fibrils that lacked a dense core, which we termed filamentous plaques (Figure 4A). Interestingly, we observed that these plaques were highly intermingled with microglia processes (Figure 4A). Processes that directly contacted thioflavin S-positive amyloid filaments were highly enriched in Trem2 (Figure 4B). These processes appeared to closely wrap around individual amyloid filaments as evidenced by the fact that the membrane-bound Trem2 was highly colocalized with the filaments, while the parent microglia branches filled with cytoplasmic Iba1 were immediately adjacent (Figure 4C). We also observed instances in which more mesh-like clusters of fibrils were fully wrapped by fine Trem2-positive microglia processes that appeared to cap individual fibril endings. (Figure 4D). This suggests that these early interactions between microglia processes and amyloid filaments could be of importance in determining the degree of fibril compaction.

To explore this possibility, we examined the nanostructures within diffuse fibrils revealed by super-resolution STORM imaging. Within individual plaques, we observed fibrils with variable widths ranging from 30 nm (about the resolution limit of our STORM imaging) to 160 nm (Figures 4E and 4F). Consistent with atomic-force microscopy data in vitro (Stine et al., 1996), this suggests that A $\beta$  fibrils coil together to form bundle-like structures of different widths in vivo. Interestingly, *Trem2* deficiency led to an increased proportion of thin fibril bundles (~40 nm) and decreased proportion of thicker ones (average 68 nm in *Trem2*<sup>+/+</sup>, 57 nm in *Trem2*<sup>+/-</sup>, and 48 nm in *Trem2*<sup>-/-</sup>) (Figure 4G). Furthermore, we observed branched structures extending orthogonally from the main A $\beta$  fibril bundle (Figure 4H), which were markedly increased in plaques from *Trem2*-deficient mice (Figure 4I). Together, the increased numbers of diffuse thin fibers projecting outward for greater lengths and the increased

### **Figure 2. Defective Microglia Barrier but Normal A $\beta$ Phagocytosis in *Trem2* or *DAP12* Haplodeficiency**

(A) Confocal images of Iba1-immunostained microglia (white) around thioflavin S+ amyloid plaques (cyan) in *5XFAD* mice with different *Trem2* genotypes or in *APPSP1-21* mice with different *DAP12* genotypes. Cyan asterisks indicate locations of the plaque. Red arrows point to the polarized microglia processes.  
 (B) Quantification of microglia process polarization away from or near plaques in *5XFAD* mice with different *Trem2* genotypes. n = 3 mice for each group; 540 microglia analyzed.  
 (C and D) Quantification of microglia plaque coverage (“barrier”) around plaques in *5XFAD* mice with different *Trem2* genotypes (C) and *APPSP1-21* mice with different *DAP12* genotypes (D). n = 6 mice for each group, 2,887 plaques for *5XFAD:Trem2* and 598 plaques for *APPSP1-21:DAP12*.  
 (E) Microglia barrier (white) interdigitates with the surface of an amyloid plaque (cyan) in wild-type *5XFAD* mice. Dotted cyan and red lines indicate thresholded borders of plaque and microglia, respectively.  
 (F) Dysmorphic microglia processes (white) with looping structures (red arrows) in mice with *Trem2* or *DAP12* deficiency.  
 (G) Confocal images of A $\beta$  immunolabeling (4G8) within microglial phagosomes (CD68+; green) in *Trem2*<sup>+/+</sup> (left) and *Trem2*<sup>-/-</sup> (right) from *5XFAD* brain slices. Yellow arrows indicate colocalized 4G8+ A $\beta$  (magenta) and CD68+ (green) vesicles.  
 (H) Quantification of CD68+ vesicle area and 4G8 fluorescence per microglia. n = 3 mice for each group and 321 cells. Student’s t tests were used for all statistical comparisons, \*\*p < 0.01, \*\*\*p < 0.001; n.s.: p > 0.05; a.u., arbitrary unit. Data presented as mean  $\pm$  SEM. All analyses were performed with mouse somatosensory cortex.



(legend on next page)

orthogonal branches, implies that the surface-to-volume ratio of amyloid fibers in *Trem2*-deficient mice is significantly greater than in wild-type mice (we estimate an ~300%–400% increase; see Supplemental Information). This phenomenon would be predicted to dramatically increase the contact area between amyloid fibrils and the adjacent exposed cellular structures. Importantly, while the total number of amyloid plaques was not significantly different between *Trem2*-deficient and wild-type mice (Figure 4J and Figure S3), we observed a significant increase in the proportion of filamentous plaques in both *Trem2*<sup>+/-</sup> and *Trem2*<sup>-/-</sup> mice (Figure 4J). The increase in filamentous plaques coupled with the greater surface area of individual plaques in *Trem2*<sup>+/-</sup> mice may lead to worsened neurotoxicity.

### Decreased Amyloid Plaque Compaction in *Trem2* or *DAP12* Deficiency Leads to Severe Axonal Dystrophy

To directly test the degree of neurotoxicity, we measured the volume of axonal dystrophy around individual amyloid plaques using immunohistochemistry for Lamp1, a lysosomal protein highly enriched in dystrophic neurites (DN) that serves as a reliable marker for quantitative DN measurements (Condello et al., 2015, 2011; Gowrishankar et al., 2015). We classified plaques by morphology and size with specific attention to early filamentous plaques that were surprisingly associated with a massive amount of dystrophic neurites (Figures 5A and 5B). We found that *Trem2* or *DAP12*<sup>+/-</sup> and *DAP12*<sup>-/-</sup> mice had a much greater degree of axonal dystrophy than wild-type mice (Figures 5C and 5D). Interestingly, the main difference in dystrophy occurred in non-compact filamentous and small compact plaques (up to 6 μm in diameter), suggesting that the protective effect of microglia is most effective at early stages of plaque evolution. Given that filamentous plaques are associated with a surprisingly large degree of axonal dystrophy (Figure 5B), a shift of the distribution toward filamentous plaques could have critical effects on the overall degree of neural circuit disruption at early stages of amyloid accumulation.

### TREM2 R47H Mutations Disrupt the Microglia Barrier Function in Late-Onset Human AD

To determine whether our findings in mice are relevant for human AD pathogenesis, we next characterized the microglia and plaque phenotypes in postmortem human brains from sporadic

late onset AD cases and patients with R47H *TREM2* variant. Consistent with previous reports on late-onset AD, we observed different types of plaque morphologies using anti-Aβ immunolabeling (4G8) and thioflavin S (TS) staining (Figure 6A). We classified them into four categories: (1) diffuse plaques: diffuse 4G8+ fibrils lacking TS labeling; (2) filamentous plaques: 4G8+ halo and filamentous TS labeling with no plaque core; (3) compact plaques: 4G8+ halo and TS-labeled core; and (4) inert: TS-labeled core with no 4G8 halo. Interestingly, microglia processes did not display any polarization toward diffuse plaques but showed enlarged processes that robustly intermingled with both filamentous and compact plaques (Figures 6A and 6B). Moreover, plaques that had a TS-labeled core with no 4G8 halo had very few microglia processes (Figure 6A) or dystrophic neurites (Figure 7A) around them, which motivated us to call them inert.

We next quantified the relative proportions of these plaque categories in AD cases with and without the R47H *TREM2* mutation (Table S2). While we did not find a significant difference in the overall microglia density or amyloid plaque burden between genotypes (Figure S6), we did observe a robust increase in the proportion of plaques with filamentous morphology (Figure 6C). Remarkably, we observed a marked reduction in the number of surrounding microglia in both filamentous and compact plaques but we saw no significant microglia differences around diffuse and inert plaques (Figure 6C) or in non-plaque regions (Figure S6). Thus, the R47H mutation in humans leads to a specific defect of microglia plaque engagement, which is strikingly similar to the phenotype in *Trem2*- and *DAP12*-haplodeficient mice.

We then sought to determine how the observed decrease in microglia numbers in R47H mutants impacts their capacity for envelopment of individual filaments and plaque cores. Like in mice, we observed that microglia processes infiltrated filamentous plaques and had a tendency to surround individual filaments (Figure 6D). In contrast, microglia around compact plaques projected robust processes that closely enveloped the plaque surface (Figure 6E). Interestingly, while microglia in R47H mutants were able to send processes toward amyloid deposits, these appeared to be less robust and did not tightly engage with individual fibrils or the plaque surface, leading to a markedly diminished microglia coverage of amyloid aggregates (Figures 6F–6H). Thus, *TREM2* in humans likely regulates the

### Figure 3. Super-resolution STORM Imaging Reveals a Marked Reduction in Plaque Compaction in *Trem2* Haplodeficiency

(A) Confocal images of thioflavin S-labeled amyloid plaques in *Trem2*<sup>+/+</sup> and *Trem2*<sup>-/-</sup> 5XFAD mice and *DAP12*<sup>-/-</sup> APPPS1-21 mice. (B and C) Quantification of mean thioflavin S fluorescence intensity (B) and circularity (C, roundness) in plaques from 5XFAD mice with different *Trem2* genotypes and APPPS1-21 mice with different *DAP12* genotypes. n = 3 mice for each group, 747 plaques for 5XFAD:*Trem2* and 198 plaques for APPPS1-21:*DAP12*. (D and E) Immunolabeled Aβ plaque fibrils reconstructed by super-resolution STORM imaging. Images were pseudo-colored according to the reconstructed intensities. Insets in (D) show the same plaque imaged with wild-field illumination. Dashed line and asterisk in (E) indicate locations of the compact plaque core which is not labeled due to poor antibody penetration in 5XFAD *Trem2*<sup>+/-</sup> mice (Figure S6). Three insets in (E) show high zoom examples of different types of Aβ fibril organization located in plaque regions with different degree of compaction. (F) Quantification of the proportion of diffuse, mesh-like, and compact regions in amyloid plaques from 5XFAD mice with different *Trem2* copy numbers. n = 8 plaques from each genotype. Multiple t tests were used to compare different regions between genotypes. Multiple comparisons were corrected with Holm-Sidak method. \*p < 0.0005, \*\*p < 0.0001. (G) Example images of fibrils within the diffuse plaque region extending radially from the plaque center in 5XFAD mice with different *Trem2* genotypes. Dashed lines and asterisks indicate locations of the unlabeled compact plaque core. (H) Quantification of lengths of the diffuse fibrils in plaques of 5XFAD mice with different *Trem2* copy numbers. Scatterplot shows individual data point. Red bars indicate group averages by genotypes. Except for comparison in (F), Student's t tests were used for all statistical comparisons, \*\*p < 0.01, \*\*\*p < 0.001; a.u., arbitrary unit. Data presented as mean ± SEM.

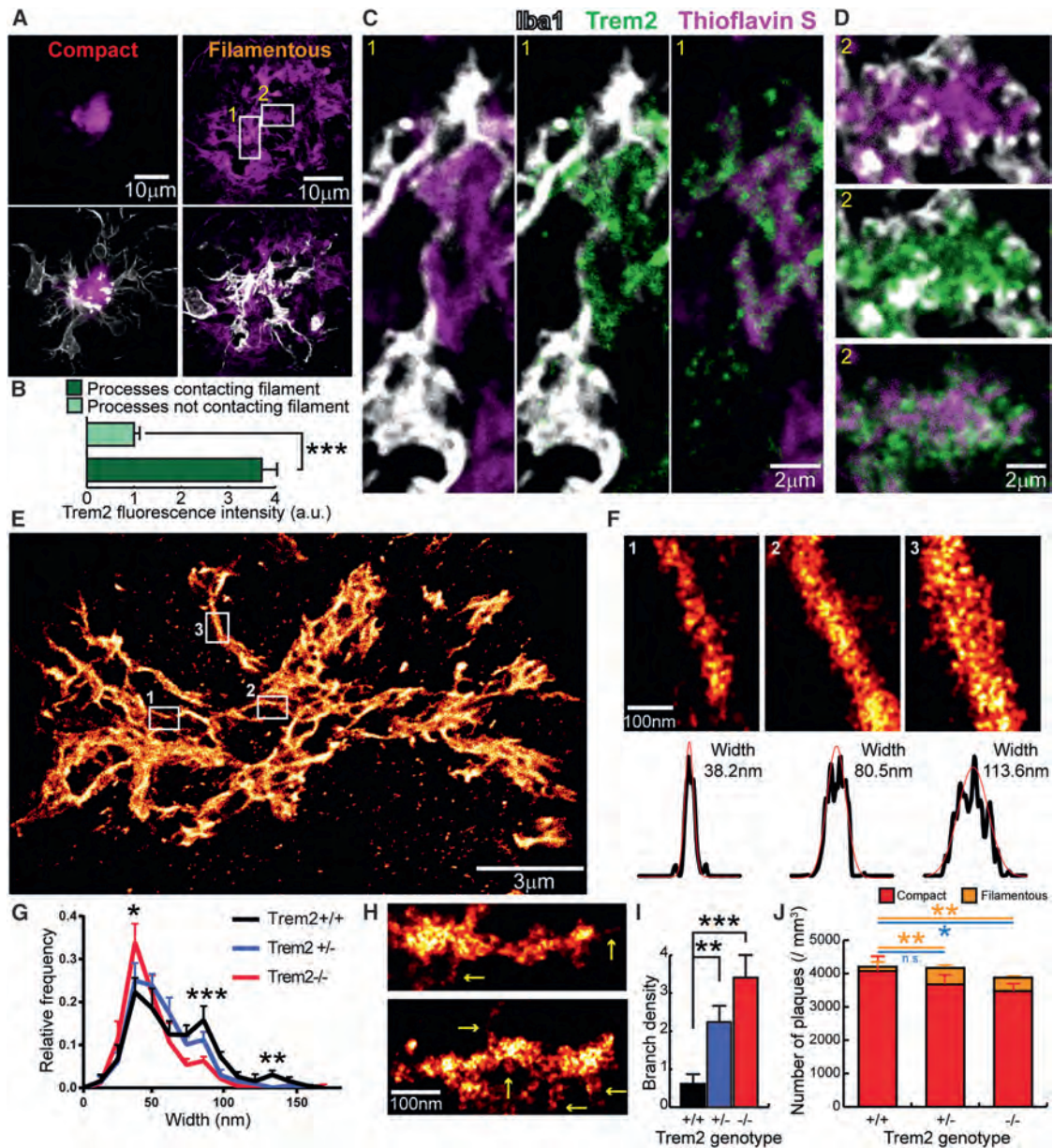


**Figure 4. Trem2 Deficiency Impairs Early-Stage Amyloid Fibril Envelopment by Microglia Leading to Increased Fibril Branching**

(A) Confocal images of filamentous and compact plaques using thioflavin S labeling (magenta) in *5XFAD* mice showing close interaction with surrounding microglia (anti-Iba1 immunostaining, white).

(B) Quantification of Trem2 fluorescence intensity in microglia processes that do and do not contact with amyloid fibrils.  $n = 30$  plaques, Student's *t* tests were used for statistical comparisons.

(C and D) Zoomed images from insets in (A), showing Trem2-enriched microglia processes wrapping around individual amyloid fibrils in a filamentous plaque.

(E and F) Examples of A $\beta$  fibril nanostructures revealed by STORM imaging. Images were pseudo-colored according to the reconstructed intensities. Three insets in (E) show examples of individual fibrils. By fitting the cross-section fluorescence intensity to a Gaussian distribution, the widths of the fibril were derived as 2.35 times the SD of the fitted curve.

(G) Distribution of the A $\beta$  fibril widths in plaques of *5XFAD* mice with different copy numbers of the *Trem2* gene.  $n = 8$  plaques from each genotype, more than 200 fibrils were measured per plaque.

(H) Examples of individual A $\beta$  fibril nanostructures branching orthogonally from the primary fiber bundle revealed by STORM imaging (yellow arrows).

(I) Quantification of the frequency of branched A $\beta$  nanostructures per 500 nm in *5XFAD* mice with different copy numbers of the *Trem2* gene.

(J) Quantification of compact (thioflavin S<sup>+</sup> core with 4G8<sup>+</sup> halo, red) and filamentous (diffuse filamentous thioflavin S labeling with 4G8<sup>+</sup> halo, orange) plaque densities in *5XFAD* mice with different copy numbers of the *Trem2* gene. Blue lines refer to statistical analyses for total plaques.  $n = 6$  mice for each group; total 2,887 plaques analyzed. Student's *t* tests were used for all statistical comparisons, \* $p < 0.05$ , \*\* $p < 0.01$ , \*\*\* $p < 0.001$ ; a.u., arbitrary unit; n.s.,  $p > 0.05$ .

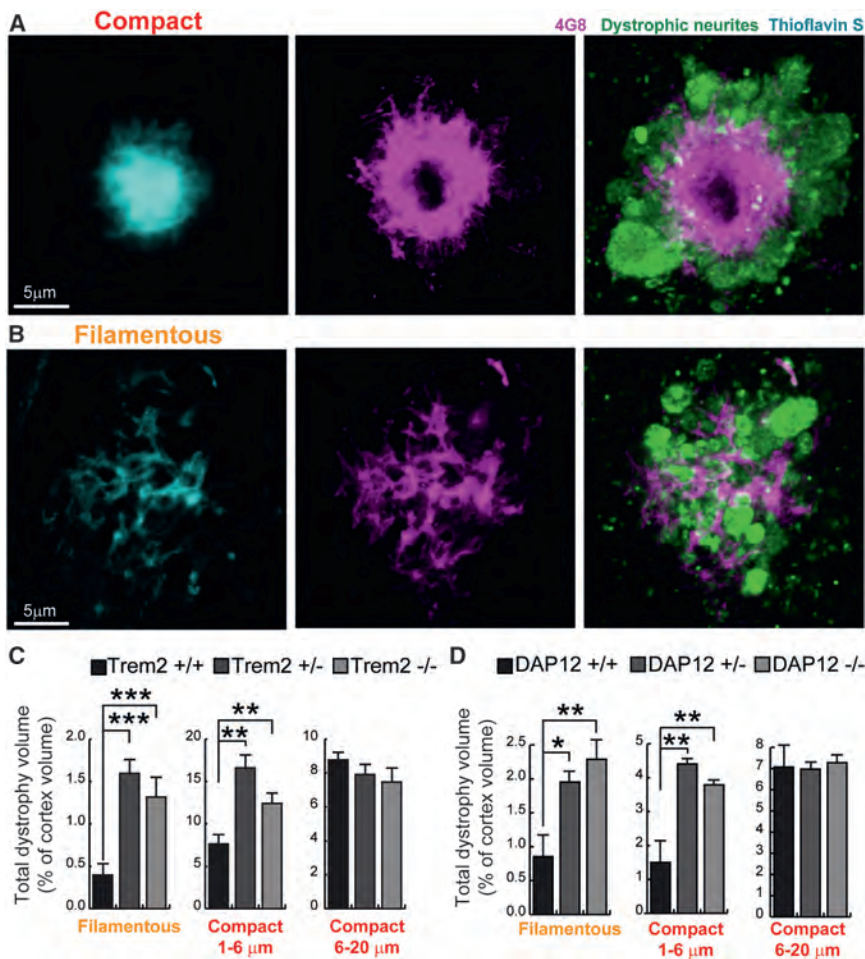


**Figure 5. *Trem2* or *DAP12* Deficiency Leads to More Severe Plaque-Associated Axonal Dystrophy**

(A and B) Visualization of Lamp1-immunolabeled axonal dystrophy (green) around compact (A) and filamentous (B) plaques in AD-like mouse brains. (C and D) Quantification of total dystrophy volume in cortex of AD-like mice with different *Trem2* (C) or *DAP12* (D) genotypes.  $n = 6$  mice for each group of *5XFAD:Trem2* mice; total 2,887 plaques analyzed.  $n = 3$  mice for each group of *APPSP1-21:DAP12* mice; total 1,076 plaques analyzed. Student's *t* tests were used for all statistical comparisons, \* $p < 0.05$ , \*\* $p < 0.01$ , \*\*\* $p < 0.001$ ; a.u., arbitrary unit. Data presented as mean  $\pm$  SEM. All analyses were performed with somatosensory cortex in mice.

we observed a strong anti-colocalization between microglia processes and hyperphosphorylated tau-positive dystrophic neurites (Figures 7E and 7F), suggesting that microglia normally exert a protective insulating effect. This function is disrupted in R47H mutants as demonstrated by a significantly reduced degree and robustness of microglia plaque coverage associated with increased neuritic abnormalities (Figure 7G).

## DISCUSSION

Our study has uncovered previously unrecognized microglia functions that may participate in the pathogenesis of Alzheimer's disease.

microglia barrier function and disruption of this function in R47H mutants is associated with inability of microglia for enveloping fibrils or amyloid deposits.

### Increased Tau Hyperphosphorylation and Axonal Dystrophy around Filamentous and Compact Plaques in Human R47H Mutants

To determine the consequences of a deficient microglia barrier in human AD with R47H *TREM2* variant, we quantified the extent of axonal dystrophy around individual plaques. Similar to mice, we found that filamentous plaques lacking a core had a surprisingly large number of dystrophic axons, as visualized by anti-APP immunohistochemistry (Figure 7A). Interestingly, we found a dramatic increase in axonal dystrophy around both filamentous and small compact plaques in R47H mutants compared to sporadic non mutant AD cases (Figure 7B).

These dystrophic swellings were associated with marked cytoskeletal abnormalities as evidenced by the extensive neuritic labeling with anti-phosphotau antibody around both filamentous and compact amyloid deposits (Figure 7C). Similar to our results quantifying APP-positive dystrophic neurites, phosphotau labeling was markedly increased in R47H AD brains compared to sporadic AD cases (Figure 7D). Consistent with our previous findings in mice (Condello et al., 2015) (Figure S1),

We examined microglia-plaque interactions in AD-like mice lacking *Trem2* and *DAP12* genes as well as in postmortem brains from human AD patients with R47H mutations. This enabled us to demonstrate that the tight envelopment of fibrils and early-stage plaques by microglia processes ("microglia barrier") may play a role in inducing amyloid fibril compaction and in reducing the surface area of potentially neurotoxic fibrils exposed to surrounding neural structures (Figure S7). This potentially neuroprotective microglial function provides a novel cellular mechanism that may explain the increased risk of Alzheimer's disease with *TREM2* genetic variants. It may also provide important insights for the more common forms of sporadic AD in which microglia senescence may drive similar functional deficits in barrier formation (Condello et al., 2015).

Microglia function in AD remains controversial with some evidence suggesting that they play a neurotoxic role by secreting reactive oxygen species and cytokines (Block et al., 2007). In advance neuropathological stages in mice, it has been shown that eliminating microglia with CSF1R antagonists leads to beneficial behavioral effects without changes in plaque numbers (Dagher et al., 2015; Olmos-Alonso et al., 2016), consistent with a toxic effect of microglia. In contrast, our results demonstrate a potentially neuroprotective role of microglia in early stages of plaque evolution, evidenced by the fact that areas covered by

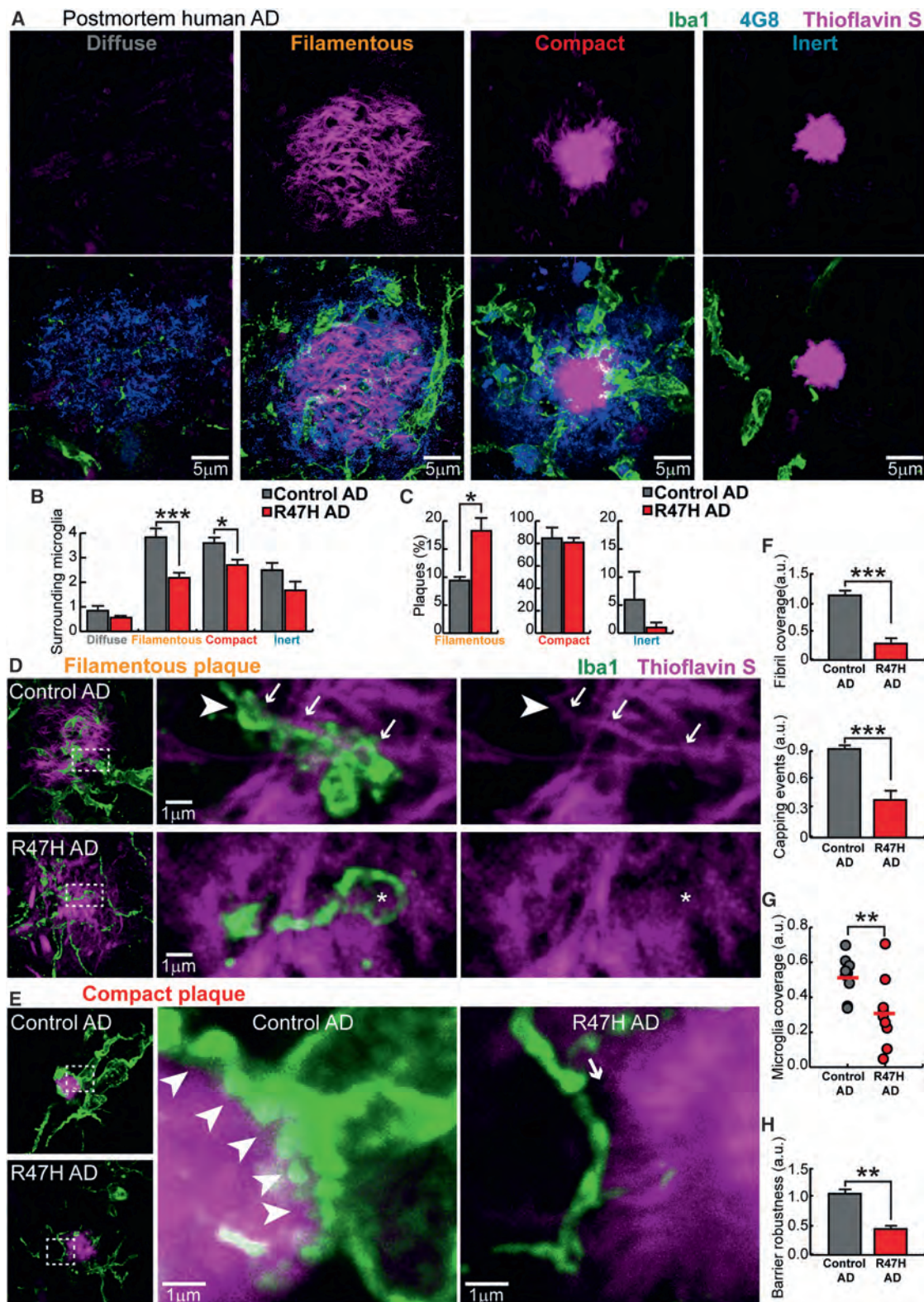


**Figure 6. *TREM2* R47H Mutations in Human AD Lead to Abnormal Microglia Coverage around Filamentous and Compact Plaques**

(A) Confocal images of thioflavin S-stained amyloid deposits (magenta), 4G8-labeled A $\beta$  (blue), and Iba1-labeled surrounding microglia (green) in human postmortem AD brains, showing four different subtypes of plaques.

(legend continued on next page)

microglia processes develop fewer dystrophic neurites (Condello et al., 2015) and by the finding that inability of microglia to engage with plaques in R47H mutations is associated with increased axonal dystrophy in humans. Furthermore, we find it unlikely that microglia are actively involved in the formation or pruning of dystrophic axons given that we never find their processes directly surrounding or engulfing individual dystrophic neurites (Figure S7) (Condello et al., 2015).

While the function of *TREM2* in peripheral immune cell responses to pathogens has been extensively studied (Colonna, 2003), its role in AD remains poorly understood. Particularly, the precise mechanisms underlying the association between increased risk for AD and R47H *TREM2* variant is not known. The present study describes a novel role for *Trem2* in the polarization of microglial processes to envelope A $\beta$  deposits and form a potentially neuroprotective barrier around them. *Trem2* or *DAP12* haploinsufficiency in AD mice dramatically reduces plaque-associated microglia and disrupts the barrier formation. Strikingly, in humans with R47H mutations, we observed a nearly identical phenotype with a marked reduction in microglia coverage of filamentous and small compact plaques that was associated with more severe axonal dystrophy and hyper-phosphorylated tau in neurites.

Surprisingly, despite in vitro studies suggesting otherwise (Kleinberger et al., 2014), we found that A $\beta$  phagocytosis by microglia in *Trem2* haploinsufficiency appears to remain normal in vivo. This result suggests that rather than defective phagocytosis, disruption of the microglia barrier could be a driving mechanism underlying increased risk for AD with single allele *TREM2* mutations in humans. In contrast, when complete protein loss occurred in *Trem2*<sup>-/-</sup> mice, we did observe a significant reduction in phagocytosis (Figures 2G and 2H). Defective phagocytosis may be more relevant for explaining the much less common Nasu-Hakola disease in which homozygous *TREM2* mutations cause a multi-organ condition associated with aggressive neurodegeneration but with very different neuropathological features from AD (Paloneva et al., 2000).

Interestingly, while in *Trem2*- and *DAP12*-deficient mice as well as R47H human mutants, microglia processes are unable to form a robust barrier, they are still moderately polarized, sending fine processes toward plaques (Figures 2A and 2B). This suggests that separate molecular mechanisms (El Khoury et al., 2003; Reed-Geaghan et al., 2009; Song et al., 2011) mediate the chemotactic plaque attraction and projection of microglia processes versus the formation of a tight and robust

envelopment of amyloid fibrils and deposits, which seems to be highly dependent on Trem2 signaling. Given the recent findings that Trem2 recognizes various types of lipids that are present in amyloid plaques (Wang et al., 2015), we postulate that the extent and types of lipids decorating the plaque surface may regulate the microglia barrier through Trem2 signaling. Consistent with this hypothesis, microglia around diffuse plaques do not have a very activated and polarized morphology (Figure 6), and spectrochemical analysis shows that diffuse plaques do not have prominent lipid coating on their surface (Liao et al., 2013; Rak et al., 2007). In contrast, as amyloid deposits become filamentous and thioflavin S positive, which likely makes them more lipophilic (Hilbich et al., 1992), they robustly attract microglia processes, consistent with recent in vivo imaging studies (Jung et al., 2015). It is therefore conceivable that conditions affecting brain lipid metabolism, such as *ApoE* genetic polymorphisms (Kim et al., 2009) or other mechanisms that alter brain lipids (Dietschy and Turley, 2004), may affect amyloid pathology by differentially modulating the formation of a microglia barrier.

Loss of microglia barrier function leads to decreased A $\beta$  fibril compaction as evidenced by our direct visualization of amyloid plaque architecture with super-resolution STORM imaging (Figures 3 and 4) and the observed reduced thioflavin S fluorescence intensity (Figure 3). STORM imaging revealed that plaques in *Trem2*<sup>+/+</sup> mice have a more compact organization with more mesh-like structures and fibrils exhibiting greater widths and shorter lengths than those in *Trem2*<sup>+/-</sup> and *Trem2*<sup>-/-</sup> mice. It also showed that in Trem2 deficiency, fibrils have more nano-scale orthogonal branches originating from the primary bundle (Figures 3H and 3I). This is consistent with our previous observations that plaque regions not covered by microglia processes have a markedly higher density of A $\beta$  protofibrils than covered regions (Condello et al., 2015).

The absolute widths measured by STORM imaging likely do not reflect the precise physical dimensions of single A $\beta$  fibrils, given resolution limits (~30 nm) and the fact that antibody labeling itself changes the size of the imaged object. Interestingly, however, the range of different widths that we observed demonstrate three main size peaks (~40 nm, 80 nm, and 120 nm), suggesting that STORM might be capable of differentiating unitary A $\beta$  fibrils (with attached primary and secondary antibodies) coiling together into larger bundles, consistent with in vitro studies using atomic-force microscopy (Stine et al., 1996). Together, these structural differences resulting from the lack of a microglia

(B) Quantification of the number of microglia within a 25  $\mu$ m radius from the plaque perimeter for each plaque subtype in AD brains with and without *TREM2* R47H mutation. Total 1,966 plaques analyzed.

(C) Quantification of the proportion of plaque subtypes that demonstrated robust microglia interactions (diffuse plaques do not attract microglia processes and were excluded in this analysis) in AD brains with and without *TREM2* R47H mutation. Total 1,474 plaques analyzed.

(D and E) Confocal images of microglia coverage of individual amyloid filaments (D) and the surface of compact plaques (E). Right panels show zoomed images from dashed boxes on the left panels. Arrows indicate microglia processes closely wrapping around an amyloid fibril with a "capping" structure (arrow head). Asterisk shows a dysmorphic loop structure formed by microglia in AD brains with *TREM2* R47H mutation. In (E), white arrow heads outline the robust microglia coverage of the plaque surface. Arrow points to the gap between a dysmorphic microglia process and the plaque border in R47H mutant.

(F) Quantification of the amyloid filaments wrapped by microglia and the capping events in individual filamentous plaques. Total 226 plaques analyzed.

(G and H) Quantification of compact plaque surface coverage (G) and barrier robustness (H) (see Figure S7) by microglia in AD with and without R47H mutations. Total 1,157 plaques analyzed. For all quantifications, n = 9 control AD patients and n = 10 R47H AD patients. Student's t tests were used for all statistical comparisons, \*p < 0.05, \*\*p < 0.01, \*\*\*p < 0.001; a.u., arbitrary unit. Data presented as mean  $\pm$  SEM. All analyses were performed on plaques from middle frontal gyrus.

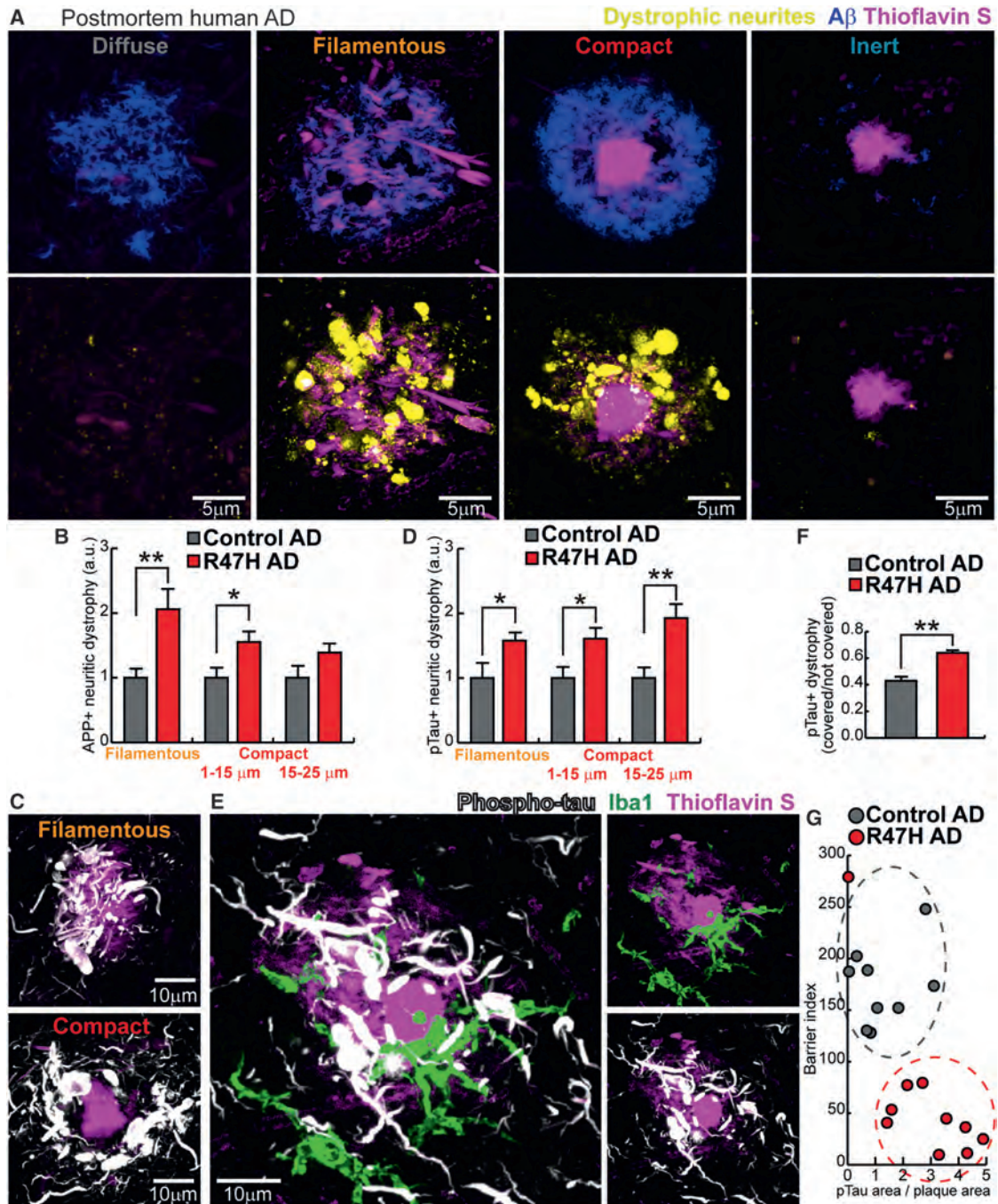


**Figure 7. R47H Mutation in Humans Is Associated with Severe Neuritic Tau Hyperphosphorylation and Axonal Dystrophy**

(A) Four subtypes of plaques in human brain. Diffuse plaques (anti A $\beta$ <sup>+</sup>, thioflavin S<sup>-</sup>); filamentous plaques (anti A $\beta$ <sup>+</sup>, filamentous thioflavin S<sup>+</sup>); compact plaques (anti A $\beta$ <sup>+</sup>, thioflavin S<sup>+</sup> compact core); inert plaques (anti A $\beta$ <sup>-</sup>, thioflavin S<sup>+</sup> compact core). Bottom: images of dystrophic neurites (labeled by anti-APP immunolabeling, yellow) around different subtypes of amyloid plaques in postmortem human brains. Notice the marked degree of dystrophy within the otherwise inconspicuous filamentous plaques.

(B) Quantification of APP<sup>+</sup> dystrophic neurites around individual plaques in AD patients with and without R47H mutations. Total 1,406 plaques analyzed.

(C) Confocal images of neurites with hyper-phosphorylated tau (white) around filamentous and compact plaques (magenta). Notice the marked degree of hyperphosphorylation in filamentous plaques.

(D) Quantification of area neurites with phosphorylated tau around individual plaques in AD patients with and without R47H mutations. Total 1,369 plaques analyzed.

(E) Microglia (green) in close contact with a plaque (magenta) but anti-colocalized with hyper-phosphorylated dystrophic neurites (white).

(legend continued on next page)

barrier are predicted to dramatically increase the surface area of an individual plaque (Supplemental Information). Differences in the degree of plaque compaction and fibril surface area may be key factors determining the degree of plaque neurotoxicity. Plaque regions not covered by microglia processes have lower degree of amyloid compaction but greater affinity for soluble A $\beta$ 42 (Figure S1) and form hotspots of potentially neurotoxic protofibrillar A $\beta$ 42 (Condello et al., 2015). Higher protofibrillar A $\beta$ 42, together with an overall increased contact area with surrounding neurites in *TREM2* deficiency, could synergistically contribute to the increased plaque neurotoxicity that we observed.

One intriguing aspect of our data is that the total number of thioflavin S compact plaques was modestly reduced in *Trem2*-deficient mice, while filamentous amyloid plaques without a compact core increased significantly. This is consistent with our model suggesting that the microglia barrier increases plaque compaction and failure of the barrier, such as in *Trem2* deficiency, shifts the balance of plaques toward a more diffuse phenotype without significantly altering total plaque number. This finding, which is dependent on the type of labels used for amyloid plaque quantification, may partly explain the initial contradicting results reported with regards to plaque density in *Trem2* deficiency (Jay et al., 2015; Wang et al., 2015).

Our surprising observation that small filamentous plaques cause a marked degree of axonal dystrophy around them in both mice and humans (Figures 5B and 7A) is consistent with the idea that less compact fibrils are more toxic than the compact ones in the plaque core. Thus, the observed shift toward a less compact plaque phenotype, coupled with the greater numbers of filamentous plaques, could significantly increase the overall degree of neural circuit damage despite a stable number of total plaques. Interestingly, our finding that diffuse plaques do not cause axonal dystrophy suggest that the transition from diffuse to  $\beta$  sheet-rich filamentous conformation (evidenced by thioflavin S labeling) is the critical neurotoxic event that leads to dystrophy consistent with recent *in vivo* imaging data (Bittner et al., 2012). While filamentous plaques represent a modest proportion of all plaques in AD-like mice (Figure 4J), we found them to be more prevalent in human sporadic AD brains (Figure 6C), which is likely due to the fact that plaque growth is protracted over decades compared to months in mice (Burgold et al., 2014; Condello et al., 2011). In addition, a plaque phenotype we called inert, because its core was intensely labeled by thioflavin S but was virtually devoid of dystrophic neurites, suggests that highly compact plaques may be minimally neurotoxic. These findings urge caution against using positron emission tomography (PET) amyloid tracers with predominant affinity to dense plaques and could partly explain the modest predictive value of current PET tracers such as PIB (Kepe et al., 2013) and the weak correlation between plaque load and cognitive dysfunction in postmortem studies (Morris et al., 2014).

Our data show that loss of the microglia barrier in mice with *Trem2* deficiency has the greatest impact on axonal dystrophy in filamentous and small compact plaques, but as plaques get bigger the difference in the degree of axonal dystrophy diminishes (Figure 5). A similar effect restricted to small plaques was previously observed when we enhanced the protective effects of the microglia barrier by genetic deletion of the chemokine receptor *CX3CR1* in mice (Condello et al., 2015). We hypothesize that the reason for this phenomenon is that in mice, the relatively rapid plaque growth may overwhelm the overall capacity of microglia neuroprotection and eventually most axons in their vicinity will be affected, thus causing the degree of measurable axonal dystrophy to plateau in large plaques. In human AD, we found that the effect of R47H mutations on the degree of axonal dystrophy was present over a broader range of plaque sizes than in mice (Figure 7). This is likely due to the fact that plaques are likely to grow much slower in humans. Thus, it is conceivable that the neuroprotective role of the microglia barrier in humans could be effective over more protracted time intervals than in transgenic mice.

While our study provides novel cellular phenomenology potentially relevant for understanding microglia function in both mice and humans, there remain uncertainties as to how the observed defective microglia barrier acts, at a more functional level, to cause pathological defects. Furthermore, while our findings demonstrate marked neuritic changes around plaques in *TREM2* deficiency, the relative functional contribution of dystrophic neurites compared to other pathologies such as synaptic loss, cell death and neurofibrillary tangles is unclear. Thus, the overall relevance of the microglia barrier function in the context of such complex neurodegenerative disorder remains to be determined.

Nevertheless, our results suggest that boosting the microglia barrier function or increasing plaque compactness by other means could constitute a novel strategy for AD therapeutics. Given the recent findings that *APOE* and *CD33* (whose genetic variants are common risk factors for AD) interact with the *TREM2* pathway (Atagi et al., 2015; Chan et al., 2015), our findings could have implications for the more prevalent forms of AD in which no mutations have been identified. Our current understanding of the cellular, molecular, and biophysical mechanisms by which microglia exert this potentially neuroprotective barrier function is limited. However, future studies elucidating such mechanisms may uncover targetable pathways that could specifically enhance the barrier function in microglia and reduce risk for AD.

## EXPERIMENTAL PROCEDURES

### Animals

All animal procedures were approved by the Institutional Animal Care and Use Committee at Yale, Weill Cornell College of Medicine and Washington University. *5XFAD* mice (Oakley et al., 2006) were cross-bred with *Trem2* knockout mice (Ulrich et al., 2014) as previously described (Wang et al., 2015). *APPS1-21* (Radde et al., 2006) mice were cross-bred with *DAP12* knockout

(F) Quantification of the degree of neuritic tau hyper-phosphorylation as a ratio between areas covered and not covered by microglia processes. Total 468 plaques analyzed.

(G) Quantification of the degree of microglia barrier (radial coverage multiply robustness; see Experimental Procedures) as a function of the degree of phosphorylated tau (normalized for plaque size). Total 1,008 plaques analyzed. For all quantifications,  $n = 9$  control humans and  $n = 10$  R47H humans. Student's *t* tests were used for all statistical comparisons, \* $p < 0.05$ , \*\* $p < 0.01$ ; a.u., arbitrary unit. Data presented as mean  $\pm$  SEM. All analyses were performed on plaques from middle frontal gyrus.

mice to obtain *DAP12*-deficient mice (Bakker et al., 2000). Unless specifically indicated, 4-month-old mice were used. *CRND8* mice (courtesy of Dr. David Westaway, University of Alberta) were also used.

### Human Postmortem Brain Tissue

Formalin-fixed human postmortem brain tissue blocks were acquired from various brain banks. Detailed demographic and clinical information can be found in Table S2, including ten AD cases with the R47H mutation (Birdsill et al., 2011; Korvatska et al., 2015) and nine cases with comparable AD pathology but not carrying the mutation. Cases were matched for age, gender, and *ApoE* genotype.

### Immunohistochemistry

Brain slices were obtained from the mouse posterior somatosensory cortex and human middle frontal gyrus. Mouse coronal sections were cut (40  $\mu$ m thick) with a cryostat and human tissue was sectioned with a vibratome. Primary antibodies incubation were 2 days at 4 $^{\circ}$ C (PBS with 0.2% Triton X-100 and 5% goat serum) and secondary antibodies for 6 hr, before mounting on slides with PermaFluor (Thermo Scientific, TA-030-FM). Heat-induced sodium citrate antigen retrieval was performed for TREM2, *DAP12*, and all human tissue staining with the following protocol: tissue was boiled in 50 mM sodium citrate with 0.05% tween-20 at 95 $^{\circ}$  for 45 min and then washed with PBS. The complete list of antibodies and reagents used in this study is included in the Supplemental Experimental Procedures.

### Confocal Microscopy

A Leica SP5 confocal microscope was used to generate all images. Laser and detector (the GaAsP hybrid detection system, photon counting mode) settings were maintained constant. For all analyses, tiled imaging using a motorized stage was used to image across one cerebral hemisphere in mice. A 3 mm $^2$  human brain region per brain slice was imaged using a 63 $\times$  oil immersion objective (N.A. 1.4) at 1,024  $\times$  10,24 pixel resolution, z-step size of 3  $\mu$ m, and identity was blinded for analyses (Yuan and Grutzendler, 2016). Images were processed with FIJI (ImageJ) software. A customized macro was used to segment individual amyloid plaque. The number of plaques analyzed ranged from 150 to 300 in each brain (see Supplemental Experimental Procedures).

### STORM Imaging

Samples were mounted in a buffer consisting of 90% glycerol and 10% 10 $\times$  PBS with an overall concentration of 10 mM cysteamine and 50 mM sodium sulfite (J.T. Baker 3922-01). Images were recorded on a modified Nikon Ti-E inverted microscope using a 60 $\times$  1.49 N.A. oil-immersion objective using an EMCCD camera (Andor IXon Ultra DU-897U-CS0-#BV). The objective was mounted on a custom mount to suppress thermal and mechanical drift and focusing was provided by a piezoelectric objective positioner (Physik Instrumente P-725.4CA). For illumination, a 642 nm solid-state laser (Omicron Lux, 20 kW/cm $^2$  at the sample) was used with a dichroic (Semrock, Di02-R635-25x36) and a band-pass filter (Semrock, BLP01-647R-25) for separation of excitation and emission. Field of view was selected using metal halide lamp (Prior Lumen 200) illumination before switching to laser illumination and was then imaged for approximately 20,000 frames using an exposure time of 25 ms and an EM-multiplication setting corresponding to a gain of 35.5. Events were detected and localized (Baddeley et al., 2009) and reconstructions were rendered using jittered triangulation (Baddeley et al., 2010) (see Supplemental Experimental Procedures).

### Statistics

Data represented as mean  $\pm$  SEM. Two-tail unpaired Student's t tests were employed for comparisons between two groups. A probability of  $p < 0.05$  was considered indicative of significant differences between groups.

### SUPPLEMENTAL INFORMATION

Supplemental Information includes Supplemental Experimental Procedures, seven figures, and two tables and can be found with this article online at <http://dx.doi.org/10.1016/j.neuron.2016.05.003>.

### AUTHOR CONTRIBUTIONS

P.Y., C.C., and J.G. designed the study. P.Y. and C.C. performed experiments. D.B. and P.Y. performed STORM microscopy and analyzed the images. P.Y., C.C., and J.G. analyzed data. P.Y., C.C., and J.G. prepared the manuscript. C.D.K., T.D.B., S.M.P., W.L., Y.W., and M.C. provided critical reagents. J.G. supervised the study.

### ACKNOWLEDGMENTS

We thank Lingling Ji (Yale University) for consultation on statistics and Katie N. Murray (Yale University) for critical reading of the manuscript. We thank the University of Washington Alzheimer's Disease Research Center Neuropathology Core for provision of human brain tissues (supported by NIA P50 AG05136). We thank Sun Health Research Institute Brain and Body Donation Program of Sun City, Arizona for the provision of human brain tissues, supported by the NINDS (U24 NS072026), the NIA (P30 AG19610), the Arizona Department of Health Services (contract 211002), and the Arizona Biomedical Research Commission (contracts 4001, 0011, 05-901 and 1001). We thank Dennis W. Dickson and Michael Deture at Mayo Clinic (Jacksonville, Florida) for providing additional human brain tissues. We thank the Helen and Robert Appel Alzheimer's Disease Research Institute for providing funding; Xiaoyu Hu for providing *DAP12* knockout mice; and Mathias Jucker for providing *APPPS1-21* mice. This project was supported by R01HL106815 and R21AG048181 (J.G.). This project was supported by National Institute of Health grants R01HL106815 and R21AG048181 (J.G.), and Alzheimer's Association Research Grant (J.G.).

Received: October 18, 2015

Revised: February 21, 2016

Accepted: April 17, 2016

Published: May 18, 2016

### REFERENCES

- Atagi, Y., Liu, C.-C., Painter, M.M., Chen, X.-F., Verbeeck, C., Zheng, H., Li, X., Rademakers, R., Kang, S.S., Xu, H., et al. (2015). Apolipoprotein E Is a Ligand for Triggering Receptor Expressed on Myeloid Cells 2 (TREM2). *J. Biol. Chem.* 290, 26043–26050.
- Baddeley, D., Jayasinghe, I.D., Cremer, C., Cannell, M.B., and Soeller, C. (2009). Light-induced dark states of organic fluochromes enable 30 nm resolution imaging in standard media. *Biophys. J.* 96, L22–L24, <http://dx.doi.org/10.1016/j.bpj.2008.11.002>.
- Baddeley, D., Cannell, M.B., and Soeller, C. (2010). Visualization of localization microscopy data. *Microsc. Microanal.* 16, 64–72, <http://dx.doi.org/10.1017/S143192760999122X>.
- Bakker, A.B., Hoek, R.M., Cerwenka, A., Blom, B., Lucian, L., McNeil, T., Murray, R., Phillips, L.H., Sedgwick, J.D., and Lanier, L.L. (2000). *DAP12*-deficient mice fail to develop autoimmunity due to impaired antigen priming. *Immunity* 13, 345–353.
- Birdsill, A.C., Walker, D.G., Lue, L., Sue, L.I., and Beach, T.G. (2011). Postmortem interval effect on RNA and gene expression in human brain tissue. *Cell Tissue Bank.* 12, 311–318.
- Bittner, T., Burgold, S., Dorostkar, M.M., Fuhrmann, M., Wegenast-Braun, B.M., Schmidt, B., Kretschmar, H., and Herms, J. (2012). Amyloid plaque formation precedes dendritic spine loss. *Acta Neuropathol.* 124, 797–807.
- Block, M.L., Zecca, L., and Hong, J.-S. (2007). Microglia-mediated neurotoxicity: uncovering the molecular mechanisms. *Nat. Rev. Neurosci.* 8, 57–69.
- Burgold, S., Filser, S., Dorostkar, M.M., Schmidt, B., and Herms, J. (2014). In vivo imaging reveals sigmoidal growth kinetic of  $\beta$ -amyloid plaques. *Acta Neuropathol. Commun.* 2, 30.
- Chan, G., White, C.C., Winn, P.A., Cimpean, M., Replogle, J.M., Glick, L.R., Cueddon, N.E., Ryan, K.J., Johnson, K.A., Schneider, J.A., et al. (2015). CD33 modulates TREM2: convergence of Alzheimer loci. *Nat. Neurosci.* 18, 1556–1558.

- Colonna, M. (2003). TREMs in the immune system and beyond. *Nat. Rev. Immunol.* 3, 445–453.
- Condello, C., Schain, A., and Grutzendler, J. (2011). Multicolor time-stamp reveals the dynamics and toxicity of amyloid deposition. *Sci. Rep.* 1, 19.
- Condello, C., Yuan, P., Schain, A., and Grutzendler, J. (2015). Microglia constitute a barrier that prevents neurotoxic protofibrillar A $\beta$ 42 hotspots around plaques. *Nat. Commun.* 6, 6176.
- Dagher, N.N., Najafi, A.R., Kayala, K.M.N., Elmore, M.R.P., White, T.E., Medeiros, R., West, B.L., and Green, K.N. (2015). Colony-stimulating factor 1 receptor inhibition prevents microglial plaque association and improves cognition in 3xTg-AD mice. *J. Neuroinflammation* 12, 139.
- Davalos, D., Grutzendler, J., Yang, G., Kim, J.V., Zuo, Y., Jung, S., Littman, D.R., Dustin, M.L., and Gan, W.-B.B. (2005). ATP mediates rapid microglial response to local brain injury in vivo. *Nat. Neurosci.* 8, 752–758.
- Dietschy, J.M., and Turley, S.D. (2004). Thematic review series: brain lipids. Cholesterol metabolism in the central nervous system during early development and in the mature animal. *J. Lipid Res.* 45, 1375–1397.
- El Khoury, J.B., Moore, K.J., Means, T.K., Leung, J., Terada, K., Toft, M., Freeman, M.W., and Luster, A.D. (2003). CD36 mediates the innate host response to beta-amyloid. *J. Exp. Med.* 197, 1657–1666.
- Frank, S., Burbach, G.J., Bonin, M., Walter, M., Streit, W., Bechmann, I., and Deller, T. (2008). TREM2 is upregulated in amyloid plaque-associated microglia in aged APP23 transgenic mice. *Glia* 56, 1438–1447.
- Gowrishankar, S., Yuan, P., Wu, Y., Schrag, M., Paradise, S., Grutzendler, J., De Camilli, P., and Ferguson, S.M. (2015). Massive accumulation of luminal protease-deficient axonal lysosomes at Alzheimer's disease amyloid plaques. *Proc. Natl. Acad. Sci. USA* 112, E3699–E3708.
- Guerreiro, R., Wojtas, A., Bras, J., Carrasquillo, M., Rogaeve, E., Majounie, E., Cruchaga, C., Sassi, C., Kauwe, J.S.K., Younkin, S., et al.; Alzheimer Genetic Analysis Group (2013). TREM2 variants in Alzheimer's disease. *N. Engl. J. Med.* 368, 117–127.
- Hanisch, U.-K.K., and Kettenmann, H. (2007). Microglia: active sensor and versatile effector cells in the normal and pathologic brain. *Nat. Neurosci.* 10, 1387–1394.
- Hilbich, C., Kisters-Woike, B., Reed, J., Masters, C.L., and Beyreuther, K. (1992). Substitutions of hydrophobic amino acids reduce the amyloidogenicity of Alzheimer's disease beta A4 peptides. *J. Mol. Biol.* 228, 460–473.
- Jay, T.R., Miller, C.M., Cheng, P.J., Graham, L.C., Bemiller, S., Broihier, M.L., Xu, G., Margevicius, D., Karlo, J.C., Sousa, G.L., et al. (2015). TREM2 deficiency eliminates TREM2+ inflammatory macrophages and ameliorates pathology in Alzheimer's disease mouse models. *J. Exp. Med.* 212, 287–295.
- Jin, S.C., Benitez, B.A., Karch, C.M., Cooper, B., Skorupa, T., Carrell, D., Norton, J.B., Hsu, S., Harari, O., Cai, Y., et al. (2014). Coding variants in TREM2 increase risk for Alzheimer's disease. *Hum. Mol. Genet.* 23, 5838–5846.
- Jonsson, T., Stefansson, H., Steinberg, S., Jonsson, P.V., Snaedal, J., Bjornsson, S., Huttenlocher, J., Levey, A.I., Lah, J.J., et al. (2013). Variant of TREM2 associated with the risk of Alzheimer's disease. *N. Engl. J. Med.* 368, 107–116.
- Jung, C.K.E., Keppler, K., Steinbach, S., Blazquez-Llorca, L., and Herms, J. (2015). Fibrillar amyloid plaque formation precedes microglial activation. *PLoS ONE* 10, e0119768.
- Kepe, V., Moghbel, M.C., Långström, B., Zaidi, H., Vinters, H.V., Huang, S.-C., Satyamurthy, N., Doudet, D., Mishani, E., Cohen, R.M., et al. (2013). Amyloid- $\beta$  positron emission tomography imaging probes: a critical review. *J. Alzheimers Dis.* 36, 613–631, <http://dx.doi.org/10.3233/JAD-130485>.
- Kim, J., Basak, J.M., and Holtzman, D.M. (2009). The role of apolipoprotein E in Alzheimer's disease. *Neuron* 63, 287–303.
- Kleinberger, G., Yamanishi, Y., Suárez-Calvet, M., Czirr, E., Lohmann, E., Cuyvers, E., Struyfs, H., Pettkus, N., Wenninger-Weinzierl, A., Mazaheri, F., et al. (2014). TREM2 mutations implicated in neurodegeneration impair cell surface transport and phagocytosis. *Sci. Transl. Med.* 6, 243ra86.
- Korvatska, O., Leverenz, J.B., Jayadev, S., McMillan, P., Kurtz, I., Guo, X., Rumbaugh, M., Matsushita, M., Girirajan, S., Dorschner, M.O., et al. (2015). R47H Variant of TREM2 Associated With Alzheimer Disease in a Large Late-Onset Family: Clinical, Genetic, and Neuropathological Study. *JAMA Neurol.* 72, 920–927.
- Lee, C.Y.D., and Landreth, G.E. (2010). The role of microglia in amyloid clearance from the AD brain. *J. Neural Transm (Vienna)* 117, 949–960.
- Liao, C.R., Rak, M., Lund, J., Unger, M., Platt, E., Albeni, B.C., Hirschmugl, C.J., and Gough, K.M. (2013). Synchrotron FTIR reveals lipid around and within amyloid plaques in transgenic mice and Alzheimer's disease brain. *Analyst (Lond.)* 138, 3991–3997.
- Liu, Z., Condello, C., Schain, A., Harb, R., and Grutzendler, J. (2010). CX3CR1 in microglia regulates brain amyloid deposition through selective protofibrillar amyloid- $\beta$  phagocytosis. *J. Neurosci.* 30, 17091–17101.
- Lue, L.-F., Schmitz, C.T., Serrano, G., Sue, L.I., Beach, T.G., and Walker, D.G. (2015). TREM2 Protein Expression Changes Correlate with Alzheimer's Disease Neurodegenerative Pathologies in Post-Mortem Temporal Cortices. *Brain Pathol.* 25, 469–480.
- Matarin, M., Salih, D.A., Yasvoina, M., Cummings, D.M., Guelfi, S., Liu, W., Nahaboo Solim, M.A., Moens, T.G., Paublete, R.M., Ali, S.S., et al. (2015). A genome-wide gene-expression analysis and database in transgenic mice during development of amyloid or tau pathology. *Cell Rep.* 10, 633–644.
- Morris, G.P., Clark, I.A., and Vissel, B. (2014). Inconsistencies and controversies surrounding the amyloid hypothesis of Alzheimer's disease. *Acta Neuropathol. Commun.* 2, 135.
- Oakley, H., Cole, S.L., Logan, S., Maus, E., Shao, P., Craft, J., Guillozet-Bongaarts, A., Ohno, M., Disterhoft, J., Van Eldik, L., et al. (2006). Intraneuronal beta-amyloid aggregates, neurodegeneration, and neuron loss in transgenic mice with five familial Alzheimer's disease mutations: potential factors in amyloid plaque formation. *J. Neurosci.* 26, 10129–10140.
- Olmos-Alonso, A., Schettters, S.T.T., Sri, S., Askew, K., Mancuso, R., Vargas-Caballero, M., Holscher, C., Perry, V.H., and Gomez-Nicola, D. (2016). Pharmacological targeting of CSF1R inhibits microglial proliferation and prevents the progression of Alzheimer's-like pathology. *Brain* 139, 891–907.
- Paloneva, J., Kestilä, M., Wu, J., Salminen, A., Böhring, T., Ruotsalainen, V., Hakola, P., Bakker, A.B., Phillips, J.H., Pekkarinen, P., et al. (2000). Loss-of-function mutations in TYROBP (DAP12) result in a presenile dementia with bone cysts. *Nat. Genet.* 25, 357–361.
- Peng, Q., Malhotra, S., Torchia, J.A., Kerr, W.G., Coggeshall, K.M., and Humphrey, M.B. (2010). TREM2- and DAP12-dependent activation of PI3K requires DAP10 and is inhibited by SHIP1. *Sci. Signal.* 3, ra38.
- Radde, R., Bolmont, T., Kaeser, S.A., Coomaraswamy, J., Lindau, D., Stoltze, L., Calhoun, M.E., Jäggi, F., Wolburg, H., Gengler, S., et al. (2006). Abeta42-driven cerebral amyloidosis in transgenic mice reveals early and robust pathology. *EMBO Rep.* 7, 940–946.
- Rak, M., Del Bigio, M.R., Mai, S., Westaway, D., and Gough, K. (2007). Dense-core and diffuse Abeta plaques in TgCRND8 mice studied with synchrotron FTIR microspectroscopy. *Biopolymers* 87, 207–217.
- Reed-Geaghan, E.G., Savage, J.C., Hise, A.G., and Landreth, G.E. (2009). CD14 and toll-like receptors 2 and 4 are required for fibrillar Abeta-stimulated microglial activation. *J. Neurosci.* 29, 11982–11992.
- Ruiz, A., Dols-Icardo, O., Bullido, M.J., Pastor, P., Rodríguez-Rodríguez, E., López de Munain, A., de Pancorbo, M.M., Pérez-Tur, J., Alvarez, V., Antonell, A., et al.; dementia genetic Spanish consortium (DEGESCO) (2014). Assessing the role of the TREM2 p.R47H variant as a risk factor for Alzheimer's disease and frontotemporal dementia. *Neurobiol. Aging* 35, 444.e1–444.e4.
- Schmid, C.D., Sautkulis, L.N., Danielson, P.E., Cooper, J., Hasel, K.W., Hilbush, B.S., Sutcliffe, J.G., and Carson, M.J. (2002). Heterogeneous expression of the triggering receptor expressed on myeloid cells-2 on adult murine microglia. *J. Neurochem.* 83, 1309–1320.

- Song, M., Jin, J., Lim, J.-E., Kou, J., Pattanayak, A., Rehman, J.A., Kim, H.-D., Tahara, K., Lalonde, R., and Fukuchi, K. (2011). TLR4 mutation reduces microglial activation, increases A $\beta$  deposits and exacerbates cognitive deficits in a mouse model of Alzheimer's disease. *J. Neuroinflammation* 8, 92.
- Stalder, M., Deller, T., Staufenbiel, M., and Jucker, M. (2001). 3D-Reconstruction of microglia and amyloid in APP23 transgenic mice: no evidence of intracellular amyloid. *Neurobiol. Aging* 22, 427–434.
- Stine, W.B., Jr., Snyder, S.W., Ladrer, U.S., Wade, W.S., Miller, M.F., Perun, T.J., Holzman, T.F., and Krafft, G.A. (1996). The nanometer-scale structure of amyloid-beta visualized by atomic force microscopy. *J. Protein Chem.* 15, 193–203.
- Ulrich, J.D., Finn, M.B., Wang, Y., Shen, A., Mahan, T.E., Jiang, H., Stewart, F.R., Piccio, L., Colonna, M., and Holtzman, D.M. (2014). Altered microglial response to A $\beta$  plaques in APPPS1-21 mice heterozygous for TREM2. *Mol. Neurodegener.* 9, 20.
- Wang, Y., Cella, M., Mallinson, K., Ulrich, J.D., Young, K.L., Robinette, M.L., Gilfillan, S., Krishnan, G.M., Sudhakar, S., Zinselmeyer, B.H., et al. (2015). TREM2 lipid sensing sustains the microglial response in an Alzheimer's disease model. *Cell* 160, 1061–1071.
- Yuan, P., and Grutzendler, J. (2016). Attenuation of  $\beta$ -Amyloid Deposition and Neurotoxicity by Chemogenetic Modulation of Neural Activity. *J. Neurosci.* 36, 632–641.

# Discovery of Novel Blood-Brain Barrier Targets to Enhance Brain Uptake of Therapeutic Antibodies

Y. Joy Yu Zuchero,<sup>1,8,\*</sup> Xiaocheng Chen,<sup>2,8</sup> Nga Bien-Ly,<sup>1</sup> Daniela Bumbaca,<sup>3</sup> Raymond K. Tong,<sup>4</sup> Xiaoying Gao,<sup>5</sup> Shuo Zhang,<sup>1</sup> Kwame Hoyte,<sup>5</sup> Wilman Luk,<sup>5</sup> Melanie A. Huntley,<sup>6</sup> Lilian Phu,<sup>4</sup> Christine Tan,<sup>2</sup> Dara Kallop,<sup>7</sup> Robby M. Weimer,<sup>7</sup> Yanmei Lu,<sup>5</sup> Donald S. Kirkpatrick,<sup>4</sup> James A. Ernst,<sup>4</sup> Ben Chih,<sup>5,\*</sup> Mark S. Dennis,<sup>2</sup> and Ryan J. Watts<sup>1</sup>

<sup>1</sup>Department of Neuroscience

<sup>2</sup>Antibody Engineering

<sup>3</sup>Developmental Sciences

<sup>4</sup>Protein Chemistry

<sup>5</sup>Biochemical and Cellular Pharmacology

<sup>6</sup>Bioinformatics and Computational Biology

<sup>7</sup>Biomedical Imaging

Genentech, Inc., 1 DNA Way, South San Francisco, CA 94080, USA

<sup>8</sup>Co-first author

\*Correspondence: joy.yu929@gmail.com (Y.J.Y.Z.), chih.ben@gene.com (B.C.)

<http://dx.doi.org/10.1016/j.neuron.2015.11.024>

## SUMMARY

The blood-brain barrier (BBB) poses a major challenge for developing effective antibody therapies for neurological diseases. Using transcriptomic and proteomic profiling, we searched for proteins in mouse brain endothelial cells (BECs) that could potentially be exploited to transport antibodies across the BBB. Due to their limited protein abundance, neither antibodies against literature-identified targets nor BBB-enriched proteins identified by microarray facilitated significant antibody brain uptake. Using proteomic analysis of isolated mouse BECs, we identified multiple highly expressed proteins, including basigin, Glut1, and CD98hc. Antibodies to each of these targets were significantly enriched in the brain after administration *in vivo*. In particular, antibodies against CD98hc showed robust accumulation in brain after systemic dosing, and a significant pharmacodynamic response as measured by brain A $\beta$  reduction. The discovery of CD98hc as a robust receptor-mediated transcytosis pathway for antibody delivery to the brain expands the current approaches available for enhancing brain uptake of therapeutic antibodies.

## INTRODUCTION

Delivery of antibody therapeutics into the brain to treat central nervous system (CNS) diseases has been a major drug development challenge. With the support of astrocytes and pericytes, a monolayer of endothelial cells creates the blood-brain barrier (BBB), which serves to restrict movement of substances from the circulating blood to the CNS. Generally, only ~0.1% of circulating antibodies cross the intact BBB, severely limiting the

therapeutic utility of antibody therapeutics for CNS disorders (Poduslo et al., 1994; Yu and Watts, 2013).

Many endogenous molecules in circulation are able to cross the BBB via specific receptors and transporters expressed on the luminal side of brain endothelial cells. These membrane protein pathways provide a promising route for delivering antibodies across the BBB by utilizing receptor-mediated transcytosis (RMT) (Fishman et al., 1987; Roberts et al., 1993; Jones and Shusta 2007; Watts and Dennis 2013). For example, systemic administration of antibodies against the transferrin receptor (TfR), which is highly expressed on BECs, dramatically enhances CNS delivery of these antibodies across the BBB in both rodents and nonhuman primates (Jefferies et al., 1984; Kissel et al., 1998; Yu et al., 2011; Couch et al., 2013; Yu et al., 2014). However, targeting TfR with antibodies posed safety liabilities (Couch et al., 2013). Although mitigation strategies could be developed, the identification of additional RMT targets for enhanced brain delivery is warranted. A number of other BBB receptors have been explored for RMT, but their ability to transport therapeutically relevant doses of antibodies into the brain remains to be demonstrated.

In the current study, we generated antibodies against several potential protein targets and tested for their uptake in brain *in vivo*. We first addressed whether antibodies against previously studied RMT targets could accumulate in brain. We also tested RMT targets identified by differential gene expression analysis via microarray. Finally, an unbiased proteomics approach was used to identify highly expressed transmembrane proteins from isolated mouse primary BECs. Using this approach, three transmembrane BEC proteins were identified as novel candidates for transporting therapeutic antibodies across the BBB.

## RESULTS

### Receptor-Mediated Transcytosis Evaluation of Lrp1 and InsR

Several murine RMT targets were evaluated for their ability to transport antibodies across the BBB using the screening

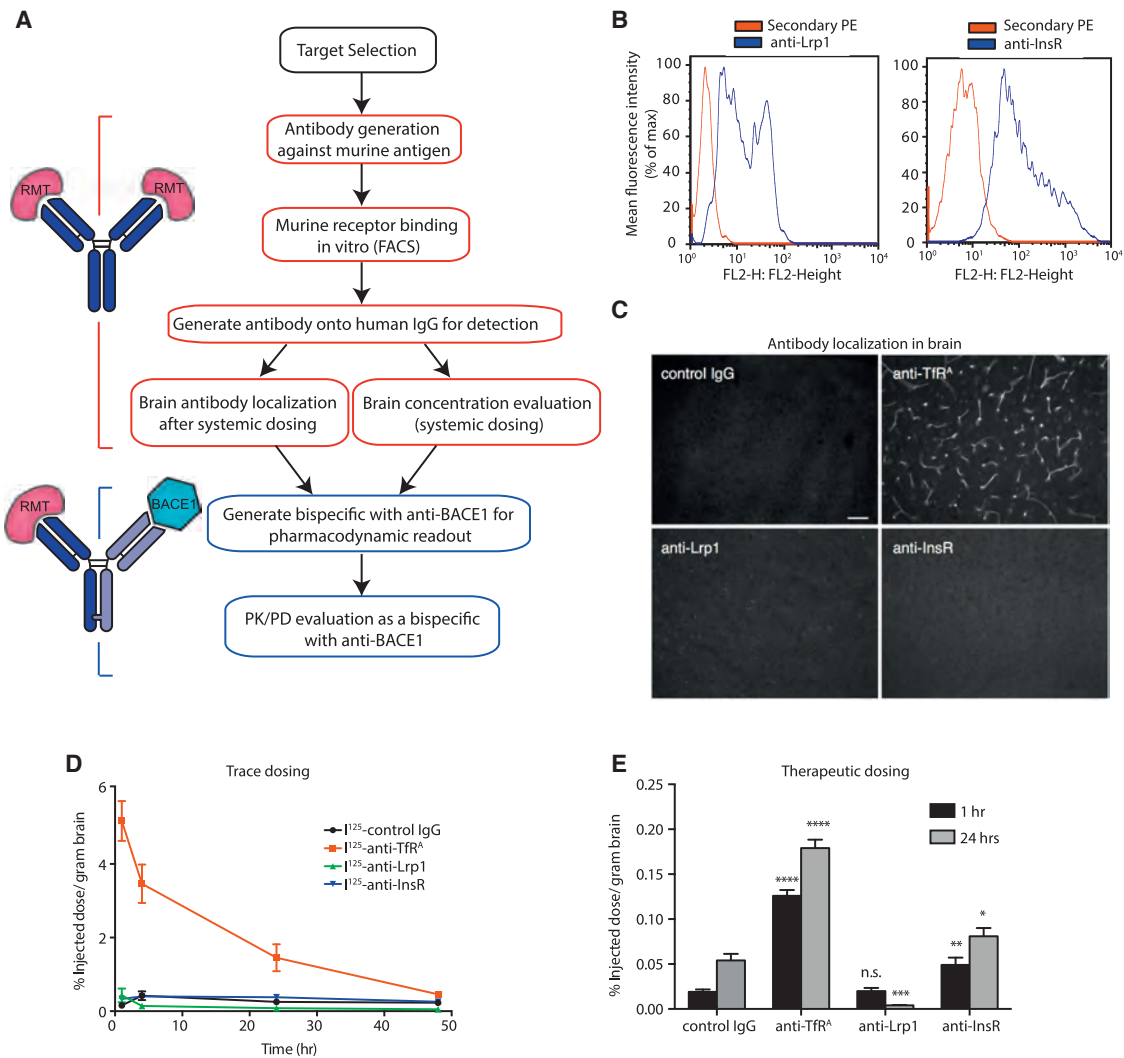


### Figure 1. Lack of Brain Uptake of Antibodies Targeting Lrp1 and InsR

(A) Screening cascade used to determine success of potential receptor-mediated transport (RMT) targets.

(B) Phage-derived anti-Lrp1 and anti-InsR antibodies bind to their corresponding murine receptors transfected in HEK293 cells by flow cytometry. See also Figure S1 for FACS profiles showing a lack of nonspecific binding in untransfected HEK293 cells.

(C) Immunohistochemical staining with fluorescent anti-human secondary IgG of antibody localization in mouse cortical tissue 1 hr after a 5 mg/kg intravenous injection of the indicated antibody. Scale bar, 50  $\mu$ m.

(D) Brain uptake of trace doses of  $^{125}$ I-labeled antibodies at various time points postdose after intravenous administration in wild-type mice, quantified as mean  $\pm$  SEM percent injected dose per gram of brain tissue (n = 3 per group and time point).

(E) Antibody concentrations in brain 1 and 24 hr after a 20 mg/kg dose of the indicated antibody. Bar graphs represent mean  $\pm$  SEM (n = 6 per group and time point; \*p  $\leq$  0.05, \*\*p  $\leq$  0.01, \*\*\*p  $\leq$  0.001, \*\*\*\*p  $\leq$  0.0001 compared to control IgG at the same time point).

cascade outlined in Figure 1A. Antibodies that bound specifically to murine antigen as assessed by flow cytometry (FACS) were tested qualitatively for their ability to target mouse brain in vivo by immunostaining mouse cortical tissue 1 hr after a 5 mg/kg dose. Because binding affinity of the antibody to the RMT target can influence brain uptake depending on the dosing paradigm, both a radiolabeled trace dose ( $\sim$ 0.1 mg/kg) and a higher therapeutically relevant dose (20 mg/kg) were then used to assess brain uptake of potential RMT antibodies (Yu et al., 2011). As a final assessment, selected antibodies were engineered as bispe-

cific antibodies containing a monovalent anti-BACE1 arm. This allows a direct demonstration of antibody delivery into the brain by measuring  $\beta$ -amyloid (A $\beta$ ) concentrations as a function of BACE1 inhibition (Yu et al., 2011).

We first evaluated two commonly studied RMT targets, low-density lipoprotein receptor-related protein 1 (Lrp1) and insulin receptor (InsR), for their ability to deliver antibodies into mouse brains. Antibodies against murine Lrp1 and InsR were generated from naive antibody phage libraries. FACS analysis using HEK293 cells expressing murine Lrp1 or InsR confirmed positive

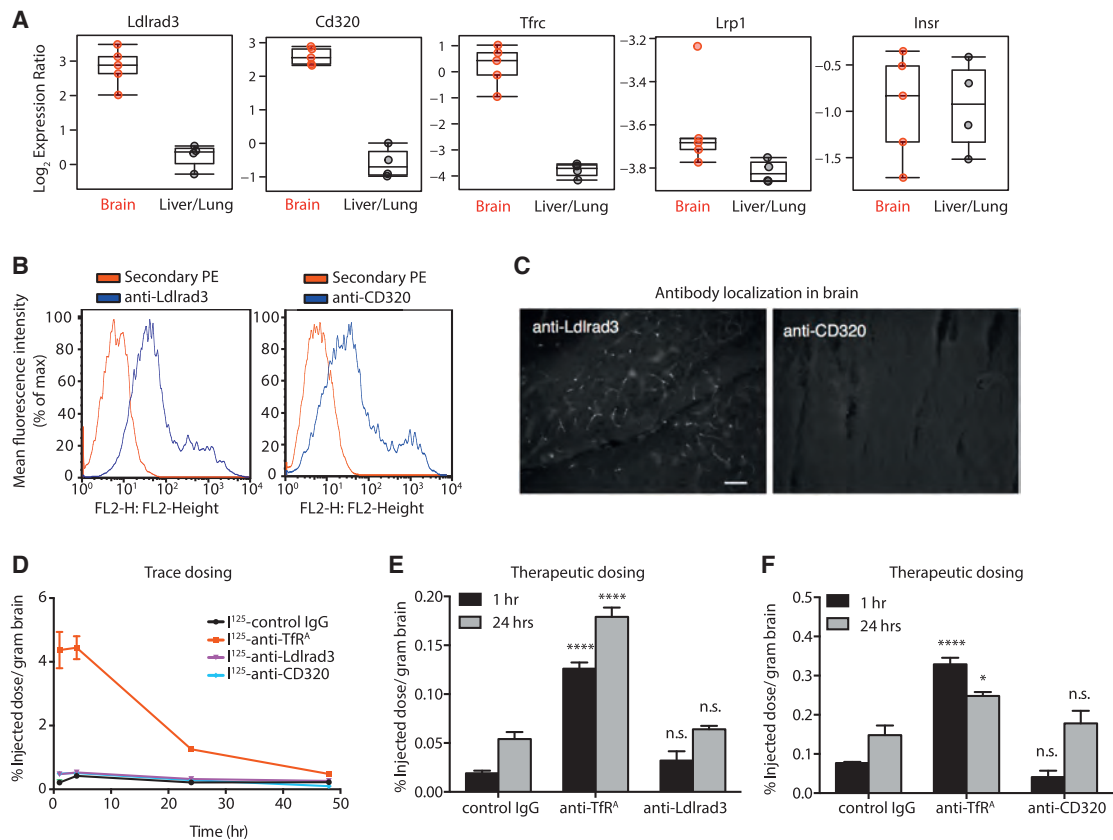


**Figure 2. mRNA Enrichment at the BBB Is Not Sufficient to Identify an RMT Target**

(A) Microarray expression profiling of FACS-purified brain and liver/lung endothelial cells from wild-type mice identifies genes enriched at the BBB (Tam et al., 2012).

(B) FACS analysis of anti-Ldlrad3 and anti-CD320 antibodies shows binding to their corresponding murine antigens expressed in HEK293 cells.

(C) Immunohistochemical staining of antibody localization in mouse cortical tissue 1 hr after a 5 mg/kg intravenous injection of the indicated antibody. Scale bar, 50  $\mu$ m.

(D) Brain uptake of trace doses of <sup>125</sup>I-labeled antibodies at various time points postdose after intravenous administration in wild-type mice, quantified as mean  $\pm$  SEM percent injected dose per gram of brain tissue (n = 3 per group and time point).

(E and F) Antibody concentrations in brain 1 and 24 hr after a 20 mg/kg dose of the indicated antibody. Data in (E) were obtained concurrently with data in Figure 1E as part of a single experiment; thus the same control IgG and anti-TfR<sup>A</sup> are shown. Bar graphs represent mean  $\pm$  SEM (n = 6 per group and time point; \*p  $\leq$  0.05, \*\*\*\*p  $\leq$  0.0001 compared to control IgG at the same time point).

binding (Figure 1B). However, these antibodies did not appear to localize to brain vasculature in vivo as assessed by immunostaining of mouse cortical tissue 1 hr after a 5 mg/kg dose (Figure 1C). As a positive control, an anti-TfR<sup>A</sup> exhibited pronounced brain vascular distribution following systemic administration (Yu et al., 2011, 2014; Couch et al., 2013).

To determine whether anti-Lrp1 and anti-InsR can accumulate in brain, radiolabeled <sup>125</sup>I-control IgG, <sup>125</sup>I-anti-TfR<sup>A</sup>, <sup>125</sup>I-anti-Lrp1, or <sup>125</sup>I-anti-InsR were IV injected into wild-type mice, and radioactivity was measured. A significant increase in brain uptake, as measured by percent of injected dose per gram of brain tissue, was observed only for <sup>125</sup>I-anti-TfR<sup>A</sup>, whereas brain uptake of both <sup>125</sup>I-anti-Lrp1 and <sup>125</sup>I-anti-InsR were similar to <sup>125</sup>I-control IgG (Figure 1D). Using a higher therapeutically relevant dose (20 mg/kg) of anti-Lrp1 did not improve brain accumulation of antibody above that observed for a control IgG, while anti-InsR exhibited a modest increase in brain levels at both

time points, but well below anti-TfR<sup>A</sup> (Figure 1E). Together, these results show that of these widely studied receptors, only antibodies against TfR exhibit robust brain uptake.

### mRNA Enrichment at the BBB Is Not Sufficient to Identify an RMT Target

To identify novel RMT targets, we first took a gene expression analysis approach and reasoned that RMT candidates specifically expressed by BECs could target therapeutics selectively to brain by reducing target-mediated clearance in peripheral organs and improving pharmacokinetics (PK) in vivo. A previous microarray expression profile of FACS-purified mouse brain endothelial cells (Tam et al., 2012) identified two single-pass transmembrane proteins, *Ldlrad3* and *CD320*, each selectively expressed at a higher level by BECs relative to liver and lung endothelial cells (Figure 2A). Interestingly, *Tfrc* had higher mRNA expression at the BEC, while *Lrp1* and *Insr* lacked any

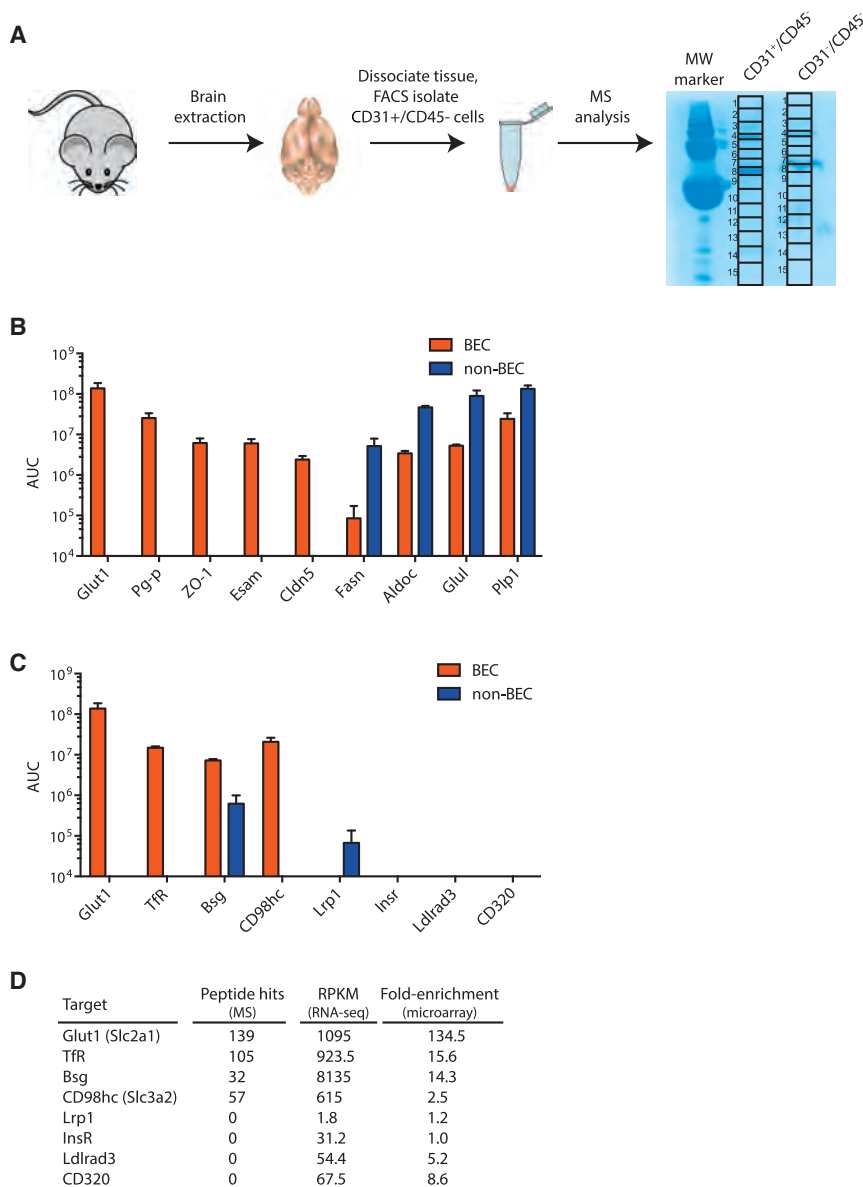


**Figure 3. Proteomic Identification of Highly Expressed Transmembrane Proteins at the BBB**

(A) Primary wild-type mouse brain endothelial cells (CD31+/CD45-) were isolated by FACS as previously described (Tam et al., 2012) and analyzed by mass spectrometry (see Experimental Procedures for details).

(B) AUC represents the average of two technical replicates for the integrated intensity of the top three most abundant peptide counts as determined by mass spectrometry for endothelial cell proteins (Glut1, Pg-p, ZO-1, Esam, Cldn5) and other brain cell-specific proteins (Fasn, Aldoc, Glul, Pip1).

(C) AUC integrated intensity for the top three most abundant peptide counts as determined by mass spectrometry for previously evaluated (i.e., TfR, Lrp1, InsR, Ldlrad3, CD320) and newly identified (i.e., Glut1, basigin, CD98hc) RMT candidates.

(D) Summary table of potential RMT targets identified by microarray, RNA-seq (Zhang et al., 2014), and mass spectrometry.

Similar results were observed using a higher therapeutic dose (Figures 2E and 2F). Together, these results indicate that enrichment of plasma membrane receptors in BECs alone is not likely sufficient to identify candidate RMT targets that support antibody transport across the BBB.

### Proteomic Identification of Highly Expressed Transmembrane Proteins at the BBB

Although relative transcript levels of *Ldlrad3* and *Cd320* were selectively enriched in BECs, we reasoned that their absolute protein level at the BBB may be a limiting factor to sufficiently transport antibody across the BBB, as suggested by the poor brain immunostaining (Figure 2C). We thus employed a proteomics approach to identify transmembrane proteins that are highly expressed in BECs to investigate whether protein levels would better predict potential RMT receptors.

We used FACS to isolate CD31-positive/CD45-negative BECs from wild-type mice as previously described (Tam et al., 2012) (Figure 3A). The mass spectrometry analysis of FACS-purified BECs identified established endothelial cell-specific proteins as expected (Figure 3B). Peptide counts from the negatively selected non-BEC lysate (i.e., CD31-negative/CD45-negative) revealed an abundance of glial-specific proteins indicating a mixed population of glial cells and neurons (Zhang et al., 2014).

In the BEC population, peptide counts revealed TfR to be the highest single-pass transmembrane protein, while protein levels of Lrp1, InsR, Ldlrad3, and CD320 were all below detection (Figure 3C). Interestingly, some peptide counts of Lrp1 were detected in the non-BEC population, which is consistent with previous reports that Lrp1 expression is restricted to neurons,

enhanced BEC expression compared to liver and lung endothelial cells, suggesting some commonly studied RMT targets lack selective enrichment at the BBB.

Antibodies against mouse *Ldlrad3* and *CD320* were generated to investigate whether these selectively expressed receptors could enhance brain uptake. FACS analysis using HEK293 cells expressing murine receptor was used to confirm antigen-specific cell surface binding for both antibodies (Figure 2B). Immunostaining of cortical brain tissue 1 hr after a 5 mg/kg dose revealed modest immunoreactivity for anti-*Ldlrad3* and a lack of antibody localization for anti-*CD320* (Figure 2C). Following an intravenous trace dose of <sup>125</sup>I-control IgG, <sup>125</sup>I-anti-TfR<sup>A</sup>, <sup>125</sup>I-anti-*Ldlrad3*, or <sup>125</sup>I-anti-*CD320* administered to wild-type mice, only <sup>125</sup>I-anti-TfR<sup>A</sup> exhibited significant uptake in brain. <sup>125</sup>I-anti-*Ldlrad3* and <sup>125</sup>I-anti-*CD320* accumulated in brain at levels comparable to <sup>125</sup>I-control IgG (Figure 2D).

pericytes, and other glial cells (Lillis et al., 2005; Tooyama et al., 1995; Zhang et al., 2014). Thus, the poor brain antibody delivery of previously described RMT targets (LRP and InsR) is likely explained by the low abundance of these proteins on BECs.

Importantly, this proteomics analysis revealed several highly abundant transmembrane proteins that have not been previously studied for RMT of antibodies. These include the extracellular matrix metalloproteinase inducer basigin (Bsg), the glucose transporter Glut1, and the solute carrier CD98 heavy chain (CD98hc) (Figure 3C). In agreement with our results, a recently published comprehensive RNA-seq transcriptome analysis of distinct cell populations in the mouse brain also reveals high absolute mRNA levels for *Tfrc*, *Bsg*, *Slc2a1* (Glut1), and *Slc3a2* (CD98hc) and very low absolute mRNA levels for *Lrp1*, *Insr*, *Ldlrad3*, and *Cd320* on BECs (Figure 3D; Zhang et al., 2014). To test whether high protein levels at the BBB correlates with potentially high transport capacity, we generated antibodies against these abundantly expressed targets and evaluated their RMT potential in vivo.

### Evaluation of Antibodies against Highly Expressed BBB Proteins for RMT

A total of five distinct antibodies against murine basigin, Glut1, and CD98hc were generated and evaluated: two for anti-Bsg (A and B), one for anti-Glut1, and two for anti-CD98hc (A and B). Binding was confirmed by FACs using HEK293 cells expressing the respective murine antigen (Figure 4A). In vivo antibody binding was assessed by immunostaining of cortical tissue 1 hr postdose from wild-type mice IV injected with a 5 mg/kg dose. Pronounced vascular localization was observed with all five antibodies at levels comparable to what was previously observed with anti-TfR<sup>A</sup> (Figure 4B, compared to Figure 1C).

A radiolabel trace dose of the higher-affinity I<sup>125</sup>-anti-Bsg<sup>A</sup> revealed a significant accumulation in brain for the duration of the study, while there was only a modest accumulation in the lower-affinity I<sup>125</sup>-anti-Bsg<sup>B</sup> compared to I<sup>125</sup>-control IgG (Figure 4C). The difference between the two anti-Bsg clones may be due to differences in their binding epitope and/or affinity to Bsg. The latter possibility would be consistent with the affinity-dependent differences previously observed with anti-TfR antibody variants at trace dose levels (Yu et al., 2011). I<sup>125</sup>-anti-Glut1 also accumulated in brain compared to I<sup>125</sup>-control IgG at all time points postdose (Figure 4D). Most strikingly, brain concentrations of both I<sup>125</sup>-anti-CD98hc<sup>A</sup> and I<sup>125</sup>-anti-CD98hc<sup>B</sup> were the highest of the three RMT targets evaluated, with both anti-CD98hc clones reaching brain levels ~80- to 90-fold above control IgG and ~4- to 5-fold above I<sup>125</sup>-anti-TfR<sup>A</sup> at their peaks (Figure 4E, note differences in scale from Figures 4C and 4D). Other tissue distribution was also examined and we found greater accumulation of anti-CD98hc antibodies in liver and lung compared to control IgG (data not shown).

When wild-type mice were IV injected with a higher therapeutic dose of 20 mg/kg, ~2- to 4-fold higher levels of anti-Bsg<sup>A</sup> and anti-Bsg<sup>B</sup> were observed in brain at 1 and 24 hr relative to control IgG, comparable to anti-TfR<sup>A</sup> at both time points (Figures 4F and see Figure S2A available online). In a similar experiment using a 20 mg/kg dose of anti-Glut1, brain concentrations of anti-Glut1 were ~1.5- to 3-fold higher than control

IgG and comparable to anti-TfR<sup>A</sup> at both time points (Figures 4G and S2B).

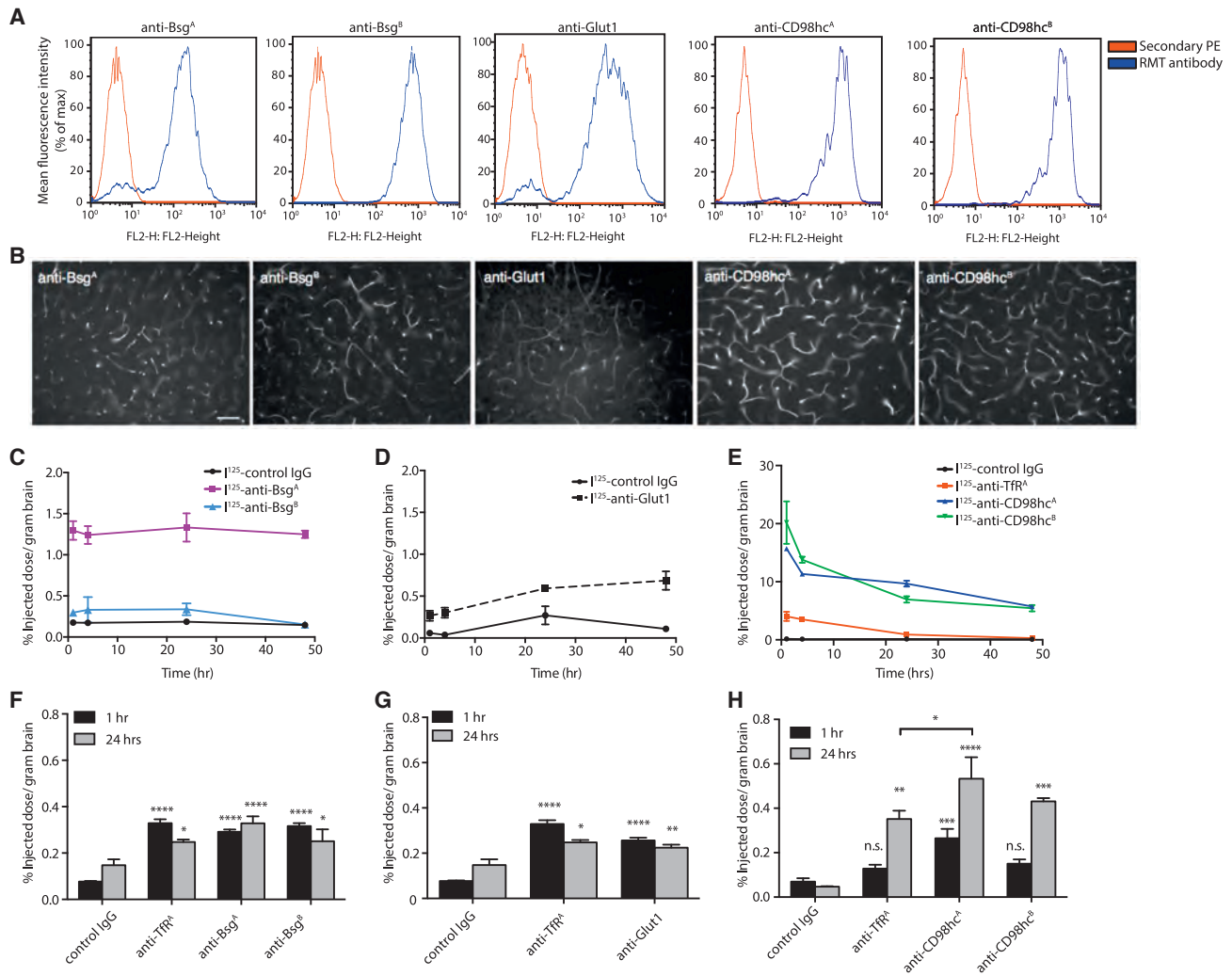
Of the three RMT candidates, systemic injections of CD98hc antibodies revealed the highest brain concentrations. Brain concentrations of anti-CD98hc<sup>A</sup> and anti-CD98hc<sup>B</sup> were ~9- and 11-fold over that of control IgG, respectively, at 24 hr postdose (Figures 4H and S2C). Furthermore, at 24 hr, brain levels of anti-CD98hc<sup>A</sup> were significantly higher than that of anti-TfR<sup>A</sup>. Although all three RMT candidates showed brain uptake by trace and therapeutic dosing, these in vivo studies reveal CD98hc to be the most robust RMT candidate.

To further confirm that dosed antibodies definitively cross the BBB and penetrate parenchyma, we assessed the amount of antibody retained in the parenchyma fraction after microvessel depletion of brain homogenates by ELISA. Dosed antibody was clearly detected for all three targets compared to the control antibody, suggesting there was significant passage of antibody across the BBB which bound to the parenchyma isolates (Figure S2D). Consistent with trace and therapeutic dose studies, anti-CD98hc antibody in the parenchyma fraction showed the greatest brain concentration (Figure S2D). The minimal uptake of anti-Glut1 may be a consequence of the specific expression of Glut1 (*Slc2a1*) in BECs; the protocol to deplete microvessels may not allow for an accurate quantification of remaining antibody in the parenchymal fraction where no antigen is expressed. Thus, antibodies against CD98hc were selected for further in vivo validation as bispecific antibodies as a result of multiple lines of evidence showing the most robust uptake in brain.

### Evaluation of Anti-CD98hc/BACE1

In order to provide a robust CNS pharmacodynamic (PD) readout that would confirm the ability of an antibody to cross the BBB, we generated bispecific antibodies that bind to CD98hc on one arm, and to the amyloid precursor protein (APP) cleavage enzyme  $\beta$ -secretase (BACE1) on the other arm (Atwal et al., 2011). BACE1 is an enzyme that is considered to be the primary generator of A $\beta$  found in plaques in the brains of Alzheimer's disease patients (Vassar et al., 1999). We previously generated an antibody against BACE1 to inhibit enzymatic activity and thereby reduce A $\beta$  production (Atwal et al., 2011). However, this antibody has poor BBB penetration and was ineffective at reducing brain A $\beta$  unless dosed at very high concentrations, or paired with anti-TfR as a bispecific antibody (Atwal et al., 2011; Yu et al., 2011). Both anti-CD98hc<sup>A</sup> and anti-CD98hc<sup>B</sup> were reformatted as bispecific antibodies to allow for a direct assessment of CD98hc-mediated antibody transport across the BBB into the parenchyma through the measurement of brain A $\beta$  levels (refer to Figure 1A).

A reduction in CD98hc binding affinity was observed when bivalent anti-CD98hc was converted into a monovalent/bispecific format as measured by competitive ELISA (Figure 5A). While the affinity of anti-CD98hc<sup>A</sup> was reduced only ~2-fold, the affinity of anti-CD98hc<sup>B</sup> was reduced by ~100-fold, indicating that avidity plays an important role in the bivalent binding of this particular antibody. Radiolabel trace dosing revealed significantly higher peak brain uptake at 1 hr postdose of anti-CD98hc<sup>A</sup>/BACE1 compared to both control IgG and anti-TfR<sup>A</sup>/BACE1 (Figure 5B;  $p < 0.0001$ ). The lower affinity anti-CD98hc<sup>B</sup>/BACE1 exhibited



increased brain uptake compared to control IgG but was below that of anti-CD98hc<sup>A</sup>/BACE1, likely due to the substantial reduction in binding affinity to CD98hc as a bispecific antibody (Yu et al., 2011). To determine extent and duration of anti-CD98hc/BACE1 brain uptake and PD response, a single 50 mg/kg IV injection of either control IgG or anti-CD98hc/BACE1 was administered in wild-type mice. Plasma clearance of the higher affinity anti-CD98hc<sup>A</sup>/BACE1 antibody was much faster compared to the lower affinity anti-CD98hc<sup>B</sup>/BACE1, as would be expected for a target-mediated clearance mechanism (Figure 5C). Both anti-CD98hc/BACE1 bispecifics showed significant brain accumulation up to 4 days postdose (Figure 5D). Brain concentrations of

anti-CD98hc<sup>B</sup>/BACE1 remained elevated at day 7 postdose, while the concentration of anti-CD98hc<sup>A</sup>/BACE1 was comparable to control IgG at this later time point. Taken together, the lower affinity anti-CD98hc<sup>B</sup>/BACE1 produced better peripheral and brain exposure over time compared to the higher affinity anti-CD98hc<sup>A</sup>/BACE1 (Figures 5C and 5D). A similar inverse relationship between antibody affinity and brain exposure was also previously observed for anti-TfR/BACE1 antibodies (Couch et al., 2013). Importantly, both CD98hc/BACE1 antibodies reduced brain A $\beta$  by  $\sim$ 30%–45% compared to control IgG-treated mice up to 4 days postdose, demonstrating successful transport of these antibodies into the brain parenchyma (Figures 5E and 5F).

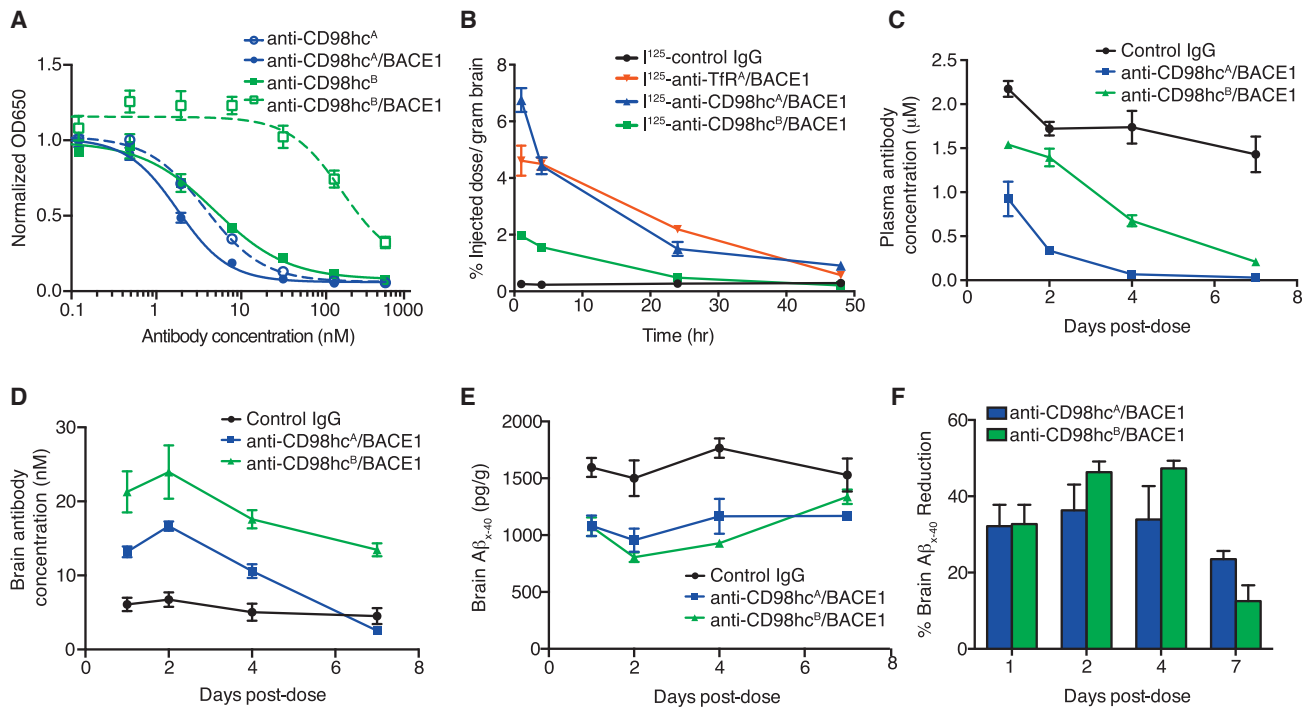


**Figure 5. CD98hc as a Novel BBB Transport Target**

(A) Competitive ELISA comparison of bivalent anti-CD98hc (solid) versus bispecific anti-CD98hc/BACE1 antibodies (dashed) binding to murine CD98hc (IC<sub>50</sub>: anti-CD98hc<sup>A</sup>- 1.5 nM, anti-CD98hc<sup>A</sup>/BACE1- 4.0 nM anti-CD98hc<sup>B</sup>- 4.6 nM, anti-CD98hc<sup>B</sup>/BACE1- 164.4 nM)

(B) Brain uptake of trace doses of <sup>125</sup>I-labeled antibodies at various time points postdose after intravenous administration in wild-type mice, quantified as mean ± SEM percent injected dose per gram of brain tissue (n = 3 per group and time point).

(C–F) Antibody concentrations in plasma (C) and brain (D), and Aβ<sub>x-40</sub> concentrations in brain (E) and percent Aβ<sub>x-40</sub> reduction compared to control IgG (F) at each time point after a single 50 mg/kg intravenous administration of antibody. See also related Figure S3.

We also performed *in vivo* two-photon microscopy to visualize the real-time trafficking of fluorescently labeled CD98hc/BACE1 bispecific variants within the parenchyma and subcortical vasculature of therapeutically dosed mice (Figure S3). Compared to mice dosed with control IgG and anti-CD98hc<sup>B</sup>/BACE1, we detected a distinct difference in the vascular clearance of anti-CD98hc<sup>A</sup>/BACE1, as predicted by the faster plasma PK of the higher affinity variant (Figure S3). In addition, we observed greater diffuse signal in the parenchyma of mice dosed with fluorescently labeled anti-CD98hc<sup>B</sup>/BACE1 by 48 hr, and to a lesser extent anti-CD98hc<sup>A</sup>/BACE1, indicating enhanced crossing of the antibody through the BBB.

### Antibody Treatments Do Not Alter Endogenous CD98hc Expression and Function

Immunocytochemistry on primary mouse BECs revealed that a majority of CD98hc localized to the plasma membrane with some colocalization with caveolin1- and EEA1-positive puncta (Figure S4). Very few puncta colocalized with TfR, a marker of recycling endosomes. We previously observed that antibodies against TfR drive lysosomal degradation of TfR in an affinity-dependent manner, leading to decreased TfR levels both *in vitro* and *in vivo* (Bien-Ly et al., 2014). Thus, we examined the endogenous levels of CD98hc in IMCD3 cells. IMCD3s were used as CD98hc is highly expressed in the kidney tubules, and this cell

line also form tight junction barrier with uniform CD98hc expression levels. Cells treated with increasing concentrations of anti-CD98hc bispecific antibodies did not change the expression level or stability of CD98hc (Figures 6A and 6B). We also examined whether antibody treatment induced changes in the subcellular localization of CD98hc. Consistent with the western blot results, a majority of CD98hc remained on the plasma membrane and with no increased trafficking of CD98hc to Lamp1-positive lysosomes (Figures 6C and 6D). Moreover, neither CD98hc bispecific affinity variant affected total brain CD98hc expression in brain lysates from mice that were dosed with 50 mg/kg of anti-CD98hc/BACE1 between 1 and 7 days (Figures 6E–6I).

We also evaluated the CD98hc amino acid transport level in the presence or absence of the anti-CD98hc antibodies. As a positive control, we observed transport inhibition by the system-L-specific substrate BCH (2-amino-2-norbornane-carboxylic acid). No inhibition was observed with anti-CD98hc antibody treatments (Figure 6J). Taken together, these data indicate that CD98hc is a novel high-capacity RMT pathway capable of delivering antibody therapeutics across the BBB without perturbing CD98hc biology.

### DISCUSSION

The idea of utilizing endogenous proteins expressed at the BBB for brain transport of therapeutics into the CNS has been studied

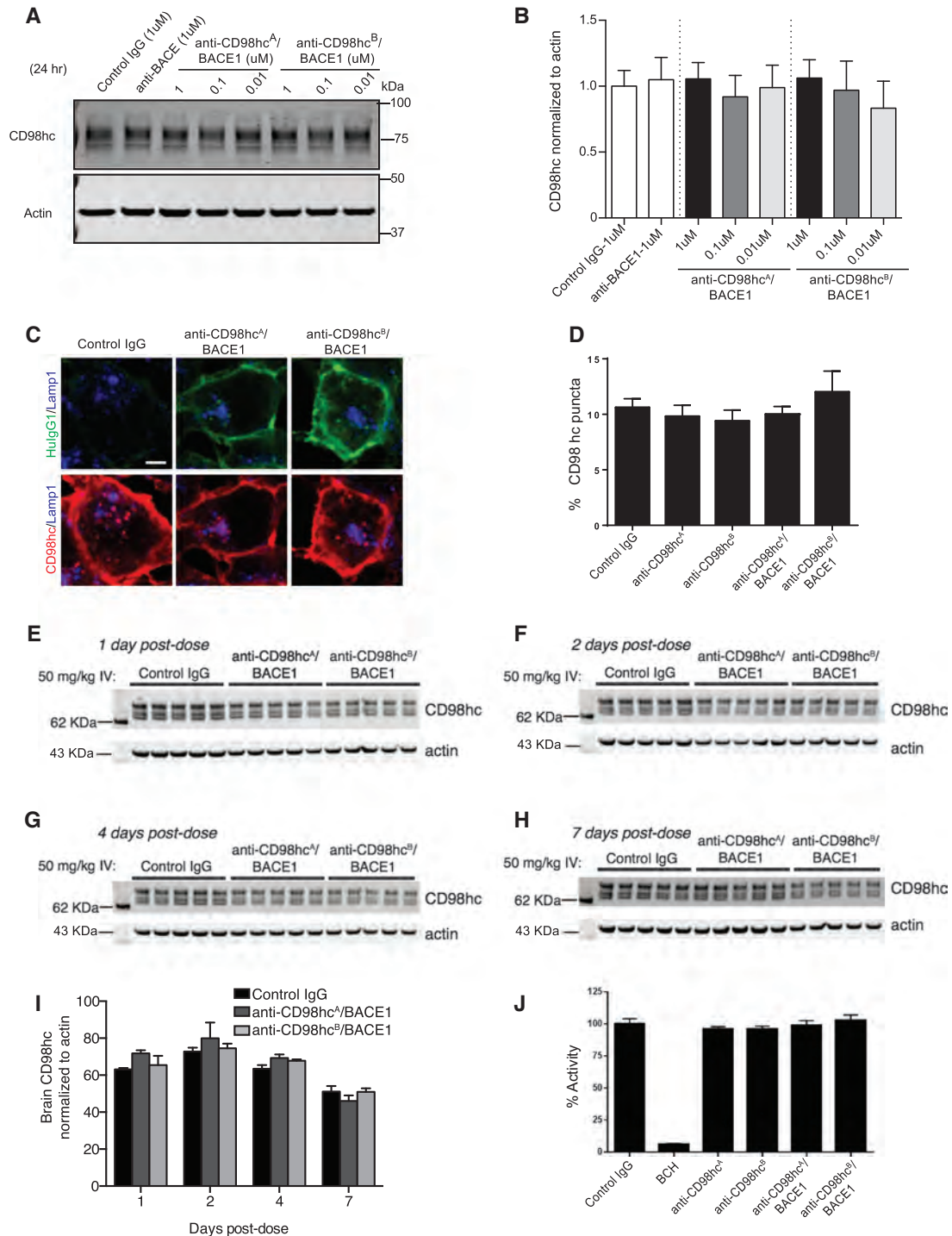


**Figure 6. CD98hc Expression, Stability, and Function Are Unperturbed by Antibody Treatment**

(A) Wild-type IMCD3 cells were treated with the indicated antibodies and concentrations for 24 hr. Lysates were probed for endogenous CD98hc and actin as the loading control.

(B) Quantification of the western blots averaged from three independent experiments each performed in triplicate. Bars represent mean  $\pm$  SEM (n = 3).

(C) IMCD3 cells stably overexpressing mouse CD98hc were treated with 1  $\mu$ M of the indicated antibodies for 1 hr at 37 $^{\circ}$ C, fixed, and stained for human IgG, mouse CD98hc, and lysosomal marker, Lamp1. Representative images of cellular uptake of Control IgG, anti-CD98hc<sup>A</sup>/BACE1, and anti-CD98hc<sup>B</sup>/BACE1 costained with Lamp1.

(D) CD98hc puncta were analyzed and quantified for colocalization with Lamp1. Bars represent mean  $\pm$  SEM (n = 5). Scale bar, 5  $\mu$ m

(legend continued on next page)

for decades (Walus et al., 1996; Boado et al., 2007; Jones and Shusta, 2007; Yu and Watts 2013). Due to its prominent expression on brain endothelial cells, TfR has been the most studied target (Jefferies et al., 1984; Lee et al., 2000; Jones and Shusta 2007; Yu and Watts 2013). Although many studies have reported additional RMT pathways for deliver across the BBB, none have shown transport of therapeutically relevant doses of antibody into the brain parenchyma with the exception of antibodies against TfR. Recently we demonstrated antibodies against TfR significantly accumulate in the brain parenchyma when administered systemically in both mice and primates (Yu et al., 2011, 2014; Couch et al., 2013). What remained to be convincingly demonstrated is whether other plasma membrane BEC proteins can be utilized in a similar manner, thus expanding the potential molecular approaches available to enhance large molecule transport across the BBB.

Although Lrp1 and InsR have been explored for RMT across the BBB (Pardridge et al., 1995; Wu et al., 1997; Boado et al., 2007; Karkan et al., 2008; Bertrand et al., 2011), we were unable to demonstrate appreciable brain uptake of antibodies against these targets. Our mass spectrometry analysis of isolated mouse BECs identified very little detectable signal for these targets, suggesting relatively low abundance at the BBB. Our results are also consistent with the reported low absolute mRNA expression in brain endothelial cells for both Lrp1 and InsR from a recently published quantitative RNA-seq dataset of distinct cell populations in the mouse brain (Zhang et al., 2014). Low protein abundance was also found for transmembrane targets that were previously identified as being highly enriched by relative mRNA expression in brain endothelial cells, such as Ldlrad3 and CD320. Retrospectively, it was not surprising that we were unable to observe an increase in brain uptake of antibodies against these enriched targets, as their low protein expression does not support a notable enhancement of delivery across the BBB in mice. Thus, using only selective mRNA expression criterion does not predict capacity for brain uptake of antibodies.

We next turned to protein abundance analysis using mass spectrometry of freshly isolated mouse BECs and identified three highly expressed transmembrane proteins: basigin, Glut1, and CD98hc. We demonstrated that antibodies against these highly expressed targets resulted in increased antibody transport into the brain. Thus high protein abundance at the BBB is likely an essential criterion when selecting a RMT target to improve brain uptake of systemically administered antibodies. Because receptor abundance is likely different between human and mouse brain endothelial cells, further confirmation of the targets identified through our mouse studies by proteomics analysis of human brain endothelial cells is necessary. Interestingly, proteomics on human brain microvasculature showed

that both CD98hc (4F2hc) and Glut1 are highly expressed (Uchida et al., 2011), which suggests that both targets hold the potential to translate into human therapeutics.

To our knowledge, this is the first demonstration that CD98hc, the most promising of the three targets identified from our BBB proteomics analysis, is a robust RMT target for transport of large molecules into the brain. CD98hc is a member of the solute carrier family and heterodimerizes with a number of CD98 light chain members to form amino acid transporters at the BBB (Boado et al., 1999). CD98hc ranked as having the second highest peptide count for a single-pass transmembrane protein identified from our data set (with TfR being the highest). The intracellular portion of CD98hc functions to mediate integrin signaling, which plays a role in both cell growth and tumorigenesis (Feral et al., 2007; Cantor and Ginsberg, 2012). Our bivalent antibodies against CD98hc exhibited significant increases in brain uptake at both trace and therapeutic dose levels after systemic administration. Importantly, CNS uptake of systemically administered anti-CD98hc<sup>A</sup>/BACE1 and anti-CD98hc<sup>B</sup>/BACE1 is further demonstrated by significant reduction in brain A $\beta$  levels.

The plasma PK of the two anti-CD98hc/BACE1 clones correlated with their binding affinity to CD98hc, likely due to target-mediated plasma clearance since CD98hc is also expressed in peripheral tissues (Parmacek et al., 1989; Nakamura et al., 1999). Lowering CD98hc affinity reduces target-mediated clearance, thus increasing peripheral exposure over time and ultimately leading to sustained brain uptake. This inverse relationship between antibody affinity for a BBB target and brain exposure of antibody over time is consistent with previous observations using affinity variants of anti-TfR/BACE1, and further substantiates a general principle of improving brain uptake with a RMT target binding affinity that may be lower than most conventional therapeutic antibodies (Couch et al., 2013). The optimal affinity range for maximizing brain uptake and exposure for each RMT target likely depends on the therapeutic dose, the duration of the desired effect, and the inherent biology and function of the RMT receptor at the BBB. Based on previous findings with anti-TfR, further reductions in anti-CD98hc affinity may produce even better peripheral PK, resulting in increased brain accumulation (Yu et al., 2011). Thus, additional affinity variants of anti-CD98hc should be explored to optimize CD98hc-dependent brain transport capacity.

Although we show that antibody treatments did not affect CD98hc localization, stability and biological function (i.e., amino acid transport), the ability to target CD98hc safely with antibodies has yet to be fully investigated. Noteworthy, an anti-CD98hc antibody (IGN523) with full effector function has been investigated in a phase I study for patients with acute myeloid leukemia (Igenica Biotherapeutics, Inc.), with no adverse events reported thus far. The possibility of retaining effector function

(E–H) Western blot analysis of CD98hc expression in brain lysates after a single 50 mg/kg dose of the indicated antibodies at various days postdose (n = 5 per group and time point).

(I) Quantification of CD98hc levels in the western blots. All graphs represent mean  $\pm$  SEM (n = 5 per group and time point).

(J) IMCD3 cells stably overexpressing mouse CD98hc cells were treated with 1  $\mu$ M of indicated antibodies for 24 hr, and amino acid uptake activity was assessed by the amount total internalized HPG, a methionine analog. BCH (2-amino-2-norbornane-carboxylic acid), an inhibitor of a system L amino acid transporter, was used as a positive control. Methionine uptake was expressed as a percentage of Control IgG and plotted against each data point. Bars represent mean  $\pm$  SEM (n = 12). See also related Figure S4.

with anti-CD98hc antibodies could be beneficial for therapeutic targets where Fc gamma receptor activation may play an important role in efficacy (e.g., anti-A $\beta$ ), which was not possible with anti-TfR antibodies due to high TfR expression on immature red blood cells causing their rapid depletion (Couch et al., 2013).

In summary, we have identified three promising new RMT targets for enhancing brain uptake of antibody therapeutics. These novel candidates were discovered using an unbiased mass spectrometry-based analysis screening for the most abundantly expressed BEC transmembrane proteins. In particular, we identified CD98hc as a promising novel RMT target that can deliver antibodies across the BBB and produce a robust PD response in the brain, thus broadening the possibilities for developing BBB platforms that can deliver therapeutic antibodies to the brain.

## EXPERIMENTAL PROCEDURES

### Antibody Generation

The Lrp1 complementary repeat domains 5 and 6 were expressed in *E. coli* as His-tagged recombinant protein. His-tagged CD320 and CD98hc extracellular domains were expressed in Chinese hamster ovary (CHO) cells, and the extracellular domain of murine Basigin (Bsg) was expressed as murine Fc-tagged protein in CHO cells. These recombinant proteins were then purified on nickel or protein A columns. Recombinant InsR was purchased from R&D system (#1544-IR-050). Recombinant Ldlrad3 was purchased from Novus Biologicals (catalog #H00143458-P01). The anti-Lrp1, anti-InsR, and anti-Ldlrad3 antibodies were selected from human antibody phage libraries. The anti-CD320, anti-Bsg, and anti-CD98hc antibodies were generated using the murine extracellular domains of the corresponding proteins to immunize mice, rats, or hamsters using standard protocols. The anti-Glut1 antibody was generated by DNA immunization in mouse using plasmid coding for the full-length Glut. The hybridomas that were generated were screened by ELISA for antigen binding and by FACs for recognition of the antigen transiently expressed on HEK cells. All antibodies were reformatted as chimeras containing a human Fc for all studies. Affinities are listed in Figure S2E.

### Naive Phage Library Sorting

A total of 10  $\mu$ g/mL of the recombinant antigen was coated overnight on NUNC 96-well Maxisorp immunoplates and preblocked with PBST (PBS and 1% bovine serum albumin [BSA] and 0.05% Tween 20). The natural synthetic diversity phage antibody libraries (Lee et al., 2004; Liang et al., 2007), preblocked with PBST, were subsequently added to the plates and incubated overnight at room temperature (RT). The plates were washed with PBST and bound phage were eluted with 50 mM HCl and 500 mM NaCl for 30 min and neutralized with 1M Tris base. Recovered phage particles were amplified in *E. coli* XL-1 blue cells. During subsequent selection rounds, the incubation time was reduced to 2–3 hr and the stringency of washing was gradually increased. Unique phage antibodies that bind specifically to the antigen were chosen and reformatted to full length IgGs by cloning VL and VH regions of individual clones into the LPG3 and LPG4 vectors, respectively, and transiently expressed in mammalian CHO cells.

### Development of Antibodies against RMT Targets

Balb/c mice (Charles River Laboratories International, Inc., Wilmington, MA, USA), Lewis rats (Charles River, Hollister, CA), or Armenian hamsters (Cytogen, MA) were immunized with purified antigen extracellular domain via footpad or intraperitoneal, at 3–4 days interval in Ribi adjuvant (Sigma) or plasmid DNA encoding the full-length antigen in the presence of GM-CSF diluted in Ringer's solution via hydrodynamic tail vein delivery (HTV), weekly injections. Following 6–12 injections, immune serum titers were evaluated by direct ELISA and FACS binding to transiently transfected HEK293 cells. Splenocytes and/or lymphocytes from animals demonstrating FACS binding were fused with mouse myeloma cells (X63.Ag8.653; American Type Culture

Collection, Manassas, VA, USA) by electrofusion (Hybrimmune; Harvard Apparatus, Inc., Holliston, MA, USA). After 10–14 days, hybridoma supernatants were harvested and screened for IgG secretion by direct ELISA or FACS. Final hybridoma clones demonstrating FACS binding were reformatted into human IgG1 or effectorless, kappa backbone. The reformatted antibodies are expressed and supernatants purified by affinity chromatography using MabSelect Sure (GE Healthcare, Piscataway, NJ, USA), eluted in 50 mM phosphoric acid (pH 3.0) plus 20X PBS (pH 11) and stored at 4°C.

### FACs Analysis

Purified antibodies were screened on HEK293 cells transfected with the corresponding antigens. Cells were collected from flasks/dishes, washed with phosphate-buffered saline (PBS), and added to 96-well U-bottom plates (BD Falcon 353077) at 1,000,000 cells per well. Samples were added to cells (100  $\mu$ L/well) and incubated at 4°C for 30–60 min. Plates were then centrifuged (1,200 rpm, 5 min, 4°C) and washed twice with PBS/1% FBS (200  $\mu$ L per well). R-Phycoerythrin-conjugated Ziege anti-human IgG Fc (Jackson ImmunoResearch 109-116-098; 100  $\mu$ L diluted in PBS) was then added and the plates incubated at 4°C (covered) for 30 min. After the final wash, the cells were fixed in PBS containing 1% formalin and read using a FACScalibur flow cytometer (BD). Mean fluorescence intensity (MFI) of each sample was then measured using the FlowJo software (Treestar, Inc.).

### Competition Enzyme-Linked Immunosorbent Assay

Nunc 96-well Maxisorp immunoplates were coated overnight at 4°C with antigen (2  $\mu$ g/ml) and blocked for 1 hr at RT with blocking buffer PBST. Serial dilutions of bivalent or bispecific antibodies were subsequently added to the plates with a sub-saturating concentration of biotinylated bispecific antibody at RT for an hour. Plates were washed with wash buffer (PBS with 0.05% Tween 20) and incubated for 30 min with horseradish peroxidase (HRP)-conjugated streptavidin, and developed with tetramethylbenzidine (TMB) substrate. Absorbance was measured spectrophotometrically at 650 nm.

### Radiolabel Trace Dosing

#### Radioiodination

All antibodies used in the studies were radioiodinated with iodine-125 (<sup>125</sup>I) using the indirect iodogen addition method as previously described (Chizzonite et al., 1991). The radiolabeled proteins were purified using NAP5™ columns pre-equilibrated in PBS. They were shown to be intact by size-exclusion HPLC.

#### In Vivo Biodistribution in C57BL/6 Female Mice

The Institutional Animal Care and Use Committees (IACUC) of Genentech Laboratory Animal Resources, in compliance with the Association for Assessment and Accreditation of Laboratory Animal Care regulations, approved all in vivo protocols, housing, and anesthesia. Female C57BL/6 mice 6–8 weeks of age (17–22 g) were obtained from Charles River Laboratories (Hollister, CA). They were administered with 5  $\mu$ Ci of the radioiodinated antibodies via IV bolus. At 1, 4, 24, and 48 hr postdose, blood (processed for plasma), brain, liver, lungs, spleen, bone marrow, and muscle (gastrocnemius) were collected (n = 3/antibody) and stored frozen until analyzed for total radioactivity on a gamma counter (2480 Wizard<sup>2</sup> Automatic Gamma Counter, PerkinElmer, Waltham, MA). The radioactivity level in each sample was calculated and expressed as percentage of Injected Dose per gram or milliliter of sample (% ID/g or % ID/mL). The % ID/g-time data were plotted using GraphPad Prism (Version 6.05) and the area under the concentration time curve (AUC) was determined. The standard deviations (SD) for the AUC estimates were calculated using the method described by Bailer (Bailer, 1988).

### Immunostaining

Wild-type mice were IV injected with 5 mg/kg of antibody followed by PBS perfusion 1 hr postdose. Brains were drop fixed in 4% paraformaldehyde (PFA) overnight at 4°C, followed by 30% sucrose overnight at 4°C. Brain tissue was sectioned at 35  $\mu$ m thickness on a sliding microtome, blocked for 1–3 hr in 5% BSA 0.3% Triton, incubated with 1:500 Alexa Fluor 488 anti-human secondary antibody (Life Technologies) in 1% BSA 0.3% Triton for 2 hr at RT. Mounted slides were subsequently analyzed by Leica fluorescence microscopy.

### Measuring Antibody Concentrations and Mouse $A\beta_{x-40}$ in Brain and Plasma

All mice used in therapeutic dosing studies were female C57BL/6 wild-type mice, ages 6–8 weeks. Mice were intravenously injected with antibody and taken down at the indicated times postinjection. Prior to perfusion with PBS, whole blood was collected in plasma microtainer tubes (BD Diagnostics) and spun down at 14,000 rpm for 2 min. Plasma supernatant was isolated for antibody and mouse  $A\beta_{x-40}$  measurements where appropriate. Brains were extracted and tissues were homogenized in 1% NP-40 (Cal-Biochem) in PBS containing Complete Mini EDTA-free protease inhibitor cocktail tablets (Roche Diagnostics). Homogenized brain samples were rotated at 4°C for 1 hr before spinning at 14,000 rpm for 20 min. Supernatant was isolated for brain antibody measurement. For PK/PD studies, one hemisphere was isolated for  $A\beta_{x-40}$  measurements and homogenized in 5M guanidine hydrochloride buffer. Samples rotated for 3 hr at RT prior to diluting (1:10) in 0.25% casein, 5 mM EDTA (pH 8.0), in PBS containing freshly added aprotinin (20  $\mu$ g/ml) and leupeptin (10  $\mu$ g/ml). Diluted homogenates were spun at 14,000 rpm for 20 min, and supernatants were isolated for mouse  $A\beta_{x-40}$  measurements.

### PK Assays

Antibody concentrations in mouse serum, and brain samples were measured using an ELISA. NUNC 384 well Maxisorp immunoplates (Neptune, NJ) were coated with F(ab')<sub>2</sub> fragment of donkey anti-human IgG, Fc fragment-specific polyclonal antibody (Jackson ImmunoResearch, West Grove, PA). After blocking the plates, each antibody was used as a standard to quantify the respective antibody concentrations. Standards and samples were incubated on plates for 2 hr at RT with mild agitation. Bound antibody was detected with HRP-conjugated F(ab')<sub>2</sub> goat anti-human IgG, Fc specific polyclonal antibody (Jackson ImmunoResearch). Concentrations were determined from the standard curve using a four-parameter nonlinear regression program. The assay had lower limit of quantitation values of 3.12 ng/ml in serum and 1.56 ng/ml in brain. For anti-CD98hc brain samples, antibody concentrations in mouse serum and brain samples were measured using an ELISA on the GYROS platform (Gyros Ab, Sweden) due to strong matrix interference specific to these antibodies. The Gyros assay uses the same antibody pairs as the plate format. The assay had lower limit of quantitation (LLOQ) values of 5 ng/ml in serum and brain.

### PD Assays

$A\beta_{x-40}$  concentrations in plasma and brain samples were measured using an ELISA similar to methods for PK analysis above. Briefly, rabbit polyclonal antibody specific for the C terminus of  $A\beta_{40}$  (Millipore, Bedford, MA) was coated onto plates, and biotinylated anti-mouse  $A\beta$  monoclonal antibody M3.2 (Covance, Dedham, MA) was used for detection. The assay had LLOQ values of 1.96 pg/ml in plasma and 39.1 pg/g in brain.

### Primary Mouse Brain Endothelial Cell Isolation and Mass Spectrometry

Brain endothelial cells (BEC; CD31+/CD45–) were isolated by flow cytometry from 40 adult female C57BL/6 mice (6–8 weeks of age). A negatively sorted population (CD31–/CD45–) was collected in parallel for comparison. In total, approximately  $5 \times 10^5$  cells were sorted to acquire a BEC population with a purity of ~92%. Isolated BECs and the negatively selected control cells were lysed in RIPA buffer in the presence of protease inhibitors and separated by SDS-PAGE on a 4%–12% Bis-Tris gel. Of the BEC lysate, 10% was used for a silver stained gel, 10% for a western blot against transferrin receptor (TfR) and the remainder loaded in a single lane and stained with Simply Blue Coomassie. In parallel lanes adjacent to the BEC lysate, lysates stemming from ~5,000, ~5,000, and ~40,000 CD31–/CD45– cells from the negatively selected population were run for silver staining, anti-TfR western, and Coomassie staining, respectively.

For mass spectrometry analysis, the Coomassie-stained gel lane corresponding to the BEC lysate (CD31+/CD45–) and the negative control (CD31–/CD45–) lysates were each cut into 15 sections from top to bottom. Each gel lane was subjected to in gel trypsin digestion using standard methods, as previously described (Zhang et al., 2011). Gel slices were diced into 1 mm cubes and destained by serial washes with 10 $\times$  gel volumes of 50 mM ammonium bicarbonate, 50% acetonitrile (pH 8.0), then 10 $\times$  gel volumes 100% acetonitrile for 15 min each. In-gel reduction and alkylation

were performed with 25 mM dithiothreitol/100 mM ammonium bicarbonate (30 min, 50°C), and 50 mM iodoacetamide/100 mM ammonium bicarbonate (20 min, RT in the dark), respectively. Gel pieces were subsequently washed and dehydrated with an additional 10 $\times$  gel volumes of 100% acetonitrile. Trypsin solution was prepared at a concentration of 10 ng/ $\mu$ L trypsin in 50 mM ammonium bicarbonate (pH 8.0) with 5% acetonitrile and added to the gel pieces on ice. Gel pieces were soaked in trypsin solution for 1 hr on ice and in-gel digestion performed overnight at 37°C. Digested peptides were collected and gel pieces extracted an additional time with 50% acetonitrile/5% formic acid. Samples were dried to completion in a SpeedVac and resuspended in 3% acetonitrile/5% formic acid for analysis.

For mass spectrometry analysis, peptides were injected onto a 0.1 mm  $\times$  100 cm C18 column packed with 1.7 mm BEH-130 resin (Waters, Milford MA) at a flow rate of 1.5 ml/min for 10 min using a NanoAcquity UPLC. Peptides were separated using a two-stage linear gradient where solvent B (98% acetonitrile/2% water/0.1% formic acid) ramped from 5% to 25% over 20 min and then from 25% to 50% over 2 min. Buffer A was comprised of (98% water/2% acetonitrile/0.1% formic acid). Peptides were introduced to an Orbitrap Velos (ThermoFisher Scientific, San Jose, CA) mass spectrometer using the ADVANCE Captive Spray Ionization source (Microm-Bruker, Auburn, CA). Orbitrap full-MS (MS1) spectra were collected at 60,000 resolution and used to trigger data dependent MS2 scans in the linear ion trap on the top eight most intense ions. MS2 spectra were searched using Mascot against a concatenated target-decoy database of mouse proteins from UniProt. Peptide spectral matches were sequentially filtered to 5% peptide false discovery rate (pepFDR) using a linear discriminant analysis, and subsequently to a 2% protein false discovery rate (final pepFDR < 0.5%). Area under curve (AUC) represents the average of two technical replicates for the integrated intensity of the top three most abundant peptide hits as previously described (Ahrné et al., 2013).

### Immunocytochemistry

IMCD3 cells stably overexpressing mouse CD98hc were plated in 384-well optical plates (Perkin Elmer) and grown for 1–2 days after confluence. Cells were treated for 1 hr at 1  $\mu$ M with anti-CD98hc bispecifics, washed with PBS, fixed with 4% PFA/4% sucrose/PBS for 5–10 min at RT, followed by ice cold 100% methanol fixation for 20 min. Cells were blocked with 1% donkey serum, 2% BSA, 0.1% Triton X-100 in PBS for 30 min RT. Primary antibodies used were mouse anti-Lamp1 (BD, 1:200) and goat anti-CD98hc (Santa Cruz 1:200), diluted in block, and incubated overnight at 4°C. The following secondary antibodies were used: donkey anti-human IgG Alexa 405, donkey anti-goat Cy3, and donkey anti-rabbit Alexa 647 (Jackson ImmunoResearch).

### Image Acquisition and Colocalization Analysis

Images were taken on a Phoenix high content system with a 40 $\times$  NA1.1 water lens in confocal mode. Laser lines 375, 488, 550, and 640 were used. Four images per well were taken and 150–200 cells in each image. Five wells per condition were imaged, thus more than 3,000 cells are analyzed per treatment. Images were transferred into ImageXpress 5.1 for analysis. For each individual channel to be analyzed, the background was removed using the TopHat function, and then the “adapted threshold” function was used to create stained object masks over the original channel image for analysis. To quantify only stained intracellular puncta, CD98hc membrane staining was excluded from analysis based on size. Total number of CD98hc puncta was quantified from the entire image consisting of about 150–200 cells. To identify internalized CD98hc staining colocalized with Lamp1, the “keep marked object” function was used to identify overlapping objects from two different channels. Total number of colocalized CD98hc puncta was quantified from the entire image and sums of each well were reported by the program and exported to Excel. Percent CD98hc puncta colocalized is calculated as number of colocalized CD98hc puncta with Lamp1 divided by the total number of total CD98hc puncta. Averages from 5 wells were calculated and graphed in Prism.

### Amino Acid Uptake Assay

IMCD3 cells stably overexpressing CD98hc were plated in 384-well plates (Perkin Elmer) the day before. Antibodies were added to cells the next morning and incubated for 24 hr at 1  $\mu$ M in growth media. Four wells per condition were

used and the experiment was repeated 3 times. After 24 hr, cells were equilibrated for 30 min at 37°C with Met-Free DMEM. To measure amino acid uptake by the cell, the amino acid methionine analog, homopropargylglycine (HPG, Life Technologies C10186), was added to the cells at 50  $\mu$ M final concentration. A total of 10 mM BCH (Sigma) was used as positive control and was added the same time as HPG. After 30 min incubation at 37°C, additional growth media was added for another 30 min. Cells were then washed with PBS and lysed in RIPA buffer with Complete protease inhibitors (Roche). All liquid handling was done with a Bravo automation system using a 384 tip head. Cell lysates were transferred to 384-well plates and incubated at 4°C overnight. The transported methionine was detected by biotinylation via the click tag on HPG. Plates were washed three times, and click reaction was performed according to manufacturer instructions (Life Technologies B10184). The total amount of biotinylated methionine was detected using ECL. Results were plotted in GraphPad Prism.

### Western Blot Analysis

Mouse brain tissues were isolated after PBS perfusion and homogenized in 1% NP-40 with protease inhibitors as described above (see "Measuring Antibody Concentrations and Mouse A $\beta_{x-40}$  in Brain and Plasma"). Approximately 20  $\mu$ g of protein was loaded onto 4%–12% Bis-Tris Novex gels (Life Technologies). Gels were transferred onto nitrocellulose membranes using the iBlot system (Life Technologies), and western blotting was performed using Odyssey blocking buffer reagents and secondary antibodies (LICOR). Mouse cross-reactive goat anti-CD98hc (Santa Cruz, M-20, 1:200) was used to detect CD98hc in brain lysates. Rabbit anti- $\beta$ -actin (Abcam8227, 1:2000) served as a loading control. Western membranes were imaged and quantified using manufacturer supplied software and system (Odyssey/LICOR).

Wild-type IMCD3 cells were plated in 48-well plates overnight, incubated with antibodies for 24 hr, washed with PBS, and then lysed with RIPA buffer supplemented with Complete protease inhibitors (Roche). Three wells per condition were used and the experiment was repeated three times. Lysates were probed for CD98hc with goat anti-CD98hc (Santa Cruz) and actin (Abcam) by western blot as described above.

### Statistical Analysis

All values are expressed as mean  $\pm$  SEM, unless otherwise indicated, and p values were assessed by ordinary one-way or two-way ANOVA, with Dunnett multiple comparisons test using Graphpad Prism Version 6.

### SUPPLEMENTAL INFORMATION

Supplemental Information includes four figures and Supplemental Experimental Procedures and can be found with this article at <http://dx.doi.org/10.1016/j.neuron.2015.11.024>.

### AUTHOR CONTRIBUTIONS

Y.J.Y.Z. and R.J.W. designed the project. Y.J.Y.Z., X.C., D.B., S.Z., M.S.D., and R.J.W. designed, performed, oversaw, and analyzed various *in vivo* experiments. X.C., M.S.D., and C.T. generated and engineered the antibodies and performed *in vitro* binding experiments. R.K.T. and J.A.E. purified and refolded the antibodies and antigens. K.H., W.L., Y.L., X.G., and B.C. ran and analyzed PK/PD assays. L.P. and D.S.K. performed the mass spectrometry experiments, and M.H. performed bioinformatics analysis on the resulting proteomics data set. D.K. and R.W. performed *in vivo* imaging experiments. N.B.-L. performed microvessel depletion experiments, and X.G. and B.C. analyzed antibody concentration by quantitative ELISA. N.B.-L., X.G., and B.C. performed *in vitro* CD98hc degradation assays. X.G. and B.C. performed *in vitro* ICC and amino acid uptake functional assays. Y.J.Y.Z. wrote the manuscript with extensive comments from X.C., N.B.-L., B.C., M.S.D., and R.J.W.

### ACKNOWLEDGMENTS

We thank Yin Zhang for phaging the anti-Lrp1 clone, and Wendy Sandoval and Yutian Gan for antibody assessment by mass spectrometry, structural biology

expression (SB-EXP) for subcloning, and research materials for mammalian protein expression. All authors are paid employees of Genentech, Inc. Genentech has filed patents on the subject matter.

Received: June 5, 2015

Revised: October 13, 2015

Accepted: November 11, 2015

Published: December 10, 2015

### REFERENCES

- Ahrné, E., Molzahn, L., Glatter, T., and Schmidt, A. (2013). Critical assessment of proteome-wide label-free absolute abundance estimation strategies. *Proteomics* *13*, 2567–2578.
- Atwal, J.K., Chen, Y., Chiu, C., Mortensen, D.L., Meilandt, W.J., Liu, Y., Heise, C.E., Hoyte, K., Luk, W., Lu, Y., et al. (2011). A therapeutic antibody targeting BACE1 inhibits amyloid- $\beta$  production *in vivo*. *Sci. Transl. Med.* *3*, 84ra43.
- Bailer, A.J. (1988). Testing for the equality of area under the curves when using destructive measurement techniques. *J. Pharma. Biopharm.* *16*, 303–309.
- Bertrand, Y., Currie, J.-C., Poirier, J., Demeule, M., Abulrob, A., Fatehi, D., Stanimirovic, D., Sartelet, H., Castaigne, J.-P., and Béliveau, R. (2011). Influence of glioma tumour microenvironment on the transport of ANG1005 via low-density lipoprotein receptor-related protein 1. *Br. J. Cancer* *105*, 1697–1707.
- Bien-Ly, N., Yu, Y.J., Bumbaca, D., Elstrott, J., Boswell, C.A., Zhang, Y., Luk, W., Lu, Y., Dennis, M.S., Weimer, R.M., et al. (2014). Transferrin receptor (TfR) trafficking determines brain uptake of TfR antibody affinity variants. *J. Exp. Med.* *211*, 233–244.
- Boado, R.J., Li, J.Y., Nagaya, M., Zhang, C., and Pardridge, W.M. (1999). Selective expression of the large neutral amino acid transporter at the blood-brain barrier. *Proc. Natl. Acad. Sci. USA* *96*, 12079–12084.
- Boado, R.J., Zhang, Y., Zhang, Y., and Pardridge, W.M. (2007). Humanization of anti-human insulin receptor antibody for drug targeting across the human blood-brain barrier. *Biotechnol. Bioeng.* *96*, 381–391.
- Cantor, J.M., and Ginsberg, M.H. (2012). CD98 at the crossroads of adaptive immunity and cancer. *J. Cell Sci.* *125*, 1373–1382.
- Chizzonite, R., Truitt, T., Podlaski, F.J., Wolitzky, A.G., Quinn, P.M., Nunes, P., Stern, A.S., and Gately, M.K. (1991). IL-12: monoclonal antibodies specific for the 40-kDa subunit block receptor binding and biologic activity on activated human lymphoblasts. *J. Immunol.* *147*, 1548–1556.
- Couch, J.A., Yu, Y.J., Zhang, Y., Tarrant, J.M., Fuji, R.N., Meilandt, W.J., Solano, H., Tong, R.K., Hoyte, K., Luk, W., et al. (2013). Addressing safety liabilities of TfR bispecific antibodies that cross the blood-brain barrier. *Sci. Transl. Med.* *5*, 183ra57, 1–12.
- Feral, C.C., Zijlstra, A., Tkachenko, E., Prager, G., Gardel, M.L., Slepak, M., and Ginsberg, M.H. (2007). CD98hc (SLC3A2) participates in fibronectin matrix assembly by mediating integrin signaling. *J. Cell Biol.* *178*, 701–711.
- Fishman, J.B., Rubin, J.B., Handrahan, J.V., Connor, J.R., and Fine, R.E. (1987). Receptor-mediated transcytosis of transferrin across the blood-brain barrier. *J. Neurosci. Res.* *18*, 299–304.
- Jefferies, W.A., Brandon, M.R., Hunt, S.V., Williams, A.F., Gatter, K.C., and Mason, D.Y. (1984). Transferrin receptor on endothelium of brain capillaries. *Nature* *312*, 162–163.
- Jones, A.R., and Shusta, E.V. (2007). Blood-brain barrier transport of therapeutics via receptor-mediation. *Pharm. Res.* *24*, 1759–1771.
- Karkan, D., Pfeifer, C., Vitalis, T.Z., Arthur, G., Ujije, M., Chen, Q., Tsai, S., Koliatis, G., Gabathuler, R., and Jefferies, W.A. (2008). A unique carrier for delivery of therapeutic compounds beyond the blood-brain barrier. *PLoS ONE* *3*, e2469.
- Kissel, K., Hamm, S., Schulz, M., Vecchi, A., Garlanda, C., and Engelhardt, B. (1998). Immunohistochemical localization of the murine transferrin receptor (TfR) on blood-tissue barriers using a novel anti-TfR monoclonal antibody. *Histochem. Cell Biol.* *110*, 63–72.

- Lee, H.J., Engelhardt, B., Lesley, J., Bickel, U., and Pardridge, W.M. (2000). Targeting rat anti-mouse transferrin receptor monoclonal antibodies through blood-brain barrier in mouse. *J. Pharmacol. Exp. Ther.* *292*, 1048–1052.
- Lee, C.V., Liang, W.C., Dennis, M.S., Eigenbrot, C., Sidhu, S.S., and Fuh, G. (2004). High-affinity human antibodies from phage-displayed synthetic Fab libraries with a single framework scaffold. *J. Mol. Biol.* *340*, 1073–1093.
- Liang, W.C., Dennis, M.S.S., Stawicki, S., Chanthery, Y., Pan, Q., Chen, Y., Eigenbrot, C., Yin, J., Koch, A.W., Wu, X., et al. (2007). Function blocking antibodies to neuropilin-1 generated from a designed human synthetic antibody phage library. *J. Mol. Biol.* *366*, 815–829.
- Lillis, A.P., Mikhailenko, I., and Strickland, D.K. (2005). Beyond endocytosis: LRP function in cell migration, proliferation and vascular permeability. *J. Thromb. Haemost.* *3*, 1884–1893.
- Nakamura, E., Sato, M., Yang, H., Miyagawa, F., Harasaki, M., Tomita, K., Matsuoka, S., Noma, A., Iwai, K., and Minato, N. (1999). 4F2 (CD98) heavy chain is associated covalently with an amino acid transporter and controls intracellular trafficking and membrane topology of 4F2 heterodimer. *J. Biol. Chem.* *274*, 3009–3016.
- Pardridge, W.M., Kang, Y.S., Buciak, J.L., and Yang, J. (1995). Human insulin receptor monoclonal antibody undergoes high affinity binding to human brain capillaries in vitro and rapid transcytosis through the blood-brain barrier in vivo in the primate. *Pharm. Res.* *12*, 807–816.
- Parmacek, M.S., Karpinski, B.A., Gottesdiener, K.M., Thompson, C.B., and Leiden, J.M. (1989). Structure, expression and regulation of the murine 4F2 heavy chain. *Nucleic Acids Res.* *17*, 1915–1931.
- Poduslo, J.F., Curran, G.L., and Berg, C.T. (1994). Macromolecular permeability across the blood-nerve and blood-brain barriers. *Proc. Natl. Acad. Sci. USA* *91*, 5705–5709.
- Roberts, R.L., Fine, R.E., and Sandra, A. (1993). Receptor-mediated endocytosis of transferrin at the blood-brain barrier. *J. Cell Sci.* *104*, 521–532.
- Tam, S.J., Richmond, D.L., Kaminker, J.S., Modrusan, Z., Martin-McNulty, B., Cao, T.C., Weimer, R.M., Carano, R.A.D., van Bruggen, N., and Watts, R.J. (2012). Death receptors DR6 and TROY regulate brain vascular development. *Dev. Cell* *22*, 403–417.
- Tooyama, I., Kawamata, T., Akiyama, H., Kimura, H., Moestrup, S.K., Gliemann, J., Matsuo, A., and McGeer, P.L. (1995). Subcellular localization of the low density lipoprotein receptor-related protein (alpha 2-macroglobulin receptor) in human brain. *Brain Res.* *691*, 235–238.
- Uchida, Y., Ohtsuki, S., Katsukura, Y., Ikeda, C., Suzuki, T., Kamiie, J., and Terasaki, T. (2011). Quantitative targeted absolute proteomics of human blood-brain barrier transporters and receptors. *J. Neurochem.* *117*, 333–345.
- Vassar, R., Bennett, B.D., Babu-Khan, S., Kahn, S., Mendiaz, E.A., Denis, P., Teplow, D.B., Ross, S., Amarante, P., Loeloff, R., et al. (1999). Beta-secretase cleavage of Alzheimer's amyloid precursor protein by the transmembrane aspartic protease BACE. *Science* *286*, 735–741.
- Walus, L.R., Pardridge, W.M., Starzyk, R.M., and Friden, P.M. (1996). Enhanced uptake of rCD4 across the rodent and primate blood-brain barrier after conjugation to anti-transferrin receptor antibodies. *J. Pharm. Exp. Therap.* *277*, 1067–1075.
- Watts, R.J., and Dennis, M.S. (2013). Bispecific antibodies for delivery into the brain. *Curr. Opin. Chem. Biol.* *17*, 393–399.
- Wu, D., Yang, J., and Pardridge, W.M. (1997). Drug targeting of a peptide radiopharmaceutical through the primate blood-brain barrier in vivo with a monoclonal antibody to the human insulin receptor. *J. Clin. Invest.* *100*, 1804–1812.
- Yu, Y.J., and Watts, R.J. (2013). Developing therapeutic antibodies for neurodegenerative disease. *Neurotherapeutics* *10*, 459–472.
- Yu, Y.J., Zhang, Y., Kenrick, M., Hoyte, K., Luk, W., Lu, Y., Atwal, J., Elliott, J.M., Prabhu, S., Watts, R.J., and Dennis, M.S. (2011). Boosting brain uptake of a therapeutic antibody by reducing its affinity for a transcytosis target. *Sci. Transl. Med.* *3*, 84ra44.
- Yu, Y.J., Atwal, J.K., Zhang, Y., Tong, R.K., Wildsmith, K.R., Tan, C., Bien-Ly, N., Hersom, M., Maloney, J.A., Meilandt, W.J., et al. (2014). Therapeutic bispecific antibodies cross the blood-brain barrier in nonhuman primates. *Sci. Transl. Med.* *6*, 261ra154.
- Zhang, Y., Chen, K., Sloan, S.A., Bennett, M.L., Scholze, A.R., O'Keeffe, S., Phatnani, H.P., Guarnieri, P., Caneda, C., Ruderisch, N., et al. (2014). An RNA-Sequencing Transcriptome and Splicing Database of Glia, Neurons, and Vascular Cells of the Cerebral Cortex. *J. Neurosci.* *36*, 11929–11947.

# Positive Allosteric Modulators of GluN2A-Containing NMDARs with Distinct Modes of Action and Impacts on Circuit Function

David H. Hackos,<sup>1,6</sup> Patrick J. Lupardus,<sup>2,6</sup> Teddy Grand,<sup>5</sup> Yelin Chen,<sup>1,7</sup> Tzu-Ming Wang,<sup>1</sup> Paul Reynen,<sup>3</sup> Amy Gustafson,<sup>3</sup> Heidi J.A. Wallweber,<sup>2</sup> Matthew Volgraf,<sup>4</sup> Benjamin D. Sellers,<sup>4</sup> Jacob B. Schwarz,<sup>4</sup> Pierre Paoletti,<sup>5</sup> Morgan Sheng,<sup>1</sup> Qiang Zhou,<sup>1,8</sup> and Jesse E. Hanson<sup>1,\*</sup>

<sup>1</sup>Department of Neuroscience

<sup>2</sup>Department of Structural Biology

<sup>3</sup>Department of Biochemical and Cellular Pharmacology

<sup>4</sup>Department of Discovery Chemistry

Genentech, Inc., 1 DNA Way, South San Francisco, CA 94080, USA

<sup>5</sup>Ecole Normale Supérieure, PSL Research University, Institut de Biologie de l'Ecole Normale Supérieure (IBENS), Centre National de la Recherche Scientifique (CNRS) UMR8197, INSERM U1024, 75005 Paris, France

<sup>6</sup>Co-first author

<sup>7</sup>Present address: Interdisciplinary Research Center on Biology and Chemistry, Shanghai Institute of Organic Chemistry, Chinese Academy of Sciences, Shanghai 200032, China

<sup>8</sup>Present address: School of Chemical Biology and Biotechnology, Peking University Shenzhen Graduate School, Shenzhen, China

\*Correspondence: hanson.jesse@gene.com

<http://dx.doi.org/10.1016/j.neuron.2016.01.016>

## SUMMARY

To enhance physiological function of NMDA receptors (NMDARs), we identified positive allosteric modulators (PAMs) of NMDARs with selectivity for GluN2A subunit-containing receptors. X-ray crystallography revealed a binding site at the GluN1-GluN2A dimer interface of the extracellular ligand-binding domains (LBDs). Despite the similarity between the LBDs of NMDARs and AMPA receptors (AMPA), GluN2A PAMs with good selectivity against AMPARs were identified. Potentiation was observed with recombinant triheteromeric GluN1/GluN2A/GluN2B NMDARs and with synaptically activated NMDARs in brain slices from wild-type (WT), but not GluN2A knockout (KO), mice. Individual GluN2A PAMs exhibited variable degrees of glutamate (Glu) dependence, impact on NMDAR Glu EC<sub>50</sub>, and slowing of channel deactivation. These distinct PAMs also exhibited differential impacts during synaptic plasticity induction. The identification of a new NMDAR modulatory site and characterization of GluN2A-selective PAMs provide powerful molecular tools to dissect NMDAR function and demonstrate the feasibility of a therapeutically desirable type of NMDAR enhancement.

## INTRODUCTION

NMDA receptors (NMDARs) are glutamate-gated ion channels that play critical roles in synaptic signaling and plasticity and

NMDAR dysfunction is implicated in a variety of nervous system disorders (Paoletti et al., 2013; Soto et al., 2014; Traynelis et al., 2010; Zhou and Sheng, 2013). NMDAR hypofunction in particular may play a role in the pathophysiology of schizophrenia (Coyle et al., 2003; Gonzalez-Burgos and Lewis, 2012). This idea originally arose from observations that NMDAR antagonists can transiently induce the positive, negative, and cognitive symptoms of schizophrenia in healthy individuals (Javitt and Zukin, 1991; Krystal et al., 1994), and it subsequently has been supported by behavioral alterations in animal models with genetically or pharmacologically reduced NMDAR function (Belforte et al., 2010; Mohn et al., 1999; Rujescu et al., 2006). NMDAR hypofunction also has been implicated in other neurological disorders. For example, NMDAR mutations, including microdeletions and predicted loss-of-function mutations, have been identified in patients with epilepsy-aphasia disorders (Carvill et al., 2013; Lemke et al., 2013; Lesca et al., 2013), and impairment of synaptic NMDAR function has been found in animal models of Alzheimer's disease (Zádori et al., 2014). Decreased NMDAR function may in principle be corrected by pharmacologically boosting activation of the remaining functional NMDARs, yet this approach risks eliciting excitotoxicity through excessive activation of NMDARs (Heng et al., 2009; Liu et al., 2007; Milnerwood et al., 2010; Tu et al., 2010; Zeron et al., 2002). Therefore, to selectively enhance physiological NMDAR function, we set out to discover molecules that act as positive allosteric modulators (PAMs) to enhance the natural physiological pattern of activation of these receptors while avoiding indiscriminate activation caused by stimulation with orthosteric agonists.

To further ensure enhancement of physiological, but not pathological, activation of NMDARs, we sought to discover PAMs with selectivity for GluN2A subunit-containing NMDARs. The GluN2 subunit composition is a critical determinant of the physiological and pathological contributions of NMDAR activation

(Paoletti et al., 2013). During brain development, there is a switch from an early dominance of GluN2B subunit expression to incorporation of GluN2A subunits at mature synapses (Sheng et al., 1994; Williams et al., 1993). It recently has become clear that mature synapses contain not only GluN2A diheteromers (GluN1/GluN2A composition), but also a significant portion of triheteromers (GluN1/GluN2A/GluN2B), which play key roles in synaptic plasticity and signaling (Gray et al., 2011; Rauner and Köhr, 2011; Soares and Lee, 2013; Tovar et al., 2013). At the same time, experiments using antagonists that preferentially inhibit GluN2B diheteromers (GluN1/GluN2B) (Hansen et al., 2014; Hatton and Paoletti, 2005; Stroebel et al., 2014) have shown that this type of NMDAR can mediate excitotoxicity when excessively activated (Costa et al., 2012; Ferreira et al., 2012; Röncke et al., 2011). Hypotheses for the deleterious effects of activating GluN2B diheteromers include the nature of the downstream signaling pathways to which they couple and/or their preferential extrasynaptic localization (Hardingham and Bading, 2010; Martel et al., 2012; Zhou and Sheng, 2013). In any case, pharmacological over-activation of GluN2B diheteromers in particular could risk pathogenic consequences. Therefore, the discovery of NMDAR enhancers that selectively potentiate GluN2A-containing NMDARs without affecting GluN2B diheteromeric receptors would not only provide a valuable tool for dissecting physiological NMDAR function, but also could represent an attractive therapeutic approach.

Here we describe a novel class of compounds that act as PAMs at GluN2A-containing NMDARs and thus enhance the normal synaptic activation of NMDARs without causing activation in the absence of stimulation. X-ray crystallography reveals that these compounds act via a novel NMDAR positive modulator binding site at the interface between the GluN1 and GluN2A ligand-binding domains (LBDs), a site that is analogous to a known PAM site found in AMPA receptors (AMPA receptors). These GluN2A PAMs potentiate recombinant diheteromeric and triheteromeric NMDARs as well as native NMDARs in brain slices during synaptic activation. Distinct but chemically related GluN2A PAMs alter channel deactivation kinetics and Glu affinity to varying degrees and also show differing dependence on Glu concentration. These distinct GluN2A PAMs also show differential impacts on synaptic plasticity that correlate with differences in their ability to affect synapses on pyramidal neurons versus interneurons. GluN2A PAMs therefore represent novel tools that can provide insight into the mechanisms of NMDAR activation and the subunit-specific roles of NMDARs in circuit function. This new class of selective NMDAR modulator also demonstrates that NMDARs can be pharmacologically targeted in a manner that may be therapeutically desirable for neurological disorders involving NMDAR hypofunction.

## RESULTS

### Discovery of Potent and Selective GluN2A PAMs

To screen for compounds that can enhance NMDAR activation in response to application of Glu in the presence of saturating glycine (Gly), we established a cell-based  $\text{Ca}^{2+}$  influx assay using HEK293 cells stably expressing GluN1 and GluN2A. A library of 1.4 million compounds was tested for the ability to increase

the  $\text{Ca}^{2+}$  influx fluorescence signal significantly above the signal obtained by subsaturating (EC30) Glu alone. GNE-3476 was identified as a hit in this high-throughput screen (HTS), with 6  $\mu\text{M}$  compound leading to a marked enhancement of the response to EC30 Glu (Figures 1A and 1B). Follow-up assays showed a dose-dependent enhancement of NMDAR activation by GNE-3476 (estimated  $\text{EC}_{50} = 10.3 \mu\text{M}$ ) (Figure 1C). Subsequent medicinal chemistry efforts (Supplemental Experimental Procedures) led to GluN2A PAMs with enhanced potency in the  $\text{Ca}^{2+}$  influx assay compared to GNE-3476, as exemplified by GNE-3419 (2.03  $\mu\text{M}$   $\text{EC}_{50}$ ), GNE-6901 (0.33  $\mu\text{M}$ ), and GNE-8324 (2.43  $\mu\text{M}$ ) (Figure 1C). Electrophysiological measurements of NMDAR currents in *Xenopus* oocytes expressing GluN1 and GluN2A confirmed that these compounds act as allosteric modulators rather than orthosteric agonists, with robust potentiation of the response to saturating Glu (100  $\mu\text{M}$ ) under various conditions where compound alone resulted in little to no signal (Figures 1D and S1). We next assessed selectivity of these more potent GluN2A PAMs by determining the dose-response relationship from cell lines expressing GluN1 paired with GluN2B, GluN2C, or GluN2D (Figures 1E–1G). Little or no compound-induced potentiation was detected in the GluN2B and GluN2C cell lines. While significant potentiation of GluN1/GluN2D NMDARs was seen with GNE-3419 and GNE-6901, the potency was 10-fold lower with GluN2D compared to GluN2A NMDARs.

### GluN2A PAMs Bind at the Inter-domain Interface of the GluN1/GluN2A LBDs

The amino-terminal domains (ATDs) of NMDARs can bind an array of ligands that act as subunit-specific allosteric modulators (Zhu and Paoletti, 2015). Yet functional characterization of NMDARs with chimeric ATDs or ATD deletions demonstrated that the ATD was not required for PAM effects (Figures S2A and S2B). To examine the LBD as a potential binding site, we crystallized and solved a 2.1-Å structure of the isolated human GluN1/GluN2A LBD dimer in complex with GNE-6901. The binding site of GNE-6901 was found to lie at the inter-domain interface between GluN1 and GluN2A LBDs (Figures 2A and 2B). This site is analogous to the binding site of AMPAR PAM molecules such as cyclothiazide (Sun et al., 2002) and aniracetam (Jin et al., 2005). Yet while the AMPAR PAMs bind a symmetric interface formed between two GluA1 LBD homodimers, the heterodimeric GluN1/GluN2A LBD interface exhibits elements of both symmetry and asymmetry (Figures 2C–2E). Comparison of the binding site of GNE-6901 to an apo GluN1/GluN2A structure (Figure 2C) reveals that the side chains of GluN1 Y535 and GluN2A E530 change rotamer conformations to permit binding of GNE-6901. To test whether these rotamer movements are important for PAM effects on the channel, we mutated GluN1 Y535 and GluN2A E530 to alanine individually or in combination, and we performed functional analysis using oocyte electrophysiology. These alanine mutants showed increased potentiation of NMDAR currents by GNE-6901 while minimally affecting the compound  $\text{EC}_{50}$  (Figure S2G), suggesting that rearrangements of the GluN1 Y535 and GluN2A E530 side chains (which are required for formation of the GNE-6901 binding site) do not appear to be required for mediating potentiation.

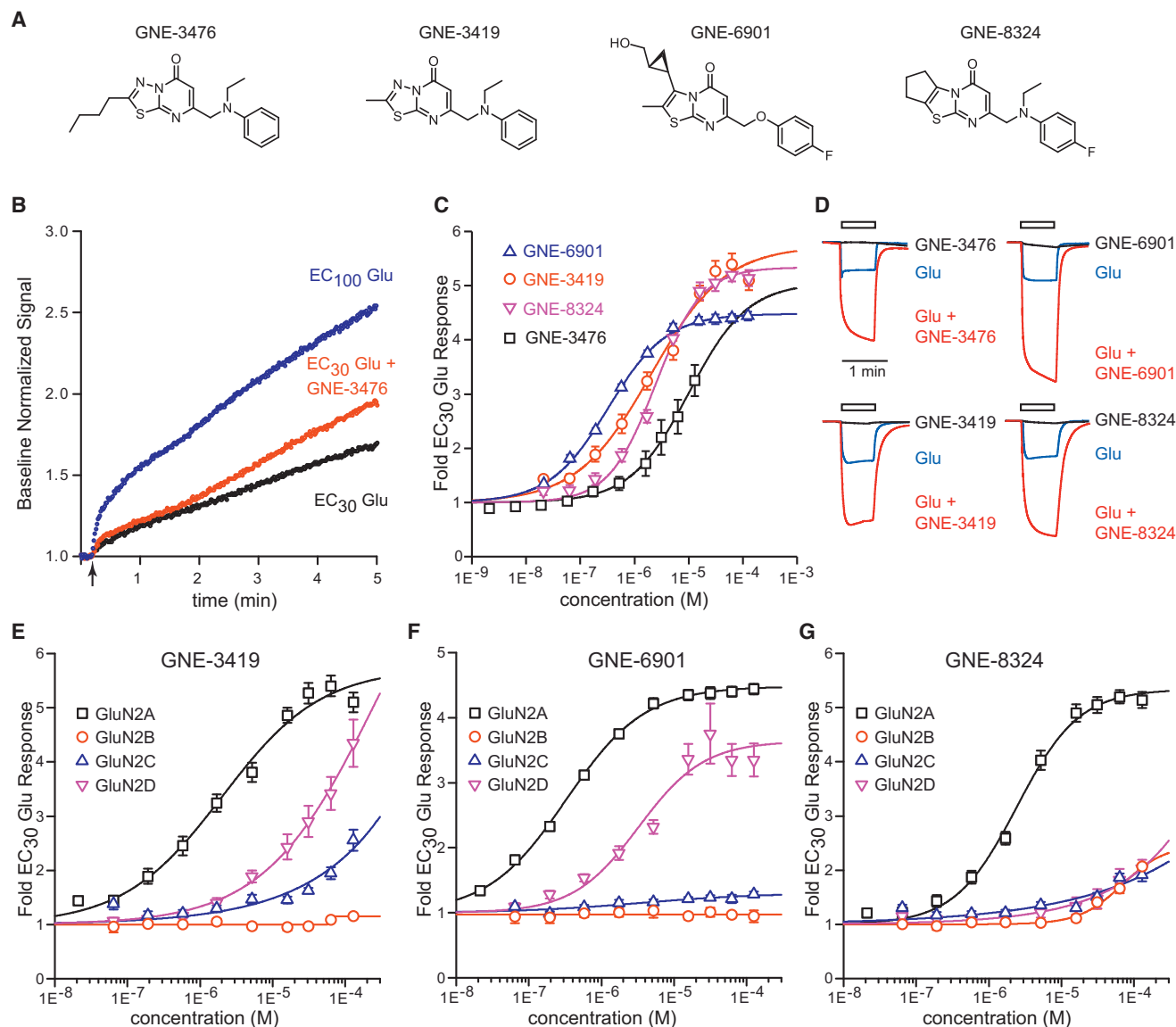


**Figure 1. Discovery of Potent and GluN2A-Selective NMDAR PAMs**

(A) Chemical structures of the GluN2A PAMs characterized in this study are shown.

(B)  $\text{Ca}^{2+}$  influx measurements from GluN1/GluN2A-expressing HEK cells show an enhanced response to  $\text{EC}_{30}$  Glu stimulation (arrow indicates onset) when  $6 \mu\text{M}$  GNE-3476 was co-applied during the HTS.

(C) Fold potentiation of the  $\text{EC}_{30}$  Glu response is shown as a function of dose for GNE-3476, GNE-3419, GNE-8324, and GNE-6901. Data are shown as mean  $\pm$  SEM ( $n = 12$  dose-response curves/compound).

(D) NMDAR currents were measured in oocytes expressing GluN1 and GluN2A to confirm that compounds acted as PAMs rather than agonists. Under conditions where little or no current was induced by  $30 \mu\text{M}$  compound in the absence of exogenous Glu application, co-application of  $100 \mu\text{M}$  Glu with  $30 \mu\text{M}$  compound resulted in significant potentiation relative to Glu alone.  $50 \mu\text{M}$  Gly was present continuously and  $5 \mu\text{M}$  AP5 was present to minimize activation by ambient Glu. Scale bar represents 1 min and current values on the y axes have been normalized to Glu-alone response amplitudes for each experiment.

(E–G)  $\text{Ca}^{2+}$  influx dose-response data for GNE-3419 (E), GNE-6901 (F), and GNE-8324 (G) are shown for HEK cell lines expressing GluN1 paired with GluN2A (reproduced from B), GluN2B, GluN2C, or GluN2D.

Data are shown as mean  $\pm$  SEM ( $n = 4$ – $12$  dose-response curves/compound/GluN2 subtype).

While no previous NMDAR modulators have been shown to bind at the GluN1/GluN2A LBD interface, chimera and mutational analyses have identified interface residues required for the action of the GluN2A-selective negative allosteric modulator (NAM) TCN-201 (Hansen et al., 2012). To compare the binding

modes of this well-characterized class of NAM with GNE-6901, we attempted co-crystallization of the GluN1/GluN2A LBD with TCN-201 and related compounds. While TCN-201 (compound 1; Bettini et al., 2010) did not lead to an X-ray structure, we were able to obtain a  $2.5\text{-\AA}$  structure of the highly related GluN2A

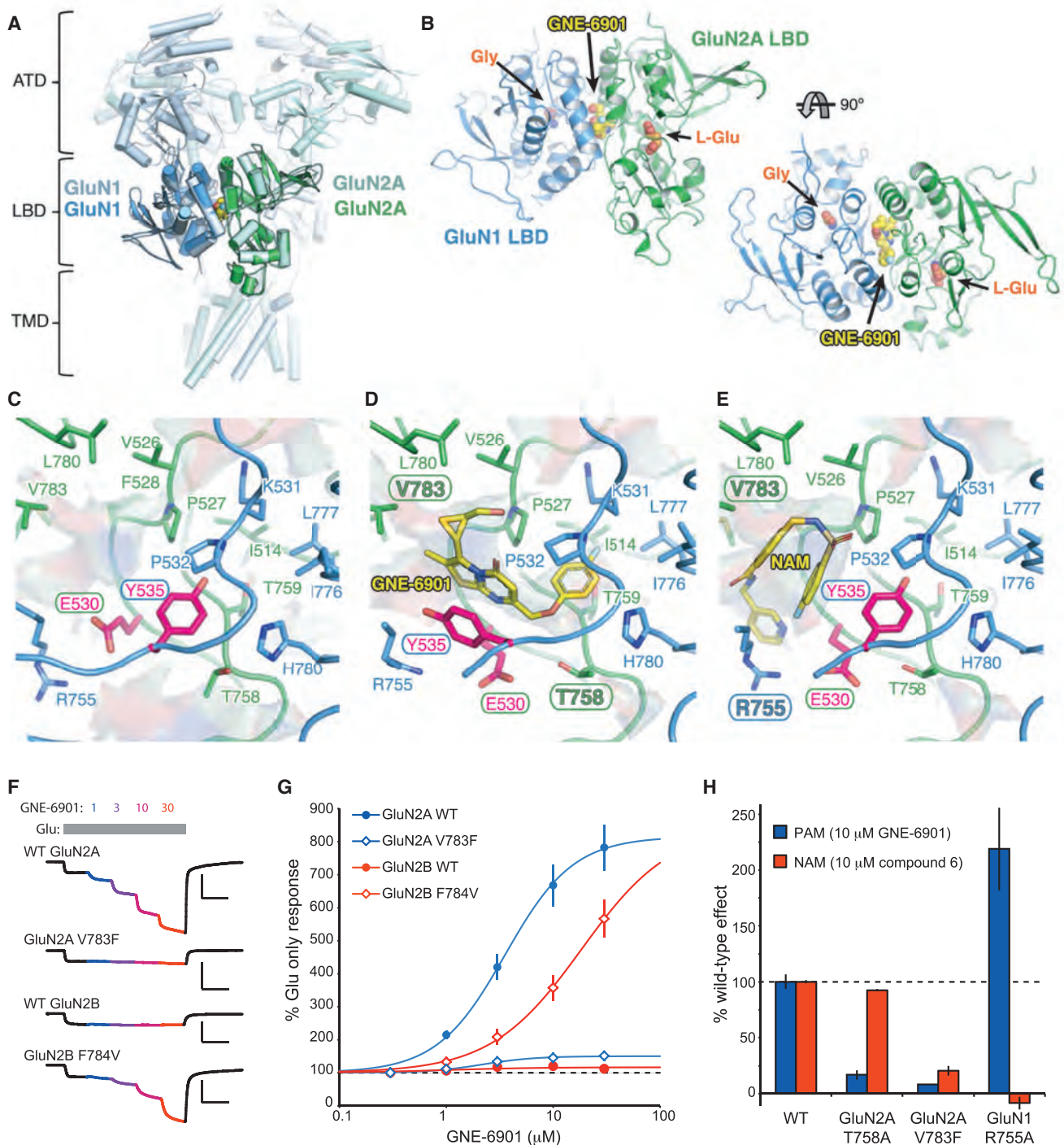


**Figure 2. Identification of an NMDAR Modulator-Binding Site at the GluN1/GluN2A LBD Interface**

(A) Cartoon representation of the human GluN1/GluN2A ligand-binding domain (LBD) structure bound to GNE-6901 presented in this paper overlaid with the full-length *Xenopus* GluN1/GluN2B receptor (PDB: 4TLL, Lee et al., 2014). The amino-terminal domains (ATDs) and trans-membrane domains (TMDs) also are labeled to show the overall position of the LBD in the context of the full-length channel. For the human LBD bound to GNE-6901, GluN1 is shown in dark blue, GluN2A is shown in dark green, and compound is shown as yellow spheres; for the full-length receptor, GluN1 is colored light blue and GluN2B light green. Colors used are consistent throughout this figure.

(B) The LBD crystal structure in complex with GNE-6901 is shown in the same orientation as depicted in (A) (upper left) and rotated 90° to show a top view (bottom right). Glutamate (L-Glu), Glycine (Gly), and GNE-6901 are shown as spheres and binding sites are labeled.

(legend continued on next page)

NAM, compound 6 (Bettini et al., 2010). This structure revealed that compound 6 binds to a distinct but overlapping region of the inter-domain interface as the GluN2A PAMs (Figure 2E). Interestingly, the side chain rotamer conformation of GluN1 Y535 is similar to that found in the apo conformation, while GluN2A E530 moves into a conformation similar to that of the PAM-bound structure to accommodate the pyridine ring of compound 6. Together, these structures identify similar but unique binding sites for GluN2A-selective PAMs and NAMs.

In comparing our compound-bound GluN1/GluN2A LBD structure with the full-length GluN1/GluN2B structure (Karakas and Furukawa, 2014; Lee et al., 2014), we identified an important difference in the PAM-binding site targeted by GNE-6901. V783 in GluN2A is a key border residue of the PAM-binding site, and it is in direct van der Waals contact with the methyl group on the thiazolopyrimidinone core of GNE-6901 (Figure 2D). The much larger corresponding residue, F784 in GluN2B, protrudes into the binding site and may prevent PAM binding to GluN1/GluN2B NMDARs. To test the functional importance of this residue in PAM selectivity, we expressed GluN2A NMDARs with a V783F mutation, as well as GluN2B NMDARs with the converse F784V mutation, in oocytes and tested their sensitivity to GNE-6901. The V783F mutation in GluN2A virtually abolished GNE-6901 sensitivity, while the F784V mutation in GluN2B conferred an ability of GNE-6901 to potentiate GluN1/GluN2B NMDARs (Figures 2F and 2G). This striking swap of sensitivity between GluN2A and GluN2B NMDARs by exchange of a single residue demonstrates that GluN2A V783 is a key determinant of PAM selectivity. Further experiments show that the corresponding residue in GluN2D, which corresponds to a Leucine (L811), is also a determinant of the less potent PAM effect of GNE-6901 observed on GluN2D receptors (Figures S2C–S2F).

Interestingly, GluN2A V783 was identified previously as essential for the action of the NAM TCN-201 (Hansen et al., 2012). To better characterize the overlapping binding sites of our series of PAMs and the prior series of NAMs, we performed mutational analysis to confirm unique and shared structural determinants. Consistent with predictions from our structures and prior work with TCN-201, we found that while GluN2A V783F blocks the effects of both GNE-6901 and the NAM (compound 6), GluN2A T758A blocks the PAM effect, but not the NAM effect, and GluN1 R755A blocks the NAM effect, but not the PAM effect (Figures 2H and S2H–S2J). This demonstration of both common and specific structural determinants of PAMs and NAMs confirms the overlapping nature of the binding sites.

### Selectivity against AMPARs

Given that the GluN1/GluN2 heterodimer interface where GNE-6901 binds is equivalent to the binding site of AMPAR PAMs, we tested the selectivity of our GluN2A PAMs against AMPARs using a  $\text{Ca}^{2+}$  influx assay in cell lines expressing GluA2 AMPARs. These experiments revealed that, while GNE-3419 potentiates both flip and flop variants of GluA2, GNE-6901 and GNE-8324 show no appreciable activity on these AMPARs (Figures 3A and 3B). To further dissect mechanisms of NMDAR versus AMPAR selectivity, we attempted to co-crystallize these compounds with the AMPAR LBD dimer (Armstrong and Gouaux, 2000). Consistent with the functional effect on AMPARs, soaking of GNE-3419 in AMPAR crystals resulted in a compound-bound structure, which revealed that GNE-3419 binds in the AMPAR dimer interface (Figure 3C) in a position equivalent to the PAM-binding site in GluN1/GluN2A (Figure 3D). The corresponding residue to GluN2A V783 in the AMPAR flip isoform is Serine 786, and our structure demonstrates that this Ser residue is not large enough to disrupt the AMPAR-binding pocket. While we did not crystallize the AMPAR LBD with the flop Asn residue at this position (Asn786), our functional assays indicate Asn also does not disrupt GNE-3419 potentiation (Figure 3B). To test for potentiation of native AMPARs during physiological activation, we examined AMPAR excitatory postsynaptic potentials (EPSPs) in hippocampal CA1 pyramidal neurons during Schaffer collateral stimulation. These experiments were consistent with the cell-based assay, with robust potentiation of AMPAR EPSPs by GNE-3419 and no detectable impact of GNE-6901 (Figures 3E and 3F).

Surprisingly, the potentiation of the AMPAR EPSP by GNE-3419 could be reversed with the addition of GNE-6901. Conversely, pre-incubation with GNE-6901 prevented potentiation by subsequent addition of GNE-3419 (Figures S3A–S3D). This dose-dependent antagonism of the GNE-3419 potentiation of AMPARs by GNE-6901, coupled with the absence of any impact of GNE-6901 alone on the AMPAR EPSPs, indicates that GNE-6901 may act as a silent allosteric modulator (SAM) of AMPARs. In other words, the functional selectivity achieved for GluN2A PAMs against AMPARs may be due to a lack of efficacy rather than potency at AMPARs.

Given the high degree of sequence similarity between AMPA and kainate receptors (KARs) at the PAM-binding site (Figure S2C), we tested if GNE-3419 might potentiate KARs as well as AMPARs using voltage-clamp measurements from oocytes expressing GluK2. While the positive control PAM,

(C) View of the PAM-binding site from an unbound apo structure of the human GluN1/GluN2A LBD. Key interface residues are shown as stick models and residues that move upon PAM binding (GluN1 Y535 and GluN2A E530) are highlighted in magenta. Solvent-accessible surface area in the interface is shown as a transparent surface. (C)–(E) are rotated 90° to the right compared to the LBD representation in (A).

(D) View of GNE-6901 bound in the PAM-binding site of the GluN1/GluN2A LBD is shown.

(E) The GluN2A-selective NAM (compound 6, Bettini et al., 2010) bound to GluN1/GluN2A LBD is shown. Note that the NAM binds in a partially overlapping region of the heterodimer interface as the PAM.

(F) Example traces from NMDAR currents measured in oocytes expressing mutant or WT GluN2A or GluN2B are shown; 1, 3, 10, and 30  $\mu\text{M}$  GNE-6901 were sequentially added during application of 300 nM Glu. Scale bars represent 1 min and 1  $\mu\text{A}$  (top two traces) or 0.5  $\mu\text{A}$  (bottom two traces).

(G) Dose-response data for each type of channel are shown. Data are shown as mean  $\pm$  SEM ( $n = 10$ –12 oocytes/dose-response curve).

(H) Impacts of point mutations of the residues highlighted in (D) and (E) on PAM and NAM effects. PAM effects are normalized to the average potentiation observed with 10  $\mu\text{M}$  GNE-6901 and NAM effects to the average inhibition observed with 10  $\mu\text{M}$  compound 6. Data are summarized from (G) and Figures S2H and S2I and are shown as mean  $\pm$  SEM.

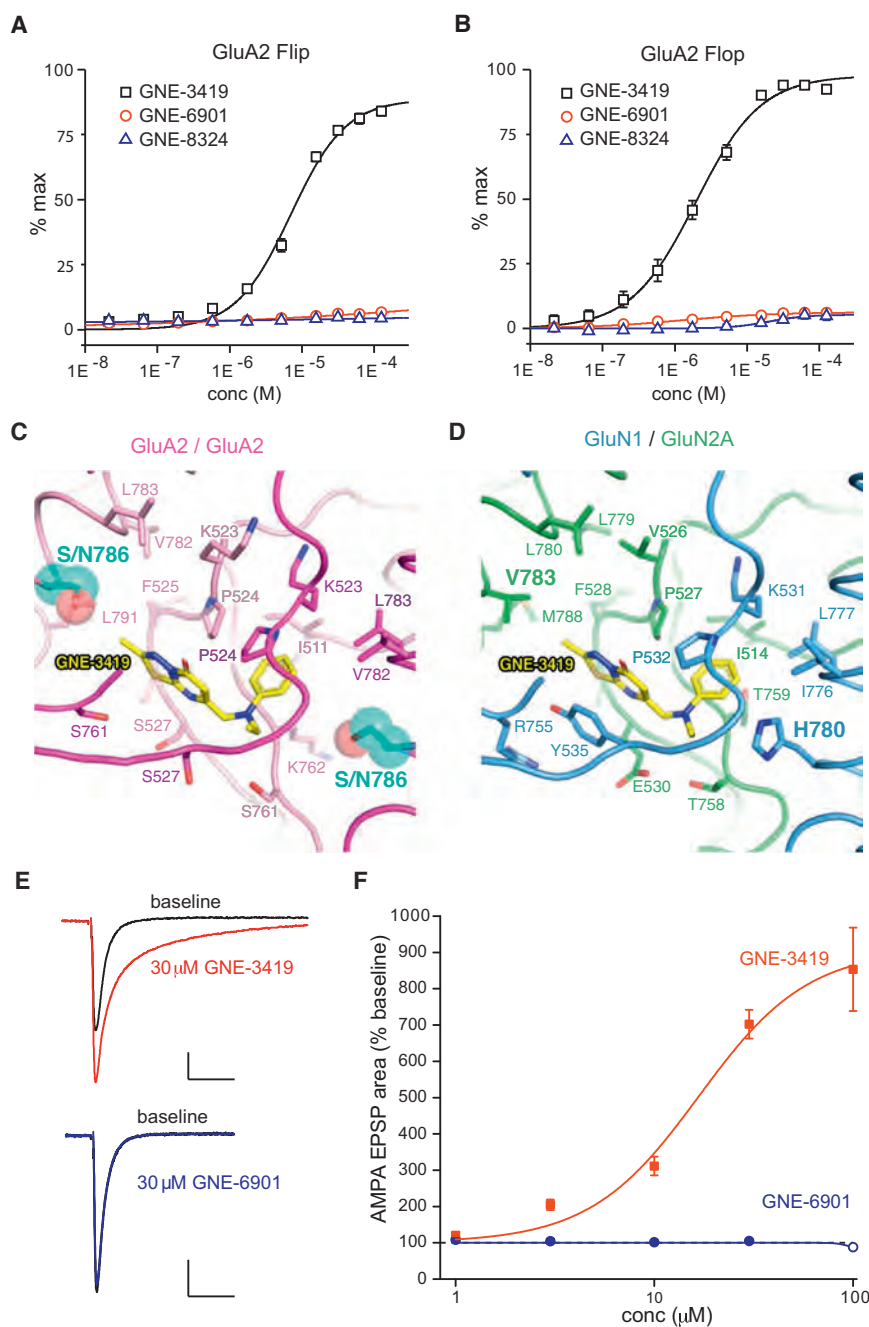


**Figure 3. Characterization of Selectivity against AMPARs**

(A and B)  $\text{Ca}^{2+}$  influx measurements from cell lines expressing the flip (A) or flop (B) variant of GluA2 are shown in response to Glu application in the presence of increasing PAM concentrations. Data are shown as mean  $\pm$  SEM ( $n = 4$ –10 dose-responses/compound).

(C) The crystal structure of GNE-3419 in complex with the GluA2 LBD is shown. The individual GluA2 monomers are shown as cartoon models in light pink and dark pink. Residues that interact with GNE-3419 are shown as stick models. The binding site includes a residue that differs between flip (S786, corresponding to this structure) and flop (N786) isoforms (highlighted in cyan).

(D) The structure of GNE-3419 in complex with the GluN1/GluN2A LBD is shown in the same orientation as the GluA2 structure in (C). Residues that interact with GNE-3419 are shown as stick models. The GluN1/GluN2A residues analogous to the flip residue S786 are highlighted with large labels.

(E) Evoked AMPA EPSPs recorded from CA1 pyramidal neurons in hippocampal brain slices are shown. Average EPSPs before (black) and after application of 30  $\mu\text{M}$  GNE-3419 (red) or GNE-6901 (blue) are shown. Scale bars represent 50 ms and 0.5 mV.

(F) Dose-response data show the percentage potentiation of AMPAR EPSP area in response to GNE-3419 (red) or GNE-6901 (blue) application. Open circle indicates that incomplete solubility was observed for GNE-6901 at the highest concentration tested. Data are shown as mean  $\pm$  SEM ( $n = 5$ –9 brain slices/dose/compound).

Concanavalin A (ConA), which blocks KAR desensitization, revealed robust Glu-evoked currents, GNE-6901, GNE-8324, and GNE-3419 all failed to act on GluK2 in a similar manner. Parallel experiments with GluA2 confirmed that GNE-3419, but not the other PAMs, could block AMPAR desensitization in this same experimental paradigm (Figures S3E and S3F), supporting selectivity against KARs.

#### Potentiation of Triheteromeric and Synaptic NMDARs

While the cell-based assays used to test GluN2A PAMs demonstrated potentiation of GluN2A, but not GluN2B-containing

NMDAR subunit composition with ectopic retention signals (Stroebel et al., 2014). These experiments revealed that triheteromeric receptors also are potentiated by GNE-6901 (Figures 4A and 4B). Consistent with the presence of a single PAM-binding site in each triheteromer as compared to the two binding sites per GluN2A diheteromer, potentiation of triheteromers was of a smaller magnitude than that of GluN2A diheteromers. Similarly, we also observed that GNE-8324 could potentiate both diheteromers and triheteromers (Figures S4A and S4B). In addition, potentiation by both PAMs was independent of the GluN1 splice variant (Figures S4C–S4F).

To directly test the impact of GNE-6901 on synaptically activated NMDARs, we performed whole-cell recordings of pharmacologically isolated NMDAR excitatory postsynaptic currents (EPSCs) in CA1 pyramidal neurons in response to Schaffer collateral stimulation in brain slices. To test specificity for GluN2A NMDARs, recordings were performed in slices from GluN2A knockout (KO) mice as well as wild-type (WT) mice. In WT mice, a clear potentiation of the NMDAR EPSC was observed when GNE-6901 was applied to brain slices, with a greater relative potentiation of EPSC area compared to peak amplitude that was associated with a slowing of the decay time of the EPSC (Figures 4C–4G). In GluN2A KO mice there was a longer baseline decay time constant for the NMDAR EPSCs compared to WT mice ( $254.8 \pm 45.6$  versus  $74.6 \pm 8.5$  ms), which is consistent with the presence of synaptic GluN2B diheteromers in the absence of GluN2A subunits in these mice. There was no effect of GNE-6901 application on NMDAR EPSCs in the GluN2A KO mice, with only a small rundown of the NMDAR EPSC evident during the recording period (Figures 4C–4H).

#### Different GluN2A PAMs Have Distinct Impacts on NMDAR Channel Function

To examine modulation of NMDAR channel function with higher resolution, we performed whole-cell patch-clamp recordings on CHO cells stably expressing GluN1 and GluN2A using a rapid solution switching system. These experiments confirmed the PAM effects on NMDARs. While Glu or Gly alone applied in the presence of GNE-6901 or GNE-8324 resulted in minimal current, the magnitude of the current elicited by Glu and Gly co-application was enhanced in the presence of the GluN2A PAMs (Figure S5). Dose-response experiments using a brief pulse (2 s) of 100  $\mu$ M Glu in the presence of 50  $\mu$ M Gly confirmed the greater potency of GNE-6901 compared to GNE-8324 (Figures 5A–5C). Notably, both PAMs can increase NMDAR currents even during the presence of saturating agonist concentrations. However, striking differences between GNE-6901 and GNE-8324 were apparent during channel deactivation following the removal of Glu in the constant presence of Gly. While GNE-6901 resulted in a relatively modest slowing of the rate of deactivation following the removal of Glu, GNE-8324 caused a profound slowing of glutamate deactivation kinetics (Figures 5A, 5B, and 5D). In contrast, when Gly was removed in the constant presence of Glu, NMDAR currents rapidly deactivated in the presence of either PAM (Figures 5E and 5F), demonstrating a specific interaction of PAMs with Glu, but not Gly.

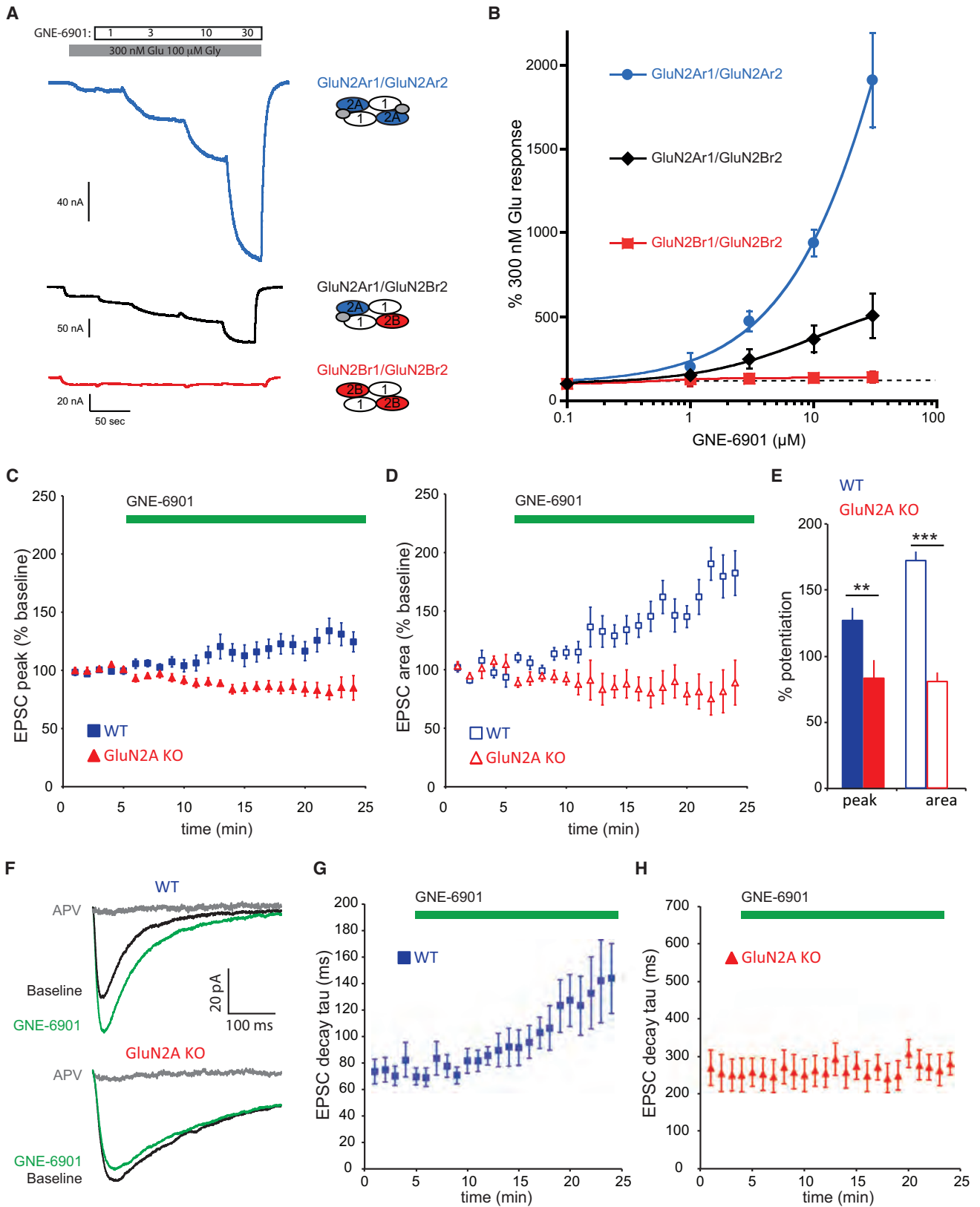
To further examine the interactions of GNE-6901 and GNE-8324 with the agonists, Gly and Glu potencies were assessed in the presence or absence of near saturating concentrations of each PAM (10  $\mu$ M GNE-6901 and 30  $\mu$ M GNE-8324). These experiments showed that neither PAM had significant impacts on Gly potency (Figures 6A–6C, S6A, and S6D). On the other hand, GNE-8324 significantly increased the potency of Glu at the NMDAR, while GNE-6901 had a much smaller impact on Glu potency (Figures 6D–6F, S6B, and S6E). We next examined the converse question of whether GNE-8324 potency was more dependent on Glu concentration than GNE-6901. In these experiments, we observed potentiation of NMDAR currents eli-

cited by the two PAMs in the presence of either saturating (100  $\mu$ M) or low (0.1  $\mu$ M) pre-applied Glu. GNE-8324 potency was found to be strongly dependent on Glu concentration, while there was only a modest effect of Glu concentration on GNE-6901 potency (Figures 6G–6I, S6C, S6F, and S6G). Thus, while both GNE-6901 and GNE-8324 enhance the NMDAR current during Glu application, these two PAMs have striking differences. Compared to GNE-6901, GNE-8324 exhibits the following: (1) greater slowing of glutamate deactivation kinetics, (2) greater impact on NMDAR Glu potency, and (3) greater dependence of its potency on Glu concentration. These results suggest that, while both GNE-6901 and GNE-8324 are GluN2A-selective PAMs, their modes of action differ, potentially resulting in different effects during physiological activation of NMDARs.

#### Differential Impacts of GluN2A PAMs during Synaptic Plasticity Induction

To test the impacts of GNE-6901 and GNE-8324 in an intact circuit, we examined synaptic potentiation of Schaffer collateral inputs to CA1 pyramidal neurons. Short-term potentiation (STP) and long-term potentiation (LTP), two aspects of plasticity that depend on NMDAR activation (Malenka and Nicoll, 1993; Park et al., 2014), were assessed following one, two, and three bouts of a weak plasticity induction stimulus in the presence of vehicle (DMSO) or PAMs at concentrations expected to have near maximal effects (10  $\mu$ M GNE-6901 and 30  $\mu$ M GNE-8324). When potentiation was induced under physiological conditions, we observed an overall significant effect of treatment on LTP and STP (Figure 7A). Compared to vehicle, slices treated with GNE-6901 showed a trend toward enhanced LTP and exhibited significantly enhanced STP ( $p < 0.001$ ), while slices treated with GNE-8324 showed a trend toward impaired LTP and exhibited significantly impaired STP ( $p < 0.01$ ). Overall, both LTP ( $p < 0.01$ ) and STP ( $p < 0.001$ ) were significantly greater with GNE-6901 compared to GNE-8324 (Figure 7B).

NMDARs are present on both pyramidal neurons where they mediate induction of synaptic potentiation at the Schaffer collateral synapses, as well as on interneurons where they can contribute to polysynaptic inhibition of pyramidal neurons and oppose the induction of potentiation (Hanson et al., 2013). Therefore, the above results could potentially reflect a mixture of effects of GluN2A PAMs on pyramidal neurons and on interneurons recruited during plasticity induction. To examine the role of interneurons in the effects of the PAMs, we repeated these experiments in the presence of the GABA<sub>A</sub>R antagonist picrotoxin (PTX) to eliminate fast synaptic inhibition (Figures 7C and 7D). Under these conditions, GNE-6901 significantly potentiated both LTP ( $p < 0.01$ ) and STP ( $p < 0.001$ ). However, in contrast to the reduction of potentiation seen with GNE-8324 when inhibition was intact, in this experiment GNE-8324 had no effect on LTP and significantly enhanced STP ( $p < 0.05$ ). Both LTP ( $p < 0.01$ ) and STP ( $p < 0.05$ ) were still significantly greater with GNE-6901 compared to GNE-8324 in the absence of inhibition. This impairment of synaptic potentiation by GNE-8324 in the presence, but not in the absence, of inhibition was confirmed in experiments using a stronger induction protocol (Figure S7).



(legend on next page)

To better understand why GNE-8324 exhibits a relative lack of effect on plasticity with inhibition blocked but prominent effect with intact inhibition (while GNE-6901 enhances plasticity in both cases), we directly measured the impacts of each PAM on pyramidal neuron and interneuron NMDAR responses. While GNE-6901 significantly increased the area of synaptically activated NMDAR responses on pyramidal neurons ( $p < 0.05$ ), GNE-8324 did not produce a significant effect (Figures 8A–8C). At the same time, whole-cell recordings targeting stratum radiatum interneurons showed that both PAMs significantly enhanced NMDAR EPSC area ( $p < 0.01$ ) (Figures 8D–8F). Both PAMs delayed interneuron NMDAR EPSC decay to a similar magnitude as was observed with GNE-6901 in pyramidal neurons (Figure S8). The basis for the unequal ability of GNE-8324 to potentiate interneuron versus pyramidal neuron NMDARs could result from the unique biophysical properties of this PAM in combination with potential variations in synaptic neurotransmitter levels at different synapses.

To examine the PAM effects on NMDAR responses in the context of the bursts of stimulation that were used to induce LTP, isolated burst-evoked NMDARs were recorded from pyramidal neurons (Figure 8G). When inhibition was blocked, there was a small enhancement of burst-evoked responses by GNE-8324 that trended toward significance ( $p = 0.14$ ), while GNE-6901 showed a more robust and significant enhancement ( $p = 0.001$ ) (Figure 8H). This is consistent with the modest versus robust enhancement of NMDAR-dependent plasticity by GNE-8324 and GNE-6901, respectively. When these experiments were repeated with intact inhibition, GNE-8324 significantly impaired the burst-evoked NMDAR response ( $p = 0.008$ ), while GNE-6901 continued to cause a significant enhancement ( $p = 0.0005$ ) (Figure 8I), again paralleling the results of the NMDAR-dependent plasticity experiments. Overall these results suggest that, during plasticity induction, the robust pyramidal neuron impact of GNE-6901, but not GNE-8324, overrides the inhibition-dependent impacts of the PAMs. Thus, these two distinct GluN2A PAMs that differ in their impacts on NMDAR biophysical properties also differ in their effects during neuronal circuit function.

## DISCUSSION

Here we report a novel class of NMDAR PAM that is selective for GluN2A subunit-containing NMDARs. Positive modulation

and selectivity were demonstrated using multiple assay platforms on recombinant and native receptors including  $\text{Ca}^{2+}$  influx from cell lines and electrophysiology recordings from cell lines, *Xenopus* oocytes, and mouse brain slices. Importantly, triheteromeric GluN1/GluN2A/GluN2B receptors, which represent a major species of synaptic NMDARs, also could be potentiated, and enhancement of synaptically activated NMDARs in WT, but not GluN2A KO, mice confirmed the physiological selectivity of positive modulation established by the *in vitro* analyses.

The binding site of GluN2A PAMs at the GluN1-GluN2A heterodimer interface was identified using X-ray crystallography, which to our knowledge represents the first structure of an NMDAR modulator bound to the LBD region and, thus, defines a new site for allosteric modulation of NMDARs. Previous structural and functional analysis identified a critical role for the GluN1/GluN2 LBD dimer interface in NMDAR activation, leading to a model in which the aromatic side chain of GluN1 Y535 binds to a hydrophobic pocket in GluN2A, thus stabilizing the activated Glu-bound conformation (Furukawa et al., 2005). Interestingly, our structure shows that rotation of the GluN1 Y535 side chain is required to accommodate PAM binding, with the phenyl group of the PAM compounds instead mimicking the Y535 aromatic side chain (Figures 2C and 2D). While rotation of GluN1 Y535 out of this pocket is necessary to accommodate PAM binding, mutational analysis suggests the presence of this side chain is not essential for potentiation (Figure S2G). Overall we hypothesize that GluN2A PAMs stabilize the inter-domain interface to a greater extent than is achieved by the normal inter-subunit interactions that are displaced by PAM binding. This enhanced interaction between subunits is predicted to stabilize the Glu/Gly-bound conformation of the LBD and promote channel activation. Regarding selectivity, residue V783, which we demonstrated is critical for the GluN2A selectivity of our PAMs (Figure 2), previously was found to be important for the selective negative modulation of NMDARs by TCN-201 (Hansen et al., 2012). Notably, our crystal structure of a related NAM from the same class of compounds as TCN-201 shows a partially overlapping binding pocket with GluN2A PAMs, and we confirmed both unique and overlapping structural determinants for the classes of compounds (Figure 2). The convergence of the binding sites of two distinct classes of GluN2A-selective modulators with opposite effects on channel activity within an overlapping

### Figure 4. Potentiation of Recombinant Triheteromeric NMDARs and Synaptically Activated NMDARs in Brain Slices

(A) Example GNE-6901 dose-response recordings from oocytes expressing GluN1 paired with GluN2Ar1/GluN2Ar2 (GluN2A diheteromers), GluN2Ar1/GluN2Br2 (GluN2A/GluN2B triheteromers), or GluN2Br1/GluN2Br2 (GluN2B diheteromers) are shown.

(B) GNE-6901 dose-response data for GluN2Ar1/GluN2Ar2, GluN2Ar1/GluN2Br2, or GluN2Br1/GluN2Br2 NMDARs. Cartoon representations of the NMDAR LBD subunit composition illustrate the 2, 1, and 0 PAM-binding sites (gray circles) in GluN2A diheteromers, GluN2A/GluN2B triheteromers, and GluN2B diheteromers, respectively. Data are shown as mean  $\pm$  SD ( $n = 5$ –13 oocytes/dose).

(C and D) Isolated NMDAR EPSCs were recorded from WT or GluN2A KO mice. Baseline-normalized EPSC peak (A) and area (B) are shown during application of 30  $\mu\text{M}$  GNE-6901. Data are shown as mean  $\pm$  SEM ( $n = 10$  WT mice and  $n = 6$  KO mice). The gradual time course of compound effect may reflect penetration into the slice or use dependence.

(E) Potentiation of NMDAR EPSC peak and area in WT and GluN2A KO mice was calculated from the normalized current magnitude at the end of the recordings. Data are shown as mean  $\pm$  SEM. WT potentiation of peak and area were significantly different from the GluN2A KO control (\*\* $p < 0.01$  and \*\*\* $p < 0.001$ ).

(F) Example NMDAR EPSCs are shown during baseline (black), after 30  $\mu\text{M}$  GNE-6901 application (green), and after blockade by 50  $\mu\text{M}$  D-APV at the end of the experiment (gray). Note the slower time course of NMDAR EPSCs in GluN2A KO mice (scale bar represents 100 ms and 20 pA for both sets of traces).

(G and H) NMDAR EPSC decay time constants from single exponential fits of the falling portion of the EPSC are shown for slices from WT (E) and GluN2A KO mice (F) during GNE-6901 application.

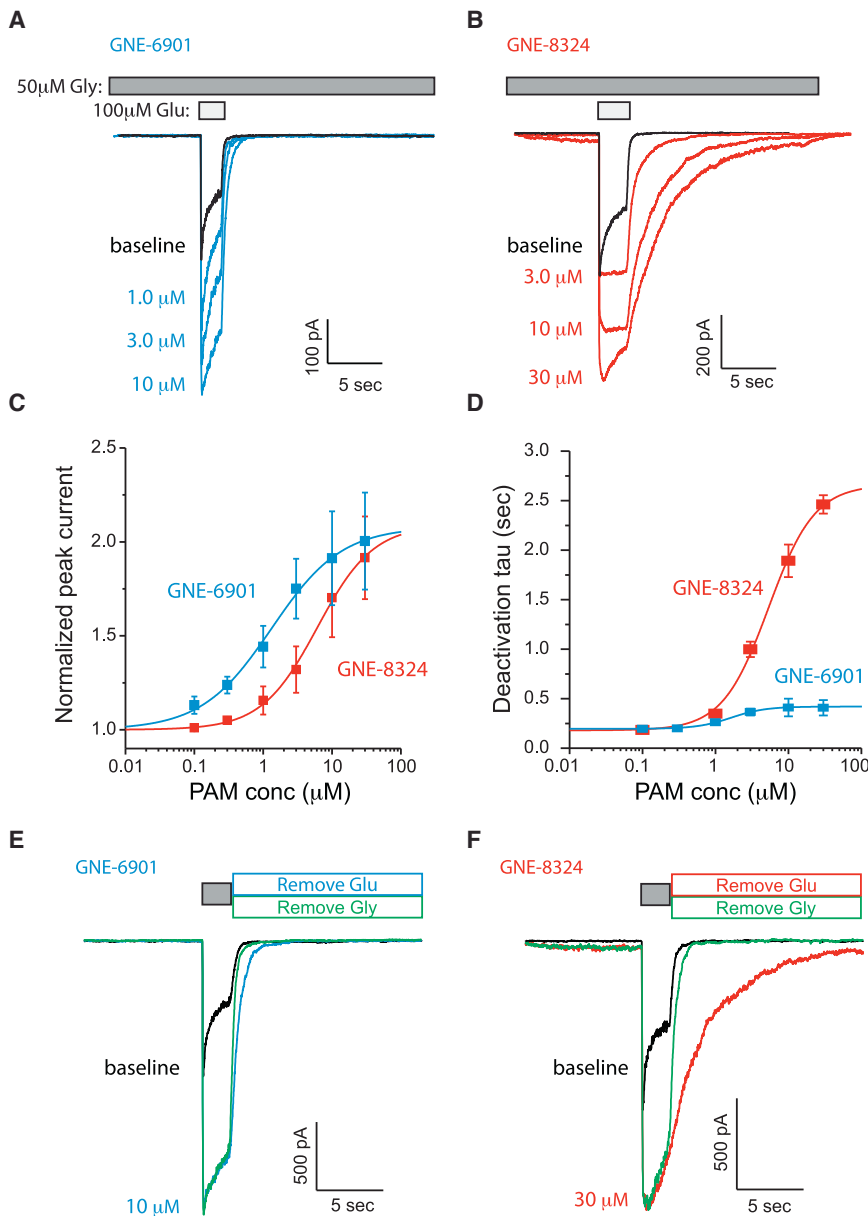


**Figure 5. Effects of GNE-6901 and GNE-8324 on NMDAR Currents Using Rapid Agonist Application**

(A) The dose dependence of GluN2A current potentiation is shown with overlaid traces of the NMDAR current in response to a brief application of 100  $\mu$ M Glu in the constant presence of 50  $\mu$ M Gly. Example traces are shown for baseline (black) and various concentrations of GNE-6901 (blue).

(B) The dose dependence of GluN2A current potentiation is shown for GNE-8324. Example traces are shown for baseline (black) and various concentrations of GNE-8324 (red). Note that while both GNE-6901 and GNE-8324 potentiate peak currents, only GNE-8324 significantly slows deactivation following the removal of Glu.

(C) GNE-6901 potentiates peak currents with an  $EC_{50}$  of  $1.33 \pm 0.22$   $\mu$ M and a maximum potentiation of  $2.08 \pm 0.42$ -fold over baseline, while GNE-8324 potentiates peak currents with an  $EC_{50}$  of  $6.1 \pm 1.06$   $\mu$ M and a maximum potentiation of  $2.09 \pm 0.27$ -fold over baseline. Data are shown as mean  $\pm$  SEM ( $n = 5$ –7 patches/experiment).

(D) Deactivation kinetics are shown as a function of PAM concentration. GNE-6901 slows deactivation tau by  $2.1 \pm 0.71$ -fold over baseline (baseline tau =  $186.2 \pm 17.4$  ms) with an  $EC_{50}$  of  $1.64 \pm 0.33$   $\mu$ M, while GNE-8324 slows tau by  $14.8 \pm 2.7$ -fold over baseline with an  $EC_{50}$  of  $5.4 \pm 1.6$   $\mu$ M. Note that GNE-8324 shows much greater slowing of deactivation kinetics relative to GNE-6901. Data are shown as mean  $\pm$  SEM ( $n = 9$ –11 patches/experiment).

(E) Example recordings showing GluN2A currents either in the absence (baseline) or presence of 10  $\mu$ M GNE-6901. The gray box represents the presence of both 100  $\mu$ M Glu and 50  $\mu$ M Gly. The black trace represents the baseline recording without GNE-6901 where Glu was removed in the presence of Gly, and the blue trace represents currents measured in the presence of 10  $\mu$ M GNE-6901 where Glu was removed in the presence of Gly. The green trace represents the converse experiment where Gly was rapidly removed in the presence of Glu in the presence of 10  $\mu$ M GNE-6901.

(F) Example recordings showing the same experimental paradigm as in (E) except with 30  $\mu$ M GNE-8324. Note that delayed deactivation was only observed when Glu was removed in the presence of Gly, but not in the converse experiment.

inter-subunit interface underscores the unique value of this site for selective modulation of NMDARs.

The LBD plays a critical role in AMPAR and NMDAR activation (Mayer, 2011; Furukawa et al., 2005; Gielen et al., 2008) and is the binding site of AMPAR PAMs (Jin et al., 2005; Sun et al., 2002). While some of the identified NMDAR PAMs were found to achieve significant selectivity against AMPARs (Figure 3), the structural basis for this selectivity is not immediately obvious. Intriguingly, functional experiments showed that while the selective compound GNE-6901 had no significant effect on AMPARs by itself, it could compete with the AMPAR potentiation caused by GNE-3419 (Figure S3). One hypothesis to explain this interaction is that some of our compounds can function as SAMs at the

LBD interface site of AMPARs, and, despite having no direct effect, can compete with the binding of compounds that do exhibit AMPAR PAM activity. We were not able to obtain a crystal structure of our AMPAR-selective compounds to verify this hypothesis. However, silent competitive inhibition of small-molecule modulators via inefficacious binding is not unprecedented, as exemplified by fluoxetine at the GABA<sub>A</sub>R benzodiazepine site (Rudolph and Knoflach, 2011) and substituted 4MP-TQS series compounds at nAChRs (Gill-Thind et al., 2015).

The detailed characterization of PAM effects on NMDAR channel function provides further insight into the basis of this allosteric modulation. In particular, the slowing of channel deactivation following removal of Glu, but not Gly (Figure 5), shows

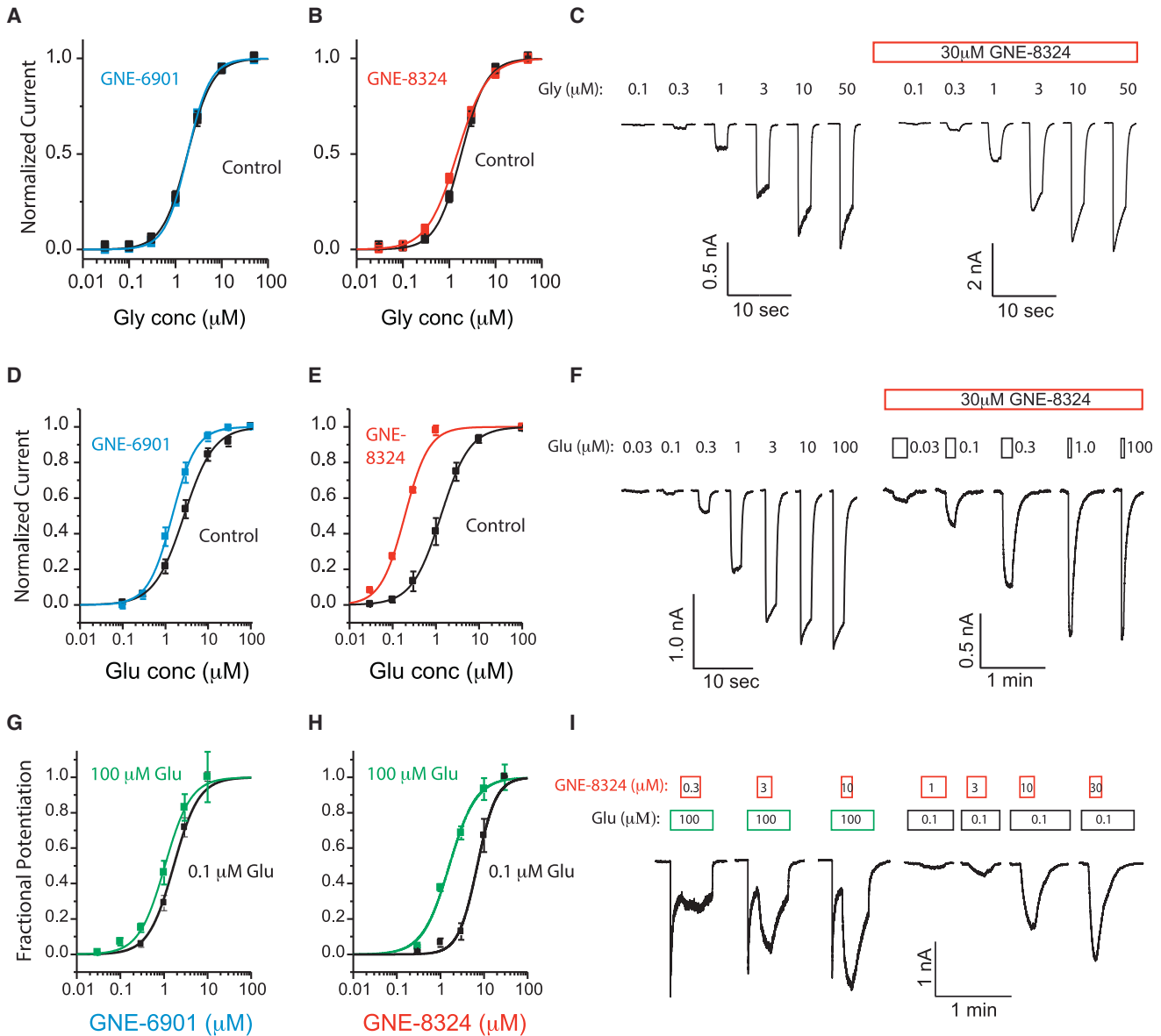


**Figure 6. GNE-6901 and GNE-8324 Have Differential Effects on NMDAR Glu Potency and Differential Dependence on Glu Concentration**

(A) Lack of effect of GNE-6901 (10  $\mu\text{M}$ ) on Gly potency (baseline  $\text{EC}_{50}$  =  $1.82 \pm 0.14 \mu\text{M}$ ; GNE-6901 =  $1.83 \pm 0.16 \mu\text{M}$ ;  $p > 0.05$ ). Data are shown as mean  $\pm$  SEM ( $n = 5-7$  patches/experiment).

(B) Lack of effect of GNE-8324 (30  $\mu\text{M}$ ) on Gly potency (baseline  $\text{EC}_{50}$  =  $1.82 \pm 0.14 \mu\text{M}$ ; GNE-8324 =  $1.48 \pm 0.2 \mu\text{M}$ ;  $p > 0.05$ ) is shown.

(C) GNE-8324 example traces. The  $\text{EC}_{50}$  for Gly was measured before and after the addition of 30  $\mu\text{M}$  GNE-8324 in the continuous presence of 100  $\mu\text{M}$  Glu. Brief 2-s pulses of Gly at varying concentrations were used to determine the  $\text{EC}_{50}$  values.

(D) Small effect of GNE-6901 (10  $\mu\text{M}$ ) on Glu potency (baseline  $\text{EC}_{50}$  =  $2.7 \pm 0.26 \mu\text{M}$ ; GNE-6901 =  $1.4 \pm 0.35 \mu\text{M}$ ;  $p < 0.05$ ) is shown.

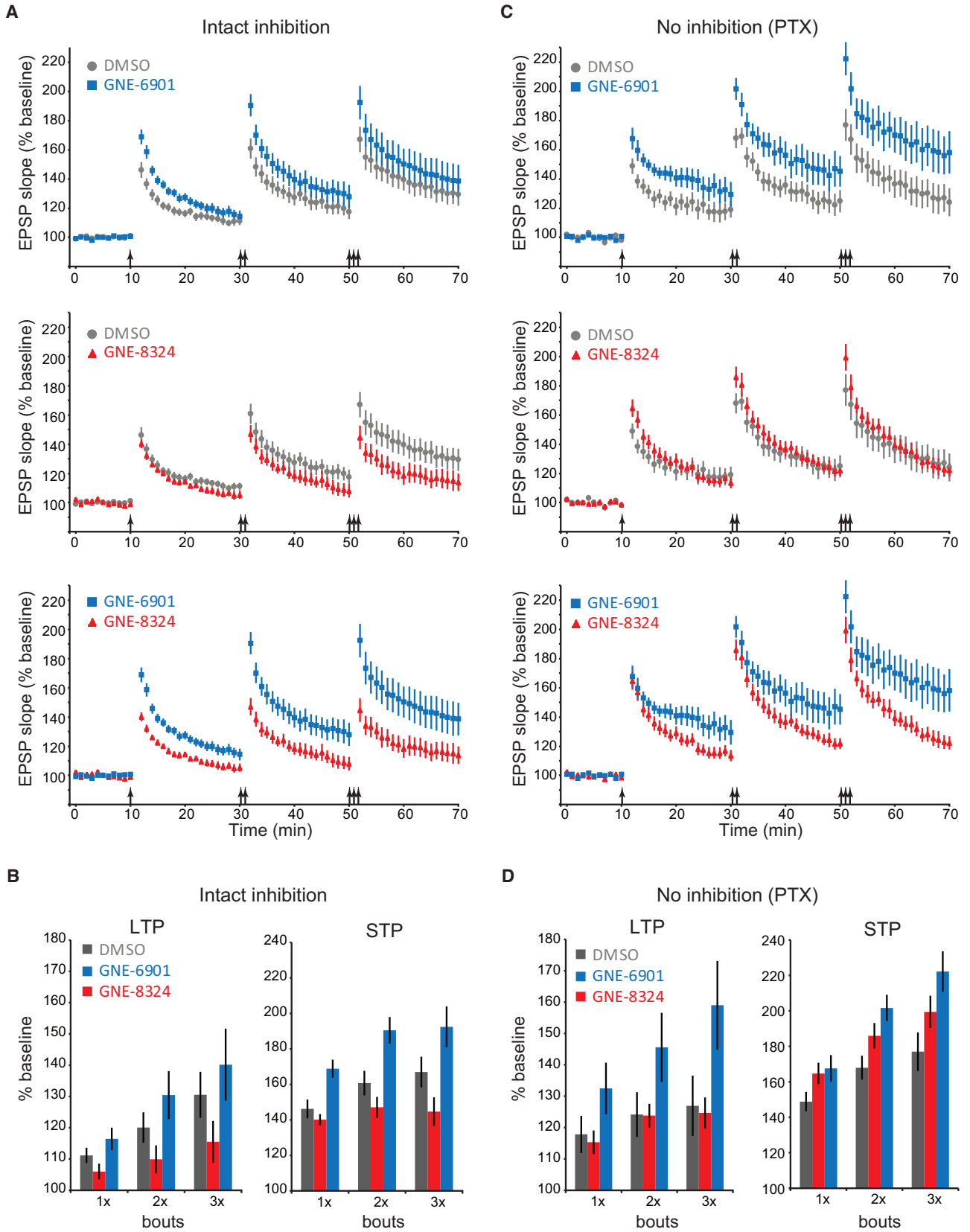
(E) Large effect of GNE-8324 (30  $\mu\text{M}$ ) on Glu potency (baseline  $\text{EC}_{50}$  =  $1.3 \pm 0.13 \mu\text{M}$ ; GNE-8324 =  $0.19 \pm 0.05 \mu\text{M}$ ;  $p < 0.01$ ) is shown.

(F) GNE-8324 example traces. The  $\text{EC}_{50}$  for Glu was measured before and after the addition of 30  $\mu\text{M}$  GNE-8324 in the continuous presence of 50  $\mu\text{M}$  Gly. Brief 2-s pulses of Glu at various concentrations were used to determine the  $\text{EC}_{50}$  values.

(G) Small effect of Glu concentration on GNE-6901  $\text{EC}_{50}$  (low Glu  $\text{EC}_{50}$  =  $1.7 \pm 0.12 \mu\text{M}$ ; high Glu =  $1.0 \pm 0.27 \mu\text{M}$ ;  $p < 0.05$ ) is shown.

(H) Large effect of Glu on GNE-8324  $\text{EC}_{50}$  (low Glu  $\text{EC}_{50}$  =  $7.1 \pm 1.3 \mu\text{M}$ ; high Glu =  $1.59 \pm 0.12 \mu\text{M}$ ;  $p < 0.01$ ) is shown.

(I) GNE-8324 example traces. Pulses of GNE-8324 at various concentrations were tested in the presence of either low Glu (0.1  $\mu\text{M}$ ) or high Glu (100  $\mu\text{M}$ ), all in the continuous presence of 50  $\mu\text{M}$  Gly. Examples of continuously recorded raw data for all experiments in this figure with GNE-6901 and GNE-8324 are shown in Figure S6.



(legend on next page)

that while the modulator-binding site is located between the binding sites for the agonist and co-agonist, only Glu deactivation kinetics is affected. This is supported by the shift in NMDAR Glu, but not Gly, potency in the presence of GluN2A PAMs (Figure 6). Thus, while both GNE-6901 and GNE-8324 enhanced NMDAR currents during saturating agonist application, these compounds were differentiated by the magnitude of effects on Glu potency and slowing of deactivation following Glu removal, with GNE-8324 having much larger effects. A simple model of the transitions between unbound LBDs, LBDs bound by either PAM or Glu, and LBDs bound by both PAM and Glu, predicts that the magnitude of PAM effect on Glu affinity should be roughly equivalent to the magnitude of Glu effect on PAM affinity (Figures S6H–S6J). Indeed, this is what we observed, with a small impact of GNE-6901 on Glu potency (<2-fold shift), matching the small dependence of GNE-6901 potency on Glu concentration (<2-fold shift), and a larger impact of GNE-8324 on Glu potency (6.8-fold shift), approximately matching the larger dependence of GNE-8324 potency on Glu concentration (4.5-fold shift) (Figure 6). The structural basis for the differences in the nature of potentiation by GNE-6901 and GNE-8324 is not obvious from our data, however, as alignment of the crystal structures of compound-bound LBDs only show subtle differences.

In addition to qualitative differences at the level of NMDAR current modulation, GNE-6901 and GNE-8324 also showed qualitative differences in their impacts during LTP induction (Figure 7). Under basal recording conditions, these compounds exerted opposite effects on synaptic plasticity, with GNE-6901 significantly enhancing and GNE-8324 significantly impairing STP, and similar opposite trends were observed for the impacts of the PAMs on LTP. However, when inhibition, which can be recruited by polysynaptic activation during plasticity induction, was blocked, GNE-8324 no longer impaired plasticity, but rather a small but significant enhancement of STP was seen. At the same time, an even more robust enhancement of plasticity by GNE-6901 was seen in the absence of inhibition. These results suggest that, in general, GluN2A PAMs can have at least two sites of action during plasticity induction as follows: (1) potentiation of pyramidal neuron NMDARs, which directly mediate STP and LTP (Malenka and Nicoll, 1993; Park et al., 2014); and (2) potentiation

of NMDARs on interneurons, which results in interneuron activation and pyramidal neuron hyperpolarization, thus opposing induction of synaptic potentiation.

Direct measurement of NMDAR responses in pyramidal neurons and interneurons showed that, while both PAMs enhance interneuron NMDARs, GNE-6901, but not GNE-8324, enhances pyramidal neuron NMDARs (Figure 8). Thus, the differential plasticity impacts can be explained by the dominance of pyramidal neuron effects of GNE-6901 over inhibition-dependent effects, while in the case of GNE-8324, inhibition-dependent effects dominate due to the lack of pyramidal neuron effects. One possibility is that the relative lack of GNE-8324 effects on pyramidal neurons derives from the significantly greater glutamate dependence of GNE-8324 compared to GNE-6901 (Figures 6G and 6H). This could hamper the ability of GNE-8324 to impact NMDARs at synapses onto pyramidal neurons where high-density transporters on astrocytes rapidly clear extracellular glutamate to maintain very low synaptic glutamate levels within milliseconds of presynaptic release (Clements et al., 1992). On the other hand, we speculate that astrocyte membranes near hippocampal interneurons could contain lower transporter densities than those surrounding synapses on pyramidal neurons, thus allowing stronger effects of Glu-dependent PAMs. This would be similar to the case in the cerebellum, where parallel fiber synapses onto interneurons are surrounded by lower transporter densities than those synapsing onto Purkinje cells (Chaudhry et al., 1995).

Overall, the identification of compounds that allow selective positive modulation of GluN2A NMDARs should be useful for dissecting NMDAR activation mechanisms, exploring cell-type-specific roles for GluN2A-containing NMDARs, and understanding the roles of GluN2A NMDARs in various brain circuits. These tools will not only provide insight into the physiological roles of GluN2A-containing NMDARs but also offer a means to test potential therapeutic benefits of NMDAR enhancement in model systems related to schizophrenia, epilepsy, and Alzheimer's and other diseases. For example, while current efforts to target NMDAR hypofunction in schizophrenia have relied on indirect and nonspecific enhancement of NMDARs via elevating Gly levels or activating mGluRs (Dunlop and Brandon, 2015), we have demonstrated that direct and selective pharmacological enhancement of GluN2A-containing NMDARs is possible.

### Figure 7. Differential Effects of GNE-6901 and GNE-8324 on LTP Induction

(A) LTP was induced with one, then two, then three bouts of a weak induction protocol (arrows). Experiments were performed in the presence of 10  $\mu$ M GNE-6901 (blue,  $n = 13$  slices), 30  $\mu$ M GNE-8324 (red,  $n = 12$  slices), or DMSO vehicle control (gray,  $n = 12$ ). For clarity, data from each pair of conditions are plotted separately (shown as mean  $\pm$  SEM). PAM concentrations were selected based on having approximate maximal effects on peak current recorded from GluN2A cell lines.

(B) LTP was quantified as the average baseline-normalized EPSP slope during the last 5 min of each portion of the experiment (following one, two, or three bouts). There was a significant effect of treatment ( $F(2,101) = 6.24$ ;  $p = 0.003$ ) and bout number ( $F(2,101) = 5.52$ ;  $p = 0.005$ ) on LTP, but no significant interaction between treatment and bout number ( $F(4,101) = 0.34$ ;  $p = 0.85$ ). STP was quantified from the normalized EPSP slope of the data point collected 1 min after induction. There was a significant effect of treatment ( $F(2,101) = 23.30$ ;  $p < 0.001$ ) and bout number ( $F(2,101) = 4.39$ ;  $p = 0.015$ ) on STP, but no significant interaction between treatment and bout number ( $F(4,101) = 0.55$ ;  $p = 0.70$ ). Data are shown as mean  $\pm$  SEM. Additional statistical analysis of comparisons between treatment groups is reported in the main text.

(C) LTP experiments were performed as in (A) but in the presence of 100  $\mu$ M PTX to block synaptic inhibition (GNE-6901,  $n = 11$ ; GNE-8324,  $n = 11$ ; DMSO,  $n = 12$ ). (D) LTP and STP in the presence of PTX were quantified as in (B). There was a significant effect of treatment ( $F(2,93) = 8.00$ ;  $p < 0.001$ ), but not bout number ( $F(2,93) = 2.51$ ;  $p = 0.087$ ) on LTP. There was a significant effect of treatment ( $F(2,93) = 12.13$ ;  $p < 0.001$ ) and bout ( $F(2,93) = 17.51$ ;  $p < 0.001$ ) on STP, but no significant interaction between treatment and bout number ( $F(4,93) = 0.71$ ;  $p = 0.59$ ). Data are shown as mean  $\pm$  SEM and additional statistical analysis of comparisons between treatment groups is reported in the main text.

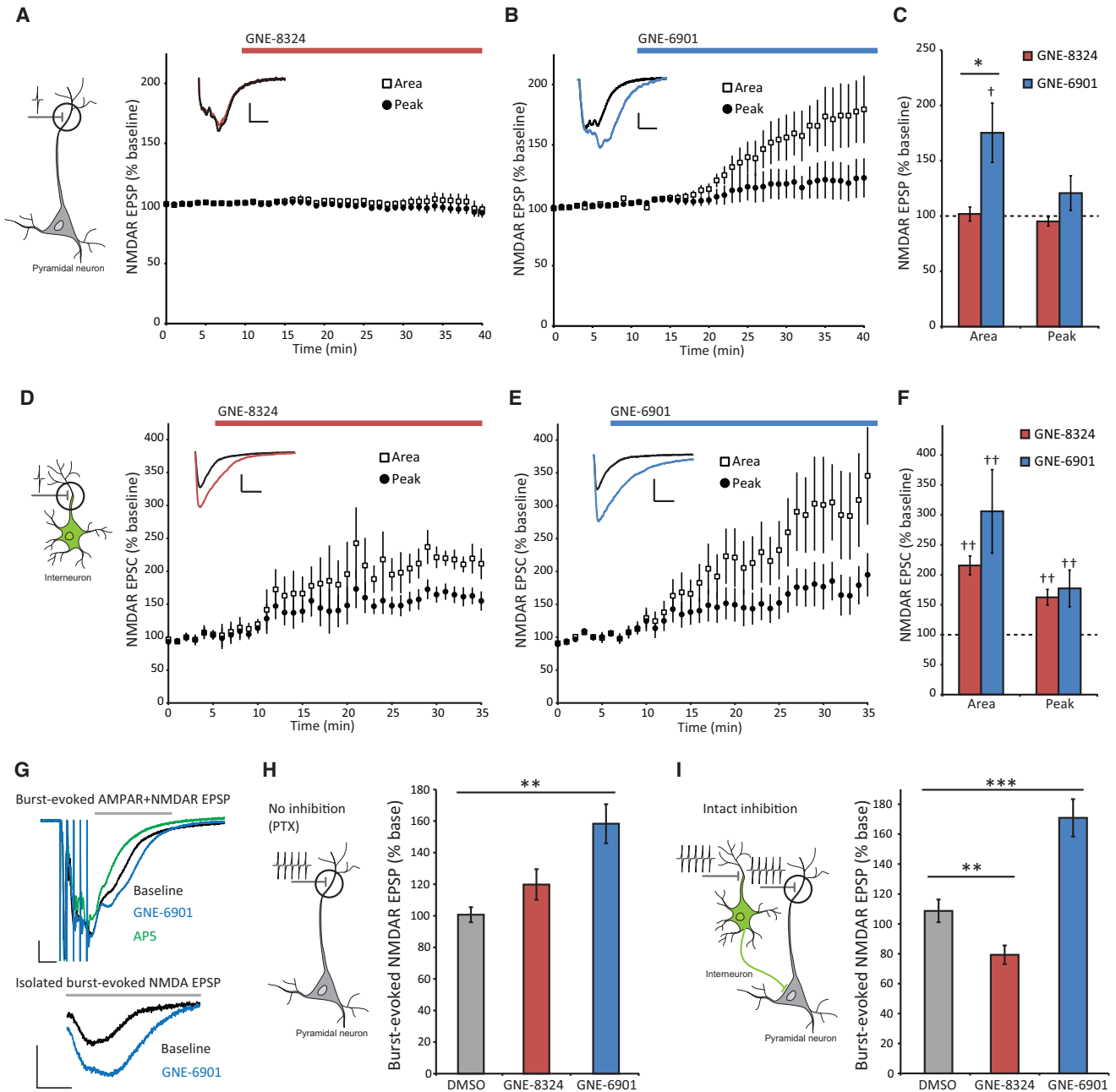


**Figure 8. Effects of GNE-6901 and GNE-8324 on Pyramidal Neuron and Interneuron NMDAR Responses**

(A) Isolated NMDAR EPSPs were recorded from CA1 pyramidal neurons in response to single electrical stimulations of presynaptic fibers. Application of 30  $\mu$ M GNE-8324 had little effect on pyramidal neuron NMDAR EPSPs ( $n = 9$ , example traces are inset; scale bars, 0.25 mV and 50 ms). (B) Application of 10  $\mu$ M GNE-6901 potentiated pyramidal neuron NMDAR EPSPs ( $n = 10$ , example traces are inset; scale bars, 0.25 mV and 50 ms). (C) GNE-6901 significantly enhanced the pyramidal neuron NMDAR EPSP area measured at the last 5 min of the recording compared to baseline ( $\dagger p < 0.05$ ). The NMDAR EPSP area at the end of the experiment was significantly greater for GNE-6901 compared to GNE-8324 ( $* p < 0.05$ ). (D) Isolated NMDAR EPSCs were recorded using whole-cell recordings targeted to GFP-positive neurons in the stratum radiatum of CA1 from GAD67-GFP reporter mice. Application of 30  $\mu$ M GNE-8324 potentiated interneuron NMDAR EPSCs ( $n = 9$ , example traces are inset; scale bars, 100 pA and 50 ms). (E) Application of 10  $\mu$ M GNE-6901 potentiated interneuron NMDAR EPSCs ( $n = 9$ , example traces are inset; scale bars, 100 pA and 50 ms). (F) GNE-6901 and GNE-8324 both significantly enhanced the peak and area of interneuron NMDAR EPSCs measured at the last 5 min of the recording compared to baseline ( $\dagger\dagger p < 0.01$ ). Neither NMDAR EPSC area nor peak at the end of the experiment significantly differed between GNE-6901 and GNE-8324 ( $p > 0.05$ ). (G) Burst-evoked NMDAR EPSPs in pyramidal neurons were measured in response to five pulses at 100 Hz. Because burst-evoked responses were observed to run down under the conditions for isolated NMDAR EPSPs, mixed AMPAR + NMDAR EPSPs were measured, which allowed a stable baseline response to be obtained. After recordings stabilized, PAM was applied for 40 min, followed by D-AP5 application to block the NMDAR component of the response (top).

(legend continued on next page)

Although the compounds reported here do not have appropriate properties for use in vivo, the discovery of a new allosteric site at the LBD interface expands on the previous knowledge of NMDAR allosteric sites, which previously have been mostly restricted to the ATD region (Zhu and Paoletti, 2015). Similar to AMPARs, the LBD dimer interface now emerges as a key allosteric locus for fine-tuning of NMDAR activity in a subunit-specific manner, which should provide the basis for future development of therapeutics for brain disorders.

## EXPERIMENTAL PROCEDURES

Additional details of the procedures are provided in the Supplemental Experimental Procedures.

### Cell Lines

Doxycycline-inducible (Dox) cell lines that express either GluN1/GluN2A or GluN1/GluN2B were generated in both CHO and HEK293 parental cell lines, and Dox-inducible cell lines that express either GluN1/GluN2C or GluN1/GluN2D were obtained from Chantest. The cDNAs for Dox-inducible cell lines that express either the flip or flop isoform of the human GluA2 AMPAR included a Gln at position 607 to impart  $\text{Ca}^{2+}$  permeability (which is absent when there is an Arg at this position as normally results from highly efficient RNA editing of the Gln codon in genomic DNA) in order to enable  $\text{Ca}^{2+}$  influx assays.

### $\text{Ca}^{2+}$ Influx Assays

The HTS of 1.4 million compounds was conducted using a  $\text{Ca}^{2+}$  influx assay utilizing GluN1/GluN2A-expressing HEK cells. Cells were loaded with a  $\text{Ca}^{2+}$ -sensitive dye and plated in acidic buffer to prevent channel opening. The proton block was reversed at the time of assay by the addition of test compound in neutralizing buffer containing saturating glycine. Endogenous glutamate from cells was present at a concentration producing submaximal activation, allowing for detection of compounds that enhance NMDAR  $\text{Ca}^{2+}$  influx.

### Purification and Crystallization of the GluN1/GluN2A and GluA2 LBD Complexes

For the human GluN1 LBD, a construct containing residues M394–K544 (S1) and R663–S800 (S2) connected by a Gly-Thr linker was generated based on the strategy for rat GluN1 LBD (Furukawa and Gouaux, 2003). The human GluN2A LBD construct, containing residues P401–R539 (S1) and Q661–N802 (S2) connected by a Gly-Thr linker, was based on the strategy for rat GluN2A LBD (Furukawa et al., 2005). For the human GluA2 LBD, a construct (previously described as S1S2J variant) was generated containing residues N392–K506 (S1) and P632–S775 (S2) connected by a Gly-Thr linker (Armstrong and Gouaux, 2000). This construct contained GluA2 flip residue Ser754 and flop residues Asn744, Ala745, and Leu758.

### Animals

All animal studies were approved by the Genentech Institutional Animal Care and Use Committee (IACUC) and conducted in accordance with the NIH Guide for the Care and Use of Laboratory Animals. The 6- to 9-week-old GluN2A KO mice (Kadotani et al., 1996) and WT littermates were used for whole-cell recordings from pyramidal neurons, and GAD67-GFP knockin mice were used

when targeting interneurons. The 2- to 3-month-old C57BL/6 mice were used for field recordings.

### Electrophysiology

For two-electrode voltage-clamp (TEVC) recordings of diheteromeric NMDARs, *Xenopus* oocytes were injected with mRNA for hGluN1-1a and hGluN2A or hGluN2B, using either WT or mutant mRNA. Experiments comparing GluN1-1a and GluN1-1b splice variants were performed using rGluN1-1a, rGluN1-1b, and rGluN2A. Similarly, experiments with chimeric/deleted ATD subunits were performed using rodent clones. Selective expression of triheteromeric NMDARs in *Xenopus* oocytes was performed as previously described (Stroebel et al., 2014).

Whole-cell patch-clamp recordings from cell lines were performed using the Dynaflo Resolve rapid solution exchange system (Collectricon). This system consists of a quartz glass perfusion chip with a linear array of 16 continuously flowing perfusion channels that are moved past the patched cell with a solution exchange time of ~10–30 ms.

Field EPSP recordings were made from the stratum radiatum of area CA1 of the hippocampus in response to electrical stimulation of the Schaffer collateral pathway. For experiments examining the direct effects of compounds on AMPAR EPSPs, 50  $\mu\text{M}$  D-(-)-2-amino-5-phosphonopentanoic acid (AP5) was included. Field NMDAR EPSPs were recorded in the presence of 10  $\mu\text{M}$  NBQX, 100  $\mu\text{M}$  PTX, and 10  $\mu\text{M}$  strychnine with reduced  $\text{Mg}^{2+}$  (0.2 mM). For plasticity experiments, a single bout of weak induction stimuli consisted of five pulses at 100 Hz, and plasticity was induced using one, two, or three bouts of this protocol (30-s inter-bout interval). EPSP measurement resumed 1 min after induction so that post-tetanic potentiation (PTP), which is a presynaptic phenomenon, did not contribute to the measurement of STP, which, along with LTP, is a postsynaptic NMDAR-dependent phenomenon (Malenka and Nicoll, 1993; Park et al., 2014). Statistical significances of LTP and STP were assessed using a two-way ANOVA with treatment and bout number as factors, and burst-evoked EPSPs were assessed with a one-way ANOVA with treatment as a factor. When there was a significant effect of treatment, follow-up tests assessing significance of differences between different treatments were performed using the Holm-Sidak method. In experiments where only two groups were compared, significance was assessed using a t test.

Whole-cell recordings of NMDAR EPSCs in CA1 pyramidal neurons in response to local stimulation were recorded at a holding potential of  $-70$  mV in the presence of reduced  $\text{Mg}^{2+}$  (0.5 mM), and they were isolated using 10  $\mu\text{M}$  NBQX disodium salt and 100  $\mu\text{M}$  PTX. AP5 applied at the end of the recording confirmed isolation of pure NMDAR EPSCs.

### ACCESSION NUMBERS

The accession numbers for the structures reported in this paper are PDB: 5H8F (apo GluN1/N2A), 5H8H (GNE3419 GluN1/N2A), 5H8N (compound 6 GluN1/N2A), 5H8Q (GNE8324 GluN1/N2A), 5H8R (GNE6901 GluN1/N2A), and 5H8S (GNE3419 GluA1).

### SUPPLEMENTAL INFORMATION

Supplemental Information includes Supplemental Experimental Procedures, eight figures, and one table and can be found with this article online at <http://dx.doi.org/10.1016/j.neuron.2016.01.016>.

Subtraction of the isolated AMPA response measured in AP5 was used to calculate the baseline and PAM-treated NMDAR EPSPs (bottom). To minimize contamination from stimulus artifacts and population spikes, the burst-evoked NMDAR EPSP was quantified from the portion of the response immediately following stimulation (gray bar). Scale bars, 0.5 mV and 25 ms.

(H) When burst-evoked NMDAR EPSPs were recorded with inhibition blocked ( $n = 10$ , GNE-6901;  $n = 11$ , GNE-8324;  $n = 12$ , DMSO), there was a significant effect of treatment ( $F(2,30) = 10.52$ ;  $p < 0.001$ ), which corresponded with a trend toward increased area with GNE-8324 and a significant increase with GNE-6901 compared to vehicle (\*\* $p < 0.01$ ).

(I) When burst-evoked NMDAR EPSPs were recorded with intact inhibition ( $n = 11$ , GNE-6901;  $n = 12$ , GNE-8324;  $n = 10$ , DMSO), there was a significant effect of treatment ( $F(2,30) = 26.99$ ;  $p < 0.001$ ), which corresponded with a significantly reduced area with GNE-8324 (\*\* $p < 0.01$ ) and a significantly increased area with GNE-6901 compared to vehicle (\*\* $p < 0.001$ ).

Data are shown as mean  $\pm$  SEM.

## AUTHOR CONTRIBUTIONS

D.H.H., P.J.L., P.P., M.S., Q.Z., and J.E.H. conceived and designed experiments. D.H.H., P.J.L., T.G., Y.C., T.-M.W., P.R., A.G., H.J.A.W., and J.E.H. conducted experiments. M.V., B.D.S., and J.B.S. designed and synthesized chemicals. D.H.H., P.J.L., P.P., M.S., and J.E.H. wrote the paper.

## ACKNOWLEDGMENTS

The authors thank Kimberly Scearce-Levie and Justin Elstrott for providing valuable comments on the manuscript, Yichin Liu and James Herrington for advice on the design of  $\text{Ca}^{2+}$  influx assays, Antonio DiPasquale (UC Berkeley X-ray Crystallography Facility) for small molecule X-ray crystallography support, and Pharmaron for chemistry support. The Stanford Synchrotron Radiation Lightsource (SSRL) is supported by the U.S. Department of Energy (DOE) Office of Science under contract DE-AC02-76SF00515. The SSRL Structural Molecular Biology Program is supported by the DOE Office of Biological and Environmental Research and by the NIH, National Institute of General Medical Sciences (including P41GM103393). Beamline 08ID-1 at the Canadian Light Source is supported by the Natural Sciences and Engineering Research Council of Canada, the National Research Council Canada, the Canadian Institutes of Health Research, the Province of Saskatchewan, Western Economic Diversification Canada, and the University of Saskatchewan. The Advanced Photon Source is a U.S. DOE Office of Science User Facility operated by Argonne National Laboratory under contract DE-AC02-06CH11357. T.G. and P.P. were supported by grants from the Pierre-Gilles-de-Gennes Foundation and the Fondation pour la Recherche Médicale (FRM, Equipe FRM DEQ20130326520). D.H.H., P.J.L., T.-M.W., P.R., A.G., H.J.A.W., M.V., B.D.S., J.B.S., M.S., Q.Z., and J.E.H. are current or former employees of Genentech, Inc.

Received: June 19, 2015

Revised: November 24, 2015

Accepted: January 6, 2016

Published: February 11, 2016

## REFERENCES

- Armstrong, N., and Gouaux, E. (2000). Mechanisms for activation and antagonism of an AMPA-sensitive glutamate receptor: crystal structures of the GluR2 ligand binding core. *Neuron* 28, 165–181.
- Belforte, J.E., Zsiros, V., Sklar, E.R., Jiang, Z., Yu, G., Li, Y., Quinlan, E.M., and Nakazawa, K. (2010). Postnatal NMDA receptor ablation in corticolimbic interneurons confers schizophrenia-like phenotypes. *Nat. Neurosci.* 13, 76–83.
- Bettini, E., Sava, A., Griffante, C., Carignani, C., Buson, A., Capelli, A.M., Negri, M., Andreatta, F., Senar-Sancho, S.A., Guiral, L., and Cardullo, F. (2010). Identification and characterization of novel NMDA receptor antagonists selective for NR2A- over NR2B-containing receptors. *J. Pharmacol. Exp. Ther.* 335, 636–644.
- Carvill, G.L., Regan, B.M., Yendle, S.C., O’Roak, B.J., Lozovaya, N., Bruneau, N., Burnashev, N., Khan, A., Cook, J., Geraghty, E., et al. (2013). GRIN2A mutations cause epilepsy-aphasia spectrum disorders. *Nat. Genet.* 45, 1073–1076.
- Chaudhry, F.A., Lehre, K.P., van Lookeren Campagne, M., Ottersen, O.P., Danbolt, N.C., and Storm-Mathisen, J. (1995). Glutamate transporters in glial plasma membranes: highly differentiated localizations revealed by quantitative ultrastructural immunocytochemistry. *Neuron* 15, 711–720.
- Clements, J.D., Lester, R.A., Tong, G., Jahr, C.E., and Westbrook, G.L. (1992). The time course of glutamate in the synaptic cleft. *Science* 258, 1498–1501.
- Costa, R.O., Lacor, P.N., Ferreira, I.L., Resende, R., Auberson, Y.P., Klein, W.L., Oliveira, C.R., Rego, A.C., and Pereira, C.M. (2012). Endoplasmic reticulum stress occurs downstream of GluN2B subunit of N-methyl-D-aspartate receptor in mature hippocampal cultures treated with amyloid- $\beta$  oligomers. *Aging Cell* 11, 823–833.
- Coyle, J.T., Tsai, G., and Goff, D. (2003). Converging evidence of NMDA receptor hypofunction in the pathophysiology of schizophrenia. *Ann. N.Y. Acad. Sci.* 1003, 318–327.
- Dunlop, J., and Brandon, N.J. (2015). Schizophrenia drug discovery and development in an evolving era: are new drug targets fulfilling expectations? *J. Psychopharmacol. (Oxford)* 29, 230–238.
- Ferreira, I.L., Bajouco, L.M., Mota, S.I., Auberson, Y.P., Oliveira, C.R., and Rego, A.C. (2012). Amyloid beta peptide 1–42 disturbs intracellular calcium homeostasis through activation of GluN2B-containing N-methyl-D-aspartate receptors in cortical cultures. *Cell Calcium* 51, 95–106.
- Furukawa, H., and Gouaux, E. (2003). Mechanisms of activation, inhibition and specificity: crystal structures of the NMDA receptor NR1 ligand-binding core. *EMBO J.* 22, 2873–2885.
- Furukawa, H., Singh, S.K., Mancusso, R., and Gouaux, E. (2005). Subunit arrangement and function in NMDA receptors. *Nature* 438, 185–192.
- Gielen, M., Le Goff, A., Stroebel, D., Johnson, J.W., Neyton, J., and Paoletti, P. (2008). Structural rearrangements of NR1/NR2A NMDA receptors during allosteric inhibition. *Neuron* 57, 80–93.
- Gill-Thind, J.K., Dhankher, P., D’Oyley, J.M., Sheppard, T.D., and Millar, N.S. (2015). Structurally similar allosteric modulators of  $\alpha 7$  nicotinic acetylcholine receptors exhibit five distinct pharmacological effects. *J. Biol. Chem.* 290, 3552–3562.
- Gonzalez-Burgos, G., and Lewis, D.A. (2012). NMDA receptor hypofunction, parvalbumin-positive neurons, and cortical gamma oscillations in schizophrenia. *Schizophr. Bull.* 38, 950–957.
- Gray, J.A., Shi, Y., Usui, H., During, M.J., Sakimura, K., and Nicoll, R.A. (2011). Distinct modes of AMPA receptor suppression at developing synapses by GluN2A and GluN2B: single-cell NMDA receptor subunit deletion in vivo. *Neuron* 71, 1085–1101.
- Hansen, K.B., Ogden, K.K., and Traynelis, S.F. (2012). Subunit-selective allosteric inhibition of glycine binding to NMDA receptors. *J. Neurosci.* 32, 6197–6208.
- Hansen, K.B., Ogden, K.K., Yuan, H., and Traynelis, S.F. (2014). Distinct functional and pharmacological properties of Triheteromeric GluN1/GluN2A/GluN2B NMDA receptors. *Neuron* 81, 1084–1096.
- Hanson, J.E., Weber, M., Meilandt, W.J., Wu, T., Luu, T., Deng, L., Shamloo, M., Sheng, M., Scearce-Levie, K., and Zhou, Q. (2013). GluN2B antagonism affects interneurons and leads to immediate and persistent changes in synaptic plasticity, oscillations, and behavior. *Neuropsychopharmacology* 38, 1221–1233.
- Hardingham, G.E., and Bading, H. (2010). Synaptic versus extrasynaptic NMDA receptor signalling: implications for neurodegenerative disorders. *Nat. Rev. Neurosci.* 11, 682–696.
- Hatton, C.J., and Paoletti, P. (2005). Modulation of triheteromeric NMDA receptors by N-terminal domain ligands. *Neuron* 46, 261–274.
- Heng, M.Y., Detloff, P.J., Wang, P.L., Tsien, J.Z., and Albin, R.L. (2009). In vivo evidence for NMDA receptor-mediated excitotoxicity in a murine genetic model of Huntington disease. *J. Neurosci.* 29, 3200–3205.
- Javitt, D.C., and Zukin, S.R. (1991). Recent advances in the phencyclidine model of schizophrenia. *Am. J. Psychiatry* 148, 1301–1308.
- Jin, R., Clark, S., Weeks, A.M., Dudman, J.T., Gouaux, E., and Partin, K.M. (2005). Mechanism of positive allosteric modulators acting on AMPA receptors. *J. Neurosci.* 25, 9027–9036.
- Kadotani, H., Hirano, T., Masugi, M., Nakamura, K., Nakao, K., Katsuki, M., and Nakanishi, S. (1996). Motor discoordination results from combined gene disruption of the NMDA receptor NR2A and NR2C subunits, but not from single disruption of the NR2A or NR2C subunit. *J. Neurosci.* 16, 7859–7867.
- Karakas, E., and Furukawa, H. (2014). Crystal structure of a heterotetrameric NMDA receptor ion channel. *Science* 344, 992–997.
- Krystal, J.H., Karper, L.P., Seibyl, J.P., Freeman, G.K., Delaney, R., Bremner, J.D., Heninger, G.R., Bowers, M.B., Jr., and Charney, D.S. (1994). Subanesthetic effects of the noncompetitive NMDA antagonist, ketamine, in

- humans. Psychotomimetic, perceptual, cognitive, and neuroendocrine responses. *Arch. Gen. Psychiatry* 51, 199–214.
- Lee, C.H., Lü, W., Michel, J.C., Goehring, A., Du, J., Song, X., and Gouaux, E. (2014). NMDA receptor structures reveal subunit arrangement and pore architecture. *Nature* 511, 191–197.
- Lemke, J.R., Lal, D., Reinthaler, E.M., Steiner, I., Nothnagel, M., Alber, M., Geider, K., Laube, B., Schwake, M., Finsterwalder, K., et al. (2013). Mutations in GRIN2A cause idiopathic focal epilepsy with rolandic spikes. *Nat. Genet.* 45, 1067–1072.
- Lesca, G., Rudolf, G., Bruneau, N., Lozovaya, N., Labalme, A., Boutry-Kryza, N., Salmi, M., Tsitsadze, T., Addis, L., Motte, J., et al. (2013). GRIN2A mutations in acquired epileptic aphasia and related childhood focal epilepsies and encephalopathies with speech and language dysfunction. *Nat. Genet.* 45, 1061–1066.
- Liu, Y., Wong, T.P., Aarts, M., Rooyackers, A., Liu, L., Lai, T.W., Wu, D.C., Lu, J., Tymianski, M., Craig, A.M., and Wang, Y.T. (2007). NMDA receptor subunits have differential roles in mediating excitotoxic neuronal death both in vitro and in vivo. *J. Neurosci.* 27, 2846–2857.
- Malenka, R.C., and Nicoll, R.A. (1993). NMDA-receptor-dependent synaptic plasticity: multiple forms and mechanisms. *Trends Neurosci.* 16, 521–527.
- Martel, M.A., Ryan, T.J., Bell, K.F., Fowler, J.H., McMahon, A., Al-Mubarak, B., Komiya, N.H., Horsburgh, K., Kind, P.C., Grant, S.G., et al. (2012). The subtype of GluN2 C-terminal domain determines the response to excitotoxic insults. *Neuron* 74, 543–556.
- Mayer, M.L. (2011). Emerging models of glutamate receptor ion channel structure and function. *Structure* 19, 1370–1380.
- Milnerwood, A.J., Gladding, C.M., Pouladi, M.A., Kaufman, A.M., Hines, R.M., Boyd, J.D., Ko, R.W., Vasuta, O.C., Graham, R.K., Hayden, M.R., et al. (2010). Early increase in extrasynaptic NMDA receptor signaling and expression contributes to phenotype onset in Huntington's disease mice. *Neuron* 65, 178–190.
- Mohn, A.R., Gainetdinov, R.R., Caron, M.G., and Koller, B.H. (1999). Mice with reduced NMDA receptor expression display behaviors related to schizophrenia. *Cell* 98, 427–436.
- Paoletti, P., Bellone, C., and Zhou, Q. (2013). NMDA receptor subunit diversity: impact on receptor properties, synaptic plasticity and disease. *Nat. Rev. Neurosci.* 14, 383–400.
- Park, P., Volianskis, A., Sanderson, T.M., Bortolotto, Z.A., Jane, D.E., Zhuo, M., Kaang, B.K., and Collingridge, G.L. (2014). NMDA receptor-dependent long-term potentiation comprises a family of temporally overlapping forms of synaptic plasticity that are induced by different patterns of stimulation. *Philos. Trans. R. Soc. Lond. B Biol. Sci.* 369, 20130131.
- Rauner, C., and Köhr, G. (2011). Triheteromeric NR1/NR2A/NR2B receptors constitute the major N-methyl-D-aspartate receptor population in adult hippocampal synapses. *J. Biol. Chem.* 286, 7558–7566.
- Rönicke, R., Mikhaylova, M., Rönicke, S., Meinhardt, J., Schröder, U.H., Fändrich, M., Reiser, G., Kreutz, M.R., and Reymann, K.G. (2011). Early neuronal dysfunction by amyloid  $\beta$  oligomers depends on activation of NR2B-containing NMDA receptors. *Neurobiol. Aging* 32, 2219–2228.
- Rudolph, U., and Knoflach, F. (2011). Beyond classical benzodiazepines: novel therapeutic potential of GABAA receptor subtypes. *Nat. Rev. Drug Discov.* 10, 685–697.
- Rujescu, D., Bender, A., Keck, M., Hartmann, A.M., Ohl, F., Raeder, H., Giegling, I., Genius, J., McCarley, R.W., Möller, H.J., and Grunze, H. (2006). A pharmacological model for psychosis based on N-methyl-D-aspartate receptor hypofunction: molecular, cellular, functional and behavioral abnormalities. *Biol. Psychiatry* 59, 721–729.
- Sheng, M., Cummings, J., Roldan, L.A., Jan, Y.N., and Jan, L.Y. (1994). Changing subunit composition of heteromeric NMDA receptors during development of rat cortex. *Nature* 368, 144–147.
- Soares, C., and Lee, K.F. (2013). A prominent role for triheteromeric GluN1/GluN2A/GluN2B NMDARs at central synapses. *J. Neurosci.* 33, 14975–14977.
- Soto, D., Altafaj, X., Sindreu, C., and Bayés, A. (2014). Glutamate receptor mutations in psychiatric and neurodevelopmental disorders. *Commun. Integr. Biol.* 7, e27887.
- Stroebel, D., Carvalho, S., Grand, T., Zhu, S., and Paoletti, P. (2014). Controlling NMDA receptor subunit composition using ectopic retention signals. *J. Neurosci.* 34, 16630–16636.
- Sun, Y., Olson, R., Horning, M., Armstrong, N., Mayer, M., and Gouaux, E. (2002). Mechanism of glutamate receptor desensitization. *Nature* 417, 245–253.
- Tovar, K.R., McGinley, M.J., and Westbrook, G.L. (2013). Triheteromeric NMDA receptors at hippocampal synapses. *J. Neurosci.* 33, 9150–9160.
- Traynelis, S.F., Wollmuth, L.P., McBain, C.J., Menniti, F.S., Vance, K.M., Ogden, K.K., Hansen, K.B., Yuan, H., Myers, S.J., and Dingledine, R. (2010). Glutamate receptor ion channels: structure, regulation, and function. *Pharmacol. Rev.* 62, 405–496.
- Tu, W., Xu, X., Peng, L., Zhong, X., Zhang, W., Soundarapandian, M.M., Balel, C., Wang, M., Jia, N., Zhang, W., et al. (2010). DAPK1 interaction with NMDA receptor NR2B subunits mediates brain damage in stroke. *Cell* 140, 222–234.
- Williams, K., Russell, S.L., Shen, Y.M., and Molinoff, P.B. (1993). Developmental switch in the expression of NMDA receptors occurs in vivo and in vitro. *Neuron* 10, 267–278.
- Zádori, D., Veres, G., Szalárdy, L., Klivényi, P., Toldi, J., and Vécsei, L. (2014). Glutamatergic dysfunctioning in Alzheimer's disease and related therapeutic targets. *J. Alzheimers Dis.* 42 (Suppl 3), S177–S187.
- Zeron, M.M., Hansson, O., Chen, N., Wellington, C.L., Leavitt, B.R., Brundin, P., Hayden, M.R., and Raymond, L.A. (2002). Increased sensitivity to N-methyl-D-aspartate receptor-mediated excitotoxicity in a mouse model of Huntington's disease. *Neuron* 33, 849–860.
- Zhou, Q., and Sheng, M. (2013). NMDA receptors in nervous system diseases. *Neuropharmacology* 74, 69–75.
- Zhu, S., and Paoletti, P. (2015). Allosteric modulators of NMDA receptors: multiple sites and mechanisms. *Curr. Opin. Pharmacol.* 20, 14–23.

# Transsynaptic Modulation of Kainate Receptor Functions by C1q-like Proteins

Keiko Matsuda,<sup>1,2,7</sup> Timotheus Budisantoso,<sup>1,2,7</sup> Nikolaos Mitakidis,<sup>3</sup> Yuki Sugaya,<sup>4</sup> Eriko Miura,<sup>1,2</sup> Wataru Kakegawa,<sup>1,2</sup> Miwako Yamasaki,<sup>2,5</sup> Kohtarou Konno,<sup>2,5</sup> Motokazu Uchigashima,<sup>2,5</sup> Manabu Abe,<sup>2,6</sup> Izumi Watanabe,<sup>2,6</sup> Masanobu Kano,<sup>4</sup> Masahiko Watanabe,<sup>2,5</sup> Kenji Sakimura,<sup>2,6</sup> A. Radu Aricescu,<sup>3,8,\*</sup> and Michisuke Yuzaki<sup>1,2,8,\*</sup>

<sup>1</sup>Department of Physiology, Keio University School of Medicine, Tokyo 160-8582, Japan

<sup>2</sup>Core Research for Evolutional Science and Technology, Japan Science and Technology Agency, Tokyo 102-0075, Japan

<sup>3</sup>Division of Structural Biology, Wellcome Trust Centre for Human Genetics, University of Oxford, Oxford OX3 7BN, UK

<sup>4</sup>Department of Neurophysiology, Graduate School of Medicine, The University of Tokyo, Tokyo 113-0033, Japan

<sup>5</sup>Department of Anatomy, Hokkaido University Graduate School of Medicine, Sapporo 060-8638, Japan

<sup>6</sup>Department of Cellular Neurobiology, Brain Research Institute, Niigata University, Niigata 951-8585, Japan

<sup>7</sup>Co-first author

<sup>8</sup>Co-senior author

\*Correspondence: radu@strubi.ox.ac.uk (A.R.A.), myuzaki@a5.keio.jp (M.Y.)

<http://dx.doi.org/10.1016/j.neuron.2016.04.001>

## SUMMARY

Postsynaptic kainate-type glutamate receptors (KARs) regulate synaptic network activity through their slow channel kinetics, most prominently at mossy fiber (MF)-CA3 synapses in the hippocampus. Nevertheless, how KARs cluster and function at these synapses has been unclear. Here, we show that C1q-like proteins C1qI2 and C1qI3, produced by MFs, serve as extracellular organizers to recruit functional postsynaptic KAR complexes to the CA3 pyramidal neurons. C1qI2 and C1qI3 specifically bound the amino-terminal domains of postsynaptic GluK2 and GluK4 KAR subunits and the presynaptic neurexin 3 containing a specific sequence *in vitro*. In C1qI2/3 double-null mice, CA3 synaptic responses lost the slow, KAR-mediated components. Furthermore, despite induction of MF sprouting in a temporal lobe epilepsy model, KARs were not recruited to postsynaptic sites in C1qI2/3 double-null mice, leading to reduced recurrent circuit activities. C1q family proteins, broadly expressed, are likely to modulate KAR function throughout the brain and represent promising antiepileptic targets.

## INTRODUCTION

The vast majority of excitatory neurotransmission in the vertebrate brain is mediated by ionotropic glutamate receptors (iGluRs) comprised of four subfamilies: AMPA (GluA1–GluA4), NMDA (GluN1–GluN3), kainate (GluK1–GluK5), and delta (GluD1 and GluD2). Different types of iGluRs are expressed at confined subcellular locations to achieve specific functions in neuronal circuits (Traynelis et al., 2010). While AMPA receptors (AMPA) mediate fast neurotransmission at the postsynaptic site, NMDA receptors (NMDARs) regulate synaptic plasticity and cell survival

at postsynaptic and extrasynaptic sites, respectively (Hardingham and Bading, 2010). GluD2 is exclusively localized at the postsynaptic site of cerebellar Purkinje cells and gates long-term depression (LTD) of synaptic plasticity (Kohda et al., 2013). On the other hand, kainate receptors (KARs) have more diverse functions at both pre- and postsynaptic sites: KARs modulate neurotransmitter release at certain presynaptic sites and regulate synaptic network activity through their slow-channel kinetics at postsynaptic sites (Contractor et al., 2011; Lerma and Marques, 2013). Although recent high-resolution proteomics unraveled molecular diversity of native iGluR complexes (Schwenk et al., 2012; Shanks et al., 2012), it remains mostly unclear how certain iGluR subtypes are targeted to and function at specific subcellular sites.

C1q family proteins, related to the C1q complement component (Kishore et al., 2004), have recently been identified as a new class of synapse organizers (Yuzaki, 2008). Cbln1, belonging to the cerebellin subfamily of C1q proteins, is released from cerebellar granule cells and plays a crucial role in the formation and function of parallel fiber-Purkinje cell synapses by binding presynaptic neurexins containing a splice site 4 insert (Nrx+SS4) and the postsynaptic GluD2 to form a molecular triad that spans the synaptic cleft (Matsuda et al., 2010; Matsuda and Yuzaki, 2011; Uemura et al., 2010). Cbln1 not only regulates synapse formation, but also determines clustering of postsynaptic GluD2 by binding to its amino-terminal domain (ATD) (Matsuda et al., 2010). Similarly, neuronal pentraxins cause AMPAR clustering by mainly binding the ATD of GluA4 AMPARs in certain inhibitory neurons (Pelkey et al., 2015; Sia et al., 2007). These findings suggest that the ATD of iGluRs, the region most distal from the postsynaptic membrane, is used for interaction with proteins at the synaptic cleft to regulate the localization of iGluRs and/or their function at synapses. Nevertheless, synaptic proteins that specifically interact with the ATD of KARs have not been identified so far.

KARs are highly enriched on the postsynaptic side of mossy fiber (MF)-pyramidal cell synapses in the hippocampal CA3 region and enhance synaptic integration during repetitive MF activities (Carta et al., 2014; Castillo et al., 1997). Intriguingly,

mRNAs encoding the C1q-like (C1q) subfamily C1q2 and C1q3 are highly expressed in dentate gyrus granule cells (DGCs) that send MFs (Iijima et al., 2010; Shimono et al., 2010). C1q1, a C1q subfamily member, is released from presynaptic sites and regulates maturation of synapses between climbing fibers and Purkinje cells by binding to brain angiogenesis inhibitor 3 (Bai3) in Purkinje cells (Kakegawa et al., 2015). Thus, we examined roles of C1q2 and C1q3 at MF-CA3 synapses. We demonstrate that C1q2 and C1q3 directly bind the ATD of postsynaptic GluK2 and GluK4 KARs, as well as a presynaptic Nr3 isoform that contains a specific sequence encoded by exon25b in splice site 5, which we refer to as Nr3+SS5<sup>25b</sup>. We found that the Nr3+SS5<sup>25b</sup>-C1q2/3 complex is necessary and sufficient to recruit KARs at postsynaptic sites in vitro. In C1q2/3 double-null mice, no postsynaptic KARs were recruited to MF-CA3 synapses in control conditions, or to sprouted MFs in a temporal lobe epilepsy model, leading to reduced network activities. These results elucidate the physiological and pathological importance of the Nr3-C1q2/3 signaling in regulating postsynaptic KAR functions.

## RESULTS

### C1q2 and C1q3 Proteins Are Localized at the MF-CA3 Synaptic Cleft

We first investigated whether C1q2 and C1q3 proteins produced in DGCs (Iijima et al., 2010) can reach synapses in the wild-type (WT) hippocampus, specifically the stratum lucidum in the CA3 region. Immunohistochemical (IHC) analyses revealed that punctate C1q2 (Shimono et al., 2010) and C1q3 immunoreactivities were highly localized in WT CA3 stratum lucidum (Figures 1A and 1B). Using immunogold electron microscopy (EM), we confirmed that C1q2 was mainly localized at the presynaptic MF terminals and their synaptic clefts (Figure 1C). Similarly, super-resolution fluorescence microscopy revealed that endogenous C1q2 and C1q3 were mainly localized between postsynaptic density 95 (PSD95)- and Bassoon-positive puncta in the CA3 stratum lucidum (Figure 1D). These findings indicate that C1q2/3 produced in the DGCs reach and localize at MF-CA3 synaptic clefts.

To investigate the physiological functions of C1q2/3, we generated mice in which the C1q2 and C1q3 genes were disrupted (Figures S1A–S1C, available online). IHC (Figures 1A and 1B) and immunogold EM (Figure 1C) analyses revealed essentially no C1q2 and C1q3 immunoreactivities in C1q2 null and C1q3 null hippocampus, respectively. Unexpectedly, gross anatomy of the hippocampus (Figure S1D) and MF projection patterns (Figure S1E) were unaffected in these mice. Similarly, the distribution of PSD95 immunoreactivities (Figure S1F) was unaffected in C1q2 or C1q3 null CA3 stratum lucidum. To exclude potential functional redundancy between C1q2 and C1q3, we generated double-null (C1q2/3 null) mice (Figure S1C). C1q2 and C1q3 double heterozygous breeding pairs produced the expected frequencies of double homozygous null offspring (6%). C1q2/3 null mice were fertile and produced offspring with normal sex ratios (52% female). No differences in body weights were observed between WT and C1q2/3 null mice at birth (WT, 1.33 ± 0.03 g, n = 31; C1q2/3 null, 1.30 ±

0.02 g, n = 40; p > 0.05) and at postnatal 4 weeks (male WT, 12.6 ± 0.4 g, n = 13; male C1q2/3 null, 12.7 ± 0.5 g, n = 12, p > 0.05; female WT, 11.8 ± 0.3 g, n = 18; male C1q2/3 null, 11.7 ± 0.4 g, n = 19, p > 0.05). Gross anatomy of the hippocampus (Figure S1D), MF projection patterns (Figure S1E), the distribution of PSD95 (Figure S1F), and vGluT1 (Figure S1G) immunoreactivities were also unaffected in C1q2/3 null mice. These results suggest that unlike other C1q family proteins, such as Cbln1 (Matsuda et al., 2010; Uemura et al., 2010) and C1q1 (Kakegawa et al., 2015), C1q2/3 do not regulate synapse formation per se in the hippocampus.

### The ATDs of GluK2/4 Serve as Postsynaptic Receptors for C1q2/3 In Vitro and In Vivo

Localization of C1q2 and C1q3 immunoreactivities closely matched that of GluK2/3 KAR in the CA3 stratum lucidum (Figure 1A). Since GluD1 and GluD2 serve as postsynaptic receptors for Cbln1 through their ATDs (Matsuda et al., 2010), we hypothesized that ATDs of KARs may be associated with C1q2/3. To test this hypothesis, we first performed cell-based binding assays by expressing the ATD of various iGluRs on the surface of HEK293 cells and applying HA-tagged recombinant full-length C1q2 and C1q3 (Figure 2A). Interestingly, C1q2 and C1q3 specifically bound to cells expressing the AMPAR subunit GluA1, as well as the KAR subunits GluK2 and GluK4 (Figures 2A and 2B). C1q2 and C1q3 did not show any binding to the ATDs of other AMPA, kainate, NMDA, or delta receptor subunits (Figures 2A and 2B). To further investigate the interaction specificity between C1q2/3 and GluK ATDs, we created various chimeric proteins between the ATDs of GluK2 and GluK3 because despite the sequence similarity of their ATDs (Figure S3A), C1q2/3 specifically bound to GluK2 (Figures 2A and 2B). Cell-based binding assays (Figure S3B) revealed that L3 and L4 regions, but not L1 and L2 regions, of GluK2 were required for binding to C1q3 (Figure S3C). In addition, C1q3 binding to GluK2-ATD was significantly reduced when three amino acid residues in the L3 region (K306–D308) or nine residues in the L4 region (V329–F337) were substituted with the corresponding residues of GluK3-ATD (Figure S3C), indicating that these residues of GluK2-ATD are involved in binding C1q3.

To test whether C1q2 and C1q3 associate with these receptors in vivo, we next examined GluK2 null (Figures S2A–S2C) and GluK4 null (Akashi et al., 2009) hippocampi. IHC analyses revealed that C1q2 (Figure 2C) and C1q3 (Figure 2D) immunoreactivities were significantly reduced in the CA3 stratum lucidum of GluK2 null and GluK4 null hippocampi. In contrast, C1q2 immunoreactivity was unaffected in the hippocampal CA3 regions in GluA1 null mouse (Figure S2D), indicating that GluA1 does not serve as an endogenous receptor for C1q2 and C1q3 at MF-CA3 synapses.

GluK2 is highly expressed at postsynaptic sites, but functional KARs are also reported at presynaptic sites of MF-CA3 synapses (Contractor et al., 2000; Kamiya and Ozawa, 2000; Lerma and Marques, 2013). Thus, to clarify the contribution by the postsynaptic GluK2, we next knocked out the gene encoding GluK2 in CA3 pyramidal neurons by crossing GluK4-Cre driver mice (GluK4<sup>Cre/+</sup>), which predominantly induced recombination in CA3 pyramidal neurons (Akashi et al., 2009), with GluK2<sup>fllox/fllox</sup>

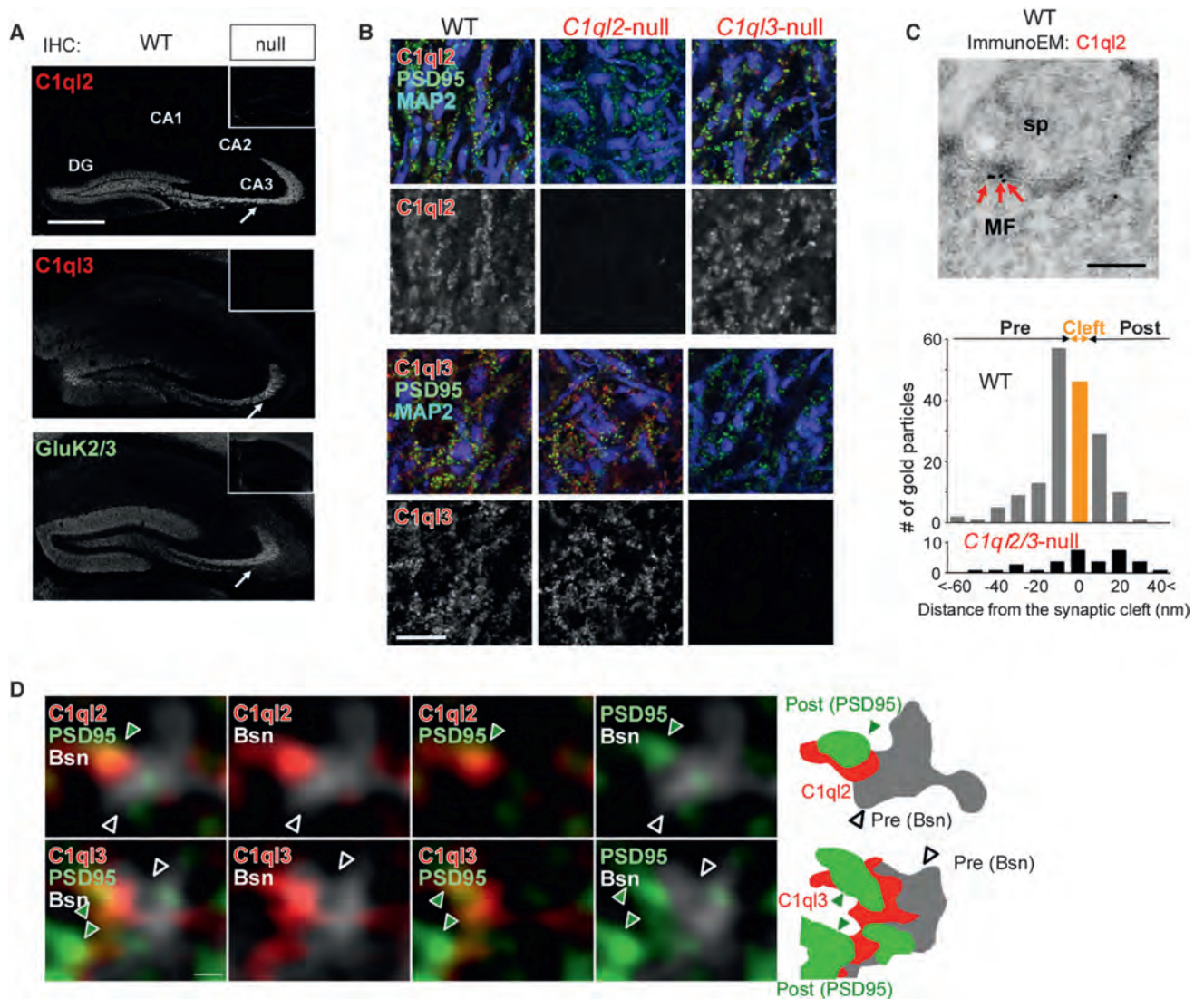


**Figure 1. C1q2 and C1q3 Are Localized at MF-CA3 Synapses**

(A) Endogenous C1q2, C1q3, and GluK2/3 immunoreactivities in WT hippocampus. Arrows indicate CA3 stratum lucidum. Insets show immunoreactivity in mice lacking a corresponding gene to confirm antibody specificity. Scale bar, 500  $\mu$ m.

(B) Representative IHC images indicating loss of C1q2 and C1q3 immunoreactivities (red) in *C1q2* null and *C1q3* null CA3 stratum lucidum, respectively. No differences were observed in PSD95 (green) and MAP2 (blue) immunoreactivities. Scale bar, 10  $\mu$ m.

(C) Postembedding immunogold EM image of endogenous C1q2 in WT MF-CA3 synapses. Red arrows indicate gold particles labeling C1q2. sp, pyramidal cell spine; MF, mossy fiber terminal. Scale bar, 200 nm. Histogram shows distribution of C1q2-positive particles at MF synapses in WT and *C1q2/3* null mice ( $n = 2$  mice each).

(D) Super-resolution structured illumination (SIM) microscopic images of endogenous C1q2 (upper, red) or C1q3 (lower, red), PSD95 (green), and Bassoon (white). Unfilled and filled triangles indicate presynaptic Bassoon-immunopositive and postsynaptic PSD95-immunopositive structures, respectively. Scale bar, 200 nm.

See also Figure S1.

mice. IHC analyses revealed that C1q2 immunoreactivity in the CA3 stratum lucidum in *GluK2*<sup>flx/flx</sup>, *GluK4*<sup>Cre/+</sup> mice was reduced to the level similar to that in *GluK2* null mice (Figure S2F), suggesting that postsynaptic GluK2 was mainly responsible for C1q2 localization at these synapses. Finally, we used surface plasmon resonance (SPR) to measure the interactions between the trimeric gC1q domains of C1q2 and C1q3 and the dimeric

GluK2 ATD (Figure 2E), and found these to be in the low micromolar range (5.6  $\mu$ M and 3.38  $\mu$ M, respectively; Figure 2F). None of the gC1q constructs bound to the ATDs of GluK3 or GluK5 (Figures 2F, S3D, and S3E). Taken together, these results indicate that GluK2 and GluK4 serve as endogenous receptors for C1q2 and C1q3 at the MF-CA3 synapses in the hippocampus by directly binding the globular domains of C1q2/3 via the ATDs.

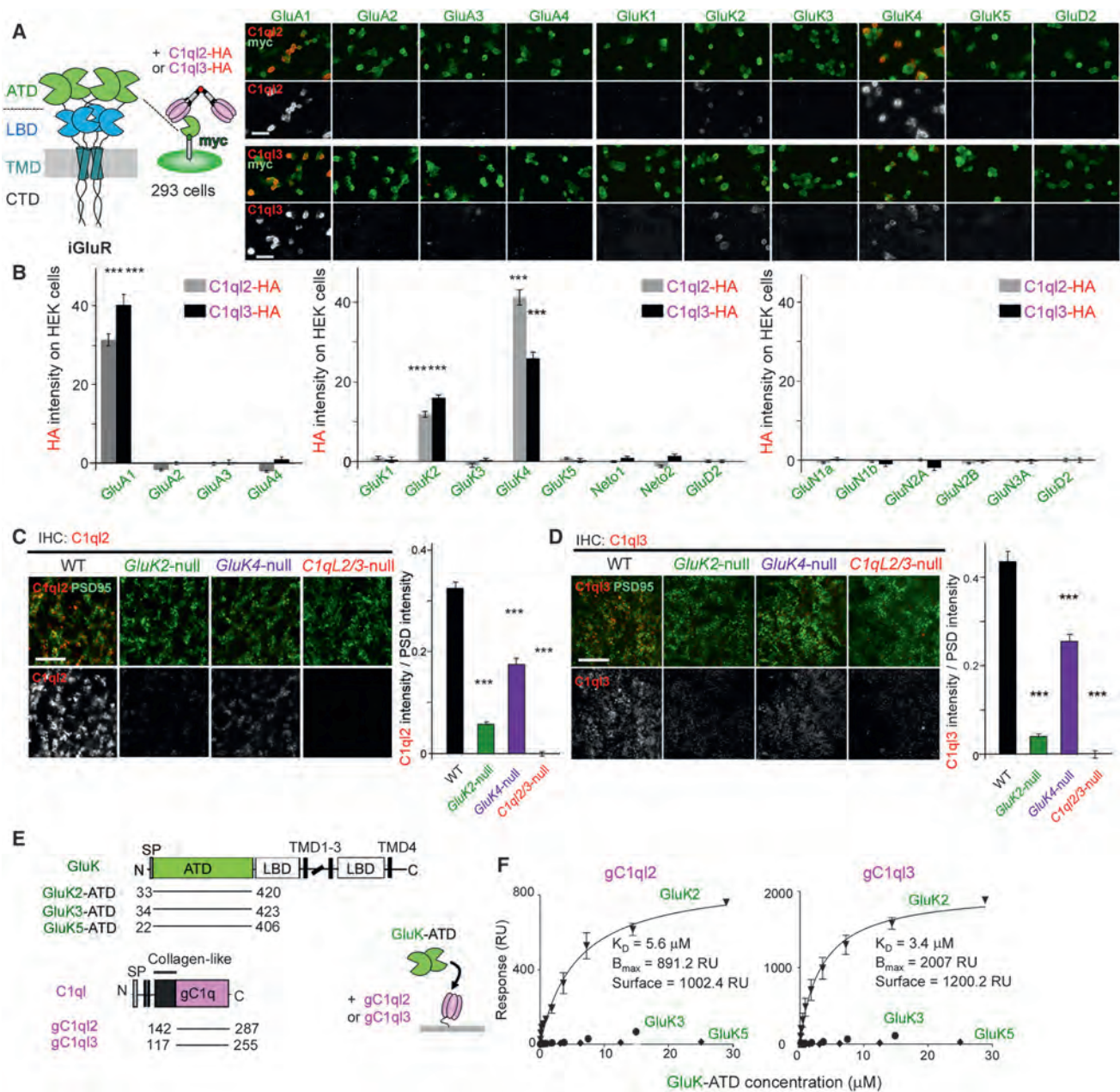


**Figure 2. Direct Interaction between C1qL2/3 and ATDs of iGluRs**

(A) Cell-based binding assay. Diagram shows domain organization of iGluR. ATD, amino-terminal domain; LBD, ligand-binding domain; TMD, transmembrane domain; CTD, C-terminal domain. Panels show cell-surface C1qL2-HA (upper panels) or C1qL3-HA (lower panels) immunoreactivity (red) on HEK293 cells expressing the ATD of iGluR-myc (green). Scale bars, 50  $\mu$ m.

(B) The graphs show mean HA immunoreactivity in the myc-positive area. HA immunoreactivity in HEK293 cells was compared with those expressing GluK2-ATD. At least  $n = 14$  fields were analyzed in two independent experiments.  $***p < 0.001$ .

(C and D) Reduction of synaptic C1qL2 and C1qL3 in *GluK2* null and *GluK4* null mice. Representative IHC images show endogenous C1qL2 (C; red) or C1qL3 (D; red) and PSD95 (green) immunoreactivities in WT, *GluK2* null, *GluK4* null, and double *C1qL2/3* null hippocampus. Scale bars, 10  $\mu$ m. The graphs show relative fluorescence intensities of C1qL2 (C;  $n = 24$ –30 regions from 4–5 mice for each genotype) or C1qL3 (D;  $n = 12$  regions from 2 mice for each genotype) normalized by those of PSD95 in randomly selected CA3 regions.  $***p < 0.001$  versus WT.

(E) Diagram of GluK (upper) and C1q (lower) domain organization and construct design. N, amino-terminus; C, carboxy-terminus; SP, secretion signal peptide; Collagen-like, collagen-like region; gC1q, globular C1q domain. GluK numbering corresponds to rat proteins; C1q numbering corresponds to mouse proteins.

(F) SPR assay. The ATD of GluK2, but not GluK3 or GluK5, bound directly to gC1qL2 and gC1qL3.

Data are presented as mean  $\pm$  SEM. See also Figures S2 and S3.

### C1qI2 and C1qI3: Master Regulators of Postsynaptic KAR Complexes

What functions do C1qI2/3 play at MF-CA3 synapses? Interestingly, IHC analyses revealed that although synaptic GluK2/3 immunoreactivity in the CA3 stratum lucidum was unaffected in single *C1qI2* null or *C1qI3* null mice (Figure S1H), it markedly decreased in double *C1qI2/3* null mice (Figures 3A and S1H). In contrast, no changes were observed for GluA1 immunoreactivity in *C1qI2/3* null mice (Figure S2E). Immunogold EM analysis further confirmed loss of GluK2/3 immunoreactivity, which was mainly observed at the postsynaptic site in WT CA3 pyramidal neurons (Petralia et al., 1994), in both *C1qI2/3* null and *GluK2* null mice, despite the absence of changes in PSD lengths (Figure 3B). In contrast, immunoblot analysis showed that total GluK2/3 protein levels were unchanged in *C1qI2/3* null CA3 regions (Figure 3C). In addition, extrasynaptic GluK2/3 immunoreactivity was clearly present in the CA3 region of *C1qI2/3* null mice (Figure S2C). These results indicate that postsynaptic localization, but not the amount of KARs, was regulated by C1qI2 and C1qI3 in CA3 pyramidal neurons.

Neuropilin and tolloid-like 1 (Neto1), an auxiliary KAR subunit that determines the slow EPSC (excitatory postsynaptic current) kinetics, is specifically expressed on the postsynaptic side of MF-CA3 synapses (Copits and Swanson, 2012; Straub et al., 2011). IHC analyses revealed that Neto1 immunoreactivity decreased significantly in the CA3 stratum lucidum of *C1qI2/3* null mice, but not in single *C1qI2* null or *C1qI3* null mice (Figure 3D). Unlike KARs, the extracellular domains of Neto proteins did not show any binding to recombinant C1qI2 or C1qI3 in cell-based binding assays (Figure 2B, middle). Similarly, immunoreactivities of GluK4 and GluK5, KAR subunits that require GluK1–GluK3 for surface expression and determine the high affinities for kainate, were significantly reduced in the CA3 stratum lucidum to the levels observed in *GluK2* null mice (Figure 3E). These results indicate that C1qI2/3 likely regulate postsynaptic localization of Neto1 and GluK5 indirectly, by binding to GluK2/4, and that C1qI2/3 serve as anterograde master regulators for postsynaptic localization and function of KAR complexes in CA3 pyramidal neurons.

To clarify whether C1qI2 or C1qI3 alone could regulate localization of KARs in vivo, we next examined synapses formed on DGCs by hilar mossy cells, which expressed only C1qI3, but not C1qI2, mRNA (Figure S4A). IHC analyses revealed that GluK2 and GluK5 immunoreactivities (Figures S4B and S4C) were severely reduced at the mossy cell-DGC synapses in the inner molecular layer of *C1qI3* null, but not in *C1qI2* null dentate gyrus, indicating that C1qI3 alone was sufficient to recruit postsynaptic KARs on DGCs in vivo. These data suggest that the reason why localization of postsynaptic KAR complexes were unaffected in single *C1qI2* or *C1qI3* null MF-CA3 synapses (Figures 3D and S1H) was because either C1qI2 or C1qI3 alone could recruit KAR complexes to these synapses.

In addition to the hippocampus, KARs are expressed in various brain regions, including the cerebellum and the striatum (Figures S4D and S4E). Immunoblot analyses revealed presence of C1qI3, but not C1qI2, in the striatum, and absence of C1qI2 and C1qI3 in the cerebellum (Figure S4F). Consistent with these findings, KAR immunoreactivity was unaffected in *C1qI2/3* null

cerebellum (Figure S4D). By contrast, synaptic KARs disappeared in *C1qI2/3* null, as well as in *GluK2* null striatum (Figure S4E). Since C1qI2/3 mRNA signals are absent in the striatum (Iijima et al., 2010), these results indicate that like C1qI2/3 provided by MFs, C1qI3 derived from projecting fibers to the striatum, such as corticostriatal inputs, may regulate synaptic localization of KARs in the striatum. Together, although there may be other mechanisms by which KAR trafficking is controlled, C1qI2/3 likely regulate synaptic localization and function of KARs in multiple brain regions.

Bai3, a cell-adhesion G-protein-coupled receptor, was previously shown to serve as a receptor for C1qI-like proteins C1qI1–C1qI4 in vitro and in vivo (Bolliger et al., 2011; Kakegawa et al., 2015). To explore the possibility that Bai3, or its closely related member Bai2 (Kakegawa et al., 2015), plays a similar role at MF-CA3 synapses, we examined double *Bai2/3* null mice. Although C1qI1 immunoreactivity was completely lost in the *Bai3* null cerebellum (Kakegawa et al., 2015), C1qI2/3 immunoreactivities were unaffected at MF-CA3 synapses in double *Bai2/3* null mice (Figures S5A and S5B). Similarly, no changes were observed for GluK2/3 immunoreactivity in the CA3 stratum lucidum of *Bai2/3* null mice (Figure S5C). Interestingly, IHC analysis revealed that Bai3 immunoreactivity was very low in the CA3 stratum lucidum (Figure S5D). These results indicate that Bai3 is unlikely involved in C1qI2/3-KAR signaling at MF-CA3 synapses, and that C1qI proteins may play distinct roles depending on their postsynaptic receptor type.

### C1qI2/3 Directly Bind to Nr3x Containing the SS5<sup>25b</sup> Insert

A unique feature of the secreted synaptic organizer Cbln1 is that it functions as a connector between pre- and postsynaptic receptors, Nr3x+SS4 and GluD2, respectively (Matsuda et al., 2010; Uemura et al., 2010). To explore the possibility that C1qI2/3 may also interact with neurexins, we performed cell-based binding assays by expressing various major Nr3x isoforms in HEK293 cells (Figure 4A). We found that full-length C1qI2 and C1qI3 specifically bound HEK293 cells expressing Nr3x3 $\beta$  (Figure 4B). While the SS4 insert was essential for Cbln1 to bind to all Nr3x isoforms, the presence or absence of SS4 in Nr3x1 $\beta$ , Nr3x2 $\beta$ , and Nr3x3 $\beta$  did not affect their binding to C1qI2 or C1qI3 (Figure 4B). Another alternative splicing at site 5 (SS5) is reported to produce an isoform unique to Nr3x that contains a sequence encoded by exon 25b (SS5<sup>25b</sup>) in approximately half of Nr3x3 $\beta$  transcripts (Schreiner et al., 2014; Treutlein et al., 2014). Interestingly, Nr3x3 $\beta$  lacking SS5<sup>25b</sup> significantly lost binding ability to C1qI2/3 (Figure 4B). Although certain Nr3x2 isoforms contain an equivalent sequence encoded by exon 23 at SS5 (Figures 4A and S6A), the presence of this sequence did not affect its binding to C1qI3 (Figures 4C and 4D). Although Nr3x3 $\beta$  also contains a  $\beta$ -specific region encoded by exon 18 (Figure 4A), we found that C1qI3 bound Nr3x3 $\beta$  lacking this  $\beta$ -specific sequence (Figures 4C and 4D). Indeed, C1qI3 bound Nr3x3 $\alpha$  lacking the  $\beta$ -specific sequence but containing SS5<sup>25b</sup> (Figure S6B). These results indicate that the SS5<sup>25b</sup> sequence, encoded by exon 25b of Nr3x, provides a binding site for C1qI2/3.

To further define the determinants of interaction between C1qI2/3 and Nr3x3 $\beta$ , we used SPR assays (Figure 4E). The

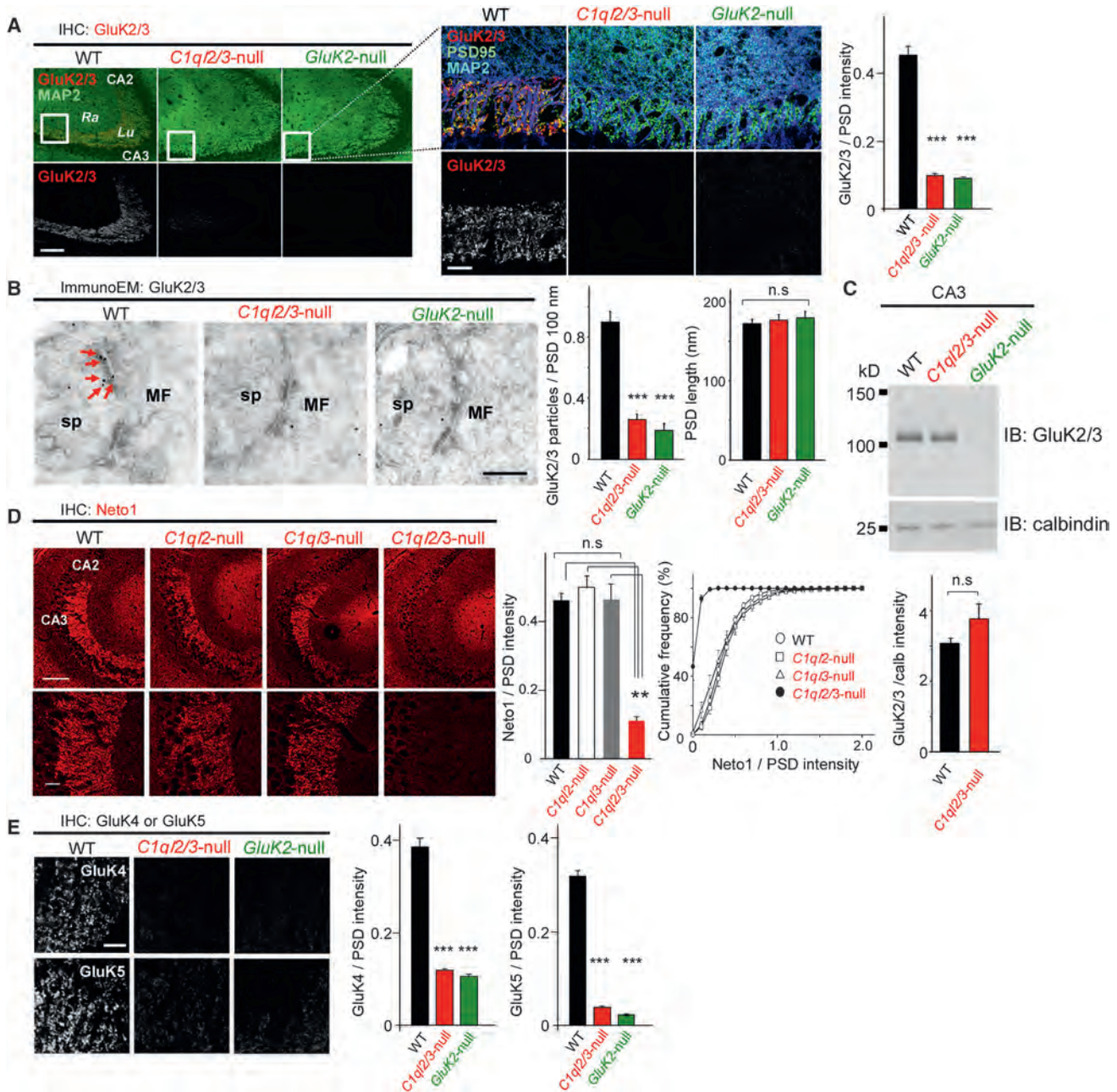


**Figure 3. C1q2 and C1q3 Determine Postsynaptic KAR Localization at MF-CA3 Synapses**

(A) Absence of synaptic GluK2/3 in *C1q2/3* null hippocampus. Representative IHC images show endogenous GluK2/3 (red), PSD95 (green), and MAP2 (green or blue) immunoreactivities in WT, *C1q2/3* null, and *GluK2* null CA3 regions. The boxed regions are enlarged in the right panels. Scale bars, 100  $\mu$ m (left) and 20  $\mu$ m (right). The graph shows relative fluorescence intensities of GluK2/3 normalized by those of PSD95 in randomly selected CA3 regions ( $n = 24\text{--}30$  regions from 4–5 mice for each genotype). \*\*\* $p < 0.001$  versus WT.

(B) Postembedding immunogold EM images of endogenous GluK2/3 (arrows) at MF-CA3 synapses in WT, *C1q2/3* null, and *GluK2* null hippocampus. sp, pyramidal cell spine; MF, mossy fiber terminal. Scale bar, 200 nm. The mean number of gold particle per 100 nm of postsynaptic density (PSD) (left graph) and the length of PSD (right graph) are summarized. \*\*\* $p < 0.001$  versus WT. n.s., no significance ( $n > 100$  synapses from 2 mice for each genotype).

(C) Representative immunoblot image indicating no difference in total GluK2/3 proteins between WT and *C1q2/3* null hippocampal CA3 regions. CA3 regions were excised and subjected to the immunoblot analyses using anti-GluK2/3 and anti-calbindin (an MF marker) antibodies. The lower graph shows averaged GluK2/3 band intensities normalized by those of calbindin. n.s., no significance versus WT ( $n = 3$  from 3 mice for each genotype).

(D) Reduced Neto1 immunoreactivity in *C1q2/3* null, but not in WT, *C1q2* null, or *C1q3* null hippocampus. Bottom panels show enlarged views of CA3 stratum lucidum. Scale bars, 100  $\mu$ m (top) and 20  $\mu$ m (bottom). The middle graph shows relative fluorescence intensities of Neto1 normalized by those of PSD95 in randomly selected CA3 regions ( $n = 8$  regions from 4 mice for each genotype). \*\* $p < 0.01$ ; n.s., no significance by Kruskal-Wallis test and Steel-Dwass post hoc test. Cumulative plot of Neto1 immunoreactivity on PSD95 immunopositive puncta is shown on the right.

(legend continued on next page)

ectodomain of  $\text{Nrx3}\beta\text{+SS5}^{25b}$ , but not that of  $\text{Nrx3}\beta\text{--SS5}^{25b}$ , bound the gC1q domains of C1q2/3 in the low micromolar range (14.9  $\mu\text{M}$  and 8.6  $\mu\text{M}$ , respectively; Figures 4F and S6C). Subsequently, we narrowed down the minimal binding site within the region encoded by  $\text{Nrx3}$  exon 25b and found that a sequence consisting of 17 amino acids, which we refer to as S5-9 (Figure S6A), bound C1q3 (Figure S6D). SPR measurements revealed that the gC1q domain of C1q3 bound the isolated S5-9 peptide with an affinity comparable to the ectodomain of  $\text{Nrx3}\beta\text{+SS5}^{25b}$  ( $K_D = 4.7 \mu\text{M}$ ; Figures 4G and S6E). Although full-length C1q2/3 weakly bound  $\text{Nrx3}$  that does not contain the  $\text{SS5}^{25b}$  sequence (Figures 4C, 4D, 4H, and S6C), exon 25b of  $\text{Nrx3}$  is likely used as a specific splicing determinant for its association with C1q2/3.

### The $\text{Nrx3}\text{-C1q2/3}$ Complexes Serve as Synaptic Partners for KARs In Vitro

To define the roles for  $\text{Nrx3}\text{-C1q2/3}$  interactions in organizing KAR-containing synapses, we expressed  $\text{Nrx3}\beta\text{+SS5}^{25b}$  together with C1q2 and C1q3 (C1q2+3) on the surface of HEK293 cells and cocultured them with  $\text{C1q2/3}$  null hippocampal neurons. We found that endogenous  $\text{GluK2/3}$ , as well as neuroligin 1 (NL1, a receptor that binds to all  $\text{Nrx}$  isoforms) and PSD95, accumulated in hippocampal neurons contacting HEK293 cells (Figure 5A). However, when  $\text{Nrx3}\beta\text{+SS5}^{25b}$  was expressed without C1q2+3, NL1 and PSD95, but not  $\text{GluK2/3}$ , formed clusters in  $\text{C1q2/3}$  null hippocampal neurons (Figure 5A). Conversely, when  $\text{Nrx3}\beta\text{+SS5}^{25b}$  lacking the laminin/neurexin/sex-hormone-binding globulin (LNS) domain, which is necessary and sufficient for its binding to NL1 (Gokce and Südhof, 2013), was coexpressed with C1q2+3 in HEK293 cells, only  $\text{GluK2/3}$  were recruited in the contacted hippocampal neurons (Figure 5B). These data suggest that  $\text{Nrx3}\beta\text{+SS5}^{25b}$  may participate in hemisynapse formation by using two distinct domains, the LNS domain and the  $\text{SS5}^{25b}$  sequence, for NL1 and C1q2/3 interactions, respectively. Coexpression of  $\text{Nrx3}\beta\text{+SS5}^{25b}$  together with either C1q2 or C1q3 alone in HEK293 cells also caused accumulation of  $\text{GluK2/3}$  in  $\text{C1q2/3}$  null hippocampal neurons (Figure 5C).

To further define the role of the  $\text{Nrx3}\text{-C1q2/3}$  complex components in synapse organization, we used a bead-induced synaptic differentiation assay (Matsuda et al., 2010). When beads coated with C1q3 (Figure 5D) were cocultured with  $\text{C1q2/3}$  null hippocampal neurons, endogenous  $\text{GluK2/3}$  receptors were recruited around the beads. These data indicate that  $\text{Nrx3}$  serves as a scaffold to accumulate C1q2/3 for recruiting postsynaptic KARs.

### C1q2/3 Regulate Postsynaptic Functions of KAR at MF-CA3 Synapses In Vivo

To define the functional roles of C1q2/3 in MF-CA3 synaptic transmission, we next performed whole-cell patch-clamp re-

cordings from CA3 pyramidal neurons in  $\text{C1q2/3}$  null hippocampal slices. KAR-mediated EPSC components were evaluated in the presence of 60  $\mu\text{M}$  GYKI52466, a selective AMPAR antagonist. MF-evoked EPSCs were reduced to approximately 15% (Figure 6A). MF-EPSCs were more strongly inhibited by GYKI52466 in  $\text{GluK2}$  null mice (Figure 6A, top traces and graph), and the remaining MF-EPSCs did not show slow decay (Figure 6A, bottom traces and graph), indicating that slow EPSC components in WT mice were mostly mediated by KARs ( $\text{EPSC}_{\text{KA}}$ ), which could be isolated by GYKI52466. Importantly, the amplitude (Figure 6A, top) and the decay time constant (Figure 6A, bottom) of MF-evoked EPSCs were reduced in  $\text{C1q2/3}$  null mice to levels similar to those of  $\text{GluK2}$  null mice. The slow decay contributed to  $\text{EPSC}_{\text{KA}}$  summation when MFs were stimulated at high frequency in WT, but not in  $\text{C1q2/3}$  null, hippocampal slices (Figure 6B). Similarly, the likelihood of action potential initiation during repetitive MF stimulation was significantly lower in  $\text{C1q2/3}$  null CA3 pyramidal neurons (Figure 6C). In contrast, the amplitude and kinetics of AMPAR-mediated quantal EPSCs elicited by MF stimulation in the presence of  $\text{Sr}^{2+}$  were similar between WT and  $\text{C1q2/3}$  null CA3 neurons (Figure 6D). Similarly, the ratios between NMDAR and AMPAR components of MF-EPSCs in WT and  $\text{C1q2/3}$  null CA3 pyramidal neurons were comparable (Figure 6E). These results indicate that postsynaptic KARs, but not AMPARs or NMDARs, were selectively regulated by C1q2/3 and enhanced synaptic integration during repetitive MF activities.

$\text{GluK2}$  and  $\text{GluK5}$  are also thought to be expressed at the presynaptic site of MFs and to regulate glutamate release (Contractor et al., 2000; Kamiya and Ozawa, 2000; Lerma and Marques, 2013). To examine whether the functions of presynaptic KARs were regulated by C1q2/3, we tested the effect of low concentrations of kainate on MF-EPSCs. In WT and  $\text{C1q2/3}$  null, but not in  $\text{GluK2}$  null hippocampus (Contractor et al., 2000), MF-EPSCs were significantly reduced by 3  $\mu\text{M}$  kainate (Figure 6F), reflecting the function of presynaptic KARs. Similarly, although the paired-pulse facilitation ratios (PPRs) of EPSCs, which reflect glutamate release probability, were similar in WT,  $\text{C1q2/3}$  null, and  $\text{GluK2}$  null CA3 synapse at 50 ms intervals, treatment with 3  $\mu\text{M}$  KA failed to increase the PPR in  $\text{GluK2}$  null, but not in WT and  $\text{C1q2/3}$  null CA3 synapses (Figure 6F). These results are consistent with those obtained from IHC and EM analyses, further indicating that C1q2/3 do not affect the function of presynaptic KARs at MF-CA3 synapses.

### C1q2/3 Recruit Postsynaptic KARs at Sprouted MFs in a Chronic Epilepsy Model

In human temporal lobe epilepsy, sprouting of hippocampal MFs and accumulation of associated KARs lead to the formation of pathological recurrent excitatory circuits in the DGCs (Lerma and Marques, 2013; Peret et al., 2014). To examine how C1q2/3 contribute to this pathological condition, we used an

(E) Loss of synaptic high-affinity KARs. Representative IHC images show  $\text{GluK4}$  (upper) or  $\text{GluK5}$  (lower) immunoreactivities in  $\text{C1q2/3}$  null and  $\text{GluK2}$  null CA3 stratum lucidum. Scale bar, 10  $\mu\text{m}$ . The graphs show averaged  $\text{GluK4}$  (left;  $n = 12\text{--}17$  regions from 3–4 mice for each genotype) or  $\text{GluK5}$  (right,  $n = 24\text{--}30$  regions from 4–5 mice for each genotype) immunoreactivities normalized by those of PSD95 in randomly selected CA3 regions. Data are presented as mean  $\pm$  SEM. See also Figures S4 and S5.

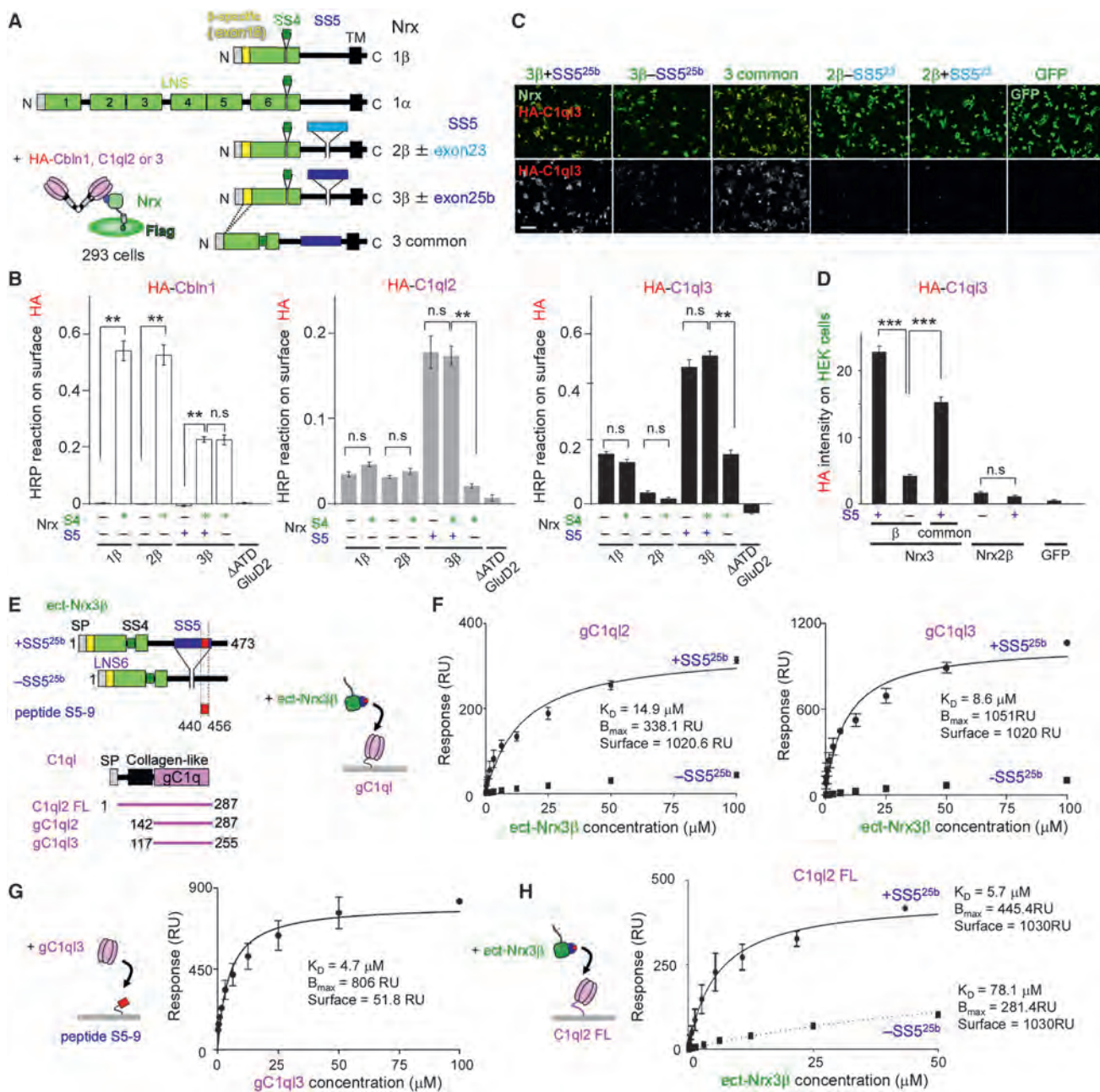


**Figure 4. Direct Interaction between C1ql2/3 and Nrx3+SS5<sup>25b</sup>**

(A) Diagram of domain organization of neurexin (Nrx) isoforms and construct design. N, amino-terminus; C, carboxy-terminus; SS4, splice site 4; SS5, splice site 5; light green boxes, LNS (laminin, neurexin, sex-hormone-binding protein) domain 1–6; yellow boxes, Nrxβ-specific region.

(B) Enzyme-linked immunosorbent assay showing interaction of Nrx with C1ql2, C1ql3, or Cbln1. HA-C1ql2, C1ql3, or Cbln1 was incubated with HEK293 cells expressing various Nrx isoforms, followed by an anti-HA antibody and peroxidase-conjugated secondary antibody. The graph shows intensities of peroxidase reaction in HEK293 cells. Data are from ten independent experiments. \*\**p* < 0.01; n.s., no significance, by Kruskal-Wallis test and Steel-Dwass post hoc test.

(C and D) Cell-based binding assay showing that a sequence encoded by exon 25b, but not β-specific exon 18, determines binding specificity of Nrx3β to C1ql3. Panels (C) show cell-surface HA-C1ql3 immunoreactivity (red) in HEK293 cells expressing various isoforms of Flag-tagged Nrx or GFP alone (green). Scale bar, 100 μm. The graph (D) shows mean HA immunoreactivity in the Flag- or GFP-positive area. At least *n* = 16 fields were analyzed in two independent experiments. \*\*\**p* < 0.001; n.s., no significance by Kruskal-Wallis test and Steel-Dwass post hoc test.

(E) Diagram of Nrx3β ectodomain (ect-Nrx3β) and C1q-like proteins. SP, secretion signal peptide; SS4, SS5, splice sites 4 and 5; LNS6, LNS6 common to both Nrxα and Nrxβ; gC1q, global C1q domain. The core 17 amino acid sequence within the region encoded by exon 25b (SS5<sup>25b</sup>) is referred to as S5-9. Numbering corresponds to mouse proteins.

(F) Equilibrium SPR analysis of binding between ect-Nrx3β ± SS5<sup>25b</sup> and immobilized gC1ql2 and gC1ql3. The ect-Nrx3β+SS5<sup>25b</sup>, but not –SS5<sup>25b</sup>, bound to gC1ql2 and gC1ql3.

(legend continued on next page)

in vitro epilepsy model, in which organotypic hippocampal slice cultures were treated with pilocarpine (Peret et al., 2014). Six days after the treatment, IHC analyses of the dentate gyrus revealed similar levels of sprouted MFs in WT and *C1ql2/3* null mice (Figure 7A) (Peret et al., 2014). Whole-cell recordings from pilocarpine-treated DGCs (Figure 7B) showed slowly decaying spontaneous EPSCs (the time constant,  $6.1 \pm 0.2$  ms,  $n = 19$ ), which was quite similar to the one ( $\sim 6.2$  ms) previously reported in DGCs in pilocarpine-treated organotypic hippocampal slices in the presence of GYKI53655, another selective AMPAR antagonist (Peret et al., 2014). These results indicate that postsynaptic KARs were recruited to WT DGCs. In contrast, essentially no slow spontaneous EPSCs were recorded in pilocarpine-treated *C1ql2/3* null DGCs in the presence or absence of GYKI52466 (Figure 7B), as reported for pilocarpine-treated *GluK2* null DGCs (Peret et al., 2014). Extracellular field recordings also revealed stereotyped spontaneous interictal-like activity consisting of the paroxysmal discharge (PD) followed by recurrent bursts (RBs) (Figure 7C), which likely reflect recurrent circuit activities in pilocarpine-treated hippocampal slices (Peret et al., 2014). Interestingly, the frequency power spectrogram (Figure 7C) revealed a marked reduction of power during RBs, but not PD, in *C1ql2/3* null, as well as in *GluK2* null DGCs. These results indicate that although pilocarpine induced MF sprouting, KARs were not recruited to *C1ql2/3* null DGCs, and the lack of postsynaptic KARs contributed to the reduction of recurrent burst activities.

To examine the pathological role of *C1ql2/3* in vivo, we next employed a pilocarpine-induced chronic epilepsy model in mice (Peret et al., 2014). One to two months after the occurrence of status epilepticus, we performed continuous video-electroencephalographic recording from the dentate gyrus of freely moving WT and *C1ql2/3* null mice for 3 days. Although both genotypes displayed ictal discharges (Figure 7D) associated with generalized tonic-clonic seizures, the number of ictal events was significantly reduced in *C1ql2/3* null mice (Figure 7E). IHC analysis revealed numerous ZnT3- and Bassoon-immunopositive sprouted MFs in both WT and *C1ql2/3* null dentate gyrus (Figures 7F and S7A). Importantly, sprouted MF terminals in the dentate gyrus were immunopositive for *C1ql2* (Figure S7B) and colocalized with KARs (Figures 7F and S7C) in WT, but not in *C1ql2/3* null dentate gyrus. Together, these results indicate that *C1ql2/3* originating from sprouted MFs recruit postsynaptic KARs in DGCs, contributing to recurrent circuit activities in the chronic epilepsy model in vitro and in vivo (Figure 7G).

## DISCUSSION

In this study, we showed that MF-derived *C1ql2* and *C1ql3* serve as extracellular organizers to recruit functional postsynaptic KAR complexes, including Neto1 and high-affinity KAR subunits, to the CA3 pyramidal neurons (Figure 7G). *C1ql2* and *C1ql3* specif-

ically bound the ATD of postsynaptic *GluK2* and *GluK4* KARs and the presynaptic *Nrx3+SS5<sup>25b</sup>*. Considering that *C1q*-like proteins are expressed in multiple brain regions (Iijima et al., 2010), we propose that they are likely involved in recruitment and functional control of KARs at a broad variety of synapses. Our results suggest that *C1q*-like proteins serve as much broader feed-forward signals than previously appreciated and impact directly on glutamatergic circuit formation and function, illustrating a novel, and possibly general, principle of iGluR regulation.

### Presynaptically Derived Anchors for Postsynaptic Targeting of iGluRs

Precise targeting of specific iGluRs to the postsynaptic sites is crucial for the function of neuronal circuits. PSD-95 family proteins, such as PSD-93, PSD-95, and SAP-102, play essential roles in synaptic trafficking, stabilization, and function of postsynaptic AMPARs and, to a lesser extent, NMDARs (Elias et al., 2006), by binding to the C termini of transmembrane AMPAR regulatory proteins (TARPs) and *GluN2* subunits, respectively. Similarly, PDZ-domain proteins, such as GRIP, PICK1, syntenin, and PSD-95, bind to the C termini of KARs and play important roles in clustering and stabilizing them at postsynaptic sites (Hirbec et al., 2003; Pahl et al., 2014). However, it is not completely clear how PDZ proteins are targeted to specific postsynaptic sites to mediate the clustering of certain members of postsynaptic iGluRs (Elias and Nicoll, 2007). Indeed, the molecular mechanisms for the highly restricted expression of postsynaptic KARs at MF-CA3 synapses have been unclear (Carta et al., 2014; Pahl et al., 2014).

Recruitment of postsynaptic receptors by presynaptically derived soluble factors represents an alternative, or complementary, strategy to ensure their accumulation at a site apposed to its presynaptic counterpart. For example, agrin, a prototypical presynaptic protein at neuromuscular junctions, induces acetylcholine receptor clustering indirectly by binding to the ectodomain of MuSK (Gautam et al., 1996). Recently, MADD-4B (punctin) was identified as a secreted anterograde organizer of GABAergic synapses through its binding to neuroligin and UNC-40 in *C. elegans* muscles (Maro et al., 2015; Tu et al., 2015). Neuronal pentraxins contribute to clustering and stabilizing postsynaptic AMPARs in parvalbumin-positive interneurons, binding mainly to the *GluA4* subunit (Pelkey et al., 2015; Sia et al., 2007).

In contrast to the examples above, *C1q* family proteins are unique in that they are exclusively produced by specific presynaptic neurons and appear to directly anchor postsynaptic receptors to presynaptic membranes. Parallel fibers secrete Cbln1 to accumulate and regulate the function of a postsynaptic iGluR member, *GluD2*, in cerebellar Purkinje cells through the direct binding (Matsuda et al., 2010; Uemura et al., 2010). We now report that *C1ql2* and *C1ql3*, provided by MFs, recruit

(G) Equilibrium SPR analysis of binding between gC1ql3 and immobilized peptide S5-9. Peptide S5-9 bound directly to gC1ql3.

(H) Equilibrium SPR analysis of binding between ect-Nrx3 $\beta$  + SS5<sup>25b</sup> and immobilized full-length *C1ql2* (*C1ql2* FL). The ect-Nrx3 $\beta$ +SS5<sup>25b</sup> bound to *C1ql2* FL with a higher affinity than ect-Nrx3 $\beta$ -SS5<sup>25b</sup> did.

Data are presented as mean  $\pm$  SEM. See also Figure S6.

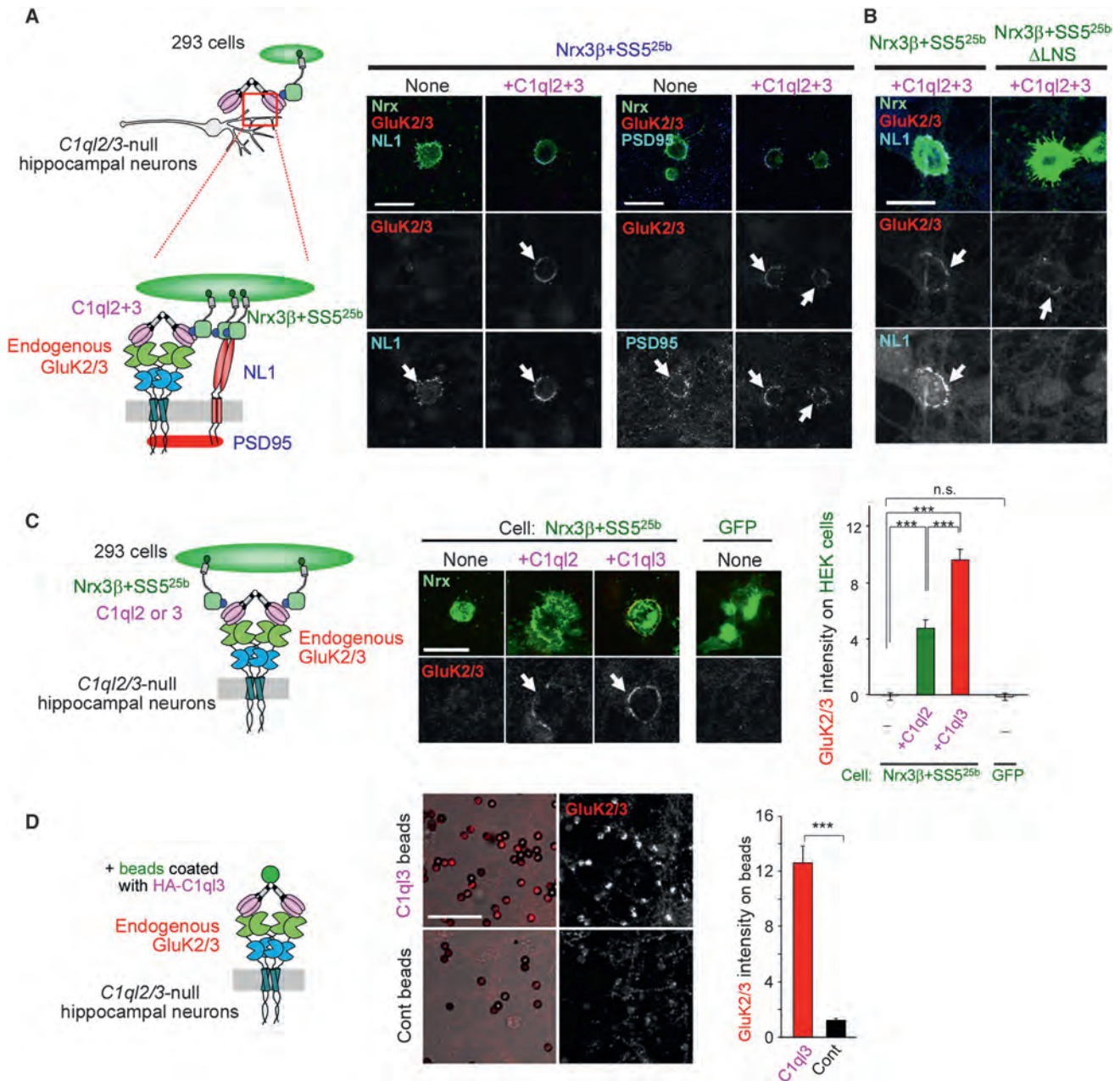


**Figure 5. Nr3-C1q2/3 Signaling Recruits KARs in Cultured Hippocampal Neurons**

(A and B) HEK293 cells coexpressing C1q2, C1q3, and Nr3β recruit KARs in C1q2/3 null hippocampal neurons. HEK293 cells expressing Flag-tagged Nr3β containing SS5<sup>25b</sup> (Nr3β+SS5<sup>25b</sup>; green) were cocultured with C1q2/3 null hippocampal neurons. Panels in (A) show accumulation of NL1 (left) and PSD95 (right) immunoreactivities (blue) in juxtaposed hippocampal neurons. GluK2/3 immunoreactivity (red) clustered only when C1q2 and C1q3 (C1q2+3) were coexpressed in HEK293 cells. Panels in (B) show that HEK293 cells expressing Nr3β lacking the LNS6 domain (Nr3β+SS5<sup>25b</sup>ΔLNS) accumulated GluK2/3 (red), but not NL1 (blue), immunoreactivities in hippocampal neurons. Scale bar, 25 μm.

(C) HEK293 cells coexpressing Nr3β+SS5<sup>25b</sup> and either C1q2 or C1q3 recruit KARs in C1q2/3 null hippocampal neurons. Panels show accumulation of GluK2/3 immunoreactivity (red) in hippocampal neurons juxtaposed to HEK293 cells coexpressing Nr3β+SS5<sup>25b</sup> (green) and either C1q2 or C1q3. Scale bar, 25 μm. The graph shows the mean GluK2/3 immunoreactivity accumulated around HEK293 cells. At least n > 100 cells were analyzed from two independent experiments. \*\*\*p < 0.001 by Kruskal-Wallis test and Scheffe post hoc test.

(D) C1q3 directly serves as a synaptic organizer for KARs. Beads coated with HA-C1q3, but not uncoated beads (control), accumulated GluK2/3 immunoreactivity (red) in C1q2/3 null cultured hippocampal neurons. Scale bar, 20 μm. The graph shows the mean GluK2/3 immunoreactivity on the beads. At least n > 300 beads were analyzed from two independent experiments. \*\*\*p < 0.001 by Mann-Whitney U test. Data are presented as mean ± SEM.

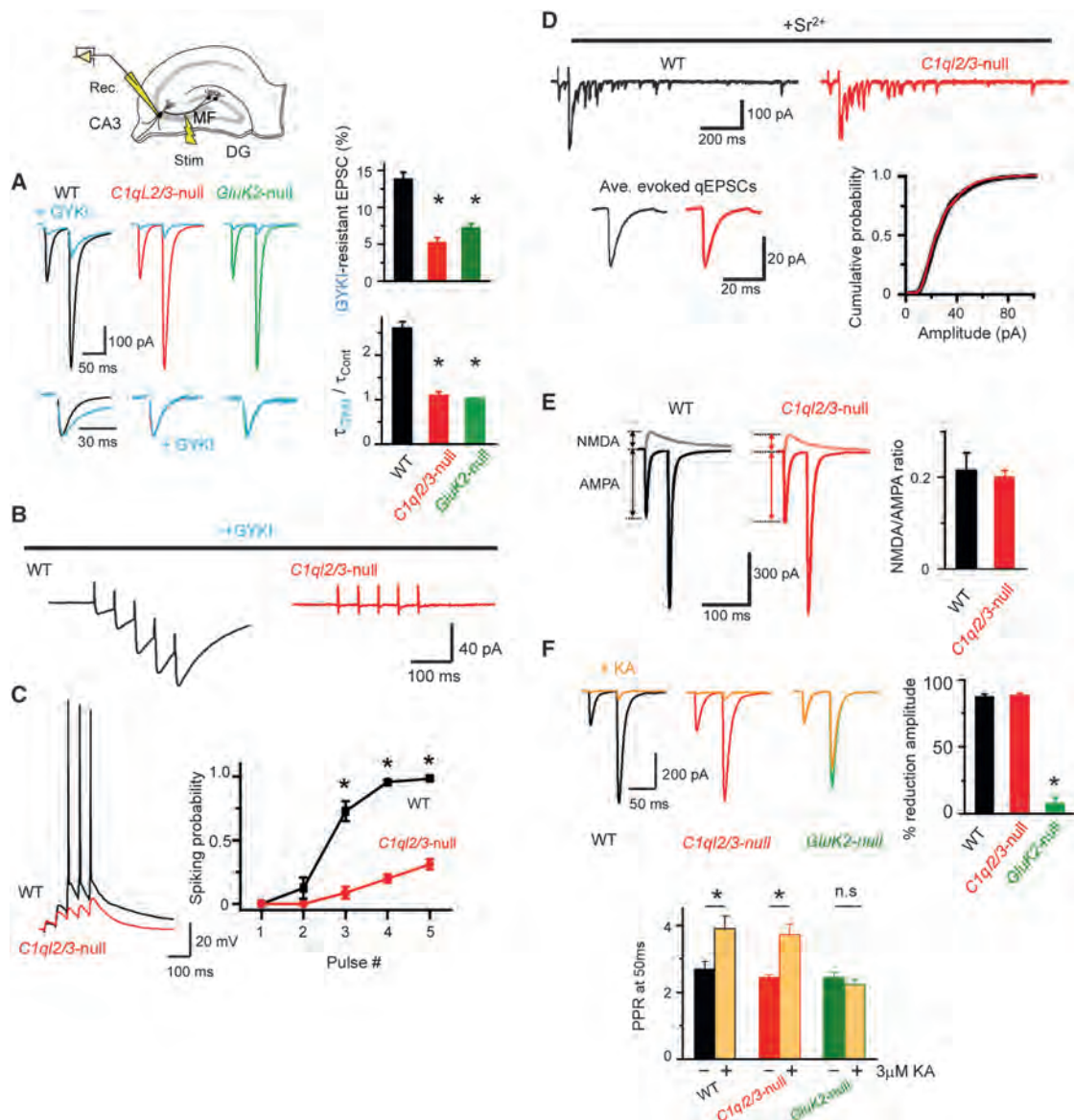


### Figure 6. C1qL2/3 Determine Postsynaptic KAR Functions in the Hippocampus

(A) Loss of postsynaptic KAR-mediated EPSCs in *C1qL2/3* null hippocampus. MF-evoked EPSCs were recorded in the absence and presence of 60  $\mu$ M GYKI52466 (GYKI) combined with 25  $\mu$ M D-AP-5 (blue lines) to evaluate KAR-mediated EPSCs in WT (black,  $n = 19$  from 7 mice), *C1qL2/3* null (red,  $n = 13$  from 6 mice), or *GluK2* null (green,  $n = 9$  from 4 mice) CA3 neurons at  $-70$  mV. The top graph shows mean amplitudes of GYKI-resistant MF-EPSCs. Lower enlarged traces show slowly decaying GYKI-resistant MF-EPSCs in WT, but not in *C1qL2/3* null or *GluK2* null CA3 neurons. The bottom graph shows the mean ratio of decay time constants before and after application of GYKI. \* $p < 0.05$  versus WT by one-way ANOVA followed by Bonferroni post hoc analysis.

(B) *C1qL2/3* modulate KAR-mediated summation of MF-EPSCs. Representative traces show that MF stimulation at 20 Hz five times in the presence of GYKI (100  $\mu$ M) and D-AP5 (25  $\mu$ M) evoked EPSC summation in WT (black,  $n = 11$  from 3 mice), but not in *C1qL2/3* null (red,  $n = 11$  from 3 mice), CA3 pyramidal neurons.

(C) *C1qL2/3* modulate likelihood of action potential initiation during repetitive MF stimulation. Representative EPSP traces show that MF stimulation at 20 Hz five times resulted in action potential generation in WT (black,  $n = 11$  from 4 mice), but not in *C1qL2/3* null (red,  $n = 10$  from 4 mice), CA3 pyramidal neurons. The graph shows spiking probability plotted against the number of MF stimulation. \* $p < 0.05$  by Mann-Whitney U test.

(D) No changes in postsynaptic AMPARs. Representative traces show asynchronous MF-evoked EPSCs in WT (black,  $n = 7$  cells) and *C1qL2/3* null (red,  $n = 9$  cells) CA3 pyramidal neurons clamped at  $-80$  mV in the presence of 8 mM Sr<sup>2+</sup>, 50  $\mu$ M D-AP5, and 5  $\mu$ M UBP310. Averaged asynchronous EPSCs (aEPSCs, bottom) indicate no differences in the amplitude and kinetics. The graph shows cumulative plot of aEPSCs in WT (black) and *C1qL2/3* null CA3 neurons (red).

(E) No changes in the postsynaptic AMPA/NMDA ratio. MF-evoked EPSCs were recorded at  $-80$  mV (thick lines) to estimate AMPAR-mediated components and at  $+40$  mV in the presence of 20  $\mu$ M CNQX (thin lines) to evaluate NMDAR components in WT ( $n = 8$ ) and *C1qL2/3* null ( $n = 9$ ) CA3 pyramidal neurons. The graph shows averaged AMPA/NMDA ratio in each genotype. \* $p < 0.05$  by Mann-Whitney U test.

(legend continued on next page)

KARs in CA3 pyramidal neurons by directly binding to GluK2 and GluK4 KARs.

### The Role of iGluR ATDs

The extracellular region of each iGluR subunit consists of one ATD and one ligand-binding domain (LBD), both of which belong to the periplasmic binding protein superfamily. Although the ATDs can make up nearly half of the full-length protein chains, their functional significance is not completely clear. The ATDs assist subtype-selective subunit assembly in AMPARs and KARs (Ayalon and Stern-Bach, 2001; Kumar et al., 2011; Rossmann et al., 2011) and allosterically modify NMDAR channel activities (Gielen et al., 2009; Karakas et al., 2011). An increasing number of soluble and transmembrane synaptic proteins are reported to bind iGluR ATDs. For example, neuronal pentraxins bind GluA4 (Pelkey et al., 2015; Sia et al., 2007), N-cadherin binds GluA2 (Saglietti et al., 2007), EphB binds GluN1 (Dalva et al., 2000), and Cbln1 binds GluD1 and GluD2 (Matsuda et al., 2010; Uemura et al., 2010). We have now demonstrated that C1q2 and C1q3 bind the ATDs of GluA1, GluK2, and GluK4. These findings suggest that the ATDs of iGluRs, which extend ~13 nm away from the postsynaptic site (Karakas et al., 2015), are strategically suitable for interactions with synaptic proteins that regulate the positioning, and thus function, of iGluRs. We propose that yet-undefined synaptic proteins bind the ATDs of all iGluR family members currently “orphan” to modulate their functions at synapses. At least some of these unknown iGluR partners may belong to the C1q superfamily.

Unlike KARs, postsynaptic localization of GluA1 was unaffected in *C1q2/3* null MF-CA3 synapses in vivo (Figure S2E). Indeed, the amplitude and kinetics of AMPAR-mediated quantal EPSCs elicited by MF stimulation were similar between WT and *C1q2/3* null CA3 neurons (Figure 6D). These results indicate that *C1q2/3* do not regulate localization and functions of postsynaptic AMPARs, at least at MF-CA3 synapses. However, considering that *C1q2/3* specifically bind GluA1, we speculate that *C1q2/3* may affect localization and/or functions of AMPARs consisting predominantly of GluA1, which may occur during plasticity (Shi et al., 2001) and in glia (Douyard et al., 2007). Although several amino acid residues in the L3 and L4 regions of GluK2-ATD were involved in binding C1q3 (Figures S3A–S3C), similar motifs are not found in the corresponding regions of the ATDs of GluA1. Thus, further studies are needed to clarify how *C1q2/3* bind the ATD of GluA1 to impact AMPAR functions.

Although allosteric interactions between the ATD and LBD were demonstrated to date only for NMDARs, recent studies indicate that AMPA and kainate receptor ectodomains could also adopt conformations linked to allosteric regulation (Cais et al., 2014; Dutta et al., 2015; Krieger et al., 2015). Indeed, although approximately half GluD2 is still localized at postsyn-

aptic sites of the parallel fiber-Purkinje cell synapses in *Cbln1* null cerebellum, the GluD2-dependent LTD is completely abolished in *Cbln1* null mice (Hirai et al., 2005). Since D-Serine binding to the LBD of GluD2 activates downstream signaling to induce LTD (Kakegawa et al., 2011), the failure to induce LTD in *Cbln1* null Purkinje cells suggests that *Nrx-Cbln1* binding to the ATD allosterically regulates the LBD response to D-Serine to modulate GluD2 signaling at synapses. Thus, binding of *Nrx-C1q2/3* to the ATD of KARs, and perhaps binding of other synaptic molecules to iGluR ATDs, may not only modulate the location of receptors, but is also likely to regulate iGluR signaling by restricting the range of relative LBD motions.

### *Nrx3* Containing the SS5<sup>25b</sup> Sequence Binds C1q-like Proteins

Neurexins are encoded by three genes (*NRXN1–NRXN3* in human), each of which uses two promoters to generate  $\alpha$  and  $\beta$  transcripts. Furthermore, alternative splicing of *Nrx* genes at six sites generates thousands of distinct isoforms in various brain regions (Schreiner et al., 2014; Treutlein et al., 2014). Such extensive variation in *Nrx* isoforms is thought to be used as a synapse-selective code to interact with distinct postsynaptic receptors. Indeed, the SS4 insert is crucial for *Nrxs* to bind Cbln1 (Matsuda and Yuzaki, 2011; Uemura et al., 2010), whereas it blocks interaction of *Nrxs* with latrophilin and LRRTMs (Boucard et al., 2012; Ko et al., 2009) and may modulate the affinity of *Nrxs* to neuroligin isoforms (Boucard et al., 2005; Chih et al., 2006; Koehnke et al., 2010). However, whether other *Nrx* splicing sites play similar roles has remained unclear. Our finding that a sequence encoded by exon 25b in the splice site 5 of *Nrx3* critically determines its binding affinity to C1q2/3 (Figure 4) suggests that there remain yet-undefined partners for *Nrxs* regulated by alternative splicing. Because C1q2/3 immunoreactivities were significantly reduced in *GluK2* or *GluK4* null hippocampus (Figure 2), *Nrxs* may not be sufficient to stabilize C1q2/3 at synapses. Further studies are warranted to clarify how *Nrx* splicing isoforms regulate synaptic functions.

The sequence critical for binding to C1q3 consists of 17 amino acids and is specific to *Nrx3* (Figure S6). Interestingly, *NRXN3* single-nucleotide polymorphisms (SNPs) are associated with addiction and obesity (Hishimoto et al., 2007; Lachman et al., 2007), and a SNP near the splice site 5 alters expression of *Nrx3+SS5<sup>25b</sup>* (Hishimoto et al., 2007). Furthermore, de novo and inherited deletions in *NRXN3* were reported for autism spectrum disorders (ASDs) (Vaags et al., 2012). Similarly, mutations in *GRIK2* gene encoding GluK2 were linked to ASDs (Jamain et al., 2002), intellectual disability, and epilepsy (Córdoba et al., 2015; Motzack et al., 2007). We also demonstrated that C1q2 and C1q3 modulate synaptic network activities in a temporal lobe epilepsy model, as well as in control conditions, by regulating localization and function of postsynaptic KARs in the

(F) Normal presynaptic KAR functions at *C1q2/3* null MF-CA3 synapses. Representative traces show that MF-EPSCs at interstimulus interval of 50 ms were inhibited by 3  $\mu$ M kainate (orange) in WT (black,  $n = 7$  from 3 mice) and *C1q2/3* null (red,  $n = 10$  from 4 mice), but not in *GluK2* null (green,  $n = 7$  from 3 mice), CA3 pyramidal neurons in the presence of 25  $\mu$ M D-AP-5. The graphs show the percentages of kainate-induced reduction of amplitudes (top) and the paired-pulse facilitation ratio (PPR; bottom) of MF-EPSCs. \* $p < 0.05$  versus WT; n.s., no significance, by one-way ANOVA followed by Bonferroni post hoc analysis. Data are presented as mean  $\pm$  SEM.

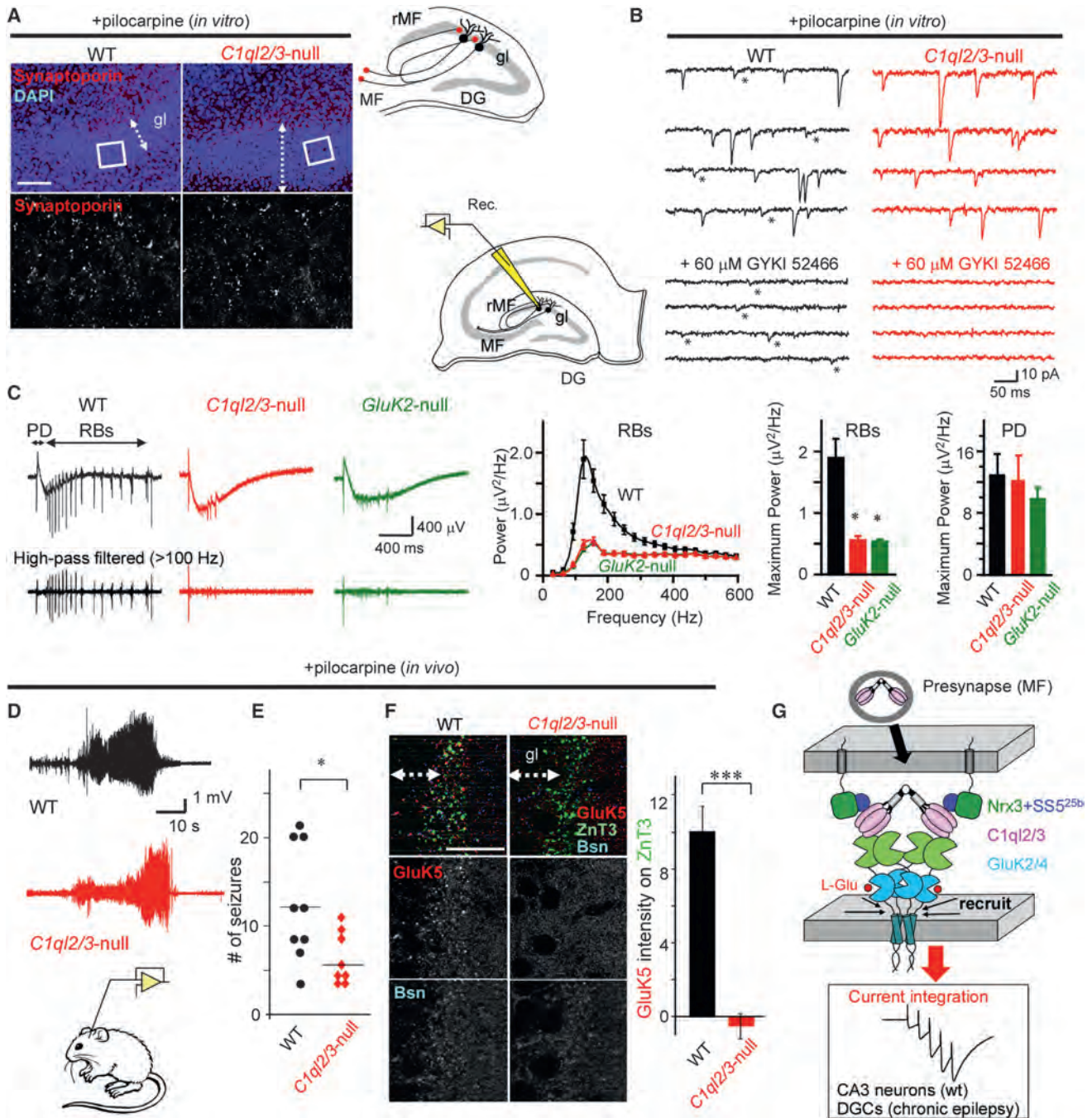


**Figure 7. C1qI2/3 Regulate Postsynaptic Localization of KARs in Sprouted MFs and Contribute to Recurrent Circuit Activities in Chronic Epilepsy Models**

(A–C) *In vitro* model.

(A) The representative IHC image shows similar levels of sprouted recurrent MF terminals (rMF) immunopositive for synaptoporphin (red) and DAPI (blue) in the granular layer of the dentate gyrus (*gl*, dotted lines) in WT and *C1qI2/3* null cultured hippocampal slices treated with pilocarpine. The boxed regions are enlarged in the bottom. Scale bar, 100  $\mu$ m.

(B) Spontaneous EPSCs recorded from WT (black, *n* = 19 slices), but not *C1qI2/3* null (red, *n* = 38 slices), DGCs show KAR-mediated components. Holding potential, –80 mV. Asterisks indicate slow representative KAR-mediated EPSCs, which were resistant to 60  $\mu$ M GYKI52466 and 50  $\mu$ M D-AP-5 (lower traces).

(C) Extracellular field recordings of spontaneous epileptiform activity in the dentate gyrus (in ACSF containing 5 mM K<sup>+</sup> and 100  $\mu$ M picrotoxin) from WT (black, *n* = 42 slices), *C1qI2/3* null (red, *n* = 32 slices), or *GluK2* null slices (green, *n* = 28 slices). Interictal-like activity consists of paroxysmal discharge (PD) followed by recurrent bursts (RBs). High-pass filtered (>100 Hz) traces are shown in the bottom. Graphs show power spectrum analysis of filtered RBs (left), maximum power of RBs (middle), and PDs (right) in each group. \**p* < 0.05 versus WT by one-way ANOVA followed by Bonferroni post hoc analysis.

(legend continued on next page)

mouse hippocampus (Figure 7G). A detailed characterization of the molecular interaction networks involving Nrxs, C1q-like molecules, and iGluRs is therefore essential for understanding and exploring new drug targets for neuropsychiatric and neurodevelopmental disorders.

## EXPERIMENTAL PROCEDURES

### Animals

*C1ql2* null mice (TG0022) were purchased from Texas Institute for Genomic Medicine. *C1ql3* floxed mice were generated by homologous recombination targeting exon 2 of *C1ql3* gene. *GluK2* floxed mice were generated by homologous recombination targeting exon 14 of *Grik2* gene. To generate *C1ql3* null or *GluK2* null mice, the floxed mice were crossed with the telencephalin-*Cre* transgenic mice (Fuse et al., 2004). All procedures related to animal care and treatment were approved by the Animal Resource Committee of Keio University.

### Preparation of Recombinant Proteins

A hemagglutinin (HA)-tagged C1q3 or C1q2 protein was expressed in HEK293 tSA cells as described previously (Kakegawa et al., 2015). Histidine (His)-tagged gC1q1, gC1q2, or gC1q3 proteins; GluK-ATD; or ectodomain of neurexin (Nrx) 3 $\beta$  for SPR assays were expressed in HEK293T cells as previously described (Aricescu et al., 2006).

### Cell-Based C1q2/3 Binding Assays

HEK293 cells transfected with pDisplay vectors containing myc-tagged iGluR ATDs or Flag-tagged Nrx3 constructs were incubated with equivalent concentrations (13–25 nM) of HA-tagged C1q2, C1q3, or Cbln1 for 4 hr, fixed with 4% paraformaldehyde, and immunostained. The intensity of HA immunoreactivity within the myc-immunopositive cell area was quantified.

### Primary Cultures

Hippocampal cultures were prepared from embryonic day 17 to day-of-birth *C1ql2/3* null mice as previously described (Matsuda et al., 2013) and cocultured with HA-C1q3 immobilized to avidin beads (Dyna) or HEK293 cells transfected with Nrx3 $\beta$ -Flag. The intensity of GluK2/3 immunoreactivity within segmented beads or Flag-immunopositive areas was quantified.

### SPR

SPR experiments were performed with streptavidin-coated CM5 chips using a Biacore T200 instrument (GE Healthcare). Proteins carrying a C-terminal Avitag were biotinylated using biotin ligase (BirA). Sensorgrams were analyzed using equilibrium and kinetics binding models.

### Immunogold EM

GluK2 or C1q2 was labeled with gold-conjugated antibodies. The density of the immunogold particles per 100 nm length of postsynaptic densities on the electron micrographs was analyzed.

### Electrophysiology

Whole-cell voltage-clamp and extracellular field recordings were made in hippocampal slices from WT, *C1ql2/3* null, and *GluK2* null mice at post-natal day (P)12–P20. Excitatory postsynaptic currents were recorded from CA3 pyramidal cells and dentate gyrus granule cells.

### In Vitro Model of Temporal Lobe Epilepsy

Brain slice cultures containing the hippocampus and the entorhinal cortex (350  $\mu$ m thickness) were prepared from *GluK2* null, *C1ql2/3* null, and WT mice at P9–P10 as previously described (Peret et al., 2014). Pilocarpine (0.5  $\mu$ M) was added to the medium at 5 days in vitro (DIV) and incubated for 2 days. Slices were used for experiments at 9–12 DIV.

### In Vivo Model of Temporal Lobe Epilepsy

Scopolamine (2 mg/kg) was administered intraperitoneally (i.p.) 30 min before application of pilocarpine (250 mg/kg, i.p.) to age- and gender-matched *C1ql2/3* null and WT mice at P60–P90. Intrahippocampal electroencephalographic (EEG) recordings were performed in freely moving animals.

### Data Analysis and Statistics

All values are presented as the mean  $\pm$  SEM, and statistical significance between multiple groups was determined by Kruskal-Wallis test followed by Steel post hoc test, unless otherwise noted. Statistical significance between two groups with normal distribution was determined by Student's t test. Statistical significance was assumed when  $p < 0.05$ .

## SUPPLEMENTAL INFORMATION

Supplemental Information includes Supplemental Experimental Procedures and seven figures and can be found with this article online at <http://dx.doi.org/10.1016/j.neuron.2016.04.001>.

## AUTHOR CONTRIBUTIONS

K.M. designed the project, carried out the biochemical and anatomical works, analyzed the data, and wrote the paper. T.B. and W.K. carried out the electrophysiological works and analyzed the data. N.M. and A.R.A. performed SPR analyses and designed constructs. M.K. and Y.S. supervised and performed EEG experiments. E.M., M. Yamasaki, and M.U. performed the anatomical experiments. K.K. performed in situ hybridization experiments. M.A., I.W., and K.S. generated and developed mutant mice. M.W. generated essential antibodies. M. Yuzaki and A.R.A. designed and supervised the project and wrote the paper.

## ACKNOWLEDGMENTS

We thank S. Narumi, J. Motohashi, and K. Suzuki for their technical assistance and M. Yamazaki and K. Akashi for production of *C1ql3* and *GluK2* null mice. We also thank H. Sakuma and T. Watanabe (Zeiss) for their support on super-resolution microscopy analysis. This work was supported by the Grant-in-Aid from the MEXT (K.M., T.B., and M. Yuzaki), the CREST from the JST (M. Yuzaki), the Keio Gijyuku Fukuzawa Memorial Fund for the Advancement of Education and Research (K.M.), the Human Frontier Research Program (RGP0065/2014 to M. Yuzaki and A.R.A.), the UK Medical Research Council (A.R.A.), and a Wellcome Trust D.Phil. studentship (N.M.). Further support from the Wellcome Trust Core Award Grant Number 090532/Z/09/Z is acknowledged. A.R.A. is an MRC Senior Research Fellow.

Received: November 2, 2015

Revised: February 29, 2016

Accepted: March 30, 2016

Published: April 28, 2016

(D–F) In vivo model.

(D) Typical ictal traces recorded from the dentate gyrus of pilocarpine-treated WT (black) and *C1ql2/3* null (red) mice.

(E) Number of ictal events in WT ( $n = 9$ ) and *C1ql2/3* null mice ( $n = 8$ ) per 72 hr. \* $p < 0.05$  by Mann-Whitney U test.

(F) Sprouted MFs do not recruit GluK5 in *C1ql2/3* null hippocampus. IHC analyses show sprouted MF terminals immunopositive for ZnT3 (green) and Bassoon (Bsn; blue) in the supra-granular layer of the dentate gyrus of pilocarpine-treated mice. GluK5 immunoreactivity (red) colocalized with ZnT3-positive MF terminals in WT, but not in *C1ql2/3* null, dentate gyrus. Granule layer is indicated by dotted lines (gl). Scale bar, 25  $\mu$ m. The right graph shows mean GluK5 fluorescence intensities on ZnT3-immunopositive MF terminals. \*\*\* $p < 0.001$ .  $n = 9$  regions from 3 mice for each genotype.

(G) Proposed molecular model leading to transsynaptic modulation of kainate receptor function by neurexin and C1ql proteins.

Data are presented as mean  $\pm$  SEM. See also Figure S7.

## REFERENCES

- Akashi, K., Kakizaki, T., Kamiya, H., Fukaya, M., Yamasaki, M., Abe, M., Natsume, R., Watanabe, M., and Sakimura, K. (2009). NMDA receptor GluN2B (GluR epsilon 2/NR2B) subunit is crucial for channel function, postsynaptic macromolecular organization, and actin cytoskeleton at hippocampal CA3 synapses. *J. Neurosci.* *29*, 10869–10882.
- Aricescu, A.R., Lu, W., and Jones, E.Y. (2006). A time- and cost-efficient system for high-level protein production in mammalian cells. *Acta Crystallogr. D Biol. Crystallogr.* *62*, 1243–1250.
- Ayalon, G., and Stern-Bach, Y. (2001). Functional assembly of AMPA and kainate receptors is mediated by several discrete protein-protein interactions. *Neuron* *31*, 103–113.
- Bolliger, M.F., Martinelli, D.C., and Südhof, T.C. (2011). The cell-adhesion G protein-coupled receptor BAI3 is a high-affinity receptor for C1q-like proteins. *Proc. Natl. Acad. Sci. USA* *108*, 2534–2539.
- Boucard, A.A., Chubykin, A.A., Comoletti, D., Taylor, P., and Südhof, T.C. (2005). A splice code for trans-synaptic cell adhesion mediated by binding of neuroligin 1 to alpha- and beta-neurexins. *Neuron* *48*, 229–236.
- Boucard, A.A., Ko, J., and Südhof, T.C. (2012). High affinity neurexin binding to cell adhesion G-protein-coupled receptor C1RL1/latrophilin-1 produces an intercellular adhesion complex. *J. Biol. Chem.* *287*, 9399–9413.
- Cais, O., Herguedas, B., Krol, K., Cull-Candy, S.G., Farrant, M., and Greger, I.H. (2014). Mapping the interaction sites between AMPA receptors and TARPs reveals a role for the receptor N-terminal domain in channel gating. *Cell Rep.* *9*, 728–740.
- Carta, M., Fièvre, S., Gorlewicz, A., and Mulle, C. (2014). Kainate receptors in the hippocampus. *Eur. J. Neurosci.* *39*, 1835–1844.
- Castillo, P.E., Malenka, R.C., and Nicoll, R.A. (1997). Kainate receptors mediate a slow postsynaptic current in hippocampal CA3 neurons. *Nature* *388*, 182–186.
- Chih, B., Gollan, L., and Scheiffele, P. (2006). Alternative splicing controls selective trans-synaptic interactions of the neuroligin-neurexin complex. *Neuron* *51*, 171–178.
- Contractor, A., Swanson, G.T., Sailer, A., O’Gorman, S., and Heinemann, S.F. (2000). Identification of the kainate receptor subunits underlying modulation of excitatory synaptic transmission in the CA3 region of the hippocampus. *J. Neurosci.* *20*, 8269–8278.
- Contractor, A., Mulle, C., and Swanson, G.T. (2011). Kainate receptors coming of age: milestones of two decades of research. *Trends Neurosci.* *34*, 154–163.
- Copits, B.A., and Swanson, G.T. (2012). Dancing partners at the synapse: auxiliary subunits that shape kainate receptor function. *Nat. Rev. Neurosci.* *13*, 675–686.
- Córdoba, M., Rodríguez, S., González Morón, D., Medina, N., and Kauffman, M.A. (2015). Expanding the spectrum of Grik2 mutations: intellectual disability, behavioural disorder, epilepsy and dystonia. *Clin. Genet.* *87*, 293–295.
- Dalva, M.B., Takasu, M.A., Lin, M.Z., Shamah, S.M., Hu, L., Gale, N.W., and Greenberg, M.E. (2000). EphB receptors interact with NMDA receptors and regulate excitatory synapse formation. *Cell* *103*, 945–956.
- Douyard, J., Shen, L., Haganir, R.L., and Rubio, M.E. (2007). Differential neuronal and glial expression of GluR1 AMPA receptor subunit and the scaffolding proteins SAP97 and 4.1N during rat cerebellar development. *J. Comp. Neurol.* *502*, 141–156.
- Dutta, A., Krieger, J., Lee, J.Y., García-Nafria, J., Greger, I.H., and Bahar, I. (2015). Cooperative dynamics of intact AMPA and NMDA glutamate receptors: similarities and subfamily-specific differences. *Structure* *23*, 1692–1704.
- Elias, G.M., and Nicoll, R.A. (2007). Synaptic trafficking of glutamate receptors by MAGUK scaffolding proteins. *Trends Cell Biol.* *17*, 343–352.
- Elias, G.M., Funke, L., Stein, V., Grant, S.G., Bredt, D.S., and Nicoll, R.A. (2006). Synapse-specific and developmentally regulated targeting of AMPA receptors by a family of MAGUK scaffolding proteins. *Neuron* *52*, 307–320.
- Fuse, T., Kanai, Y., Kanai-Azuma, M., Suzuki, M., Nakamura, K., Mori, H., Hayashi, Y., and Mishina, M. (2004). Conditional activation of RhoA suppresses the epithelial to mesenchymal transition at the primitive streak during mouse gastrulation. *Biochem. Biophys. Res. Commun.* *318*, 665–672.
- Gautam, M., Noakes, P.G., Moscoso, L., Rupp, F., Scheller, R.H., Merlie, J.P., and Sanes, J.R. (1996). Defective neuromuscular synaptogenesis in agrin-deficient mutant mice. *Cell* *85*, 525–535.
- Gielen, M., Siegler Retchless, B., Mony, L., Johnson, J.W., and Paoletti, P. (2009). Mechanism of differential control of NMDA receptor activity by NR2 subunits. *Nature* *459*, 703–707.
- Gokce, O., and Südhof, T.C. (2013). Membrane-tethered monomeric neurexin LNS-domain triggers synapse formation. *J. Neurosci.* *33*, 14617–14628.
- Hardingham, G.E., and Bading, H. (2010). Synaptic versus extrasynaptic NMDA receptor signalling: implications for neurodegenerative disorders. *Nat. Rev. Neurosci.* *11*, 682–696.
- Hirai, H., Pang, Z., Bao, D., Miyazaki, T., Li, L., Miura, E., Parris, J., Rong, Y., Watanabe, M., Yuzaki, M., and Morgan, J.I. (2005). Cbln1 is essential for synaptic integrity and plasticity in the cerebellum. *Nat. Neurosci.* *8*, 1534–1541.
- Hirbec, H., Francis, J.C., Lauri, S.E., Braithwaite, S.P., Coussen, F., Mülle, C., Dev, K.K., Coutinho, V., Meyer, G., Isaac, J.T., et al. (2003). Rapid and differential regulation of AMPA and kainate receptors at hippocampal mossy fibre synapses by PICK1 and GRIP. *Neuron* *37*, 625–638.
- Hishimoto, A., Liu, Q.R., Drgon, T., Pletnikova, O., Walther, D., Zhu, X.G., Troncoso, J.C., and Uhl, G.R. (2007). Neurexin 3 polymorphisms are associated with alcohol dependence and altered expression of specific isoforms. *Hum. Mol. Genet.* *16*, 2880–2891.
- Iijima, T., Miura, E., Watanabe, M., and Yuzaki, M. (2010). Distinct expression of C1q-like family mRNAs in mouse brain and biochemical characterization of their encoded proteins. *Eur. J. Neurosci.* *31*, 1606–1615.
- Jamain, S., Betancur, C., Quach, H., Philippe, A., Fellous, M., Giros, B., Gillberg, C., Leboyer, M., and Bourgeron, T.; Paris Autism Research International Sibpair (PARIS) Study (2002). Linkage and association of the glutamate receptor 6 gene with autism. *Mol. Psychiatry* *7*, 302–310.
- Kakegawa, W., Miyoshi, Y., Hamase, K., Matsuda, S., Matsuda, K., Kohda, K., Emi, K., Motohashi, J., Konno, R., Zaitzu, K., and Yuzaki, M. (2011). D-serine regulates cerebellar LTD and motor coordination through the  $\delta 2$  glutamate receptor. *Nat. Neurosci.* *14*, 603–611.
- Kakegawa, W., Mitakidis, N., Miura, E., Abe, M., Matsuda, K., Takeo, Y.H., Kohda, K., Motohashi, J., Takahashi, A., Nagao, S., et al. (2015). Anterograde C1q1 signaling is required in order to determine and maintain a single-winner climbing fiber in the mouse cerebellum. *Neuron* *85*, 316–329.
- Kamiya, H., and Ozawa, S. (2000). Kainate receptor-mediated presynaptic inhibition at the mouse hippocampal mossy fibre synapse. *J. Physiol.* *523*, 653–665.
- Karakas, E., Simorowski, N., and Furukawa, H. (2011). Subunit arrangement and phenylethanolamine binding in GluN1/GluN2B NMDA receptors. *Nature* *475*, 249–253.
- Karakas, E., Regan, M.C., and Furukawa, H. (2015). Emerging structural insights into the function of ionotropic glutamate receptors. *Trends Biochem. Sci.* *40*, 328–337.
- Kishore, U., Gaboriaud, C., Waters, P., Shrive, A.K., Greenhough, T.J., Reid, K.B., Sim, R.B., and Arlaud, G.J. (2004). C1q and tumor necrosis factor superfamily: modularity and versatility. *Trends Immunol.* *25*, 551–561.
- Ko, J., Fuccillo, M.V., Malenka, R.C., and Südhof, T.C. (2009). LRRTM2 functions as a neurexin ligand in promoting excitatory synapse formation. *Neuron* *64*, 791–798.
- Koehnke, J., Katsamba, P.S., Ahlsen, G., Bahna, F., Vendome, J., Honig, B., Shapiro, L., and Jin, X. (2010). Splice form dependence of beta-neurexin/neuroligin binding interactions. *Neuron* *67*, 61–74.
- Kohda, K., Kakegawa, W., Matsuda, S., Yamamoto, T., Hirano, H., and Yuzaki, M. (2013). The  $\delta 2$  glutamate receptor gates long-term depression by coordinating interactions between two AMPA receptor phosphorylation sites. *Proc. Natl. Acad. Sci. USA* *110*, E948–E957.

- Krieger, J., Bahar, I., and Greger, I.H. (2015). Structure, dynamics, and allosteric potential of ionotropic glutamate receptor N-terminal domains. *Biophys. J.* *109*, 1136–1148.
- Kumar, J., Schuck, P., and Mayer, M.L. (2011). Structure and assembly mechanism for heteromeric kainate receptors. *Neuron* *71*, 319–331.
- Lachman, H.M., Fann, C.S., Bartzis, M., Evgrafov, O.V., Rosenthal, R.N., Nunes, E.V., Miner, C., Santana, M., Gaffney, J., Riddick, A., et al. (2007). Genomewide suggestive linkage of opioid dependence to chromosome 14q. *Hum. Mol. Genet.* *16*, 1327–1334.
- Lehma, J., and Marques, J.M. (2013). Kainate receptors in health and disease. *Neuron* *80*, 292–311.
- Maro, G.S., Gao, S., Olechwiec, A.M., Hung, W.L., Liu, M., Özkan, E., Zhen, M., and Shen, K. (2015). MADD-4/punctin and neuroligin organize C. elegans GABAergic postsynapses through neuroligin. *Neuron* *86*, 1420–1432.
- Matsuda, K., and Yuzaki, M. (2011). Cbln family proteins promote synapse formation by regulating distinct neuroligin signaling pathways in various brain regions. *Eur. J. Neurosci.* *33*, 1447–1461.
- Matsuda, K., Miura, E., Miyazaki, T., Kakegawa, W., Emi, K., Narumi, S., Fukazawa, Y., Ito-Ishida, A., Kondo, T., Shigemoto, R., et al. (2010). Cbln1 is a ligand for an orphan glutamate receptor delta2, a bidirectional synapse organizer. *Science* *328*, 363–368.
- Matsuda, S., Kakegawa, W., Budisantoso, T., Nomura, T., Kohda, K., and Yuzaki, M. (2013). Stargazin regulates AMPA receptor trafficking through adaptor protein complexes during long-term depression. *Nat. Commun.* *4*, 2759.
- Motazacker, M.M., Rost, B.R., Hucho, T., Garshasbi, M., Kahrizi, K., Ullmann, R., Abedini, S.S., Nieh, S.E., Amini, S.H., Goswami, C., et al. (2007). A defect in the ionotropic glutamate receptor 6 gene (GRIK2) is associated with autosomal recessive mental retardation. *Am. J. Hum. Genet.* *81*, 792–798.
- Pahl, S., Tapken, D., Haering, S.C., and Hollmann, M. (2014). Trafficking of kainate receptors. *Membranes (Basel)* *4*, 565–595.
- Pelkey, K.A., Barksdale, E., Craig, M.T., Yuan, X., Sukumaran, M., Vargish, G.A., Mitchell, R.M., Wyeth, M.S., Petralia, R.S., Chittajallu, R., et al. (2015). Pentraxins coordinate excitatory synapse maturation and circuit integration of parvalbumin interneurons. *Neuron* *85*, 1257–1272.
- Peret, A., Christie, L.A., Ouedraogo, D.W., Gorlewicz, A., Epsztein, J., Mülle, C., and Crépel, V. (2014). Contribution of aberrant GluK2-containing kainate receptors to chronic seizures in temporal lobe epilepsy. *Cell Rep.* *8*, 347–354.
- Petralia, R.S., Wang, Y.X., and Wenthold, R.J. (1994). Histological and ultrastructural localization of the kainate receptor subunits, KA2 and GluR6/7, in the rat nervous system using selective antipeptide antibodies. *J. Comp. Neurol.* *349*, 85–110.
- Rossmann, M., Sukumaran, M., Penn, A.C., Veprintsev, D.B., Babu, M.M., and Greger, I.H. (2011). Subunit-selective N-terminal domain associations organize the formation of AMPA receptor heteromers. *EMBO J.* *30*, 959–971.
- Saglietti, L., Dequidt, C., Kamieniarz, K., Rousset, M.C., Valnegri, P., Thoumine, O., Beretta, F., Fagni, L., Choquet, D., Sala, C., et al. (2007). Extracellular interactions between GluR2 and N-cadherin in spine regulation. *Neuron* *54*, 461–477.
- Schreiner, D., Nguyen, T.M., Russo, G., Heber, S., Patrignani, A., Ahmé, E., and Scheffele, P. (2014). Targeted combinatorial alternative splicing generates brain region-specific repertoires of neuroligins. *Neuron* *84*, 386–398.
- Schwenk, J., Harmel, N., Brechet, A., Zolles, G., Berkefeld, H., Müller, C.S., Bild, W., Baehrens, D., Hüber, B., Kulik, A., et al. (2012). High-resolution proteomics unravel architecture and molecular diversity of native AMPA receptor complexes. *Neuron* *74*, 621–633.
- Shanks, N.F., Savas, J.N., Maruo, T., Cais, O., Hirao, A., Oe, S., Ghosh, A., Noda, Y., Greger, I.H., Yates, J.R., 3rd, and Nakagawa, T. (2012). Differences in AMPA and kainate receptor interactomes facilitate identification of AMPA receptor auxiliary subunit GSG1L. *Cell Rep.* *1*, 590–598.
- Shi, S., Hayashi, Y., Esteban, J.A., and Mainow, R. (2001). Subunit-specific rules governing AMPA receptor trafficking to synapses in hippocampal pyramidal neurons. *Cell* *105*, 331–343.
- Shimono, C., Manabe, R., Yamada, T., Fukuda, S., Kawai, J., Furutani, Y., Tsutsui, K., Ikenaka, K., Hayashizaki, Y., and Sekiguchi, K. (2010). Identification and characterization of nCLP2, a novel C1q family protein expressed in the central nervous system. *J. Biochem.* *147*, 565–579.
- Sia, G.M., Béique, J.C., Rumbaugh, G., Cho, R., Worley, P.F., and Huganir, R.L. (2007). Interaction of the N-terminal domain of the AMPA receptor GluR4 subunit with the neuronal pentraxin NP1 mediates GluR4 synaptic recruitment. *Neuron* *55*, 87–102.
- Straub, C., Hunt, D.L., Yamasaki, M., Kim, K.S., Watanabe, M., Castillo, P.E., and Tomita, S. (2011). Distinct functions of kainate receptors in the brain are determined by the auxiliary subunit Neto1. *Nat. Neurosci.* *14*, 866–873.
- Traynelis, S.F., Wollmuth, L.P., McBain, C.J., Menniti, F.S., Vance, K.M., Ogden, K.K., Hansen, K.B., Yuan, H., Myers, S.J., and Dingledine, R. (2010). Glutamate receptor ion channels: structure, regulation, and function. *Pharmacol. Rev.* *62*, 405–496.
- Treutlein, B., Gokce, O., Quake, S.R., and Südhof, T.C. (2014). Cartography of neuroligin alternative splicing mapped by single-molecule long-read mRNA sequencing. *Proc. Natl. Acad. Sci. USA* *111*, E1291–E1299.
- Tu, H., Pinan-Lucarré, B., Ji, T., Jospin, M., and Bessereau, J.L. (2015). C. elegans punctin clusters GABA(A) receptors via neuroligin binding and UNC-40/DCC recruitment. *Neuron* *86*, 1407–1419.
- Uemura, T., Lee, S.J., Yasumura, M., Takeuchi, T., Yoshida, T., Ra, M., Taguchi, R., Sakimura, K., and Mishina, M. (2010). Trans-synaptic interaction of GluRdelta2 and Neuroligin through Cbln1 mediates synapse formation in the cerebellum. *Cell* *141*, 1068–1079.
- Vaags, A.K., Lionel, A.C., Sato, D., Goodenberger, M., Stein, Q.P., Curran, S., Ogilvie, C., Ahn, J.W., Drmic, I., Senman, L., et al. (2012). Rare deletions at the neuroligin 3 locus in autism spectrum disorder. *Am. J. Hum. Genet.* *90*, 133–141.
- Yuzaki, M. (2008). Cbln and C1q family proteins: new transneuronal cytokines. *Cell. Mol. Life Sci.* *65*, 1698–1705.

# Divergent Routing of Positive and Negative Information from the Amygdala during Memory Retrieval

Anna Beyeler,<sup>1,2</sup> Praneeth Namburi,<sup>1,2</sup> Gordon F. Globber,<sup>1</sup> Clémence Simonnet,<sup>1</sup> Gwendolyn G. Calhoun,<sup>1</sup> Garrett F. Conyers,<sup>1</sup> Robert Luck,<sup>1</sup> Craig P. Wildes,<sup>1</sup> and Kay M. Tye<sup>1,\*</sup>

<sup>1</sup>The Picower Institute for Learning and Memory, Department of Brain and Cognitive Sciences, Massachusetts Institute of Technology, Cambridge, MA 02139, USA

<sup>2</sup>Co-first author

\*Correspondence: kaytye@mit.edu

<http://dx.doi.org/10.1016/j.neuron.2016.03.004>

## SUMMARY

Although the basolateral amygdala (BLA) is known to play a critical role in the formation of memories of both positive and negative valence, the coding and routing of valence-related information is poorly understood. Here, we recorded BLA neurons during the retrieval of associative memories and used optogenetic-mediated phototagging to identify populations of neurons that synapse in the nucleus accumbens (NAc), the central amygdala (CeA), or ventral hippocampus (vHPC). We found that despite heterogeneous neural responses within each population, the proportions of BLA-NAc neurons excited by reward predictive cues and of BLA-CeA neurons excited by aversion predictive cues were higher than within the entire BLA. Although the BLA-vHPC projection is known to drive behaviors of innate negative valence, these neurons did not preferentially code for learned negative valence. Together, these findings suggest that valence encoding in the BLA is at least partially mediated via divergent activity of anatomically defined neural populations.

## INTRODUCTION

The ability to appropriately recognize stimuli imbued with either positive or negative valence is critical for survival as well as mental health. The neural circuits underlying the assignment of valence to environmental stimuli are thought to be highly conserved in the mammalian brain (Janak and Tye, 2015) and are dysfunctional in psychopathologies including anxiety, depression, and addiction (Allsop et al., 2014; Etkin and Wager, 2007; Lammell et al., 2014; Mervaala et al., 2000; Tye et al., 2011, 2013). Distributed and interconnected brain structures have been tied to valence coding (Berridge and Robinson, 2003; Namburi et al., 2015a; Nieh et al., 2013), but real-time dynamics within circuits processing valence information during

behavioral selection remain largely unexplored. The basolateral complex of the amygdala (BLA) receives inputs from multiple sensory modalities (Bordi and LeDoux, 1992; Fontanini et al., 2009; McDonald, 1998; Pitkänen, 2000) and neurons therein respond to cues of both positive and negative valence (Paton et al., 2006; Shabel and Janak, 2009). However, the BLA contains a diversity of neurons projecting to different downstream targets (Pitkänen, 2000) known to drive opposing behaviors (i.e., approach and avoidance, Namburi et al., 2015b; Stuber et al., 2011), and the naturally occurring firing patterns of these distinct subsets of BLA neurons during information processing remain unknown.

Previous evidence suggests that valence assignment during memory retrieval is supported by differences in real-time activity among anatomically defined populations of BLA neurons. The BLA and nucleus accumbens (NAc) have been implicated in the formation of cue-reward associations (Ambroggi et al., 2008; Namburi et al., 2015b; Tye et al., 2008) and optogenetic activation of BLA terminals in the NAc drives positive reinforcement (Britt et al., 2012; Stuber et al., 2011). By contrast, the assignment of negative valence has been linked to BLA projections to the central amygdala (CeA; Amorapanth et al., 1999; Ciochi et al., 2010; Goosens and Maren, 2001), and disconnection between the BLA and the CeA abolishes fear responses to cues associated with an aversive outcome (Jimenez and Maren, 2009). Valence processing in the BLA may also mediate innate emotional states; both the BLA and the ventral hippocampus (vHPC) are linked to anxiety (Adhikari, 2014; Etkin et al., 2009; Somerville et al., 2004) and optogenetic activation of BLA terminals in the vHPC increases anxiety-related behaviors (Felix-Ortiz et al., 2013).

We recently showed that projection-target-defined populations of BLA neurons play distinct roles in valence learning (Namburi et al., 2015b). However, the real-time activity and mechanisms by which the BLA produces distinct emotional and motivational states have yet to be identified.

Here, we hypothesized that during the retrieval of positive or negative associative memories, opposite valences are encoded by anatomically divergent BLA circuits. Using an intersectional, dual-virus approach, we employed optogenetic-mediated “phototagging” in combination with large-scale *in vivo* electrophysiological recordings to reveal the specific neural code of BLA

neurons that synapse in the NAc, CeA, or vHPC, in response to the presentation of cues associated with either rewarding or aversive outcomes.

## RESULTS

### Optogenetic-Mediated Photoidentification of BLA Projection Neurons during Retrieval

In order to “photoidentify” distinct populations of BLA neurons, we used a dual-virus approach to express the light-activated cation channel channelrhodopsin-2 (ChR2) in a subpopulation of BLA neurons, defined by axonal termination within a specific downstream region (NAc, CeA, or vHPC; Figure 1A). To this end, we used an anterograde viral vector carrying a construct allowing for cre-dependent ChR2 expression in the BLA and a retrograde viral vector carrying cre-recombinase in the downstream target (see Experimental Procedures; Nieh et al., 2015; Senn et al., 2014). This strategy allows specific targeting and identification of BLA neurons terminating in the region of interest and avoids spurious identification of BLA neurons sending axons of passage through this region, which is a shortcoming of electrical and optical antidromic stimulation. So that we could evaluate the activity of photoidentified cells during valence retrieval, we trained mice to discriminate between two auditory stimuli: one associated with a rewarding outcome of positive valence (sucrose) and the second associated with an aversive outcome of negative valence (quinine; Figures 1B and 1C). After mice learned the reward predictive significance of the conditioned stimulus associated with sucrose delivery (CS-S), as indicated by licking after tone onset and before the delivery of sucrose (Figures 1C and 1D), we introduced a second auditory conditioned stimulus (CS-Q) associated with the delivery of a bitter tastant (quinine; Figure 1B). Mice initially generalized the two tones, exhibiting licking responses for both the CS-S and CS-Q, and progressively learned to discriminate between the two stimuli (Figure 1E; Movie S1). When the mice reached performance criteria for the sucrose association (at least 70% of sucrose deliveries collected during the session) and for the quinine association (at least 70% of quinine deliveries avoided during the session), we performed acute recordings in the BLA over 2 successive days in 21 animals (Figures 1D–1G and S1).

### Half of BLA Neurons Respond to Sucrose and/or Quinine Cues

To determine the functional response profiles of BLA neurons, we performed recordings with silicon optrodes (Figure 2A), and analyzed neural data after histological confirmation of the placement of the recording electrodes and of the spread of viral expression (Figures 1G, S1, and S2A). During each recording session, ~30 sucrose and ~30 quinine trials were presented, and the firing rate of every isolated unit was analyzed in response to the two cues. Of the 1,626 neurons recorded in the BLA, 50% of the neurons were task responsive, meaning that they showed a significant firing rate change in response to one or both cues (Wilcoxon signed-rank test,  $p < 0.01$ ; Figures 2B–2D; Table S1). 28% of neurons significantly changed firing rate selectively

during the conditioned stimulus associated with sucrose (CS-S) and 9% selectively during the conditioned stimulus associated with quinine (CS-Q). 13% of the units significantly changed their firing rate in response to both cues in a qualitatively similar manner (either excitatory or inhibitory responses), which we termed the “same” way, and less than one percent changed their firing rate in response to both cues in qualitatively distinct directions, which we termed “opposite” ways (Figure 2C). When averaging the proportion of cells responding with excitation or inhibition within the three categories (responsive to the CS-S only, responsive to the CS-Q only, and responsive to both cues in the same way), we found that  $53\% \pm 2\%$  of the units showed excitatory responses, while  $47\% \pm 2\%$  showed inhibitory responses (Figure 2E, illustrated as percentage of total units).

We also tested the response of each unit to the unconditioned stimulus (US; Figure S2) and found that 32% of the units responding to the CS also significantly changed their firing rate during the first 500 ms after the delivery of the US (sucrose or quinine), while 18% responded to the US without changing their firing rate to the cues (Figures S2C and S2D). Overall, 50% of the units responded to the delivery of the US (Figure S2E). 37% of the units responded only during the sucrose delivery, 6% responded only during quinine delivery, and 7% responded during both US deliveries (5.7% in a “same” qualitative way and 1.5% in qualitatively “opposite” ways; Figures S2E and S2F). Overall, we found that more cells were inhibited than excited by the US, irrespective of valence ( $34\% \pm 3\%$  excitatory compared to  $66\% \pm 3\%$  inhibitory responses; Figure S2F).

### BLA Projectors Send Collaterals to Multiple Downstream Targets

Because previous studies suggest that a subset of BLA neurons collateralize to multiple downstream targets (Shinonaga et al., 1994), we estimated the extent of collateralization in each of the BLA neural populations projecting to the NAc, CeA, and vHPC by measuring fluorescence in multiple downstream structures of the BLA (Figures 3A and 3B) from animals expressing ChR2-eYFP selectively in one projector population (BLA-NAc, BLA-CeA, or BLA-vHPC). This approach allowed us to evaluate the presence of neurites from each of these projection-target-defined populations; however, the presence of fluorescent processes may include fibers of passage and not faithfully represent functional synaptic terminals.

We estimated the extent of collateralization based on membrane fluorescence relative to a reference location, shown in Figure 3B. Each of the three BLA projector populations sent collaterals to multiple downstream targets (Figure 3C); however, the fluorescence within the intended target structure always surpassed that in the collateral regions we examined (Figure 3D). In the images we collected, the average relative fluorescence from BLA-NAc projector neurites outside the NAc was  $33\% \pm 9\%$ . The collateral fluorescence observed for BLA-vHPC projectors was  $24\% \pm 5\%$  and only  $17\% \pm 4\%$  for BLA-CeA projectors. We found that BLA-NAc projectors expressed neurites extending across the NAc subregions, and outside the NAc to the medial prefrontal cortex (mPFC), CeA, and vHPC

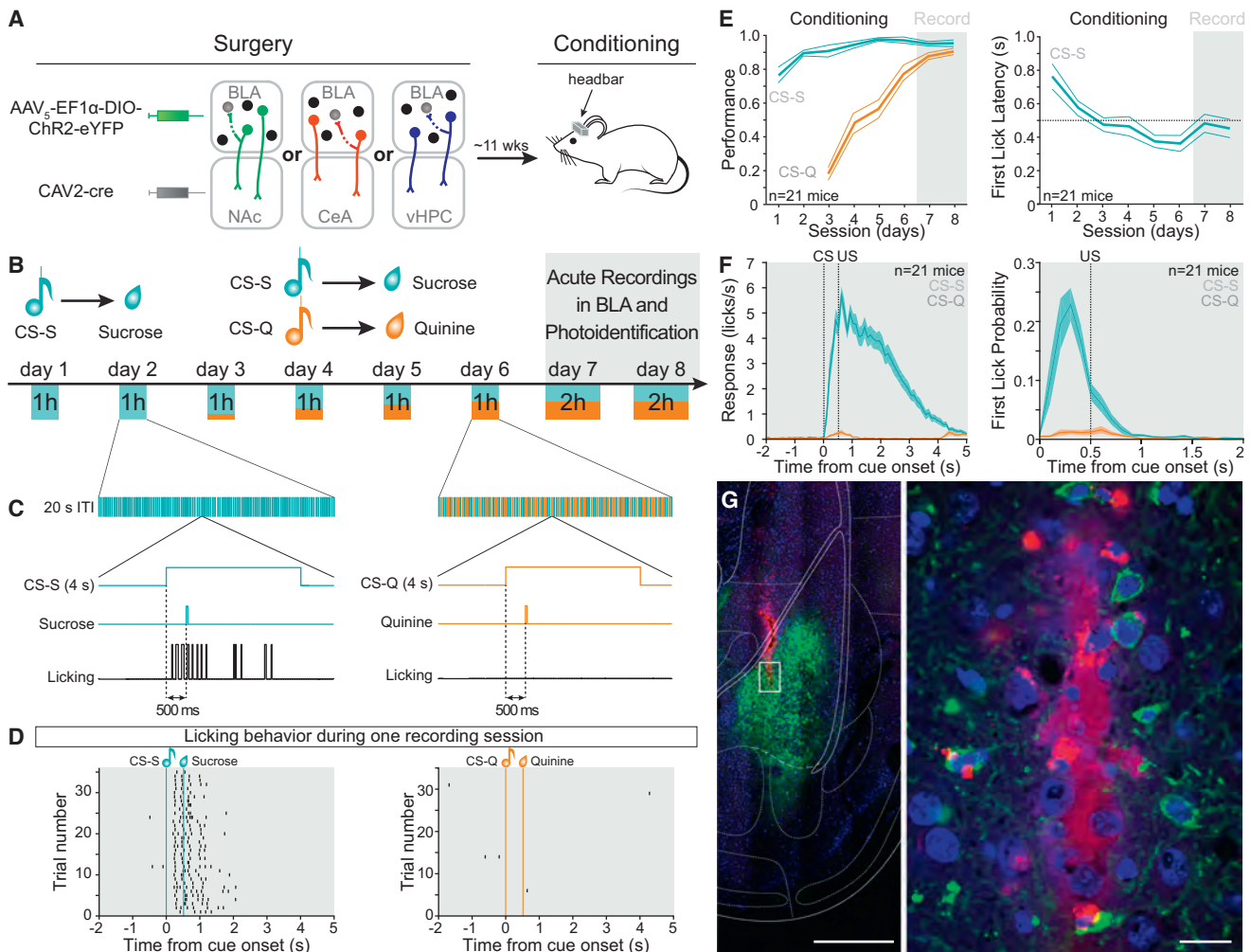


### Figure 1. Experimental Design and Behavioral Training

(A) Anterograde AAV<sub>5</sub>-EF1 $\alpha$ -DIO-ChR2-eYFP was injected in the BLA and retrograde CAV2-cre was injected in one of the following downstream targets: NAc, CeA, or vHPC. A head bar was cemented to the skull to enable subsequent head-fixed training and recording.

(B) Schematic of conditioning and retrieval task. On days 1–2, an auditory cue (CS-S) was paired with a sucrose delivery and on days 3–6, a second auditory cue (CS-Q) was paired with quinine deliveries. The number of quinine cues was gradually increased from 10% to 50% of total trials. On days 7–8, during the retrieval of rewarding and aversive associations, an optrode was inserted into the BLA to record neural activity, and laser stimulation was used to photoidentify neurons expressing ChR2.

(C) Time courses of a reward trial (left) and an aversive trial (right). The cues were played for 4 s and a 3  $\mu$ L drop of solution (sucrose or quinine) was delivered  $\sim$ 500 ms after the onset of the cue. Anticipatory licking before the sucrose delivery indicates acquisition of the reward association and no licking indicates expression of the aversive association.

(D) Licking behavior of a representative mouse in response to the CS-S (left raster) and the CS-Q (right raster) presentations during a recording session.

(E) Performance for the reward association (CS-S performance = sucrose trials with licks/number of sucrose trials) and for the aversive association (CS-Q performance = quinine trials without licks/number of quinine trials) increased during learning of the task (left) and the latency of the first lick after the CS-S onset decreased across training (right). The thinner lines represent the SEM, and the dashed line at 500 ms indicates the time of US delivery.

(F) Licking behavior during the recording sessions, averaged across all animals. Left panel represents the licking behavior and right panel represents the probability of first lick in response to the cues. The shaded areas represent SEM.

(G) Representative image of a recording track in the BLA. The recording optrode was coated with red fluorescent microspheres before insertion into the brain (left image, scale bar represents 500  $\mu$ m). The area containing the tip of the electrode in the BLA (white rectangle on the left image) is enlarged to the right. Scale bar reflects 20  $\mu$ m. Blue is DAPI, green is eYFP, and red is red fluorescent microspheres.

(Figures 3C–3D and S3). The relative fluorescence of BLA-NAc projectors in the CeA was 57% of the fluorescence in NAc ventro-lateral core, which could be partly due to axons of passage that do not locally terminate or form functional synapses. The

BLA-vHPC projector population displayed more fluorescence in the medial than in the lateral NAc shell (paired t test,  $t = 3.77$ ,  $p < 0.05$ ). However, there was no detectable difference in the amount of membrane fluorescence of BLA-CeA projectors

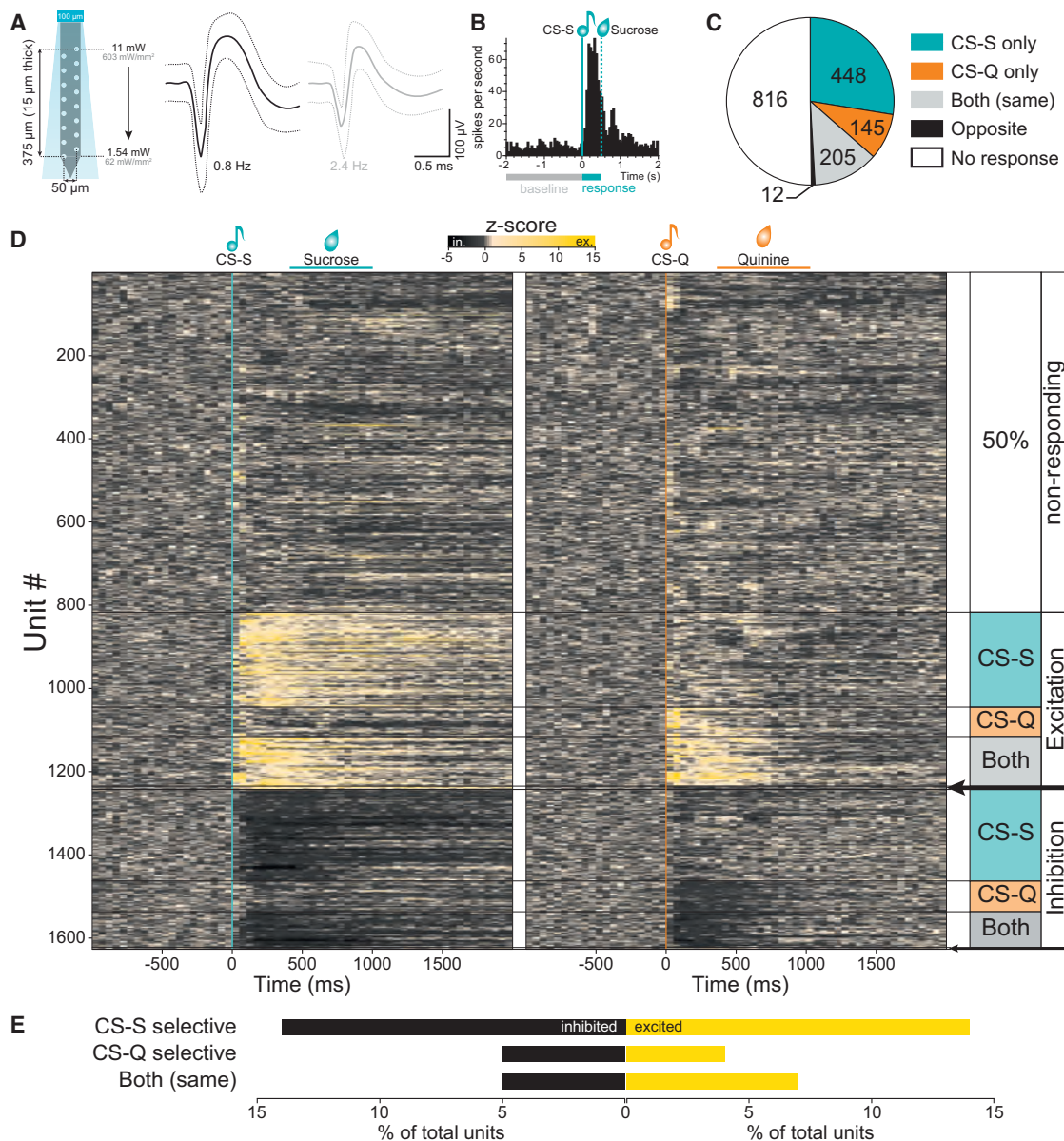


**Figure 2. BLA Units Respond to Matched Modality Sucrose and/or Quinine Cues**

(A) Schematic of the optrode used to record neural activity. The blue quadrilateral represents the theoretical light cone. Right: the average waveform of two units isolated from one recording site (average  $\pm$  99.7% confidence interval).

(B) Peri-stimulus time histogram (PSTH) of the firing rate of a single unit, to the onset of 30 sucrose-predicting cues (CS-S). For each unit, a Wilcoxon signed-rank test determined whether the firing rate during the first 500 ms of the cue was significantly different from the 2 s baseline window ( $p < 0.01$ ).

(C) 1,626 BLA units were recorded from 21 mice. 810 (50%) had a significantly different firing rates during the first 500 ms of the cue compared to the 2 s before the cue (Wilcoxon signed-rank test,  $p < 0.01$ ). 28% responded selectively to the CS-S, 9% to the CS-Q, 13% responded to both cues in the same way, and less than 1% responded to both cues in an opposite way.

(D) Heat maps of the Z score of all recorded units in response to the CS-S (vertical teal line, left map) and in response to the CS-Q (vertical orange line, right map). 26% of the units showed a significant excitatory response to one and/or the other auditory cue (Wilcoxon signed-rank test,  $p < 0.01$ ). 14% of the units were selectively excited by the CS-S and 4% by the CS-Q, while 7% were excited by both cues. 24% of the units showed a significant inhibitory response to one and/or the other cue. 14% were selectively inhibited by the CS-S and 5% by the CS-Q, while 5% were inhibited by both cues. The black arrows indicate units responding to both cues in an opposite manner (top arrow: excited by the CS-S and inhibited by the CS-Q [0.5%]; bottom arrow: inhibited by the CS-S and excited by the CS-Q [0.2%]).

(E) Proportion of units responding to the rewarding cue only (CS-S selective), to the aversive cue only (CS-Q selective), or to both cues in the same way, with an inhibitory response (black) or with an excitatory response (yellow).

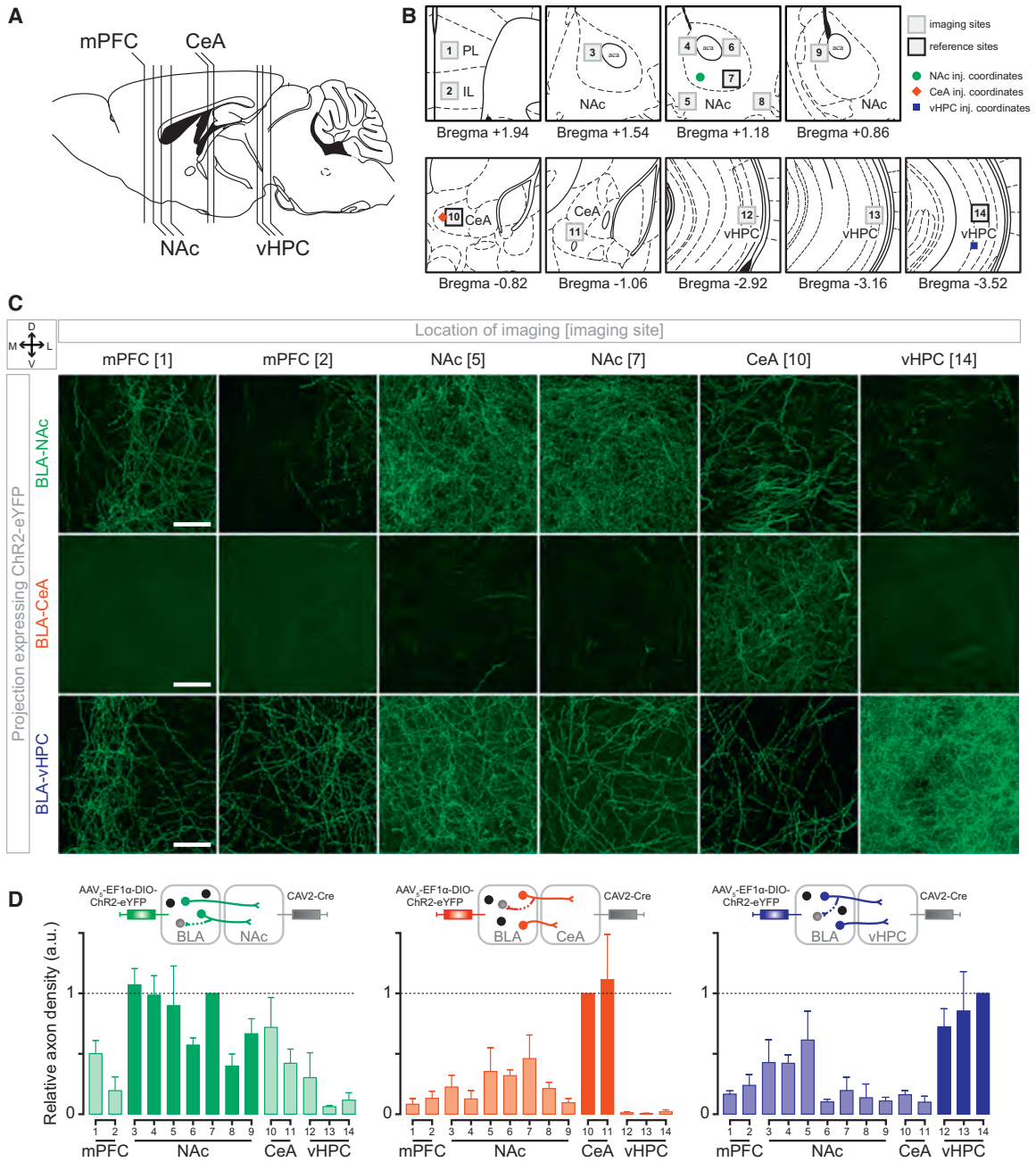


**Figure 3. Evidence of Collateralization of BLA Projection Neurons**

(A) Sagittal view representing the relative position of brain sections imaged to quantify membrane fluorescence of neurites expressing ChR2-eYFP.

(B) Coronal locations of the 14 sites imaged for each mouse. Locations proximal to the injection coordinates were used as reference sites (black outlines) to compare the fluorescence intensity with other imaging sites (gray outlines).

(C) Confocal images containing a section of (from left to right): the prelimbic (PL) and infralimbic (IL) medial prefrontal cortex (mPFC), the NAc medial shell and lateral core, the medial CeA and the vHPC from one mouse expressing ChR2-eYFP in BLA-NAc projectors (top row), in BLA-CeA projectors (middle row), or in BLA-vHPC projectors (bottom row). Scale bars represent 50  $\mu$ m.

(D) Quantification of the fluorescent pixels per confocal image for each experimental group (BLA-NAc  $n = 3$  mice, except for mPFC where  $n = 2$ , BLA-CeA  $n = 4$  mice and BLA-vHPC,  $n = 3$  mice). The relative axon density represents the fraction of fluorescent pixels normalized within each animal. The number of fluorescent pixels was obtained by thresholding the maximum intensity projection (MIP) of the confocal z stack ( $>0.5$ , see Figure S3). Error bars represent SEM.

between the medial and lateral NAc shell (paired *t* test,  $t = 0.67$ ,  $p = 0.27$ ). Notably, among our samples, BLA-CeA projectors scarcely expressed membrane fluorescence in the vHPC ( $\sim 1\%$  relative eYFP fluorescence).

To quantify the extent of synaptic terminals from BLA-NAc projectors in the CeA, we expressed synaptophysin fused to the fluorescent protein mCherry (Calhoun et al., 1996; Oh et al., 2014). In mice expressing mCherry in the synaptic terminals and eYFP in the cell membranes of BLA-NAc projectors, the relative mCherry fluorescence in the CeA was only 20% (Figures S3A and S3B), while the relative eYFP fluorescence was 57% (Figure 3D). This finding suggests that BLA-NAc projectors collateralize to the CeA, albeit to a lesser extent than expected by quantifying neurite fluorescence alone, which likely includes fibers of passage.

### ChR2-Expressing Neurons Have Shorter Photoresponse Latencies Compared to Non-expressing Neighbors

The BLA is known to be an epileptogenic region (Ben-Ari et al., 1980) and recurrent collaterals between pyramidal cells in the BLA have been anatomically described (McDonald, 1984). To unequivocally distinguish the BLA projection neurons expressing ChR2-eYFP (ChR2+) from the non-expressing neighbors that receive excitatory inputs from projectors in vivo, we empirically determined the photoresponse latencies ex vivo, where visual and electrophysiological validation of opsin expression is possible (Figures 4A, 4B, and S4). We classified neurons in three categories using whole-cell patch-clamp recordings in the BLA (Figures 4B and 4C): (1) projectors that exhibit a peak/steady-state current, characteristic of ChR2-expressing neurons in response to a 1 s blue light illumination (ChR2+, 21% of 91 cells), (2) ChR2-negative neighbors receiving direct or indirect synaptic input from ChR2-expressing projectors (responsive neighbors, 25%), and (3) ChR2-negative neighbors that did not respond to illumination (non-responsive neighbors, 54%). We then measured the latencies of the light-evoked action potentials (APs) or excitatory postsynaptic potentials (EPSPs) from the onset of a 5 ms light pulse to the peak of the response, in mice expressing ChR2 in BLA-NAc projectors ( $n = 40$  cells), in BLA-CeA projectors ( $n = 19$  cells), or in BLA-vHPC projectors ( $n = 32$  cells; Figure 4D). While all ChR2+ projectors fired after photostimulation, only one of the responsive neighbors reached a suprathreshold response, with a latency of 17.3 ms (BLA-NAc neighbor; Figures 4E and 4F). Firing latencies ranged from 2 to 8 ms for BLA-NAc projectors and were significantly shorter than the light-evoked EPSP latencies of their responsive neighbors (10–36 ms, Student's *t* test,  $***p < 0.01$ ). BLA-CeA projectors expressing ChR2 responded faster than their responsive neighbors (1–5 versus 12–18 ms, Student's *t* test,  $***p < 0.01$ ). Finally, the photoresponse latencies of BLA-vHPC projectors ranged from 2 to 5 ms and were shorter than the photoresponse latencies of their responsive neighbors (11–24 ms, Student's *t* test,  $***p < 0.01$ ; Figure 4F). Based on these data, we defined the in vivo photoresponse latency threshold as  $< 9$  ms for the NAc-projecting BLA neurons, and  $< 6$  ms for both the BLA-CeA and BLA-vHPC projectors.

### BLA Projector Populations Differentially Respond to Sucrose and Quinine Cues

In order to perform optogenetic-mediated “phototagging” to identify BLA projectors in vivo, at the end of every recording session, we provided different patterns of photostimulation to compute the photoresponse latency and classify neurons as ChR2-expressing projectors (Figure 5A; see Experimental Procedures). After applying the identification threshold defined by our ex vivo recordings, we found a similar distribution of latencies across the three projector populations (Kolmogorov-Smirnov tests,  $p > 0.05$ ; Figure 5B). There were no detectable differences in the distribution of firing rates between the BLA-NAc and BLA-vHPC populations compared to the distribution in the BLA (Kolmogorov-Smirnov tests,  $p > 0.05$ ), while BLA-CeA projectors have a different distribution of firing rates compared to all BLA neurons (Kolmogorov-Smirnov test,  $p < 0.01$ ; Figure 5C). Finally, there were no detectable differences in the distribution of the action potential duration (peak-trough) between each of the three projector populations compared to the BLA distribution (Kolmogorov-Smirnov tests,  $p > 0.05$ ; Figure 5D). Altogether, 7% of the units recorded met our criteria for phototagging (Figure 5E; see Experimental Procedures). Compared to the entire set of BLA neurons, in which 50% were cue-responsive, we found that BLA-NAc, BLA-CeA, and BLA-vHPC projecting populations contained 61%, 52%, and 69% cue-responsive units, respectively (Figure 5F).

To visualize the response of each projector population to sucrose and quinine cues without applying any predetermined categories, we computed the average *Z* score of all recorded BLA neurons, BLA-NAc, BLA-CeA, and BLA-vHPC projectors (Figure 6A) in response to the sucrose cue (CS-S) and to the quinine cue (CS-Q). We compared *Z* score distances between the CS-S and CS-Q among the four populations (average within cell differences for BLA = 0.28, BLA-NAc = 0.63, BLA-CeA =  $-0.69$ , and BLA-vHPC = 1.26; Figure 6B) and found that the response profile of BLA-CeA projectors differed from each of the other three groups (Kruskal-Wallis test,  $p < 0.001$ , BLA-CeA post hoc comparisons: to BLA-NAc  $***p < 0.001$ , to BLA  $*p < 0.05$ , and to BLA-vHPC  $**p < 0.01$ ; Figure 6B).

To compare CS representation dynamics in BLA projector populations, we projected the *Z* score time course of each neuron from 500 ms before to 500 ms after cue-onset onto a two-dimensional space using principal components analysis (PCA; Figures 6C, 6D, and S6). The time period between 100 and 500 ms after the cue-onset contributed to the component explaining the highest amount of variance in the dataset (PC1), while the first 100 ms following cue-onset contributed the most to the second principal component (PC2; Figure 6C). Interestingly, PC1 separates responses to the sucrose and quinine cues in all populations as illustrated by the separation of the CS-S and CS-Q vectors along PC1 (Figures 6D, S6B, and S6C). Additionally, PC2 separates the responses between the projector populations, especially separating CeA projectors from NAc and vHPC projectors (Figures 6D and S6C). Altogether, the PCA of the *Z* score time course suggests that the late cue-response ( $\geq 100$  ms) contains more information regarding the valence of the cue, while the early cue-response ( $\leq 100$  ms) contains more information regarding the projection target of the cell.

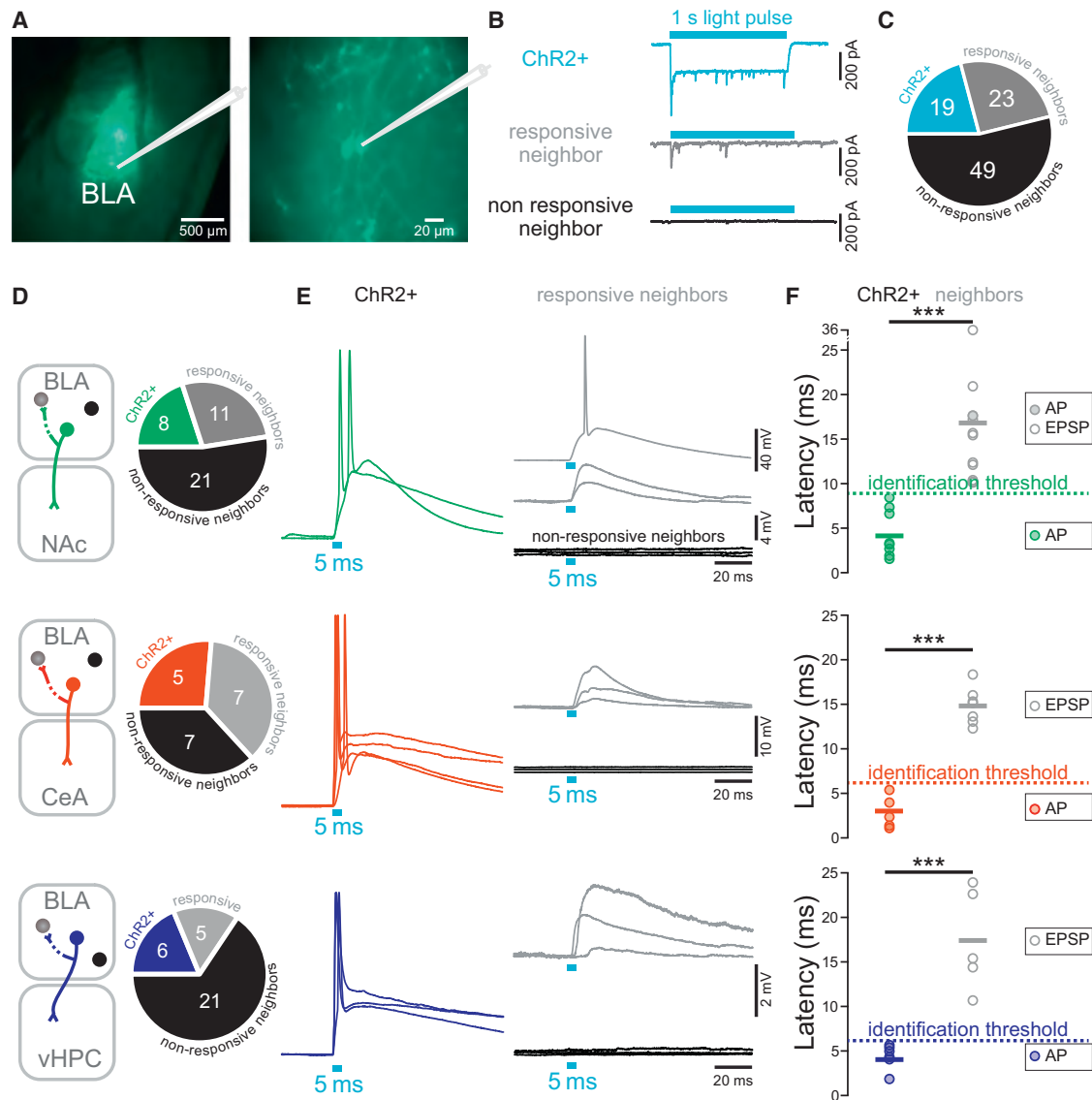


#### Figure 4. Empirical Determination of Photoresponse Latency Threshold Ex Vivo

(A) Left: differential interference contrast (DIC) image of a 300- $\mu\text{m}$ -thick coronal brain section of a mouse expressing ChR2-eYFP in BLA-NAc projectors, with green fluorescence image overlaid. Right: BLA-NAc projectors expressing ChR2-eYFP and recorded in whole-cell patch clamp.

(B) Representative peak/steady-state current of a neuron expressing ChR2 (ChR2+, sky-blue trace) in response to a 1 s light pulse (sky-blue rectangle). In non-expressing neighboring cells, light stimulation either evoked a transient current (gray trace) or the cells did not respond (black trace).

(C) Proportion of all cells recorded ex vivo expressing ChR2-eYFP (ChR2+, 21%, sky-blue), responsive neighbors (25%, gray), and non-responsive neighbors (54%, black). Numbers indicate the number of recorded neurons.

(D) Proportion of ChR2+ neurons, responsive neighbors, and non-responsive neighbors recorded in the BLA of mice expressing ChR2-eYFP in BLA-NAc (green), BLA-CeA (red), or BLA-vHPC (dark blue) projectors.

(E) Representative traces of neural responses to a 5 ms light pulse of BLA projectors expressing ChR2-eYFP (green, red, or dark blue traces), in responsive neighbors (gray traces) and non-responsive neighbors (black traces).

(F) Light-evoked peak response latency in BLA-NAc, BLA-CeA, and BLA-vHPC projectors expressing ChR2 and in non-expressing neighbors. Light-evoked response latencies are significantly shorter in BLA-NAc (unpaired t test,  $t_{17} = 4.64$ ,  $***p < 0.001$ ), BLA-CeA (unpaired t test,  $t_{10} = 10.64$ ,  $***p < 0.001$ ), and BLA-vHPC (unpaired t test,  $t_9 = 5.62$ ,  $***p < 0.001$ ) projectors compared to their non-expressing neighbors. The distribution of the latency in expressing and non-expressing cells was used to define the latency threshold for in vivo photoidentification (9 ms for BLA-NAc projectors and 6 ms for BLA-CeA and BLA-vHPC projectors).

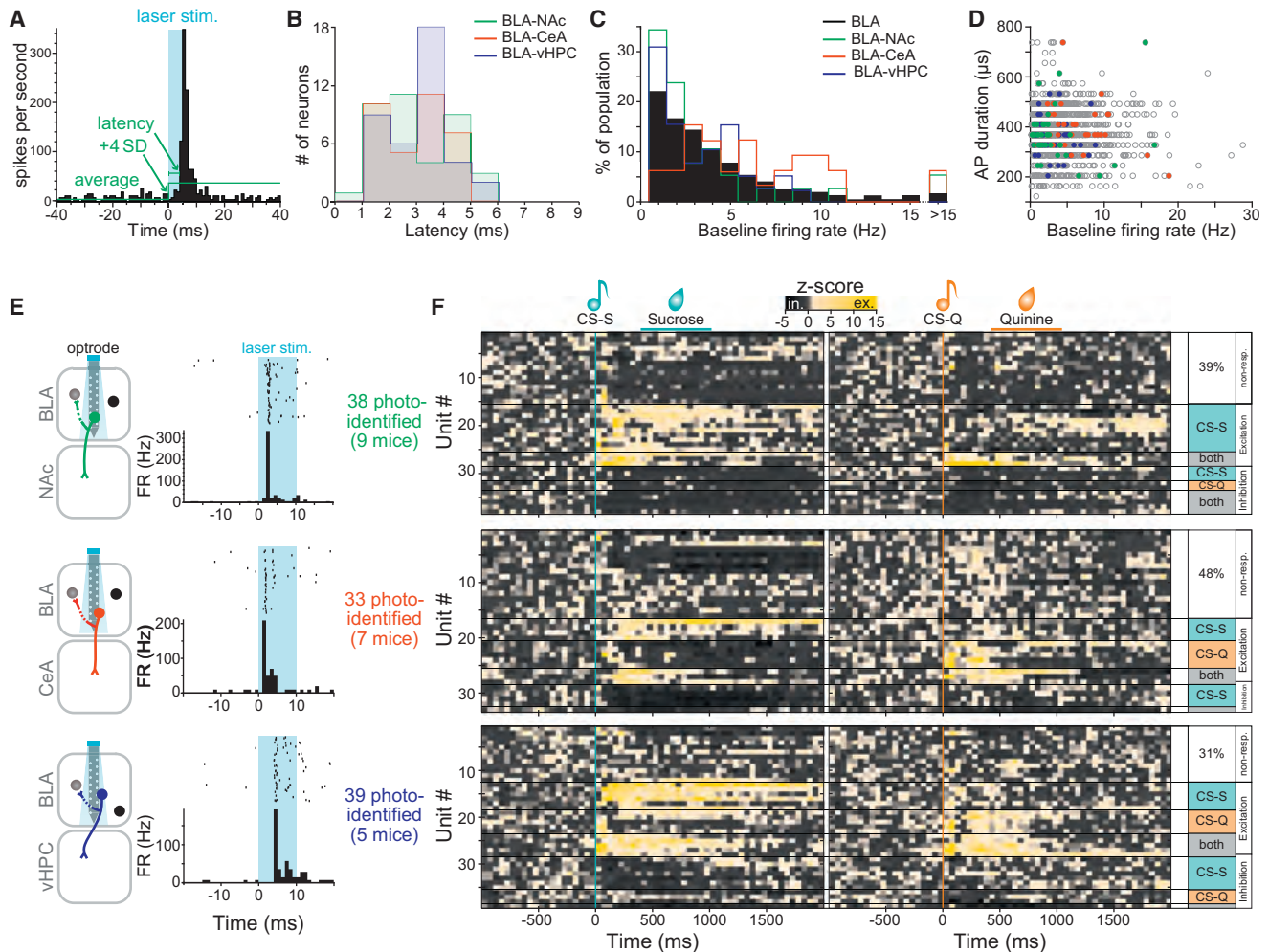


**Figure 5. Neural Response of BLA Projection Neurons to Cues Predicting Sucrose or Quinine**  
 (A) Photoresponse latencies in vivo were calculated by measuring the time from stimulation onset to the first bin in which firing rate increased at least 4 SDs above baseline.  
 (B) No differences were detected in photoresponse latency distributions among BLA-NAc, BLA-CeA, and BLA-vHPC projectors (Kolmogorov-Smirnov tests,  $p > 0.05$ ).  
 (C) The distribution of firing rates in BLA-NAc and BLA-vHPC projectors was not different from the BLA distribution (Kolmogorov-Smirnov tests,  $p > 0.05$ ), while the firing rate distribution in BLA-CeA projectors was different from the BLA distribution (Kolmogorov-Smirnov tests,  $p < 0.01$ ).  
 (D) Scatterplot depicting the action potential (AP) duration (peak-trough) as a function of the firing rate of all the recorded units (gray) and in the three photo-identified populations (BLA-NAc in green, BLA-CeA in red, and BLA-vHPC in blue).  
 (E) Representative examples of firing rate (FR) in response to 10 ms photostimulation for units photoidentified as BLA-NAc (green), BLA-CeA (red), or BLA-vHPC (blue) projectors.  
 (F) Heat maps of the Z scores of all the units photoidentified as BLA-NAc projectors (top), BLA-CeA projectors (middle), or BLA-vHPC projectors (bottom) in response to the CS-S (teal line, left) and to the CS-Q (orange line, right).

**BLA Neurons Projecting to NAc and CeA Preferentially Code for Opposite Valence**

After classification of the units depending on their qualitative response type, we found heterogeneity within each population (Figures 7A and 7B). We categorized the functional responses into six classes: selectively excited by the CS-S, selectively excited by the CS-Q, excited by both cues, selectively inhibited by the CS-S, selectively inhibited by the CS-Q, or inhibited by both cues (Figures 7C and 7D). Examination of the population profiles of specific projector responses reveals noteworthy ab-

ences: for example, zero BLA-NAc neurons were excited by the CS-Q and zero BLA-CeA neurons were inhibited by the CS-Q (Figure 7C).

When comparing the proportions of neurons excited or inhibited by one cue (Figure 7D), we found a larger proportion of BLA-NAc projectors excited by the CS-S (10/13 units; 77%), compared to the entire BLA neural population (228/448 units, 51% in the BLA, binomial distribution,  $^+p < 0.1$ ; Figure 7D). We also found that all BLA-CeA projectors responding only to the quinine cue showed an excitatory response (5/5 units; 100%),

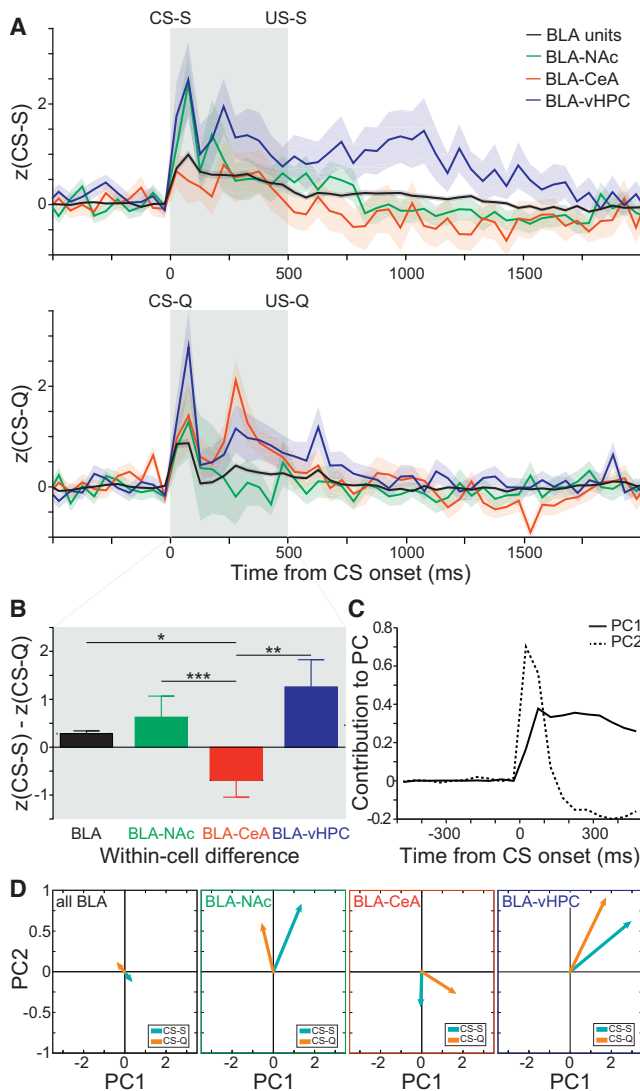


**Figure 6. Category-Independent Coding Properties of BLA Populations**

We first analyzed responses within each population independent of qualitative classifications.

(A) Z score time courses averaged across all BLA units (black), all BLA-NAc projectors (green), all BLA-CeA projectors (red), or all BLA-vHPC projectors (blue), in response to the CS-S (top) and in response to the CS-Q (bottom). Shaded areas represent the SEM. The gray shaded box depicts the interval from CS onset to US onset.

(B) Difference between CS-S and CS-Q Z scores, averaged from the onset of the CS to the US delivery, for each BLA units (black bar) and for neurons of the three projector populations (green, red, and blue bars). Positive values indicate greater magnitude responsiveness to the CS-S, while negative values indicate greater magnitude responsiveness to the CS-Q. BLA-CeA projectors respond more to the CS-Q than the CS-S compared to all other populations (Kruskal-Wallis test  $p < 0.01$ , BLA-CeA post hoc comparisons: to BLA-NAc  $***p < 0.001$ , to BLA  $*p < 0.05$ , and to BLA-vHPC  $**p < 0.01$ ). Error bars represent SEM.

(C) The Z score time course of each neuron from  $-500$  ms to  $500$  ms relative to cue-onset was projected onto two dimensions using principal component analysis (PCA). In order to visualize the time periods that contribute most significantly to the principal components depicted in (D), we plotted the contribution of each  $50$  ms time bin to principal component 1 (PC1) and

compared to  $71/145$  units (49%) of the BLA units (binomial distribution,  $*p < 0.05$ ). We also observed that all recorded BLA-NAc projectors that responded only to the quinine cue showed inhibitory responses ( $2/2$  units, 100%; Figures 7C and 7D). Regarding responses to the unconditioned stimuli (Figures S5 and S7), we did not detect differences in the proportion of excitatory and inhibitory responses to the sucrose and quinine deliveries (binomial distribution,  $p > 0.05$ ).

Finally, we compared the response profiles to the conditioned stimuli in the BLA neural population as a whole and in the three projection-target-defined BLA populations using different classification criteria for the representation of valence previously described in the literature (Figure 7E; for review see Namburi et al., 2015a).

Using a simple classification emphasizing cue selectivity (termed “valence selectivity” in Namburi et al., 2015a), we can categorize neurons based upon their selectivity to the sucrose predictive (CS-S) or quinine predictive (CS-Q) cue, regardless of the response direction (excitation or inhibition). Among all recorded BLA neurons that responded selectively to one cue, we found  $\sim 3$ -fold more neurons selective to the CS-S ( $448/593$ , 76%; Figure 7E, left) than units selective to the CS-Q. We did not detect differences in the proportion of units selectively responding to the CS-S in the three projector populations compared to the whole BLA population ( $13/15$ , 87% in BLA-NAc;  $8/13$ , 62% in BLA-CeA;  $13/21$ , 62% in BLA-vHPC, binomial tests,  $p > 0.05$ ; Figure 7E).

Another classification, the “valence index,” defines the proportion of cells encoding valence as those with distinct responses to the CS-S and CS-Q (i.e., combining units responding selectively to one of the cues with units showing opposite responses to both cues) relative to all CS-responsive cells (Figure 7E, middle). By using this classification, we found that within the BLA task-responsive units we sampled, the majority encode valence during the retrieval of the positive and negative associations ( $605/810$ , 75%). This proportion was not detectably different in the three projector populations compared to the BLA population ( $15/23$ , 65% in BLA-NAc;  $13/17$ , 76% in BLA-CeA;  $21/27$ , 78% in BLA-vHPC, binomial tests,  $p > 0.05$ ; Figure 7E).

Within the context of BLA projector populations, we utilize a third classification, the “valence bias,” which defines the proportion of a population encoding positive or negative valence among all the cells encoding valence (Figure 7E, right). Using this metric, positive valence is encoded at a population level by neurons that increase their firing upon presentation of the reward-predicting cue (CS-S), that decrease their firing in response to a cue predicting an aversive outcome (CS-Q), or exhibit both of these opposing responses. Contrastingly, negative valence is encoded at the population level by cells inhibited by reward-predicting cues

principal component 2 (PC2). Bins prior to the cue onset did not contribute to either principal component, whereas the first time bins after CS onset contribute most strongly to PC2 and subsequent bins contribute to PC1.

(D) Neural responses to the sucrose predictive cue (CS-S) and quinine predictive cue (CS-Q) in all BLA units, BLA-NAc, BLA-CeA, and BLA-vHPC projector populations, visualized along PC1 and PC2. Neural dynamics in principal component (PC) space across all neurons in each population were averaged for each cue to obtain the position of the vectors.

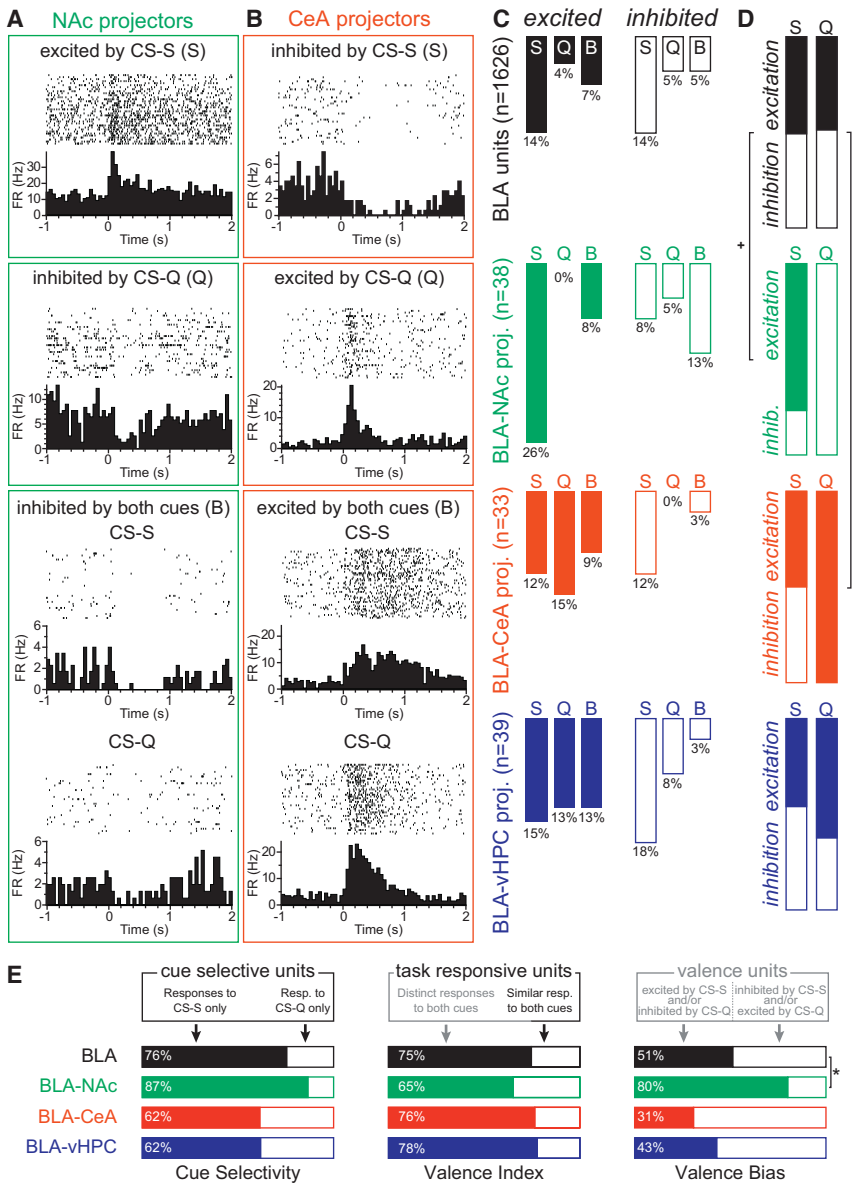


**Figure 7. Distinct Roles in Coding Positive and Negative Valence Defined by Projection Target**

For these analyses, we grouped neurons based upon their qualitative response to the CS-S and CS-Q.

(A) PSTHs of the firing rates (FR) of three units photoidentified as BLA-Nac projectors, one showing an excitatory response to the cue associated with sucrose (CS-S, top), one showing an inhibitory response to the cue associated with quinine (CS-Q, middle), and one showing an inhibitory response to both cues (B, bottom).

(B) Perievent raster histograms of the firing rates of three units photoidentified as BLA-CeA projectors, one inhibited by the cue associated with sucrose (CS-S, top), one excited by the cue associated with quinine (CS-Q, middle), and one excited by both cues (B, bottom).

(C) Distribution of units excited (left, filled bars) or inhibited (right, open bars) by the CS-S [S], by the CS-Q [Q], or by both cues in the same way [B], in all the BLA units (black), in the BLA-Nac photoidentified units (green), in the BLA-CeA photoidentified units (red) and in BLA-vHPC photoidentified units (blue).

(D) Proportion of units excited and inhibited by the sucrose cue (S) or the quinine cue (Q), in the four neural populations. A larger proportion of BLA-Nac neurons (77%) showed phasic excitations to the CS-S than in the nonspecific BLA neural population as a whole (51%; binomial distribution,  $*p = 0.093$ ). A larger proportion of BLA-CeA neurons (100%) showed phasic excitation to the CS-Q than in the nonspecific BLA neural population (49%; binomial distribution,  $*p < 0.05$ ).

(E) Valence definitions applied to all BLA units and the three projector populations. Cue selectivity: proportion of cue responsive cells responding exclusively to the sucrose cue (filled bars) or to the quinine cues (open bars). Valence index: proportion of task-responsive cells encoding valence (including those responsive to only one cue, or responding oppositely to both cues; closed bars) compared to those responding in the same way to both cues. Valence bias: relative proportion of

neurons responding to positive valence (filled bars) and negative valence (open bars). The BLA-Nac projector population has a greater proportion of cells encoding positive valence than the nonspecific BLA population based upon this valence bias metric (binomial distribution,  $*p < 0.05$ ).

and/or excited by cues predicting aversive outcomes. Using this operational definition in our dataset, we found that 51% of valence encoding BLA neurons code for positive valence (310/605 cells), whereas 49% code for negative valence (295/605 cells). Within the BLA projector populations, we found a significantly larger proportion of BLA-Nac projectors encoding positive valence (12/15 cells, 80%) compared to the whole BLA (binomial test  $*p < 0.05$ ; Figure 7E). Within our sample, fewer BLA-CeA projectors encoded positive valence (4/13 cells, 31%) and instead tended to preferentially encode negative valence (9/13 cells, 69%). In contrast, positive and negative valence encoding neurons were evenly represented among valence-responsive BLA-vHPC neurons (9/21 cells, 43% encoding positive valence; Figure 7E).

Altogether, quantitative analysis of the neural response of BLA populations (all BLA, BLA-Nac, BLA-CeA, and BLA-vHPC) and analysis of the proportion of units responding with excitation and inhibition to the cues of positive and negative valence both show that BLA-Nac and BLA-CeA populations have divergent profiles in response to cues predicting rewarding and aversive outcomes.

## DISCUSSION

### Divergent Circuits for Encoding Positive and Negative Valence

To assess valence encoding in BLA neurons projecting to the Nac, CeA, or vHPC, we recorded photoidentified cells during

the retrieval of rewarding and aversive Pavlovian associations. Within this behavioral task, two cues of the same sensory modality (tones) were predictive of either a positive or negative outcome, themselves of matched modality (the tastants, sucrose or quinine). In so doing, we observed heterogeneous responses to the conditioned stimuli within BLA projector populations, yet provided evidence that information regarding the sucrose and quinine predictive cues is differentially routed to divergent circuits (Figures 6 and 7).

### **BLA Neurons Respond to Cues Associated with Positive and Negative Valence**

Our results are consistent with previous studies reporting that intermingled neurons in the BLA respond to the valence of learned cues in rats (Shabel and Janak, 2009) and monkeys (Fuster and Uyeda, 1971; Paton et al., 2006; Zhang et al., 2013b). The proportion of cue-responsive BLA units that we identify in mice is similar to that recorded by Fuster and Uyeda in monkeys (53%, while we found 50%). Moreover, the proportions of units differentially modulated by cues predicting positive or negative outcomes (responding to the CS-S only, to the CS-Q only, or to both cues in an opposite manner) are also strikingly consistent between mice and monkeys in these two studies (37% in both). Fuster and Uyeda also identified a similar proportion of units responding to both cues in the same qualitative way (excited by both cues or inhibited by both cues; 16%, while we found 13%). These marked similarities suggest that the coding properties of BLA neurons are preserved across mammalian phylogeny.

The critical novel finding that we present is that projection-target-defined populations of BLA neurons play distinct roles in valence retrieval *in vivo*. These distinctions are not exclusively based upon opposing excitatory responses, but also involve inhibitory responses. When all BLA neurons are considered together, approximately half of the cells responding selectively to the CS-S, selectively to the CS-Q, or similarly to both cues displayed inhibitory responses (Figure 2D). As most of the BLA neurons displayed low but stable firing rates (Figure 5D), this suggests that inhibition of an ensemble of cells during a specific cue may carry valence information through a decrease in synaptic activation of the downstream target(s) of these cells.

### **Design Advantages**

Here, we introduce important advances for photostimulation-assisted identification of neural populations within a recurrent excitatory network. Recently, the *in vivo* activity of projection-target-defined cells has been examined by expressing ChR2 in neurons of interest and using light-evoked firing as an instrument to identify these neurons in intact animals (Ciocchi et al., 2015; Jennings et al., 2013; Zhang et al., 2013a). However, two confounds could undermine the stringent identification of projection-target-defined neurons using these methods. First, lateral synaptic contacts between glutamatergic neurons may result in the inclusion of non-projectors in the photoidentified group. To avoid the inappropriate inclusion of indirectly excited, non-expressing neighboring cells, we have refined this method by establishing projection-specific cutoffs for photostimulation-evoked action potential latency based upon direct *ex vivo* obser-

vations. The second confound arises from “antidromic” phototagging approaches that can inaccurately identify neurons via antidromic activation of fibers of passage. Here, we circumvent this confound using a dual-virus recombination strategy, which requires co-infection at terminal and somatic sites in order for ChR2 expression to occur. Using this approach, we eliminate the need for antidromic stimulation and collision tests and can photoidentify cells at the level of the soma.

We have also taken strides to facilitate the interpretation of our neural data as they relate to valence encoding. Previous studies examining valence processing in the BLA have used different sensory modalities for the conditioned stimuli paired with rewarding and aversive outcomes (Shabel and Janak, 2009), as well as for the outcomes themselves. For instance, palatable foods or liquids are often presented as rewarding unconditioned stimuli, whereas electric shocks or air puffs are used as aversive unconditioned stimuli (Cohen et al., 2012; Fuster and Uyeda, 1971; Paton et al., 2006; Shabel and Janak, 2009). These discrepancies in stimulus modality require sensory processing along distinct streams, which may result in the recruitment of distinct subpopulations of BLA neurons independent of valence processing. To reduce this potential confound, we matched the modality of the rewarding and aversive unconditioned stimuli (gustatory) and conditioned stimuli (auditory).

To further reduce variability in the detection of sensory signals during the behavioral task, we head restrained mice. In a head-fixed configuration, the mice receive auditory conditioned stimuli at a consistent intensity throughout all trials. Further, acute recordings in head-fixed mice allow for multiple recording tracks within each animal, increasing the yield of recorded units and photoidentified cells compared to previous studies.

### **“Both” Cells and Collaterals: Hypotheses**

We found evidence of collateralization to multiple downstream targets among BLA projector populations. We hypothesize that certain cells collateralize within these distributed circuits to enhance overall arousal through increased excitability of post-synaptic cells in the entire valence system. Congruent with this idea, a recent study identified a population of dorsal hippocampal neurons sending collaterals to the NAc, the BLA, and the mPFC, which was activated across behavioral conditions of different valence (Ciocchi et al., 2015). We speculate that BLA neurons targeting multiple downstream structures respond similarly to positive and negative valence in order to increase overall arousal in response to salient conditioned stimuli.

An alternative possibility is that certain valence encoding neurons in the BLA project to multiple downstream targets in order to promote behavioral flexibility. Within natural environments, valence exists on a continuum wherein sensory cues predict rewards and dangers of various magnitude, and these pairings are often subject to change. In order to survive, an animal must shift behavioral strategies when environmental contingencies change. Individual BLA neurons that innervate multiple projection targets have the ability to send information both to canonical fear and reward pathways. These cells may track changing environmental contingencies via selective strengthening of inputs to one target over the other(s), potentially through the formation of increased synaptic contacts, through

compartment-specific changes in release probability following axo-axonal excitation, or through downstream local inhibition.

### Valence: Operational Definitions

If we consider all cells in a population, and define valence coding within that population to be its net responsivity to either a rewarding or an aversive cue, our results indicate that all the assayed BLA populations increase activity in response to positive and negative valence (Figure 6A). However, if we further calculate the difference between the responses induced by the sucrose cue and by the quinine cue (Figure 6B), we find that cells in the entire BLA population, the BLA-NAc projector population, and the BLA-vHPC population tend to be more excited/less inhibited by the sucrose cue compared to the quinine cue, whereas the cells in the BLA-CeA projector population were overall more excited/less inhibited by the quinine cue compared to the sucrose cue. These results suggest that the BLA-NAc projector population is sending a stronger excitatory drive to the NAc in response to reward predictive cues than to aversion predictive cues and that, conversely, the BLA-CeA projector population is sending a stronger excitatory drive to the CeA during retrieval of an aversive association.

Within the recorded BLA populations, we found that cells responding exclusively to the reward predictive cue were over-represented among cue-selective neurons (Figure 7E). As the mice did not consume the quinine during most trials, the bias in cue selectivity may represent the relative magnitude of valence predicted by the two cues (sucrose consumption versus quinine smell). Alternatively, the bias toward neurons responding to the reward predictive cue could reflect a larger computational load required to take action (go) compared to that required to suppress action (no go).

To further decode the nature of valence processing during the retrieval of associative memories, we classified BLA neural responses to the sucrose predictive cue and the quinine predictive cue based upon their directionality. The valence index quantifies the proportion of a task-responsive population that encodes valence. Within this classification, neurons that respond similarly to both cues are not considered to be valence encoding, as these neurons might encode the salience of the cues or general arousal. Using this definition, among the task-responsive cells, we found that 75% of BLA neurons encoded valence, and this proportion was similar regardless of their projection target.

Among the valence encoding BLA neurons identified using the valence index, we examined the relative proportion of cells encoding positive or negative valence using the valence bias metric (Figure 7E). Despite the limitation that the downstream cell type contacted by BLA projectors is unknown, we found that a larger proportion of BLA-NAc projectors encode positive valence compared to the entire BLA, whereas the BLA-CeA projectors tend to preferentially encode negative valence. By contrast, and to our surprise, positive and negative valence encoding neurons were equally represented among valence-responsive BLA-vHPC neurons. Given that activation of this projection is anxiogenic (Felix-Ortiz et al., 2013), we hypothesized that BLA neurons projecting to the vHPC would code for negative valence during retrieval. Our contrasting findings raise the possibility that innate and learned emotional valence could be processed by

distinct circuitry emerging from the BLA. For this reason, we examined neural responses to the unconditioned stimuli.

### Innate versus Learned Valence: Responses to the US

While the value of the predictive cues must be learned across multiple conditioning sessions, the valence of sucrose and quinine are innate and do not require training. Analyzing responses of BLA neurons to these stimuli presents two limitations, however. First, the US is delivered during the CS, and second, the rewarding US (sucrose) is consumed by the animal, whereas the aversive US (quinine) can be smelled but is not consumed after the mice acquired the association (Figure 1D; Movie S1). The majority of the BLA neurons selectively responding to the sucrose or quinine delivery changed their firing upon the sucrose delivery (595/698, 85%, Figures S2E and 7E). This disparity may be because the sucrose is actively consumed, whereas the quinine is avoided.

Among the US-valence-responsive BLA neurons we recorded, the majority encode innate negative valence (518/723, 58%), while 305/723 (42%) encoded innate positive valence (Figure S7D). Compared to our findings regarding responses to conditioned stimuli, in which 49% of valence-encoding BLA neurons encoded negative valence, these results suggest that a greater proportion of BLA neurons encoded innate negative valence than learned negative valence. This encoding of the innate valence of the US by BLA neurons may promote the attribution of valence to the CS during learning (Gore et al., 2015).

If we categorize the units depending on their response type to the US and calculate the US-valence bias (Figure S7D), we find that the NAc projector population preferentially encodes innate positive valence (11/18, 61%), and that CeA projectors we recorded preferentially encode innate negative valence (12/17, 71%). If we assume that most of the BLA-CeA projectors that we recorded in this study are projecting to the viral injection site in the CeM, and consider anxiety-related behaviors as a state of innate negative valence, our results are consistent with previous findings showing that activation of the BLA-CeA projection is anxiolytic, via disynaptic inhibition of the CeM through feedforward recruitment of the CeL by the BLA (Tye et al., 2011).

Surprisingly, we found that the vHPC projectors did not preferentially encode innate negative valence (9/19, 47%), despite our previous finding that activation of the BLA-vHPC is anxiogenic (Felix-Ortiz and Tye, 2014; Felix-Ortiz et al., 2013). This discrepancy may result from recruitment of different BLA-vHPC projectors for the initiation of anxiety-like behaviors and the processing of discrete sensory stimuli.

### Looking Forward

The heterogeneity of response types within different populations suggests that combinatorial activity within the BLA in response to a conditioned cue ultimately recruits the motor output that triggers the appropriate behavior. Despite this heterogeneity, our results suggest that BLA-NAc projectors preferentially encode positive valence, when valence is defined (1) as the differential response of the entire population to rewarding versus aversive cues (Figures 6A and 6B), (2) as excitation/inhibition balance of cue selective cells (Figure 7D), or (3) as a valence bias (Figure 7E). Conversely, we found that BLA-CeA projectors preferentially encode negative valence when valence is defined using any of

these three definitions. However, other BLA outputs including projections to the bed nucleus of the stria terminalis, the prefrontal cortex, anterior cingulate cortex, and orbitofrontal cortex represent promising avenues for future study of valence processing in anatomically defined BLA populations. The results that we present here detail functional differences in valence encoding based upon anatomically defined circuits and offer insight toward mechanisms by which emotional and motivational information may be routed through the brain.

## EXPERIMENTAL PROCEDURES

### Stereotaxic Surgery and Viral Vectors

All procedures were carried out in accordance with the guidelines from the NIH and with approval of the MIT committee on animal care (CAC). Adult wild-type male C57BL/6J mice were used. We injected an anterograde adeno-associated viral vector (AAV<sub>5</sub>), carrying ChR2 fused to eYFP in a cre-recombinase-dependent double-inverted open reading frame (DIO) construct, under the control of the pan-neuronal promoter EF1 $\alpha$  (AAV<sub>5</sub>-EF1 $\alpha$ -DIO-ChR2-eYFP) in the BLA to transduce local cell bodies, and injected a retrogradely traveling canine adenovirus of type 2 carrying cre-recombinase (CAV2-cre), into the downstream target of interest (NAc, CeA, or vHPC).

### Behavioral Conditioning

~3 months after surgery, mice were food restricted and head fixed daily over 6 days to learn to associate two auditory cues with two gustatory outcomes of positive and negative valence. During the first days, the mice learned to associate one conditioned stimulus (CS-S) with a delivery of sucrose before we introduced a second conditioned stimulus (CS-Q) associated with a delivery of an aversive solution (quinine). When the mice showed anticipatory licking in response to the CS-S and reached a performance criterion of 70% successful trials for sucrose (lick) and for quinine (no lick), we performed acute recordings in the BLA over 2 consecutive days in 21 animals (Figures 1 and S1).

### In Vivo Electrophysiology

Once the mice recovered from surgery, they were head fixed and a silicon optrode coated with red fluorescent microspheres was lowered into the BLA. The optrode was then lowered at ~1  $\mu$ m/s until we observed a neural response to 473 laser stimulation. We then started a recording session presenting ~30 sucrose and ~30 quinine interleaved trials. Following completion of the task, a phototagging session, during which pseudorandomly dispersed stimulations of 1 s constant light, 10 s of 1 Hz (10 ms pulses), 2 s of 10 Hz (5 ms pulses), and 100 ms of 100 Hz (5 ms pulses) were delivered, with at least five iterations each.

### Ex Vivo Electrophysiology

Coronal sections of 300  $\mu$ m containing the BLA were collected from animals that had the same viral surgery as the animals used for in vivo recordings. Whole-cell patch-clamp recordings were taken from visually identified fluorescent projectors and neighboring non-expressing cells. BLA cells expressing ChR2 were activated using a 470 nm LED. Response latencies of action potentials (APs) and excitatory postsynaptic potentials (EPSPs) were measured for 20 pulses of 5 ms delivered at 10 Hz and averaged for each neuron (Figure S4).

### Confocal Microscopy

Mice included in this study were trained, recorded, and perfused before the brain was extracted for histological verification of the viral injections and the recording location. Brains were fixed, frozen, and sliced in 50  $\mu$ m coronal sections. Sections were then incubated with a DNA-specific fluorescent probe, slide mounted, and imaged using an Olympus FV1000 confocal laser-scanning microscope.

### Statistical Analysis

Changes in neural firing rate in response to the CS and US were tested using a Wilcoxon signed-rank test comparing an experimental window of 500 ms to a

baseline window of 2 s (Figures 2B and S2C; Table S1). Significance threshold was placed at  $p < 0.01$  to classify a neuron as responding to the event. We used the same signed-rank test for light responses (100 ms baseline window and experimental window of 9 ms for BLA-NAc projectors and 6 ms for BLA-CeA and BLA-vHPC projectors), in addition to a threshold on the light-evoked response magnitude (average Z score  $> 0.5$ ). Paired statistical comparisons were made with a two-tailed paired Student's t test. Comparison of distributions was performed using a two sample Kolmogorov-Smirnov test. Comparisons of Z score differences were realized with a non-parametric Kruskal-Wallis test. Comparisons of proportion of excitation and inhibition within populations were made using binomial distribution tests. Threshold for significance was placed at \* $p < 0.1$ , \*\* $p < 0.05$ , \*\*\* $p < 0.01$ , and \*\*\*\* $p < 0.001$ ). All data are shown as mean  $\pm$  SEM.

## SUPPLEMENTAL INFORMATION

Supplemental Information includes Supplemental Experimental Procedures, seven figures, one table, and one movie and can be found with this article online at <http://dx.doi.org/10.1016/j.neuron.2016.03.004>.

## AUTHOR CONTRIBUTIONS

Conceptualization, A.B., P.N., and K.M.T.; Methodology, A.B., P.N., R.L., and G.F.C.; Investigation, A.B., P.N., G.F.G., G.G.C., and C.S.; Software, P.N.; Writing – Original Draft, A.B.; Writing – Review & Editing, A.B., G.G.C., P.N., C.P.W., and K.M.T.; Funding Acquisition, K.M.T., A.B., P.N., and G.G.C.; Resources, K.M.T. and C.P.W.; Supervision, K.M.T.

## ACKNOWLEDGMENTS

We thank the entire K.M.T. laboratory for helpful discussion. We thank E.J. Kremer for providing the CAV2-cre vector, R. Neve for the HSV and AAV<sub>9</sub> vectors, and the UNC vector core for the AAV<sub>5</sub> vectors. K.M.T. is a New York Stem Cell Foundation – Robertson Investigator and McKnight Scholar and this work was supported by funding from the JPB Foundation, PIIF, PNDRF, JFDP, Whitehall Foundation, Klingenstein Foundation, NARSAD, Alfred P. Sloan Foundation, New York Stem Cell Foundation, Whitehead Career Development Chair, NIH R01-MH102441-01 (NIMH), and NIH Director's New Innovator Award DP2-DK-102256-01 (NIDDK). A.B. was supported by a fellowship from the Swiss National Science Foundation and NARSAD. P.N. was supported by Singleton, Leventhal, and Whitaker fellowships. G.G.C. was supported by JFDP and NARSAD.

Received: September 18, 2015

Revised: January 8, 2016

Accepted: February 16, 2016

Published: March 31, 2016

## REFERENCES

- Adhikari, A. (2014). Distributed circuits underlying anxiety. *Front. Behav. Neurosci.* 8, 112.
- Allsop, S.A., Vander Weele, C.M., Wichmann, R., and Tye, K.M. (2014). Optogenetic insights on the relationship between anxiety-related behaviors and social deficits. *Front. Behav. Neurosci.* 8, 241.
- Ambroggi, F., Ishikawa, A., Fields, H.L., and Nicola, S.M. (2008). Basolateral amygdala neurons facilitate reward-seeking behavior by exciting nucleus accumbens neurons. *Neuron* 59, 648–661.
- Amorapanth, P., Nader, K., and LeDoux, J.E. (1999). Lesions of periaqueductal gray dissociate-conditioned freezing from conditioned suppression behavior in rats. *Learn. Mem.* 6, 491–499.
- Ben-Ari, Y., Tremblay, E., and Ottersen, O.P. (1980). Injections of kainic acid into the amygdaloid complex of the rat: an electrographic, clinical and histological study in relation to the pathology of epilepsy. *Neuroscience* 5, 515–528.

- Berridge, K.C., and Robinson, T.E. (2003). Parsing reward. *Trends Neurosci.* 26, 507–513.
- Bordi, F., and LeDoux, J. (1992). Sensory tuning beyond the sensory system: an initial analysis of auditory response properties of neurons in the lateral amygdaloid nucleus and overlying areas of the striatum. *J. Neurosci.* 12, 2493–2503.
- Britt, J.P., Benaliouad, F., McDevitt, R.A., Stuber, G.D., Wise, R.A., and Bonci, A. (2012). Synaptic and behavioral profile of multiple glutamatergic inputs to the nucleus accumbens. *Neuron* 76, 790–803.
- Calhoun, M.E., Jucker, M., Martin, L.J., Thinakaran, G., Price, D.L., and Mouton, P.R. (1996). Comparative evaluation of synaptophysin-based methods for quantification of synapses. *J. Neurocytol.* 25, 821–828.
- Ciocchi, S., Herry, C., Grenier, F., Wolff, S.B.E., Letzkus, J.J., Vlachos, I., Ehrlich, I., Sprengel, R., Deisseroth, K., Stadler, M.B., et al. (2010). Encoding of conditioned fear in central amygdala inhibitory circuits. *Nature* 468, 277–282.
- Ciocchi, S., Passecker, J., Malagon-Vina, H., Mikus, N., and Klausberger, T. (2015). Brain computation. Selective information routing by ventral hippocampal CA1 projection neurons. *Science* 348, 560–563.
- Cohen, J.Y., Haesler, S., Vong, L., Lowell, B.B., and Uchida, N. (2012). Neuron-type-specific signals for reward and punishment in the ventral tegmental area. *Nature* 482, 85–88.
- Etkin, A., and Wager, T.D. (2007). Functional neuroimaging of anxiety: a meta-analysis of emotional processing in PTSD, social anxiety disorder, and specific phobia. *Am. J. Psychiatry* 164, 1476–1488.
- Etkin, A., Prater, K.E., Schatzberg, A.F., Menon, V., and Greicius, M.D. (2009). Disrupted amygdalar subregion functional connectivity and evidence of a compensatory network in generalized anxiety disorder. *Arch. Gen. Psychiatry* 66, 1361–1372.
- Felix-Ortiz, A.C., and Tye, K.M. (2014). Amygdala inputs to the ventral hippocampus bidirectionally modulate social behavior. *J. Neurosci.* 34, 586–595.
- Felix-Ortiz, A.C., Beyeler, A., Seo, C., Leppla, C.A., Wildes, C.P., and Tye, K.M. (2013). BLA to vHPC inputs modulate anxiety-related behaviors. *Neuron* 79, 658–664.
- Fontanini, A., Grossman, S.E., Figueroa, J.A., and Katz, D.B. (2009). Distinct subtypes of basolateral amygdala taste neurons reflect palatability and reward. *J. Neurosci.* 29, 2486–2495.
- Fuster, J.M., and Uyeda, A.A. (1971). Reactivity of limbic neurons of the monkey to appetitive and aversive signals. *Electroencephalogr. Clin. Neurophysiol.* 30, 281–293.
- Goosens, K.A., and Maren, S. (2001). Contextual and auditory fear conditioning are mediated by the lateral, basal, and central amygdaloid nuclei in rats. *Learn. Mem.* 8, 148–155.
- Gore, F., Schwartz, E.C., Brangers, B.C., Aladi, S., Stujenske, J.M., Likhtik, E., Russo, M.J., Gordon, J.A., Salzman, C.D., and Axel, R. (2015). Neural Representations of Unconditioned Stimuli in Basolateral Amygdala Mediate Innate and Learned Responses. *Cell* 162, 134–145.
- Janak, P.H., and Tye, K.M. (2015). From circuits to behaviour in the amygdala. *Nature* 517, 284–292.
- Jennings, J.H., Sparta, D.R., Stamatakis, A.M., Ung, R.L., Pleil, K.E., Kash, T.L., and Stuber, G.D. (2013). Distinct extended amygdala circuits for divergent motivational states. *Nature* 496, 224–228.
- Jimenez, S.A., and Maren, S. (2009). Nuclear disconnection within the amygdala reveals a direct pathway to fear. *Learn. Mem.* 16, 766–768.
- Lammel, S., Tye, K.M., and Warden, M.R. (2014). Progress in understanding mood disorders: optogenetic dissection of neural circuits. *Genes Brain Behav.* 13, 38–51.
- McDonald, A.J. (1984). Neuronal organization of the lateral and basolateral amygdaloid nuclei in the rat. *J. Comp. Neurol.* 222, 589–606.
- McDonald, A.J. (1998). Cortical pathways to the mammalian amygdala. *Prog. Neurobiol.* 55, 257–332.
- Mervaala, E., Föhr, J., Könönen, M., Valkonen-Korhonen, M., Vainio, P., Partanen, K., Partanen, J., Tiihonen, J., Viinamäki, H., Karjalainen, A.K., and Lehtonen, J. (2000). Quantitative MRI of the hippocampus and amygdala in severe depression. *Psychol. Med.* 30, 117–125.
- Namburi, P., Al-Hasani, R., Calhoun, G.G., Bruchas, M.R., and Tye, K.M. (2015a). Architectural representation of valence in the limbic system. *Neuropsychopharmacology*. Published online December 9, 2015. <http://dx.doi.org/10.1038/npp.2015.358>.
- Namburi, P., Beyeler, A., Yorozu, S., Calhoun, G.G., Halbert, S.A., Wichmann, R., Holden, S.S., Mertens, K.L., Anahtar, M., Felix-Ortiz, A.C., et al. (2015b). A circuit mechanism for differentiating positive and negative associations. *Nature* 520, 675–678.
- Nieh, E.H., Kim, S.-Y., Namburi, P., and Tye, K.M. (2013). Optogenetic dissection of neural circuits underlying emotional valence and motivated behaviors. *Brain Res.* 1511, 73–92.
- Nieh, E.H., Matthews, G.A., Allsop, S.A., Presbrey, K.N., Leppla, C.A., Wichmann, R., Neve, R., Wildes, C.P., and Tye, K.M. (2015). Decoding neural circuits that control compulsive sucrose seeking. *Cell* 160, 528–541.
- Oh, S.W., Harris, J.A., Ng, L., Winslow, B., Cain, N., Mihalas, S., Wang, Q., Lau, C., Kuan, L., Henry, A.M., et al. (2014). A mesoscale connectome of the mouse brain. *Nature* 508, 207–214.
- Paton, J.J., Belova, M.A., Morrison, S.E., and Salzman, C.D. (2006). The primate amygdala represents the positive and negative value of visual stimuli during learning. *Nature* 439, 865–870.
- Pitkänen, A. (2000). *The Amygdala: A Functional Analysis* (Oxford University Press).
- Senn, V., Wolff, S.B.E., Herry, C., Grenier, F., Ehrlich, I., Gründemann, J., Fadok, J.P., Müller, C., Letzkus, J.J., and Lüthi, A. (2014). Long-range connectivity defines behavioral specificity of amygdala neurons. *Neuron* 81, 428–437.
- Shabel, S.J., and Janak, P.H. (2009). Substantial similarity in amygdala neuronal activity during conditioned appetitive and aversive emotional arousal. *Proc. Natl. Acad. Sci. USA* 106, 15031–15036.
- Shinonaga, Y., Takada, M., and Mizuno, N. (1994). Topographic organization of collateral projections from the basolateral amygdaloid nucleus to both the prefrontal cortex and nucleus accumbens in the rat. *Neuroscience* 58, 389–397.
- Somerville, L.H., Kim, H., Johnstone, T., Alexander, A.L., and Whalen, P.J. (2004). Human amygdala responses during presentation of happy and neutral faces: correlations with state anxiety. *Biol. Psychiatry* 55, 897–903.
- Stuber, G.D., Sparta, D.R., Stamatakis, A.M., van Leeuwen, W.A., Hardjoprajitno, J.E., Cho, S., Tye, K.M., Kempadoo, K.A., Zhang, F., Deisseroth, K., and Bonci, A. (2011). Excitatory transmission from the amygdala to nucleus accumbens facilitates reward seeking. *Nature* 475, 377–380.
- Tye, K.M., Stuber, G.D., de Ridder, B., Bonci, A., and Janak, P.H. (2008). Rapid strengthening of thalamo-amygdala synapses mediates cue-reward learning. *Nature* 453, 1253–1257.
- Tye, K.M., Prakash, R., Kim, S.-Y., Fenno, L.E., Grosenick, L., Zarabi, H., Thompson, K.R., Gradinaru, V., Ramakrishnan, C., and Deisseroth, K. (2011). Amygdala circuitry mediating reversible and bidirectional control of anxiety. *Nature* 471, 358–362.
- Tye, K.M., Mirzabekov, J.J., Warden, M.R., Ferenczi, E.A., Tsai, H.-C., Finkelstein, J., Kim, S.-Y., Adhikari, A., Thompson, K.R., Andalman, A.S., et al. (2013). Dopamine neurons modulate neural encoding and expression of depression-related behaviour. *Nature* 493, 537–541.
- Zhang, S.-J., Ye, J., Miao, C., Tsao, A., Cerniauskas, I., Ledergerber, D., Moser, M.-B., and Moser, E.I. (2013a). Optogenetic dissection of entorhinal-hippocampal functional connectivity. *Science* 340, 1232627.
- Zhang, W., Schneider, D.M., Belova, M.A., Morrison, S.E., Paton, J.J., and Salzman, C.D. (2013b). Functional circuits and anatomical distribution of response properties in the primate amygdala. *J. Neurosci.* 33, 722–733.



# OUR NETWORK IS YOUR NETWORK

## With Cell Press Webinars, our network is your network!

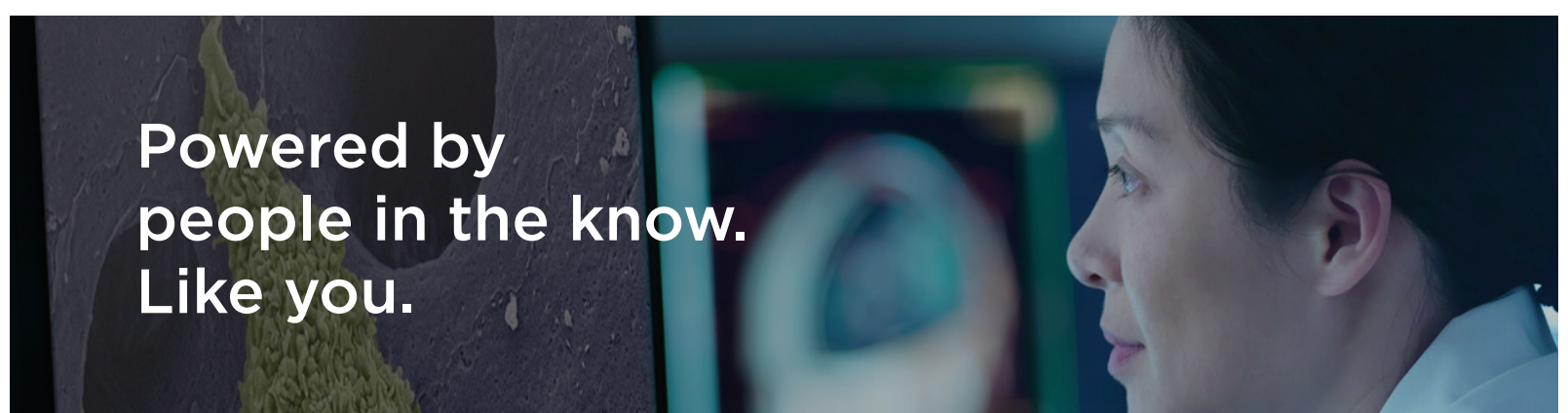
Cell Press Webinars give you access to hot topics in emerging research and the application of new technology.

Watch essential, need-to-know webcasts via live streaming or on demand from the comfort and convenience of your office, lab, or home.

Need-to-know topics, editorially curated

World-class presenters, experts in their field

Moderated by Cell Press editors



Powered by  
people in the know.  
Like you.

Tap into our network today!  
Visit [www.cell.com/webinars](http://www.cell.com/webinars)

**CellPress**  
Webinars

# Distinct Contribution of Adult-Born Hippocampal Granule Cells to Context Encoding

Nathan B. Danielson,<sup>3,4</sup> Patrick Kaifosh,<sup>3,4</sup> Jeffrey D. Zaremba,<sup>3,4</sup> Matthew Lovett-Barron,<sup>3,6</sup> Joseph Tsai,<sup>3,4</sup> Christine A. Denny,<sup>1,2</sup> Elizabeth M. Balough,<sup>3,4</sup> Alexander R. Goldberg,<sup>2</sup> Liam J. Drew,<sup>1,2,7</sup> René Hen,<sup>1,2,3,5</sup> Attila Losonczy,<sup>3,5,\*</sup> and Mazen A. Kheirbek<sup>1,2,8,9</sup>

<sup>1</sup>Department of Psychiatry, Columbia University, New York, NY 10032, USA

<sup>2</sup>Division of Integrative Neuroscience, New York State Psychiatric Institute, New York, NY 10032, USA

<sup>3</sup>Department of Neuroscience

<sup>4</sup>Doctoral Program in Neurobiology and Behavior

<sup>5</sup>Kavli Institute for Brain Science

Columbia University, New York, NY 10032, USA

<sup>6</sup>Department of Bioengineering, Stanford University, Stanford, CA 94305, USA

<sup>7</sup>Wolfson Institute for Biomedical Research, UCL, London WC1E 0BT, UK

<sup>8</sup>Department of Psychiatry

<sup>9</sup>Center for Integrative Neuroscience

University of California, San Francisco, San Francisco, CA 94158, USA

\*Correspondence: al2856@cumc.columbia.edu

<http://dx.doi.org/10.1016/j.neuron.2016.02.019>

## SUMMARY

Adult-born granule cells (abGCs) have been implicated in cognition and mood; however, it remains unknown how these cells behave *in vivo*. Here, we have used two-photon calcium imaging to monitor the activity of young abGCs in awake behaving mice. We find that young adult-born neurons fire at a higher rate *in vivo* but paradoxically exhibit less spatial tuning than their mature counterparts. When presented with different contexts, mature granule cells underwent robust remapping of their spatial representations, and the few spatially tuned adult-born cells remapped to a similar degree. We next used optogenetic silencing to confirm the direct involvement of abGCs in context encoding and discrimination, consistent with their proposed role in pattern separation. These results provide the first *in vivo* characterization of abGCs and reveal their participation in the encoding of novel information.

## INTRODUCTION

Hippocampal neurogenesis in the adult mammalian brain is a process by which new dentate gyrus (DG) granule cells (GCs) are generated and functionally integrated into hippocampal circuitry (Drew et al., 2013; Toni et al., 2007, 2008; van Praag et al., 2002). In both rodents and humans, a significant fraction of DG neurons are replaced by neurons generated in adulthood (Imayoshi et al., 2008; Spalding et al., 2013). Why this is the case and precisely how young adult-born GCs (abGCs) alter hippocampal circuit function remain open questions.

Behavioral studies have implicated abGCs in memory formation (Zhao et al., 2008); stress and anxiety (Snyder et al., 2011); responses to antidepressant treatments (David et al., 2009; Santarelli et al., 2003); and, most recently, in behaviors requiring contextual discrimination, consistent with a role in pattern separation (Clelland et al., 2009; Kheirbek et al., 2012a; Nakashiba et al., 2012; Sahay et al., 2011a). However, such studies have primarily inferred functions of abGCs from experiments in which adult neurogenesis was chronically ablated or enhanced, *i.e.*, long-term manipulations that may induce compensatory changes (Singer et al., 2011) and/or result in the recruitment of alternative behavioral or cognitive strategies. Furthermore, in these designs abGCs are either absent or more abundant during all phases of testing.

Hypotheses attempting to explain the role of abGCs range from modulating the activity of mature GCs (mGCs) through interactions with local interneurons, to themselves providing the DG's principal output signals (Piatti et al., 2013; Sahay et al., 2011b). Brain slice preparations have provided additional insight into the possible mechanisms by which they may uniquely influence circuit function (Dieni et al., 2013; Marín-Burgin et al., 2012; Temprana et al., 2015; van Praag et al., 2002). For example, adult-born neurons undergo a period of heightened synaptic plasticity 4–6 weeks postmitosis, a critical period during which they have been proposed to have a distinct contribution to behavior (Denny et al., 2012; Ge et al., 2007; Kheirbek et al., 2012b; Schmidt-Hieber et al., 2004). Further observed differences in excitability and plasticity could allow abGCs to encode and transfer information differently than mGCs (Ge et al., 2007; Gu et al., 2012; Schmidt-Hieber et al., 2004; van Praag et al., 2002). However, at present there are no data from the intact brain directly comparing the firing patterns of these subpopulations during behavior. This is because *in vivo* identification of mGCs and abGCs with electrophysiological approaches remains technically challenging (Jung and McNaughton, 1993; Leutgeb et al.,

2007; Neunuebel and Knierim, 2012; Pernía-Andrade and Jonas, 2014). Studies using immediate early gene expression as a proxy for neuronal activation have not identified significant differences in the recruitment of mGCs and abGCs (Stone et al., 2011) during contextual encoding, but this methodology fails to capture the dynamic nature of neuronal encoding.

Here, we have recorded the activity of abGCs *in vivo*, providing the first functional characterization of identified abGCs. Although these cells are more active than mGCs *in vivo*, they are less spatially tuned. Furthermore, we found that mGCs robustly discriminated contexts on the basis of their spatial tuning, while the small population of spatially tuned abGCs seemed to discriminate contexts to a similar or lesser degree, depending on the inclusion criteria and remapping metric applied. We confirmed this online participation of abGCs to the encoding of novel information by transiently suppressing abGCs's activity in distinct epochs of conditioning paradigms, where we showed their essential role in behavioral pattern separation. These experiments extend our understanding of the unique contribution of abGCs to behavior and provide the first characterization of their activity *in vivo*.

## RESULTS

### Two-Photon Calcium Imaging of DG GCs *In Vivo*

To gain insight into how abGCs behave *in vivo*, we sought to directly observe their activity in the intact brain in response to the manipulation of spatial and contextual cues. This was achieved by performing calcium imaging of the DG in head-restrained mice as they explored a linear virtual environment (Kaifosh et al., 2013; Lovett-Barron et al., 2014) (Figure 1A). Use of this method allowed us to image the activity of abGCs and mGCs simultaneously, which is not yet technically feasible in freely moving mice. To label abGCs, NestinCreER<sup>T2</sup> mice (Dravinsky et al., 2011) were crossed with a conditional tdTomato reporter line (*Nestin<sup>tdTomato</sup>*) and pulsed with tamoxifen (TMX) 6 weeks prior to imaging. This led to labeling of  $89.5\% \pm 3.8\%$  of the DCX population of immature cells 6 weeks after induction, indicating  $\sim 10\%$  of abGCs were not labeled and thus were not characterized as abGCs. Mice were stereotactically injected in the dorsal DG with a virus expressing GCaMP6f in all GCs. Implantation of a chronic imaging window over the dorsal DG provided the optical access necessary for cell-type-specific imaging of the DG GC layer (Figures 1A and S1, available online). This preparation did not impair hippocampal-dependent contextual conditioning, nor did it impact the overall level of activity in the DG. In addition, window implantation did not impact total number of tdTomato+ abGCs, their dendritic morphology, or the number of proliferating cells in the implanted hemisphere.

In total, we imaged 7,950 mGCs (tdTomato negative) and 446 abGCs (tdTomato positive) from 11 fields of view (FOVs) across 6 mice (Figure S1). The same FOV (Figure S2) was imaged over three trials in which the mouse explored two linear virtual contexts. On the first trial, the mouse explored one of the two contexts (A; chosen at random), then for both the second and third trials it explored the second context (B). This paradigm allowed us to compare activity levels, spatial firing patterns, and remapping dynamics in abGCs and mGCs simultaneously.

### abGCs Are More Active Than mGCs *In Vivo*

Consistent with electrophysiological studies reporting sparse GC activity (Alme et al., 2010; Leutgeb et al., 2007; Pernía-Andrade and Jonas, 2014; Schmidt-Hieber et al., 2014), detected calcium transients (Figure S2A) were observed at very low rates in both abGCs and mGCs (Figures 1B–1D; Movie S1). The level of activity was dependent on the animal's behavioral state (Leutgeb et al., 2007; Neunuebel and Knierim, 2012), as calcium transients during running were observed at nearly 2-fold higher rate than during nonrunning epochs (Figure S2C). Running-related calcium transients occurred at significantly greater rates in abGCs than in mGCs across all transients (Figures 1B and 1C) as well as across FOVs (Figure 1D). This difference was most pronounced in the FOVs that displayed the highest levels of activity. The increased activity observed *in vivo* is consistent with reports of greater responsiveness to perforant path activation of abGCs *in vitro* (Marín-Burgin et al., 2012). In addition to having a lower overall fraction of silent cells, the abGC population also contained a higher fraction of highly active cells (Figure 1C, inset). Additionally, across FOVs, we did not detect differences between mGCs and abGCs in the amplitude or duration of detected transients suggesting similar activity-induced calcium dynamics in the two populations (Figure S2B).

### abGCs Are Less Spatially Tuned Than mGCs

We next assessed the degree to which abGCs and mGCs were spatially tuned (Figure 2). To limit noise in estimates of the spatial tuning metrics, we included only GC recordings with four or more running-related transients during the trial. For each such GC recording, we calculated a tuning vector as the mean of the vectors pointing in the direction of the mouse's position at the time of each transient onset, inversely weighted by the mouse's occupancy of that position (Figures 2A, 2B, and S3). This vector's orientation and length defined the cell's tuning direction and tuning specificity, respectively. The mean spatial tuning specificity was significantly lower for abGCs than for mGCs (Figure 2C). We did not observe significant reward-related or velocity-related activity in our recordings (Figure S4).

To assess the statistical significance of the tuning specificity difference, for each GC we generated a null distribution by randomly shuffling calcium transient onset times and repeatedly recomputing the tuning specificity. This allowed us to calculate the p value as the fraction of this null distribution that exceeded the GC's tuning specificity. The p value distributions for both mGCs and abGCs differed significantly from chance levels, indicating that spatially tuned cells existed within both populations (Figure 2D). However, the p value distribution for mGC populations was lower than that for abGCs (Figure 2D), suggesting that as a population the mGCs demonstrate a higher degree of spatial tuning than abGCs. Across all significance thresholds, a higher fraction of mature neurons would be categorized as spatially tuned than of young neurons. These findings indicate that abGCs differ from mGCs not just in their level of activity but also in the spatial information carried by their activity.

To investigate whether the observed difference in spatial tuning was dependent on the value of our inclusion threshold, we compared the spatial tuning p values of mGCs and abGCs for

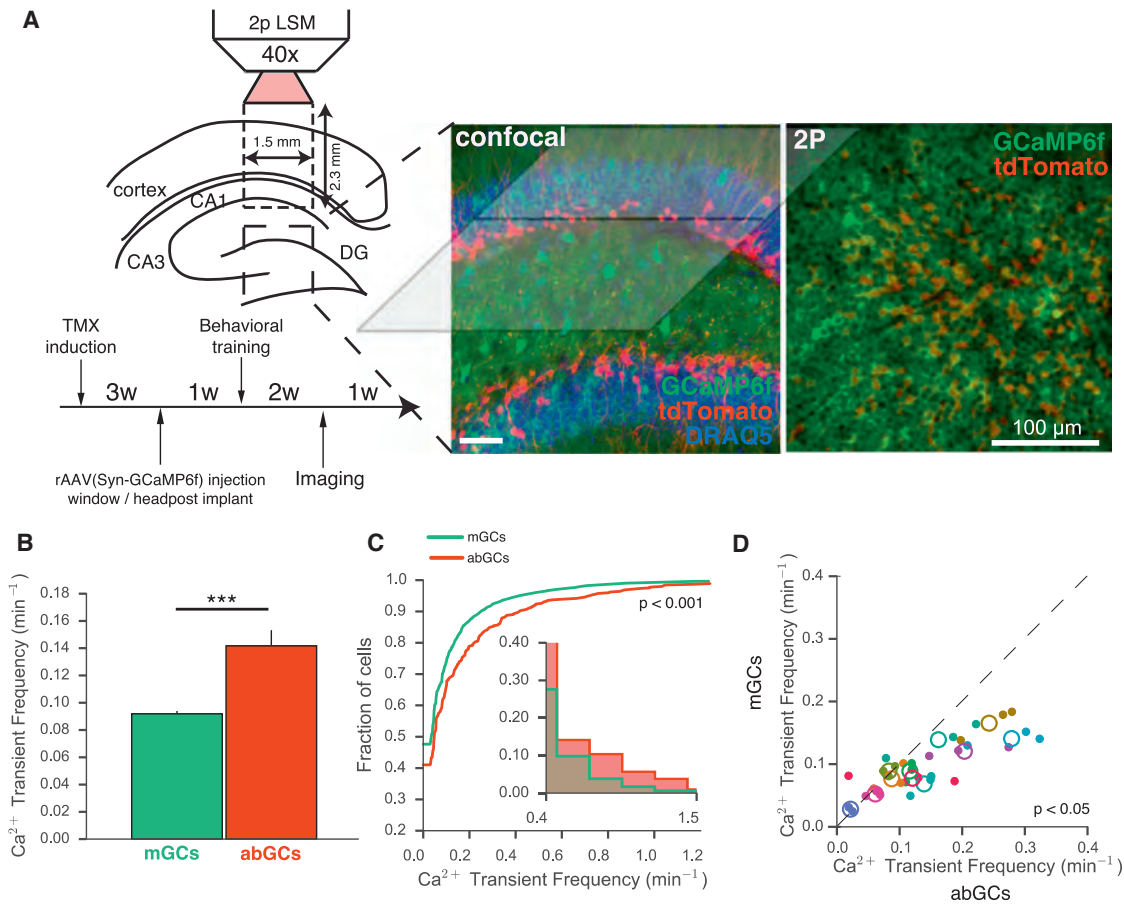


### Figure 1. Functional Imaging of abGCs and mGCs

(A) Left: experimental schematic. Two-photon line-scanning microscopy allows for the recording of large populations of GCs in surgically exposed dorsal DG. Experimental timeline as indicated. Middle: confocal image of recovered tissue illustrating the geometry of the preparation. GCs (stained with DRAQ5) express GCaMP6f, with abGCs also expressing tdTomato. Right: time-averaged *in vivo* two-photon image of a representative FOV ( $300 \times 300 \mu\text{m}$ ), containing  $\sim 1,000$  GCs.

(B) abGCs exhibit a higher rate of running-related calcium transients than mGCs ( $p < 0.001$ ;  $n = 7,950$  mGCs, 446 abGCs across 11 FOV in 6 mice; Welch's  $t$  test,  $t_{(8,396)} = -4.14$ ; each measure is the average of 1–3 recordings for that cell).

(C) Distribution of firing rates across abGCs and mGCs demonstrates significantly different population-level activity ( $p < 0.001$ ; Kolmogorov-Smirnov (KS) test, KS Stat = 0.10).

(D) Scatter of mean abGC and mGC running-related firing rates within each recording session (closed circles) and averaged across sessions for each FOV (open circles). Color reflects FOV as specified in Figure S6. Across imaging fields abGCs were significantly more active than mGCs ( $p < 0.05$ ;  $n = 11$  FOV; paired  $t$  test,  $t_{(20)} = 2.88$ ). The same results were obtained when including all transients (data not shown).

Error bars are mean  $\pm$  SEM.

different minimum numbers of running-related transients (Figure 2E). At all inclusion thresholds, mean  $p$  values were lower for mGCs than for abGCs. As expected for a population in which there was no relationship between spatial tuning and activity level, the  $p$  values for mGCs decreased monotonically with increasing inclusion threshold (statistical power increases, and hence  $p$  values decrease with greater numbers of transients). The lack of a similar decrease in abGCs suggests a dependence of tuning on activity, whereby the most active abGCs tend to be least tuned (see Figure S3).

It is important to note that a lower tuning specificity could be consistent with an interpretation of multiple place fields, and a difference in this metric could either be attributable to inconsis-

tent tuning or to tuning that is consistent but multi-peaked or broader. Estimating the precise number of fields was not possible due to the sparsity of events observed. However, in order to account for the possibility of multi-peaked tuning profiles, we also calculated the mutual information between the occupancy-normalized  $\text{Ca}^{2+}$  transient rate maps and the mouse's position. The traditional definition of spatial information (Skaggs et al., 1993), based on the method of sieves, is a highly biased estimator in the setting of sparse firing rates, as were observed in our data (Paninski, 2003), therefore it was not possible to quantify absolute spatial information rates in these cells. However, a  $p$  value analysis derived similarly to that of tuning specificity above is immune to this bias, since both the calculated and

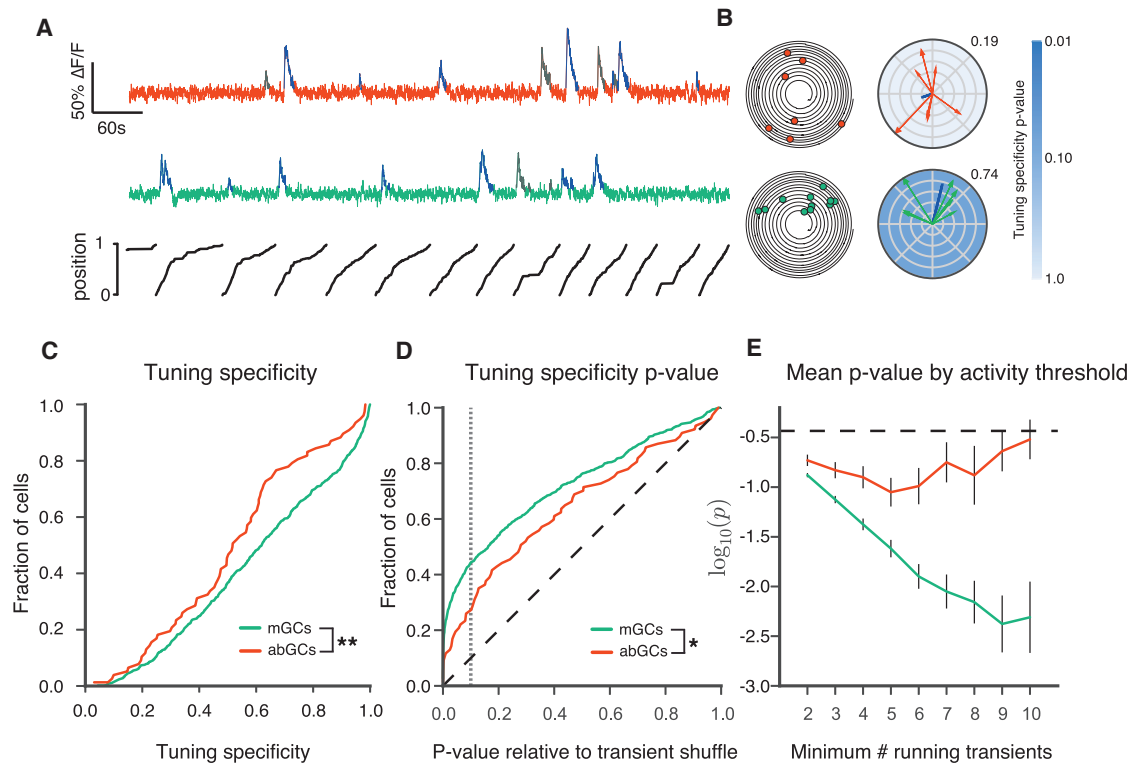


**Figure 2. Spatial Tuning of abGCs and mGCs**

(A) Time series of calcium signals from an example abGC (red) and mGC (green), with position of the mouse along the circular treadmill belt plotted below. Running-related calcium transients are indicated in blue (all others in gray).

(B) Left: trajectory plot of position (angular coordinate) and time (radial coordinate) with running-related calcium transients as dots along the trajectory. Right: spatial tuning plots for example mGC (green) and abGC (red). Vectors indicate the animal's position at the time of each running-related transient onset, with magnitude determined by the inverse of the fraction of time spent at that position. Blue lines indicate the calculated tuning vectors, whose orientation and magnitude correspond to the tuning direction and specificity, respectively. Tuning specificity is given next to each plot. Tuning specificity p value is indicated by blue shading.

(C) Cumulative distributions of tuning specificity values for active mGCs and abGCs ( $\geq$  four running-related transients). The abGC distribution was significantly left shifted as compared to the mGC distribution with few sharply tuned cells ( $p < 0.01$ ;  $n = 639$  mGCs, 77 abGCs from 11 FOVs in 6 mice; two-sample KS Test, KS Stat = 0.217,  $p < 0.01$ ).

(D) Cumulative distributions of tuning specificity p values. The p value distributions for mGCs and abGCs differed significantly from each other ( $p < 0.05$ ; KS test, KS Stat = 0.18) and from the uniform distribution (diagonal dashed line) expected in the case of a nonspatially tuned population ( $p < 0.001$  for both mGCs and abGCs; KS test, abGCs, KS Stat = 0.25, mGCs KS Stat = 0.35). Gray dashed line indicates  $p = 0.1$ .

(E) Mean logarithm of the p value for mGCs and abGCs with differing inclusion thresholds for the number of running-related calcium transients. For mGCs, the p values monotonically decrease with increasing inclusion threshold, consistent with the increased statistical power provided by a greater numbers of transients. The lack of such a decrease in the adult-born population suggests that the more active abGCs tend to be less tuned or consist of a mixed population of tuned and untuned cells. The dashed black line shows the expected value for an untuned population.

Error bars are mean  $\pm$  SEM.

shuffled distributions are calculated in the same manner (see Experimental Procedures). This analysis, which is independent of the tuning specificity metric and does not inherently select for singly peaked tuning profiles, confirmed our primary results. Spatial information p values and tuning specificity p values were linearly related on a logarithmic scale, yielding largely overlapping populations of cells (Figures 4A and 4B). The spatial information p value distributions for both populations differed significantly from chance levels, but the mGC p value distribution was significantly lower than that of abGCs, again suggesting that as a population abGCs are relatively less spatially tuned (Figure 4C). We also observed a similar relationship between the minimum number of transients and the mean spatial information

p value as was described in the tuning specificity analysis (Figure 4D). We saw no consistent evidence of multi-peaked firing in the tuning profiles of recordings that satisfied the spatial information, but not the tuning specificity criterion. In summary, this spatial information-based analysis further supports our finding that as a population, abGCs are less sharply tuned than the mGC population.

### Contextual Discrimination by abGCs and mGCs

We next assessed the context specificity of spatial representations within the population of spatially tuned mGCs and abGCs (Figure 3). We compared the similarity of GCs' spatial tuning between two sequential exposures to either similar ("A-B") or

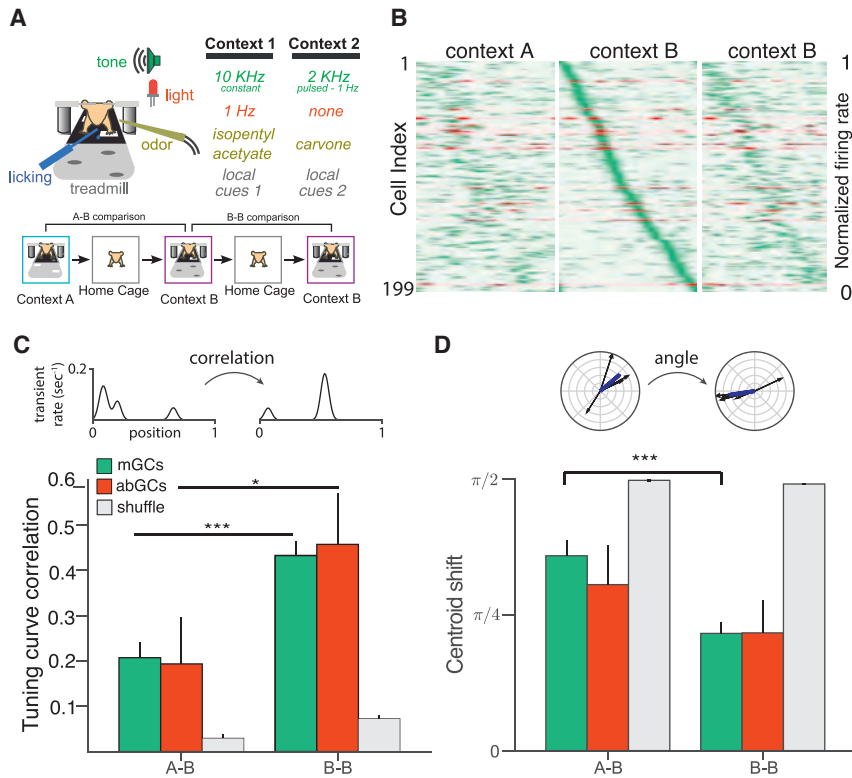


**Figure 3. Contextual Coding by abGCs and mGCs**

(A) Experimental schematic. Mice ran for three 12 min sessions in contexts A, B, and B (1 hr between runs). A and B refer to either context 1 or 2 (chosen randomly for each experiment).

(B) Remapping of spatial rate maps across sequential context exposures. Smoothed calcium transient rates, normalized to peak for each cell, are plotted as a function of position during three contextual exposures (A, B, B). Cells (mGCs, green; abGCs, red) are ordered according to the position of peak activity during the first exposure to context B. Data is shown for GCs with sufficient tuning specificity and activity ( $p < 0.1$ , at least four transients) in at least one experiment.

(C and D) Context specificity of spatial representations. Tuning curve correlations of 1D rate maps (C) and centroid shifts (angle between tuning directions) (D) between sequential exposures to different (A-B) or the same (B-B) contexts for all cells shown in (B) (A-B:  $n = 180$  mGCs, 14 abGCs; B-B:  $n = 174$  mGCs, 9 abGCs). The rate map correlations of both populations were more similar in the B-B condition than in A-B (Mann-Whitney U, mGCs:  $U_{(150)} = 5,291$ ,  $p < 0.001$ ; abGCs:  $U_{(18)} = 23.0$ ,  $p < 0.05$ ). In mGCs the tuning shift was larger in the A-B condition than in B-B, although this did not reach significance in abGCs (mGCs:  $U_{(150)} = 5,714$ ,  $p < 0.001$ ; abGCs:  $U_{(18)} = 40.0$ ,  $p = 0.34$ ). In both conditions, the similarity of spatial representations exceeded chance levels as estimated by shuffling cell identity (gray). Error bars are mean  $\pm$  SEM.

identical (“B-B”) contexts. The similar contexts A and B shared the same treadmill belt but had different olfactory, auditory, visual, and tactile cues (Figure 3A). We focused our analysis on cells with significant and well-estimated spatial tuning (at least four running-related transients in both sessions and tuning specificity  $p$  value below 0.1 in at least one session; Figure 3B). Spatially tuned mGCs displayed a higher correlation of their tuning curves (Figures 3C, S5A, and S5B) and a smaller centroid shift (angle between tuning directions; Figures 3D, S5A, and S5B) in the B-B condition than in the A-B condition. The small number of spatially tuned abGCs satisfying the inclusion criteria displayed a significantly higher correlation of tuning curves in the B-B condition than in A-B, but this result did not hold for the centroid shift metric. When basing the inclusion criteria on the spatial information  $p$  value, rather than on the tuning specificity, we similarly observed that mGCs remapped to a greater degree in the A-B than the B-B conditions as assessed by both metrics (Figures 4E and 4F). abGCs did not demonstrate a significant difference in remapping in the A-B versus B-B comparison, though it is important to note that this was difficult to assess given the low number of abGCs meeting the inclusion threshold. While the A-B-B paradigm allowed us to measure reorganization in response to the manipulation of a novel context, B-B-A and other related paradigms will allow for assessment of reorganization in a more familiar environment.

We next investigated whether DG GCs can discriminate between similar contexts solely on the basis of their activity level

throughout the exposure to these contexts, which would be indicative of rate remapping (Figures 5, S5C, and S5D). To determine this, we computed population vectors (Figure 5A) whose components were the time-averaged calcium transient rate (Figure 5B) or the transient AUC rate (Figure 5C) for each cell during the trial. By measuring the angle between population vectors ( $\Theta_{B-B}$ ,  $\Theta_{A-B}$ ) we found that for both mGCs and abGCs the population vectors were as closely aligned between sequential exposures to the same (B-B) versus different (A-B) contexts. To control for the disparities in sample size between adult-born and mature populations, we studied the pseudopopulation vectors (Figure 5D) obtained by pooling GCs across all FOVs. The contextual specificity ( $\Theta_{B-B} - \Theta_{A-B}$ ) for the abGC pseudopopulation fell well within the distribution obtained from random subsamplings of the mGC pseudopopulations for both the transient rate (Figure 5E) and transient AUC rate (Figure 5F) vectors. This indicates that in our experimental paradigm, both abGCs and mGCs discriminate between contexts at the level of their spatial tuning rather than through spatially independent changes in firing rate.

### abGCs Actively Participate in the Encoding of Novel Information

Finally, we asked whether abGCs are required for encoding a novel environment. In order to address this question, we expressed *archaerhodopsin* (*Arch*) in abGCs by crossing the

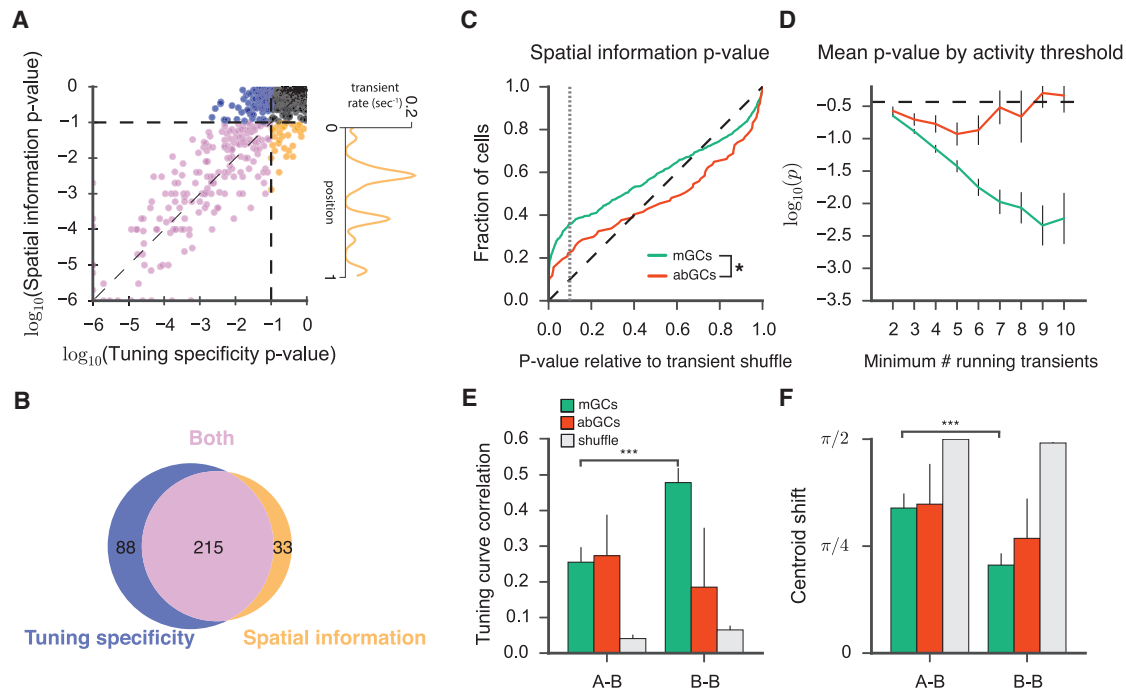


**Figure 4. Spatial Information in abGCs**

(A) For each cell firing at least four running-related transients, we calculated the spatial information p value and tuning specificity p value by shuffling the events in time and repeatedly recalculating either corresponding metric. Values are highly correlated on a log scale ( $r = 0.91$ , Pearson's R). Cells are colored according to whether they met the tuning specificity p value inclusion criterion only (blue), the spatial information p value criterion only (gold), both (purple), and neither (black). Right panel: the tuning profile of a cell meeting the spatial information, but not the tuning specificity, criteria is shown.

(B) Venn diagram demonstrates overlap in populations meeting the two inclusion criteria ( $p < 0.10$ ).

(C) Cumulative distributions of spatial information p values. The p value distributions for mGCs and abGCs differed significantly from each other (KS test, KS Stat = 0.17,  $p < 0.05$ ) and from the uniform distribution (diagonal dashed line) expected in the case of a nonspatially tuned population (KS test; mGCs: KS Stat = 0.26,  $p < 0.001$ ; abGCs: KS Stat = 0.146,  $p < 0.05$ ). Gray dashed line indicates  $p = 0.1$ .

(D) Mean logarithm of the p value for mGCs and abGCs with differing inclusion thresholds for the number of running-related calcium transients. A similar relationship is seen as described in Figure 2E.

(E and F) Contextual discrimination analysis with inclusion criteria based on spatial information p value. For mGCs (A-B,  $n = 100$ ; B-B,  $n = 106$ ) the tuning curve correlation (E; Mann-Whitney U,  $U_{(204)} = 3,597$ ,  $p < 0.001$ ) and centroid shift (F; Mann-Whitney U,  $U_{(204)} = 3,798$ ,  $p < 0.001$ ) were both significantly more similar in the B-B condition than in A-B. This relationship was not observed (Mann-Whitney U; E;  $U_{(14)} = 26.0$ ,  $p = 0.45$ ; F;  $U_{(14)} = 23.0$ ,  $p = 0.32$ ) in the few abGCs (A-B,  $n = 11$ ; B-B,  $n = 5$ ) meeting the spatial information inclusion criterion.

Error bars are mean  $\pm$  SEM.

NestinCreER<sup>T2</sup> mouse line with conditional Arch-eGFP mice (Madisen et al., 2012) (*Nestin<sup>Arch</sup>*; Figure 6A). *Nestin<sup>Arch</sup>* mice given TMX in adulthood expressed the transgene in ~80%–90% of abGCs in the DG (Figure S6). Targeted fiber optic implantation allowed local light delivery and thus control of 6-week-old and younger DG abGCs expressing Arch during behavior (Figure 6A). To examine effects on context encoding, mice received local illumination of the dorsal DG as they explored a conditioning context before receiving a single foot shock; they were then exposed to this same context 24 hr later in the absence of light. *Nestin<sup>Arch</sup>* mice froze significantly less than control mice, indicating that activity in abGCs was required for effective contextual encoding (Figure 6B). Optical stimulation of abGCs impaired conditioning, presumably by disrupting the circuit (Figure S6). Optical modulation of abGCs did not impact shock reactivity, anxiety-related behavior, or general locomotor activity (Table S1).

We next tested whether transient inhibition of abGCs impacts behavioral pattern separation, the ability to discriminate between similar contexts, which has been proposed to require abGCs (Clelland et al., 2009; Kheirbek et al., 2012a; Nakashiba et al., 2012; Sahay et al., 2011a). We suppressed abGC activity either during exposure to the conditioning context A or to the similar, nonconditioned context B (Figures 6C and 6D). While silencing abGCs during exposure to the conditioning context did not impair the development of a discriminatory response (Figure 6C), silencing these cells during exposure to the similar context resulted in impaired discrimination (Figure 6D), indicating that activity of the abGCs is required for behavioral pattern separation specifically during exposure to the ambiguous context. *Nestin<sup>Arch</sup>* mice could discriminate between very distinct contexts and between similar contexts when silencing was performed after the mice had already learned to discriminate (Figure S6). Together, these data extend our understanding of the role played by abGCs during pattern separation on a behavioral level.

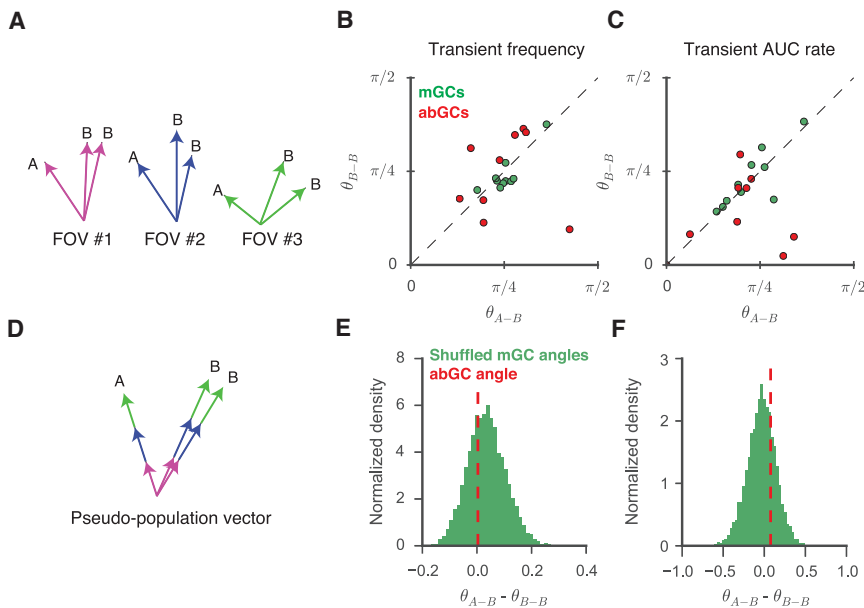


**Figure 5. Mean Activity in GCs Does Not Code for Context**

(A) Schematic of population vector analysis. Activity-based vectors were defined for each experiment, and angles were measured between sequential exposures to the same ( $\theta_{B-B}$ ) or similar ( $\theta_{A-B}$ ) contexts.

(B and C) Scatter of population vector angles across the two conditions in which vector components are defined as transient frequency (B) or rate of transient AUC (area under the curve of significant  $\text{Ca}^{2+}$  transients divided by the total time) (C). Each point corresponds to mature (green) or newborn (red) cells from one FOV. For neither abGC (B; paired t test,  $T_{(16)} = 0.04$ ,  $p = 0.97$ ; C;  $T_{(16)} = 1.25$ ,  $p = 0.25$ ) nor mGC (B;  $T_{(18)} = 1.53$ ,  $p = 0.16$ ; C;  $T_{(18)} = -0.32$ ,  $p = 0.76$ ) populations were the vectors more similar for sequential exposures to the same context than for sequential exposures to different contexts.

(D) For each contextual exposure, we calculated a single pseudopopulation vector by concatenating the newborn population vectors from all FOVs. Schematic is drawn to illustrate the case of activity-based discrimination.

(E and F) Lack of evidence for activity-based discrimination ( $\theta_{A-B} - \theta_{B-B}$ ) for either transient frequency (E) and transient AUC rate (F). The dotted red line indicates the difference in the angles between the abGC pseudopopulation vectors. The difference was consistent with the distribution (green histogram) of such differences attained by repeatedly randomly downsampling similarly constructed pseudopopulations of mature cells (E, percentile = 34; F, percentile = 73; see Experimental Procedures).

## DISCUSSION

The results presented herein expand our understanding of the contribution of abGCs to the function of the DG. We found that activity was sparse in both the mGC and abGC populations, consistent with *in vivo* extracellular electrophysiological studies and intracellular recordings (Alme et al., 2010; Leutgeb et al., 2007; Pernia-Andrade and Jonas, 2014; Schmidt-Hieber et al., 2014). By monitoring for the first time *in vivo* the activity of this population of cells while mice explored multisensory contexts, we reveal that GCs 6 weeks and younger fire at a higher rate *in vivo* than the mature population, complementing recent findings showing that young GCs are more excitable *in vitro* preparations (Marín-Burgin et al., 2012). In the absence of combined electrophysiological recordings, we cannot eliminate the possibility that transient differences in  $\text{Ca}^{2+}$  buffering might affect our activity estimates (Brandt et al., 2003), though we detected no consistent differences in the amplitude or duration of detected somatic  $\text{Ca}^{2+}$  transients (see also Marín-Burgin et al., 2012) at the FOV or individual mouse level.

We further found that abGCs were less spatially tuned than mGCs. The lower tuning specificity we observed could either be attributable to less stable spatial firing patterns or to the presence of stable but multi-peaked tuning profiles, as might be expected from recent electrophysiological recordings describing broader, multi-peaked tuning profiles at the hilar-GCL border, where most abGCs reside (Alme et al., 2010; Neunuebel and Knierim, 2012). In addition to a lower tuning specificity, however, we found that abGCs fire with relatively less spatial information. Although our behavioral paradigm did not allow for the systematic study of time coding (Kraus et al., 2013; MacDonald et al.,

2011) in the GC population, we did not find that GC activity was related to other dimensions of the task, such as reward or velocity (Kropff et al., 2015).

Our results also suggested the existence of a relationship between activity and tuning in abGCs, in which the highly active abGCs are less spatially tuned. These results may be related to the maturational heterogeneity of the labeled cells and are consistent with a model in which young abGCs are initially more active and less spatially tuned but within 6 weeks become more similar to the less active and more spatially tuned mature cells. It is important to note that the *Nestin<sup>tdTomato</sup>* labeling system does not provide an exact birthdate of the recorded neurons but rather results in the cumulative labeling of abGCs 6 weeks and younger. Consequently, we are unable to unequivocally distinguish abGCs between 0 and 6 weeks in our recordings. The recorded abGCs exhibited strong state-dependent modulation (Figure S2C), presumably driven by their glutamatergic innervation and local integration into the DG circuit. As both of these developmental events have been demonstrated to occur after approximately 3 weeks of development (Espósito et al., 2005; Ge et al., 2006, 2007; Toni et al., 2007), this suggests that our functional characterization was based predominantly on cells in the 3–6 week age range. Future studies incorporating the imaging techniques described here with retroviral approaches for labeling age-matched cohorts of abGCs will allow for a more detailed determination of the developmental timeline of abGC properties *in vivo*. Such future studies will allow us to track (in the 3–6 week range) the transition from an immature to a mature functional phenotype.

Our *in vivo* imaging data suggest that the small population of spatially tuned abGCs differentiated novel contexts on the basis

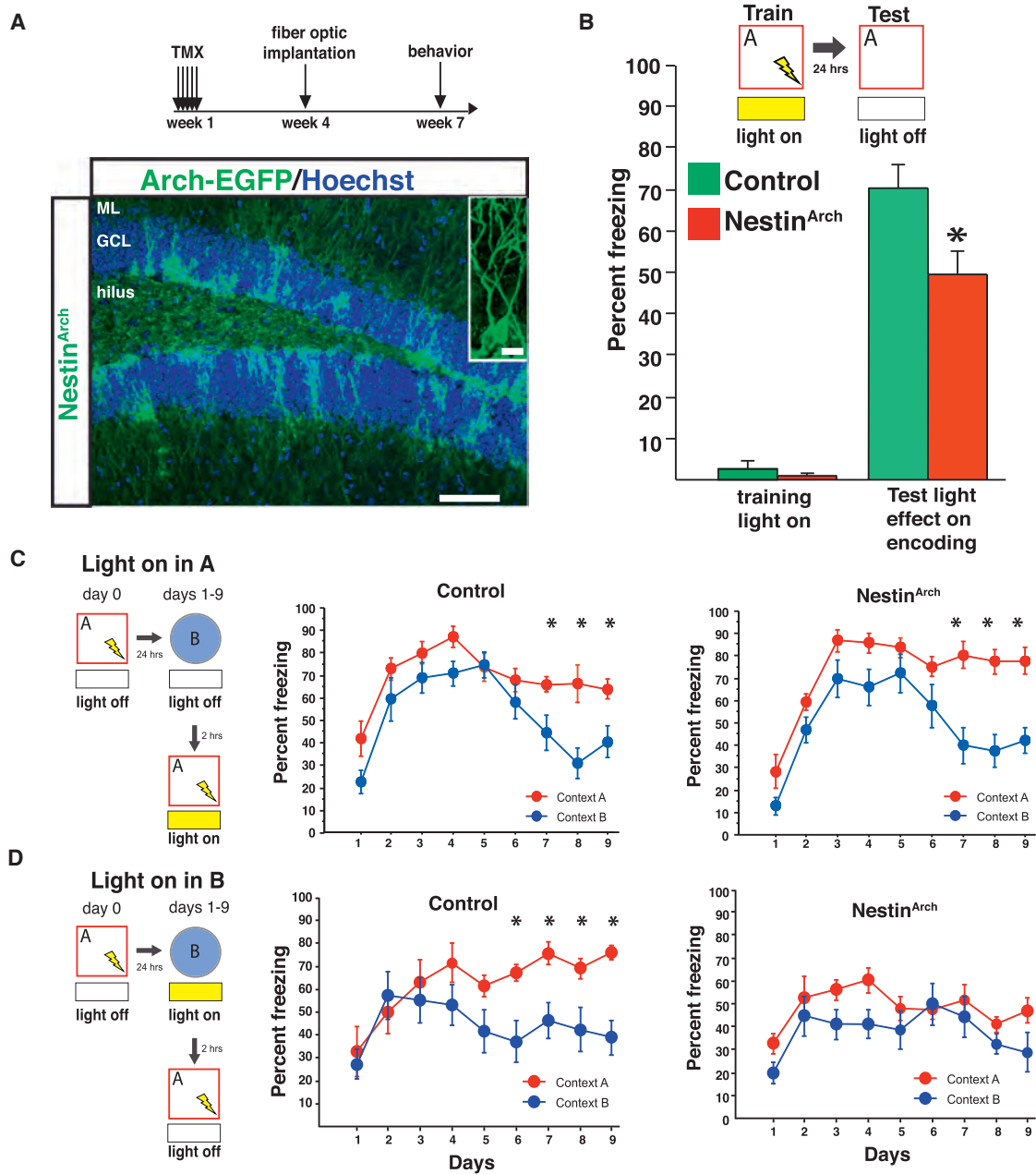


**Figure 6. abGCs Participate in Memory Encoding and Discrimination**

(A) Experimental design. Right: expression of Arch in abGCs (Scale bar, 100  $\mu$ m; inset, 10  $\mu$ m).

(B) Yellow-light inhibition of dorsal abGCs during training impaired encoding of contextual fear ( $n = 8$  control, 9 Nestin<sup>Arch</sup>; group effect  $F_{(1,15)} = 6.3$ ,  $p = 0.02$ ; group $\times$ training interaction  $F_{(1,15)} = 5.4$ ,  $p = 0.03$ ; on test day  $t_{15} = -2.5$ ,  $p = 0.02$ ).

(C and D) Acute inhibition of abGCs impairs behavioral pattern separation. (C) Mice discriminated when abGCs were inhibited in the conditioning context ( $n = 7$  control, 8 Nestin<sup>Arch</sup>; group $\times$ day $\times$ context interaction  $F_{(8,208)} = 0.581$ ,  $p = 0.79$ . Control: context effect  $F_{(1,12)} = 7.243$ ,  $p = 0.02$ ; day $\times$ context interaction  $F_{(8,96)} = 2.094$ ,  $p = 0.0436$ . Nestin<sup>Arch</sup>: context effect  $F_{(1,14)} = 10.631$ ,  $p = 0.006$ ; day $\times$ context effect  $F_{(8,112)} = 3.706$ ,  $p = 0.007$ ). (D) Mice did not discriminate when abGCs were inhibited in the unconditioned context ( $n = 8$  control, 7 Nestin<sup>Arch</sup>; group $\times$ day $\times$ context interaction  $F_{(8,208)} = 1.9$ ,  $p = 0.04$ . Control: context effect  $F_{(1,13)} = 4.8$ ,  $p = 0.04$ ; day $\times$ context interaction  $F_{(8,104)} = 3.1$ ,  $p = 0.004$ . Nestin<sup>Arch</sup>: context effect  $F_{(1,12)} = 4.1$ ,  $p = 0.06$ ; day $\times$ context effect  $F_{(8,96)} = 0.6$ ,  $p = 0.74$ ). Error bars are mean  $\pm$  SEM.

of their spatial tuning to a similar and possibly weaker degree than mGCs, depending on the metric and inclusion criteria applied. This, combined with the fact that we observed so few

well-tuned abGCs in spite of our large number of recordings, suggests that the unique role of abGCs in contextual discrimination behaviors may not be attributable to the spatial distribution

of their firing or the remapping of their fields. The broader tuning profile of abGCs (compared to mGCs) is consistent with computational models of GC dynamics and might support the encoding of novel features in the environment (Aimone et al., 2011; Temprana et al., 2015). This would also be consistent with our finding that silencing these neurons during exposure to the novel context (but not the familiar one) prevents contextual discrimination learning. Alternatively, the abGC population may modulate local excitatory/inhibitory tone in the DG and CA3 (Gu et al., 2012; Restivo et al., 2015; Toni et al., 2008) and could consequently shape spatial and contextual representations. There is indeed evidence from ablation studies that abGCs may modulate the activity of mGCs, possibly via their influence on the DG microcircuit (Burghardt et al., 2012; Drew et al., 2015; Ikrar et al., 2013; Lacefield et al., 2012; Park et al., 2015). Future studies should test this hypothesis directly by using the methods described here to assess changes in mGC spatial and contextual representations following inhibition of abGCs.

In addition, we find that transient inhibition of abGCs impairs behavior, specifically contextual encoding and discrimination, consistent with a proposed role in behavioral pattern separation (Clelland et al., 2009; Kheirbek et al., 2012a, 2012b; Nakashiba et al., 2012; Sahay et al., 2011a). These studies complement recent optogenetic studies describing a role for DG GCs in memory processes (Denny et al., 2014; Gu et al., 2012; Kheirbek et al., 2013). Furthermore, we demonstrate that in a pattern separation task, activity of the abGCs is required during exposure to the novel ambiguous context, but not during exposure to the conditioning context. This is likely due to a deficit in contextual encoding, due to an inability in *Nestin<sup>Arch</sup>* mice to encode context B as the safe context. This is in agreement with our results in one-trial contextual fear conditioning, where silencing abGCs during the first exposure to context A impaired the ability to encode this context. In the pattern separation experiment, when abGC silencing takes place in context A, freezing keeps increasing because learning is reinforced each day by a foot shock. In contrast, when silencing takes place in context B, freezing decreases in both contexts. This suggests that in these conditions, mice were confused when exposed to both contexts A and B and could no longer encode them as safe or fearful nor discriminate between them.

It is important to note that in this study, the behavior measured during optical inhibition of abGCs in contextual fear discrimination tasks differed from that in the head-fixed preparation during imaging. It was not possible for us to perform our behavioral and imaging experiments in identical conditions, as animals are known to freeze in response to an unconditioned stimulus in our head-fixed paradigm, and thus we cannot measure spatial tuning and remapping in a fear-conditioned animal. Future experiments combining freely moving *in vivo* imaging designs (Ziv et al., 2013) with behavioral pattern separation tasks will allow for analysis of changes in abGC response profiles to novel or conditioned contexts.

Our experimental preparation required a partial lesion of ipsilateral area CA1 in order to obtain high-resolution optical access to the DG. While DG-mediated behavior was normal in the experimental animals (Figures S1D and S1E), we cannot rule out the possibility that chronic circuit reorganization or the implementa-

tion of an alternate circuit strategy might occur in this preparation. Although the implant did not impact overall levels of neurogenesis, or the morphological features of recorded abGCs, we cannot exclude the possibility that the properties of abGCs and mGCs may be differentially affected by the surgical preparation, due, for example, to the potential disruption of grid cell activity in the medial entorhinal cortex (Bonnievie et al., 2013). In the future, less-invasive techniques should complement the results of this study.

Our data not only demonstrate the importance of abGCs for encoding and disambiguating contextual information but also provide insights into the circuit dynamics underlying these processes. Impairments in pattern separation have been proposed to contribute to the excessive generalization of memory often seen in anxiety and depression as well as in age-related disorders such as mild cognitive impairment (Kheirbek et al., 2012a; Leal et al., 2014; Yassa et al., 2011). A mechanistic understanding of how abGCs contribute to hippocampus-dependent memory processing will provide insights not only into the normal function of adult hippocampal neurogenesis but also into the therapeutic potential of this unique form of plasticity.

## EXPERIMENTAL PROCEDURES

Full details of the experimental procedures are provided in the Supplemental Information.

### Mice, Viruses, and Stereotactic Surgery

All experiments were conducted in accordance with the U.S. NIH guidelines and with the approval of the Columbia University and New York State Psychiatric Institute Institutional Animal Care and Use Committees. Male *Ai9*, *Ai35*, *Nestin-CreERT<sup>2</sup>*, and controls were generated as previously described (Dranovsky et al., 2011; Madisen et al., 2010, 2012). For imaging experiments, recombinant adeno-associated viruses carrying the GCaMP6f gene were obtained from the Penn Vector Core (AAV1.Syn.GCaMP6f.WPRE.SV40) with titer of  $2\text{--}4 \times 10^{13}$ . The dorsal DG of male mice (8 weeks of age) was stereotactically injected at  $-1.5$  mm AP;  $-2.3$  mm ML; and  $-1.8$ ,  $-1.65$ ,  $-1.5$  mm DV relative to the cortical surface. Mice were then surgically implanted with an imaging window over the left dorsal DG and implanted with a stainless-steel headpost for head fixation during imaging experiments (see Supplemental Information). For optogenetic experiments, male mice (8 weeks of age) were surgically implanted with fiber optics targeted to the dorsal DG ( $\pm 1$  mm ML,  $-1.5$  mm AP,  $-1.7$  mm DV) using published protocols (Kheirbek et al., 2013).

### In Vivo Two-Photon Imaging

We used the same imaging system as described previously (Kaifosh et al., 2013; Lovett-Barron et al., 2014), with the addition of an 8 kHz resonant galvanometer (Bruker). All images were acquired with a Nikon 40 $\times$  NIR water-immersion objective (0.8 NA, 3.5 mm WD) in distilled water. We continuously acquired red (tdTomato) and green (GCaMP6f) channels separated by an emission cube set (green, HQ525/70 m-2p; red, HQ607/45 m-2p; 575dxcx, Chroma Technology) at 1024  $\times$  1024 pixels covering 300  $\mu\text{m}$   $\times$  300  $\mu\text{m}$  at 15 Hz with photomultiplier tubes (green GCaMP fluorescence, GaAsP PMT, Hamamatsu Model 7422P-40; red tdTomato fluorescence, multialkali PMT, Hamamatsu R3896). A custom dual stage preamp ( $1.4 \times 10^5$  dB, Bruker) was used to amplify signals prior to digitization.

For training, mice were water restricted (>90% predeprivation weight) and trained to run on a cue-deplete burlap treadmill belt for water reward over the course of 1–2 weeks. We applied a progressively restrictive water reward schedule, with mice initially receiving 40 randomly placed rewards per lap and ultimately receiving 3 randomly placed rewards per lap. Mice were habituated to the optical instrumentation, then trained for 20 min daily until they regularly ran at least one lap per minute. For contexts, similar to our previous work, each

context (1 and 2) consisted of the same treadmill belt (the same sequence of three joined fabric ribbons) but was distinct in its visual, auditory, tactile, and olfactory stimuli (Figure 4A) (Lovett-Barron et al., 2014). During imaging sessions, mice received three randomly placed water rewards per lap, with reward positions changing randomly each lap. To allow for comparison of GC activity between similar contexts, the same three fabrics were used in the same order, but the locations of all of the tactile cues were shuffled between the two belts.

### Imaging Analysis

#### Processing of $Ca^{2+}$ Fluorescence Data

All imaging data were analyzed using the SIMA software package (Kaifosh et al., 2014). Motion correction was performed using a 2D Hidden Markov Model (Dombeck et al., 2007; Kaifosh et al., 2013), with modifications to accommodate the specific features of data acquired with resonant galvanometers. Only the green GCaMP channel was used for estimating motion artifacts. In cases where motion artifacts were not adequately corrected, the affected data were discarded from further analysis. The especially sparse activity of dentate GCs prevented the successful application of activity-based segmentation methods. Therefore, we used the SIMA project's ROI Buddy graphical user interface (Kaifosh et al., 2014) to draw regions of interest (ROIs) over GC somata visible in the time-averaged image of the motion-corrected green/GCaMP6f channel. We also used this software to determine the correspondence of ROIs across datasets from different trials in which the same FOV was imaged. To prevent the introduction of any bias, the red tdTomato channel was not viewed when drawing ROIs but only referenced after all ROIs had been drawn in order to tag ROIs over tdTomato-expressing cells as newborn GCs.

Dynamic GCaMP6f fluorescence signals were extracted from ROIs using SIMA according to the previously described formulation (Kaifosh et al., 2014). We then computed the relative fluorescence changes ( $\Delta F/F$ ) (as described in Jia et al., 2011), with uniform smoothing window  $t_1 = 3$  s and baseline size  $t_2 = 60$  s. We detected statistically significant calcium transients as described previously (Dombeck et al., 2007; Lovett-Barron et al., 2014). In order to improve our sensitivity, we then recalculated the baseline of the raw signal after masking frames identified previously as occurring during a significant transient.  $\Delta F/F$  was then recalculated and transients re-estimated. Transients less than 1 s were removed to reduce false positives. This iterative procedure was repeated three times and effectively removed the transient contamination from the calculated baseline.

#### Spatial Tuning Vector and Tuning Specificity $p$ Value Analysis

When evaluating the spatial tuning of GCs, we restricted our analysis to running-related epochs, defined as consecutive frames of forward locomotion (defined as an imaging frame in which at least one forward pair of beam breaks occurred) at least 1 s in duration and with a minimum peak speed of 5 cm/sec. Consecutive epochs separated by  $<0.5$  s were merged. Running-related transients were defined as those that were initiated during a running-related epoch. Transient start was defined as the first imaging frame with mean fluorescence  $\geq 2\sigma$ , with  $\sigma$  equal to the SD of the baseline frames. Offset was defined as the first frame with mean fluorescence  $\leq 0.5\sigma$  (Dombeck et al., 2007). The spatial tuning vector was calculated as  $\sum_{j=1}^N \frac{e^{\theta_j}}{\sum_{j=1}^N e^{\theta_j}}$ , where  $\theta_j$  is the position of the mouse at the onset time of the  $j^{\text{th}}$  running-related transient, and  $e^{\theta_j}$  is the fraction of running frames acquired at position  $\theta_j$ . Only the animal's position at the time of transient onset was used for constructing the tuning vector and rate maps (see Remapping Analysis section below), as the calcium decay kinetics are intrinsic to the GCaMP6f indicator and are not sensitive to the animal's running speed (a similar onset-based approach was implemented previously by Ziv et al., 2013). In order to assess the significance of the spatial selectivity, for each cell we generated a null tuning distribution by shuffling the transient onset times (restricted to running frames) and repeatedly recomputing the tuning specificity. This process was repeated 100,000 times, and the  $p$  value was defined as the fraction of this distribution that exceeded the GC's tuning specificity.

#### Spatial Information $p$ Value Analysis

For each cell we first computed the spatial information content (Skaggs et al., 1993) as  $I_N = \sum_{i=1}^N \lambda_i \ln \frac{\lambda_i}{p_i}$ , where  $\lambda_i$  and  $p_i$  are the transient rate and fraction of time spent in the  $i^{\text{th}}$  bin,  $\lambda$  is the overall firing rate, and  $N$  is the number of bins.

We computed  $I_N$  for multiple values of  $N=2, 4, 5, 8, 10, 20, 25$ , and 100. We then created 100,000 random reassignments of the transient onset times within the running-related epochs and recomputed the values of  $I_N^s$ , where  $s$  is the index of the shuffle. To roughly correct for biases in the calculation of mutual information, we then subtracted the mean of this null distribution from all estimates to obtain values  $\hat{I}_N = I_N - \frac{1}{100,000} \sum_{s=1}^{100,000} I_N^s$ . Finally, we computed a single estimate of the information content for the true transient onset times,  $\hat{I} = \max_N \hat{I}_N$ , and for the shuffles,  $\hat{I}_s = \max_N I_N^s$ . The spatial tuning  $p$  value was taken as the fraction of values of  $s$  for which  $\hat{I}$  exceeded  $\hat{I}_s$ .

#### Remapping Analysis

Rate maps were formed by dividing the number of transients starting in each bin by the occupancy of that bin. We calculated rate maps with 100 position bins and smoothed with a Gaussian kernel ( $\sigma = 3$  bins). The tuning curve correlation for each cell was defined as the Pearson correlation coefficient between tuning curves for a cell in the two sequential context exposures. The centroid shift for each cell was defined as the angle (in radians) between the tuning directions calculated for the two context exposures. For both metrics, the shuffle distributions were calculated by estimating the tuning curve correlations or tuning shifts when cells were paired by a subsampled Cartesian product of cell identities (1,000 pairs per shuffle).

#### Behavioral Testing

In Arch experiments, the patch cables were interfaced to an FC/PC rotary joint (Doric lenses), which was attached on the other end to a 593.5 nm laser diode that was controlled by a Master-8 stimulator (AMPI). Fear conditioning took place in Coulbourn Instruments fear conditioning boxes. See Supplemental Information for full details of behavioral procedures.

#### Statistics

For all optogenetic behavioral data, data were analyzed using ANOVA with repeated measurements where appropriate. All tests are described in the appropriate figure legends. Group numbers were based on previous optogenetic and two-photon imaging experiments (Kheirbek et al., 2013; Lovett-Barron et al., 2014). For imaging data, for all normally distributed data, a Welch's two-sample  $t$  test was used for comparison of means with  $n - 1$  degrees of freedom. The Mann-Whitney  $U$  test was used for comparison of means in non-normally distributed data with  $n - 1$  degrees of freedom. A paired student's  $t$  test was used for comparison of means in paired data with  $n - 1$  degrees of freedom. The one-sided Kolmogorov-Smirnov (KS) test was used for testing the hypothesis that a distribution was drawn from an underlying theoretical distribution with  $n - 1$  degrees of freedom (uniformity in the case of Figure 2E). The two-sided two-sample KS test with  $n - 1$  degrees of freedom was used for testing the null hypothesis that two empirical distributions were drawn from the same continuous underlying distribution.

#### SUPPLEMENTAL INFORMATION

Supplemental Information includes Supplemental Experimental Procedures, six figures, one table, and one movie and can be found with this article online at <http://dx.doi.org/10.1016/j.neuron.2016.02.019>.

#### AUTHOR CONTRIBUTIONS

N.B.D., R.H., A.L., and M.A.K. conceived the project, designed the experiments, and wrote the manuscript. N.B.D., P.K., J.D.Z., A.L., and M.A.K. performed experiments and analyzed data. M.L.-B., J.T., C.A.D., E.M.B., A.R.G., and L.J.D. assisted with experiments and provided essential reagents, expertise, and input to the manuscript.

#### ACKNOWLEDGMENTS

We thank L. Looger, S. Fusi, and A. Fenton for discussion and comments; H. Zeng for Ai32 and Ai35 mice; and the GENIE Program at the Janelia Farm Research Campus for GCaMP6f. N.B.D. is supported by NINDS F30NS090819. P.K. is a Howard Hughes Medical Institute International Pre-doctoral Fellow. M.L.-B. was supported by a Canadian Natural Sciences

and Engineering Research Council postgraduate scholarship. A.L. is supported by NIMH 1R01MH100631, 1U01NS090583, 1R01NS094668, the Searle Scholars Program, the Human Frontier Science Program, and the McKnight Memory and Cognitive Disorders Award. R.H. is supported by NIH R37 MH068542, NIA R01 AG043688, New York State Stem Cell Science (NYSTEM), and the Hope for Depression Research Foundation. M.A.K. was supported by NIMH K01MH099371, NARSAD, and NYSTEM.

Received: December 4, 2015

Revised: January 29, 2016

Accepted: February 10, 2016

Published: March 10, 2016

## REFERENCES

- Aimone, J.B., Deng, W., and Gage, F.H. (2011). Resolving new memories: a critical look at the dentate gyrus, adult neurogenesis, and pattern separation. *Neuron* 70, 589–596.
- Alme, C.B., Buzzetti, R.A., Marrone, D.F., Leutgeb, J.K., Chawla, M.K., Schaner, M.J., Bohanick, J.D., Khoboko, T., Leutgeb, S., Moser, E.I., et al. (2010). Hippocampal granule cells opt for early retirement. *Hippocampus* 20, 1109–1123.
- Bonnevie, T., Dunn, B., Fyhn, M., Hafting, T., Derdikman, D., Kubie, J.L., Roudi, Y., Moser, E.I., and Moser, M.B. (2013). Grid cells require excitatory drive from the hippocampus. *Nat. Neurosci.* 16, 309–317.
- Brandt, M.D., Jessberger, S., Steiner, B., Kronenberg, G., Reuter, K., Bick-Sander, A., von der Behrens, W., and Kempermann, G. (2003). Transient calretinin expression defines early postmitotic step of neuronal differentiation in adult hippocampal neurogenesis of mice. *Mol. Cell. Neurosci.* 24, 603–613.
- Burghardt, N.S., Park, E.H., Hen, R., and Fenton, A.A. (2012). Adult-born hippocampal neurons promote cognitive flexibility in mice. *Hippocampus* 22, 1795–1808.
- Clelland, C.D., Choi, M., Romberg, C., Clemenson, G.D., Jr., Fragniere, A., Tyers, P., Jessberger, S., Saksida, L.M., Barker, R.A., Gage, F.H., and Bussey, T.J. (2009). A functional role for adult hippocampal neurogenesis in spatial pattern separation. *Science* 325, 210–213.
- David, D.J., Samuels, B.A., Rainer, Q., Wang, J.W., Marsteller, D., Mendez, I., Drew, M., Craig, D.A., Guiard, B.P., Guilloux, J.P., et al. (2009). Neurogenesis-dependent and -independent effects of fluoxetine in an animal model of anxiety/depression. *Neuron* 62, 479–493.
- Denny, C.A., Burghardt, N.S., Schachter, D.M., Hen, R., and Drew, M.R. (2012). 4- to 6-week-old adult-born hippocampal neurons influence novelty-evoked exploration and contextual fear conditioning. *Hippocampus* 22, 1188–1201.
- Denny, C.A., Kheirbek, M.A., Alba, E.L., Tanaka, K.F., Brachman, R.A., Laughman, K.B., Tomm, N.K., Turi, G.F., Losonczy, A., and Hen, R. (2014). Hippocampal memory traces are differentially modulated by experience, time, and adult neurogenesis. *Neuron* 83, 189–201.
- Dieni, C.V., Nietz, A.K., Panichi, R., Wadiche, J.I., and Overstreet-Wadiche, L. (2013). Distinct determinants of sparse activation during granule cell maturation. *J. Neurosci.* 33, 19131–19142.
- Dombeck, D.A., Khabbaz, A.N., Collman, F., Adelman, T.L., and Tank, D.W. (2007). Imaging large-scale neural activity with cellular resolution in awake, mobile mice. *Neuron* 56, 43–57.
- Dranovsky, A., Picchini, A.M., Moadel, T., Sisti, A.C., Yamada, A., Kimura, S., Leonardo, E.D., and Hen, R. (2011). Experience dictates stem cell fate in the adult hippocampus. *Neuron* 70, 908–923.
- Drew, L.J., Fusi, S., and Hen, R. (2013). Adult neurogenesis in the mammalian hippocampus: why the dentate gyrus? *Learn. Mem.* 20, 710–729.
- Drew, L.J., Kheirbek, M.A., Luna, V.M., Denny, C.A., Cloidt, M.A., Wu, M.V., Jain, S., Scharfman, H.E., and Hen, R. (2015). Activation of local inhibitory circuits in the dentate gyrus by adult-born neurons. *Hippocampus*. Published online December 14, 2015. <http://dx.doi.org/10.1002/hipo.22557>.
- Espósito, M.S., Piatti, V.C., Laplagne, D.A., Morgenstern, N.A., Ferrari, C.C., Pitossi, F.J., and Schinder, A.F. (2005). Neuronal differentiation in the adult hippocampus recapitulates embryonic development. *J. Neurosci.* 25, 10074–10086.
- Ge, S., Goh, E.L., Sailor, K.A., Kitabatake, Y., Ming, G.L., and Song, H. (2006). GABA regulates synaptic integration of newly generated neurons in the adult brain. *Nature* 439, 589–593.
- Ge, S., Yang, C.H., Hsu, K.S., Ming, G.L., and Song, H. (2007). A critical period for enhanced synaptic plasticity in newly generated neurons of the adult brain. *Neuron* 54, 559–566.
- Gu, Y., Arruda-Carvalho, M., Wang, J., Janoschka, S.R., Josselyn, S.A., Frankland, P.W., and Ge, S. (2012). Optical controlling reveals time-dependent roles for adult-born dentate granule cells. *Nat. Neurosci.* 15, 1700–1706.
- Ikrar, T., Guo, N., He, K., Besnard, A., Levinson, S., Hill, A., Lee, H.K., Hen, R., Xu, X., and Sahay, A. (2013). Adult neurogenesis modifies excitability of the dentate gyrus. *Front. Neural Circuits* 7, 204.
- Imayoshi, I., Sakamoto, M., Ohtsuka, T., Takao, K., Miyakawa, T., Yamaguchi, M., Mori, K., Ikeda, T., Itohara, S., and Kageyama, R. (2008). Roles of continuous neurogenesis in the structural and functional integrity of the adult forebrain. *Nat. Neurosci.* 11, 1153–1161.
- Jia, H., Rochefort, N.L., Chen, X., and Konnerth, A. (2011). In vivo two-photon imaging of sensory-evoked dendritic calcium signals in cortical neurons. *Nat. Protoc.* 6, 28–35.
- Jung, M.W., and McNaughton, B.L. (1993). Spatial selectivity of unit activity in the hippocampal granular layer. *Hippocampus* 3, 165–182.
- Kaifosh, P., Lovett-Barron, M., Turi, G.F., Reardon, T.R., and Losonczy, A. (2013). Septo-hippocampal GABAergic signaling across multiple modalities in awake mice. *Nat. Neurosci.* 16, 1182–1184.
- Kaifosh, P., Zaremba, J.D., Danielson, N.B., and Losonczy, A. (2014). SIMA: Python software for analysis of dynamic fluorescence imaging data. *Front. Neuroinform.* 8, 80.
- Kheirbek, M.A., Klemenhagen, K.C., Sahay, A., and Hen, R. (2012a). Neurogenesis and generalization: a new approach to stratify and treat anxiety disorders. *Nat. Neurosci.* 15, 1613–1620.
- Kheirbek, M.A., Tannenholz, L., and Hen, R. (2012b). NR2B-dependent plasticity of adult-born granule cells is necessary for context discrimination. *J. Neurosci.* 32, 8696–8702.
- Kheirbek, M.A., Drew, L.J., Burghardt, N.S., Costantini, D.O., Tannenholz, L., Ahmari, S.E., Zeng, H., Fenton, A.A., and Hen, R. (2013). Differential control of learning and anxiety along the dorsoventral axis of the dentate gyrus. *Neuron* 77, 955–968.
- Kraus, B.J., Robinson, R.J., 2nd, White, J.A., Eichenbaum, H., and Hasselmo, M.E. (2013). Hippocampal “time cells”: time versus path integration. *Neuron* 78, 1090–1101.
- Kropff, E., Carmichael, J.E., Moser, M.B., and Moser, E.I. (2015). Speed cells in the medial entorhinal cortex. *Nature* 523, 419–424.
- Lacefield, C.O., Itskov, V., Reardon, T., Hen, R., and Gordon, J.A. (2012). Effects of adult-generated granule cells on coordinated network activity in the dentate gyrus. *Hippocampus* 22, 106–116.
- Leal, S.L., Tighe, S.K., Jones, C.K., and Yassa, M.A. (2014). Pattern separation of emotional information in hippocampal dentate and CA3. *Hippocampus* 24, 1146–1155.
- Leutgeb, J.K., Leutgeb, S., Moser, M.B., and Moser, E.I. (2007). Pattern separation in the dentate gyrus and CA3 of the hippocampus. *Science* 315, 961–966.
- Lovett-Barron, M., Kaifosh, P., Kheirbek, M.A., Danielson, N., Zaremba, J.D., Reardon, T.R., Turi, G.F., Hen, R., Zemelman, B.V., and Losonczy, A. (2014). Dendritic inhibition in the hippocampus supports fear learning. *Science* 343, 857–863.
- MacDonald, C.J., Lepage, K.Q., Eden, U.T., and Eichenbaum, H. (2011). Hippocampal “time cells” bridge the gap in memory for discontinuous events. *Neuron* 71, 737–749.

- Madisen, L., Zwingman, T.A., Sunkin, S.M., Oh, S.W., Zariwala, H.A., Gu, H., Ng, L.L., Palmiter, R.D., Hawrylycz, M.J., Jones, A.R., et al. (2010). A robust and high-throughput Cre reporting and characterization system for the whole mouse brain. *Nat. Neurosci.* *13*, 133–140.
- Madisen, L., Mao, T., Koch, H., Zhuo, J.M., Berenyi, A., Fujisawa, S., Hsu, Y.W., Garcia, A.J., 3rd, Gu, X., Zanella, S., et al. (2012). A toolbox of Cre-dependent optogenetic transgenic mice for light-induced activation and silencing. *Nat. Neurosci.* *15*, 793–802.
- Marín-Burgin, A., Mongiat, L.A., Pardi, M.B., and Schinder, A.F. (2012). Unique processing during a period of high excitation/inhibition balance in adult-born neurons. *Science* *335*, 1238–1242.
- Nakashiba, T., Cushman, J.D., Pelkey, K.A., Renaudineau, S., Buhl, D.L., McHugh, T.J., Rodriguez Barrera, V., Chittajallu, R., Iwamoto, K.S., McBain, C.J., et al. (2012). Young dentate granule cells mediate pattern separation, whereas old granule cells facilitate pattern completion. *Cell* *149*, 188–201.
- Neunuebel, J.P., and Knierim, J.J. (2012). Spatial firing correlates of physiologically distinct cell types of the rat dentate gyrus. *J. Neurosci.* *32*, 3848–3858.
- Paninski, L. (2003). Estimation of entropy and mutual information. *Neural Comput.* *15*, 1191–1253.
- Park, E.H., Burghardt, N.S., Dvorak, D., Hen, R., and Fenton, A.A. (2015). Experience-dependent regulation of dentate gyrus excitability by adult-born granule cells. *J. Neurosci.* *35*, 11656–11666.
- Pernía-Andrade, A.J., and Jonas, P. (2014). Theta-gamma-modulated synaptic currents in hippocampal granule cells in vivo define a mechanism for network oscillations. *Neuron* *81*, 140–152.
- Piatti, V.C., Ewell, L.A., and Leutgeb, J.K. (2013). Neurogenesis in the dentate gyrus: carrying the message or dictating the tone. *Front. Neurosci.* *7*, 50.
- Restivo, L., Niibori, Y., Mercaldo, V., Josselyn, S.A., and Frankland, P.W. (2015). Development of adult-generated cell connectivity with excitatory and inhibitory cell populations in the hippocampus. *J. Neurosci.* *35*, 10600–10612.
- Sahay, A., Scobie, K.N., Hill, A.S., O'Carroll, C.M., Kheirbek, M.A., Burghardt, N.S., Fenton, A.A., Dranovsky, A., and Hen, R. (2011a). Increasing adult hippocampal neurogenesis is sufficient to improve pattern separation. *Nature* *472*, 466–470.
- Sahay, A., Wilson, D.A., and Hen, R. (2011b). Pattern separation: a common function for new neurons in hippocampus and olfactory bulb. *Neuron* *70*, 582–588.
- Santarelli, L., Saxe, M., Gross, C., Surget, A., Battaglia, F., Dulawa, S., Weisstaub, N., Lee, J., Duman, R., Arancio, O., et al. (2003). Requirement of hippocampal neurogenesis for the behavioral effects of antidepressants. *Science* *301*, 805–809.
- Schmidt-Hieber, C., Jonas, P., and Bischofberger, J. (2004). Enhanced synaptic plasticity in newly generated granule cells of the adult hippocampus. *Nature* *429*, 184–187.
- Schmidt-Hieber, C., Wei, H., and Hausser, M. (2014). Synaptic mechanisms of sparse activity in hippocampal granule cells during mouse navigation (Society for Neuroscience).
- Singer, B.H., Gamelli, A.E., Fuller, C.L., Temme, S.J., Parent, J.M., and Murphy, G.G. (2011). Compensatory network changes in the dentate gyrus restore long-term potentiation following ablation of neurogenesis in young-adult mice. *Proc. Natl. Acad. Sci. USA* *108*, 5437–5442.
- Skaggs, W.E., McNaughton, B.L., Gothard, K.M., and Markus, E.J. (1993). An information-theoretic approach to deciphering the hippocampal code. In *Advances in Neural Information Processing Systems (NIPS)*, 5, S.J. Hanson, J.D. Cowan, and C.L. Giles, eds, pp. 1030–1037.
- Snyder, J.S., Soumier, A., Brewer, M., Pickel, J., and Cameron, H.A. (2011). Adult hippocampal neurogenesis buffers stress responses and depressive behaviour. *Nature* *476*, 458–461.
- Spalding, K.L., Bergmann, O., Alkass, K., Bernard, S., Salehpour, M., Huttner, H.B., Boström, E., Westerlund, I., Vial, C., Buchholz, B.A., et al. (2013). Dynamics of hippocampal neurogenesis in adult humans. *Cell* *153*, 1219–1227.
- Stone, S.S., Teixeira, C.M., Zaslavsky, K., Wheeler, A.L., Martinez-Canabal, A., Wang, A.H., Sakaguchi, M., Lozano, A.M., and Frankland, P.W. (2011). Functional convergence of developmentally and adult-generated granule cells in dentate gyrus circuits supporting hippocampus-dependent memory. *Hippocampus* *21*, 1348–1362.
- Temprana, S.G., Mongiat, L.A., Yang, S.M., Trinchero, M.F., Alvarez, D.D., Kropff, E., Giacomini, D., Beltramone, N., Lanuza, G.M., and Schinder, A.F. (2015). Delayed coupling to feedback inhibition during a critical period for the integration of adult-born granule cells. *Neuron* *85*, 116–130.
- Toni, N., Teng, E.M., Bushong, E.A., Aimone, J.B., Zhao, C., Consiglio, A., van Praag, H., Martone, M.E., Ellisman, M.H., and Gage, F.H. (2007). Synapse formation on neurons born in the adult hippocampus. *Nat. Neurosci.* *10*, 727–734.
- Toni, N., Laplagne, D.A., Zhao, C., Lombardi, G., Ribak, C.E., Gage, F.H., and Schinder, A.F. (2008). Neurons born in the adult dentate gyrus form functional synapses with target cells. *Nat. Neurosci.* *11*, 901–907.
- van Praag, H., Schinder, A.F., Christie, B.R., Toni, N., Palmer, T.D., and Gage, F.H. (2002). Functional neurogenesis in the adult hippocampus. *Nature* *415*, 1030–1034.
- Yassa, M.A., Mattfeld, A.T., Stark, S.M., and Stark, C.E. (2011). Age-related memory deficits linked to circuit-specific disruptions in the hippocampus. *Proc. Natl. Acad. Sci. USA* *108*, 8873–8878.
- Zhao, C., Deng, W., and Gage, F.H. (2008). Mechanisms and functional implications of adult neurogenesis. *Cell* *132*, 645–660.
- Ziv, Y., Burns, L.D., Cocker, E.D., Hamel, E.O., Ghosh, K.K., Kitch, L.J., El Gamal, A., and Schnitzer, M.J. (2013). Long-term dynamics of CA1 hippocampal place codes. *Nat. Neurosci.* *16*, 264–266.

# Congenital Nystagmus Gene FRMD7 Is Necessary for Establishing a Neuronal Circuit Asymmetry for Direction Selectivity

Keisuke Yonehara,<sup>1,9,10</sup> Michele Fiscella,<sup>2,10</sup> Antonia Drinnenberg,<sup>1,3,10</sup> Federico Esposti,<sup>1</sup> Stuart Trenholm,<sup>1</sup> Jacek Krol,<sup>1</sup> Felix Franke,<sup>2</sup> Brigitte Gross Scherf,<sup>1</sup> Akos Kusnyerik,<sup>4</sup> Jan Müller,<sup>2</sup> Arnold Szabo,<sup>5</sup> Josephine Jüttner,<sup>1</sup> Francisco Cordoba,<sup>6</sup> Ashrithpal Police Reddy,<sup>1</sup> János Németh,<sup>4</sup> Zoltán Zsolt Nagy,<sup>4</sup> Francis Munier,<sup>7</sup> Andreas Hierlemann,<sup>2</sup> and Botond Roska<sup>1,8,\*</sup>

<sup>1</sup>Neural Circuit Laboratories, Friedrich Miescher Institute for Biomedical Research, Maulbeerstrasse 66, 4058 Basel, Switzerland

<sup>2</sup>Bio Engineering Laboratory, Department of Biosystems Science and Engineering of ETH Zurich, Mattenstrasse 26, 4058 Basel, Switzerland

<sup>3</sup>University of Basel, Petersplatz 1, 4003 Basel, Switzerland

<sup>4</sup>Department of Ophthalmology, Semmelweis University, Mária u. 39, 1085 Budapest, Hungary

<sup>5</sup>Department of Human Morphology and Developmental Biology, Faculty of Medicine, Semmelweis University, Tűzoltó u. 58, 1094 Budapest, Hungary

<sup>6</sup>Laboratory and Animal Services, Novartis Institute for Biomedical Research, Fabrikstrasse 28, 4056 Basel, Switzerland

<sup>7</sup>Jules-Gonin Eye Hospital, Avenue de France 15, 1000 Lausanne, Switzerland

<sup>8</sup>Department of Ophthalmology, University of Basel, Mittlere Strasse 91, 4031 Basel, Switzerland

<sup>9</sup>Present address: The Danish Research Institute of Translational Neuroscience – DANDRITE, Nordic EMBL Partnership for Molecular Medicine, Department of Biomedicine, Aarhus University, Ole Worms Alle 3, 8000 Aarhus C, Denmark

<sup>10</sup>Co-first author

\*Correspondence: botond.roska@fmi.ch

<http://dx.doi.org/10.1016/j.neuron.2015.11.032>

This is an open access article under the CC BY-NC-ND license (<http://creativecommons.org/licenses/by-nc-nd/4.0/>).

## SUMMARY

Neuronal circuit asymmetries are important components of brain circuits, but the molecular pathways leading to their establishment remain unknown. Here we found that the mutation of FRMD7, a gene that is defective in human congenital nystagmus, leads to the selective loss of the horizontal optokinetic reflex in mice, as it does in humans. This is accompanied by the selective loss of horizontal direction selectivity in retinal ganglion cells and the transition from asymmetric to symmetric inhibitory input to horizontal direction-selective ganglion cells. In wild-type retinas, we found FRMD7 specifically expressed in starburst amacrine cells, the interneuron type that provides asymmetric inhibition to direction-selective retinal ganglion cells. This work identifies FRMD7 as a key regulator in establishing a neuronal circuit asymmetry, and it suggests the involvement of a specific inhibitory neuron type in the pathophysiology of a neurological disease.

## INTRODUCTION

Neuronal circuit asymmetries are important building blocks of the nervous system. Sensory circuits rely on circuit asymmetries to detect external features, like the position of sound sources, the orientation of visual objects, or the direction of visual motion.

In both invertebrates and vertebrates, neurons have been identified that respond selectively to the direction of visual motion as follows: vigorously to motion in a preferred direction, but only weakly to motion in the opposite null direction (Borst and Euler, 2011). Direction-selective neurons are already present at the sensory periphery, in the lobula and lobular plate of flies and in the retina of vertebrates (Borst and Helmstaedter, 2015). Retinal direction-selective neurons have preferred directions and corresponding circuit asymmetries along the cardinal directions. Due to their accessibility for physiological recordings and genetic manipulation, these circuits serve as model systems for understanding the formation of neuronal circuit asymmetries (Wei and Feller, 2011). However, the molecules establishing the asymmetry of direction-selective circuits along the cardinal axes remain unknown.

A potential source for identifying candidate molecules involved in the development of cardinal direction selectivity are monogenic diseases, which disrupt human visual behaviors that depend on the activity of direction-selective retinal cells. A visually guided behavior that relies on the activity of retinal direction-selective neurons is the optokinetic reflex (Osterhout et al., 2015; Oyster et al., 1972; Sun et al., 2015; Yoshida et al., 2001). The optokinetic reflex is initiated by a visual scene drifting on the retina, which triggers the eye to follow it, thus keeping the image stable on the retina. The optokinetic reflex works together with the vestibulo-ocular reflex, in which eye movement is initiated by head or body motion, to stabilize the gaze while the animal moves its head or entire body (Schweigart et al., 1997). These two reflexes, driven by visual and body motions, are complementary. The optokinetic reflex dominates gaze stabilization at lower speeds and the vestibular reflex does so at higher

speeds (van Alphen et al., 2001; Faulstich et al., 2004). The optokinetic reflex can be separated from the vestibulo-ocular reflex if the head is fixed in place (Bryan and Angelaki, 2009).

A neurological disease in which the optokinetic reflex is disturbed is idiopathic congenital nystagmus. Individuals with idiopathic congenital nystagmus, which occurs in 1 in 1,500 humans, have impaired eye movements resulting in impaired vision (Gottlob and Proudlock, 2014). In 70% of the detected cases, mutations in the *FRMD7* gene on the X chromosome have been reported (Tarpey et al., 2006). Individuals without a functional *FRMD7* allele have involuntary horizontal eye oscillations (nystagmus) and lack the optokinetic reflex along the horizontal axis (Thomas et al., 2008, 2011). In contrast, along the vertical axis no nystagmus can be observed and the optokinetic reflex is unaffected. The symptoms begin in early childhood at an age of 2–3 months. While *FRMD7* expression has been localized to the retina and the vestibular system (Tarpey et al., 2006; Thomas et al., 2011), the neuronal circuit dysfunction responsible for the symptoms of the disease is unknown.

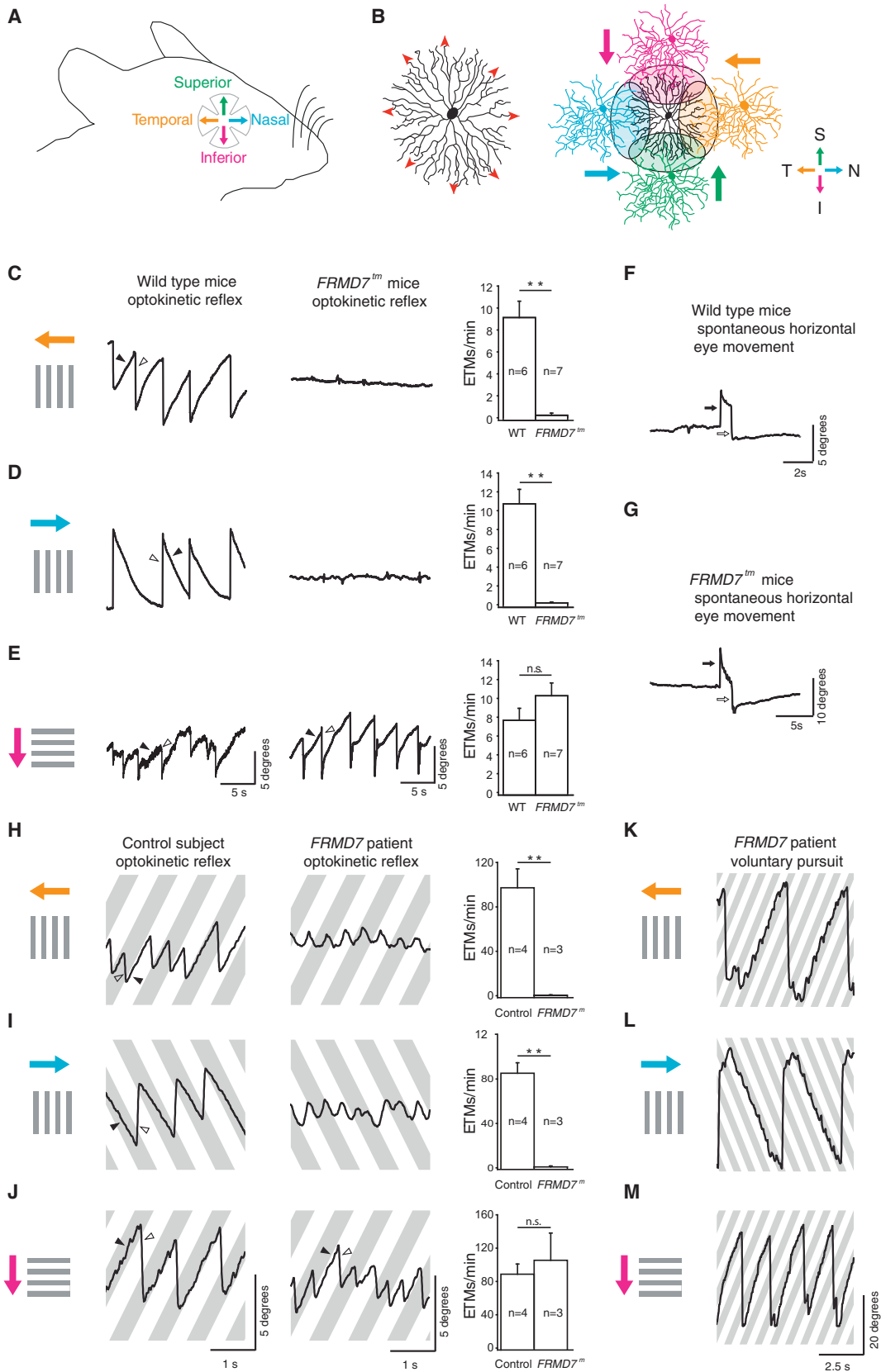
In the retina of mammals, including mice, three classes of direction-selective ganglion cells (DS cells) have been described as follows: on-off DS cells, on DS cells, and off DS cells (Sanes and Masland, 2015). The on-off cells respond to both light increments and decrements, while on cells respond only to increments and off cells only to decrements. The on-off DS cells consist of four types with preferred directions corresponding to each of the four cardinal directions (inferior, superior, temporal, and nasal; note that throughout the text the direction of motion is defined based on the direction of motion on the retina). The on DS cells can be classified into three types, with preferred motion directions being inferior, superior, and temporal. The off DS cells prefer motion in the inferior direction. Most on DS cells and a type of on-off DS cell are tuned to slow motion, while most on-off DS cells and a group of on DS cell prefer faster motion (Dhande et al., 2013; Gauvain and Murphy, 2015). DS cell types in the mouse retina are genetically determined populations of neurons: they can be labeled by distinct molecular markers and they form retinal mosaics (Sanes and Masland, 2015).

It has been suggested that slow-motion-tuned DS cells are the main source of direction-selective input driving the optokinetic reflex in response to slow drifts of the visual scene (Oyster et al., 1972). Indeed, the optokinetic reflex is lost when retinal direction selectivity is abolished by genetic ablation of starburst cells, which are a key circuit component of the retinal direction-selective circuit (Yoshida et al., 2001). Slow-motion-tuned on and on-off DS cells project their axons to the nuclei of the accessory optic system (Dhande et al., 2013; Yonehara et al., 2009), which consists of the medial terminal nucleus (MTN), the lateral terminal nucleus (LTN), and the nucleus of the optic tract (NOT)/dorsal terminal nucleus (DTN) complex (Giolli et al., 2006; Simpson, 1984; Figure 6C). In mice, the MTN receives retinal inputs from superior and inferior motion-preferring on DS cells (Dhande et al., 2013; Yonehara et al., 2009), and inferior motion-preferring on-off DS cells (Kay et al., 2011); the NOT/DTN complex receives retinal inputs from temporal motion-preferring on and on-off DS cells (Dhande et al., 2013). Direction-selective responses with preferred directions along the vertical axis have been recorded in the MTN and LTN, while responses with preferred directions

along the horizontal axis have been recorded in the NOT/DTN complex (Soodak and Simpson, 1988). Activity in the NOT/DTN complex has been shown to be required selectively for the horizontal optokinetic reflex (Hoffmann and Fischer, 2001), while MTN activity is required for the vertical optokinetic reflex (Sun et al., 2015). The accessory optic system is conserved across species, as the MTN and NOT/DTN have been anatomically identified in a number of species including mouse, rabbit, cat, monkey, and human (Giolli et al., 2006; Simpson, 1984).

The retinal circuitry underlying the direction-selective responses of on-off and on DS cells has been investigated in detail. DS cells receive excitatory input from glutamatergic bipolar cells, as well as inhibitory and excitatory inputs from starburst amacrine cells. Starburst cells release both GABA and acetylcholine (Vaney et al., 2012). The glutamatergic excitatory input from bipolar cells and the cholinergic excitatory input, which likely arrives via paracrine secretion from starburst cells (Briggman et al., 2011), are not direction selective (Lee et al., 2010; Yonehara et al., 2013; but see Pei et al., 2015). The GABAergic inhibitory input from starburst cells is spatially asymmetric: in response to motion in the null direction, inhibitory input is maximal; in response to motion in the preferred direction, inhibitory input is minimal (Vaney et al., 2012). Furthermore, active integration mechanisms in the dendrites of DS cells sharpen the spiking output of DS cells (Oesch et al., 2005; Sivyer and Williams, 2013; Trenholm et al., 2014). With the exception of the responses of a single on-off DS cell type to slow motion (Trenholm et al., 2011) and the responses of the off DS cell type (Kim et al., 2008), the inhibitory input from starburst cells is necessary for the direction-selective responses of DS cells (Fried et al., 2002; Yoshida et al., 2001).

The direction selectivity of the inhibitory input to DS cells relies on two features of the retinal circuit. The first feature is an asymmetric neurotransmitter release from starburst cells. Starburst cell processes radiate away from the soma; they act both as dendrites, receiving input from bipolar cells and other starburst cells, and as axons, providing input to DS cells and other starburst cells (Famiglietti, 1991; Kim et al., 2014). A starburst cell process preferentially releases GABA if motion occurs in a centrifugal direction along the process, from the soma to the tip (Euler et al., 2002). This asymmetric release could be due to inputs from different types of bipolar cells with different temporal characteristics along the starburst cell process (Kim et al., 2014), an excitability gradient (Gavrikov et al., 2003; Hausselt et al., 2007), or inhibitory interactions between starburst cells (Lee and Zhou, 2006). This asymmetry is radial, centered on each starburst soma, and likely has no information about the cardinal directions. Therefore, the disruption of its development would likely result in a decrease in direction selectivity along all four cardinal directions. The second circuit feature, on which direction selectivity relies, is the spatially asymmetric inhibitory connectivity between starburst cells and DS cell types (Briggman et al., 2011; Fried et al., 2002). The angle of a starburst cell process relative to the cardinal directions in the retina determines the connectivity between the starburst cell process and the DS cell type (Figures 1A and 1B). For instance, starburst processes that point nasally connect to DS cell types preferring temporal motion, and starburst processes that point superiorly connect to DS types preferring inferior motion (Briggman et al., 2011). This



(legend on next page)

spatially asymmetric connectivity is believed to be necessary for defining cardinal direction selectivity. Developmental disruption could potentially result in the loss of direction selectivity in specific directions or combinations of directions.

Spatially asymmetric inhibitory connectivity between starburst cells and DS cells forms independent of visual activity or spontaneous retinal waves (Elstrott et al., 2008), and occurs rapidly between post-natal day 6 (P6) and eye opening, from previously established symmetric inputs (Wei et al., 2011; Yonehara et al., 2011). Molecules responsible for positioning DS cell dendrites, for establishing bipolar cell input, and for defining the morphology and spacing of starburst cells have been described already (Duan et al., 2014; Sun et al., 2013), and molecules responsible for creating centrifugal direction selectivity in starburst cell processes have been proposed (Gavrikov et al., 2003). While disruption of some of these molecules results in decreased tuning of direction-selective responses (Sun et al., 2013), no molecules have been identified that are necessary for motion detection in specific directions (Duan et al., 2014; Gavrikov et al., 2003; Sun et al., 2013). Therefore, the molecular pathway responsible for setting up the circuit asymmetry along the cardinal directions has remained unidentified.

Recently, using a transcriptional map of adult retinal cell types in mice, we found that *FRMD7*, the gene in which mutations result in the lack of the horizontal optokinetic reflex in humans, is enriched in starburst cells (Siegert et al., 2012), suggesting that direction-selective circuits in the retina could be involved in the disease. The *FRMD7* gene encodes a member of the FERM domain family of proteins (Moleirinho et al., 2013) and has been implicated in the reorganization of the cytoskeleton (Pu et al., 2013). Here we investigate a potential link between the function of *FRMD7*, the development of retinal direction selectivity, and the lack of the horizontal optokinetic reflex in *FRMD7*-based congenital nystagmus.

## RESULTS

### *FRMD7* Is Required for the Horizontal Optokinetic Reflex in Mice

We compared the optokinetic reflex and spontaneous eye movements of wild-type and *FRMD7* hypomorphic mutant (*FRMD7<sup>tm</sup>*;

Experimental Procedures; Figure S1) mice (Figures 1 and S2). Head-fixed mice were presented with drifting gratings while their eye movements were tracked with a camera. In wild-type mice, a strong optokinetic reflex could be elicited in nasal, temporal, and inferior directions (Figures 1C–1E). The reflex was weak in the superior direction (Figure S2A), as has been reported previously (Yonehara et al., 2009). Similar to human subjects with *FRMD7* mutation (Thomas et al., 2011; Figures 1H–1J and S2), *FRMD7<sup>tm</sup>* mice lacked the horizontal optokinetic reflex, both in the nasal and temporal directions (Figures 1C and 1D; Movie S1), but the vertical inferior optokinetic reflex of *FRMD7<sup>tm</sup>* mice was similar to that of wild-type mice (Figure 1E). The absence of the horizontal optokinetic reflex did not appear to arise from an inability of the mice to move their eyes horizontally, as we observed spontaneous horizontal eye movements in wild-type and *FRMD7<sup>tm</sup>* mice (Figures 1F and 1G). Similarly, human subjects with *FRMD7* mutation could perform voluntary horizontal eye movements (Figures 1K and 1L). We observed no spontaneous oscillatory eye movements (nystagmus) in *FRMD7<sup>tm</sup>* mice. These results suggest that one of the symptoms, the lack of the horizontal optokinetic reflex, is shared between *FRMD7<sup>tm</sup>* mice and human subjects with *FRMD7* mutation and that the motor circuits of both humans and mice remain capable of moving the eyes horizontally.

### Lack of Horizontal Direction Selectivity in the Retina of *FRMD7<sup>tm</sup>* Mice

We investigated whether the lack of the horizontal optokinetic reflex is accompanied by altered retinal activity in *FRMD7<sup>tm</sup>* mice. We recorded the spiking activity of retinal ganglion cells in wild-type and *FRMD7<sup>tm</sup>* mice using microelectrode arrays. The retina was stimulated with light flashes and bars moving in different directions and at different velocities. Light flashes were used to segregate on and on-off cells, motion in different directions was used to determine direction selectivity, and different velocities were used to differentiate between slow- and fast-motion-preferring DS cells (Experimental Procedures). Retinas of *FRMD7<sup>tm</sup>* mice responded well to both light flashes and slow and fast motions (Figures S3A–S3C). However, in *FRMD7<sup>tm</sup>* mice the fractions of cells with direction-selective responses were significantly lower (by 52% and 44%) than in wild-type

### Figure 1. Horizontal Optokinetic Reflex Is Absent in *FRMD7<sup>tm</sup>* Mice and in Human Subjects with *FRMD7* Mutation

(A) Retinal cardinal axes are shown. (B) (Left) A schematic of a starburst cell showing the direction of centrifugal motion (red arrowheads) that evokes transmitter release. (Right) Spatial organization of synaptic connectivity between a starburst cell (center, black) and four types of DS cells, color coded according to their preferred directions (colored arrows), is shown. (C–E) Optokinetic reflex eye movements produced by wild-type (WT, left) and *FRMD7<sup>tm</sup>* (middle) mice in response to motion in the temporal (top), nasal (middle), and inferior (bottom) directions on the retina. Gray bars represent the motion stimulus and arrows colored according to the color code in (A) indicate the motion direction on the retina. The right column shows the quantification of optokinetic reflex eye-tracking movements per minute (ETMs, Supplemental Experimental Procedures) for WT and *FRMD7<sup>tm</sup>* mice in the three directions. Filled and open arrowheads indicate the slow phase and fast phase of eye movements, respectively. (F and G) Spontaneous eye movements in WT (F) and *FRMD7<sup>tm</sup>* (G) mice along horizontal axes. Open and filled arrows indicate eye movements to the left and right, respectively. (H–J) Optokinetic reflex in a control human subject (left) and a subject with *FRMD7* mutation (middle) in response to motion in the temporal (top), nasal (middle), and inferior (bottom) directions on the retina. Gray bars represent the motion stimulus and arrows colored according to the color code in (A) indicate the motion direction on the retina. The right column shows the quantification of optokinetic reflex ETMs for control human subjects and for subjects with *FRMD7* mutation in the three directions (Supplemental Experimental Procedures). Filled and open arrowheads indicate slow phase and fast phase of eye movements, respectively. (K–M) Voluntary pursuit movements in a human subject with *FRMD7* mutation in response to the motion protocols as in (H)–(J). Data are shown as mean  $\pm$  SEM; n refers to the number of animals in (C)–(E) and subjects in (H)–(J). See also Figures S1 and S2 and Movie S1.

mice when stimulated with fast and slow motions, respectively (Figure S3C).

In wild-type retinas, we recorded direction-selective responses along both the horizontal and the vertical axes: we identified fast-motion-tuned DS cells, preferring motion along the cardinal directions, and slow-motion-tuned DS cells types, preferring superior, inferior, or temporal motion (Figure 2). Similarly we found on-off DS cells preferring motion along the cardinal directions and on DS cells preferring mainly superior, inferior, or temporal motion (Figures S4A–S4C). Strikingly, in *FRMD7<sup>tm</sup>* mice, the fraction of (temporal or nasal) horizontal motion-preferring DS cells decreased by 95% (fast motion) and 93% (slow motion) compared to wild-type mice (Figure 2). The nearly complete lack of direction selectivity along the horizontal axis was found in both on and on-off DS cells (Figures S4A–S4C). Nevertheless, in *FRMD7<sup>tm</sup>* mice, the number of vertical motion-preferring direction-selective cells relative to all recorded ganglion cells remained similar to wild-type (Figure 2F). Thus, the loss of *FRMD7* leads to the specific loss of horizontal direction-selective responses in the retina.

### FRMD7 Is Selectively Expressed in Starburst Cells in the Retina

A transcriptional map of adult retinal cell types in mice suggested that *FRMD7* is enriched in adult starburst cells (Siegert et al., 2012). To test whether starburst cells specifically express *FRMD7*, we performed double-label quantitative fluorescence in situ hybridization with antisense probes for *FRMD7* mRNA and *ChAT* mRNA at different developmental times (Figures 3A, 3B, and S5A). *ChAT* is a specific marker for starburst cells. Both *FRMD7* and *ChAT* expressions were first observed at P3. Once expressed, *FRMD7* and *ChAT* mRNAs were co-localized in the same cells, both in the ganglion cell layer and in the inner nuclear layer. We did not detect signals with control sense probe for *FRMD7* mRNA (Figures 3C and S5B).

We obtained further evidence that *FRMD7* expression is specific to starburst cells using immunohistochemistry: in *FRMD7<sup>tm</sup>* mice, *lacZ* is inserted into the locus between exons 3 and 4. By performing antibody staining against LacZ and ChAT, we confirmed that the expression of LacZ is restricted to ChAT-positive cells in the retina (Figure S1F). Thus, in the developing and adult retina, *FRMD7* is specifically expressed in starburst cells, the key cell type for establishing retinal direction selectivity.

### Starburst Cells in *FRMD7<sup>tm</sup>* Mice Have Normal Morphology and Stratification

We then tested whether the morphology of starburst cells is affected in *FRMD7<sup>tm</sup>* mice. Starburst cell processes stratify into on and off sublayers as early as P3, and bistratified ganglion cell dendrites follow these processes as early as P3–P4 (Stacy and Wong, 2003). The on-off DS cells receive inhibitory input from starburst cells already at P4 (Wei et al., 2011). The density of starburst cell somas, labeled with an antibody against ChAT, was similar in wild-type and *FRMD7<sup>tm</sup>* mice, both in the ganglion cell and in the inner plexiform layer (Figures 3D and 3E). Furthermore, starburst cells extended their processes to the same depths in the inner plexiform layer in wild-type and *FRMD7<sup>tm</sup>* mice (Figure 3F).

To examine the morphology of individual starburst cells, we sparsely labeled them in both control and *FRMD7<sup>tm</sup>* mice. For this we used control *Chat-Cre* mice and *FRMD7<sup>tm</sup>;Chat-Cre* mice and infected the retina in vivo with conditional adeno-associated virus (AAV), expressing a mutant TVA receptor (TVA66T) (Miyamichi et al., 2013), and EnvA-coated SADΔG-GFP rabies virus. Confocal imaging of infected starburst cells revealed that the gross morphology of starburst cells, the size of the dendritic field, the symmetry of the processes, and the number of primary processes were similar in control and *FRMD7<sup>tm</sup>* mice (Figures 3G and 3H).

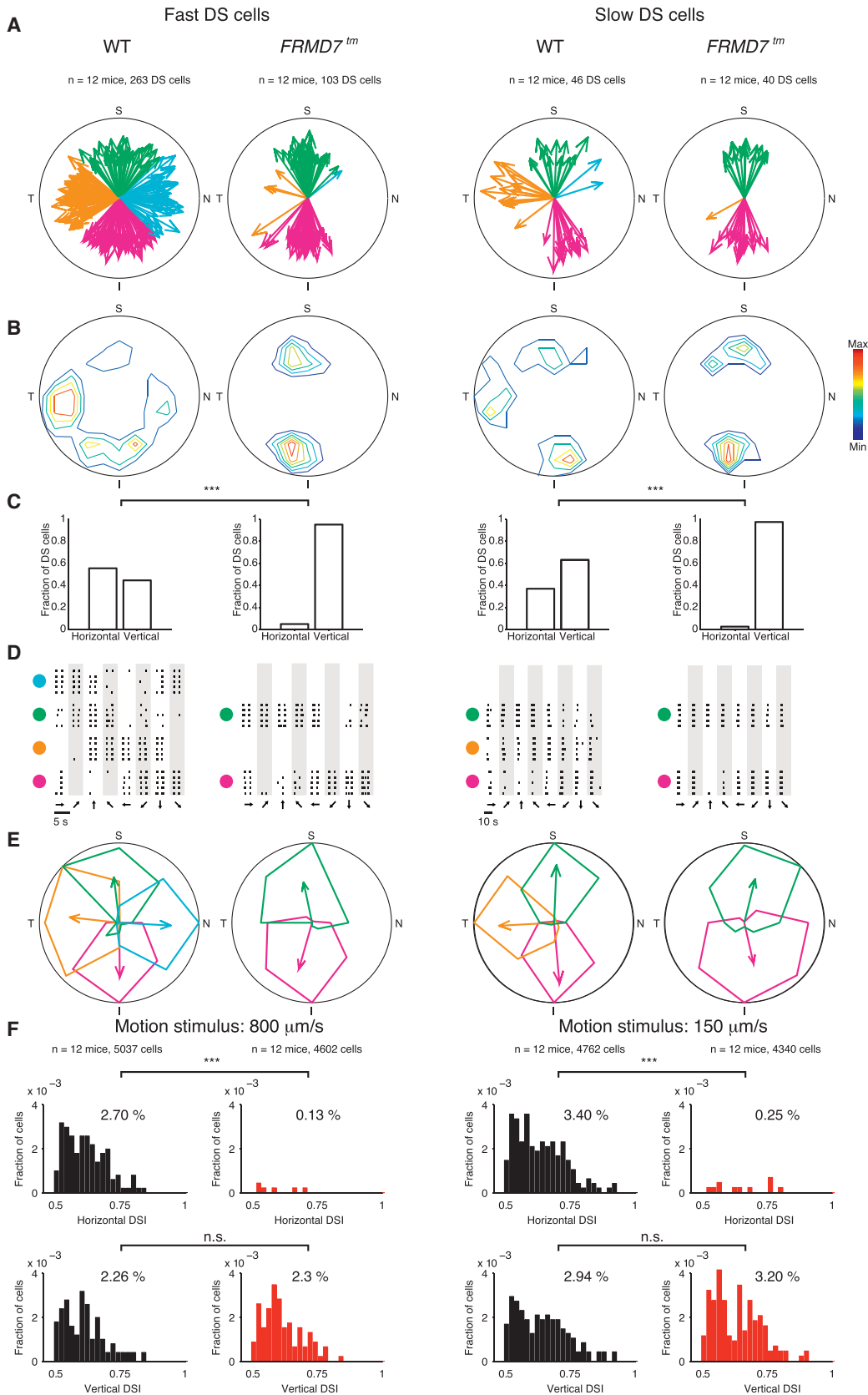
To visualize the output synapses of starburst cells, we labeled starburst cells with a fluorescently tagged presynaptic marker in both control and *FRMD7<sup>tm</sup>* mice. We infected the retinas of control *Chat-Cre* mice and *FRMD7<sup>tm</sup>;Chat-Cre* mice in vivo with AAV, expressing GFP-tagged synaptophysin in the presence of Cre recombinase. Confocal imaging of the infected starburst cells indicated no sign of abnormal density of output synapses in *FRMD7<sup>tm</sup>* mice (Figure 3I).

### Loss of the Asymmetry of Inhibitory Inputs to Horizontal DS Cells

There could be several reasons for the lack of horizontal direction selectivity in the *FRMD7<sup>tm</sup>* retinas. First, it is possible that horizontal DS cells are lost in *FRMD7<sup>tm</sup>* mice. Alternatively, horizontal DS cells might remain present, but lose their horizontal direction-selective responses due to changes in the retinal circuit. To further examine the circuit mechanism underlying the lack of horizontal direction selectivity, we used *Hoxd10-GFP* mice, in which the three on DS cell types and one temporal on-off DS cell type, but no other retinal cell type, are genetically labeled (Dhande et al., 2013). All GFP-labeled ganglion cells in *Hoxd10-GFP* mice project to the nuclei of the accessory optic system and prefer slow motion. We crossed *FRMD7<sup>tm</sup>* mice with *Hoxd10-GFP* mice and compared the labeled ganglion cell population with that of control *Hoxd10-GFP* mice. We found that the density of GFP-labeled cells was unchanged in *FRMD7<sup>tm</sup>;Hoxd10-GFP* mice compared to control mice (Figures S6B and S6C), suggesting that cells with the genetic identity of wild-type horizontal DS cells are not lost in the *FRMD7<sup>tm</sup>* background.

The lack of horizontal direction selectivity in *FRMD7<sup>tm</sup>* retinas can be a sign either of no motion responses or of responses that have similar magnitudes in all motion directions in ganglion cells that have the genetic identity of wild-type horizontal DS cells. The third possibility, that horizontal motion-preferring DS cells are converted to vertical motion-preferring cells in *FRMD7<sup>tm</sup>* retinas, is not likely since the number of vertical DS cells does not increase in *FRMD7<sup>tm</sup>* retinas compared to wild-type (Figure 2F). We performed two-photon targeted patch-clamp recordings from GFP-labeled cells (Figure S6A) in isolated retinas of control *Hoxd10-GFP* mice and *FRMD7<sup>tm</sup>;Hoxd10-GFP* mice. We recorded spiking activity, as well as inhibitory and excitatory currents, while stimulating the retina with light spots, either flashed to the receptive field center or moving across the retina in eight different directions (Figure 4).

We first analyzed GFP-labeled on-off cells since these cells belong to a single horizontal motion-preferring DS cell type in



(legend on next page)

control *Hoxd10-GFP* retinas. Targeting GFP-labeled on-off cells in *FRMD7<sup>tm</sup>;Hoxd10-GFP* retinas, therefore, allows for identifying ganglion cells with the genetic identity of wild-type horizontal DS cells in the *FRMD7<sup>tm</sup>* background. In control mice, spike recordings performed in cell-attached mode confirmed that GFP-labeled on-off cells respond to motion stimulation and preferred temporal motion (Figures 4A and 4E). In contrast, in *FRMD7<sup>tm</sup>;Hoxd10-GFP* mice, GFP-labeled on-off cells lacked direction selectivity by not responding to motion stimulation in any direction (Figures 4B and 4E). However, the spike responses to flashed spots remained similar to those in control mice (Figure 4E). To understand the cause for the lack of direction selectivity, we recorded excitatory and inhibitory currents from GFP-labeled on-off cells in whole-cell patch-clamp mode after the spike recording from the same cells was finished. The excitatory inputs during motion stimulation remained similar to those in the control (Figure S6E). As far as inhibition, in control retinas, GFP-labeled on-off cells received asymmetric inhibitory inputs: the inhibition was largest when the stimulus moved nasally, the null direction. In contrast, in *FRMD7<sup>tm</sup>;Hoxd10-GFP* mice, GFP-labeled non-DS on-off cells received symmetric inhibitory inputs: the magnitude of inhibition was similar across all directions and its value ranged between the nasal and temporal values of the motion-evoked inhibition measured in control retinas (Figures 4A, 4B, 4E, and S6I). These results suggest that the increased inhibition evoked by motion in the temporal direction abolishes motion-evoked spiking activity in GFP-labeled on-off cells and, furthermore, that the decreased magnitude of inhibition in the nasal direction is enough to suppress spiking in this direction.

We then analyzed the spiking activity of GFP-labeled on cells that were not vertically tuned. While these cells preferred horizontal motion in control mice (Figures 4C and 4F), they responded in all motion directions, indiscriminately, in *FRMD7<sup>tm</sup>;Hoxd10-GFP* mice (Figures 4D and 4F). Analysis of the inhibitory input to these cells revealed that the asymmetry of the inhibition was significantly reduced along the horizontal axis (Figure 4F). The magnitude of the inhibition lay between the nasal and temporal values of the motion-evoked inhibition measured in control retinas, but closer to the temporal side (Figure S6I). The distribution of the motion-evoked inhibitory responses of on cells was significantly different from that of on-off cells in *FRMD7<sup>tm</sup>;Hoxd10-GFP* retinas (Figure S6J).

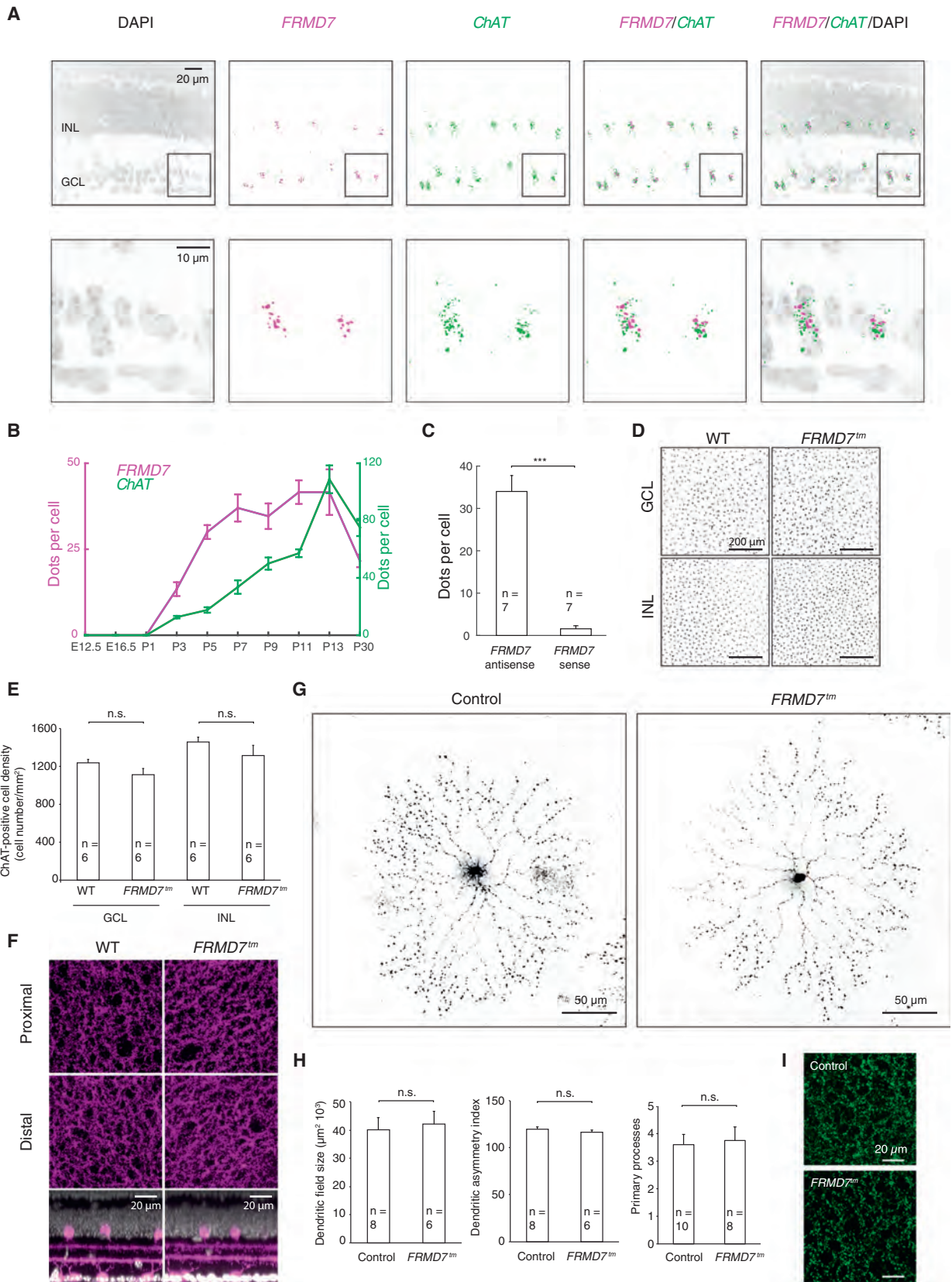
Comparing the timing of spiking, inhibition, and excitation evoked by motion stimulation in on-off and on cells revealed that, while inhibition and excitation temporally overlapped in the non-spiking on-off cells, the spiking in on cells corresponded to the sustained phase of excitation, suggesting that the reduced inhibition is unable to block the effect of this part of the excitatory input (Figures S6F–S6H). Taken together, in both GFP-labeled on-off and on cells (which were not tuned vertically) of *FRMD7<sup>tm</sup>;Hoxd10-GFP* mice, the inhibitory input is symmetric. Depending on the magnitude and time course of excitation and inhibition, the symmetric inhibition either blocks spiking in all motion directions, as in on-off cells, or leads to indiscriminate spiking in all motion directions, as found in on cells.

To examine whether the dendrites of GFP-labeled non-DS on-off and on cells in *FRMD7<sup>tm</sup>;Hoxd10-GFP* mice were mistargeted, we filled the cells with neurobiotin during the recording and subsequently reconstructed their dendritic stratification. Similar to GFP-labeled cells in control *Hoxd10-GFP* mice, the dendrites of the recorded GFP-labeled non-DS on-off and on cells in retinas of *FRMD7<sup>tm</sup>;Hoxd10-GFP* mice co-stratified with either the proximal or both the proximal and distal ChAT-positive strata (Figures 4G–4J). This is consistent with a view that the symmetric inhibitory input to GFP-labeled non-DS cells is delivered by starburst cells in *FRMD7<sup>tm</sup>* mice.

We encountered only a few GFP-labeled vertical motion-preferring DS cells in *Hoxd10-GFP* retinas, both in the control and *FRMD7<sup>tm</sup>* background. Therefore, we used a different approach to label vertical DS cells and compare their tuning in wild-type and *FRMD7<sup>tm</sup>* retinas. We injected a retrograde fluorescent tracer, cholera toxin subunit B Alexa 488 conjugate, into the MTN of wild-type and *FRMD7<sup>tm</sup>* mice. We performed two-photon targeted patch-clamp recordings from Alexa 488-labeled cells in isolated retinas (Figures 5 and S6D). We recorded spiking activity in cell-attached mode and inhibitory currents in whole-cell mode. The MTN back-labeled ganglion cells in *FRMD7<sup>tm</sup>* retinas had direction-selective spiking responses and inhibitory currents similar to the MTN back-labeled ganglion cells recorded in wild-type retinas. The preferred direction of the spiking responses and inhibitory currents opposed each other and pointed either superior or inferior (Figure 5). Thus, in *FRMD7<sup>tm</sup>* mice, vertical motion-preferring on DS cells are direction selective similar to wild-type mice.

### Figure 2. Lack of Horizontal Direction Selectivity in the Retina of *FRMD7<sup>tm</sup>* Mice

The figure shows data obtained with microelectrode arrays. In (A)–(E), the left two columns correspond to cells tuned to fast motion and the right two columns to cells tuned to slow motion (Supplemental Experimental Procedures). The radius of each circle corresponds to direction selectivity index (DSI) = 1. (A) Polar plots showing the preferred directions (direction of arrow) and DSI (length of an arrow) of individual DS cells (DSI > 0.5, each recorded DS cell is represented by an arrow) in WT and *FRMD7<sup>tm</sup>* retinas. The color code shows the different directions according to Figure 1A. (B) Contour plots showing the density of DS cells at different DSIs and preferred directions. Red indicates maximal density. (C) The proportions of horizontal (nasal and temporal) and vertical (superior and inferior) motion-preferring DS cells in WT and *FRMD7<sup>tm</sup>* retinas are shown. (D) Raster plots showing the spike responses (each black line is a spike) of example DS cells in WT and *FRMD7<sup>tm</sup>* retinas in response to motion in eight different directions, indicated by the arrows at the bottom of the plot. Responses to stimulus repetitions (n = 5) are shown in different rows. Large colored dots indicate the preferred directions of DS cells according to the color code in Figure 1A. (E) Polar plots of the normalized mean spike numbers of cells shown in (D). The preferred direction and DSI of each cell are shown by the direction and length of the corresponding (color-coded) arrow. (F) Distributions of the horizontal (top) and vertical (bottom) DSIs (Supplemental Experimental Procedures) of DS cells in WT (black) and *FRMD7<sup>tm</sup>* (red) retinas for fast (left) and slow (right) stimulus speeds are shown. See also Figures S3 and S4.



(legend on next page)

### Developmental Time Window in which FRMD7 Is Required for Establishing Horizontal Direction Selectivity

We investigated whether FRMD7 is required for the formation or for the maintenance of horizontal direction selectivity. The in situ hybridization experiments show that *FRMD7* expression is first detected at P3 (Figures 3B and S5). To narrow down the time window of FRMD7 function, we tested whether the lack of horizontal direction selectivity in *FRMD7<sup>tm</sup>* mice is already present at eye opening. We performed microelectrode array recordings from *FRMD7<sup>tm</sup>* retinas just after eye opening, at P13–P14. Whereas P13–P14 wild-type retinas had both vertical and horizontal direction-selective responses, P13–P14 retinas of *FRMD7<sup>tm</sup>* mice lacked horizontal direction-selective responses, suggesting that the mechanism leading to the loss of horizontal direction selectivity operates before eye opening (Figures S4D–S4F). Thus, FRMD7 is required for the formation of horizontal direction selectivity between birth and eye opening.

### The Accessory Optic System in *FRMD7<sup>tm</sup>* Mice

We asked whether those on and on-off DS cells in *FRMD7<sup>tm</sup>* mice that lost their horizontal direction selectivity and that normally project their axons to the NOT/DTN nuclei of the accessory optic system keep their central target. We labeled the retino-recipient areas of *FRMD7<sup>tm</sup>;Hoxd10-GFP* mice by injecting CTB conjugated to Alexa dye into one of the eyes. CTB is taken up by retinal ganglion cells and is transported to their axon terminals (Morin and Studholme, 2014). Subsequently, we examined the GFP-labeled axons in the retino-recipient brain areas labeled with CTB. We found that all nuclei of the accessory optic system, MTN and NOT/DTN, were innervated by GFP-positive axons, as in wild-type mice (Figure 6).

Next we mapped *FRMD7* and *ChAT* expression in the brain of P11 wild-type mice using fluorescence in situ hybridization (Figure S7A). The nuclei of the accessory optic system were labeled by injecting CTB conjugated to Alexa dye into both eyes at P8. *ChAT* probe was used as a landmark to identify motor nuclei. The nuclei of the accessory optic system, NOT/DTN and MTN, were negative for *FRMD7* mRNA expression. Furthermore, we did not detect *FRMD7* mRNA expression in other major visual areas, such as the lateral geniculate nucleus, primary visual cortex, and superior colliculus (data not shown). We found that *FRMD7* and *ChAT* mRNAs were co-localized in the same cells

in some motor nuclei as follows: the abducens nucleus, which innervates the lateral rectus of extraocular muscles, and the oculomotor/trochlear nuclei, which innervate the other extraocular muscles (Figure S7A). Expression of *FRMD7* mRNA also was observed in the vestibulo-ocular reflex pathway, in the vestibular nuclei (Thomas et al., 2011; Figure S7A). These results suggest that FRMD7 is expressed in select cell types in the brain.

### FRMD7 Is Distributed Symmetrically within Starburst Cell Processes

We examined where FRMD7 is localized within starburst cells. We performed immunohistochemistry with anti-FRMD7 and anti-ChAT antibodies on retinas at different developmental stages (P3, P5, and P7), and we examined the stained retinas using confocal microscopy (Figure 7). In neonatal stages, FRMD7 signals were present in the basal part of the cell body and processes (Figures 7A and 7B). To quantify the degree of asymmetry in the distribution of the FRMD7 signal within individual starburst cells, we determined the angle of FRMD7-labeled primary processes at P5 in whole-mount retinas (Figure 7C). We found no sign of an asymmetric FRMD7 localization, suggesting that the localization of FRMD7 is not biased to specific starburst cell processes.

### FRMD7 Is Expressed in *ChAT*-Expressing Cells in the Retina of Non-human Primates

To determine whether *FRMD7* is expressed in *ChAT*-expressing cells in non-human primate retinas, we first performed immunohistochemistry with antibodies against ChAT in whole-mount retinas (Figure 8A). Similar to the findings from mice, mosaics of ChAT-labeled cells were present in both the inner nuclear and ganglion cell layers of non-human primate retinas (Rodieck and Marshak, 1992). Moreover, as in mice, the ChAT antibody labeled two retinal strata in the inner plexiform layer (Figure 8A). We then performed fluorescence in situ hybridization with antisense and control sense probes for *FRMD7* mRNA and antisense probes for *ChAT* mRNA (Figures 8B and S7B). Almost all the *ChAT*-positive cells were also positive for *FRMD7*. Conversely, a substantial fraction (70%) of *FRMD7*-positive cells in both the ganglion cell layer and inner nuclear layer were *ChAT* labeled (Figure 8C). We did not detect signals with control sense probe for *FRMD7* mRNA (Figure S7B). Thus, the mosaics of ChAT-labeled cells, and the ChAT-marked retinal strata, as

### Figure 3. FRMD7 Is Specifically Expressed in Starburst Cells in the Mouse Retina

(A) Confocal images of a mouse retinal section stained by double-label quantitative fluorescence in situ hybridization using antisense probes for mouse *FRMD7* mRNA and mouse *ChAT* mRNA and DAPI. Bottom panels are magnifications of the insets in top panels.  
 (B) Fluorescent dots per cell for *FRMD7* mRNA (magenta) and *ChAT* mRNA (green) at different developmental stages are shown (see Figure S5A for images).  
 (C) Quantification of hybridization signal for control sense probe is shown (see Figure S5B for images).  
 (D) Confocal images show the inner nuclear layer (INL) and ganglion cell layer (GCL) of WT (left) and *FRMD7<sup>tm</sup>* (right) retinas stained with anti-ChAT antibody.  
 (E) Quantification of the density of ChAT-positive cells from images, as given in (D), is shown.  
 (F) Top view of confocal images of WT (left) and *FRMD7<sup>tm</sup>* (right) retinas stained with anti-ChAT antibody at the proximal (top) and distal (middle) ChAT-positive strata in the inner plexiform layer. Side view is shown at the bottom.  
 (G) Confocal images show starburst cells sparsely labeled with GFP-expressing rabies virus in *ChAT-Cre* mice in control (left) and *FRMD7<sup>tm</sup>* (right) background.  
 (H) Dendritic field size (left), dendritic asymmetry index (middle), and the number of primary processes (right) of GFP-labeled starburst cells quantified from images as shown in (G). Dendritic asymmetry index refers to the ratio of length of widest diameter to that of narrowest diameter of the dendritic arbor (%).  
 (I) Confocal images of starburst cell processes at the proximal inner plexiform layer (IPL) sublayer labeled with synaptophysin-GFP-expressing AAV in *ChAT-Cre* mice in control (top) and *FRMD7<sup>tm</sup>* (bottom) background. Data are shown as mean  $\pm$  SEM; n refers to the number of retinas in (E) and cells in (C) and (H). See also Figures S1 and S5.

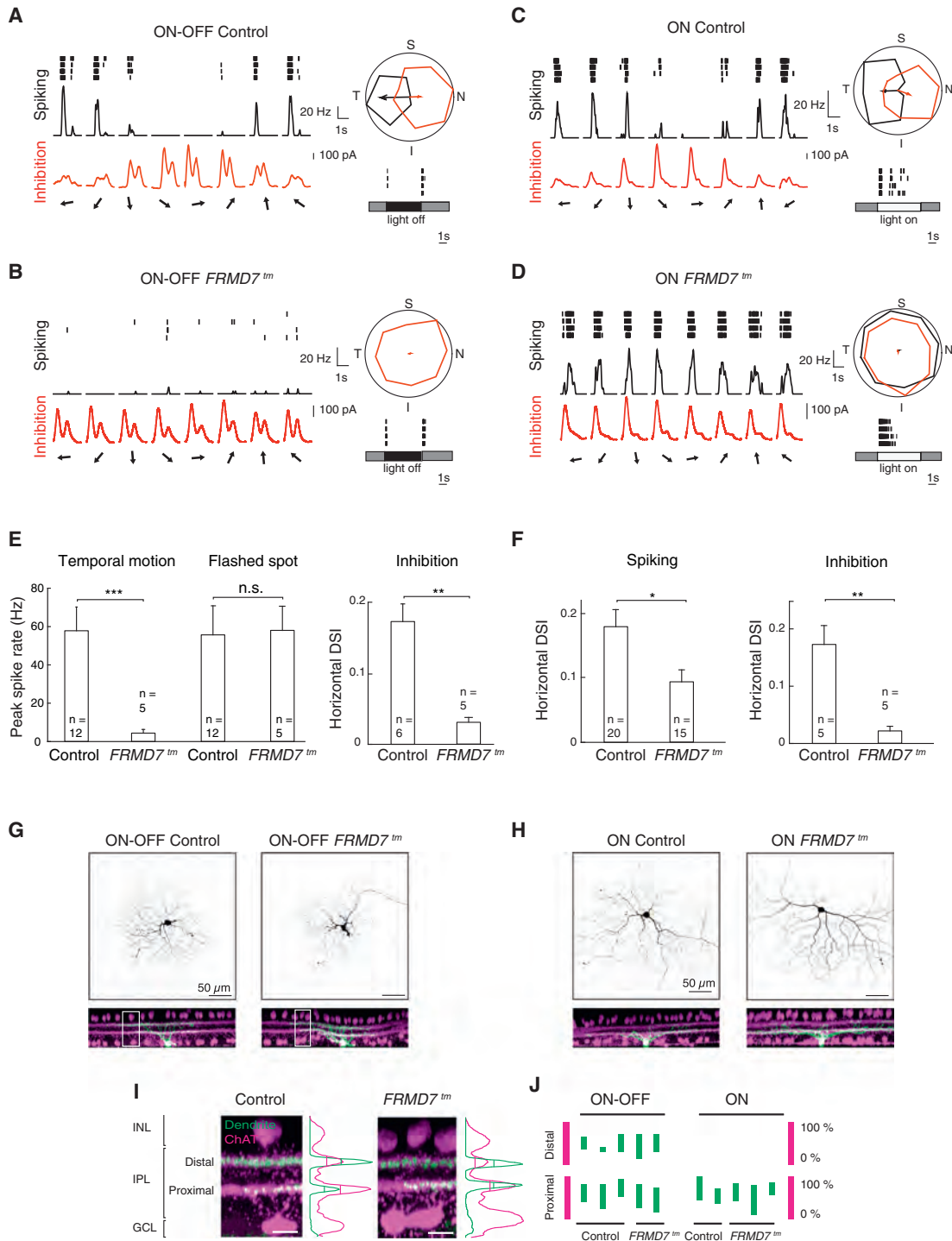


**Figure 4. Ganglion Cells in *FRMD7<sup>tm</sup>* Retinas with Genetic Identity of Horizontal Motion-Preferring DS Cells Lack Asymmetric Inhibitory Input** (A–D) Examples of cell-attached and whole-cell voltage-clamp recordings of GFP-labeled on-off cells (A and B) and on cells (C and D) in *Hoxd10-GFP* (Control; A and C) and *FRMD7<sup>tm</sup>;Hoxd10-GFP* (*FRMD7<sup>tm</sup>*; B and D) retinas. (Left column) Spike raster plot (black, top), spike rate (black, middle), and inhibition (red, bottom) in response to motion stimulus are shown. Arrows indicate the direction of motion. (Right column top) Polar plot of normalized (to the maximum) spike number (black) and peak inhibition (red) during motion stimulation is shown. The vector sum of spiking (black) and inhibitory (red) responses are shown by arrows. The vector sum for spikes was only plotted if the cell responded to stimulation (Supplemental Experimental Procedures). (Right column bottom) Spike raster plot in response to a 300-μm flashed-spot stimulus centered onto the cell body is shown. Gray, white, and dark areas indicate the stimulus contrast. N, nasal; T, temporal; S, superior; I, inferior.

(legend continued on next page)

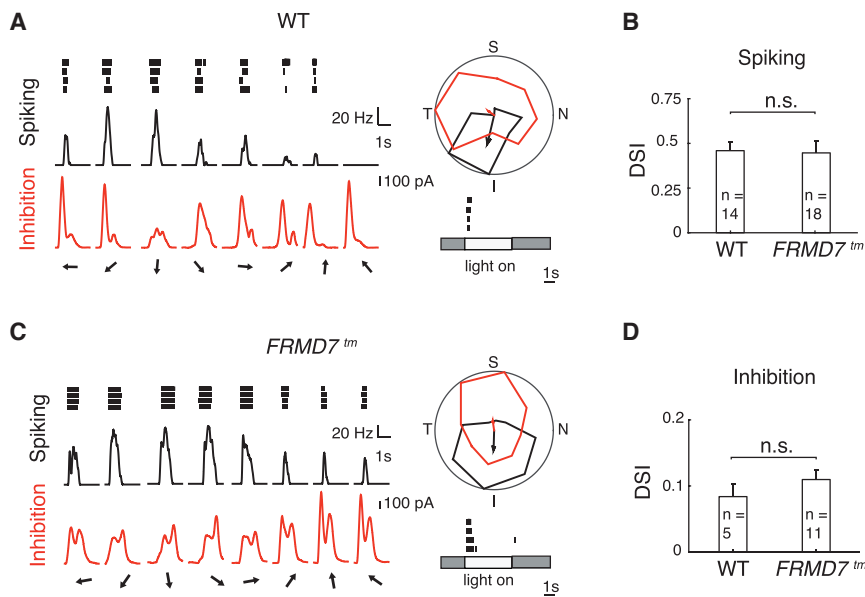


**Figure 5. Vertical Direction Selectivity and Asymmetric Inhibitory Input in MTN Back-Labeled Ganglion Cells in *FRMD7<sup>tm</sup>* Mice**

(A and C) Examples of cell-attached and whole-cell voltage-clamp recordings of MTN back-labeled ganglion cells in WT and *FRMD7<sup>tm</sup>* retinas. Spiking responses (black) and inhibitory currents (red) of vertically tuned on DS cells in WT (A) and *FRMD7<sup>tm</sup>* (C) retina are shown. (Left column) Spike raster plot (black, top), spike rate (black, middle), and inhibition (red, bottom) in response to motion stimulus are shown. Arrows indicate the direction of motion. (Right column top) Polar plot of normalized (to the maximum) spike number (black) and peak inhibition (red) during motion stimulation is shown. The vector sum of spiking (black) and inhibitory (red) responses are shown by arrows. (Right column bottom) Spike raster plot in response to a 300- $\mu$ m flashed-spot stimulus centered on the cell body is shown. Gray and white areas indicate the stimulus contrast. (B and D) Bar graphs showing DSI of spiking (B) and inhibition (D) in MTN back-labeled ganglion cells in WT and *FRMD7<sup>tm</sup>* retinas. Data points represent mean  $\pm$  SEM; n refers to the number of recorded cells. See also Figure S6.

well as the enrichment of *FRMD7* in *ChAT*-positive cells are conserved between mice and non-human primates.

## DISCUSSION

We found that *FRMD7*, a gene responsible for 70% of cases of idiopathic congenital nystagmus in humans, is required in the mouse retina to establish spatially asymmetric inhibitory inputs from starburst cells to DS cells along the horizontal axis, and is thus required for horizontal direction selectivity. The retinal expression of *FRMD7* is restricted to starburst cells in mice and enriched in *ChAT*-labeled cells in primates. Vertical direction selectivity was not dependent on *FRMD7*. Similar to results in humans, the dysfunction of *FRMD7* in mice leads to the loss of the horizontal optokinetic reflex. These results establish *FRMD7* as a member of a previously unidentified molecular pathway that is necessary for the establishment of neuronal circuit asymmetries.

### Circuit Mechanism Underlying the Lack of Horizontal Direction Selectivity in *FRMD7<sup>tm</sup>* Mouse Retina

We suggest that the lack of horizontal direction selectivity in the retina of *FRMD7<sup>tm</sup>* mice is due to the lack of asymmetric connectivity between starburst cells and ganglion cells with the genetic identity of wild-type horizontal motion-preferring DS cells. The following set of evidence supports this conclusion. First,

*FRMD7* was only expressed in *ChAT*-labeled cells (Figures 3A, 3B, 7, and S5), and *ChAT* is a selective marker of starburst cells in mice (Ivanova et al., 2010). Second, we found symmetric inhibitory currents in GFP-labeled on-off cells in the *FRMD7<sup>tm</sup>* background in a mouse line in which, in the wild-type background, all GFP-labeled on-off cells are DS cells preferring horizontal motion (Figures 4 and S6). Third, vertical direction selectivity persisted in *FRMD7<sup>tm</sup>* retinas (Figures 2 and 5). The first and second points indicate that starburst cells are the defective circuit element. The third point favors the hypothesis that, between the two key features determining asymmetric connectivity between starburst cell and DS cell and the centrifugal direction-organized asymmetric GABA release from starburst cell processes, it is the asymmetric connectivity between starburst cells and horizontal DS cells that is defective.

### Potential Role of *FRMD7* in Establishing Horizontal Asymmetric Connectivity

The results obtained are consistent with a role of *FRMD7* in the reorganization of the synaptic input from starburst cells to DS cells. During the development of wild-type mice, by P6, in both on-off and on DS cells, first symmetric connections between starburst cells and DS cells are established. These symmetric connections are then reorganized to asymmetric connections before

(E) Quantification of spiking (left) and inhibitory (right) responses in on-off cells is shown.

(F) Quantification of spiking (left) and inhibitory (right) responses in on cells. In (E) and (F), data points represent mean  $\pm$  SEM; n refers to the number of recorded cells (Supplemental Experimental Procedures).

(G and H) Confocal images of neurobiotin-filled, physiologically recorded on-off (G) and on (H) cells in top view (top) and side view (bottom). In side view, *ChAT* signals are shown (magenta) together with filled cells (green).

(I) Magnification of insets in (G). Fluorescence intensity profile for filled dendrite (green) and *ChAT* (magenta) along retinal depth is shown at the right of the images. Vertical lines in the profiles indicate the full width at half maximum within the IPL.

(J) Full width at half maximum of filled dendrites is shown as bars (green) relative to that of *ChAT*-positive proximal and distal strata (magenta).

See also Figure S6.

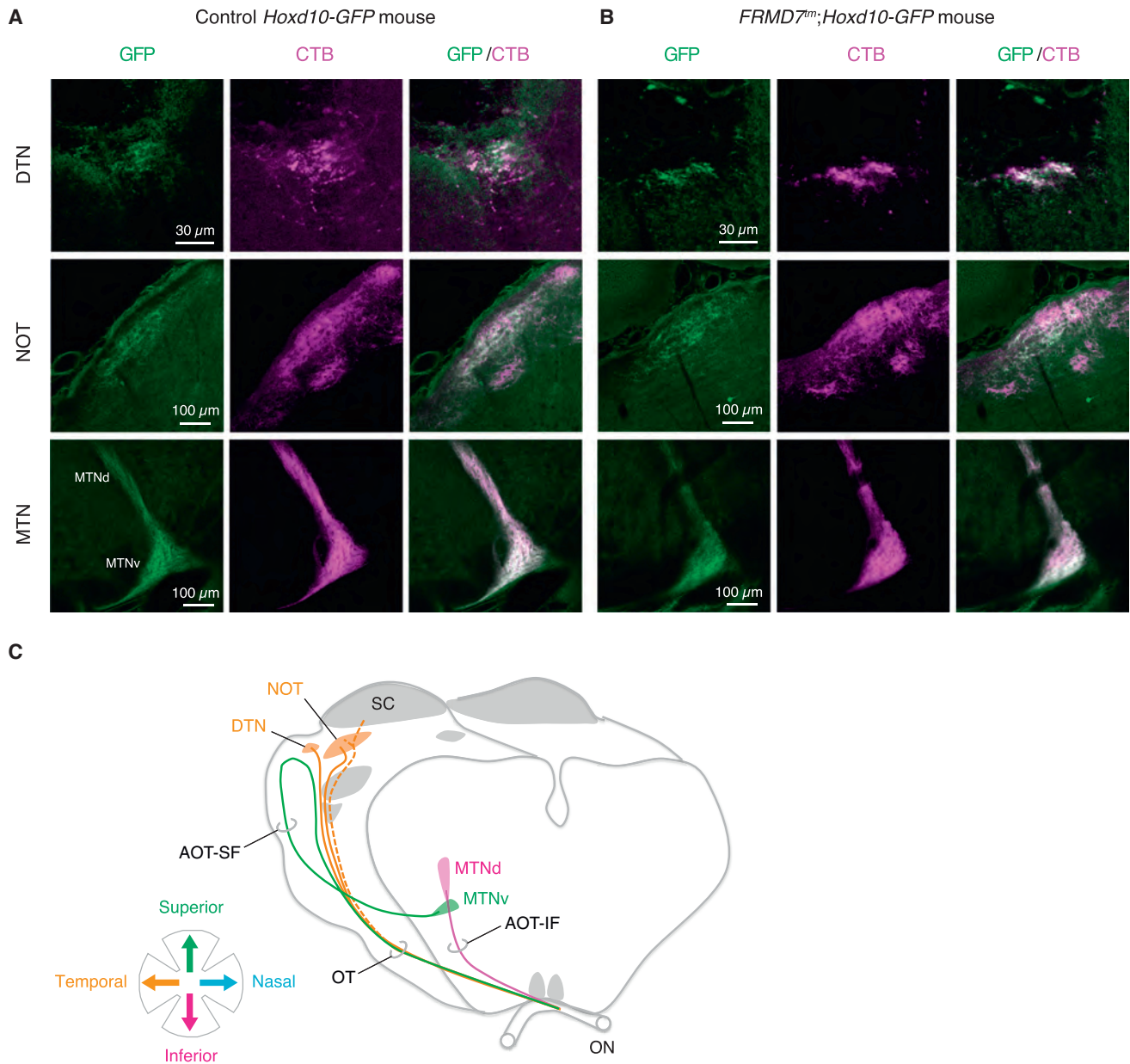


**Figure 6. Hoxd10-GFP-Labeled Retinal Ganglion Cell Axons Innervate Accessory Optic Nuclei in *FRMD7<sup>tm</sup>* Mice**

(A and B) Confocal images show DTN (top), NOT (middle), and MTN (bottom) innervated by GFP-labeled and cholera toxin subunit B-Alexa dye conjugate (CTB)-labeled retinal ganglion cell axons in control *Hoxd10-GFP* (A) and *FRMD7<sup>tm</sup>;Hoxd10-GFP* mice (B).

(C) Schematic of central targets of *Hox10-GFP*-labeled retinal ganglion cell axons. Axons and targets are color coded according to their directional tuning. AOT-IF, inferior fasciculus of the accessory optic tract; AOT-SF, superior fasciculus of the accessory optic tract; MTNd, dorsal division of the MTN; MTNv, ventral division of the MTN; SC, superior colliculus; ON, optic nerve; OT, optic tract. Schematic adapted from Pak et al. (1987) and Dhande et al. (2013). See also Figure S7.

eye opening (Wei et al., 2011; Yonehara et al., 2011). Our findings suggest that, in *FRMD7<sup>tm</sup>* mice, this symmetric-to-asymmetric transition is defective along the horizontal axis (Figure 8D).

How could *FRMD7* contribute to the establishment of the selective connectivity between nasally or temporally pointing starburst cell processes and temporal or nasal motion-preferring DS cells? To enable the correct matching of starburst cell pro-

cess and DS cell type, it is likely that nasally and temporally pointing starburst cell processes are labeled by distinct molecules or combinations of molecules. This would require a sorting machinery in the soma that knows about the horizontal directions and sends different molecules to nasally and temporally pointing processes. Since it is widely documented that the retina has a number of molecules forming nasal-temporal gradients, such as

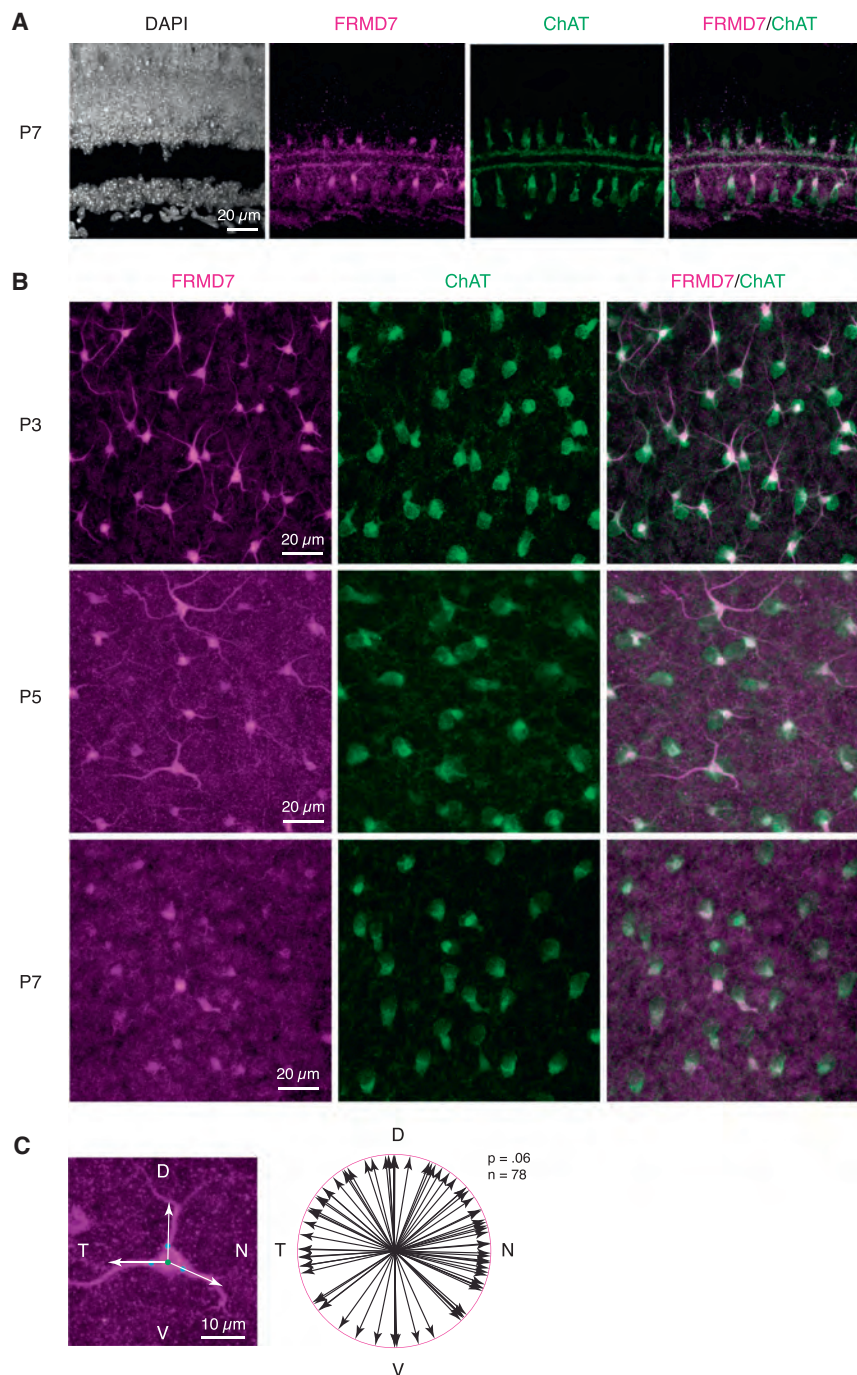


**Figure 7. FRMD7 Is Symmetrically Localized within Starburst Amacrine Cell Processes**

(A and B) Confocal images show WT retinas stained with antibody for ChAT (green) and FRMD7 (magenta) at different developmental time points (P3, P5, and P7) in side view (A) and top view of z stack of labeled cells in GCL (B). (C) Quantification of the subcellular distribution of FRMD7 within starburst cells. (Left) The direction of FRMD7-labeled processes was defined by the angle of the vector, which points from the cell body center (green dot) to the exit point of the primary processes from cell body (cyan dots). (Right) Distribution of the direction of FRMD7-labeled processes is shown.

poral processes. It is more likely that FRMD7 is part of the molecular machinery that is either involved in sensing or sorting along the horizontal axis.

While it is an open question where and how FRMD7 exerts its function in the starburst cell to establish asymmetric connectivity, the organization of the protein and the precise location of the mutations found in individuals with congenital nystagmus provide insights. The *FRMD7* gene encodes a member of the FERM domain family of proteins (Moleirinho et al., 2013). The FERM domain of FRMD7 is located in the N terminus and is thought to link FRMD7 to the cell membrane. Next to the FERM domain is a FERM-adjacent domain, which in other FERM-containing proteins is thought to be subject to phosphorylation. Notably, the mutations causing congenital nystagmus in humans are concentrated in the FERM domain and a region around the FERM-adjacent domain (Thomas et al., 2011). The C-terminal part of FRMD7 has no homology with other proteins. Other FERM domain-containing proteins are involved in the signal transduction between the plasma membrane and the actin cytoskeleton (Moleirinho et al., 2013). Indeed, the FRMD7 protein interacts with the Rho GDP-dissociation inhibitor alpha, the main regulator of Rho

ephrins and BMPs (Sakuta et al., 2006), it is likely that the knowledge of starburst cells about the opposing horizontal directions is learned from these gradients. Along the vertical axis a similar differential sorting mechanism may label superiorly and inferiorly pointing starburst cell processes. The findings that both nasal and temporal direction selectivities are abolished in *FRMD7<sup>tm</sup>* mice (Figures 2 and S4) and that FRMD7 protein was found symmetrically distributed in the processes of starburst cells (Figures 7B and 7C) suggest that FRMD7 is not a marker for nasal or tem-

GDPases, which are key regulators of the reorganization of actin cytoskeleton (Pu et al., 2013). These findings raise the possibility that FRMD7 also signals between the plasma membrane and the cytoskeleton.

#### **Circuit Mechanism Underlying the Lack of the Horizontal Optokinetic Reflex in *FRMD7<sup>tm</sup>* Mice**

We propose that the lack of horizontal direction selectivity in the retina contributes significantly to the lack of the horizontal

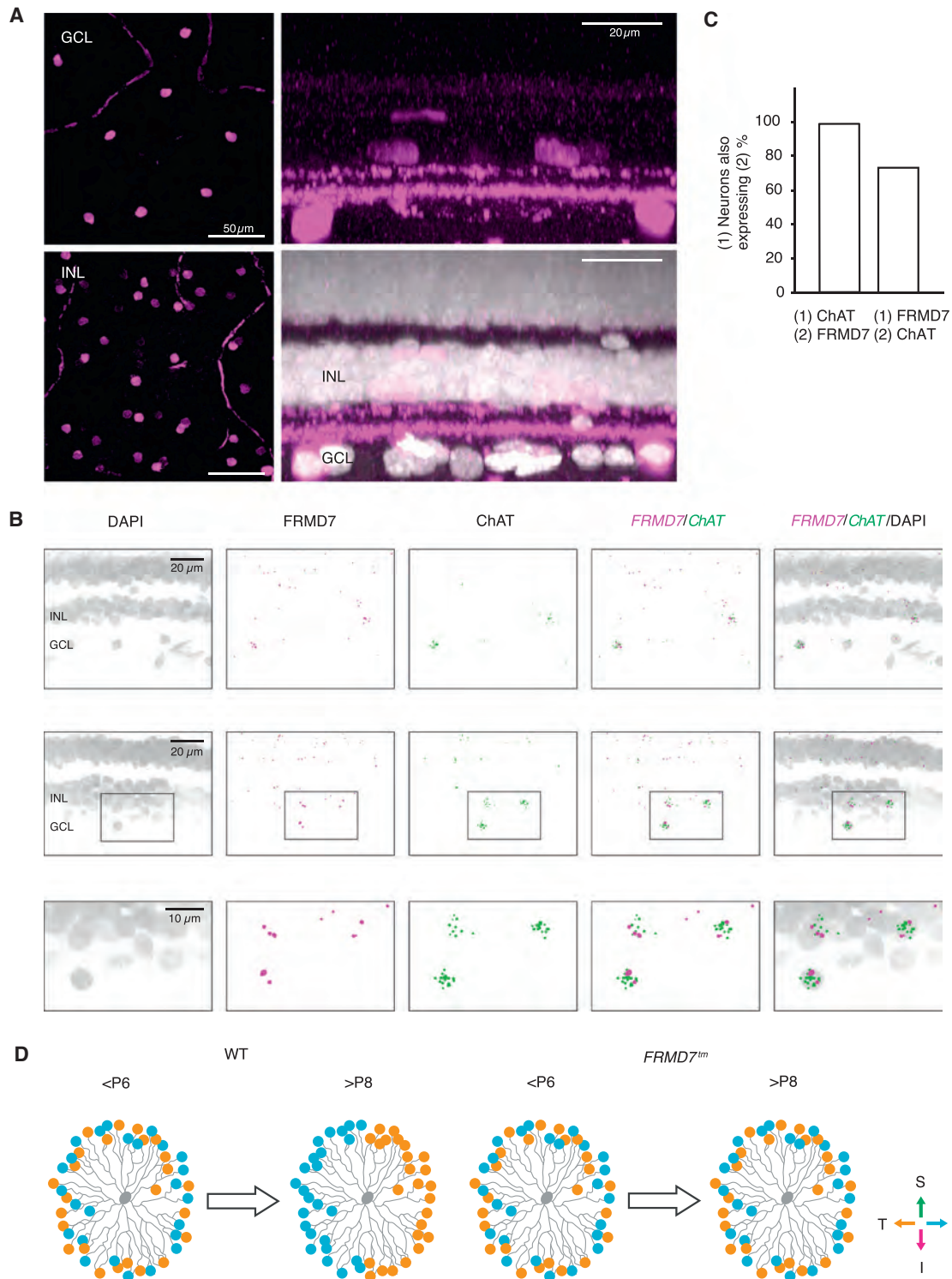


**Figure 8. FRMD7 Is Expressed in ChAT-Labeled Cells in the Retina of Non-human Primates**

(A) Confocal images show whole-mount non-human primate retinas stained with antibody for ChAT (magenta) and DAPI (white) in top view (left) and side view (right).

(B) Confocal images of retinal sections stained by double-label fluorescence in situ hybridization using antisense probes for *FRMD7* mRNA and *ChAT* mRNA as well as DAPI in non-human primate retinas. Two example regions (top and middle) and magnification of inset in middle panels (bottom) are shown.

(C) Relationship between *FRMD7* mRNA-expressing and *ChAT* mRNA-expressing cells is shown.

(legend continued on next page)

optokinetic reflex in *FRMD7<sup>tm</sup>* mice. The following evidence supports this conclusion. First, it has been shown previously that mice whose retinal direction selectivity has been abolished by the genetic ablation of starburst cells lose the optokinetic reflex (Yoshida et al., 2001). In that study, the genetic manipulation was done in the retina alone, without affecting any circuits in the brain. Second, it has been shown in cats that activity in the NOT/DTN complex, which processes horizontal direction-selective input, is required selectively for the horizontal optokinetic reflex (Hoffmann and Fischer, 2001). Third, we found that the defective DS cells in *FRMD7<sup>tm</sup>* mice project to their normal brain targets (Figure 6). Fourth, *FRMD7<sup>tm</sup>* mice were able to produce spontaneous, large-amplitude horizontal eye motions (Figures 1F and 1G). Fifth, *FRMD7<sup>tm</sup>* mice had normal vertical retinal direction selectivity (Figures 2 and 5) and showed a normal vertical optokinetic reflex (Figure 1E). Sixth, the optokinetic reflex was measured in head-fixed mice, limiting possible interactions with the vestibular system. Taken together, these results suggest that the lack of horizontal direction selectivity in the retina is sufficient to abolish the horizontal optokinetic reflex. However, as we detected *FRMD7* mRNA expression in the motor nuclei responsible for eye movements and in the vestibular nuclei (Figure S7A), we cannot rule out contributions to the defective optokinetic response from motor and vestibular nuclei.

### Circuit Mechanism Underlying the Symptoms of *FRMD7*-Based Idiopathic Congenital Nystagmus in Humans

Can *FRMD7* dysfunction in starburst cells be a contributor to, or cause of, the lack of horizontal optokinetic reflex in *FRMD7*-based congenital nystagmus in humans? The following findings support this interpretation. First, the neuronal pathways controlling the optokinetic reflex are highly conserved across mammals. Although on DS cells have not yet been recorded in primate retinas, on direction-selective cells preferring the ipsiversive direction (i.e., left NOT/DTN is activated by the leftward motion and vice versa) have been recorded in primate NOT/DTN brain areas (Distler and Hoffmann, 2011; Hoffmann, 1989), which are the targets of horizontal on DS cells in other animals (Dhande et al., 2013). Second, in adult non-human primate retinas, the same ChAT antibody, which in mice labels two mosaics of starburst cells and two retinal strata in the inner plexiform layer where the processes of starburst cells ramify, also labeled two mosaics of cells in the same nuclear layers and two retina strata in the inner plexiform layer (Rodieck and Marshak, 1992; Figure 8A). Third, *FRMD7* was expressed in those non-human primate retinal cells that were marked by ChAT (Figures 8B and 8C). Fourth, we show that human subjects with congenital nystagmus were able to produce voluntary, smooth-pursuit, horizontal eye movements (Figures 1K and 1L). Fifth, the vertical optokinetic reflex is still present in individuals with congenital nystagmus (Figure 1J). Taken together, this evidence indicates that, in primates, *FRMD7* is expressed in a retinal cell population

that has the morphological and genetic attributes of starburst cells in mice and that the motor system controlling horizontal eye movements in individuals with congenital nystagmus is functional. These findings are consistent with a hypothesis that the loss of the horizontal optokinetic reflex in humans is, at least partly, due to the loss of *FRMD7* function in starburst cells. Note that, in humans, *FRMD7* mRNA expression also has been observed in the brain regions involved in vestibulo-ocular reflex (Tarpey et al., 2006; Thomas et al., 2011). However, since the optokinetic reflex was assessed in head-fixed human subjects, a potential dysfunction in the vestibular system is unlikely to fully explain the loss of the horizontal optokinetic reflex.

In contrast to individuals with *FRMD7*-based nystagmus, we did not observe spontaneous oscillatory eye movements (nystagmus) in *FRMD7<sup>tm</sup>* mice. This lack can be explained in at least two different ways. First, it is possible that the presence of horizontal nystagmus is linked to the lack of the horizontal optokinetic reflex in humans. For example, an inhibitory interaction between the control circuits generating the optokinetic reflex and microsaccades in humans (Otero-Millan et al., 2011) may exist. When the horizontal optokinetic reflex is lost, inhibition decreases and horizontal microsaccades become larger and uncontrolled, appearing as horizontal nystagmus. As wild-type mice are not confirmed to have microsaccades, the absence of this type of eye movement may explain why there is no nystagmus in *FRMD7<sup>tm</sup>* mice. Alternatively, the two symptoms, nystagmus and the lack of the horizontal optokinetic reflex, could be caused by two independent circuit mechanisms. Indeed, the presence of horizontal nystagmus together with a normal optokinetic reflex in achromatopsia shows that the two symptoms can be independent of each other (Yee et al., 1981). It is possible that a defect in the connectivity between starburst cells and DS cells leads to the lack of the horizontal optokinetic reflex, and, independently, either a defect in the retinal fovea (Thomas et al., 2014), which is absent in mouse retinas, or a dysfunction of another brain circuit causes nystagmus.

## EXPERIMENTAL PROCEDURES

### Animal and Human Subjects

The study protocols for animals and humans were approved by the relevant Institutional Review Boards.

Further description of the experimental procedures is provided in the Supplemental Experimental Procedures.

## SUPPLEMENTAL INFORMATION

Supplemental Information includes Supplemental Experimental Procedures, seven figures, and one movie and can be found with this article online at <http://dx.doi.org/10.1016/j.neuron.2015.11.032>.

## AUTHOR CONTRIBUTIONS

K.Y. designed experiments; performed retinal experiments, in vivo injections, and in situ hybridization; grew rabies virus; developed all plasmids; analyzed

(D) Schematic of the development of horizontal asymmetric inhibitory outputs of a starburst cell (gray, center) in WT (left) and *FRMD7<sup>tm</sup>* mice (right) during the postnatal period before eye opening. Output inhibitory synapses are color coded according to the preferred directions (colored arrows) of the postsynaptic DS cell partner. Symmetric inhibitory connectivity established during the first postnatal week is reorganized into asymmetric inhibitory connectivity during the second postnatal week in WT mice (Wei et al., 2011; Yonehara et al., 2011), but not in *FRMD7<sup>tm</sup>* mice.

data; and wrote the paper. M.F. performed microelectrode array recordings, analyzed data, and wrote the paper. A.D. performed patch-clamp recordings, analyzed data, and wrote the paper. F.E. performed human eye movement recordings, analyzed data, and helped write the paper. S.T. performed human and mouse eye movement recordings, analyzed data, and helped write the paper. J.K. performed *FRMD7* mRNA analysis. F.F. developed software for microelectrode array data analysis and analyzed data. B.G.S. performed in situ hybridization and immunohistochemistry. A.K. selected patients and helped with human eye movement recordings. J.M. built the microelectrode array recording system and setup. A.S. helped with histology. J.J. made AAV viruses. F.C. helped with primate tissue collection. A.P.R. made AAV constructs. J.N., Z.Z.N., and F.M. selected and diagnosed patients. A.H. designed and supervised microelectrode array recordings and technology developments. B.R. designed experiments, analyzed data, and wrote the paper.

## ACKNOWLEDGMENTS

We thank Nathalie Stuber, Reto Baumgartner, Tamas Szikra, Zoltan Raics, Monique Lerch, Sabrina Djaffer, and Claudia Patricia Patiño Alvarez for technical support and Sara Oakeley for commenting on the manuscript. We acknowledge the following grants: Boehringer Ingelheim Fonds PhD fellowship to A.D.; Japan Society for the Promotion of Science Postdoctoral Fellowship for Research Abroad, Lundbeck Foundation, and European Research Council Starting Grant “CIRCUITASSEMBLY” to K.Y.; Human Frontier Science Program Postdoctoral Fellowship LT000173/2013 to S.T.; Gebert-Rüf Foundation, Swiss National Science Foundation, European Research Council, National Centres of Competence in Research Molecular Systems Engineering, Swiss National Science Foundation Sinergia, Swiss-Hungarian, and European Union 3X3D Imaging grants to B.R. The ETH Zurich group, M.F., F.F., J. M., and A.H. acknowledge funding through the European Research Council Advanced Grant “NeuroCMOS,” contract AdG 267351, and the Swiss National Science Foundation Sinergia Project CRSII3\_141801.

Received: July 6, 2015

Revised: August 14, 2015

Accepted: November 18, 2015

Published: December 17, 2015

## REFERENCES

- Borst, A., and Euler, T. (2011). Seeing things in motion: models, circuits, and mechanisms. *Neuron* 71, 974–994.
- Borst, A., and Helmstaedter, M. (2015). Common circuit design in fly and mammalian motion vision. *Nat. Neurosci.* 18, 1067–1076.
- Briggman, K.L., Helmstaedter, M., and Denk, W. (2011). Wiring specificity in the direction-selectivity circuit of the retina. *Nature* 471, 183–188.
- Bryan, A.S., and Angelaki, D.E. (2009). Optokinetic and vestibular responsiveness in the macaque rostral vestibular and fastigial nuclei. *J. Neurophysiol.* 101, 714–720.
- Dhande, O.S., Estevez, M.E., Quattrochi, L.E., El-Danaf, R.N., Nguyen, P.L., Berson, D.M., and Huberman, A.D. (2013). Genetic dissection of retinal inputs to brainstem nuclei controlling image stabilization. *J. Neurosci.* 33, 17797–17813.
- Distler, C., and Hoffmann, K.-P. (2011). Visual pathway for the optokinetic reflex in infant macaque monkeys. *J. Neurosci.* 31, 17659–17668.
- Duan, X., Krishnaswamy, A., De la Huerta, I., and Sanes, J.R. (2014). Type II cadherins guide assembly of a direction-selective retinal circuit. *Cell* 158, 793–807.
- Elstrott, J., Anishchenko, A., Greschner, M., Sher, A., Litke, A.M., Chichilnisky, E.J., and Feller, M.B. (2008). Direction selectivity in the retina is established independent of visual experience and cholinergic retinal waves. *Neuron* 58, 499–506.
- Euler, T., Detwiler, P.B., and Denk, W. (2002). Directionally selective calcium signals in dendrites of starburst amacrine cells. *Nature* 418, 845–852.
- Famiglietti, E.V. (1991). Synaptic organization of starburst amacrine cells in rabbit retina: analysis of serial thin sections by electron microscopy and graphic reconstruction. *J. Comp. Neurol.* 309, 40–70.
- Faulstich, B.M., Onori, K.A., and du Lac, S. (2004). Comparison of plasticity and development of mouse optokinetic and vestibulo-ocular reflexes suggests differential gain control mechanisms. *Vision Res.* 44, 3419–3427.
- Fried, S.I., Münch, T.A., and Werblin, F.S. (2002). Mechanisms and circuitry underlying directional selectivity in the retina. *Nature* 420, 411–414.
- Gauvain, G., and Murphy, G.J. (2015). Projection-specific characteristics of retinal input to the brain. *J. Neurosci.* 35, 6575–6583.
- Gavrikov, K.E., Dmitriev, A.V., Keyser, K.T., and Mangel, S.C. (2003). Cation-chloride cotransporters mediate neural computation in the retina. *Proc. Natl. Acad. Sci. USA* 100, 16047–16052.
- Giolli, R.A., Blanks, R.H.I., and Lui, F. (2006). The accessory optic system: basic organization with an update on connectivity, neurochemistry, and function. *Prog. Brain Res.* 151, 407–440.
- Gottlob, I., and Proudlock, F.A. (2014). Aetiology of infantile nystagmus. *Curr. Opin. Neurol.* 27, 83–91.
- Hauselt, S.E., Euler, T., Detwiler, P.B., and Denk, W. (2007). A dendrite-autonomous mechanism for direction selectivity in retinal starburst amacrine cells. *PLoS Biol.* 5, e185.
- Hoffmann, K.P. (1989). Control of the optokinetic reflex by the nucleus of the optic tract in primates. *Prog. Brain Res.* 80, 173–182, discussion 171–172.
- Hoffmann, K.P., and Fischer, W.H. (2001). Directional effect of inactivation of the nucleus of the optic tract on optokinetic nystagmus in the cat. *Vision Res.* 41, 3389–3398.
- Ivanova, E., Hwang, G.-S., and Pan, Z.-H. (2010). Characterization of transgenic mouse lines expressing Cre recombinase in the retina. *Neuroscience* 165, 233–243.
- Kay, J.N., De la Huerta, I., Kim, I.-J., Zhang, Y., Yamagata, M., Chu, M.W., Meister, M., and Sanes, J.R. (2011). Retinal ganglion cells with distinct directional preferences differ in molecular identity, structure, and central projections. *J. Neurosci.* 31, 7753–7762.
- Kim, I.-J., Zhang, Y., Yamagata, M., Meister, M., and Sanes, J.R. (2008). Molecular identification of a retinal cell type that responds to upward motion. *Nature* 452, 478–482.
- Kim, J.S., Greene, M.J., Zlateski, A., Lee, K., Richardson, M., Turaga, S.C., Purcaro, M., Balkam, M., Robinson, A., Behabadi, B.F., et al.; EyeWires (2014). Space-time wiring specificity supports direction selectivity in the retina. *Nature* 509, 331–336.
- Lee, S., and Zhou, Z.J. (2006). The synaptic mechanism of direction selectivity in distal processes of starburst amacrine cells. *Neuron* 51, 787–799.
- Lee, S., Kim, K., and Zhou, Z.J. (2010). Role of ACh-GABA cotransmission in detecting image motion and motion direction. *Neuron* 68, 1159–1172.
- Miyamichi, K., Shlomaï-Fuchs, Y., Shu, M., Weissbourd, B.C., Luo, L., and Mizrahi, A. (2013). Dissecting local circuits: parvalbumin interneurons underlie broad feedback control of olfactory bulb output. *Neuron* 80, 1232–1245.
- Moleirinho, S., Tilston-Lunel, A., Angus, L., Gunn-Moore, F., and Reynolds, P.A. (2013). The expanding family of FERM proteins. *Biochem. J.* 452, 183–193.
- Morin, L.P., and Studholme, K.M. (2014). Retinofugal projections in the mouse. *J. Comp. Neurol.* 522, 3733–3753.
- Oesch, N., Euler, T., and Taylor, W.R. (2005). Direction-selective dendritic action potentials in rabbit retina. *Neuron* 47, 739–750.
- Osterhout, J.A., Stafford, B.K., Nguyen, P.L., Yoshihara, Y., and Huberman, A.D. (2015). Contactin-4 mediates axon-target specificity and functional development of the accessory optic system. *Neuron* 86, 985–999.
- Otero-Millan, J., Macknik, S.L., Serra, A., Leigh, R.J., and Martinez-Conde, S. (2011). Triggering mechanisms in microsaccade and saccade generation: a novel proposal. *Ann. N Y Acad. Sci.* 1233, 107–116.

- Oyster, C.W., Takahashi, E., and Collewijn, H. (1972). Direction-selective retinal ganglion cells and control of optokinetic nystagmus in the rabbit. *Vision Res.* *12*, 183–193.
- Pak, M.W., Giolli, R.A., Pinto, L.H., Mangini, N.J., Gregory, K.M., and Venable, J.W., Jr. (1987). Retinopretectal and accessory optic projections of normal mice and the OKN-defective mutant mice beige, beige-J, and pearl. *J. Comp. Neurol.* *258*, 435–446.
- Pei, Z., Chen, Q., Koren, D., Giammarinaro, B., Acaron Ledesma, H., and Wei, W. (2015). Conditional Knock-Out of Vesicular GABA Transporter Gene from Starburst Amacrine Cells Reveals the Contributions of Multiple Synaptic Mechanisms Underlying Direction Selectivity in the Retina. *J. Neurosci.* *35*, 13219–13232.
- Pu, J., Mao, Y., Lei, X., Yan, Y., Lu, X., Tian, J., Yin, X., Zhao, G., and Zhang, B. (2013). FERM domain containing protein 7 interacts with the Rho GDP dissociation inhibitor and specifically activates Rac1 signaling. *PLoS ONE* *8*, e73108.
- Rodieck, R.W., and Marshak, D.W. (1992). Spatial density and distribution of choline acetyltransferase immunoreactive cells in human, macaque, and baboon retinas. *J. Comp. Neurol.* *321*, 46–64.
- Sakuta, H., Takahashi, H., Shintani, T., Etani, K., Aoshima, A., and Noda, M. (2006). Role of bone morphogenetic protein 2 in retinal patterning and retinotectal projection. *J. Neurosci.* *26*, 10868–10878.
- Sanes, J.R., and Masland, R.H. (2015). The types of retinal ganglion cells: current status and implications for neuronal classification. *Annu. Rev. Neurosci.* *38*, 221–246.
- Schweigart, G., Mergner, T., Evdokimidis, I., Morand, S., and Becker, W. (1997). Gaze stabilization by optokinetic reflex (OKR) and vestibulo-ocular reflex (VOR) during active head rotation in man. *Vision Res.* *37*, 1643–1652.
- Siebert, S., Cabuy, E., Scherf, B.G., Kohler, H., Panda, S., Le, Y.-Z., Fehling, H.J., Gaidatzis, D., Stadler, M.B., and Roska, B. (2012). Transcriptional code and disease map for adult retinal cell types. *Nat. Neurosci.* *15*, 487–495.
- Simpson, J.I. (1984). The accessory optic system. *Annu. Rev. Neurosci.* *7*, 13–41.
- Sivyer, B., and Williams, S.R. (2013). Direction selectivity is computed by active dendritic integration in retinal ganglion cells. *Nat. Neurosci.* *16*, 1848–1856.
- Soodak, R.E., and Simpson, J.I. (1988). The accessory optic system of rabbit. I. Basic visual response properties. *J. Neurophysiol.* *60*, 2037–2054.
- Stacy, R.C., and Wong, R.O.L. (2003). Developmental relationship between cholinergic amacrine cell processes and ganglion cell dendrites of the mouse retina. *J. Comp. Neurol.* *456*, 154–166.
- Sun, L.O., Jiang, Z., Rivlin-Etzion, M., Hand, R., Brady, C.M., Matsuoka, R.L., Yau, K.-W., Feller, M.B., and Kolodkin, A.L. (2013). On and off retinal circuit assembly by divergent molecular mechanisms. *Science* *342*, 1241974.
- Sun, L.O., Brady, C.M., Cahill, H., Al-Khindi, T., Sakuta, H., Dhande, O.S., Noda, M., Huberman, A.D., Nathans, J., and Kolodkin, A.L. (2015). Functional assembly of accessory optic system circuitry critical for compensatory eye movements. *Neuron* *86*, 971–984.
- Tarpey, P., Thomas, S., Sarvananthan, N., Mallya, U., Lisgo, S., Talbot, C.J., Roberts, E.O., Awan, M., Surendran, M., McLean, R.J., et al. (2006). Mutations in FRMD7, a newly identified member of the FERM family, cause X-linked idiopathic congenital nystagmus. *Nat. Genet.* *38*, 1242–1244.
- Thomas, S., Proudlock, F.A., Sarvananthan, N., Roberts, E.O., Awan, M., McLean, R., Surendran, M., Kumar, A.S.A., Farooq, S.J., Degg, C., et al. (2008). Phenotypical characteristics of idiopathic infantile nystagmus with and without mutations in FRMD7. *Brain* *131*, 1259–1267.
- Thomas, M.G., Crosier, M., Lindsay, S., Kumar, A., Thomas, S., Araki, M., Talbot, C.J., McLean, R.J., Surendran, M., Taylor, K., et al. (2011). The clinical and molecular genetic features of idiopathic infantile periodic alternating nystagmus. *Brain* *134*, 892–902.
- Thomas, M.G., Crosier, M., Lindsay, S., Kumar, A., Araki, M., Leroy, B.P., McLean, R.J., Sheth, V., Maconachie, G., Thomas, S., et al. (2014). Abnormal retinal development associated with FRMD7 mutations. *Hum. Mol. Genet.* *23*, 4086–4093.
- Trenholm, S., Johnson, K., Li, X., Smith, R.G., and Awatramani, G.B. (2011). Parallel mechanisms encode direction in the retina. *Neuron* *71*, 683–694.
- Trenholm, S., McLaughlin, A.J., Schwab, D.J., Turner, M.H., Smith, R.G., Rieke, F., and Awatramani, G.B. (2014). Nonlinear dendritic integration of electrical and chemical synaptic inputs drives fine-scale correlations. *Nat. Neurosci.* *17*, 1759–1766.
- van Alphen, A.M., Stahl, J.S., and De Zeeuw, C.I. (2001). The dynamic characteristics of the mouse horizontal vestibulo-ocular and optokinetic response. *Brain Res.* *890*, 296–305.
- Vaney, D.I., Sivyer, B., and Taylor, W.R. (2012). Direction selectivity in the retina: symmetry and asymmetry in structure and function. *Nat. Rev. Neurosci.* *13*, 194–208.
- Wei, W., and Feller, M.B. (2011). Organization and development of direction-selective circuits in the retina. *Trends Neurosci.* *34*, 638–645.
- Wei, W., Hamby, A.M., Zhou, K., and Feller, M.B. (2011). Development of asymmetric inhibition underlying direction selectivity in the retina. *Nature* *469*, 402–406.
- Yee, R.D., Baloh, R.W., and Honrubia, V. (1981). Eye movement abnormalities in rod monochromacy. *Ophthalmology* *88*, 1010–1018.
- Yonehara, K., Ishikane, H., Sakuta, H., Shintani, T., Nakamura-Yonehara, K., Kamiji, N.L., Usui, S., and Noda, M. (2009). Identification of retinal ganglion cells and their projections involved in central transmission of information about upward and downward image motion. *PLoS ONE* *4*, e4320.
- Yonehara, K., Balint, K., Noda, M., Nagel, G., Bamberg, E., and Roska, B. (2011). Spatially asymmetric reorganization of inhibition establishes a motion-sensitive circuit. *Nature* *469*, 407–410.
- Yonehara, K., Farrow, K., Ghanem, A., Hillier, D., Balint, K., Teixeira, M., Jüttner, J., Noda, M., Neve, R.L., Conzelmann, K.-K., and Roska, B. (2013). The first stage of cardinal direction selectivity is localized to the dendrites of retinal ganglion cells. *Neuron* *79*, 1078–1085.
- Yoshida, K., Watanabe, D., Ishikane, H., Tachibana, M., Pastan, I., and Nakanishi, S. (2001). A key role of starburst amacrine cells in originating retinal directional selectivity and optokinetic eye movement. *Neuron* *30*, 771–780.

# Go figure

With author-narrated animations



Introducing Figure360, an author-narrated animation of select figures in Cell Press primary research and review journals.

A short, digestible synopsis puts the figure in context and helps you zoom in on the most important take-home message in a matter of minutes. Why go it alone when the author can help you figure it out in less than half the time?

**Check it out at [www.cell.com/figure360](http://www.cell.com/figure360)**

**Figure360**

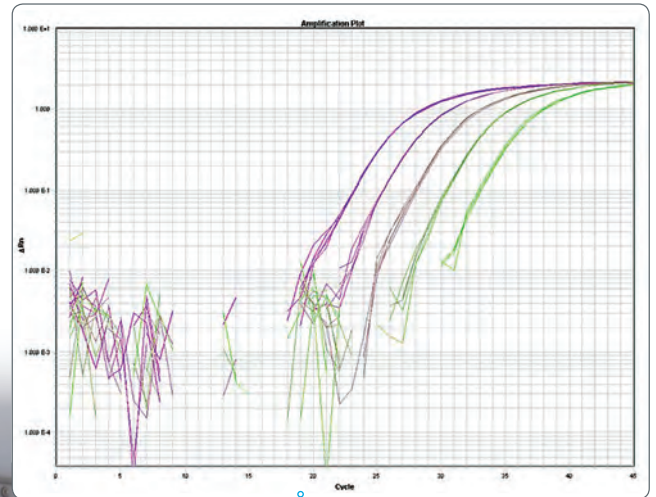
**CellPress**



# PipetmaX<sup>®</sup> + qPCR Assistant

Now everyone in your lab can automate qPCR protocols

- ▶ Easy to set up, no programming required
- ▶ Create flexible, single and multiplex qPCR methods
- ▶ Eliminate data entry errors with sample import and export
- ▶ Save time by combining multiple methods into one run



▶ Standard Amplification Curves for COX gene. Standard cDNA samples were serially diluted 5-fold and amplified in 5 replicates (dilutions left to right: 5x, 25x, 125x, 625x and 3125x).



 **GILSON<sup>®</sup>**

instruments • accessories • software • solutions ▶ Meet PipetmaX and your new qPCR Assistant at [www.gilson.com](http://www.gilson.com)  
Visit [www.gilson.com](http://www.gilson.com) to download Speaking Volumes, our interactive publication for your tablet!

# THE BENCHMARK IN ANTIBODIES

Since the day it was founded, Proteintech has been making all of its products to the highest standards possible while taking complete responsibility for the quality of each product.

- **Proteintech makes every single antibody in its 12,000-strong catalog.**
- **Each Proteintech product is unique and cannot be bought under a different label.**
- **Antibodies tested in siRNA knockdown experiment to demonstrate specificity.**
- **It works in any species and any application or get a full money-back refund.**